

PART I

INTERPRETATION OF PROJECT MAGNET DATA (1959 to 1966)

FOR AFRICA AND THE MOZAMBIQUE CHANNEL

PART II

SEISMIC RAY TRACING WITH APPLICATIONS TO AFRICA

ALAN G. GREEN, B.Sc.

A thesis submitted for the degree of Doctor of Philosophy
in the University of Newcastle upon Tyne.

1973

BEST COPY

AVAILABLE

Poor text in the original
thesis.

Some text bound close to
the spine.

Some images distorted

A B S T R A C T

PART I INTERPRETATION OF PROJECT MAGNET DATA (1959 to 1966) FOR AFRICA AND THE MOZAMBIQUE CHANNEL

This part of the thesis is concerned with the interpretation of Project MAGNET profiles over the African continent and Mozambique Channel. The paths of the continental profiles lie between latitudes 5°N. and 22°S. , while the paths of the profiles which cross the Mozambique Channel lie between latitudes 0° and 35°S. (figure (1)).

The geology and geochronology of 'equatorial' Africa are described briefly in chapter (1). In chapter (2) a new method of magnetic profile analysis is introduced and applied to a number of simulated profiles. This method forms the basis of the interpretation of the continental Project MAGNET profiles (chapter (4)). In chapter (3) the various details of the reduction of the Project MAGNET data (e.g. the interpolation of the data, removal of the regional magnetic field, removal of the diurnal magnetic field) are described. The continental Project MAGNET data are interpreted in chapter (4) while the 'oceanic' data are interpreted in chapter (5).

PART II SEISMIC RAY TRACING WITH APPLICATIONS TO AFRICA

Until recently most seismological data have been explained in terms of spherically symmetric Earth models. Improved recording techniques (e.g. seismic arrays) and the increased number of recording stations have resulted in the discovery of large lateral variations of the seismic velocity in the crust and mantle which are closely correlated with major tectonic features (e.g. ocean ridges and trenches).

It has therefore become increasingly necessary to consider laterally heterogeneous Earth models when inverting seismological data. This part of the thesis is concerned with the development and application of some computer programs to trace seismic rays through laterally heterogeneous velocity media.

In the first chapter the basic principles of seismic wave theory and the ray approximation are outlined. This will include:

- (i) A derivation of the ray path equations for a seismic ray travelling through structures in which the velocity is a function of three dimensions and two dimensions respectively. The velocity structures may be continuously varying and/or defined in discrete units bounded by velocity discontinuities.
- (ii) A derivation of the equations describing the geometrical spreading effect in velocity structures which are a function of two coordinates. The equations which represent the energy partitioning of a seismic ray at a finite velocity boundary (Zoeppritz's equations) are stated.
- (iii) The method of interpolation of the velocity data and the integration procedure.
- (iv) A brief description of the computer programs.

In chapter (2) the two dimensional computer program (i.e. the computer program which traces seismic rays through velocity structures which are a function of two dimensions) is applied to some 'standard' Earth models and in the final chapter this program is used (a) to derive a spherically symmetric velocity depth model from body wave data, which represents the average velocity beneath east and southern Africa, and (b) to test some models of the East African Rift obtained from interpretations of gravity data.

A C K N O W L E D G E M E N T S

I would like to thank Professor S.K. Runcorn, F.R.S. for the opportunity of working in his Department, and the Natural Environment Research Council for financial support.

I thank Dr. R.W. Girdler for supervising this work.

I am most grateful to Dr. D.H. Tarling and Dr. F.J. Lowes for advice and encouragement with Part I of this thesis and to A. Douglas, P.D. Marshall and Dr. H.I.S. Thirlaway for suggesting the ray tracing project.

I am also most grateful to Mrs. Marie Davison for typing this thesis.

I express my sincere gratitude to my wife, Janet, to whom I dedicate this thesis for her patience and encouragement.

C O N T E N T S

PART I INTERPRETATION OF PROJECT MAGNET DATA (1959 - 1966) FOR AFRICA AND THE MOZAMBIQUE CHANNEL

Page No.

CHAPTER 1. GEOLOGY AND GEOCHRONOLOGY OF 'EQUATORIAL' AFRICA.

1.1	Introduction	1
1.2	Precambrian A (600 to 1000 My.)	4
1.3	Precambrian B (1000 to 1600 My.)	14
1.4	Precambrian C (1600 to 2100 My.)	16
1.5	Precambrian D (> 2100 My.)	21
1.6	Palaeozoic and Karroo	25
1.7	Mesozoic	27
1.8	Cenozoic	29

CHAPTER 2. NEW METHOD OF MAGNETIC PROFILE ANALYSIS.

2.1	Introduction	33
2.2	Profile Spectra	33
2.3	Evaluation and Discussion of Terms Related to Profile Spectra	38
2.4	Practical Procedure	41
2.5	Examples	45
2.6	Some Precautions and Limitations	49
2.7	Conclusions	52

CHAPTER 3. PROJECT MAGNET DATA AND ITS REDUCTION.

3.1	Introduction	54
3.2	Instrumentation and Accuracy of Data	54
3.3	Digitisation	55
3.4	Note on Interpolation	56
3.5	Digitising Interval	56
3.6	Removal of the Regional Field	57
3.7	Removal of the Diurnal Effect	58
3.8	Residual Field	59

CHAPTER 4 INTERPRETATION OF PROJECT MAGNET PROFILES ACROSS THE AFRICAN CONTINENT

4.1	Introduction	63
4.2	Notes on the Variables which affect the Shape and Size of a Magnetic Anomaly	64
4.3	Notes on the Method of Average Width and Depth Estimation as Applied to the Project MAGNET Data	65
4.4	Magnetic Profile - Geology Interpretation	67
4.5	Summary and Discussion of the Magnetic Characteristics of African Tectonic Units	101
4.6	Discussion of the Average Depth Estimates	108
4.7	Conclusions	111

CHAPTER 5 PROJECT MAGNET PROFILES AND SEAFLOOR SPREADING

5.1	The Importance of Madagascar in the Gondwanaland Reconstructions	114
5.2	Reconstructions of Madagascar with the African Mainland	115
5.3	New Evidence Bearing on the Relationship Between Madagascar and the African Mainland	117
5.4	Postulated Movement of Madagascar Relative to the African Mainland - A New Reconstruction	122
5.5	Conclusions	126

REFERENCES TO PART I	128
----------------------	-----

APPENDIX A	Algol Computer Program for Interpolation of Distance-Time Data
APPENDIX B	Fortran Computer Programs for Average Width, Depth and Thickness Estimates.
APPENDIX C	List of Geological Maps.

CHAPTER 1. BASIC PRINCIPLES AND COMPUTATIONAL DETAILS

1.1	Basic Principles	144
1.2	Three Dimensional Analysis	145
1.3	Two Dimensional Analysis	158
1.4	Interpolation of the Velocity Data	166
1.5	Integration Procedure	176
1.6	Computer Programs	179
1.7	Summary	181

CHAPTER 2. APPLICATION OF RAY TRACING TO SYMMETRIC EARTH MODELS

2.1	Travel Times and Ray Paths - Integration Step Size	184
2.2	Relative Intensities (geometrical spreading) - Integration Step Size	185
2.3	Relative Intensities (or relative amplitudes) of Rays Traced Through Some Standard Earth Models	186

CHAPTER 3. RAY TRACING APPLIED TO AFRICA

3.1	An Average Velocity-Depth Profile for East/ Southern Africa	198
3.2	Application of RAY Tracing to Models of the East African Rift	203

REFERENCES TO PART II.	236
------------------------	-----

APPENDIX A	Fortran Computer Program to Trace Rays Through Laterally Heterogeneous Velocity Media.
------------	--

P A R T I

C H A P T E R 1.

GEOLOGY AND GEOCHRONOLOGY OF 'EQUATORIAL' AFRICA.

(1.1) Introduction

(1.2) Precambrian A (600 to 1000 My.)

(1.2.1) Type I - Rejuvenated Basement and Highly

Metamorphic Rocks

(1.2.1.1) Mozambique Belt

(1.2.1.2) North Congo Shield

(1.2.2) Type II - Low to High Grade Metasediments

and Metavolcanics

(1.2.2.1) Damaran Belt

(1.2.2.2) West Congolian Belt

(1.2.2.3) Katangan Belt

(1.2.2.4) Bukoban and Malagarasian

(1.2.2.5) Bushimay

(1.2.2.6) Platform Series of North Zaire and Adjacent Regions

(1.3) Precambrian B (1000 to 1600 My.)

(1.3.1) Kibaran Belt

(1.3.2) Irumide Belt

(1.4) Precambrian C (1600 to 2100 My.)

(1.4.1) The Limpopo Belt and Other Precambrian C Formations of the Rhodesian Shield

(1.4.2) Zambia Shield (Tumbide Belt)

(1.4.3) Kasai Shield (Lukoshian, Luizian and Lulua Belt)

(1.4.4) Ubendian and Ruizian Belt

(1.4.5) Kibali-Buganda-Toro Belt

(1.4.6) Other Regions of Precambrian C Age

(1.5) Precambrian D (> 2100 My.)

(1.5.1) Rhodesian Shield

(1.5.2) Tanganyika Shield

(1.5.3) Kasai Shield

(1.5.4) Cameroun Shield

(1.5.5) Regions of Possible Precambrian D Age

(1.6) Palaeozoic and Karroo

(1.6.1) Karroo

(1.7) Mesozoic

(1.8) Cenozoic

(1.8.1) East African Rift System

(1.8.2) Structures Related to the East African
Rift System

GEOLOGY AND GEOCHRONOLOGY OF 'EQUATORIAL' AFRICA

(1.1) Introduction

Throughout 'equatorial' Africa the relative amount of reliable geological information varies considerably and it is unfortunate that the geological maps referenced have frequently relied on extrapolation and interpolation. Even so with the amount of data available it has been possible to divide this part of Africa into a number of geochronological divisions which are then subdivided into units that have characteristic geology, metamorphism and structural trends. This chapter will summarize the general features of these divisions and subdivisions that are described in the literature.

Up to this time, two of the three modern treatises on African geology and geochronology (Clifford (1968), Cahen and Snelling (1966)) have used for the Precambrian, different names for the same major periods of orogeny, and also the same name for both the orogenic episode and a specific part of the orogenic belt. It was therefore decided to follow the terminology of the third treatise (Tectonic Map of Africa) where the Precambrian is split into four divisions A, B, C and D; where Precambrian^D is the oldest. The Phanerozoic era is discussed in its conventional three-fold divisions; Palaeozoic, Mesozoic and Cenozoic with an additional period, the Karroo, included to describe parts of the Late Palaeozoic Early Mesozoic.

In the discussion that follows a superscript will be used to indicate in which geochronological period a particular geologic or tectonic unit falls e.g. Rhodesian Shield^D. The meaning of each superscript is given in table (1). The metamorphic grade, radiometric age and dominant fold or trend direction of each tectonic unit are described in tables (2) to (6).

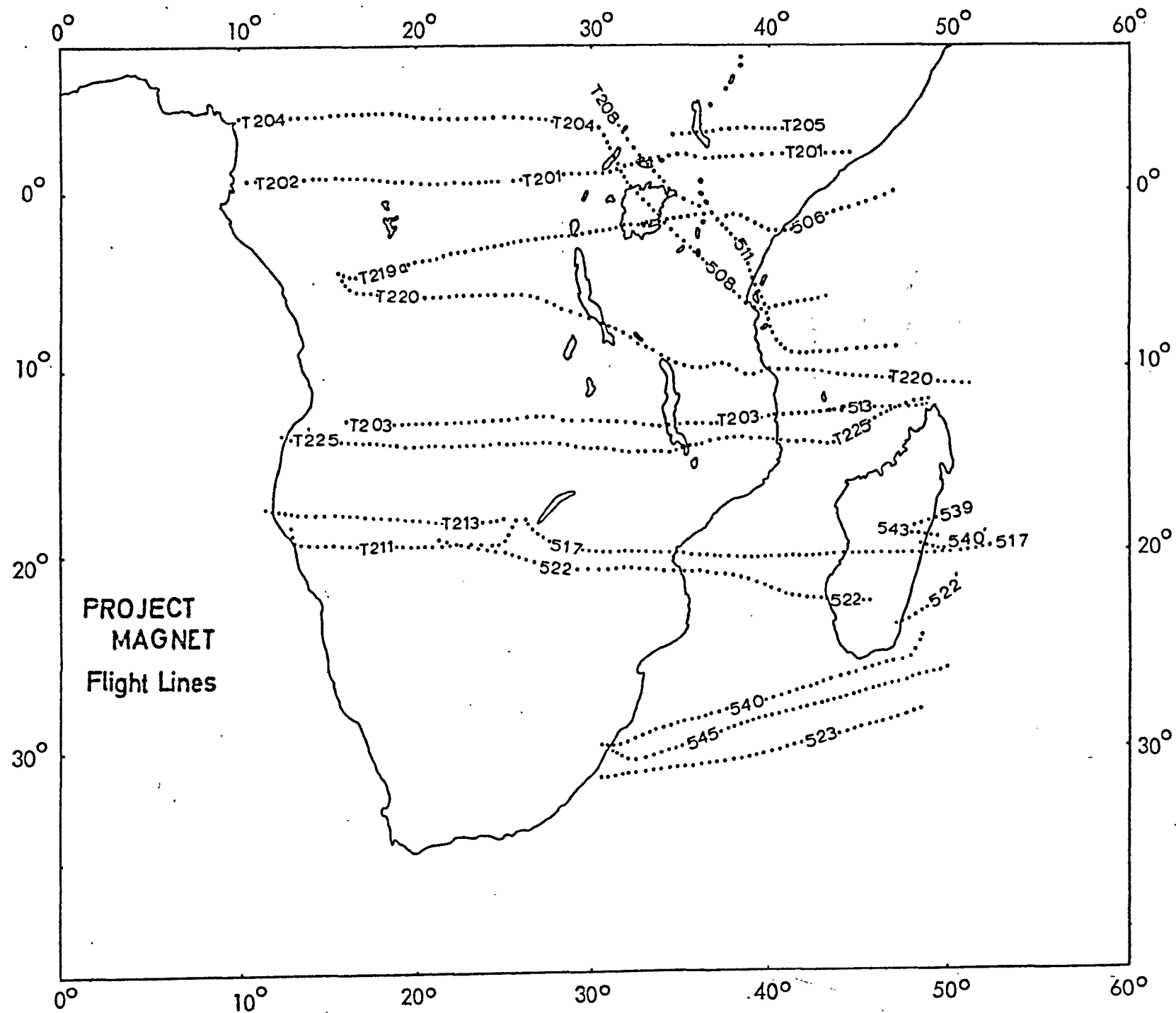


Fig.(1)

Precambrian	A	A
Precambrian	B	B
Precambrian	C	C
Precambrian	D	D
Palaeozoic		P
Mesozoic		M
Cenozoic		Ce
Karoo		K
Unknown age		?

Table (1). Superscripts used to indicate the geochronological period in which each geologic or tectonic unit falls.

(1.2) Precambrian A (600 to 1000 My.)

Vast regions of 'equatorial' Africa were affected by Precambrian A orogenic events (fig. (2) and fig. (5)). Generally the rock formations ascribed to the Precambrian A can be described in terms of two subdivisions. The first subdivision (rocks of this subdivision will be referred to as type I) consists of relic 'basement' rocks (rocks from older shield regions) interspersed with high grade metamorphic rocks whose origin is not yet clearly defined (see fig. (2) and fig. (5)). Most geologists who have recently made detailed studies of specific regions of type I rocks conclude that the high metamorphic grade was a feature of the rocks before the Precambrian A events and that these rocks were simply remobilised in Precambrian A times (Hepworth et. al. (1967), Hepworth and Kennerly (1970), Hepworth (1972), Vail (1966), Sanders (1965)). Rocks of the second subdivision (referred to as type II) include a variety of sedimentary and intercalated volcanic rocks whose deformation ranges from unfolded and unmetamorphosed to highly deformed and metamorphosed (fig. (2)).

It will be convenient to discuss this geochronological division in terms of the two types of rocks mentioned, types I and II. The regions where type II rocks are believed to grade into type I rocks, notably the margins of the Mozambique Orogenic Belt, will be discussed under the type I heading.

(1.2.1) Type I - Rejuvenated Basement and Highly Metamorphic Rocks

Orogenic belts of this type include parts of the Mozambique - Zambezi Belt of east Africa (fig. (2)) and possibly the continuous belt of 'basement' rocks extending from Cameroun through the Central African Republic and North Zaire to the Kenya - Uganda border (fig. (5)).



B-Bukoban Bu-Bushimay Bn-Bunyoro D-Damaran
 F-Francevillian KU-Kenya-Uganda Province L-Lindian
 LB-Liki Bembien M-Malagarasian Mz-Mozambique Province
 O-Oubanguien Ot-Otavi SO-Sembe Ouessou
 TK-Tanzania-Kenya Province W-West Congolian
 Z -Zambezi -Mozambique Province

- Precambrian A (Platform sediments - mostly unmetamorphosed)
- Precambrian A (Platform sediments metamorphosed)
- Precambrian A (Mozambique type)
- x

x

x

x

 Possibly Precambrian A

Fig(2).

TABLE (2)

PRECAMBRIAN A TYPE I

TECTONIC UNIT	SYSTEM OR CYCLE ETC.	METAMORPHIC GRADE	DOMINANT TREND OR FOLD AXIS	AGE RANGE OR APPROX. AGE (MY.)
MOZAMBIQUE BELT	MOZAMBIQUE PROVINCE ZAMBEZI-MOZAMBIQUE PROVINCE TANZANIA-KENYA PROVINCE KENYA-UGANDA PROVINCE	MEDIUM TO HIGH MEDIUM TO HIGH + CATACLASIS MEDIUM TO HIGH + CATACLASIS MEDIUM TO HIGH + CATACLASIS	N. + E. (SHEAR ZONES) + NNW. N. TURNING TO W. AT 17°S	450 to 700 (1100 ?) 450 to 700 (1100 ?) 450 to 700 (1100 ?) 450 to 700 (1100 ?)
UGANDA BASEMENT (WEST NILE COMPLEX)	ARUAN MIRIAN CHUAN	MEDIUM TO HIGH + CATACLASIS MEDIUM TO HIGH + CATACLASIS MEDIUM TO HIGH + CATACLASIS	N. 10° E. + N. 30° E. NE. TO E. NW.	? 650 (?) 650 (?)
NORTH CONGO SHIELD	CONGO OUTCROP CENTRAL AFRICAN REPUBLIC OUTCROP CAMEROUN OUTCROP	HIGH AND LOW MEDIUM TO HIGH MEDIUM TO HIGH	? N. N. TO E.	490 to 650 490 to 650 490 to 650

ALL AGES OBTAINED FROM CAHEN AND SNELLING (1966)

(1.2.1.1) Mozambique Belt

The high grade metamorphic rocks of the Mozambique Belt extend in a north to south direction from central Mozambique to as far north as the Gulf of Aden (Holmes (1951), Holmes and Cahan (1957), Cahan and Snelling (1966)). Several authors have postulated its southern continuation beneath the Karroo and younger formations of southern Mozambique (Cahan and Snelling (1966), Clifford (1968), Cox (1970)). This would then link up with the Precambrian 'regime' of Madagascar which is thought to have been joined to the African mainland at this time (see chapter (5)).

The rocks of this belt are surprisingly consistent from region to region; gneisses, migmatites and quartzites predominate with some intrusive granites. Within this terrain are possible relics or remnants of previous orogenies (Hepworth et al. (1967), Hepworth and Kennerly (1970), Hepworth (1972), Vail (1966), Sanders (1965)). It is therefore possible that some of the gneisses and migmatites were metamorphosed before the Mozambique Orogenesis. This is further substantiated by the local fold trends oblique to the dominantly meridional Mozambique trend (Hepworth (1972)).

The most southern outcrop of rocks affected by the Mozambique Orogeny, the Zambezi - Mozambique Province (see Cahan and Snelling (1966) for definition of Province as used here), emerges from beneath younger cover formations at approximately latitude 21° S (fig. (2)). It trends in a northerly direction until approximately latitude 17° S. where it bends 90° to become the westerly trending Zambezi Branch (or mid-Zambezi Belt) which can be traced as far west as Lake Kariba (Loney (1970), Vail and Snelling (1971)) (fig. (2)). The continuity of the belt around the 90° bend has been demonstrated by geological mapping (Vail (1966), Johnson

and Vail (1965), Johnson (1968)). The margins of the belt adjacent to the Rhodesian Shield^D have been investigated by Vail (1966) and Vail and Snelling (1971). Vail has shown that regions near to the north western margin of the belt (near to the northern outcrop of the Umkondo Sequence^C shown in fig. (4)) consist of rocks of the Rhodesian Shield^D and the overlying Frontier-Gairezi^C meta-sedimentary series which have been progressively metamorphosed up to the sillimanite grade in the east before they grade into the gneisses and migmatites of the Zambezi Branch. The continuity of the isograds around the 90° bend are further evidence of the connection between the northerly and westerly trending branches. Vail and Snelling (1971) have recently shown that the contact between the northern Rhodesian Shield and the Zambezi Branch follows a similar pattern to that observed on the north western margin. Here the rocks of the Rhodesian Shield^D, including the prominent Great Dyke^D, and the overlying Piriwiri-Lomagundi-Deweras^C sedimentary sequence show progressive increases in metamorphic grade and deformation towards the younger fold belt. The Urungwe Klippe, a large body of metamorphic rocks, is thought to have been thrust onto the Rhodesian Shield^D during an episode of the Mozambique Orogeny (Shackleton et al. (1966), Clifford et al. (1967)). It is also shown (Vail and Snelling (1971)) that 'remobilised' basement rocks outcrop throughout the marginal zones of the Zambezi-Mozambique Province. Northwest of Lake Kariba Precambrian A rocks again outcrop, but these are mostly classified under type II rocks.

North of the Zambezi Valley sediments, the Mozambique Province affects rocks in Zambia, Malawi and Mozambique (fig. (2)). To the north west, this province is bounded by the Irumide Belt^B, parts of which have been rejuvenated in the Mozambique Orogeny. The rocks

exposed here are typical of the Mozambique Belt except that in Malawi and Zambia there are some small syntectonic and post-tectonic granite and syenite complexes (Bloomfield and Hapgood (1966), Bloomfield (1961, 1970), Phillips (1961), Bishop and Van Eeden (1971)). The lower grade metasedimentary sequence recognised in north eastern Mozambique (Oberholzer (1964)) may be correlated with the upper sequence of the two tier system described later for other provinces of the Mozambique Belt. Other parts of Mozambique are little studied but most recent studies place much of this country within the Mozambique Belt.

Further north again the belt reappears as the Tanzania-Kenya Province (fig. (2)). This province abuts against the Tanganyika Shield^D on the west and is surrounded by younger sedimentary and volcanic series on all other sides. Hepworth has recently conducted a geologic-aerophotographic survey of the margin between the Tanganyika Shield^D and the Mozambique Belt (Hepworth et. al. (1967), Hepworth and Kennerly (1970), Hepworth (1972)). The conclusions arrived at are essentially the same as those of Vail (1966) and Vail and Snelling (1971) for the Zambezi-Mozambique Province. A gradation from unrejuvenated granitoid shield to the high grade gneisses of the fold belt is traced. It is claimed that the high metamorphic grade of the gneisses was in most cases a pre-Mozambique feature and that the younger ages result from a rejuvenation of the rocks of the shield.

In the mountain masses of Tanzania (Pares, Usambra, Uluguru, Kibariani, Usugar) Harpum (in Pallister (1971)) has recognised two groups of rocks which were affected by the Mozambique Orogeny. The first is a sequence of acid gneisses to granulites (including a charnokite sequence) and the second is an overlying series of quartzites, marbles, schists, meta-dolerites and metacalcareous rocks. Although migmatization is common throughout Tanzania very few granites are observed.

In Kenya, east of the Kavirondo Gulf, Baker (in Pallister (1971)) has split the rocks of the Mozambique Belt into three distinct series. The first is the Loita Series of south west Kenya which consists of a sequence of quartzites and shelf facies sediments of low metamorphic grade. This has been correlated with the Bukoban Series^A (Section (1.2.2)). The next group is the Turoka Series of marbles, quartzites schists, gneisses and migmatites. This group extends along the eastern margin of the belt into Tanzania where it forms a considerable part of the Masai Steppe. The last and by far the most abundant group is the Ukamba group of migmatites, gneisses and basic rocks which outcrop in central and south eastern Kenya. The Turoka and Ukamba groups appear to be correlated to the upper and lower groups already discussed for Tanzania. As with Tanzania it is emphasized that although widespread alkali-metasomatism produces abundant migmatites, granite batholiths are rarely found.

The next outcrop of Mozambique type rocks occur north west of the Tertiary and Quaternary volcanics of the East African Rift System as the Kenya-Uganda Province (fig. (2)). On the Kenya side of the border Sanders describes a gradation in metamorphism for this region where the Mozambique rocks abut against the Tanganyika Shield^D. This description is very similar to that already described for other provinces of the Mozambique Belt. Unaltered relic masses, a two tier sequence of metamorphism, and fold trends oblique to the dominant meridional trend are all features of this region (Sanders (1965)). Although rocks of the Mozambique Belt extend to the Gulf of Aden (Cahen and Snelling (1966)) this study is restricted to below latitude 5° N; we are therefore interested in the possible continuation of the Mozambique Orogenesis west into Uganda.

In Karamoja, north east Uganda, Macdonald (Macdonald (1961), Hepworth and Macdonald (1966)) has shown that the rocks of the Karasuk Group and the Flaggy Moroto Granulites may belong to the Mozambique Belt. Further west in central Uganda the 'basement' gneisses' are still largely undifferentiated (geological map of Uganda (1966)). Although in places these basement rocks appear to underlie the Buganda-Toro^C Belt, the few age determinations available give Precambrian A ages (Cahen and Snelling (1966)). In the West Nile district of north west Uganda detailed geological mapping has resulted in a four fold division of basement rocks; the Watian, the Aruan, the Mirian, and the Chuan. These are collectively called the 'West Nile Complex' (table (2), Hepworth and Macdonald (1966)). The Watian Series belongs to the Precambrian D. The Aruan Sequence overlies the Watian Series but has not been radiometrically dated. Stratigraphically the next sequence of rocks includes (i) the Mirian Group of medium to high grade rocks and (ii) the Chuan Group which includes the Aswa mylonite zone and the Madi Belt. Both groups show evidence of multiphase deformation. As with the two northern provinces of the Mozambique Belt, the Uganda basement lacks large granite intrusions. Hepworth and Macdonald (1966) confidently correlate the Mirian and Chuan rocks with the Mozambique rocks of the Karamoja district and this is substantiated by the relatively large number of Precambrian A radiometric ages obtained from Uganda.

(1.2.1.2) North Congo Shield

Although the geology of the North Congo Shield (fig. (5)) is still largely unknown, parts of the West Nile Complex have been traced across the Uganda-Zaire border and it is claimed that the Kibalian^C rocks lie unconformably above this complex. Exactly which units of the West

Nile Complex are present is uncertain. Very few radiometric dates have been published for the north Zaire region, but those that are available indicate Precambrian A events (Cahen and Snelling (1966), Clifford (1968)). In contrast many dates are available from the rocks of the Central African Republic where Precambrian A ages have again been obtained (Roubault et. al. (1965)). As with the Mozambique Belt two sequences of rocks are recognised. The first is a 'basement' of gneisses, migmatites, quartzites and granites, part of which is continuous with the Watian^D and the Bomu^D complexes. Overlying this 'basement' is the second sequence of metasediments which are correlated with the type II rocks of the Lindian^A (see section (1.2.2.6)).

A similar pattern of Precambrian A ages is found further west in Cameroun (Lasserre (1965), Cahen and Snelling (1966)). These occur north of the Cameroun Shield^D (fig. (5)) and consist of metasediments, granulites, migmatites and granites with gabbro and dunite intrusions. Unlike the Mozambique Belt to the east, the Central African Republic and Cameroun areas contain many large granite masses. These have been the source material for the large number of radiometric age determinations.

It seems likely from both the radiometric age data and the continuity of rock types that this vast east-west trending region (North Congo Shield in fig. (5)) has been affected by Precambrian A orogenesis. Further geological and geochronological data is required to substantiate a time connection with the Mozambique Orogeny.

(1.2.2) Type II Low to High Grade Metasediments and Metavolcanics

Various sedimentary-volcanic series which were deposited in the Precambrian A period are recognised in Equatorial Africa (fig. (2)). These rocks range from completely unaltered sediments and volcanics to

TABLE (3) PRECAMBRIAN A TYPE II

TECTONIC UNIT	SYSTEM OR CYCLE ETC.	METAMORPHIC GRADE	DOMINANT TREND OR FOLD AXIS	APPROX. AGE OR AGE RANGE (MY)
KATANGAN BELT	KATANGAN BUSHIMAY	ZERO TO MEDIUM ZERO	ARCuate + NNW + NNE FOLDS NW. + NE.	485 to 840 940 $\frac{2}{2}$
BUKOBAN	BUKOBAN ABERCORN SANDSTONE	ZERO TO VERY LOW ZERO	NW.+ NE. NONE	630 to 1000 940 $\frac{3}{2}$
WEST CONGOLIAN BELT	WEST CONGOLIAN	ZERO TO LOW (GREENSCHIST)	NNW.	450 to 740 $\frac{1}{4}$
DAMARAN BELT	OTAVI DAMARAN	ZERO LOW TO HIGH	E. E. TO NE.	450 to 570 $\frac{4}{4}$ 450 to 570 $\frac{4}{4}$
	LINDIAN + OUBANGUIEN	ZERO	NW.	755 $\frac{1}{-}$
	SANSIKWA	ZERO TO LOW	NNE. + NNW.	450 to 740 $\frac{1}{-}$

1 - Cahen and Snelling (1966) 2 - Cahen (1970) 3 - Brock and Piper (1972) 4 - Clifford (1968) 5 - Vail et. al. (1968)

metamorphosed schists and gneisses. Type II rocks form the following large formations:- (i) the Katangan of Katanga, Zambia and north western Rhodesia, (ii) the Damaran of South West Africa and southern Angola, (iii) the West Congolian of northern Angola, Gabon, Congo (Brazzaville) and Zaire, (iv) Bukoban and Malagarasian of Tanzania and east Zaire respectively, (v) Lindian, Bushimay, Oubanguien, Liki-Bembian, Sembe-Ouessou and Francevillien of Gabon, Congo, Zaire, Cameroun, and Central African Republic (fig. (2)).

(1.2.2.1) Damaran Belt

This belt is bounded by the Atlantic Ocean to the west and by younger cover formations on all other sides. Clifford (Clifford et. al. (1962), Clifford (1967)) has postulated its continuation beneath the Kalahari sediments to link with the Katangan Belt. There are two distinct grades of metamorphism recognised in this belt and this has resulted in a subdivision into the Otavi and Damaran units (see table (3)). Further north in central Angola, Cahen and Snelling (1966) report Precambrian A ages from basement rocks near to the coast (not shown on fig. (2) as this outcrop is not well defined) and it was concluded that these ages indicate a connection between the Damaran and West Congolian Orogenic Belts.

(1.2.2.2) West Congolian Belt

The rocks of this belt extend from north Angola through to central Gabon (Cahen and Lepersonne (1967)). The West Congolian Belt proper is bounded by rocks of the Mayumbian^C and Zadinian^D formations on the west and south, the Cameroun Shield^D to the north and by the Congo Basin sediments and the Kasai Shield^D on the east. The West Congolian event has also rejuvenated parts of the marginal shield regions.

(1.2.2.3) Katangan Belt

The Katangan Belt outcrops in the central region of 'equatorial' Africa (Cahen (1954), Cahen and Snelling (1966), Cahen and Lepersonne (1967)) (fig. (2) and table (3)). It is bound to the north by the Kibaran Belt^B, the Zambian Shield^D and the Irumide Belt^B; to the west by the Kalahari^{Ce} sediments of Angola and to the south by the Rhodesian Shield^D. The eastern boundary is not well defined, but the Katangan Belt probably merges with the Zambezi-Mozambique Province of type I rocks (Vail and Snelling (1971)). This suggestion is supported by the discovery of Katangan type sediments east of Lake Kariba within the Mozambique Belt (Loney in the 10th Annual Report of the Research Institute of African Geology, University of Leeds). More detailed geological and geochronological research is required to prove the continuity the Katangan and Zambezi-Mozambique Belts.

The stratigraphy of the Katangan Belt is well known (Cahen and Lepersonne (1967)) and includes sediments and low grade metasediments with some intercalated dolerite lavas. Basic rocks and granite intrusions of several ages also intrude parts of the Katangan. The grade of metamorphism increases from north to south. In the latter area the rocks attain grades of greenschists.

(1.2.2.4) Bukoban and Malagarasian

Bukoban rocks rest on a variety of older systems extending from the Uganda-Tanzania border to as far south as latitude 7°S. Near the Tanzania-Zambia border, the Abercorn series of sandstones and siliceous shales (Page (1961)) has recently been dated at 940 my. (Vail et. al. (1968)). This indicates a possible correlation with the main Bukoban rocks (Piper (1972), Brock and Piper (1972)). The

stratigraphy of the latter series is similar to that described for the Katangan Belt (Cahen and Lepersonne (1967)). Bukoban type rocks extend into Burundi as the Malagarasian (see fig. (2)).

An extensive dyke swarm is known to intrude the Bukoban System (Harpum (1954)). In various other parts of Tanzania and northern Malawi, northern Zambia, and east Zaire similar dyke swarms have been observed (Vail (1970)), and although few have been radiometrically dated Vail postulates an age correlation between them.

(1.2.2.5) Bushimay

The Bushimay Series outcrops to the north of the Katangan Belt and is bound by the Kasai Shield^D on the south west, the Kibaran Belt^B on the south east and younger cover formations on all other sides (Cahen and Lepersonne (1967) and fig. (2)). This metasedimentary series is considered to be a molasse sequence related to the Kibaran Orogeny. Cahen and Lepersonne (1967) and Cahen (1970) correlate the Bushimay Series with the lower part of the Katangan.

(1.2.2.6) Platform Series of North Zaire and Adjacent Regions

North of the Bushimay a large number of extensive Precambrian A platform sediments outcrop (fig. (2)). On the east the Lindian and Oubanguin (Ubanguin) rocks extend in patches from latitudes 4°S to 4°N and from the region near to the Lake Albert Rift (Bunyoro tillites) in the east to the Ubangi river in the west. Lindian rocks have also been found beneath the Congo Basin sediments (Cahen and Lepersonne (1967)).

To the west of these series a large number of formations collectively termed the Sansikwa (Cahen and Lepersonne (1967)) are found to outcrop almost to the west coast. The Sansikwa which here

includes the Liki-Bembian, the Francevillian, the Sembe Ouesso and the Sansikwa formations consists of various sediments, glacial beds and intercalated lavas. These have subsequently been intruded by dolerites, gabbros and quartz veins. The Sansikwa is considered to be equivalent to the lower members of the West Congolian, although it was probably deposited during the Kibaran Orogeny^B.

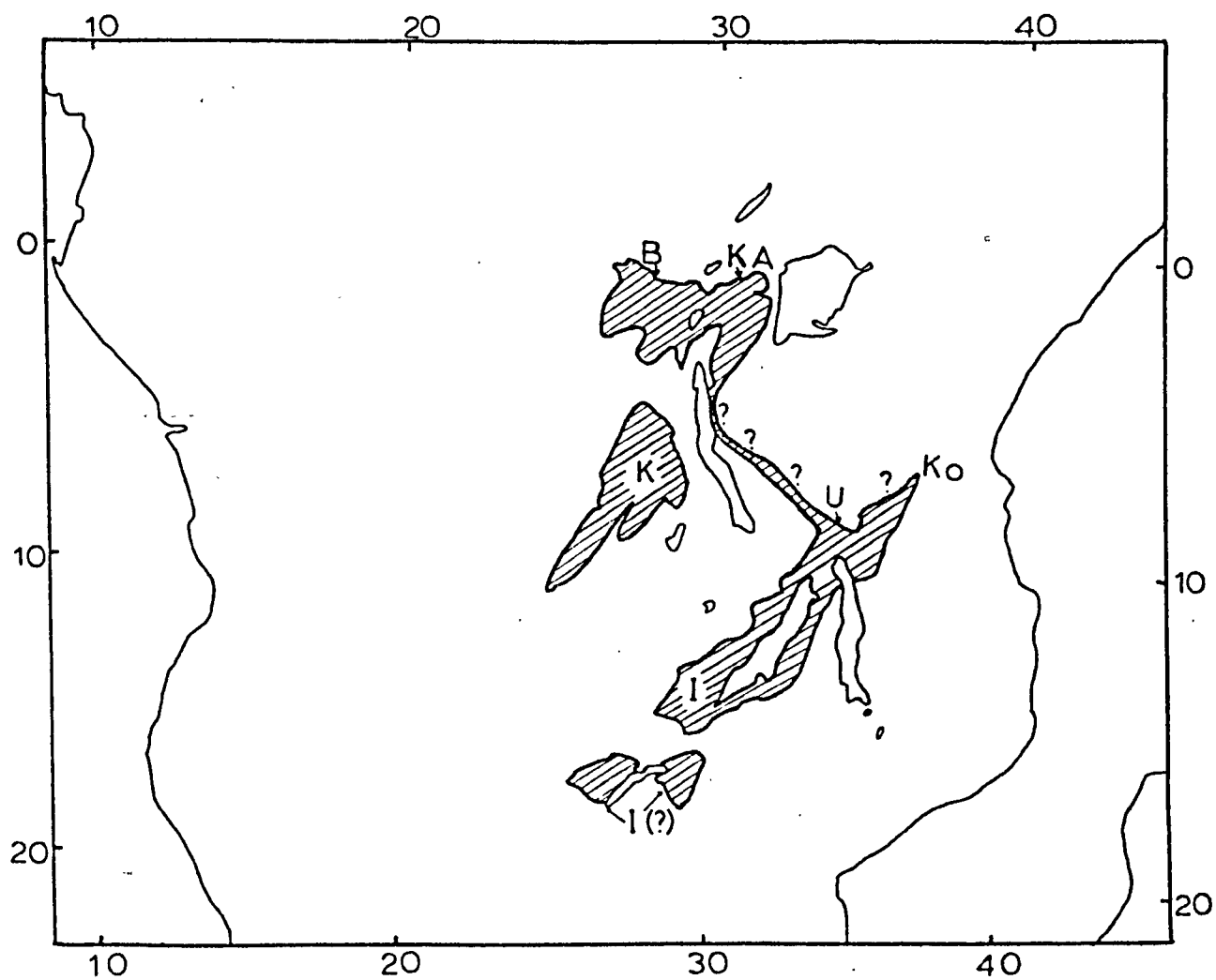
(1.3) Precambrian B (1000-1600 My.)

Most of the rocks of this division belong to two near parallel orogenic belts, each extending for approximately 2000 km. in a north to north east direction (fig. (3)). Several authors (Cahen and Snelling (1966), Vail et al. (1968), Pallister (1971)) have suggested that the two belts may be connected by a north west trending belt from the shores of Lake Malawi to the Itiaso formation on the shore of Lake Tanganyika.


(1.3.1) Kibaran Belt

The northern belt, the Kibaran, has been split by national boundaries into three sections, the Kibaran of Katanga, the Burundian of Burundi and Rwanda and the Karagwe-Ankolean of Uganda and Tanzania (fig. (3)). This belt is contained between the Katangan^A and the Bukoban^A on the east and south east and similar Precambrian A formations plus the Kasai Shield^D and the Lukoshien Belt^C on the west. Although to the north it disappears beneath the Congo Basin sediments^M, Ce radiometric dates of 800 to 1300 My. from the Ouango Massive in the Central African Republic may indicate its northern continuation (Roubault et. al. (1965)).

The Kibaran and Burundian parts of the belt are well known and its detailed stratigraphy has been described by a number of Belgian geologists (see Cahen and Lepersonne (1967) for stratigraphy and



B-Burundian I-Irumide K-Kibaran KA-Karagwe-Ankolean
Ko-Konse U-Ukingan ?-Age not proven

 Precambrian B

Fig(3)

TABLE (4)

PRECAMBRIAN B

TECTONIC UNIT	SYSTEM OR CYCLE ETC.	METAMORPHIC GRADE	DOMINANT TREND OR FOLD AXIS	MAXIMUM AGE OR AGE RANGE (MY.)
KIBARAN BELT	KIBARAN KARAGWE-ANKOLEAN BURUNDIAN	LOW TO LOWER AMPHIBOLITE LOW TO LOWER AMPHIBOLITE LOW TO LOWER AMPHIBOLITE	NNE. NNE. TO NE. + NNW. NNE. + NNW. TO NW.	850 to 1300 ² 1300 ₁ 1300 ₁
IRUMIDE BELT	IRUMIDE (MUVA) UKINGAN ITIASO AND KONSE	LOW TO AMPHIBOLITE LOW TO AMPHIBOLITE + INTENSE SHEAR METAMORPHISM VERY LOW	E TO ENE NE. + NW. NW. + NE.	900 to 1600 ^{1, 3} 1300 to 1800 ₁ 1238 ₁

¹ - Cahen and Snelling (1966) ² - Cahen and Lepersonne (1967) ³ - Vail et. al. (1968)

reference lists). Within the succession of metasediments there is an abundance of pre-tectonic, syntectonic and post tectonic granites, granodiorites, syenites and pegmatites. In addition rhyolites, gabbros and dolerite sills and dykes are found throughout the belt. The Karagwe-Ankolean section of this belt is reported to have similar rocks (Combe (1932), Halligan (1962), Cahen and Snelling (1966)) except there are no reports of rhyolites or gabbros.

A notable feature of the Kibaran Belt is the continuous range of radiometric ages obtained (850 to 1300 My. (table (4))). Cahen (1970) has interpreted this as due to an almost continuous sequence of orogenic and magmatic activity from the Kibaran to the Katangan^A.

(1.3.2) Irumide Belt

In comparison to the northern belt, the boundaries of the southern Precambrian B orogenic belt, the Irumide, is little known. Apart from the lack of detailed geologic mapping and radiometric dating, the main cause for this is the effects of earlier and later orogenic events. The presence of similar fold trends and styles and the evidence from a few radiometric dates (Vail and Dodson (1970), Vail et. al. (1968), Cahen and Snelling (1966), Clifford (1968)) suggests that this belt may extend from west of Lake Kariba in the south, to the Konse formation in central Tanzania (fig. (3)). The rocks in the Irumide Belt range from low grade metamorphosed sediments to granulites. It is probable that some of the higher grade rocks are older granulites reworked during the Irumide Orogeny. The gneisses and granites of Rhodesia, as well as parts of the Piriwiri-Lomagundi-Deweras^C sequence are thought to be the southern-most outcrops of the Irumide Belt

(Clifford et. al. (1967), Vail et. al. (1968), Clifford (1968)).

Further north the evidence for this belt has been obliterated by the Mozambique Orogeny (Zambezi-Mozambique Province of fig. (2)). It can be recognised however on both sides of the Luangwe Rift Valley^{K, Ce}. Here the 'basement' gneisses of Zambia and the overlying Muva and Kalonga metasedimentary series were all folded during the Irumide Orogeny (Ackerman and Foster (1960), Vail et. al. (1968)).

In northern Zambia and Malawi the belt outcrops as the Mafingi Series of low grade metasediments (Thatcher (1970)) and this can be correlated with the Ukingan Series on the opposite side of Lake Malawi (Cahen and Snelling (1966)). The lithology, direction of fold axis (NW. rather than NE.) and metamorphic grade of the Ukingan series are distinctly different from the rest of the Irumide Belt. It thus seems possible that the Ukingan region was not only affected by the north east trending Irumide event but was also folded by the north west trending orogenic belt of Precambrian B age which has been postulated for this region (see fig. (3)) .

It must be emphasized that many of the correlations cited from the literature for this orogenic belt were based on a comparison of trends and lithologies and there is a lack of detailed age determinations.

(1.4) Precambrian C (1600 to 2100 My.)

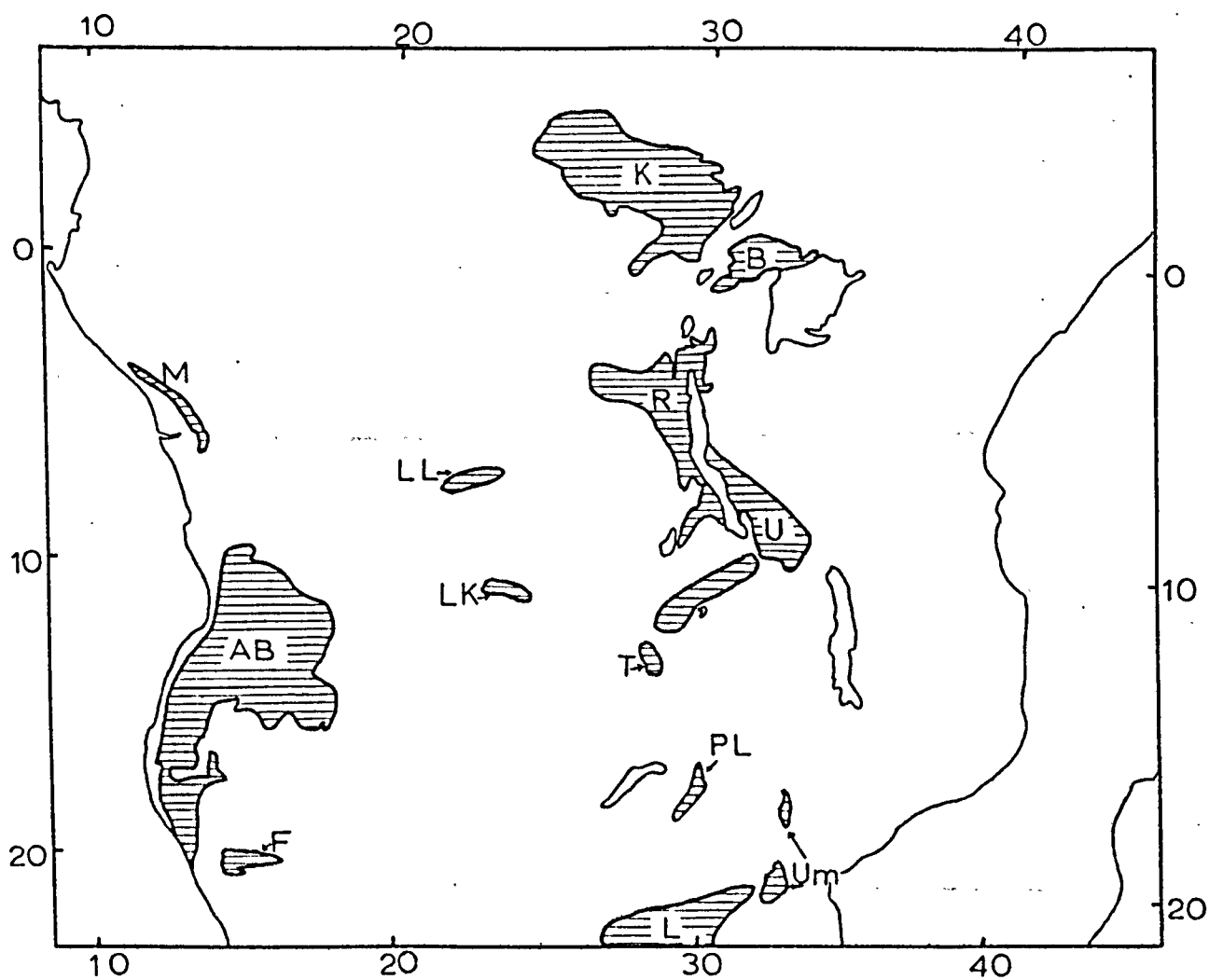
The principal outcrops of Precambrian C rocks occur in three major orogenic belts (see fig. (4)); the Limpopo Belt, the Ubendian-Ruizian Belt, and the Kibalian-Buganda-Toro Belt. There are several smaller sequences of this age recognised on the Kasai Shield^D (fig. (4) and fig. (5)), the Zambia Shield^D, and on the margins of the Rhodesian Shield^D.

(1.4.1) The Limpopo Belt and Other Precambrian C Formations of the Rhodesian Shield

The Limpopo Belt is wedged between the Rhodesian Shield^D in the north and the Transvaal Shield in the south (Vail (1968)). To the east the belt passes beneath the younger Umkondo System^C but possibly reappears further east where it is partly overprinted by the Zambezi-Mozambique Belt^A (Van Breeman et. al. (1966)). On the west this belt disappears beneath the Kalahari^{Ce} sediments. The rocks affected by the Limpopo orogenesis include a series of high grade metamorphic rocks as well as the lower grade Messina Sequence (Haughton (1963)).

The age of the Limpopo Belt has been the subject of much speculation. At first the similarity of the rocks of this belt with those of the Mozambique Belt^A led to their correlation, but subsequent radiometric dating placed a minimum age circa 2000 My. on the Limpopo Belt (Holmes and Cahen (1957)). Much new data have since been obtained to elucidate the evolution of this belt (Van Breeman et. al. (1966, 1972), Van Breeman (1970), Robertson (1968)). It has now been proposed that the major orogenic event occurred before 2500 My. and that the frequent occurrence of radiometric dates circa 2000 My. indicates a later less intense event. This may help to explain the presence of an unmetamorphosed extension of the Great Dyke^D and satellite complexes^D in the Limpopo Belt.

Two major sedimentary sequences of Precambrian C age lie on the margins of the Rhodesian Shield^D (fig. (4)). On the east the Umkondo Sequence and its correlatives the Frontier and Gairezi Series, overlie the Rhodesian Shield. The Umkondo Sequence has been metamorphosed on its eastern boundary by the Mozambique Belt^A. The



AB - Angola Basement B - Buganda-Toro F - Franzfontein
 K - Kibalian L - Limpopo LL - Luizian-Lulua LK - Lukoshian
 M - Mayumbian PL - Piriwiri-Lomagundi-Deweras R - Ruizian
 T - Tumbide U - Ubendian Um - Umkondo-Frontier-Gairezi

 Precambrian C

Fig.(4)

TABLE (5)

PRECAMBRIAN C

TECTONIC UNIT	SYSTEM OR CYCLE ETC.	METAMORPHIC GRADE	DOMINANT TREND OR FOLD AXIS	MAXIMUM AGE OR AGE RANGE (MY)
RHODESIAN SHIELD	LIMPOPO UMKONDO FRONTIER - GAIREZI LOMGUNDI - DEWERAS PIRIWIRI	HIGH (GRANULITE) ZERO TO LOW LOW TO HIGH ZERO TO LOW ZERO TO LOW	ENE. N. + E. NW. N. + NNE. + NE. N. + NNE. + NE.	2000 to 2650 $\frac{3}{2}$ 1785 $\frac{2}{2}$ 1785 1940 $\frac{4}{2}$ 1655 $\frac{2}{2}$
ZAMBIA SHIELD	TUMBIDE	LOW (?)	N. TO NE.	1635 4
KASAI SHIELD	LUKOSHIAN LUIZIAN LULUA	MODERATE (GREENSCHIST TO AMPHIBOLITE) HIGH (AMPHIBOLITE TO GRANULITE) LOW (GREENSCHIST)	N.10°W. TO W WSW. NE. + ENE	1845 to 1950 $\frac{1}{1}$ 1910 to 2120 $\frac{1}{1}$?
UBENDIAN- RUIZIAN BELT	UBENDIAN RUIZIAN	HIGH (AMPHIBOLITE TO GRANULITE) HIGH (AMPHIBOLITE TO GRANULITE)	N. TO W. N. TO W.	1800 $\frac{1}{1}, \frac{5}{2}$ 2100 $\frac{1}{1}, \frac{5}{2}$
KIBALI-BUGANDA-TORO BELT	BUGANDA TORO KIBALI	LOW TO HIGH HIGH (AMPHIBOLITE TO GRANULITE) LOW (GREENSCHIST)	ENE. + NNE. NW. TO N. WNW.	1725 to 2075 $\frac{1}{1}, \frac{5}{2}$ 1725 to 2075 $\frac{1}{1}, \frac{5}{2}$ 1725 to 2075 $\frac{1}{1}, \frac{5}{2}$
	UPPER MAYUMBIAN FINGOE	ZERO TO LOW LOW (GREENSCHIST)	NE.+ NW. NNE.TO NNW. + ENE.	1100 to 1950 $\frac{1}{1}$?

1 - Cahen and Snelling (1966)
 2 - Vail and Dodson (1970)
 3 - Van Breeman et. al. (1972)
 4 - Vail et.al. (1967)
 5 - Clifford (1968)

Umkondo Dolerite, a series of volcanics and dolerite dykes and sills, intrudes both the Umkondo and Frontier-Gairezi systems.

A possible correlative of the Umkondo Sequence is the Piriwiri-Lomagundi-Deweras Sequence which lies unconformably on the north and north west parts of the Rhodesian Shield^D (Macgregor (1951a and b), Shackleton et. al. (1966)). Metasediments are the principal rock types and these are underlain by the Deweras metavolcanics (including greenstones) (Rhodesian Geologic Map (1971), Haughton (1963), Clifford et. al. (1967)). Rocks of this sequence show a northerly increase in metamorphic grade caused by the Mozambique Orogeny^A (Vail and Snelling (1971)). There is also a westerly increase in metamorphic grade and it has been postulated that this is due to the effects of the southerly continuation of the Irumide Belt^B (Clifford et. al. (1967), Vail et. al. (1968)) (see fig. (3)).

(1.4.2) Zambia Shield (Tumbide Belt)

In the region of the Zambia Shield (fig. (4) and fig. (5)) the effects of the Tumbide Orogeny have been recognised by Ackermann (1950) and Ackerman and Foster (1960). The full extent of this orogeny is unknown because of the overprinting of the later Irumide^B and Katangan^A orogenies. The Tumbide Orogeny appears to have folded the Mosofu and Lufubu formations. Some authors (Vail et. al. (1968)) postulate that the Tumbide event also affected parts of the Zambia Shield which Clifford (1968, 1970) assigns to the Precambrian D.

(1.4.3) Kasai Shield (Lukoshian, Luizian and Lulua Belts)

Two small Precambrian C orogenic belts outcrop on the Kasai Shield (fig. (4) and fig. (5)). In the south near latitude 11°S.

the Lukoshien Belt is wedged between the Precambrian D rocks of the Kasai Shield to the north and south and its other boundaries disappear beneath Paleozoic and younger sediments of the Congo Basin (Cahen and Lepersonne (1967)). The second belt, the Luizian, overlies the Charnokite Complex^D at approximately latitude 7°S. with a marked unconformity.

The northern boundary of the Luizian Belt is formed by the Lulua Belt (see fig. (4)). The rocks of the latter form a series of sediments and volcanics which have been folded and faulted with later injection of dolerite dykes. This cycle has not been dated radiometrically, but Cahen and Snelling (1966) suggest the possibility that it may form part of the later Kibaran Belt^B.

(1.4.4) Ubendian-Ruizian Belt

North of the Zambia Shield, the Ubendian-Ruizian Belt is wedged between the Kibaran Belt^B and the Tanganyika Shield^D (fig. (4)) (McConnell (1951), Sutton et. al. (1954), Quennell et. al. (1956)). The belt extends from the Malawi Tanzania border to western Burundi where it disappears beneath younger formations. The most noteworthy feature of the Ubendian-Ruizian Belt is the number of large granite masses outcropping at the surface. The Kate Granite intrudes the Lower Plateau Series of northern Zambia and southern Tanzania (this series is a molasse of the Ubendian cycle) and it is from this granite that the minimum age of 1700 to 1800 My. is obtained. The anomalously young ages obtained from several parts of this belt (Cahen and Snelling (1966)) are probably due to the effects of the neighbouring Kibaran Orogeny^B.

(1.4.5) Kibali-Buganda-Toro Belt

North of the Kibaran^B Belt the next outcrop of Precambrian C rocks occurs as the Kibali-Buganda-Toro Belt (fig. (4)). This extends from north central Zaire into Uganda where the Nyanzian^D and Kavirondian^D Series form its eastern boundary. Lake Victoria and the Lindian Series^A form the southern and western boundaries respectively while the Uganda 'Basement'^{D, A} forms a northern boundary. In Buganda the Mubende Granite intrudes the Singo Series, a molasse of the Buganda Orogeny, to set a minimum age of 1800 My. for the age of the orogenic belt (table (5)). As with the Ubendian-Ruizian Belt there are a large number of granitic masses within the Precambrian C terrain.

(1.4.6) Other Regions of Precambrian C Age

A large number of rocks of Precambrian C age are found on the western side of the Congo Basin (fig. (4)). Here ages between 1100 and 1950 My. (table (5)) have been assigned to the Upper Mayumbian Orogeny (Cahen and Snelling (1966), Cahen and Lepersonne (1967)). Again Precambrian A events (West Congolian Orogeny) have obscured the true extent of this Precambrian C orogeny.

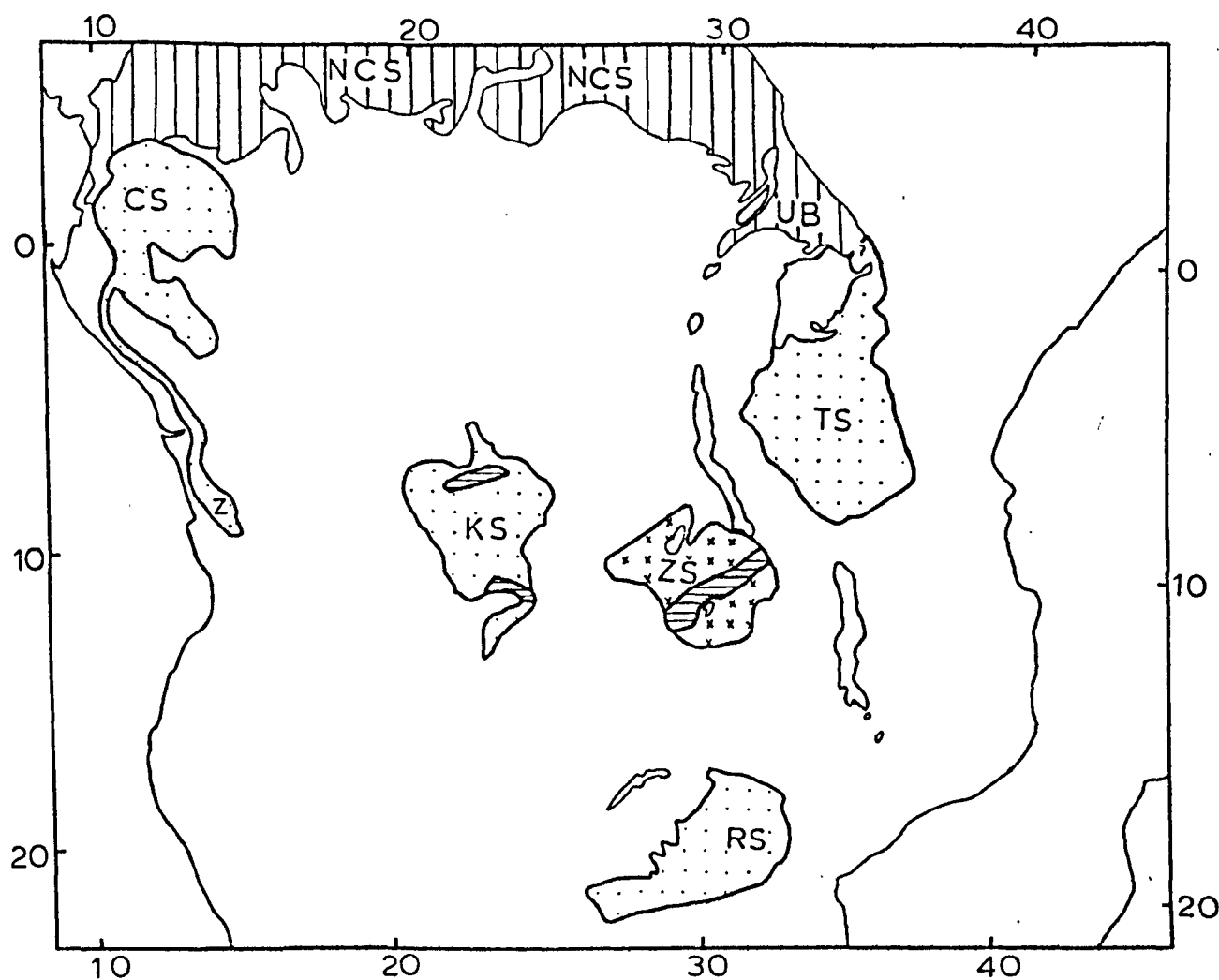
In south and central Angola several rock types, including granites and gneisses, have yielded Precambrian C ages (Cahen and Snelling (1966), Simpson (1970)). The relation between this part of the Angola basement and the Mayumbian to the north is unknown (see fig. (3)). Further south in South West Africa, within the Damaran Orogenic Belt^A, a large granite mass, the Franzfontein Granite, has yielded an age of 1700 My. indicating a possible continuation of the Angola granite regime.

(1.5) Precambrian D (>2100 My.)

Four cratonic blocks, which have remained stable areas since early Precambrian D times, are recognised in 'equatorial' Africa. These are the Rhodesian, Kasai, Tanganyika, and Cameroun Shields (fig. (5)). Although these shields or cratons have not been orogenically deformed since at least 2300 My. (see table (5)) parts of them have been the sites of later volcanic and/or plutonic activity, whereas other parts are covered by younger sedimentary sequences.

(1.5.1) Rhodesian Shield

The most southerly craton, the Rhodesian Shield, is bounded by the Limpopo Belt^C in the south, the Umkondo System^C and Mozambique Belt^A in the north and the Piriwiri-Lomagundi-Deweras^C and Kalahari^{Ce} Systems on the west and north west. Macgregor (1947, 1951a and b) has described a series of sedimentary and volcanic rocks which have been intruded by a large number of enormous granite batholiths and have been metamorphosed to form a complex series of greenschist belts (the Rhodesian Gold Belt). These belts have been divided into three systems, the Sebakwian, the Bulawayen and the Shamvaian (see Annexure to the Proceedings and Transactions of the South African Geological Society, 71, (1968)). The Great Dyke and various related basic and ultrabasic complexes were intruded at approximately the same time as the final phase of granite intrusion. The Great Dyke is a north to south trending intrusion 480 km. long with an average width of 5 to 6 km. (Worst (1960), Bichan (1970)). It consists of serpentinite, pyroxenite and gabbro. The contemporaneity of the dyke and several extensive linear dyke swarms parallel or sub-parallel to it has been shown by both radiometric (Vail and



CS - Cameroun Shield KS - Kasai Shield ZS - Zambia Shield
 RS - Rhodesian Shield TS - Tanganyika Shield Z - Zadinian

NCS - North Congo Shield



Precambrian D



Precambrian C



Unsure

Precambrian D (Geologists' view)



Precambrian A (Radiometric dating)

Fig(5)

TABLE (6) PRECAMBRIAN D

TECTONIC UNIT	SYSYEM OR CYCLE ETC.	METAMORPHIC GRADE	DOMINANT TREND OR FOLD AXIS	MAXIMUM AGE OR AGE RANGE (MY.)
TANGANYIKA SHIELD	NYANZIAN KAVIRONDIAN DODOMAN	LOW (GREENSCHIST) LOW (GREENSCHIST) HIGH (GRANULITE)	NW + NE E N 70° W	2930 to 3150 $\frac{1, 2}{1}$ 2550 to 2900 $\frac{1, 2}{1}$ 2300 to 2900
RHODESIAN SHIELD	SHAMVAIAN BULAWAYAN SEBAKWIAN GREAT DYKE	LOW MODERATE TO HIGH (AMPHIBOLITE) MODERATE TO HIGH (AMPHIBOLITE)	NE TO W NE TO NNW NE TO N	3000 $\frac{5}{2}$ 3000 $\frac{5}{2}$ 3000 $\frac{5}{6}$ 2500 to 2800
KASAI SHIELD	CHARNOKITE COMPLEX UPPER LUANYI DIRAYA	HIGH (GRANULITE) HIGH (GRANULITE) HIGH (GRANULITE)	ENE ENE ENE	2500 to 2560 $\frac{1}{1}$ 3270 $\frac{1}{1}$ 2520 to 2710
CAMEROUN SHIELD	CALCO MAGNESIUM ZADINIAN	HIGH (GRANULITE) HIGH (GRANULITE)	? ENE + NE + NW	2300 to 3200 $\frac{1}{1, 2}$ 2500
NORTH CONGO SHIELD	BOMU AND GANGU COMPLEXES WATIAN	HIGH + LOW HIGH (GRANULITE)	WSW+SE + NNE E	3500 $\frac{2}{4}$ 2660
	ZAMBIA BASEMENT	HIGH (GRANULITE)	?	2720 ? $\frac{1}{1}$

1 - Cahen and Snelling (1966) 2 - Cahen and Lepersonne (1967) 3 - Old and Rex (1971) 4 - Spooner et. al. (1970) 5- Vail and Dodson (1970) 6 - Allsop (1965)

7 - Snelling et. al. (1964)

Dobson (1970), Robertson and Van Breeman (1970)) and palaeomagnetic means (McElhinny and Opdyke (1966)).

(1.5.2) Tanganyika Shield

The Tanganyika Shield is bounded by the Ubendian Belt^C in the south and south east, various Precambrian B series in the west and the Mozambique Belt^A on the east (fig. (5)). The northern boundary is poorly defined but possibly continues northwards on the eastern side of Lake Victoria as the Bulgwe Series of Uganda. In the central and western regions, north of Lake Victoria, the shield is truncated by the Buganda-Toro Belt^C (Cahen and Snelling (1966)). Spooner et. al. (1970) have suggested that the Watian rocks of the West Nile Complex (Hepworth and MacDonald (1966)) which have been dated circa 2655 My. may have been part of an enlarged Shield. From other radiometric data quoted (Cahen and Snelling (1966), Hepworth and MacDonald (1966), Spooner et. al. (1970)) and the known distribution of Aruan[?], Mirian^A and Chuan^A rocks it was decided to include this region of Uganda in the discussion of the Precambrian A rocks.

The Tanganyika Shield proper is composed of a vast region of granitoid material (including the Older Granites) plus the remnants of three ancient systems, the Kavirondian and Nyanzian greenschist belts, and the Dodoman Belt. There are a number of granite masses also associated with these systems (the Younger Granites) (Harpum (1954), Shackleton (1946)). The Kavirondian and Nyanzian rocks outcrop in north west Tanzania, south west Kenya and south east Uganda around Lake Victoria. In Uganda the Nyanzian is known as the Bulugwe Series (Davies (1935)) and the Kavirondian as the Samia Series. The higher grade Dodoman Belt (Quennell et. al. (1956)) outcrops in much of central Tanzania (Geological Map of Tanzania (1967)). The relationships

of these three systems with one another and with the surrounding granites is still incompletely known.

(1.5.3) Kasai Shield

This shield which outcrops to the west of the Tanganyika Shield (fig. (5)) is mostly obscured beneath the Palaeozoic and younger sediments of the Congo Basin. Only its eastern boundary with the Kibaran Belt and the Bushimay Series is clearly seen. The rocks of this shield have been extensively studied by Belgian geologists (see bibliography given by Cahen and Snelling (1966), Cahen and Lepersonne (1967)). Three or possibly four orogenic cycles have been recognised on this shield. The oldest cycle, the Upper Luanyi (table (6)) outcrops south of latitude 7°S . and is overlain by part of the next cycle, the Charnokite Complex (the Kasai-Lomami Norite Gabbro and Charnokite Complex of Cahen and Lepersonne (1967)). The probable correlative of the Charnokite Complex north of latitude 7°S . is the Dibaya Complex (table (6)). The other cycles are discussed under the Precambrian C.

(1.5.4) Cameroun Shield

The Cameroun Shield outcrops to the north west of the Kasai Shield (fig. (5)). It is bound by the Precambrian A complex of Cameroun to the north, the Atlantic Ocean to the west, and various formations correlated with the West Congolian^A on all other sides. Because of the later Precambrian A events which affect regions around Cameroun and Gabon the full extent of Precambrian D rocks is not yet known in this region. One possible extension is along a thin line of country parallel to the coast which terminates as the Zadinian or Lower Mayumbian Orogenic Belt (fig. (5) and table (6)) (Cahen and Snelling (1966)).

(1.5.5) Regions of Possible Precambrian D Age

Mestraud (1971) has argued that much of the basement of Cameroun, to the north of the Cameroun Shield, and to the east through the Central African Republic and north Zaire to Uganda belong to the Precambrian D. He calls this region, with the Cameroun Shield, the North Congo Shield (see fig. (5)). Consistent Precambrian A radiometric dates (see section (1.2.1.2)) have been obtained from the North Congo Shield and most of this region is therefore discussed in the Precambrian A section. However small patches of rocks in Zaire and Uganda have yielded Precambrian D ages. In north central Zaire these rocks are known as the Bomu and Gangu formations. Cahen and Lepersonne (1967) observe that these formations may be continuous with the West Nile Complex beneath the younger cover formations. The Watian (table (6), Hepworth (1961, 1964), MacDonald (1963), Hepworth and MacDonald (1966)) is the only part of the West Nile Complex which is known to be of Precambrian D age (Spooner et. al. (1970)). This formation occurs in the West Nile district of Uganda and is observed in small patches in other parts of the Uganda basement (Uganda Geologic Map (1966)) and possibly in neighbouring regions of Zaire.

Clifford has suggested that a large region of Zambia (Zambia Shield or Bangweulu Craton) be classified Precambrian D. Lack of geological mapping and radiometric dating makes it difficult to outline this shield or to 'pin-point' the last orogenic phase in this region. Clifford's classification (1968, 1970) is based on the evidence of two radiometric dates (table (6)) obtained from detrital minerals (Holmes and Cahen (1955), Snelling et. al. (1964)) and the description of the geology given by Furon et. al. (1958). Others (Cahen and Snelling (1966), Vail et. al. (1968)) recognise the possibility that much of this

'shield' has been affected by the later Tumbide^C and Irumide^B orogenies.

(1.6) Palaeozoic and Karroo

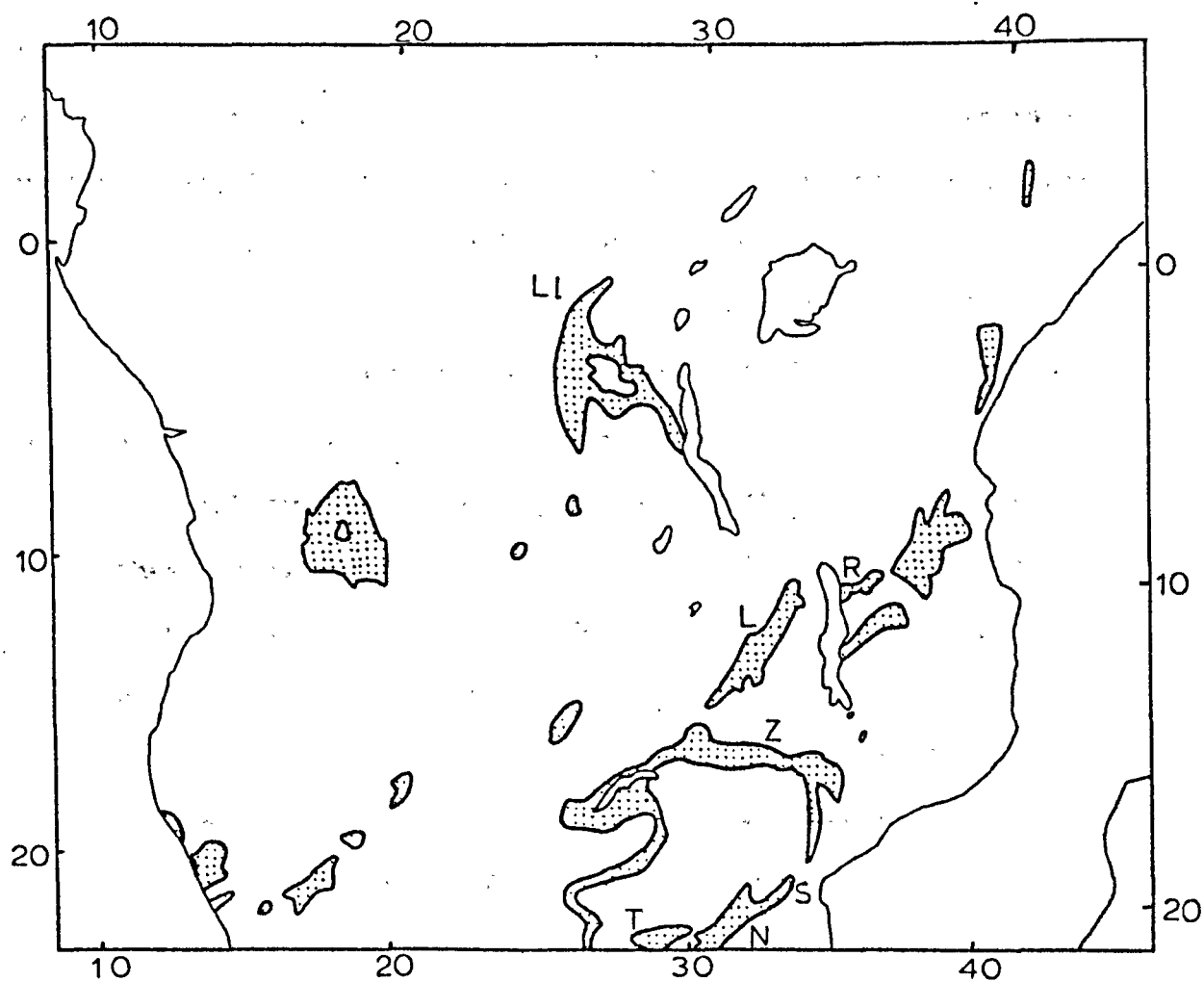
It is apparent from the radiometric dates quoted in tables (2) and (3) that many Precambrian A formations have suffered later Palaeozoic events. The only Palaeozoic sedimentary sequence found in 'equatorial' Africa is a small outcrop of Bilatian rocks west of Lake Edward in Zaire (Haughton (1963), Cahen and Lepersonne (1967)).


(1.6.1) Karroo

No major orogenies have affected 'equatorial' Africa since the Precambrian, but in the Karroo period (~ 225 to ~ 100 My.) the south and eastern areas were involved in major crustal warping and rifting (see also chapter (5) on the movements in the Mozambique Channel) (fig. (6)). During this period the main Karroo series, the Dwyka, the Eccra, the Beaufort and the Stormberg were deposited. The Karroo rocks, which are mostly flat lying, are predominantly glacial and sedimentary deposits. The end of the Karroo was marked by widespread volcanics (Stormberg Volcanics).

The history of most Karroo outcrops appears to be similar. Troughs were initiated by rifting and subsidence and this was followed by massive sedimentation. Faulting continued throughout and subsequent to the sedimentation so that many of the Karroo outcrops are fault-bounded.

In the southern part of the region, Karroo rocks practically surround the Rhodesian Shield^D (fig. (6)). On its northern margin there is the Zambezi Valley (Hitchen (1958), Tavener-Smith (1960), Haughton (1963)), while on the south and south eastern margins there are the Sabi Monocline, the Nuanetsi Syncline and the Tuli Syncline (Hapgood



L - Luangwa Valley N - Nuanetsi Syncline R - Ruhuhu
 T - Tuli Syncline S - Sabi Monocline Z - Zambezi Valley
 LI - Luabala  Karroo

Fig(6)

(1963), Cox (1970), Cox et. al (1965)). The latter structures are continuous with the Lebombo Monocline which extends southwards into South Africa. On the western margin of the Rhodesian Shield the Karroo Series rests on the basement of the shield. Extensive lava flows (Stormberg Volcanics) of rhyolite and basalt occurred in all the regions mentioned. West of the Rhodesian Shield deep bore holes have confirmed the existence of these lavas beneath the extensive Kalahari Sediments^{Ce} of Botswana and South West Africa almost to the Damaran Belt^A on the west coast (Botswana Geologic Map, South West Africa Geological Map, Bishop and Van Eeden (1971)). Various outcrops of these lavas are also observed within this belt (fig. (6)).

East and north of the Rhodesian Shield, Karroo structures are traced from the Urema Trough northwards through the Shire Rift. The presence of Stormberg Volcanics beneath the sediments of the surrounding region of coastal Mozambique is proven from the evidence of deep bore holes (Flores (1970), Pallister (1971)). Vail (1970) has traced a series of Karroo dyke swarms from the Limpopo Belt in the south through the Shire Rift to northern Malawi (Fitches (1971)) and possibly into Tanzania.

West of Lake Malawi there is a considerable volume of Karroo sediments associated with the Luangwa Valley (fig. (6) (Haughton (1963), De Swardt et. al. (1965), Bishop and Van Eeden (1971)). Only minor volcanics are observed in the valley (Zambia Geologic Map). On the eastern shore of Lake Malawi, two separate Karroo sedimentary basins (the northern one is the Ruhuhu Basin) trend in a north east direction (fig. (6)). To the east of these depressions a larger Karroo outcrop extends almost to the east coast. The northward continuation of these Karroo sediments, beneath younger formations, is indicated from the

depression observed in the basement by geophysical studies (Kent (1965) Kent et. al. (1971)). North of Dar es Salaam Karroo sediments again outcrop and extend into Kenya as far north as latitude 3°S. Several smaller patches of Karroo sediments outcrop around Lake Rukwa in Tanzania and in faulted troughs in Uganda (Haughton (1963), Pallister (1971)). Other outcrops of Karroo rocks are seen east of Lake Tanganyika in eastern Zaire (Haughton (1963), Mestraud (1971)) (the Lualaba Sequence in fig. (6)) and further west in northern Angola and western Zaire.

(1.7) Mesozoic

From the Lower Jurassic to the Lower Cretaceous the south and south eastern regions of 'equatorial' Africa were again the site of rift faulting and volcanicity. A period of between 30 and 60 My. separated the final phase of the Karroo activity (Stormberg Volcanics) and the beginning of this later cycle (Vail (1968), Flores (1970), Woolley and Garson (1970), Pallister (1971)). In some areas a continental sandstone was deposited between the volcanics of the two cycles.

Many of the major faults in Malawi were either initiated or reactivated in Post Karroo and, in some cases, Post Cretaceous times (Bloomfield and Hapgood (1966)). The Lake Malawi Rift was active at this time while the region to the south was involved in the widespread volcanicity of the Chilwa and Lupata Gorge Alkaline Provinces. A few alkaline and carbonatite centres have been found in Mozambique and these are tentatively correlated with the Chilwa Province (Oberholzer (1964)). The extent of this activity in Mozambique has been demonstrated from the results of deep drilling (Flores (1970), Pallister

(1971)). Further south many of the Karroo initiated troughs were also reactivated (Cox et. al. (1965), Vail (1968)). To the west, another major fault system of Mesozoic age can be traced in a south westerly direction from the Luangwa Valley (Bishop and Van Eeden (1971)), through the faults which bound Lake Kariba to a zone of faults recognised in Botswana (Green (1966), Vail (1968), Reeves (1972)).

In the north eastern part of 'equatorial' Africa the Mesozoic was a period of relative stability, only warping and minor reactivation of faults occurred, mainly as the result of sedimentary loading (Kent et. al. (1971), Kent (1972)). In this region there were intermittent marine transgressions from Mid-Jurassic to Cretaceous times. Other parts of 'equatorial' Africa have been tectonically inactive from the Jurassic. Inland the vast Congo and Kalahari Basins (including the Cubango Basin of Holmes (1965)) were the sites of deposition of great quantities of sediments. Although these are predominantly continental, three marine incursions have been discovered in the Congo Basin (Mestraud (1971)).

Lastly, a number of probable Cretaceous carbonatite and kimberlite intrusions have been recognised in east and south east Uganda, Kenya, Tanzania (Pallister (1971), Dawson (1970)), Rhodesia north of Bulawayo (Vail (1968)), Malawi (Bloomfield and Hapgood (1966)), Mozambique (Oberholzer (1964), Bishop and Van Eeden (1971)), Angola, South West Africa and Zaire (Haughton (1963)). Generally these intrusions have not been correlated with any major tectonic features but they may be connected with the tensions involved with the drifting of the continents at that time.

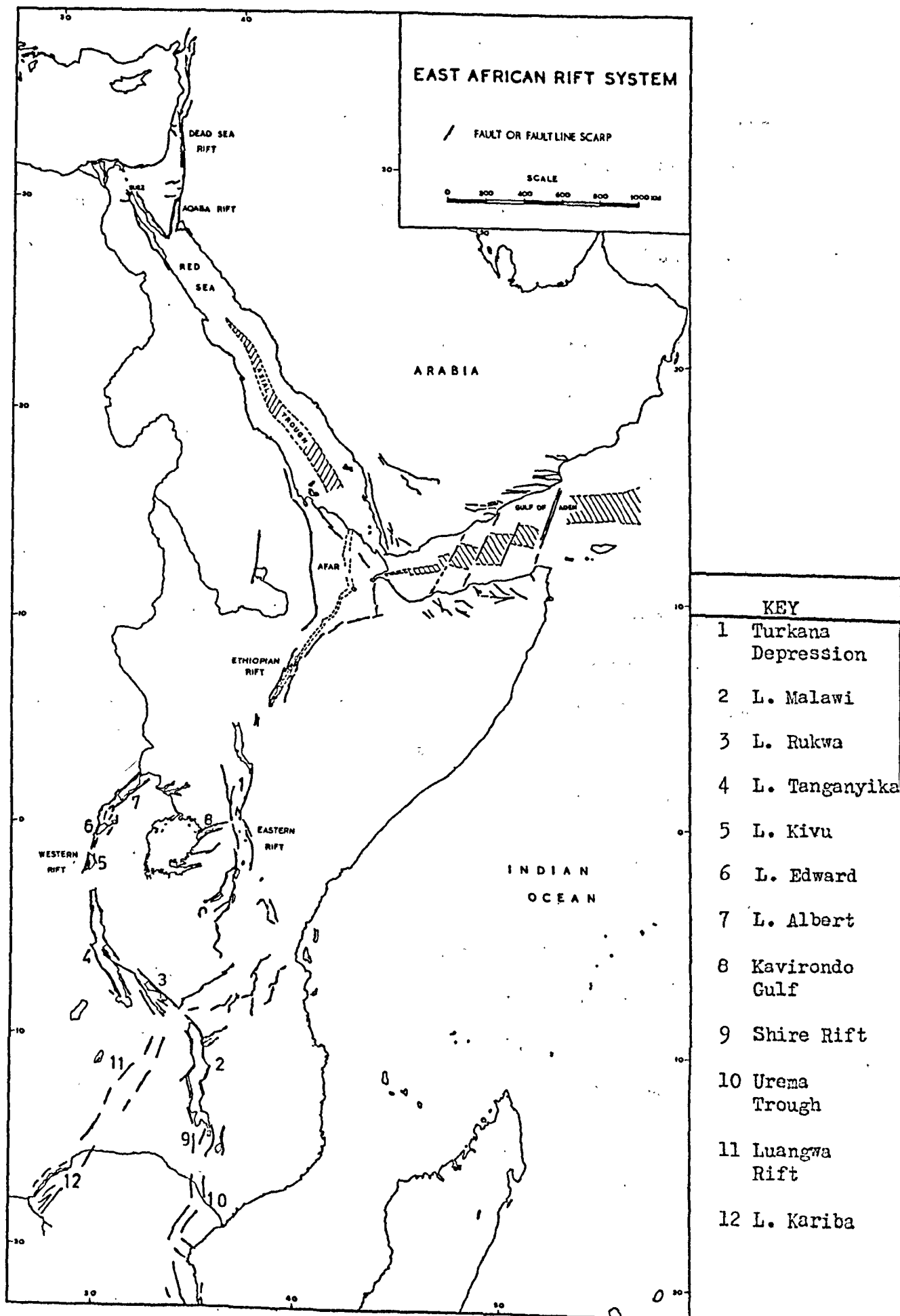
(1.8) Cenozoic

Tertiary and Quaternary tectonism and volcanism have been almost entirely confined to the eastern and north eastern parts of 'equatorial' Africa. As mentioned above most other parts of the region were the sites of mainly continental sedimentation from the Mesozoic to the present.

(1.8.1) East African Rift System

Although this discussion will only be concerned with the East African Rift south of the Turkana Depression (fig. (7)) it is important to emphasize that there is a very close relationship, in time and spacial events, between the tectonics of this area and the Ethiopian Rift System to the north (Baker et. al. (1972), King (1970), Gass (1970)). On a larger scale the shallow seismicity (Ewing and Heezen (1956), Fairhead and Girdler (1969, 1970, 1971)) and the topographic resemblance to the oceanic ridges allows the East African Rift System to be included as part of the World Rift System (Rothé (1954)).

The southern limit of the Rift System is uncertain but only the structures to the north of Lake Malawi are wholly Tertiary and later in age. All activity further south appears to be a rejuvenation of Karroo and Mesozoic structures. North of Lake Malawi the Rift splits into two branches around the perimeter of the Tanganyika Shield^D. The Western Rift (fig. (4)) cuts across older drainage systems and has very thick sediments associated with a large part of it. This branch of the Rift consists of a series of long and well defined grabens, which have very constant widths of about 45 km. (Holmes (1965)). A number of very large lakes are situated within these grabens (Lakes - Rukwa, Tanganyika, Kivu, Edward and Albert). Present day seismicity and



Fig(7)

volcanism indicates that the Western Rift is presently more active than the Eastern Rift.

The Eastern Rift is dominated by a large uplift (the Kenya Dome) which took place in the Late Pliocene-Pleistocene. Only in the region of this dome are true grabens observed in the Eastern Rift. These are the meridional Gregory Rift (Gregory (1920, 1921)) and the westerly trending Kavirondo Rift which extends to the Kavirondo Gulf on Lake Victoria (fig. (7)). The southern and northern extremities of the Eastern Rift are situated on the outer flanks of the dome. Here the Rift System consists of a series of splay faults which do not show any major grabens but instead form wide depressions 400 to 500 km. broad.

The eastern rifts, and to a much lesser extent the western rifts, are characterized by a strongly alkaline series of volcanic rocks which have been erupted from both fissures and central volcanoes. The history of the tectonic and magmatic activity of the East African Rift System is shown in table (7). It is clear that the history of the Eastern Rift is far better understood than that of the Western Rift.

(1.8.2) Structure Related to the East African Rift System

A possible southerly continuation of the East African Rift is through Malawi along the Lake Malawi Rift, the Shire Rift and into Mozambique as the Urema Trough and possibly even further south along more minor features situated along Meridian 35°E . (Oberholzer (1964)). Most of these structures are pre-Tertiary features which have been reactivated. The present day seismicity, usually of magnitude 4 and greater indicates that this region is still active (Fairhead and Girdler (1969, 1971), unpublished tectonic map of Mozambique (1964)).

A second possible southern extension is along the line of reactivated Karroo and Mesozoic structures extending from the Luangwa

PERIOD	TECTONIC ACTIVITY	MAGMATIC ACTIVITY	LOCATION	RADIOMETRIC DATES OR TIME RANGE
LATE CRETACEOUS	UPLIFT (~400 metres) SUBSIDENCE		CENTRAL KENYA EAST COAST	<u>2, 8</u>
EARLY TERTIARY	ARCHING ACCOMPANIED BY WARPING AND FAULTING		APPROXIMATELY COINCIDENT WITH PRESENT DAY RIFTS	<u>2</u>
OLIGOCENE		NUMBER OF SMALL ALKALINE COMPLEXES DEVELOPED ALONG AN AXIS OF MINOR DOMES	FROM JUST NORTH OF THE KAVIRONDO GULF THEY EXTEND FOR 60km. IN A N. TO NE. DIRECTION	<u>3, 6, 11</u> 25 to 31 My.
MIOCENE		HIGHLY EXPLOSIVE ALKALINE VOLCANOES OF NEPHILINITE WITH ASSOCIATED CARBONATITE AND PHONOLITE	EXTEND IN A NORTHERLY DIRECTION FROM THE KAVIRONDO GULF ALONG THE KENYA-UGANDA BORDER	<u>3, 6, 7, 11</u> 15 to 22 My.
	UPLIFT OF THE FLANKS OF THE RIFT SYSTEM WITH INITIATION OF THE TURKANA DEPRESSION			<u>2</u>
		ALKALI BASALTS, BASINITES WITH SOME NEPHILINITE	NORTH WEST KENYA NORTH AND CENTRAL KENYA	<u>5</u> 14 to 32 My. * (oldest rocks are in the north)
		PHONOLITE VOLCANOES	NORTH KENYA	<u>5</u> ?
	UPLIFT	PHONOLITE ERUPTIONS	KENYA DOME	<u>1, 2</u> 10 to 13.5 My.
		ERUPTION OF OVERSATURATED VOLCANICS (TRACHYTES OR QUARTZ TRACHYTES)	NORTH KENYA	<u>10</u> 24 to 38 My. (if oldest age is correct then * will have to be revised)
MIOCENE	INITIATION OF LAKE ALBERT RIFT - FOR THE TERTIARY THERE ARE NO OTHER REPORTS OF PRE-PLIOCENE ACTIVITY FOR EITHER THE WESTERN RIFT OR ANY OF THE BRANCHES WHICH MAY REPRESENT A SOUTHERN EXTENSION OF THE RIFT SYSTEM		WESTERN RIFT	<u>12</u>

Table(7) History of the East African Rift.

PERIOD	TECTONIC ACTIVITY	MAGMATIC ACTIVITY	LOCATION	RADIOMETRIC DATES OR TIME RANGE
PLIOCENE	INITIAL RIFTING	VOLCANIC ACTIVITY CHANGES TO PREDOMINANTLY TRACHYTE AND BASALT WITH SOME PHONOLITE	VOLCANIC ACTIVITY EXTENDED TO NORTH TANZANIA. FIRST ERUPTION EAST OF THE RIFT	<u>1, 2, 5, 10, 13</u> 5 - 7 My. to RECENT
	MAJOR UPLIFT (~ 1500 metres) WITH GRABEN FORMATION. SPLAY FAULTS DEVELOPED NORTH AND SOUTH OF THE KENYA DOME	NEPHILINITE, TRACHYTE VOLCANISM	WESTERN RIFT-NORTH AND SOUTH OF LAKE KIVU KENYA DOME	<u>4</u> PLIOCENE TO RECENT
PLEISTOCENE	CENTRAL GRABEN IN KENYA BROKEN UP BY SWARMS OF MINOR FAULTS ('GRID' FAULTS)	BASALT-PHONOLITE VOLCANISM	TANZANIA AND KENYA SOUTHERN JUNCTION OF OF THE EAST AND WEST RIFTS	<u>2</u> <u>4, 14</u> PLIOCENE TO RECENT
		FORMATION OF TRACHYTE CALDERA VOLCANOES	ETHIOPIA TO NORTH TANZANIA ALONG THE RIFT AXIS	<u>2</u> PLEISTOCENE TO RECENT
		BASALT, BASINITE, PHONOLITE AND TRACHYTE VOLCANISM	150 to 250 km. EAST OF THE EASTERN RIFT	<u>2</u> 1 My. to PRESENT
	MAJOR FAULTING	NEPHILINITE-CARBONATITE CENTRES ACTIVE	KENYA GRABEN NORTH KENYA, SOUTH TANZANIA, KAVIRONDO GULF.	<u>2, 12</u> <u>12</u> PLEISTOCENE TO RECENT
		VOLCANIC ACTIVITY	WESTERN RIFT	<u>4</u> PLEISTOCENE TO RECENT

1- BAKER ET. AL. (1971) 2- BAKER ET. AL. (1972) 3- KING AND SUTHERLAND (1966) 4- KING (1970) 5- KING AND CHAPMAN (1972) 6- KING ET. AL. (1972) 7- McCALL (1958)
8- SAGGERSON AND BAKER (1965) 9- WILLIAMS (1970) 10- LIPPARD (1973) 11- DAVIES (1956) 12- HEPWORTH (1964) 13- FAIRHEAD ET. AL. (1972) 14- HARKIN (1960)

Table(7) Continued.

Valley through Lake Kariba into Botswana (Vail (1968), Reeves (1972)). Reeves reports extensive low magnitude seismicity (magnitude 3 or less) for Botswana.

Finally possible rifting has been postulated, from a study of the seismicity, along a south westerly trending direction from the southern end of Lake Tanganyika towards approximately 12°S . where it takes on a meridional trend (Fairhead and Girdler (1969)).

C H A P T E R 2

NEW METHOD OF MAGNETIC PROFILE ANALYSIS

(2.1) Introduction

(2.2) Profile Spectra

(2.2.1) Spectrum of a Profile Crossing a Single Anomaly

(2.2.2) Spectrum of a Profile Crossing a Sequence of Bodies

(2.3) Evaluation and Discussion of Terms Related to Profile Spectra

(2.3.1) Geomagnetic Field Vector Term

(2.3.2) Magnetic Moment Vector Term

(2.3.3) Width of Bodies Term

(2.3.4) Thickness of Bodies Term

(2.3.5) Depth to Bodies Term

(2.4) Practical Procedure

(2.5) Examples

(2.6) Some Precautions and Limitations

(2.7) Conclusions

NEW METHOD OF MAGNETIC PROFILE ANALYSIS

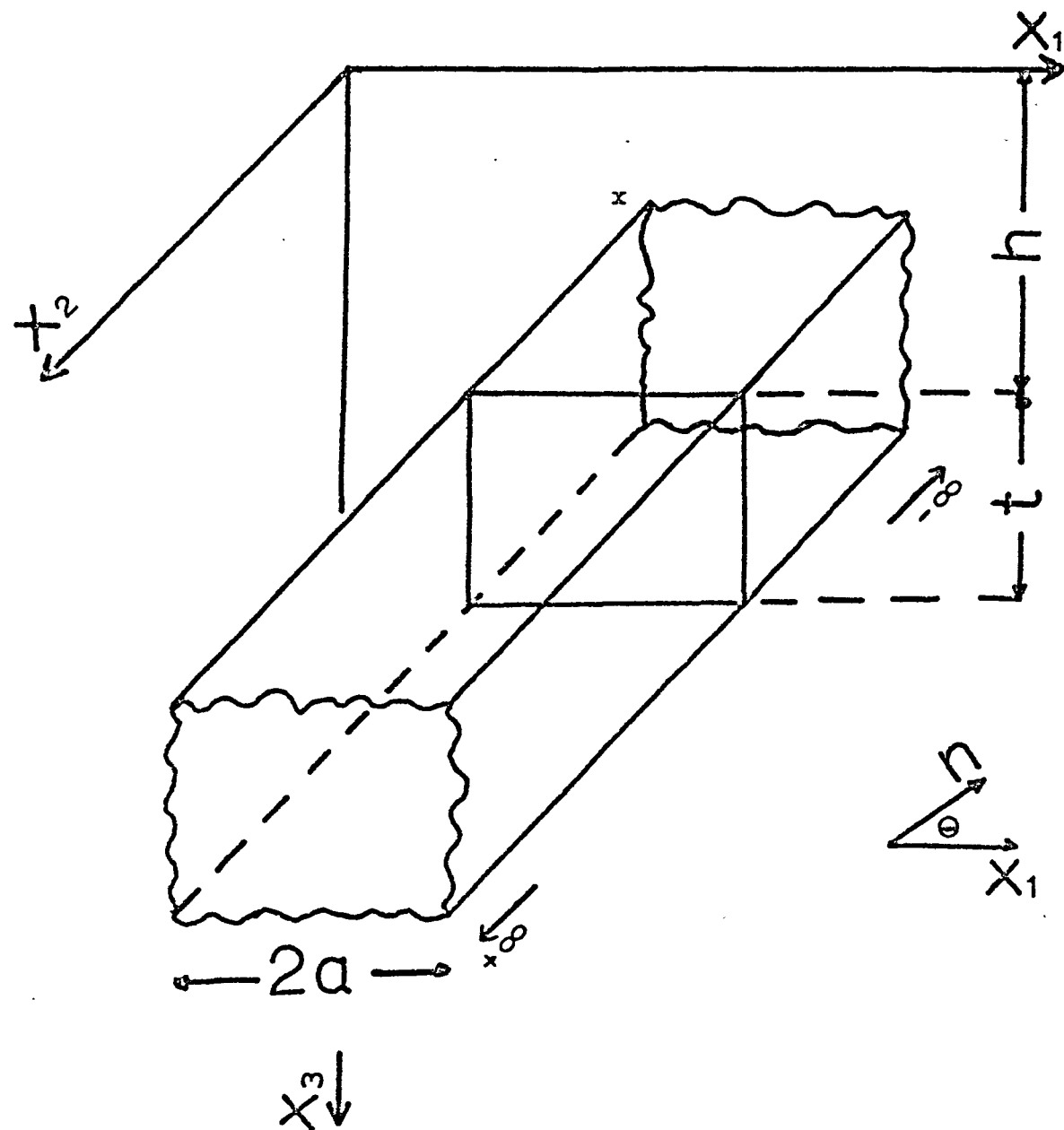
(2.1) Introduction

It is readily observed that the magnetic profiles presented in chapter (4) (e.g. figure (22)) are each composed of a large number of anomalies. From these profiles single isolated anomalies may be interpreted by the usual modelling techniques using the geology and magnetic field vector of the underlying bodies as constraints. This method is practically useless for analysing the very large amounts of profile data presented here which are contaminated with 'noise' and which cross regions for which the geology and magnetic field vector are only poorly known. The approach developed here, is the profile version of the 'Statistical Models Method' which Spector and Grant (Spector (1968), Spector and Grant (1970)) successfully applied to contoured data. This is a direct method of finding average depths to ensembles of bodies using the data in the wavenumber domain. The basic assumption is that the sources of the anomalies belong to ensembles of 'two dimensional' prisms which have widths, thicknesses, depths and magnetic moment vectors rectangularly distributed about mean values. Using this approach it is found that the slope of the energy spectrum curve depends only on the average dimensions and depths of the sources. Other advantages of using the Fourier representation of the data are also described. The techniques are then applied to a wide range of situations with considerable success.

(2.2) Profile Spectra

(2.2.1) Spectrum of a Profile Crossing a Single Anomaly

Much of the versatility of the prism model discussed by Spector and Grant (1970) applies to the 'two dimensional' prism (figure (8)) and



Fig(8) Two Dimensional Prism used as the base model.

x is the x_1 coordinate of the left hand side of the prism.

will therefore be used here as the base model for profile analysis.

A rectangular coordinate system is assumed (figure (8)), where the x_1 axis is taken to be coincident with the flight line (at constant height) and is at an angle θ with respect to geographic north (θ is positive when measured clockwise from north) and the prism extends to $\pm \infty$ in the x_2 direction.

The magnitude of the magnetic field produced at the point (x'_1, x'_2, x'_3) by the volume element (dx_1, dx_2, dx_3) at the point (x_1, x_2, x_3) is given by

$$dm = \frac{k}{2a} \frac{\partial^2}{\partial s \partial t} \left(\frac{1}{r} \right) dx_1 dx_2 dx_3 \quad (1)$$

where

r = the distance (x'_1, x'_2, x'_3) to (x_1, x_2, x_3)

$k/2a$ = the magnetic moment/unit volume

∂s = an element of length in the direction of the magnetic moment vector defined by the direction cosines l_i

∂t = an element of length in the direction of the geomagnetic field vector defined by the direction cosines L_i

$$r = ((x_i - x'_i) (x_i - x'_i))^{\frac{1}{2}}$$

where $i = 1, 2$ and 3 . Repeated index will indicate summation (e.g.

$x_i y_i = \sum_i x_i y_i$). Redefine $x_i = x_i - x'_i$.

The total field of the prism shown in figure (8) is given by (Bhattacharyya (1966))

$$m = \frac{k}{2a} \frac{\partial^2}{\partial s \partial t} \int_{h+t}^h \int_{-\infty}^{\infty} \int_{-\infty}^{x+2a} (x_i x_i)^{-\frac{1}{2}} dx_1 dx_2 dx_3 \quad (2)$$

By representing the extent of the prism in the x_1 and x_2 directions by the functions f_1 and f_2 respectively where

$$\begin{aligned} f_1(x_1) &= 1 & x + 2a \geq x_1 \geq x \\ &= 0 & x_1 < x, \quad x_1 > x + 2a \end{aligned}$$

and

$$f_2(x_2) = 1 \text{ for all } x_2$$

which have Fourier transforms

$$\begin{aligned} **F_1(v_1) &= \int_{-\infty}^{\infty} e^{iv_1 x_1} f_1(x_1) dx_1 \\ &= \frac{2 \sin(v_1 a)}{v_1} \end{aligned} \quad (3)$$

and

$$\begin{aligned} F_2(v_2) &= \int_{-\infty}^{\infty} e^{iv_2 x_2} f_2(x_2) dx_2 \\ &= \delta(v_2) \end{aligned} \quad (4)$$

(** capitals will indicate the Fourier transform of the lower case)

$$\begin{aligned} \text{where } \delta(v_2) &= 1 \text{ for } v_2 = 0 \\ \delta(v_2) &= 0 \text{ for } v_2 \neq 0 \end{aligned} \quad (5)$$

(v_1 and v_2 are the angular wavenumber equivalents of x_1 and x_2 respectively) it is possible with the help of expressions derived by Bhattacharyya (1966) to complex Fourier transform the magnitude of the total field expression (2) to obtain:

$$\begin{aligned} M(v_i) &= 2\pi k (jL_i v_i + L_3(v_i v_i)^{\frac{1}{2}}) (j1_i v_i + 1_3(v_i v_i)^{\frac{1}{2}}) \frac{\sin(v_1 a)}{v_1 a} \\ &\quad \cdot (1 - \exp(-t(v_i v_i)^{\frac{1}{2}})) \frac{\exp(-h(v_i v_i)^{\frac{1}{2}})}{(v_i v_i)^{\frac{1}{2}}} \cdot \delta(v_2) \end{aligned} \quad (6)$$

where $j = (-1)^{\frac{1}{2}}$ and $i = 1$ and 2 .

Substituting (5) into (6) shows that all the information in the wavenumber domain is contained along the $v_2 = 0$ axis; this is exactly the same information that is contained in the Fourier transform of any single profile which crosses the prism perpendicular to its infinite axis. Therefore the complex Fourier transform of a single profile crossing the prism in the x_1 direction is given by

$$M(v) = 2\pi k (jL_1 + L_3) (jl_1 + l_3) \frac{\sin(va)}{va} (1 - e^{-tv}) e^{-hv} \quad (7)$$

where v_1 has been replaced by v .

Although the problem is now two dimensional, in that profiles are being analysed, the three dimensionality of the magnetic moment and geomagnetic field vectors is still preserved because l_2 and L_2 are defined by the relation

$$l_i l_i = L_i L_i = 1 \quad (8)$$

where $i = 1, 2$ and 3 .

Finally we have that the energy (power) spectrum is given by:

$$E(v) = M(v)^2 = 4\pi^2 k^2 R_T R_K S C P \quad (9)$$

where

$$R_T = \sin^2 I_T + \cos^2 (D_T - \theta) \cos^2 I_T \quad (10)$$

I_T is the inclination of the geomagnetic field vector,

D_T is the declination of the geomagnetic field vector.

$$R_K = \sin^2 I_K + \cos^2 (D_K - \theta) \cos^2 I_K \quad (11)$$

I_K is the inclination of the magnetic moment vector,

D_K is the declination of the magnetic moment vector.

$$S = \left(\frac{\sin(va)}{va} \right)^2 \quad (12)$$

$$C = (1 - e^{-tv})^2 \quad (13)$$

$$P = e^{-2hv} \quad (14)$$

It is clear that the terms S, C, and P contain all the information on the width, thickness and depth respectively.

(2.2.2) Spectrum of a Profile Crossing a Sequence of Bodies

The above equations apply only to a single anomaly; to analyse a length of profile which may contain many anomalies, a statistical approach is required. The ensemble approach seems most suitable (Spector (1968), Spector and Grant (1970)).

To relate the measurable quantities to those defined by the ensemble theory, the fundamental postulate that the expectation (most probable value) and the ensemble average of the energy spectrum are equal is assumed. Next it is assumed that the profile contains contributions from a single ensemble defined by the parameters

$K, D_T, D_K, I_T, I_K, a, t, h,$

which are independent of each other and rectangularly distributed in the

ranges:- $(0 \text{ to } 2\bar{K}), (\bar{D}_T \pm \Delta D_T), (\bar{D}_K \pm \Delta D_K), (\bar{I}_T \pm \Delta I_T),$

$(\bar{I}_K \pm \Delta I_K), (0 \text{ to } 2\bar{a}), (0 \text{ to } 2\bar{t}), (\bar{h} \pm \Delta h).$

The case for the presence of more than one ensemble is discussed later.

The ensemble average of the energy spectrum is then given by

$$\langle E(v) \rangle = \langle 4\pi \bar{K}^2 \rangle \langle R_T \rangle \langle R_K \rangle \langle S \rangle \langle C \rangle \langle P \rangle \quad (15)$$

where $\langle \quad \rangle$ denotes ensemble average. To make the whole expression additive we simply take the logarithm to give

$$\begin{aligned} \ln \langle E(v) \rangle &= \ln \langle 4\pi \bar{K}^2 \rangle + \ln \langle R_T \rangle + \ln \langle R_K \rangle + \ln \langle S \rangle + \ln \langle C \rangle \\ &\quad + \ln \langle P \rangle \end{aligned} \quad (16)$$

It is clear that only the last three terms affect the gradient of the power spectrum versus wavenumber curve. Thus, if an estimate for the average width of the bodies can be obtained, the final gradient (width factor subtracted) will only depend on the average depths and thicknesses

of the bodies. A similar argument applies to equation (7) for single anomaly analysis. All that follows has a counterpart in the interpretation of single anomalies.

(2.3) Evaluation and Discussion of Terms Related to Profile Spectra

(2.3.1) Geomagnetic Field Vector Term $\langle R_T \rangle$

$$\langle R_T \rangle = \frac{1}{4 \Delta I_T \Delta D_T} \int_{\bar{I}_T - \Delta I_T}^{\bar{I}_T + \Delta I_T} \int_{\bar{D}_T - \Delta D_T}^{\bar{D}_T + \Delta D_T} R_T(I_T, D_T) dD_T dI_T$$

It follows that

(17)

$$\langle R_T \rangle \approx R_T(\bar{I}_T, \bar{D}_T) \text{ provided } \begin{cases} \Delta I_T < 20^\circ \\ \Delta D_T < 20^\circ \end{cases}$$

The inclination and declination of the geomagnetic field vector will vary according to the direction and length of profile, but the conditions (17) still allow long sections of profile to be analysed by this method.

(2.3.2) Magnetic Moment Vector Term $\langle R_K \rangle$

$$\langle R_K \rangle = \frac{1}{4 \Delta I_K \Delta D_K} \int_{\bar{I}_K - \Delta I_K}^{\bar{I}_K + \Delta I_K} \int_{\bar{D}_K - \Delta D_K}^{\bar{D}_K + \Delta D_K} R_K(I_K, D_K) dD_K dI_K$$

Again it follows

$$\langle R_K \rangle \approx R_K(\bar{I}_K, \bar{D}_K) \text{ provided } \begin{cases} \Delta I_K < 20^\circ \\ \Delta D_K < 20^\circ \end{cases} \quad (18)$$

If the induced component of magnetisation is dominant, this term may be set equal to $\langle R_T(I_T, D_T) \rangle$.

If the remanent component is dominant, which is very common, the $R_K(I_K, D_K)$ term may be a highly fluctuating quantity over certain adjacent lengths of profile; the sections of profile for which condition (18) may be applicable must then be analysed separately. If (I_K, D_K) are not known for the particular sequence of rocks crossed then either induced magnetisation must be assumed or much better an estimate may be obtained by using the (I_K, D_K) values from nearest neighbour rocks of the same geological age, for which palaeomagnetic results are available. It is emphasized that \bar{R}_K and \bar{R}_T are only needed if an estimate of \bar{K} is required, these factors do not affect the thickness and depth estimates.

(2.3.3) Width of Bodies Term $\langle S \rangle$

$$\langle S \rangle = \frac{1}{2\bar{a}} \int_0^{2\bar{a}} \left(\frac{\sin(va)}{va} \right)^2 da = - \left(\frac{\sin 2v\bar{a}}{2v\bar{a}} \right)^2 + \frac{1}{\bar{a}} \int_0^{2\bar{a}} \left(\frac{\sin 2va}{2va} \right) da \quad (19)$$

$$= - \left(\frac{\sin 2v\bar{a}}{2v\bar{a}} \right)^2 + \frac{1}{2v\bar{a}} \int_0^{4v\bar{a}} \left(\frac{\sin Z}{Z} \right) dZ \quad (20)$$

$$\text{where } Z = 2va$$

The second term in (20) may be conveniently evaluated numerically using Chebyshev polynomials (R. Burlirsh (1967)). Estimates of the average width $2\bar{a}$ may be obtained by finding the distance between the zeros of the second (vertical) derivative of the magnetic field which is again conveniently obtained by use of the wavenumber domain (see Practical Procedure). For induced magnetisation only the zeros of the 2nd vertical derivative curve are often found to coincide with the sides of the bodies (see also Vacquier et al (1951) and (Bhattacharyya (1965)) and for remanent magnetisation dominant, the distance between the zeros

of the second derivative curve are still found to be a fair estimator of the average widths of bodies (see also theoretical models of Bhattacharyya (1965)).

(2.3.4) Thickness of Bodies Term <C>

$$\langle C \rangle = \frac{1}{2\bar{t}} \int_0^{2\bar{t}} (1 - e^{-t\nu})^2 dt = 1 - \frac{(3 - e^{-2\bar{t}\nu})(1 - e^{-2\bar{t}\nu})}{4\bar{t}\nu} \quad (21)$$

This term is identical to the equivalent derived by Spector and Grant (1970). For sufficient length of profile this term combined with the average depth term (below) has the effect of producing a broad peak in the energy spectrum versus wavenumber curve.

(2.3.5) Depth to Bodies Term <P>

$$\langle P \rangle = \frac{1}{2\Delta h} \int_{\bar{h}-\Delta h}^{\bar{h}+\Delta h} e^{-2h\nu} dh = \frac{e^{-2\bar{h}\nu} \sinh(2\nu\Delta h)}{4\nu\Delta h} \quad (22)$$

$$\approx e^{-2\bar{h}\nu} \text{ for } \begin{cases} \Delta h < \bar{h}/2 \\ \nu < \frac{1}{\bar{h}} \end{cases} \quad (23)$$

Again this term is identical to the equivalent expression discussed by Spector and Grant (1970). It is found to be the dominating quantity in the spectrum.

A similar depth dependence for profile spectra was obtained by Treitel, Clement and Kaul (1971) who used line sources for their models. It must be emphasized that these authors erroneously used the gravity potential rather than the magnetic potential in their analysis; for their energy spectrum equation to be generally applicable to magnetic data they would need to have multiplied the complex spectrum by the Fourier transform of the $\frac{\partial}{\partial s}$ operator, where ∂s is an element of length in the direction of the magnetic moment vector.

(2.4) Practical Procedure

There are two ways to the energy spectrum of real data:-

- (i) Cosine transform the modified autocorrelation function (Blackman and Tukey (1958)).
- (ii) Smooth the modified periodogram (Jones (1965)).

With the rediscovery of the Fast Fourier transform algorithm (Cooley and Tukey (1965), Special Issue I.E.E.E. (A.U. - 15) (1967)) the latter route is by far the most efficient and offers several additional advantages for magnetic profile analysis. First, it allows the data, now in wavenumber form (raw Fourier coefficients) to be conveniently filtered. The application of the conventional filters (continuation, derivatives and cut off filters) and the design and application of more specialised filters (Spector (1968), Schouten and McCamy (1972), Blakely and Cox (1972), Le Mouel et. al. (1972)), are faster and more accurate in the wavenumber domain (Black and Schollar (1969)). Secondly, the periodogram of separate profiles which cross the same ensemble of bodies may be averaged to obtain a single, more stable estimate of the energy spectrum (Welsh (1967), Tukey (1961)). The number of degrees of freedom (Blackman and Tukey (1958)) for the spectral estimate will then increase from 2 for a single profile spectrum (unsmoothed) to $2n$ for a spectrum that is the result of averaging over n separate profile spectra (unsmoothed). Lastly, the problem of smoothing (stabilizing) a single profile spectrum or an unstable averaged spectrum is more conveniently solved in the wavenumber domain (Black (1970)). It is easier to choose a satisfactory smoothing function to be applied to the periodogram than the equivalent problem of choosing the lag window to be applied to the autocorrelation function. For example Treital et. al (1971) obtained their spectra via the modified autocorrelation function.

For maximum use of profile data, the following procedure is suggested:-

(i) Digitise the data at an interval smaller than the smallest wavelength present; this will depend on the height of the aeroplane above the source and the magnetisation of the source. Remove the regional magnetic gradient (core effect).

(ii) Fast Fourier transform the digitised data. The shortest wavelength (corresponding to the Nyquist wavenumber) will equal twice the digitising interval and the longest wavelength will equal the length of data plus the length of one interval. The Fast Fourier transform used in this study is capable of transforming any number of points which may be factorised into prime numbers upto 23 (the usual Fast Fourier transform requires that the number of points be of the form 2^n where n is an integer (Cooley and Tukey (1965))) and was written by R.C. Singleton, Stanford Research Institute (1968). The restriction to the number of points meant that on occasions upto four points of a data set had to be discarded. The Fourier coefficients may then be stored and any of the following operations performed:-

(a) Upward or downward continuation - multiply the m th coefficient by $\frac{\exp(-2\pi mH)}{T}$ where T is the length of profile and H is the change in height (positive H - upwards)(figure (8) and figures (11) to (14)),

(b) n th vertical derivative - multiply the m th coefficient by $\frac{(-2\pi m)^n}{T}$,

(c) Low pass filter - simply truncate the Fourier coefficients at the desired wavenumber (e.g. Caner (1969)).

(d) Transfer the anomaly to the pole - multiply the Fourier Transform by a term of the form $A e^{j\phi}$ where A and ϕ are both functions of

I_T , I_K , D_T , D_K , and θ (section 2.2.1) and $j = (-1)^{\frac{1}{2}}$.

Operations (a) and (b) are easily proved by taking the anomaly field vector as independent of the x_2 direction and as very small when compared to the main geomagnetic field, thus enabling the anomaly field to be represented by a harmonic expansion (see also Bhattacharyya (1965) and Henderson (1971)). The operation (d), 'transfer to the magnetic pole', has been the subject of several papers and the reader is referred to these for details of the exact form of the term $A e^{j\phi}$. Blakely and Cox (1972) give the most general derivation of this term while Schouten (Schouten (1971), Schouten and McCamy (1972)) and Le Mouel et. al. (1972) give similar formula to Blakely and Cox (1972) but the derivations are less general.

The filtered data or second derivative curve may then be rapidly obtained by passing the filtered coefficients through the Fast Fourier transform with the exponent reversed (special issue I.E.E.E. (AU-15) (1967)).

(iii) The raw Fourier coefficients may be convolved with a $(-\frac{1}{2}, \frac{1}{2}, -\frac{1}{2})$ filter to cut down leakage in the resultant energy spectrum (leakage from intermediate spectral estimates - (Bingham, Godfrey and Tukey (1967))). This filter has the effect of reducing the energy spectrum by $\frac{1}{8}$ so the final spectrum must be compensated for this (Black (1970)). The periodogram (modified) is then calculated by squaring and adding the real and imaginary modified coefficients. The periodogram can then be smoothed to give a better estimate of the energy spectrum by averaging over different profiles and/ or convolving with an appropriate set of filter coefficients. In all the examples studied by the author, a triangular filter set was found adequate to give the required stability (Cooley, Lewis and Welsh (1967)). Sharp peaks in the spectrum, which may indicate a periodicity in the underlying structure,

must be set equal to the adjacent energy values before smoothing, and replaced subsequently; this process has been termed post-whitening by Black (1970).

(iv) Using the average width of the bodies, which may be obtained by use of the 2nd derivative curve (after any necessary smoothing of the data), the width factor (20) may be calculated and subtracted from the energy spectrum. For reliable estimates, the second derivative should be used in conjunction with both the original profile and a series of upward continued versions of the profile; this is especially important when the profile contains contributions from more than one ensemble of bodies.

(v) The energy spectrum curve will now be ready for depth estimates. Appreciable changes in the dominant gradient will indicate the presence of more than a single ensemble of bodies and the linear parts of the curve must be analysed separately (Spector and Grant 1970). The average depth is given by

$$\text{gradient} = -2 \times \bar{h} \quad (24)$$

The effect of \bar{t} on the gradient of the spectrum after the first few harmonics past the peak is negligible, so that the linear parts of the curve will only depend on \bar{h} .

(vi) The presence of broad peaks may indicate that certain ensembles are depth limited with respect to the length of profile. These particular peaks are defined by

$$\frac{\partial}{\partial v} (\ln \langle C \rangle + \ln \langle P \rangle) = 0$$

or

$$-2 \bar{h} - \frac{2}{v} + \frac{4\bar{t} (1 - e^{-2\bar{t}v})^2}{4\bar{t}v - (3 - e^{-2\bar{t}v}) (1 - e^{-2\bar{t}v})} = 0 \quad (25)$$

By substituting into equation (25) a value of \bar{h} obtained from the gradient

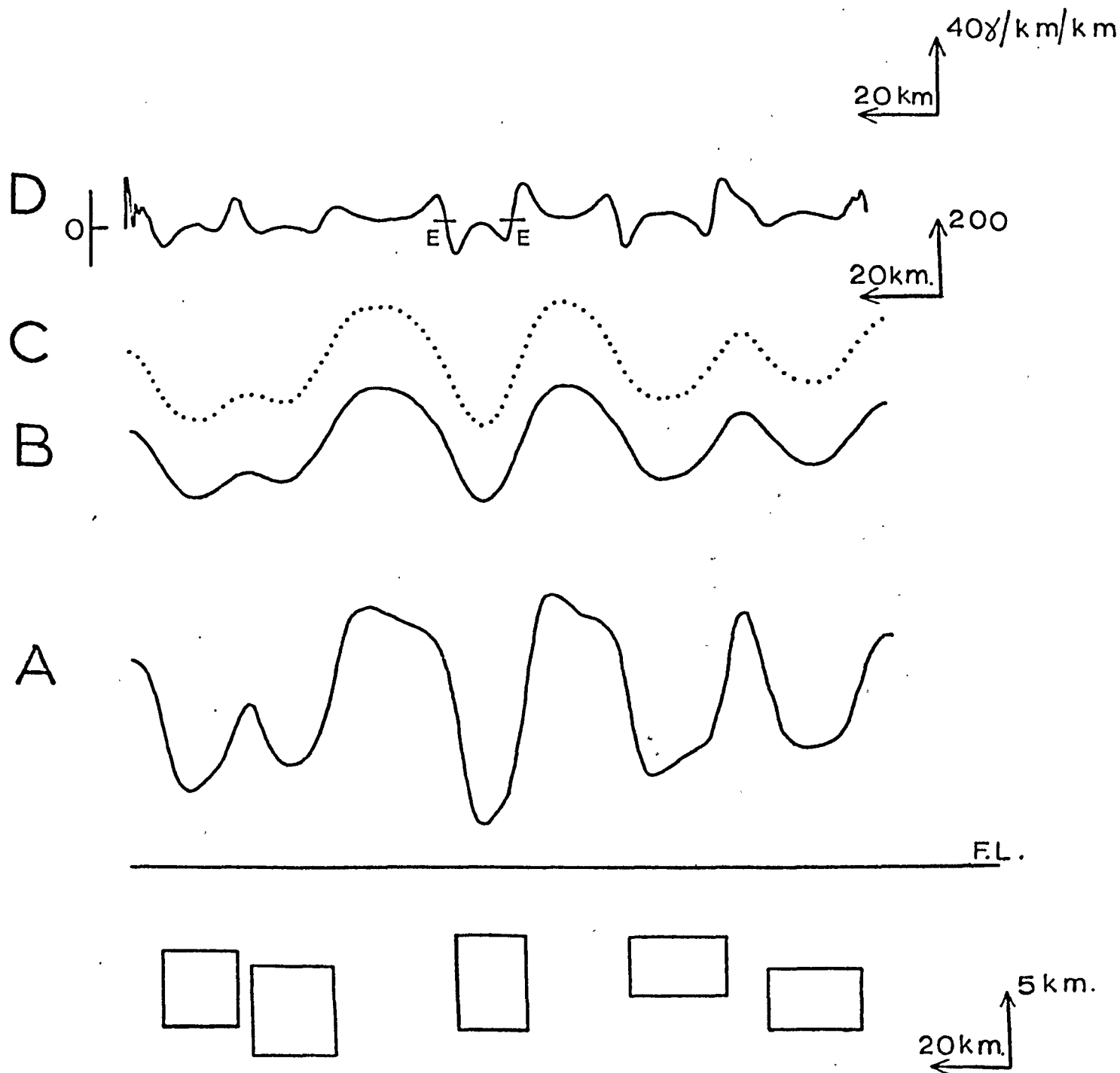
of the curve and the value of v at the peak, it is possible to obtain an estimate of \bar{t} by iteration. Unfortunately, very small errors in \bar{h} will produce a drastically incorrect value of \bar{t} . There is also the problem of discriminating between peaks due to the above effect and 'non-significant' peaks that are bound to occur when using a limited amount of data. Instead of using equation (25) to give thickness estimates it will often be advisable to just say whether or not the bodies are depth limited with respect to the length of data used. If they are not depth limited, then the sources may be considered in the calculations to have infinite thicknesses.

(2.5) Examples

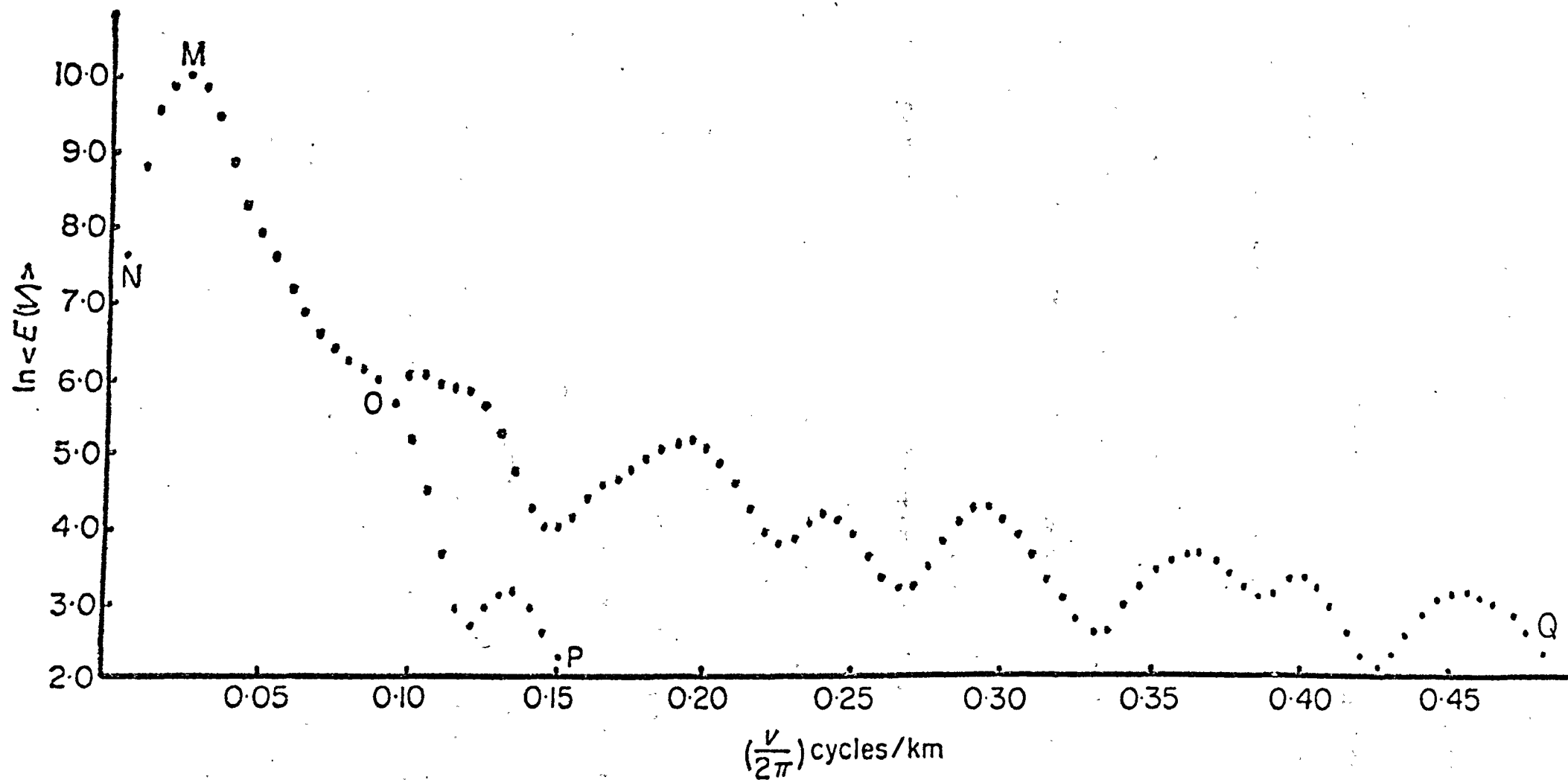
To test some of the ideas discussed, data were simulated using a two dimensional magnetic anomaly computer program (Talwani and Heirtzler (1964)). An example of a distribution of bodies, which are members of a single ensemble, is shown in figure (9) with the resultant anomaly curve (line A). Also shown are curves continued 5 km. upwards by,

- (i) the method described using data in the wavenumber domain (line B),
- (ii) recalculation of anomaly field at the new height using the two dimensional anomaly program (line C).

From a comparison of the two curves it is clear that the method described here produces a rapid and extremely good representation of the continued field (the two curves are identical on the scale shown, except at the last three points). Also shown in the figure, is the second derivative curve D and it is observed that the cross over points with the $y = 0$ axis (example marked E - E) give a fair estimate of the width of the body. These excellent results are to be compared with



Fig(9) A distribution of two dimensional magnetic prisms which belong to a single Ensemble shown with (i) computed magnetic anomaly curve (A), (ii) 5km. upward continued curve using the wavenumber domain calculation (B), (iii) analytically upward continued curve (C), (iv) second derivative curve (D). F.L. denotes flight line.



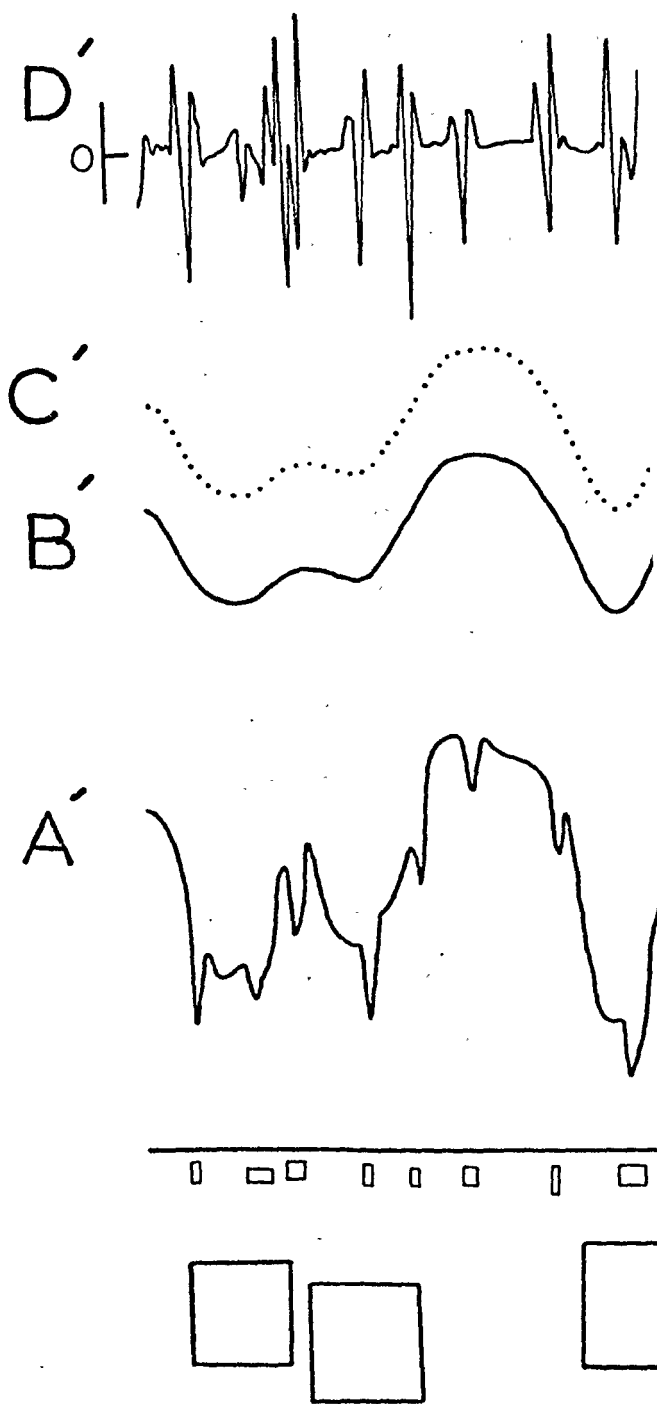
Fig(10) Log energy spectrums smoothed with a triangle filter set. The curve NMOP is the significant part of the energy spectrum for the single ensemble of bodies shown in fig(9) and the curve NMOQ is the energy spectrum for the two ensembles shown in fig(11).

those which would be obtained by convolving the data with a set of filter coefficients which approximates the above operation (Henderson and Zietz (1949)).

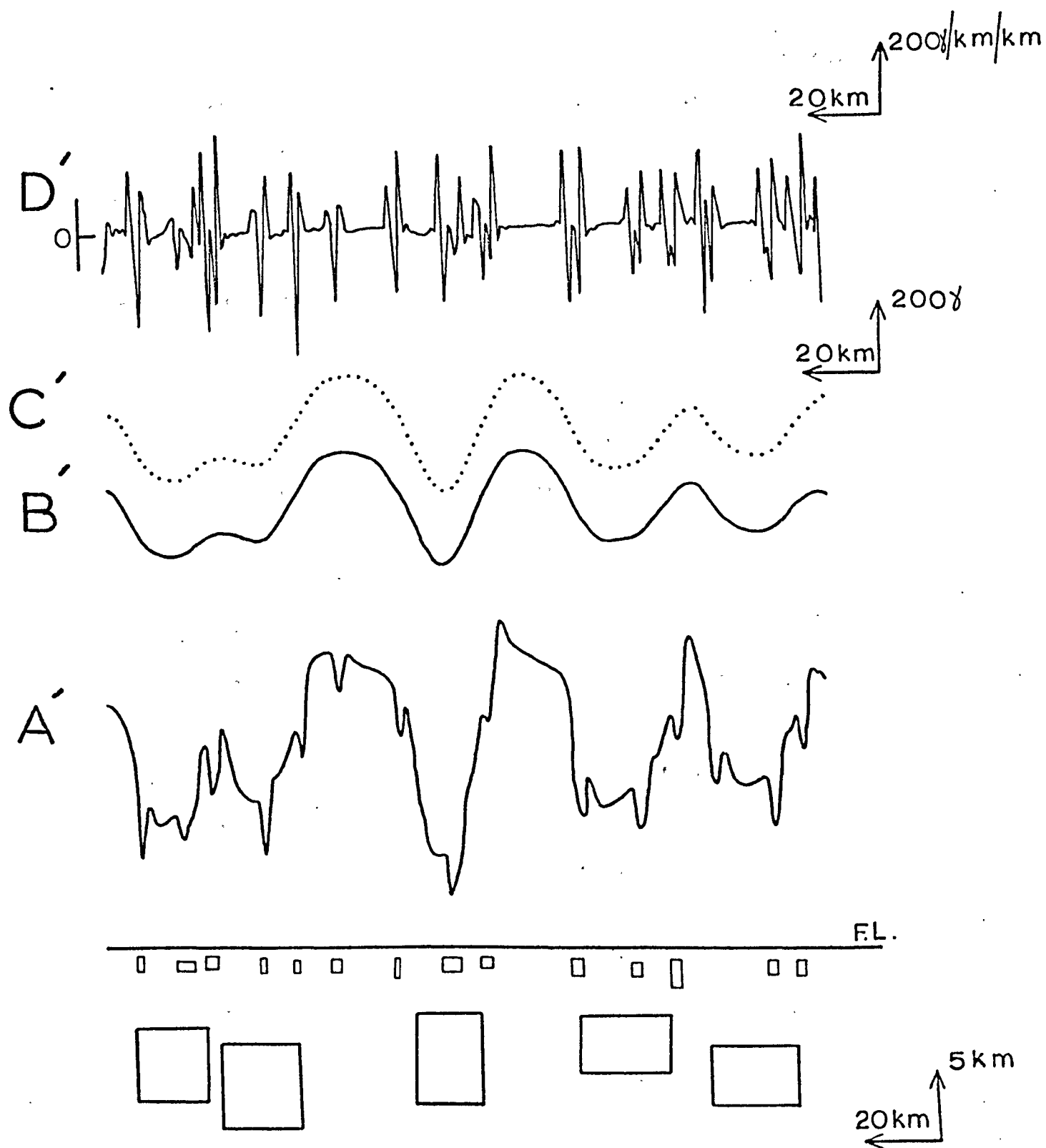
The energy spectrum with the width factor (equation (20)) removed is shown in figure (10) by the curve NMOP. All the diagrams of the energy spectrums shown here have been compensated for the effect of the width. The peak at M in figure (10) indicates that the ensemble of bodies is depth limited and the gradient of the curve which is linear in its decay as predicted, gives a depth by least squares fit of 5.3 km. which is to be compared with the true average model depth of 5.6 km. below the flight line.

In figure (11) a second distribution of bodies belonging to a different ensemble is superimposed on the previously defined pattern (compare A' of figure(11) with A of figure (9)).

This new curve A' is also upward continued 5km. to give the curve B' in figure (11) and this is compared to C', which is the analytically upward continued curve. The two curves B' and C' are identical to the curve C of figure (9) (except at the end points), demonstrating that only the effect of the broad deep seated anomalies is observed at the greater height. There seems to be no distortion (on the scale shown at least) for this configuration of bodies from the field of the shallow bodies when using this method of continuation. Again the second derivative curve D' is shown, but now it represents the effect of both sets of bodies. To separate the effect of the deep bodies from the shallow ones, the original anomaly curve was smoothed (or upward continued) until only the long wavelength anomalies remained (representing the deeper ensemble of bodies). The second derivative curve calculated for this smoothed anomaly curve, which was found to be very similar to the second derivative curve D of figure (9) was then used



Fig(11) Two sets of bodies from
ensemble of bodies cor
the curves shown are a

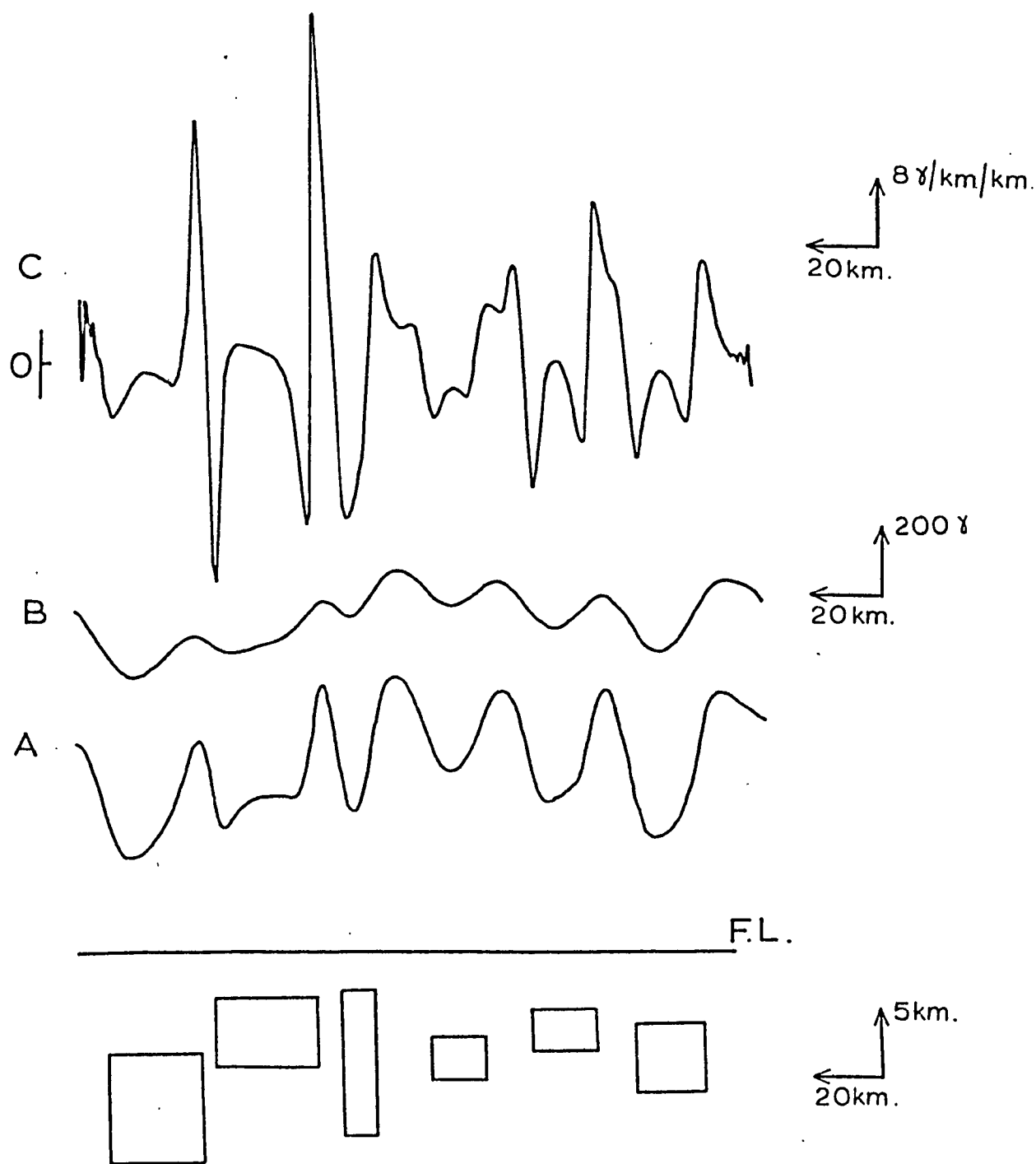


Fig(11) Two sets of bodies from separate and distinct ensembles. The lower ensemble of bodies corresponds to those shown in fig(9). All the curves shown are as for fig(9).

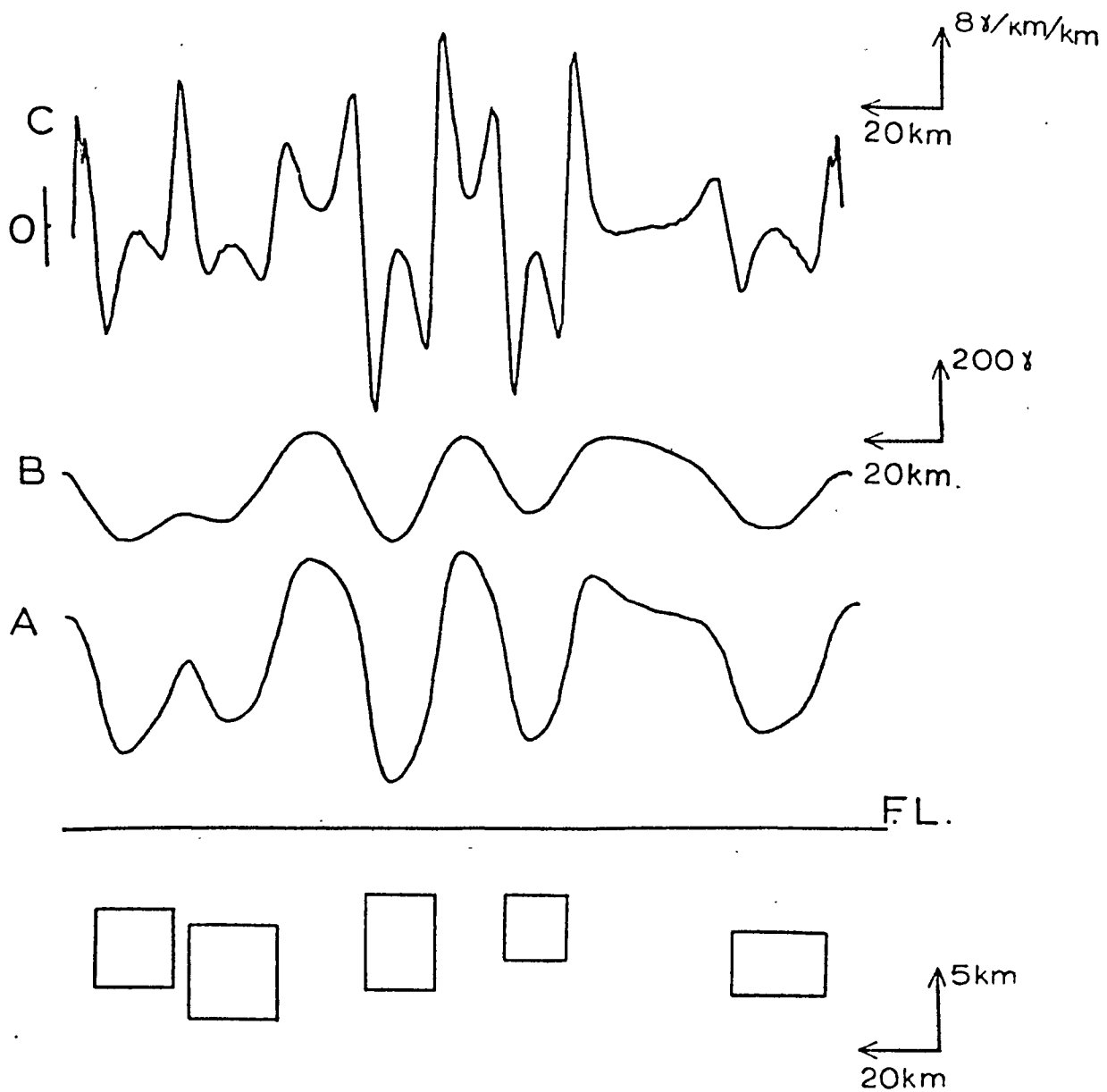
to obtain the average half width for the deeper ensemble of bodies.

By comparing the second derivative of this smoothed anomaly curve with the second derivative curve D' it was then possible to distinguish the parts of the curve D' which were attributable to the shallow ensemble of bodies and thus, an estimate of the average half width of the shallow ensemble of bodies was obtained. As the width factor (20) is not very sensitive to the value of average half width \bar{a} it was only necessary to obtain the average widths to within the order of magnitude of their true value, and generally this second derivative method produced values well within these limits. If the widths were obtained to the above accuracy then the depth estimates were found to be within 15% of the true average value. Without taking the width into account, overestimates in excess of 30% (usually greater than 50%) were obtained.

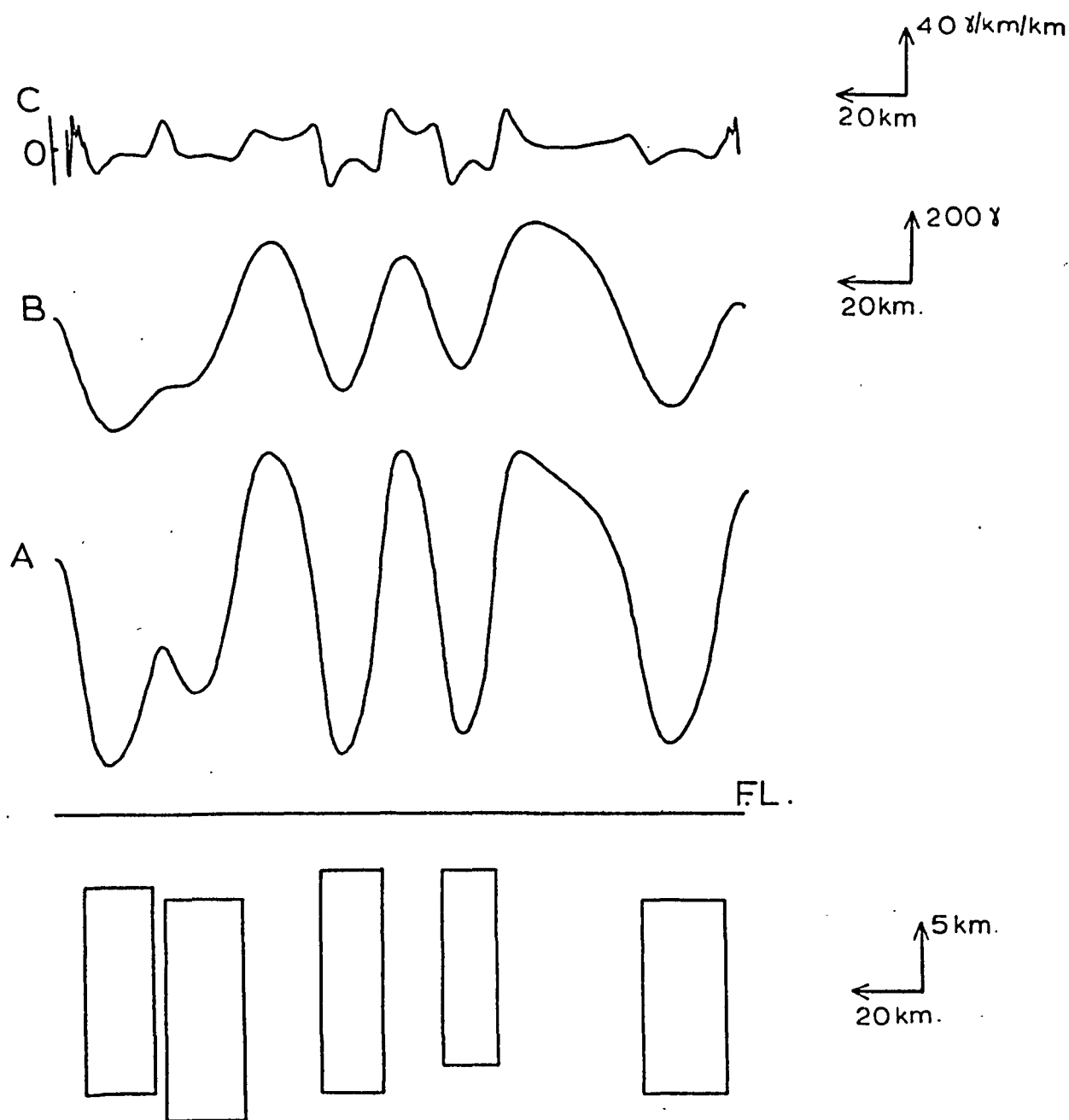
The energy spectrum for this double ensemble case is shown in figure (10) by the curve N M O Q. The smaller width of the second ensemble has been used in the width factor (20) subtracted from this curve past the point marked O; this seemed reasonable when considering the domination of the second ensemble past that point. It is clear that the energy spectrum curve marked N M O is not affected at all by the introduction of the second ensemble and, therefore, this section may be used to obtain depth estimates for the first ensemble. The linear section of curve M O yields an average depth of 6.2 km. (true average model depth 5.6 km.) for the first ensemble and the linear trend between O - Q yields an average depth of 0.54 km. (true average model depth 0.6 km.) for the second ensemble of bodies. An indication of the thickness of the second ensemble is obscured by the interaction of the two ensembles where the dominant peak would occur. Other sets of bodies belonging to single ensembles are shown in figure (12) to (14). Figure (12) shows a set of bodies with variations in depths, widths, thicknesses



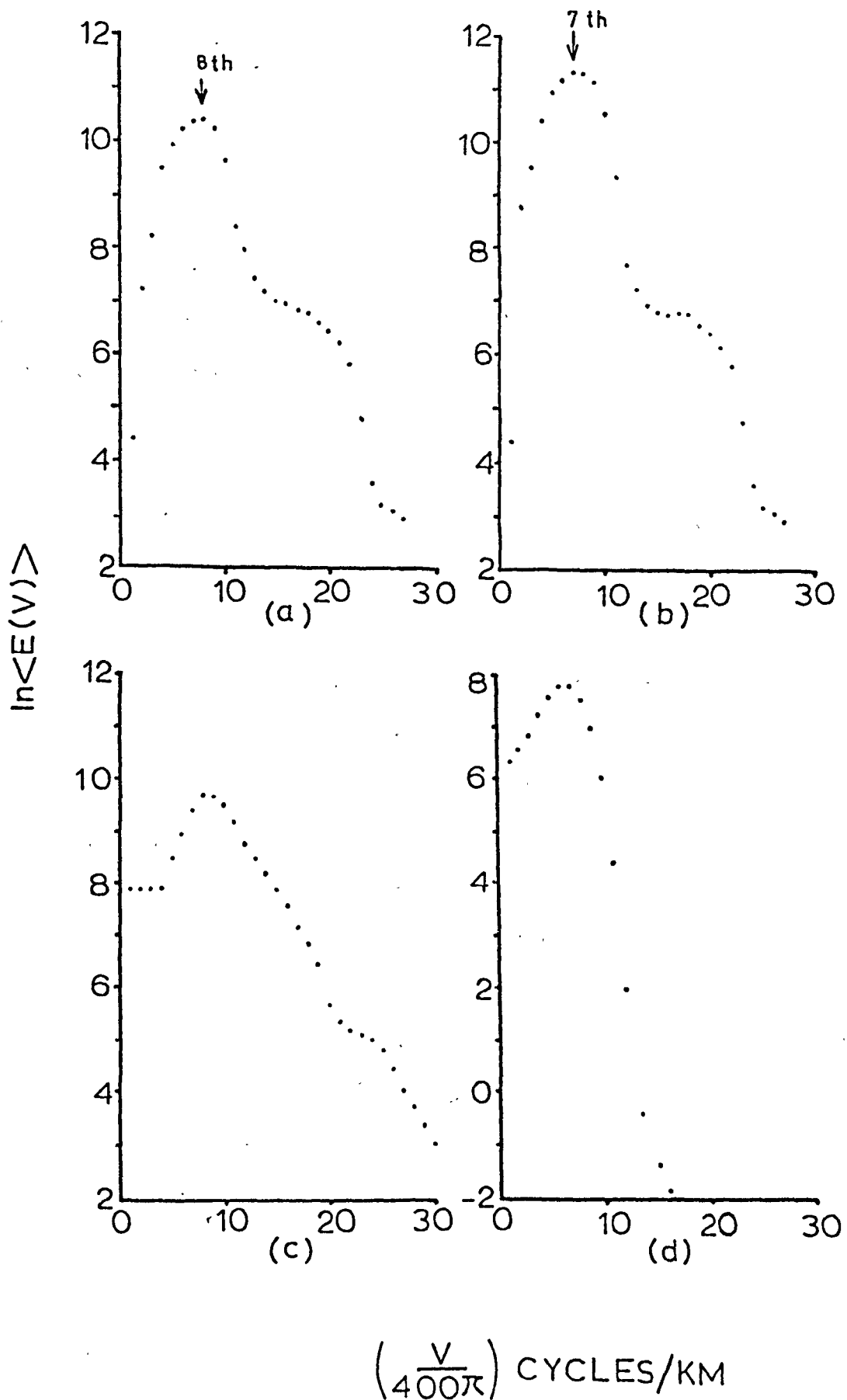
Fig(12) An ensemble of bodies with variations in depths, widths, thicknesses and magnetisation angles which extend to the limits set by the rectangular distributions in section (2.2.2) and the conditions (18) and (23). Here A is the anomaly curve, B is the 5km. upward continued curve and C is the second derivative curve.



Fig(13) An ensemble of bodies similar to, but not identical to, those shown in fig(9). All the curves shown are as for fig(12).



Fig(14) The same ensemble of bodies as shown in fig(13) but with the thickness of the bodies increased by 10 km . All the curves shown are as for fig(12)



Fig(15)

- (a) - log energy spectrum for the ensemble of bodies in fig(13).
- (b) - log energy spectrum for the ensemble of bodies in fig(14).
- (c) - log energy spectrum for the ensemble of bodies in fig(12).
- (d) - log energy spectrum for the ensemble of bodies in fig(13) but with the depth increased to 20km. (average).

and magnetization angles which extend to the limits set by the rectangular distributions discussed in section (2.2.2) and the conditions (18) and (23). Here the curve A is the anomaly curve, B is the 5 km. upward continued curve and C is the second vertical derivative curve. The average depth to the top of the bodies obtained from the gradient of the energy spectrum given in figure (15c) is 4.8 km. which compares very favourably with the true average model depth of 5.3 km.

Figure (13) shows a set of bodies similar, but not identical, to those shown in figure (9), and figure (14) shows the same set of bodies as figure (13) with the thickness of the bodies increased. The curves A to C in these figures are as for figure (12). The calculated energy spectrums are shown in figure (15a) and figure (15b). Average depths calculated from the gradients of these curves yield values of 5.4 km. and 6.0 km. which are to be compared to the true average model depths of 5.3 km. The peaks in both curves around the 7th and 8th harmonics demonstrate that the ensembles of bodies are depth limited with respect to the length of data used. The theory of sections (2.3.4) and (2.4(iv)) predicts a shift of the peak towards the lower wave-numbers for the thicker set of bodies. This is born out experimentally by figure (15a) and figure (15b) where the actual peak occurs at the 8th harmonic for the thinner set of bodies and the 7th harmonic for the thicker set (figure (15b)). Figure (15d) shows the energy spectrum for the ensemble of bodies shown in figure (13), but now the flight height is increased to a total of 20 km. above the average level of the bodies. The average depth estimated from the gradient of the spectrum is found to be 21.2 km., again a very good result.

Two further tests were conducted on sets of bodies not included

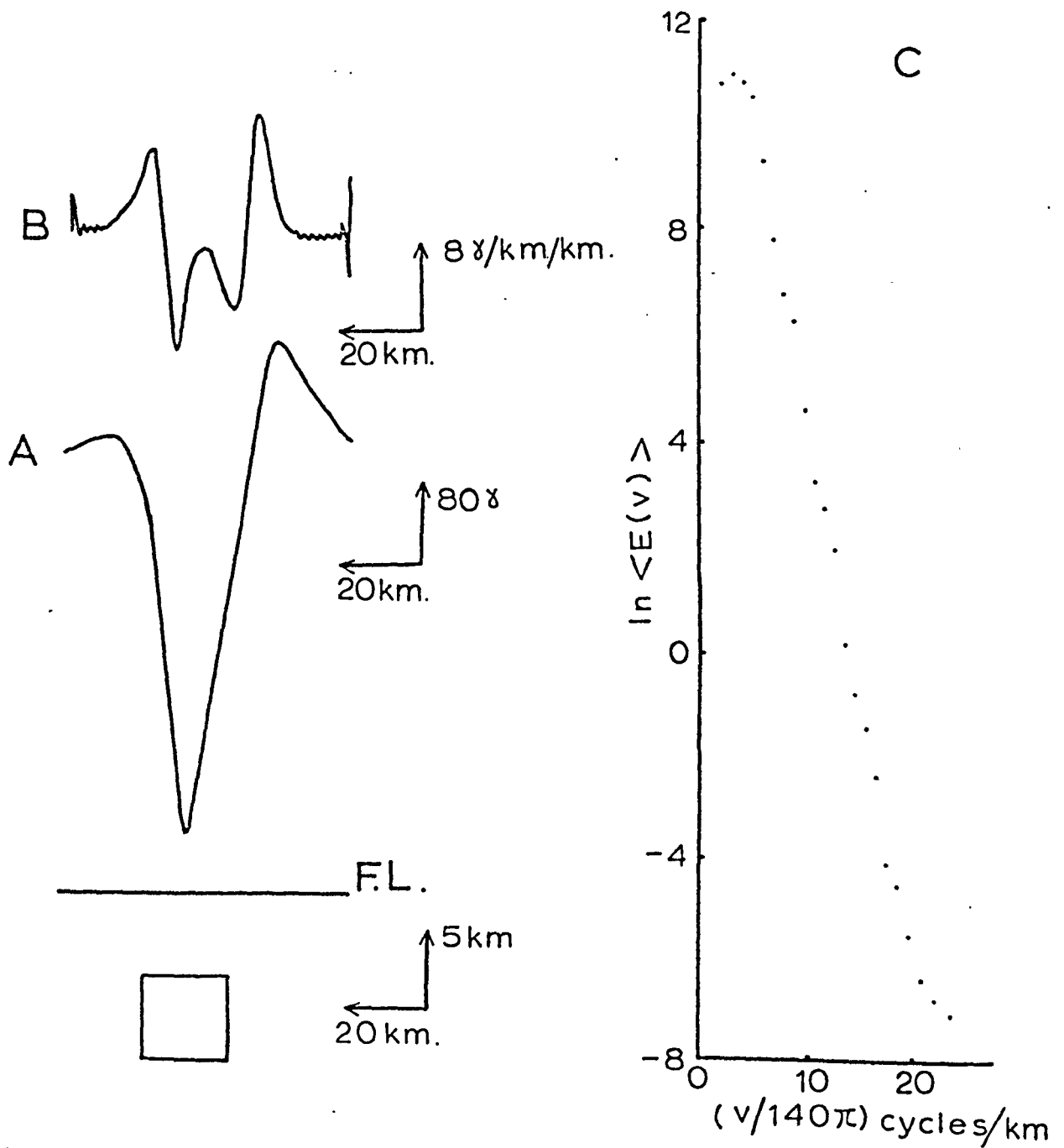
in the above theory. First a single body and its calculated anomaly curve (A), its second derivative curve (B), and energy spectrum are shown in figure (16). Exactly the same procedure was followed as for the ensembles of bodies to give a depth estimate from the gradient of the energy spectrum of 5.4 km. (true model depth 5.3 km.).

Finally the set of bodies shown in figure (13) was taken but now two of the bodies were reversely magnetised with respect to the three remaining bodies (figure (17)). The bodies marked R indicate those reversely magnetised and the curves A to C are as for figure (16). The second derivative is not so good for defining the widths but still yields estimates of average widths which are useful for the calculation of the width factor (20). Surprisingly the average depth to the top of the bodies calculated from the gradient of the energy spectrum yielded the extremely good result of 5.1 km. (true average model depth 5.3 km.). It thus seems that as long as there is not too much interaction of the anomalies from the reversely and normally magnetised bodies the method may be used for this situation. If the normally and reversely magnetised bodies are in contact (e.g. as for the ocean floor, Vine and Matthews (1963), Vine (1966)) there will be significant interaction of their anomalies and the resulting gradients of both the profile and energy spectrum curves will be altered to give anomalously shallow estimates of depth.

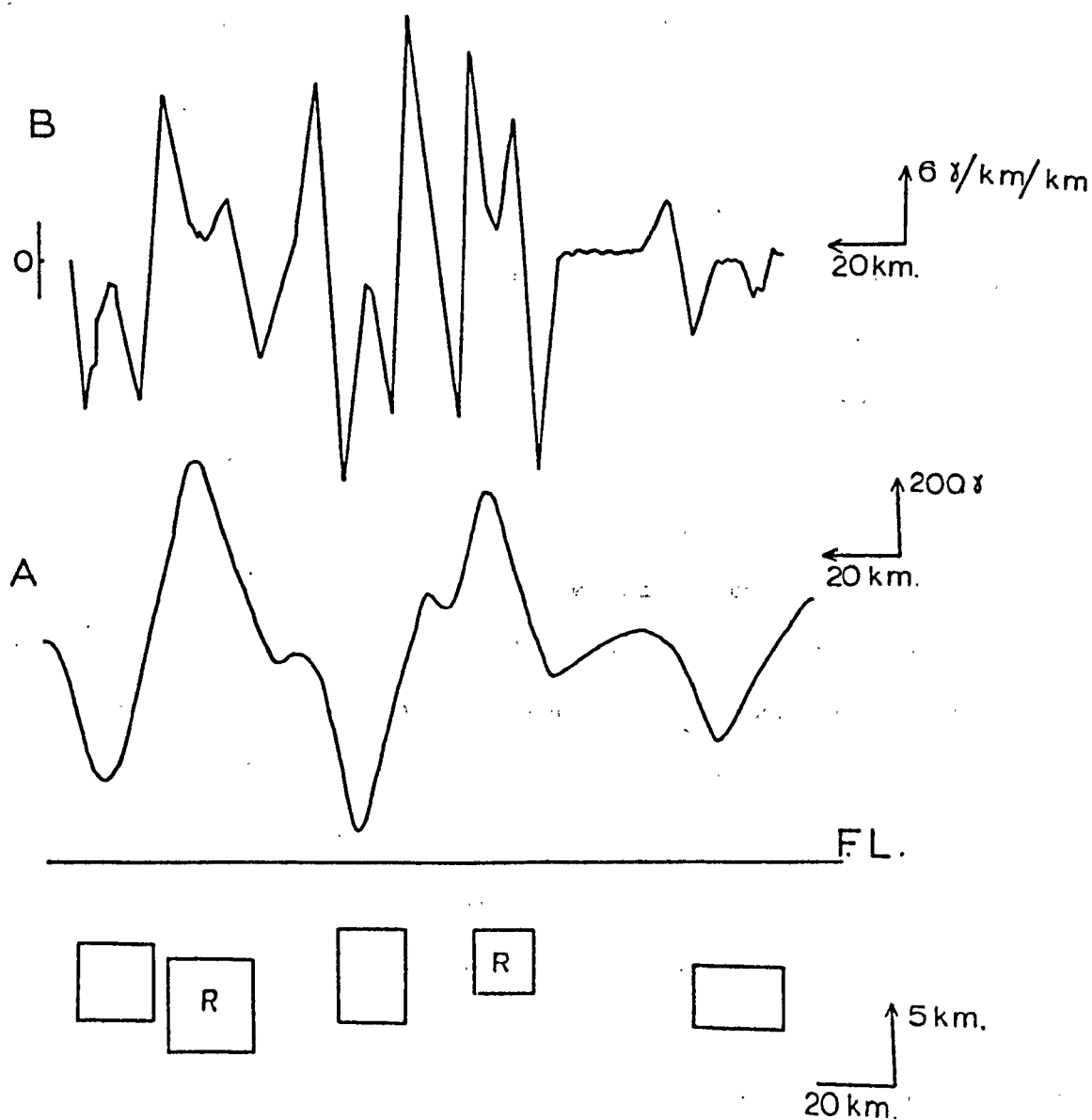
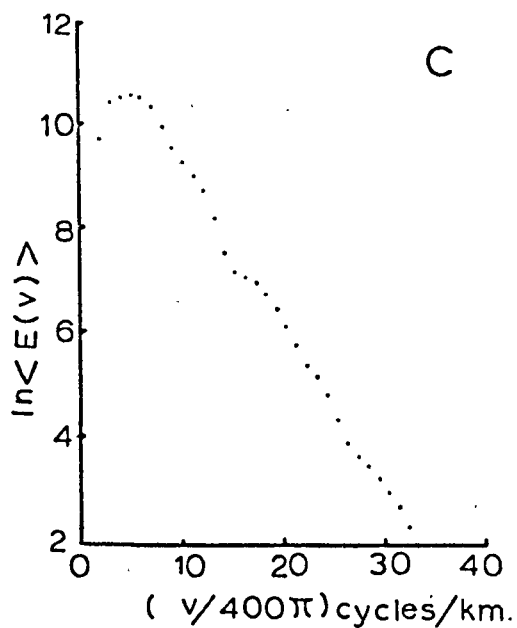
(2.6) Some Precautions and Limitations

Several salient points must be emphasized when using this method and interpreting the results:-

- (i) Inaccurate depth estimates will be obtained if insufficient data values are used. From the experiments with simulated data, 80 data points were chosen as the minimum required to obtain meaningful results.



Fig(16) A single two dimensional magnetic prism shown with (i) the computed anomaly curve (A), (ii) the second derivative curve (B), (iii) the log energy spectrum (C).



Fig(17) The same ensemble of bodies as shown in fig(13) but now two of the bodies are reversely magnetised with respect to the three remaining bodies. The reversely magnetised bodies are marked R and the curves A to C are as for fig(16).

(ii) It is not possible to obtain accurate estimates of average depths if the anomalies are separated by very large distances; large lengths of profile which contain no anomalies must be omitted.

(iii) If there is a complete series of anomalies ranging from short wavelength to long wavelength and they have comparable amplitudes, then it is very likely that the energy spectrum will yield only a single depth, which will be an estimate of the average depth to all bodies. Fortunately in practice the majority of the energy is concentrated in the longer wavelengths and in most cases the effects of the deeper seated bodies and shallow ones separate into quite distinct parts of the energy spectrum.

(iv) Oversmoothing of the energy spectrum may result in a too shallow gradient with consequent anomalous depth estimates. Trietal et. al. (1971) when using line sources, which should give maximum depths, oversmoothed their spectra by applying a narrow lag window to the autocorrelation function. In their attempt to rid the spectrum of non-significant peaks, they obtained spectra which consistently yielded shallow depth estimates rather than deeper as expected.

It is better to smooth the spectrum by convolving with successively longer filter functions (increase the number of the points in the filter by one each time) until the spectrum does not significantly alter with an extra increase in length of the filter (e.g. Jenkins and Watts (1968) give a detailed discussion of the equivalent problem of choosing the lag window to be applied to the autocorrelation function).

(v) When using real data the second derivative curve is found to be 'unstable' if there are anomalies with short wavelengths relative to the Nyquist wavelength. In chapter (4) many anomalies are found to be only five or six times the digitising interval and the second derivative curve will certainly not represent the extent of the bodies causing these

anomalies. For this reason the half width of the higher wavenumber anomalies (those with widths less than approximately ten times the digitising interval) were estimated from the width of the anomaly. The half widths of the longer wavelength anomalies were estimated using the second derivative of the smoothed anomaly curve (profile curve continued 20 km. upwards).

(vi) Two dimensional bodies have been assumed in all the calculations. It is worthwhile to look at the effect of a finite width in the third dimension. Figure (18) shows the two dimensional width factor for a body of half width 8 km. (curve B) compared to the width factor of a three dimensional body of square cross section in the horizontal plane again of half width 8 km. (Spector and Grant (1970)) (shown here as curve A). It is clear that the third dimension of finite extent has the effect of increasing the gradient of the spectrum. As the length of body perpendicular to the profile flight line increases, the effect of the horizontal extent of the body changes from that shown in curve A to that of curve B. Thus anomalies caused by three dimensional bodies will yield deeper estimates of average depths.

(vii) Finally we have assumed vertical sided prisms for our models, bodies with shallow gradient sides may be modelled to fit the anomaly at shallower depths than will be estimated here. Deeper estimates may of course be obtained by neglecting the widths of the bodies, thus assuming line sources of magnetisation as Trietal et. al. (1971) do.

Taking all these points into consideration it appears that estimates of depth calculated by the method presented here are likely to be slightly deeper than the true depth for real data, but nowhere near as inaccurate as those obtained by using the assumption of line sources. We can therefore feel confident that the depths calculated are likely to be maximum depths near to the true average depth.

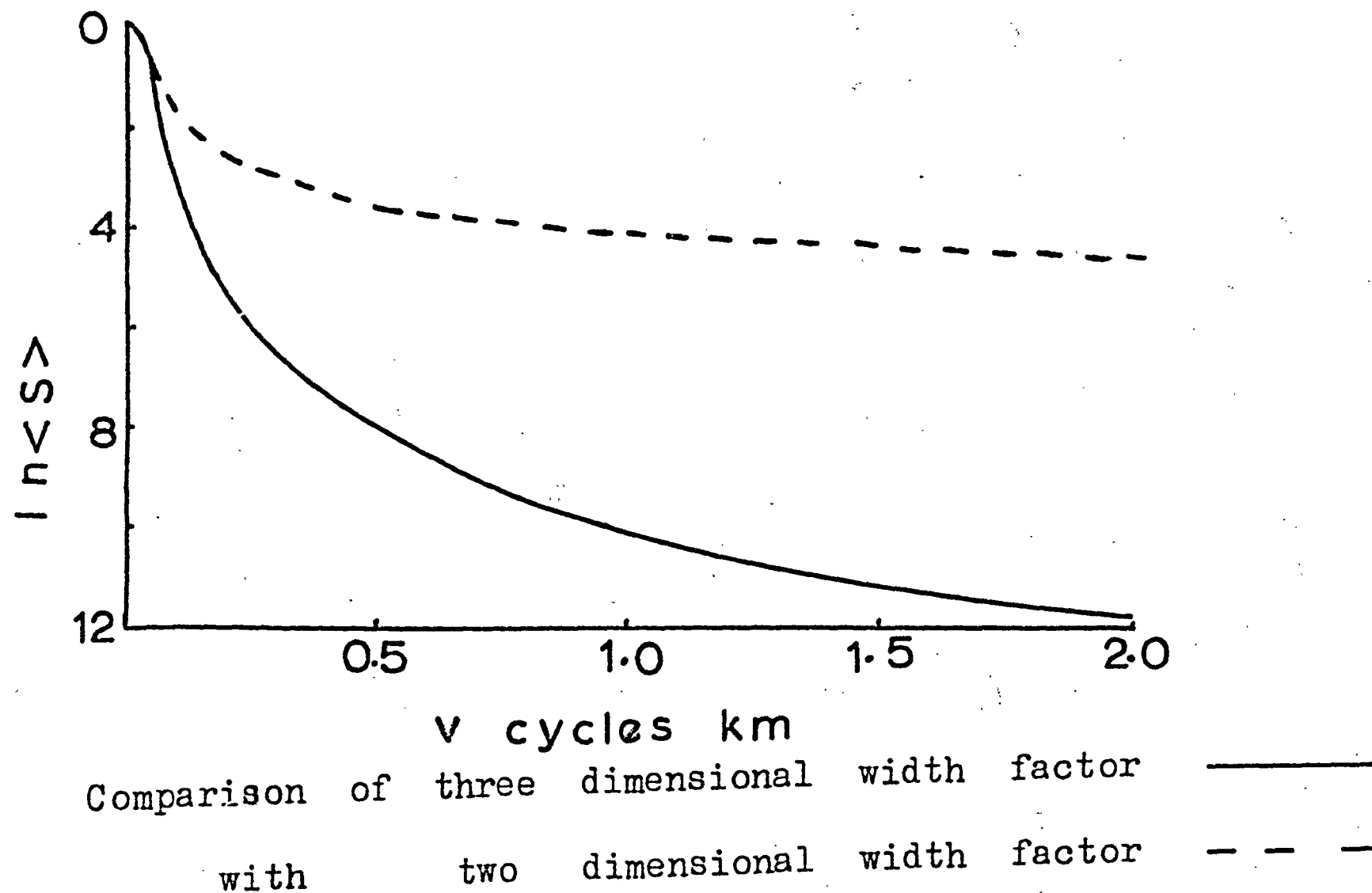


FIG (18)

(2.7) Conclusions

With the data in the wavenumber domain, average widths and depths are rapidly estimated for lengths of profile containing a large number of anomalies caused by magnetic bodies belonging to one or more ensembles. If a large number of profiles cross the same sequence of rocks then it may be possible by averaging over profiles to obtain reliable thickness estimates. This has not been possible in the present work. The first program in Appendix (B) calculates the average thickness of bodies given the average depth and the wavenumber of the peak in the spectrum by an iteration scheme based on equation (25). The second program in Appendix (B) checks this estimate by returning the wavenumber of the peak given the depth and thickness.

The wavenumber domain is also an efficient route to most of the filter operations that are commonly applied to magnetic data. The third computer program in Appendix (B) gives:

- (i) upward or downward continuation curves,
- (ii) n^{th} vertical derivative curve,
- (iii) energy spectrum with three different sets of filter coefficients applied,
- (iv) a least squares fit of a straight line to the linear parts of the energy spectrum curve, all in under 20 seconds for a profile length of 200 points using an I.B.M. 360/67 computer.

The most serious source of error, for real data, is the assumption of two dimensionality, but even the usual modelling techniques use this: the magnetic bodies are taken to be two dimensional prisms with strike perpendicular to the flight path.

C H A P T E R 3

PROJECT MAGNET DATA AND ITS REDUCTION

- (3.1) Introduction
- (3.2) Instrumentation and Accuracy of Data
- (3.3) Digitisation
- (3.4) Note on Interpolation
- (3.5) Digitising Interval
- (3.6) Removal of the Regional Field
- (3.7) Removal of the Diurnal Effect
- (3.8) Residual Field

PROJECT MAGNET DATA AND ITS REDUCTION

(3.1) Introduction

All the data used in Part I of this thesis were obtained by the United States Naval Oceanographic Office as part of their 'Airborne Geomagnetic Survey Project MAGNET' programme. The primary reason for this very large scale survey was to chart more accurately the magnetic field of the Earth. It is fortunate that the data gives sufficient detail to be useful for regional studies.

(3.2) Instrumentation and Accuracy of Data

All the measurements of the total magnetic intensity were made with a Naval Ordnance Laboratory Vector Airborne Magnetometer (N.O.L. report number 1187 (1954)) and were recorded on continuous strip charts. Microfilm copies of these data were used in this study. The Vector Airborne Magnetometer is a relative instrument so that to obtain estimates of the absolute value of the magnetic field the scale of the instrument must be calibrated relative to an absolute magnetometer. If possible, before the magnetometer readings are taken, the instrument is calibrated by either (i) comparison with a magnetometer on the runway or (ii) the aeroplane flies across a magnetic observatory and the scale of the instrument is adjusted accordingly. The effect of the aircraft's magnetic field is also compensated for by comparison with ground based measurements. Navigation fixes are given at every five minutes of flight. These are obtained primarily by celestial fixes although more accurate controls (Doppler radar, Loran A and C, visual sights) are used when possible. The probable maximum errors of these measurements have been estimated to be (G.R. Lorentzen-personal

communication (1971)):-

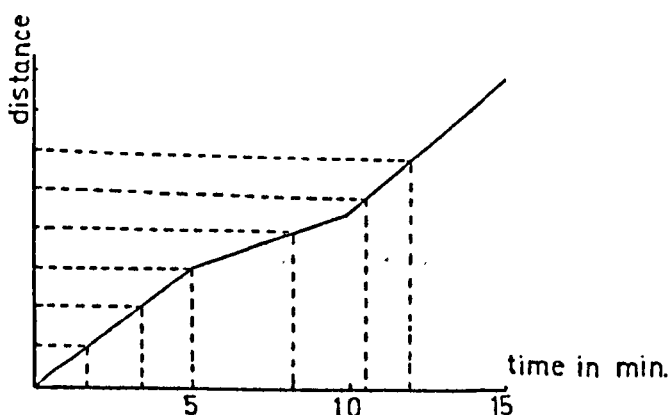
Total magnetic intensity \pm 25 gammas (absolute value)
 Navigational fix \pm 9km. for a flight height of 3km.

(3.3) Digitisation

From the navigational fixes it was possible to calculate the distance travelled by the aeroplane for each five minute interval. If we are given that (latx, lonx) and (laty, lony) are the latitudes and longitudes of the beginning and end of a five minute interval respectively, then from spherical trigonometry the distance travelled is given by:

$$\text{Distance} = \text{Radius (Earth)} \cos^{-1}(\cos(\text{latx}) \cos(\text{laty}) \cos(\text{lonx} - \text{lony}) + \sin(\text{latx}) \sin(\text{laty})).$$

Using this formula it was found that the distance travelled per five minutes could vary by a factor of two for some flights. As most methods of width and depth determination require equispaced data rather than equitime it was necessary to interpolate to find the positions on the microfilm of the equispaced values. First the distance travelled in each five minute interval was calculated. The time of each equispaced value (assuming a constant velocity per five minute interval) could then be obtained in the manner described by fig. (19).



FIG(19)

To perform this calculation by hand for approximately 112 hours of track would have been an extremely time consuming process. A computer program was therefore written which would read in latitudes, longitudes and time, perform the equivalent operation to that outlined above and return the times of the equispaced values. This computer program, which is given in Appendix (A), was written in Algol and run on the KDF 9 computer. With the knowledge of the times of the equispaced values it was then possible to read from the microfilm the corresponding magnetic intensity values.

(3.4) Note on Interpolation

The above process assumes that the aeroplane travelled with a constant velocity within each time interval. Initially the possibility of fitting a nth degree polynomial to the distance versus time curve was considered. Although this permits the possibility of acceleration to be represented in between the five minute interval marks it also allows the possibility of two times to be read for a single position and this idea was therefore discarded. A cubic spline (see Part II, chapter (1)) might be a better form of interpolation. This would yield a smooth distance versus time curve with the physically reasonable conditions of continuous velocity and acceleration across data points, but here again, with highly variable data the possibility of two times being read for a single position in space exists. Although discontinuous velocities and accelerations are a feature of linear interpolation we are guaranteed of a single time for any position of the aeroplane in space. Considering the accuracy of the navigational fixes it is concluded that the linear scheme is adequate.

(3.5) Digitising Interval

Before digitising the data it was necessary to decide on the

interval at which data points were taken. The interpolation program described in Appendix (A) was run for 1, 3 and 5km. intervals for profile T203 (see chapter (4)). The data were not digitised at all three intervals but it was clear that the 5km. interval would miss out important features while the 1km. interval was unnecessarily close. Anomalies of 1 to 2 km. width were generally of very low amplitude due to the effect of flying at high altitudes ($>1\text{km.}$). Bullard et al. (1962) arrived at similar conclusions. The 3km. interval (20 to 40 seconds of flight) was sufficient to outline practically every anomaly encountered on the profiles. Special consideration was given to the exact positions of the peaks of the anomalies in the Mozambique Channel profiles (Chapter (5)). If the equispaced positions missed the peak value then an additional value was taken at the peak and used in the compilation of those profiles. This was particularly important for the correlation of anomalies in the southern part of that region. The actual peak in the continental profiles is not so important and therefore only equispaced values were taken.

(3.6) Removal of the Regional Field

A Fourier analysis of a great circle magnetic profile demonstrates that the Earth's magnetic field may be split into two distinct magnetic components (Allredge et. al. (1963), Bullard (1967)):

- (i) geomagnetic effect (core or dynamo source)
- (ii) crustal effect.

The purpose here is to look at the latter effect and it is therefore desired to remove the geomagnetic effect. This was achieved by the now standard process of subtracting the International Geomagnetic Reference Field (IGRF, 1965.0) (I.A.G.A. (1969)) from each of the profile

values. To reduce the time of computation, the IGRF was calculated at every 102km. and a linear interpolation scheme used to calculate intermediate values. The extreme smoothness of the geomagnetic field over this distance, for this part of the world, fully justifies the linear interpolation (see MacKenzie and Sclater (1971)).

(3.7) Removal of the Diurnal Effect

The very long time of flight of some of the profiles necessitated that there should be some consideration of the effect of the magnetic diurnal variation (Chapman and Bartels (1945)) on the magnetic profiles. Observatory records (magnetograms) for the vertical and horizontal fields were obtained from Lwiro (Zaire), Niarobi (Kenya) and Addis Ababa (Ethiopia). Two conclusions can be derived from observation of the magnetograms taken on the same day as the profiles. First, no magnetic storms were recorded at the times of the flights. Secondly the records show a very consistent shape over the seven years of observation (1959 to 1966). The flight times of each profile was compared to the times of the variation of the magnetic intensity field at the nearest observatory to the flight path. If a total variation greater than 15 gammas was observed over the time of flight then the diurnal effect was estimated. This was achieved by calculating the deviation of the total magnetic intensity from the base value:-

$$dF_o = (V_o^2 + H_o^2)^{\frac{1}{2}} - (V_b^2 + H_b^2)^{\frac{1}{2}}$$

(b is the base value and o the observed value)

for every half hour interval on the magnetograms and linear interpolation used to estimate intermediate values. The gradient of the observatory records was then subtracted from the profile values.

(3.8) Residual Field

After removing the geomagnetic field and the effect of the magnetic diurnal variation, a background trend or constant value was observed on some of the profiles. The constant background field may be due to either:

(i) lack of alignment of the relative magnetometer with an absolute instrument,

or

(ii) poor representation by the IGRF of the regional field for the particular locality. Both reasons can explain the effect on the profile data. Flight 513, which showed a background field of 100 gammas crossed a region sampled by flight T225 which showed no background field at this locality. It is emphasized that the anomaly patterns were very similar, the main differences being explained by the different flight altitudes and flight directions. This would therefore be a case of lack of alignment of the magnetometer with an absolute instrument. The three most southern profiles in the Mozambique Channel (540, 545, 523) all show a large background field (~ -200 gammas) west of Madagascar. Profile 545 was traced east of the island and the background field was observed to gradually change to a large positive value ($\sim +150$ gammas). This would appear to be a case of the IGRF not being sufficiently refined for this locality.

Over some of the land profiles the background trends can also be seen to be parts of longer wavelength anomalies of widths 800 to 2000 km. with amplitudes as high as 100 to 200 gammas. In the average depth analysis of the profiles in chapter (4) the lengths of magnetic data to be analysed are split into tectonic, geologic, or magnetic units and these are usually less than 800km. length. Most

of these could therefore be compensated by removing a linear trend term. This linear term was estimated and subtracted before the energy spectrum was calculated. The removal of the linear gradient was found to only affect the first four 'harmonics' and often this did not alter the depth estimate to the first decimal place quoted.

C H A P T E R 4

INTERPRETATION OF PROJECT MAGNET PROFILES ACROSS THE AFRICA CONTINENT

(4.1) Introduction

(4.2) Notes on the Variables which affect the Shape and Size
 of a Magnetic Anomaly

(4.3) Notes on the Method of Average Width and Depth Estimation
 as Applied to the Project MAGNET Data

(4.4) Magnetic Profile - Geology Interpretation

(4.4.1) Flights T211 and 522

(4.4.2) Flights T213 and 517

(4.4.3) Flight T225

(4.4.4) Flight T203

(4.4.5) Flight T220

(4.4.6) Flight T219a

(4.4.7) Flights T201 and T202

(4.4.8) Flights T204 and T205

(4.4.9) Flight 508

(4.4.10) Flight 511

(4.4.11) Flight 506

(4.4.12) FlightT208

(4.5) Summary and Discussion of the Magnetic Characteristics
 of African Tectonic Units

(4.5.1) The Mozambique Orogenic Belt

(4.5.2) The East African Rift and Related Structures

(4.5.3) The Kalahari and Congo Basins

(4.6) Discussion of the Average Depth Estimates

(4.6.1) Shallow Ensembles

(4.6.2) Deep Ensembles

(4.6.3) Comparison of Average Depth Estimates to 'Deep'
African Magnetic Sources with Estimates from
other Continents

(4.7) Conclusions

INTERPRETATION OF PROJECT MAGNET PROFILES ACROSS THE AFRICAN CONTINENT

(4.1) Introduction

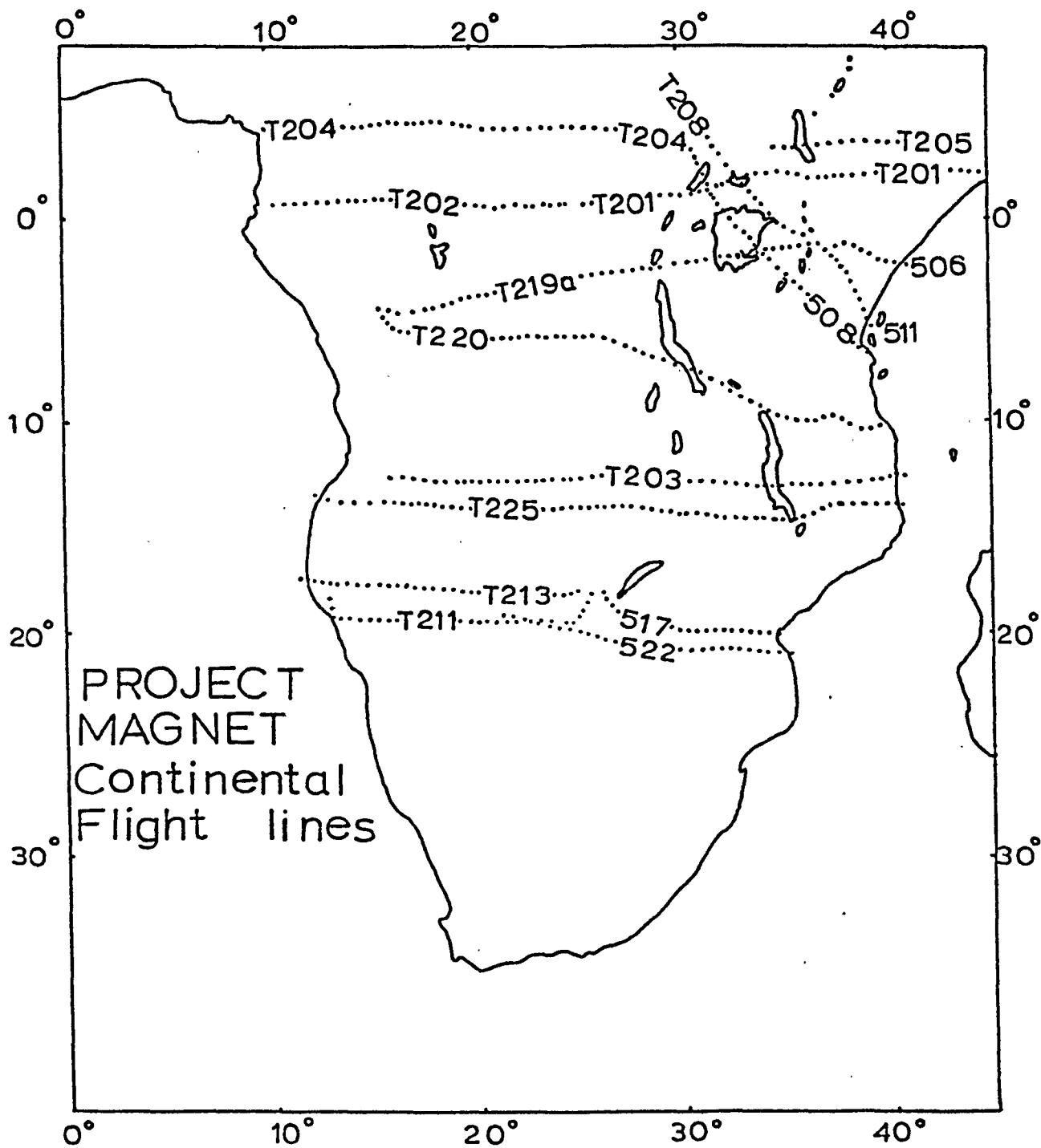
The flight paths of the Project MAGNET profiles used in this chapter are shown in figure (20). The latitudes and longitudes of the beginning and end of each profile, together with the flight dates are given in table (8). The flight paths shown were chosen for study with the following objectives:

- (i) To analyse 'transcontinental' magnetic profiles and look for any magnetic characteristics which may be related to the surface geology or tectonics. Figure (21) shows the Project MAGNET flight paths superimposed on a tectonic map of Africa (see chapter (1) for the sources of this map). The 'transcontinental' profiles are plotted together in figure (22); all transcontinental profiles are in an east to west direction (figure (20)) and most of the tectonic or geological units discussed in chapter (1) have been overflowed.
- (ii) To look at the effect, if any, of the East African Rift System on the magnetic 'pattern' of Africa. As well as the transcontinental profiles a number of shorter profiles (250 km. to 1000 km. length) are analysed for this purpose (figure (20)). These shorter profiles are plotted together in figure (23) .

As a first step the variables which affect the shape and size of a magnetic anomaly are briefly reviewed and this is followed by a note on the application of the techniques of chapter (2) to the Project MAGNET data. The magnetic profiles are then compared with the underlying geology. At this stage the average width and depth estimates are given. Some of the more important features observed in the magnetic data are discussed and this is followed by a comment on the average depth estimates.

Profile Number	Flight Date	From		To	
		Lat.	Long.	Lat.	Long.
T201	21.10.59	02° 02'N.	44° 03'E.	00° 36'N.	25° 40'E.
T202	23.10.59	00° 33'N.	24° 22'E.	00° 37'N.	10° 28'E.
T203	29.11.59	12° 48'S.	15° 51'E.	12° 36'S.	40° 50'E.
T204	21.01.60	04° 03'N.	10° 03'E.	00° 07'N.	32° 22'E.
T205	25.01.60	03° 07'N.	34° 32'E.	03° 41'N.	41° 43'E.
T208	19.11.60	00° 50'N.	36° 02'E.	03° 36'S.	31° 42'E.
T211	17.02.61	18° 16'S.	25° 39'E.	18° 34'S.	12° 57'E.
T213	08.05.61	18° 05'S.	24° 52'E.	17° 30'S.	11° 30'E.
T219a	13.11.65	01° 23'S.	36° 41'E.	04° 31'S.	15° 23'E.
T220	30.01.66	04° 49'S.	15° 42'E.	10° 06'S.	39° 57'E.
T225	18.04.64	13° 58'S.	40° 13'E.	13° 38'S.	12° 09'E.
506	12.11.65	02° 06'S.	41° 07'E.	01° 26'S.	37° 36'E.
508	22.07.64	00° 06'S.	32° 34'E.	06° 46'S.	36° 09'E.
511	15.11.60	07° 29'S.	40° 04'E.	01° 28'S.	36° 57'E.
517	12.02.61	18° 24'S.	26° 17'E.	20° 02'S.	34° 45'E.
522	04.04.64	19° 28'S.	21° 22'E.	20° 54'S.	34° 08'E.

Table (8) Flight dates and the latitudes and longitudes of the end points of the profiles analysed in Chapter (4).



Fig(20)

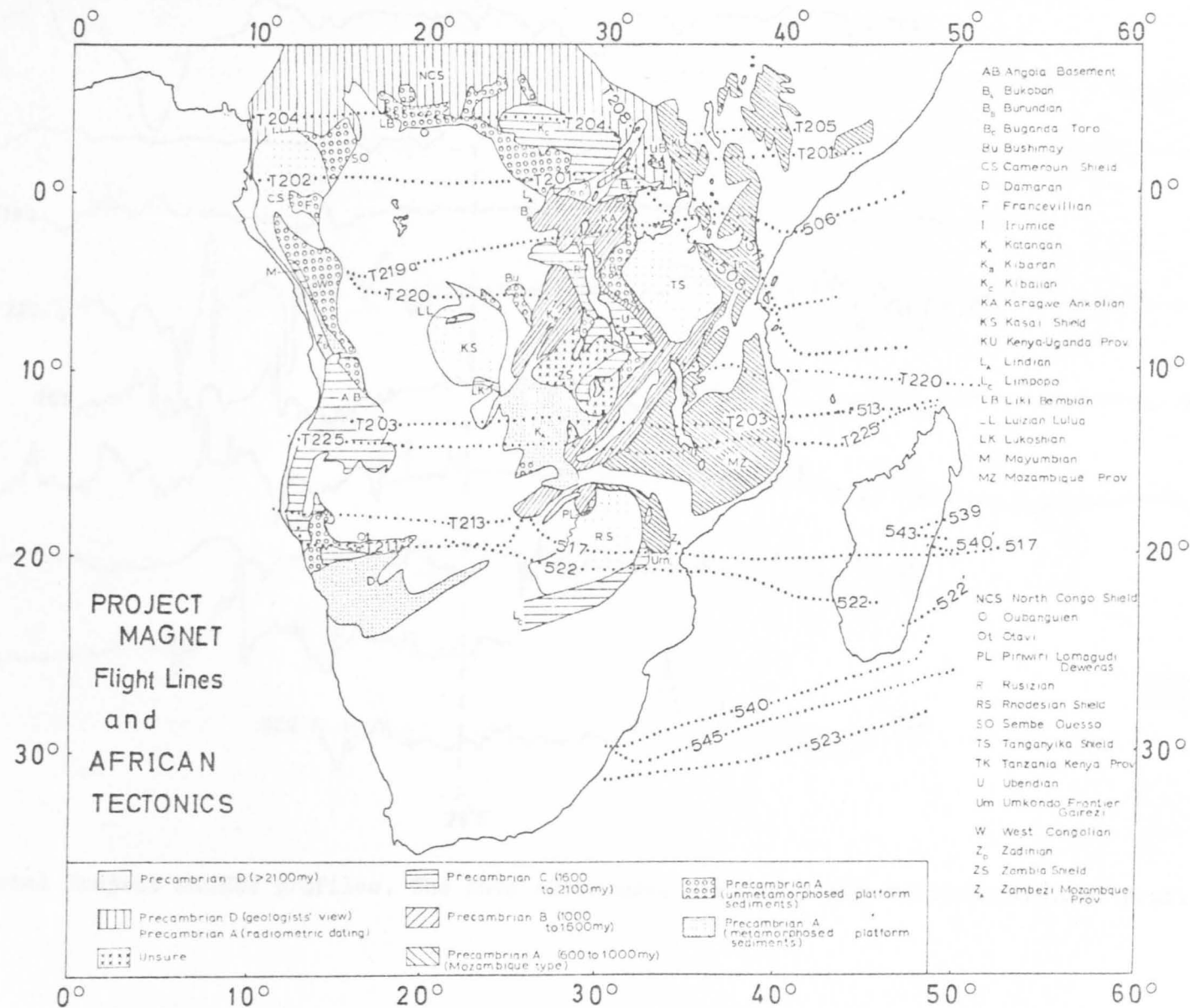


FIG.(21)

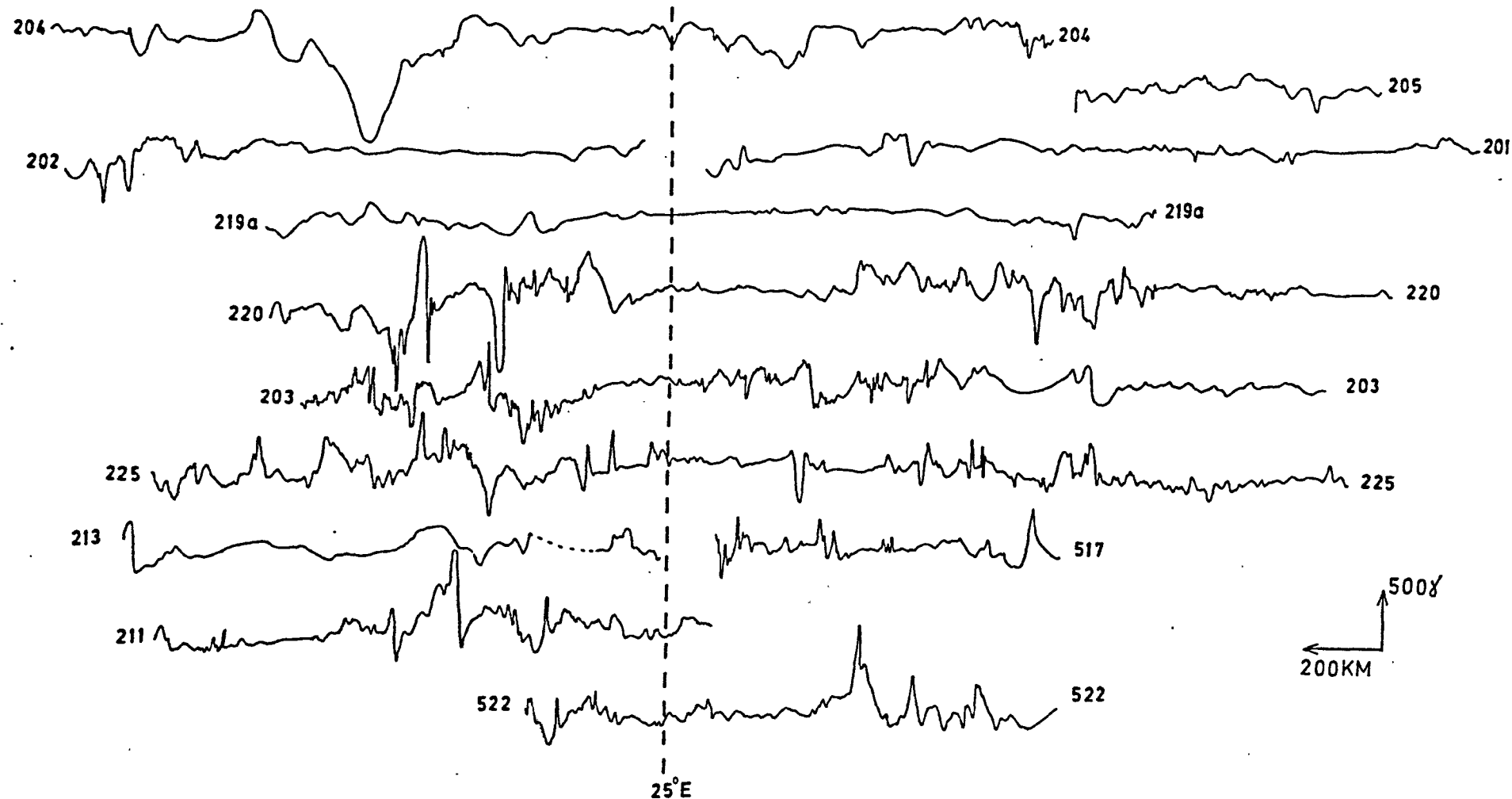


FIG (22) Transcontinental Project MAGNET profiles. The data shown here make up eight transcontinental profiles.

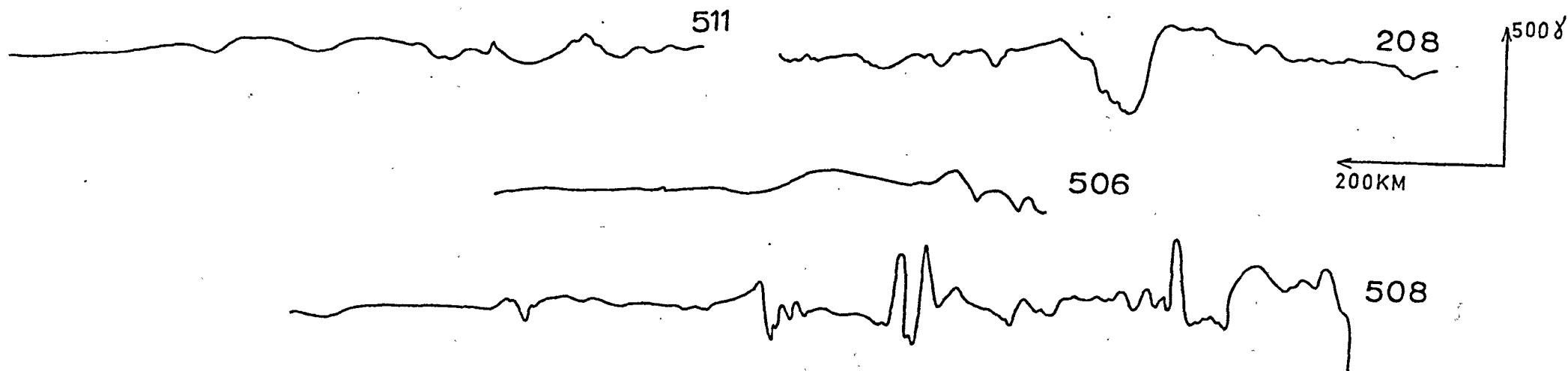


FIG (23) Extra Project MAGNET profiles used for the study of the East African Rift System.

(4.2) Notes on the Variables which Affect the Shape and Size of a Magnetic Anomaly.

A number of factors contribute to the shape and size of a magnetic anomaly. These are:

- (i) The size of the causative body (discussed in chapter (2)).
- (ii) The shape of the body.
- (iii) The strike and dip of the body. Unless other information is available, the strike of the body is usually assumed to be perpendicular to the flight path when only profiles are being analysed.

Although the effect of the dip of the body may be very important (see for example Grant and West (1965)), to obtain estimates of this parameter requires information about the magnetisation vector ((iv) and (v) below). In this study only average quantities are considered (chapter (2)) and all the magnetic bodies are taken to be two dimensional prisms with vertical sides (figure (8)).

(iv) The magnitude of the intensity of magnetisation (total vector) of the body. The magnetisation of a body is governed by the amount of magnetic minerals contained within the body. Table (9) shows the range of susceptibilities and remanent intensities of a number of common rock types. Although the range of values shown for each rock type are wide, certain 'general characteristics' of these crustal rocks may be stated (table (9)).

(v) The direction of the intensity of magnetisation vector (induced + remanent) of the body. This effect may be observed in figure (24) or figure (25), where the anomaly for a two dimensional prism (figure (8)) is plotted for various inclinations (for fixed declination) and various declinations (for fixed inclination). The simulated anomalies were obtained with the Talwani and Heirtzler (1964) computer program.

Rock Type		Susceptibility ($10^3/4$ MKS)	Remanent Intensity (A/m)	Magnetic Characteristics
Basic Extrusive	Basic Extrusive	0.0 to 11.0	0.0 to 15.0	Highly magnetic with the primary component dominant (especially submarine rocks). The magnetisation is usually stable.
	Basalt	0.3 to 2.95	0.2 to 15.0	
	Ocean Basalt	1.0 to 5.0	1.0 to 100.0	
Basic Intrusive	Basic Intrusive	0.0 to 20.0	1.0 to 60.0	Highly magnetic but large crystal size may result in low stability. Therefore secondary remanence and induction may be important.
	Diorite	0.0 to 3.0	0.1 to 1.7	
	Gabbro	0.0 to 10.0	0.1 to 4.2	
Acid Volcanic Rocks	General Acid Rocks	0.0 to 8.0	0.0 to 7.0	Acid to intermediate rocks tend to contain less magnetic minerals than basic rocks. Large crystal size may result in low stability. These rocks often occur as large plutons with resultant large anomalies.
	Rhyolite	1.1		
	Granite	0.0 to 6.0	0.0 to 4.5	
	Granodiorite	0.0 to 8.0	1.2	
Ultra Basic Rocks	Peridotite	12.5	3.18	Highly magnetic, but the large crystal sizes may result in low stability.
Altered and Metamorphic Rocks	General Metamorphic	0.0 to 5.8	0.0 to 7.0	Metamorphic and sedimentary rocks are usually low in magnetic mineral content. Induced magnetisation dominant. Basic and Ultrabasic rocks lose their magnetisation as the alteration increases.
	Schist	0.0 to 0.3	0.0	
	Gneiss	0.0 to 7.0	0.0	
	Greenstone	0.1	0.0	
	Serpentinite	14.0	0.0 to 7.0	
	Charnokite	6.0	7.0	
	Granulite	0.6	0.3 to 0.8	

Table(9) Susceptibility, remanent intensity and magnetic characteristics of some common rock types.

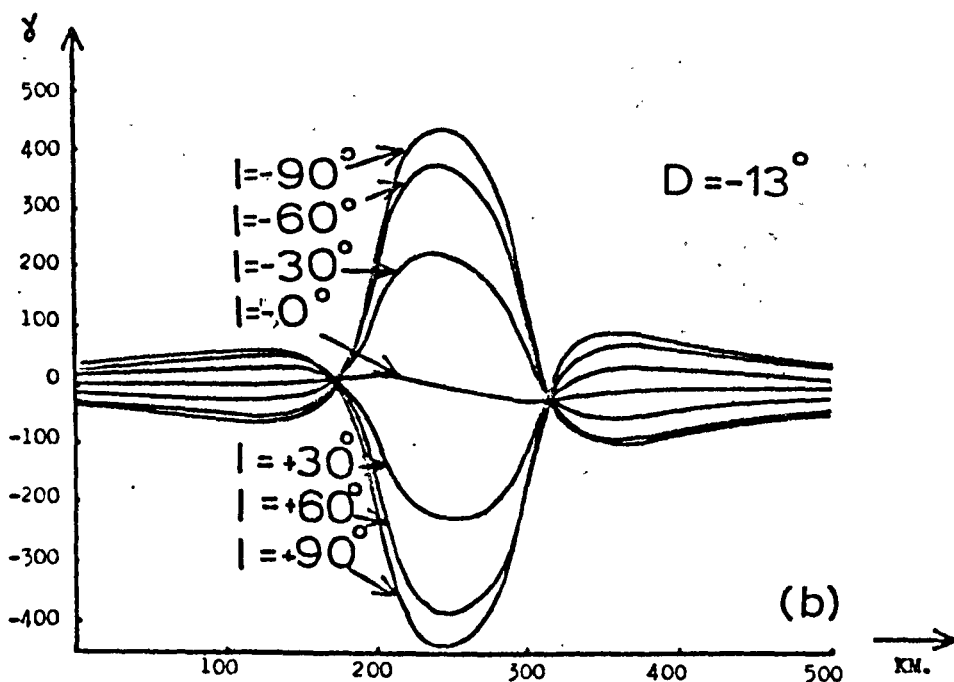
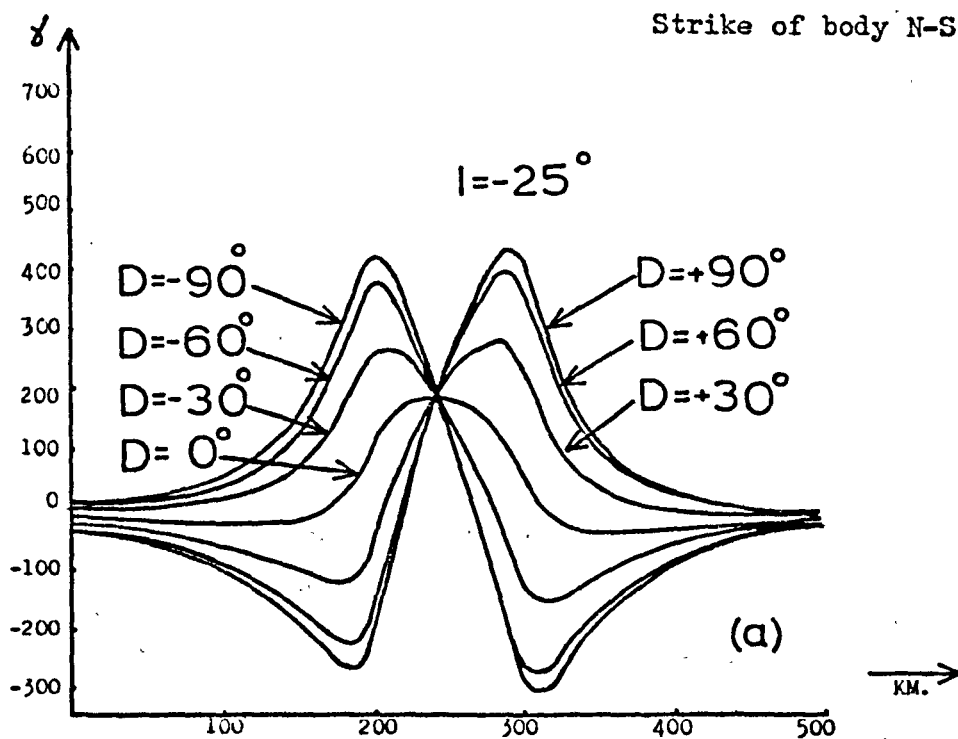
(vi) The intensity and direction of the geomagnetic field at the site of the body. This effect is seen by comparing the anomalies of figure (24), which were calculated for a body at the equator (magnetic dip = -25° , magnetic declination = -3°), with the anomalies of figure (25), which were calculated for the same body at latitude 20°S . (magnetic dip = -58° , magnetic declination = -13°). For the same intensity of magnetisation vector the size of the anomalies at latitude 20°S . are almost double those at the equator.

(4.3) Notes on the Method of Average Width and Depth Estimation as Applied to the Project Magnet Data

To obtain the maximum amount of information from each section of profile a set procedure was adopted:

(i) Each profile was upward continued by 10 km. and 20 km. (for example see figure (26)) to filter out the high wavenumber anomalies due to near surface features. Using the upward continuation filter rather than a simple low pass cut off filter (see section (2.4)) has the advantage that natural anomaly curves are maintained, those which would be observed 10 km. or 20 km. up from the original profile. The upward continued profile could be used to depth analyse the deeper sources, but this is unnecessary as the magnetic effects of the deep and shallow bodies occur in different parts of the energy spectrum for most cases.

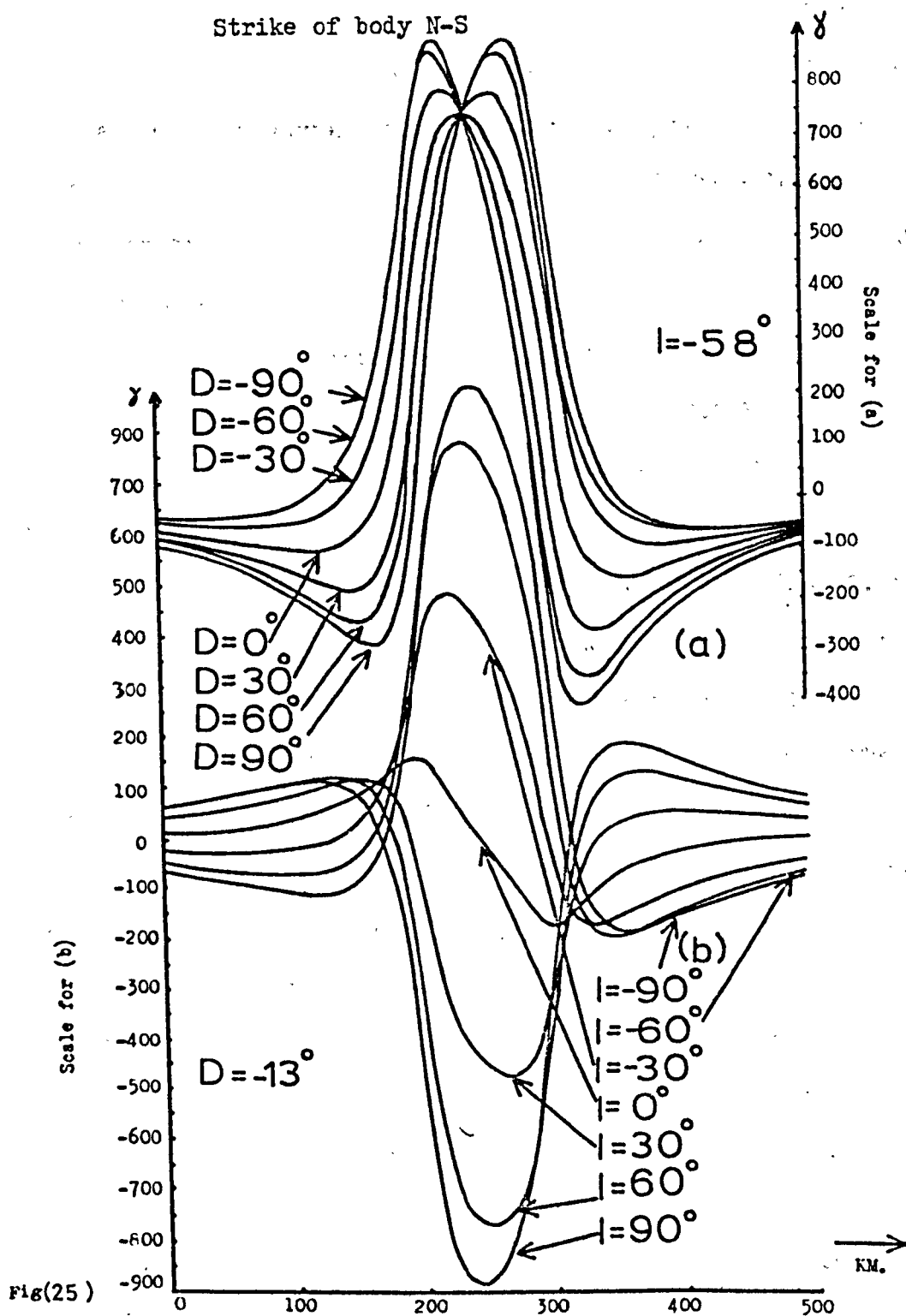
(ii) The second derivative of the 20 km. upward continued curve was computed and this was used to estimate the average width of the deep ensemble of bodies. Small excursions of the second derivative curve across the zero line, which are caused by high wavenumber anomalies not effectively filtered, were not used in the width analysis. The second derivative curves are each shown with the relevant energy spectrum (e.g. figure (27)). The energy spectrum curves show in many of the magnetically



Fig(24)

Magnetic anomaly caused by two dimensional Prism (see fig(8)) at latitude 0° (magnetic dip -25° , magnetic declination -3°). Width of body = 100km., thickness of body = 100km., height of profile above the body = 3km., magnetisation of body = 330 A/m.

(a) shows effect of varying the declination of the magnetic vector with fixed inclination (-25°).
 (b) shows effect of varying the inclination of the magnetic vector with fixed declination (-3°).



Fig(25)

Magnetic anomaly caused by two dimensional Prism (see fig(8)) at latitude 20°S (magnetic dip = -58° , magnetic declination = -13°). Width of body = 100km., thickness of body = 100km., height of profile above body = 3km., magnetisation of body = 330 A/m.

(a) shows effect of varying the declination of the magnetic vector with fixed inclination (-58°)
 (b) shows effect of varying the inclination of the magnetic vector with fixed declination (-13°)

quiet zones of the Mozambique Orogenic Belt (section (4.5.1)) a deep (4 to 20 km. depth) source of bodies. The presence of this deep set of bodies was not at all obvious in the original profiles and only appears as 30 to 50 gammas undulations in the upward continued curves (e.g. figure (44)). It was found that most of these low amplitude, long wavelength anomalies show up extremely clearly in the second derivative curves (e.g. figure (48)). Many more data points would be required to delimit the extent of the shallow, high wavenumber, sources using the second derivative method (see section (2.5)). Therefore the width of the anomaly was used as the estimate of the extent of these bodies.

(iii) The modified periodogram was computed (section (2.4)) and smoothed until a stable estimate of the energy spectrum was obtained. The stability was based on a subjective observation of the periodogram as it was convolved with successively longer filter sets. When the spectrum did not change significantly with a single increase in the length of the filter set, then it was taken to be stable. Lengths of triangular filter sets ranging from seven (weights of 1, 2, 3, 4, 3, 2, 1) to fifteen values were found adequate to smooth all the energy spectra presented in this thesis. Instead of removing high amplitude peaks in the spectrum before smoothing (these are rare in the African data) as advocated in chapter (2), regions near to peaks were omitted from the least squares depth analysis; this was necessary to analyse all the data presented within a reasonable length of time. At this stage the spectrum was truncated in the high wavenumbers at the position where it becomes flat (white spectrum) or highly oscillating, indicating the 'noise' in the data which is not accounted for in the theory of chapter (2).

(iv) If two ensembles are shown in the spectrum (see section (2.5)) then:

(a) The effect of the width of the longer wavelength anomalies (equation (20)) was removed from the high gradient slope of the spectrum using the average width obtained from the second derivative of the upward continued profile.

(b) The effect of the width of the short wavelength anomalies was removed from the shallow gradient slope of the spectrum using the average width obtained from the original profile.

(c) The gradients were obtained by a least squares fit of straight lines to the linear parts of the spectrum. Equation (24) then gives the average depths. Small oscillations due to inadequate sampling may be ignored if a long length of the spectrum is available for depth analysis. These oscillations will effect the gradient estimate if only a small length of the spectrum contributes to the ensemble; results from these parts of the spectrum must therefore be viewed with caution.

(v) If only a single ensemble of bodies was revealed in the spectrum then the procedure outlined in (iv) was again followed, but there was a choice of which anomalies were dominating the spectrum, the long or short wavelength. In most of the cases studied here, if only a single ensemble was shown in the spectrum then it occurred in the longer wavelengths and therefore the widths obtained from the second derivative of the upward continued data were used in the width factor (equation (20)). In the case where there was a continuous set of high amplitude anomalies ranging from short to long wavelength, the spectrum showed only a single linear decay over its complete length indicating that all the bodies have been included in a single ensemble. In these instances the use of the width of the longer wavelengths is not fully justified, but the result will still be a fair approximation of the 'average' depth.

(4.4) Magnetic Profile - Geology Interpretation

In the following sections each magnetic profile is shown plotted above the geology that it crosses (e.g. figure (26)). A list of the maps used to obtain the geology is given in Appendix (C). The major tectonic boundaries are also shown in these figures and these are based on:

- (i) The geological maps referenced in Appendix (C).
- (ii) The tectonic map of Africa at 1:5,000,000.
- (iii) The literature referenced in chapter (1).

In order to show a reasonable amount of detail of the geology at the scale the profiles are presented, it was necessary to resort to a numbering system to reference the rock types crossed. This system is explained by reference to tables (10) and (11).

The major tectonic or geologic boundaries shown beneath the profiles (e.g. figure (26)) define the separate lengths of data which are width and depth analysed by the method of chapter (2). In a few cases where the magnetic boundary is not well defined or does not coincide with the tectonic boundary, two or more tectonic units will be discussed in a single section. Lengths of a profile which cross a single tectonic unit but which show large variations of magnetic pattern over that length will be width and depth analysed separately; as discussed in chapter (2), average depth estimates will have no meaning if large regions of profile which contain no anomalies are included in the analysis.

By analysing the major tectonic or geologic units separately, there is a greater probability that the magnetic sources contributing to the anomaly pattern will belong to only one or two ensembles (chapter (2)).

Table(10) Key to rock formations etc. used in the figures relating the magnetic profiles to the geology. Age of the formations are in million years. If a radiometric age is not available then the formation etc. is referenced according to the geochronological divisions of chapter(2).

<u>A</u>	Angola Basement (1600 to 1700)	<u>F</u>	Frontier-Gairezi System(1785)
Ar	Aruan (A ?)	<u>G</u>	Great Dyke Complex (2500 to 2800)
As	Aswa Mylonite Zone (A ?)	<u>H</u>	Haute Sangha Formation (?)
<u>B</u>	Botswana Basement (D)	<u>J</u>	Jurassic
Ba	Bambia Plateau Series (T)	<u>K</u>	Kenya Basement (A)
Bd	Burundian (800 to 1200)	Ka	Kalahari Beds (Ce)
BK	Bwamba Pass and Kyoga Series (~750)	KA	Karagwe Ankolean (1300)
Br	Barue Formation (A)	Kh	Khoabendus Formation (>1000)
BT	Buganda Toro Belt (1800 to 2000)	Ki	Kibalian Formation (1725 to 2075)
Bu	Bukoban System (630 to 1000)	Kib	Kibaran Belt (850 to 1300)
By	Bunyoro Series (630 ?)	Kr	Karoo System (100 to 250)
Bz	Banzville Formation (>3600)	Ks	Karasuk Series (A)
<u>C</u>	Cretaceous	Kt	Katangan Belt (485 to 840)
Ca	Carboniferous	Kw	Kwango Series (P to Ce)
Cb	Cameroun Basement (500 to 650)	<u>L</u>	Lake Sediments
Ch	Cheringma (A ?)	LB	Liki Bembian Group (A)
Cm	Calco Magnesium Complex (2300)	Li	Lindian Group (A)
Cn	Cambrian	Ll	Lualaba Series (K)
Cr	Carnot Sandstone (P)	Lm	Limpopo Belt (2000 to 2650)
<u>D</u>	Devonian	Lp	du Lom, de Poli, d'Ayos (500 to 650)
Dj	Dja Series (?)	Lu	Lukuga Series (K)
Dw	Dwango Gravels (Re)	<u>M</u>	Mesozoic

Table(10) Key to rock formations etc. (continued).

Mb	Malawi Basement (450 to 700)	<u>Q</u>	Quaternary
Md	Mulden Series (A)	<u>R</u>	Rhodesian Shield (3000 to 3300)
Mi	Mityana Series (A)	Re	Recent
MO	Mbaiki and Ouakuri (?)	Ru	Ruizian Belt (2100)
Mu	Muva System (900 to 1600)	<u>S</u>	Silurian
Mz	Mozambique Belt (450 to 700)	SG	Sena and Grudga Formations (Ce)
<u>N</u>	Nyanzian and Kavirondian Belts (2550 to 3150)	SO	Sembe Ouessou Series (A)
Ns	Nosib Series (A)	SP	Stanely Pool Series (P)
<u>O</u>	Ordovician	SW	South West African Basement (?)
Oe	Oendelongo System (850 to 1300)	<u>T</u>	Tertiary
Oj	Outjo facies of the Damaran Belt (450 to 570)	Tr	Triassic
Ok	Okavango Swamp (Ce)	<u>U</u>	Unknown
OO	Older Granites (?)	Ub	Uganda Basement (?)
Og	l' Ogooue System(1900 to 2500)	Ue	Ubendian Belt (1800)
<u>Pa</u>	Palaeozoic	Uk	Ukingan Series (C)
Pc	Precambrian	Um	Umkondo System (1785)
Pe	Permian	<u>W</u>	Watian (2660)
		<u>Y</u>	Younger Granites (?)
		<u>Z</u>	Zambia Basement (C or B)

Prefixes Used

l	lower
m	middle
p	pre
t	post
u	upper

Table(11) Key to the rock types etc. used in the figures relating the magnetic profiles to the geology

I - Igneous Rocks

1	Granite	2	Rhyolite	3	Diorite	4	Andesite
5	Gabbro	6	Basalt	7	Diabase or Dolerite	8	'Basic Rocks'
9	'Ultrabasic Rocks'	10	Pegmatite	11	Alpite	12	Serpentinite
13	Pyroxenite	14	Granodiorite	15	Tuff	16	'Volcanic Rocks'
17	'Felsic Volcanic Rocks'	18	'Acid Volcanic Rocks'	19	Anorthosite	I	'Igneous Rocks'

M - Metamorphic Rocks

1	Slate	2	Phyllite	3	Schist	4	Amphibolite
5	Quartzite	6	Marble or Crystalline Limestone	7	Granulite	8	Gneiss
9	Migmatite	10	Granite	11	Charnokite	12	Metavolcanics
13	Metasediments	14	Metacalcareous Rocks	15	Metagabbros	16	Meta- Anorthosite
17	Meta-Pyroxenes	18	Granitiod Rocks	19	Conglomerate	20	Granulite
21	Banded Ironstone	22	Cataclastics	M	Metamorphic Rocks		

S - Sedimentary Rocks

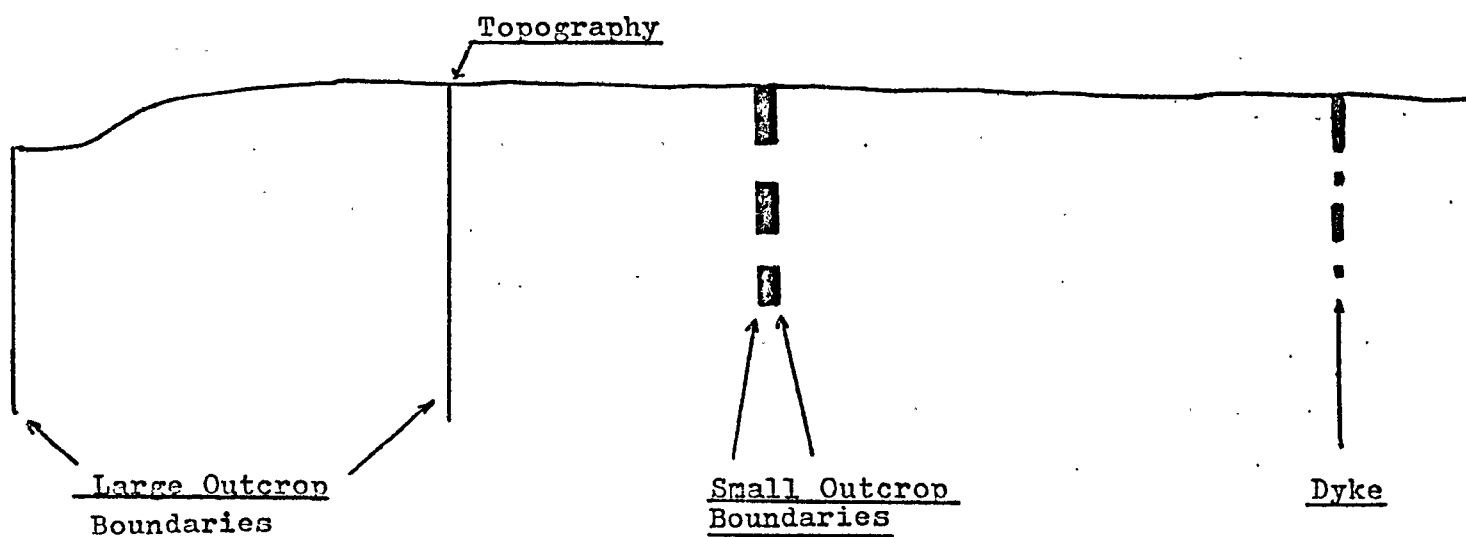
1	Sandstone (R-Redbeds)	2	Quartzite	3	Arkosite	4	Greywacke
5	Grit	6	Psammite	7	Calcareous Sandstone	8	Conglomerate
9	Limestone	10	Dolomite	11	Marl	12	Clay
13	Mudstone	14	Shale	15	Argillite	16	Glacial Deposits
17	Ironstone	18	Ferruginous Deposits	19	Alluvium	20	Coal Measures
21	Gravel	22	Sand	S	Sediments		

Table(11) Key to rock types etc. (continued)

Key to the descriptive minerals or adjectives used to classify the rocks.

a	Albite	b	Epidote	c	Chlorite	d	Calcite
e	Graphite	f	Mica	g	Biotite	h	Sericite
i	Muscovite	j	Feldspar	k	Garnet	l	Hornblend
m	Talc	n	Pyroxene	o	Sillimanite	p	Cordierite
q	Kyanite	s	Quartz	t	Acid	u	Ferrugenous
v	Magnesian						

Key to rock unit boundaries.



Unfortunately many of the units are only crossed by one or two profiles and therefore the conclusions about their magnetic characteristics (e.g. magnetic pattern, average width and depths to the principle magnetic sources) must at this stage remain tentative.

(4.4.1) Flights T211 and 522

Flights T211 and 522 constitute the most southern trans-continental path at approximately latitude 19°S . (figure (20)). From west to east these profiles cross successively (i) the Damaran Orogenic Belt, (ii) the Kalahari Basin, (iii) the Rhodesian Shield, (iv) the Limpopo Orogenic Belt, and (v) an outcrop of Karroo rocks (figure (20), figure (26), figure (28)).

(4.4.1.1) Damaran Orogenic Belt

From the west, profile T211 crosses various sedimentary and metasedimentary formations affected by the Damaran Orogeny (figure (26)). Within this terrain there are various outcrops of Karroo volcanic rocks (Geological Map of South West Africa). The large amplitude anomaly (200 gammas) recorded on the most western part of the profile is affected by a 90° change in the flight path at this position (figure (20)). For the next 350 km. the magnetic anomalies are mostly less than 30 gammas; notable exceptions are a 100 gammas anomaly and a 160 gammas anomaly which lie directly across Karroo volcanic rocks. After this, for the next 160 km., the magnetic anomalies increase to values in excess of 150 gammas with most anomalies ranging from 30 to 80 gammas amplitude with widths from 12 km. to 40 km. There is no apparent change in the underlying geology to explain this increase in magnetic activity. On the eastern margin of the Damaran Orogenic Belt a large amplitude (400 gammas peak to trough) magnetic anomaly of 100 km. width (marked b in figure(26)) is directly related to an extensive granite-gneiss mass; this correlation

is required to account for the high gradient of the anomaly.

The highly variable anomaly pattern recorded on this section of profile prevents a meaningful statistical depth analysis.

(4.4.1.2) Kalahari Basin Sediments

As profile T211 crosses onto the sediments of the Kalahari Basin there is a marked increase in the size of the magnetic anomalies (figure (26)). Large amplitude (upto 800 gammas), long and short wavelength anomalies are continuous from the western margin (figure (26)) to the eastern margin (figure (28)) of the sediments. It is worthwhile to notice the very good correspondence between profiles 522 and T211 for the region where their flight paths almost overlap (figure(20) and figure (22)).

From the energy spectrums of the Kalahari sections of profiles T211 (b to c in figure (26) and 522 (a to b in figure (28)) average depths below ground level to the sources of the high amplitude short wavelength anomalies are estimated to be 1.0 km. and 0.8 km. respectively (figure (27), figure (29)). From the original profiles an estimate of between 6 km. and 8 km. is obtained for the average half-width of this shallow ensemble of bodies (figures (26 to 29)). That a source for many of the high amplitude short wavelength anomalies is to be found at shallow depths (0.8 to 1.0 km.) is confirmed from the results of deep drilling (Geological maps of Botswana and South West Africa) which have consistently reached a basement of Karroo volcanic rocks. The magnetic profile data, together with the results of deep drilling (deep holes are shown at many localities beneath the profiles) confirm previous hypothesis on the nature of the basement to the Kalahari sediments (Haughton (1963), Green (1966)).

The energy spectrums of figure (27) and figure (29) show that

the source of many of the high amplitude long wavelength anomalies, observed clearly on the original and upward continued curves, are situated near to depths of 12.9 km. (figure (27)) and 13.1 km. (figure (29)). The second derivative of the upward continued curves show that the average half-width of these deep sources is somewhere near 33 km. (figure (27)) and 30 km. (figure (29)). These long wavelength anomalies are discussed further in section (4.5.3).

(4.4.1.3) Rhodesian Shield, Limpopo Orogenic Belt and Outcrops of
Karoo Volcanic Rocks

In the region where profile 522 crosses onto the basement rocks of Botswana (Rhodesian Shield) there is a decrease in the size of the magnetic anomalies. The magnetic relief for the first 270 km. of this section of profile (marked b-c in figure (28)) is mostly less than 100 gammas with widths of anomalies between 10 km. and 50 km. This low relief is consistent with the underlying geology of metavolcanic rocks (greenstones) interspersed with mainly gneissic and granitic rocks (see table (9) for the magnetic characteristics of these rocks).

As this profile enters a region which is extensively intruded by dykes, which are part of the Great Dyke Complex, there is a marked change in the size of the magnetic anomalies (figure (28)). The profile first traces a gentle rise of 200 gammas over a distance of 90 km. and this is followed by a 350 gammas increase over only 21 km.; the peak value coincides with a 'subsidiary' dyke of the Great Dyke (see section (1.5.1)). A drop of 650 gammas over 60 km. distance is then recorded. No distinctive features are observed at the position of the postulated extension of the Great Dyke (Worst (1960)). Gravity traverses by Podmore (1970) show a similar lack of features in this region. It is

therefore possible that the high amplitude anomaly coincident with the 'subsidiary' dyke marks an offset portion of the 'main' feeder chamber.

The very high magnetic relief is maintained as the profile crosses successively the Limpopo Orogenic Belt and a large outcrop of Karroo volcanic rocks. This northern section of the Limpopo Belt was not affected by the Precambrian C orogenesis (see section (1.5.1)), instead the Precambrian D dyke swarms, which intruded the basement, have remained unaffected since that time. These dykes and their feeder chambers are the most likely source of the magnetic anomalies observed across the orogenic belt and may contribute to the anomalies shown above the Karroo volcanic rocks (the eastern margin of the Limpopo Orogenic Belt 'disappears' beneath the Karroo volcanics). Obviously, the young volcanic rocks will also contribute to the magnetic anomaly pattern.

Over this complete section of profile (marked b-d in figure (28)) both the original and upward continued curves show two distinct magnetic regions (b-c and c-d in the figure). These regions are depth and width analysed separately. The energy spectrum of the first region (b-c) shows only a single ensemble of bodies at 6.9 km. depth below ground level (figure (30)); the tail end of the spectrum was still decaying after the last harmonic shown in figure (30) but was not sufficiently long or stable to warrant a least squares depth estimate. An average half width of 26 km. for the magnetic bodies in this region was obtained from the second derivative curve.

The energy spectrum for the second region (c-d in figure (28)) shows one ensemble of bodies at an average depth of 2.3 km. below ground level (figure(31)). Observation of the original profile curve

UPWARD CONTINUED CURVES

20KM.

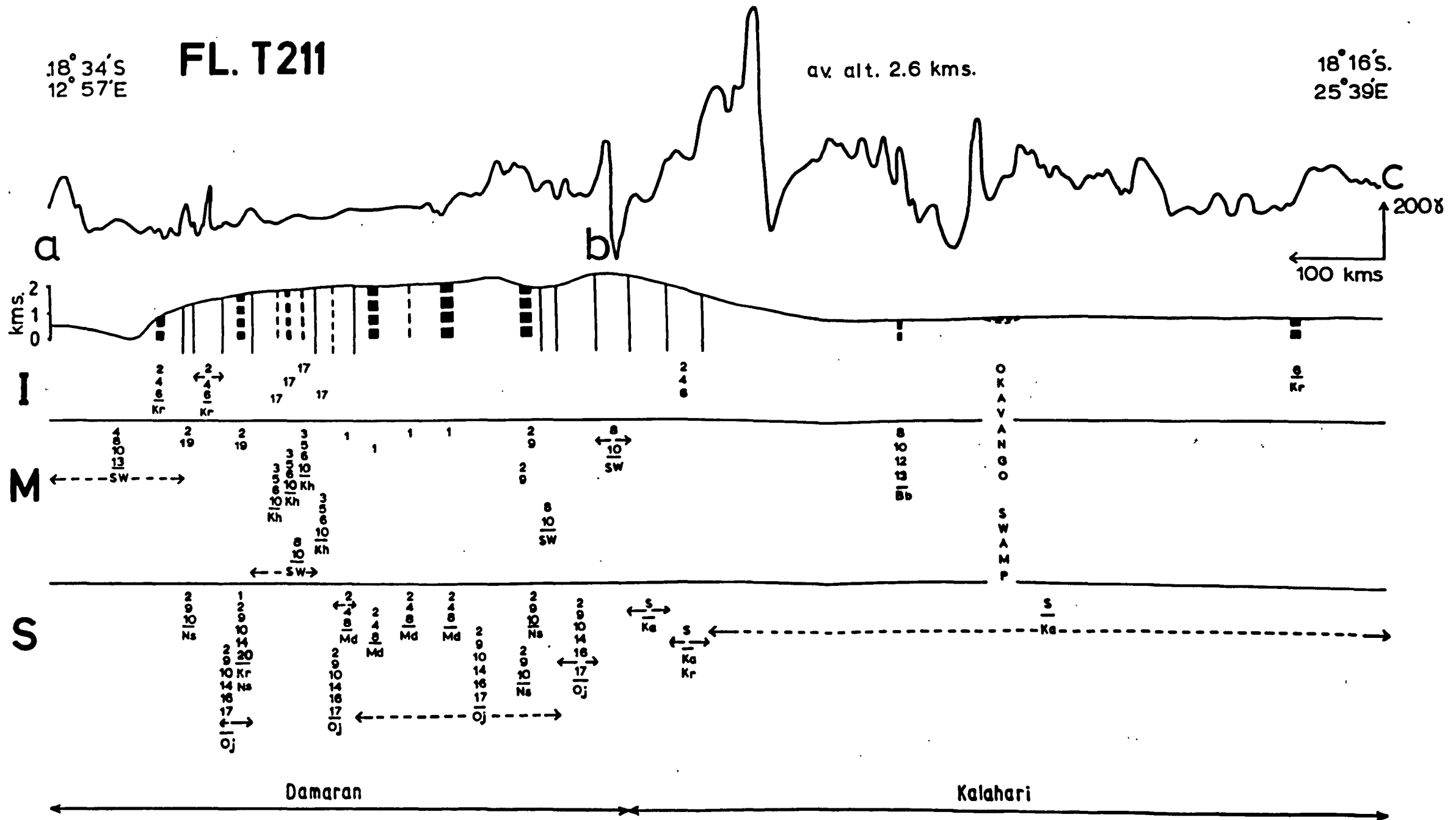
10KM.

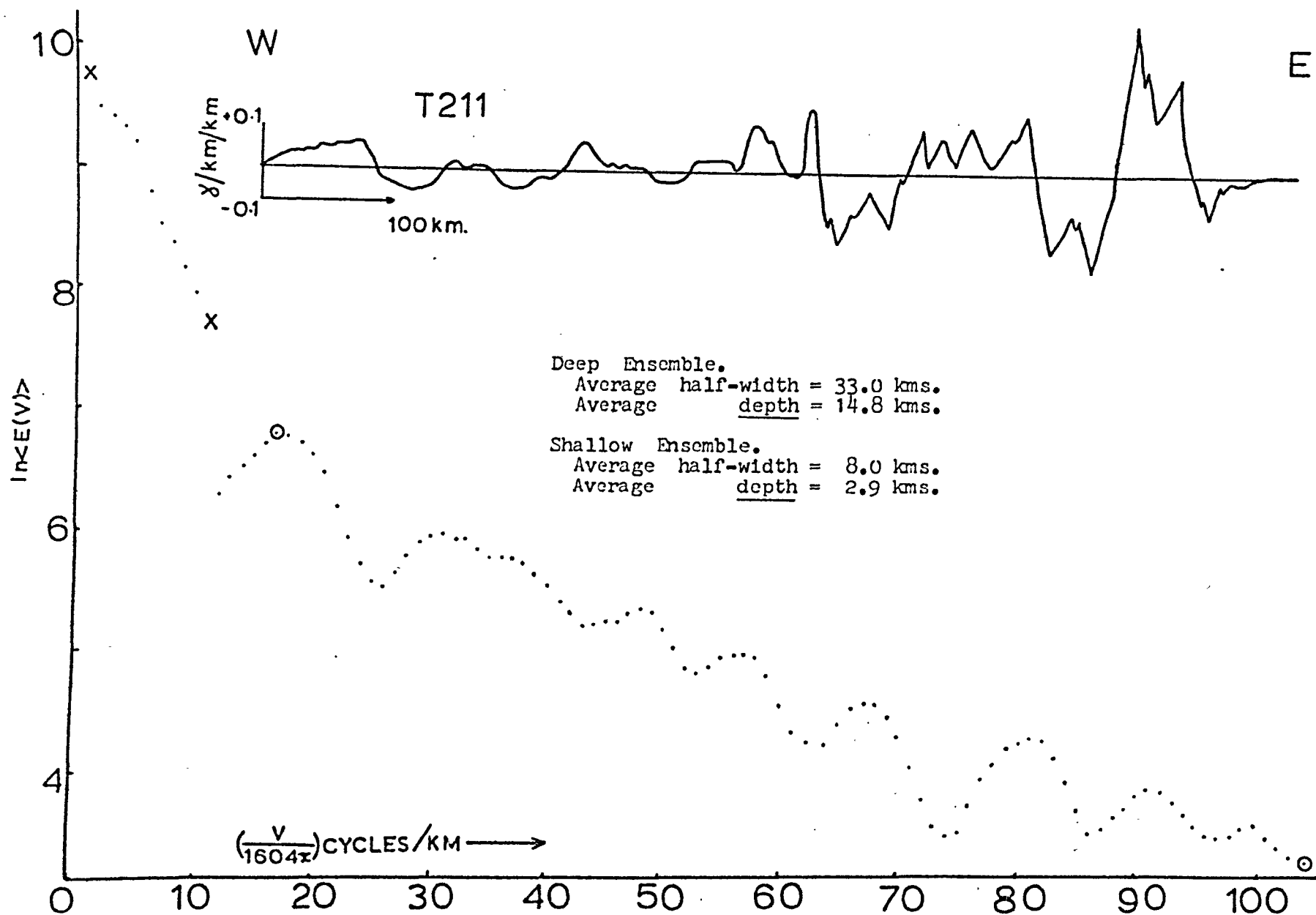
18° 34' S
12° 57' E

FL. T211

av. alt. 2.6 kms.

18° 16' S
25° 39' E





Fig(27) Energy spectrum and second derivative curve for section b - c of profile T211. Average altitude of the flight above ground = 1.9km. Therefore the average depths below ground level are 12.9km. and 1.0km.

UPWARD CONTINUED CURVES

20KM.

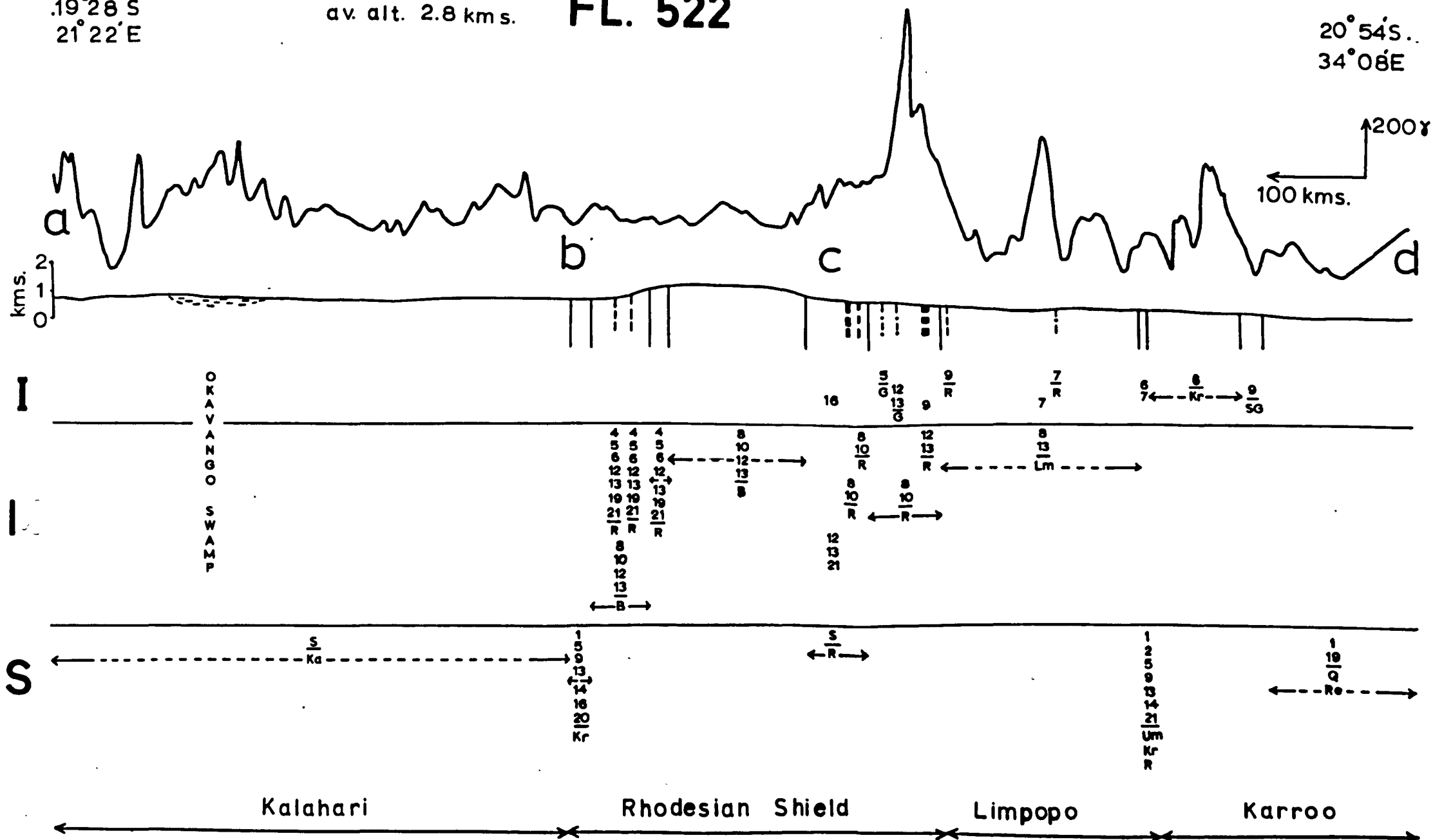
10 KM.

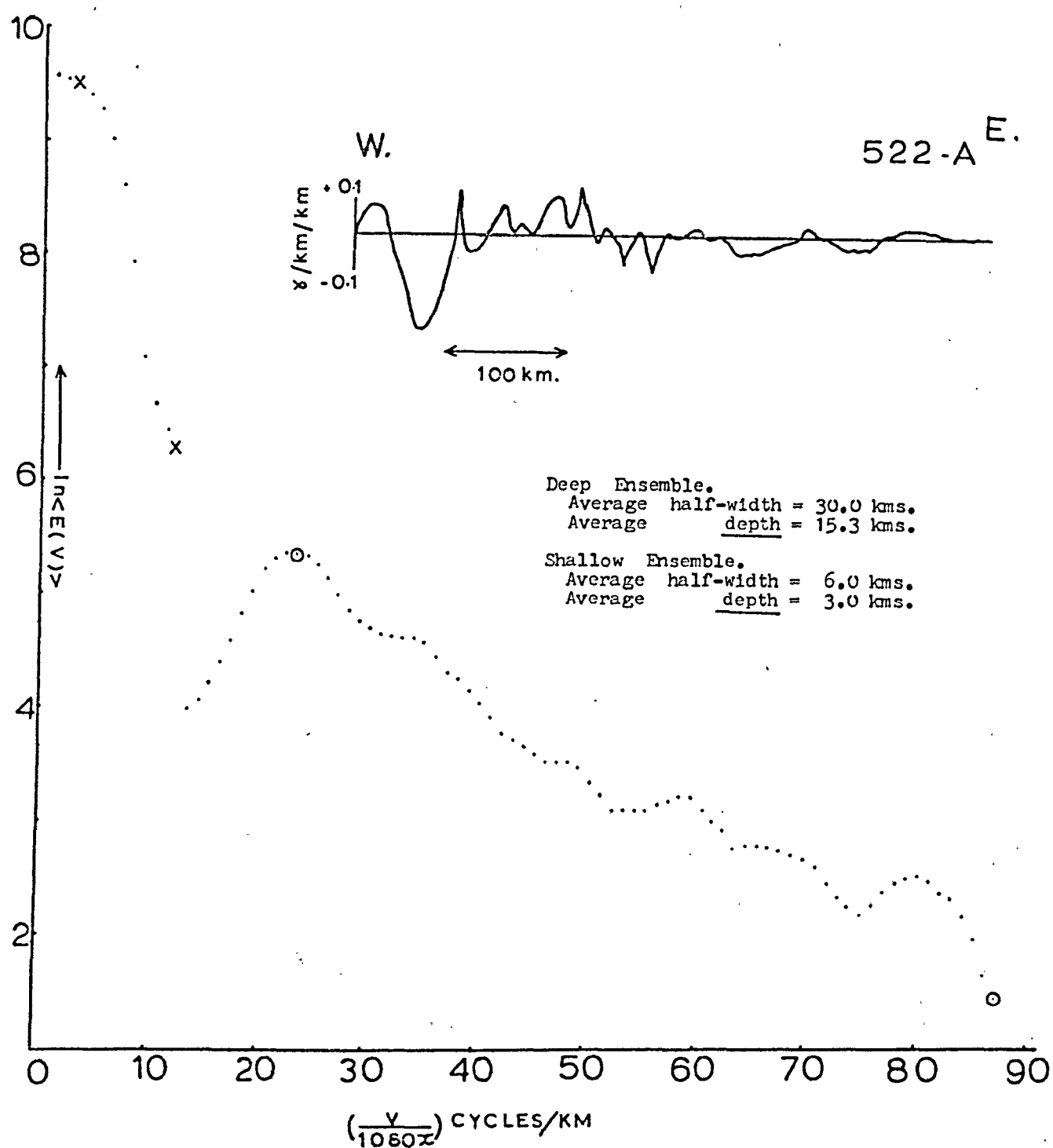
19°28'S
21°22'E

av. alt. 2.8 kms.

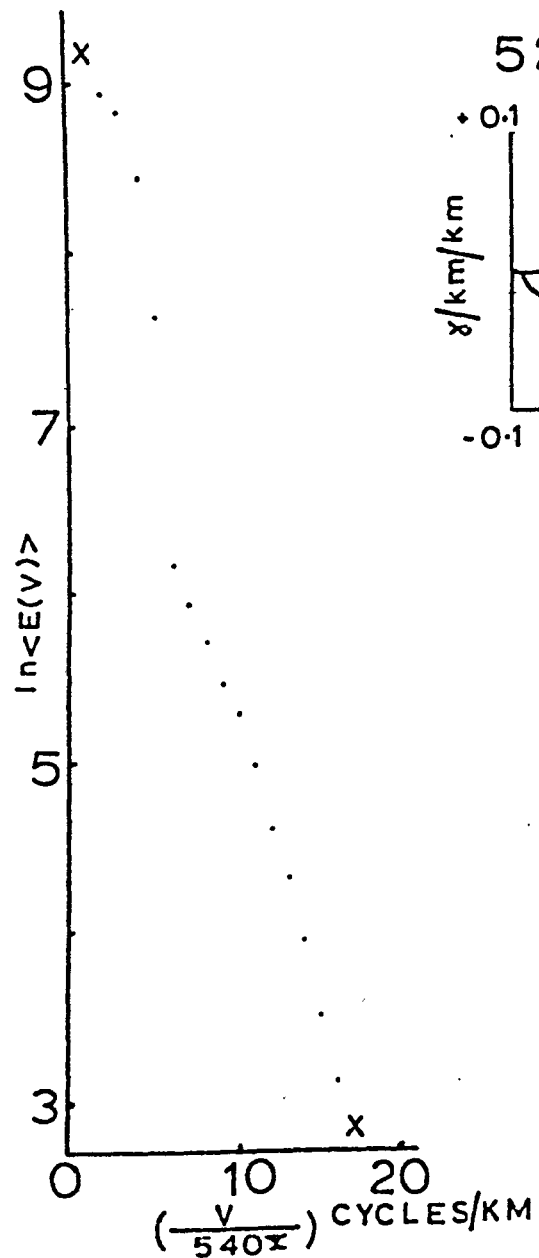
FL. 522

20°54'S..
34°08'E

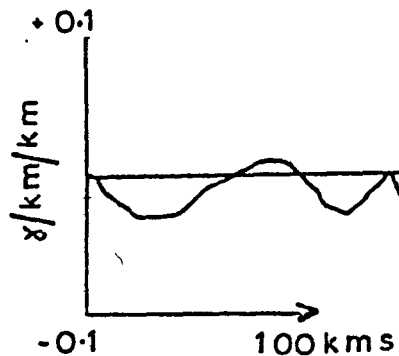




Fig(29) Energy spectrum and second derivative curve for section a - b of profile 511. Average altitude of the flight above ground = 2.2km. Therefore the average depths below ground level are 13.1km. and 0.8km.



522-B



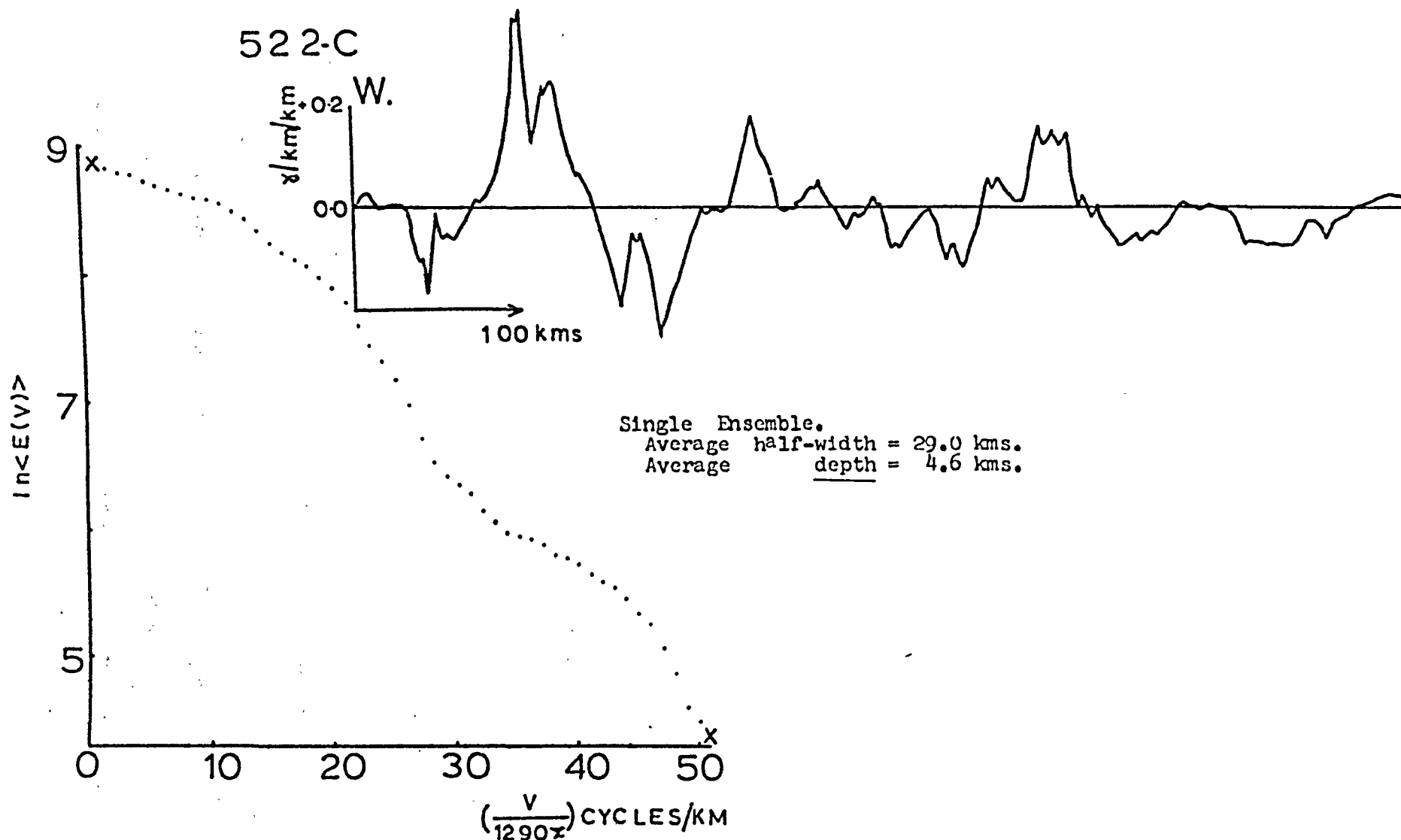
E.

Single Ensemble.

Average half-width = 26.0 kms.

Average depth = 8.6 kms.

Fig(30) Energy spectrum and second derivative curve for section b - c of profile 511. Average altitude of the flight above ground level = 1.7km. Therefore the average depth below ground level is 6.9km.



Fig(31) Energy spectrum and second derivative curve for section c - d of profile 522. Average altitude of the flight above ground = 2.3km. Therefore the average depth below ground level is 2.3km.

in figure (28) shows that the long wavelength anomalies have high gradient sides, so the shallow depth estimate is reasonable. In this case the energy spectrum shows the average effects of both long and short wavelength anomalies. The average half-width of 29 km. (figure (31)), obtained from the second derivative curve, is only representative of the long wavelength anomalies. The shallow depth estimate (2.3 km.) demonstrates the importance of the surface igneous rocks (Precambrian dykes and Karroo lavas) on the magnetic profile.

(4.4.2) Flights T213 and 517

Except for two breaks of between 100 km. and 200 km. length, flights T213 and 517 make up a transcontinental profile at approximately 18°S. (figure (20), figure (32), figure (35)). These profiles cross successively (i) the Damaran Orogenic Belt, (ii) the Kalahari Basin, and (iii) the Rhodesian Shield (figure (21), figure (32), figure (35)).

Before attempting to analyse profile T213 it is important to explain the near absence of short wavelength relief over most of its length (figure (32)). After the first 165 km. of track (the flight starts in the east) the magnetometer was stopped and adjusted (reasons not given on the microfilm data). After this the instrument appears to only respond efficiently to 'long wavelength' components of the magnetic field.

(4.4.2.1) Damaran Orogenic Belt

Lack of short wavelength magnetic anomalies excludes detailed correlation of the magnetic profile with the geology. The only large amplitude (400 gammas) magnetic anomaly, situated in the west of profile T213 (figure (32)), is probably a 'continental edge effect' (Fenwick et. al. (1968)). No change in the long wavelength magnetic pattern is

observed as the profile crosses from the exposed metamorphic rocks of the orogenic belt onto the region covered by the Kalahari sediments. It is therefore reasonable to state that the deep structure, as observed magnetically, is continuous across this margin.

To obtain a 'complete' anomaly for average depth estimation the region between the points a to b in figure (32) was analysed. The resultant energy spectrum (figure (33)) yields a single ensemble at an average depth of 8.6 km. below ground level while the second derivative curve shows an average half-width of 48 km.

(4.4.2.2) Kalahari Basin Sediments

There are no basement exposures within the Kalahari sediments crossed by profile T213 (figure (32)) but on the geological maps of South West Africa and Botswana a number of boreholes that have reached Karroo volcanic rocks are shown in the vicinity of the profile. The presence of these volcanic rocks may be correlated with the ensemble of magnetic bodies, estimated from the energy spectrum of the Kalahari Basin section of profile T213 (point c to the western margin of the sediments in figure (32)) to be at an average depth of 0.9 km. below ground level (figure (33)). This average depth estimate must be viewed with extreme caution as the anomalies of wavelengths corresponding to the harmonics used in the depth estimate are of a very low amplitude. The very low amplitude of the short wavelength anomalies prevented a realistic average width estimate and therefore the average half-width used in the width factor (equation (20)) is a value similar to that found from other profiles which cross near to the region (e.g. figure (27) or figure (29)).

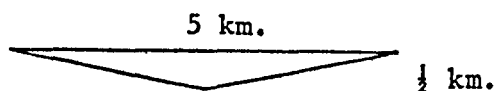
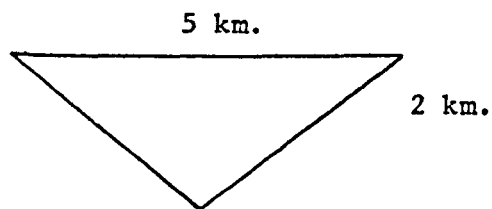
The average depth to the sources of the longer wavelength anomalies of profile T213 (see the upward continued curves in figure (32)) is found to be 17.7 km. below ground level (figure (34)) while the average half-width is estimated to be 35 km.

(4.4.2.3) Rhodesian Shield (including a region of Kalahari sediments)

The western region of the Rhodesian Shield shown on the tectonics of figure (35)) includes an area intruded by Karroo volcanic rocks which is partially covered by Kalahari sediments. The high amplitude (100 gammas to 300 gammas) short wavelength (6 km. to 15 km. width) magnetic anomalies which are continuous across this region are evidence that Karroo volcanics are basement to the sediments here.

After leaving the area underlain by Karroo volcanics the magnetic relief decreases (most anomalies are less than 100 gammas amplitude) as the flight crosses a swarm of dykes (figure (35)) which would seem to be potentially magnetic material. The lack of sizable anomalies may be explained by either (i) the narrowness of the dykes (most of the dykes shown in figure (35) are between 1 km. and 3 km. width) or (ii) metamorphic alteration of the dykes (many of the formations on the Rhodesian Shield have been altered to the greenstone facies of metamorphism). Exceptions to this low magnetic relief, marked (c) in figure (35), may be related to the Great Dyke (see section (1.5.1)). The eastern peak of these three anomalies lies directly across the main dyke. Podmore (1970) has published some Great Dyke models obtained from gravity data and Irving (1964) has collected palaeomagnetic data from this structure. It therefore seemed reasonable to obtain an estimate of the magnitude of the remanent intensity vector (although remanent magnetisation is assumed dominant, the palaeo-dip obtained from the dyke is very close to the present day magnetic dip) using the gravity models ((i) and (ii) below) and palaeomagnetic direction vector as constraints. With the Talwani and Heirtzler (1964) computer program, intensity values of 1.4A/m. and 4.0A/m., for structures (i) and (ii) respectively (below), are required to simulate the recorded 100 gammas

anomaly (figure (35)).



(i) Remanent Intensity = 1.4 A/m.

(ii) Remanent Intensity = 4 A/m.

Declination = 227.5°

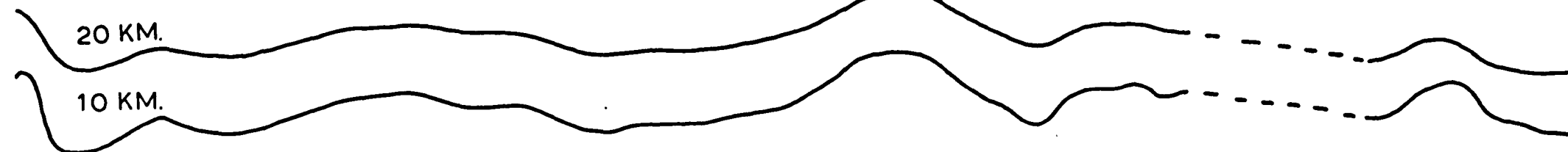
Average Palaeo-pole position -

Dip = -60.0°

These intensity values fall within the range of values shown in table (9)) for typical Great Dyke rocks (e.g. periodotite, gabbro and serpentinite). The two adjacent magnetic anomalies may be directly correlated with the subsidiary dykes found beside the main dyke; Podmore (1970) has found large gravity anomalies across these apparently more minor features. For the remainder of the Rhodesian Shield there are several medium wavelength anomalies (20 km. to 45 km. width) of 50 gammas amplitude superimposed on a broad 100 gammas undulation (figure (35)). As the profile crosses onto a region undefined tectonically (figure (35)) the magnetic relief increases dramatically. The Karroo volcanic rocks shown in this region are the most probable source of this increase in magnetic activity.

To calculate the average widths and depths of the magnetic sources, this section of profile was split into three parts based mainly on the magnetic character. The first 306 km. of profile (a to b in figure (35)) has two sources contributing to the anomaly pattern (figure (36)); a shallow source at an average depth of -0.2 km., with an average half-width of 6 km. and a deeper source at an average depth of 3.5 km. with an average half-width of 27 km. The shallow depth estimate is

UPWARD CONTINUED CURVES

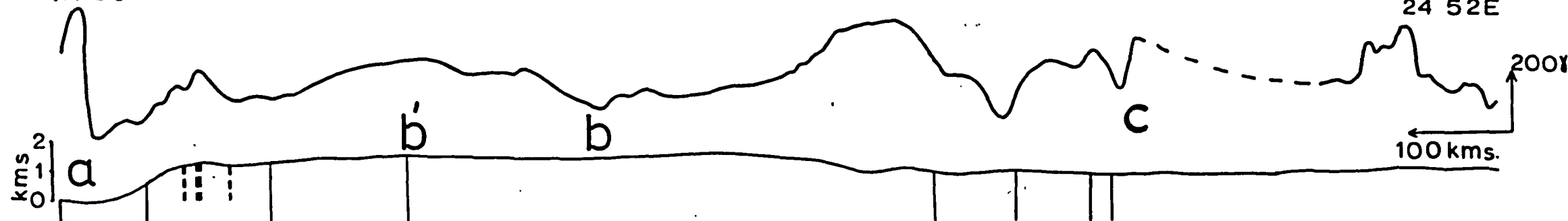


17°30'S
11°30'E

FL. T 213

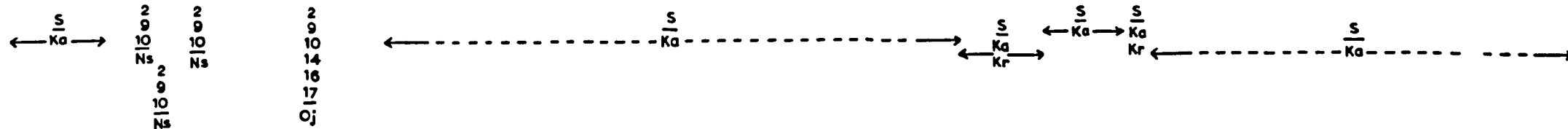
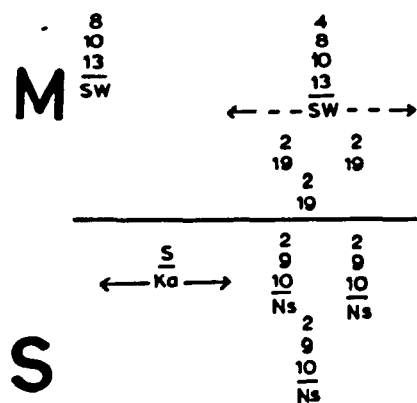
av. alt. 2.7 kms.

18°05'S.
24°52'E



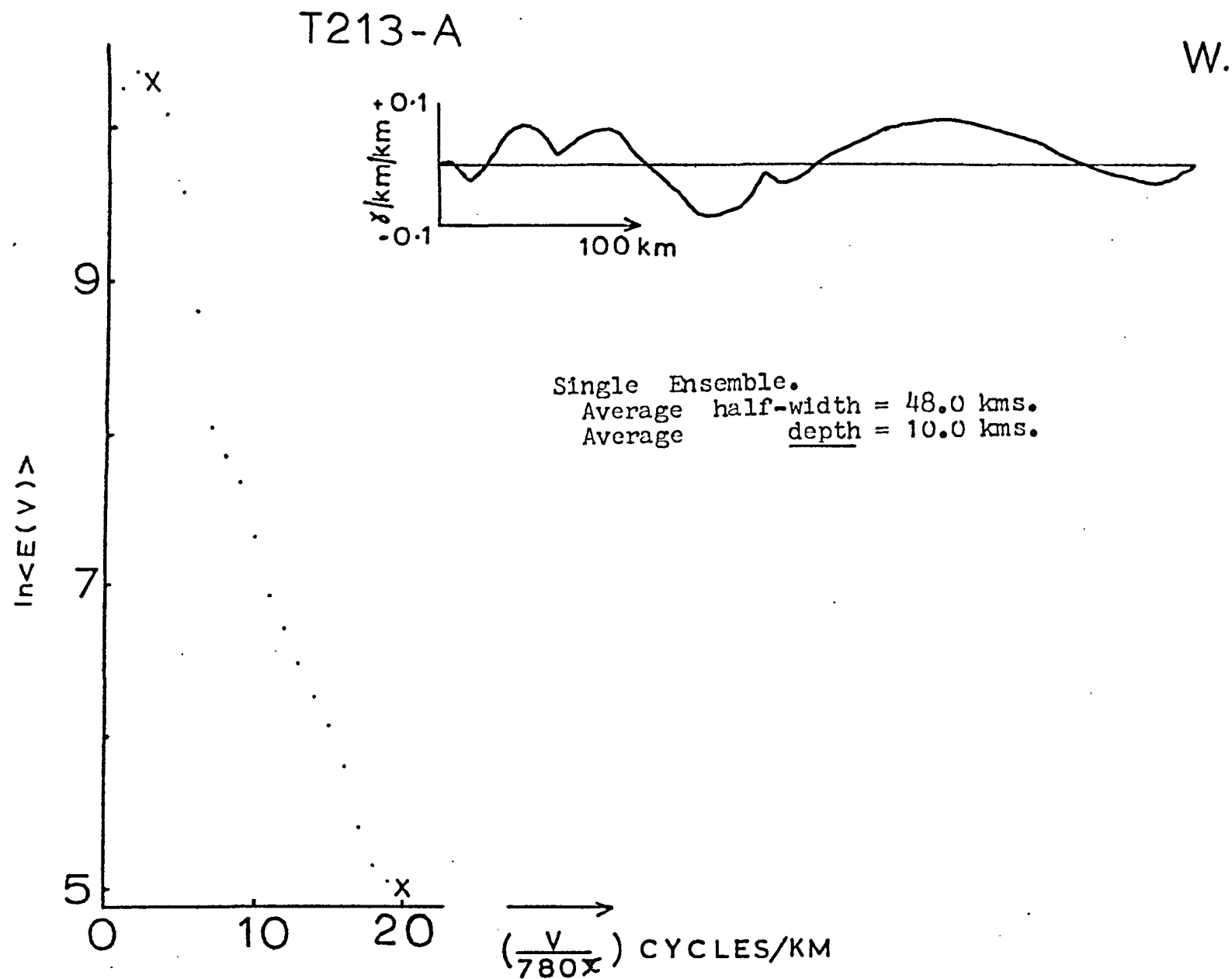
2
4
6

2
4
6



Damaran

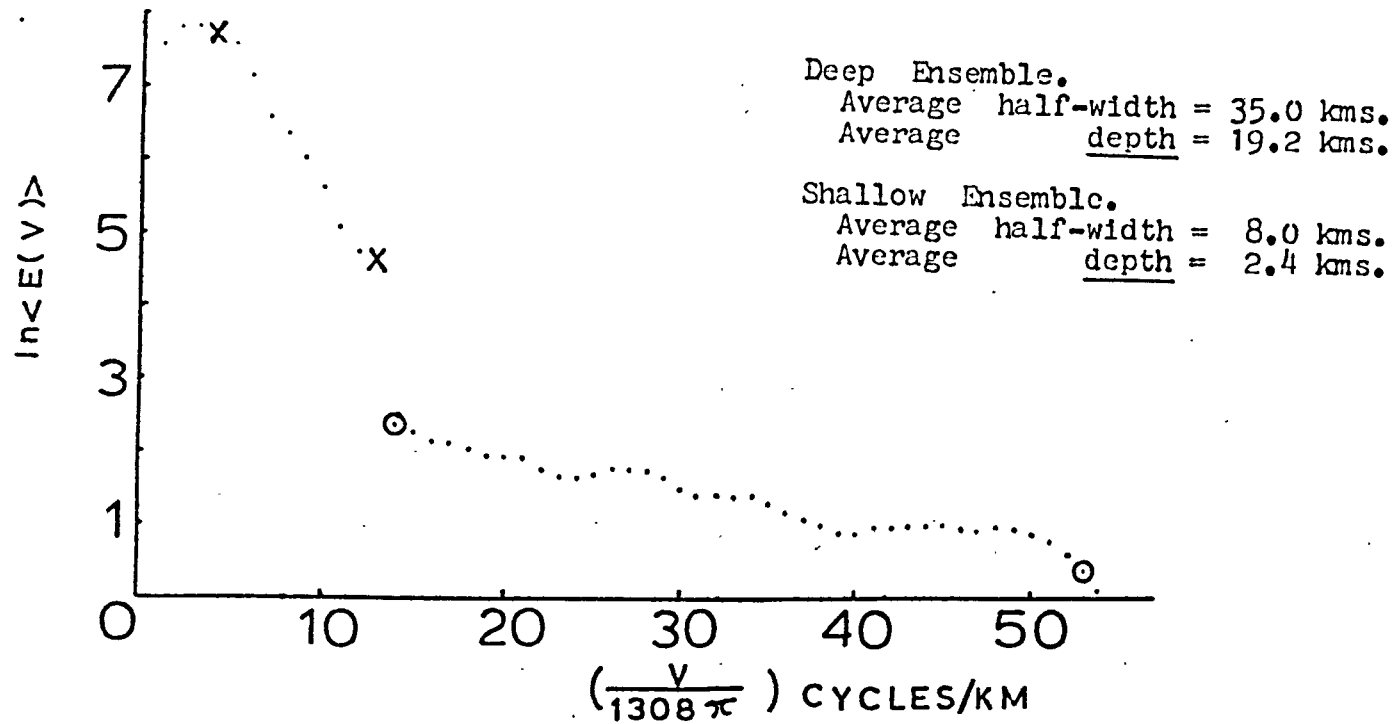
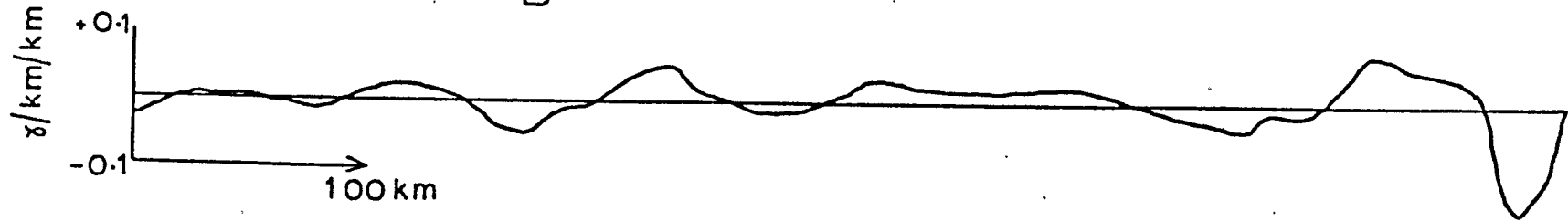
Kalahari



Fig(33) Energy spectrum and second derivative curve for section a - b of flight T213. Average altitude of flight above ground level = 1.4km. Therefore the average depth below ground level is 8.6km.

W.

T 213-B



Fig(34) Energy spectrum and second derivative curve for section b' - c of profile T213. Average altitude of flight above ground = 1.5km. Therefore the average depths are 17.7km. and 0.9km. below ground level.

UPWARD CONTINUED CURVES

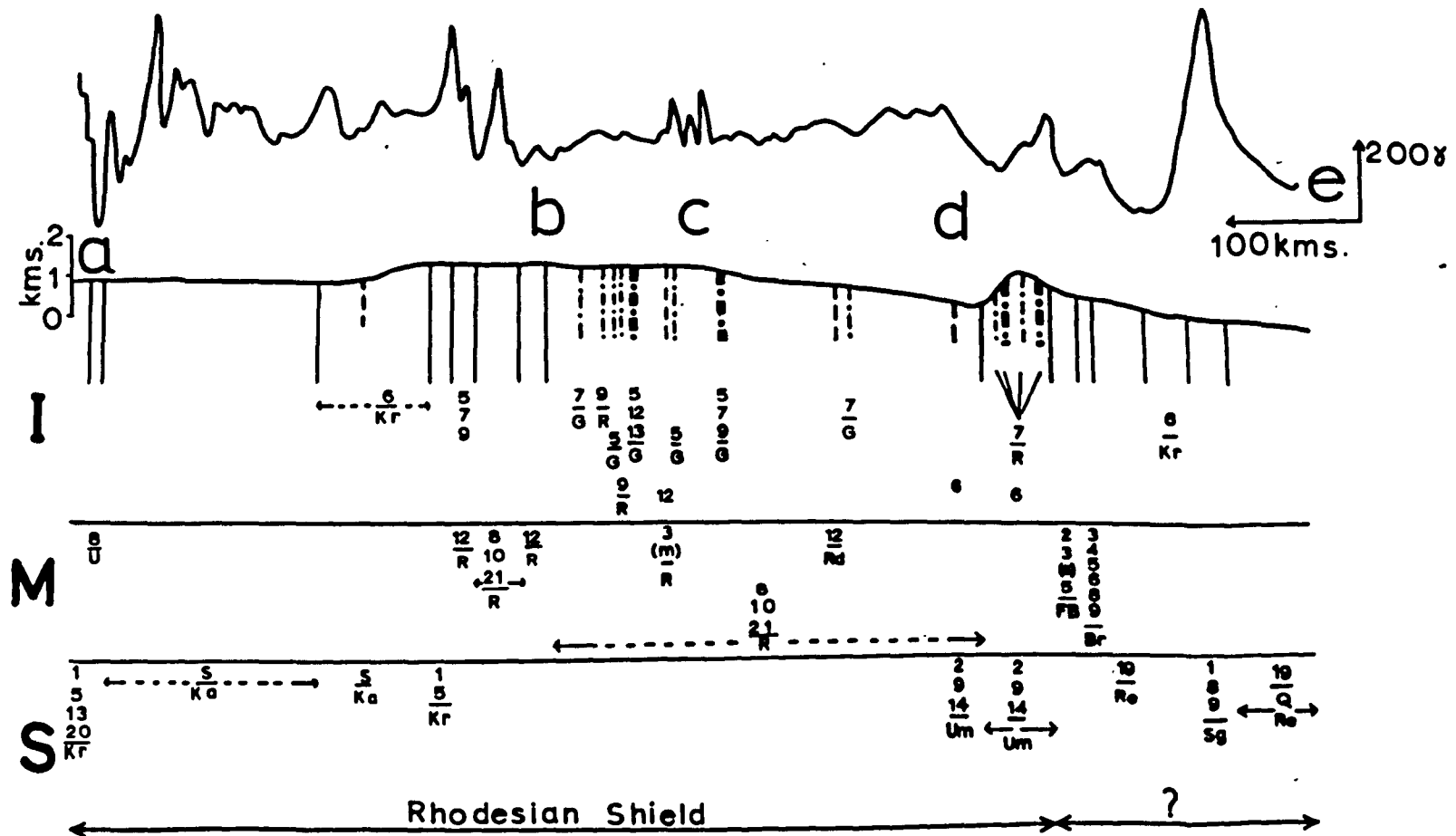
20KM.

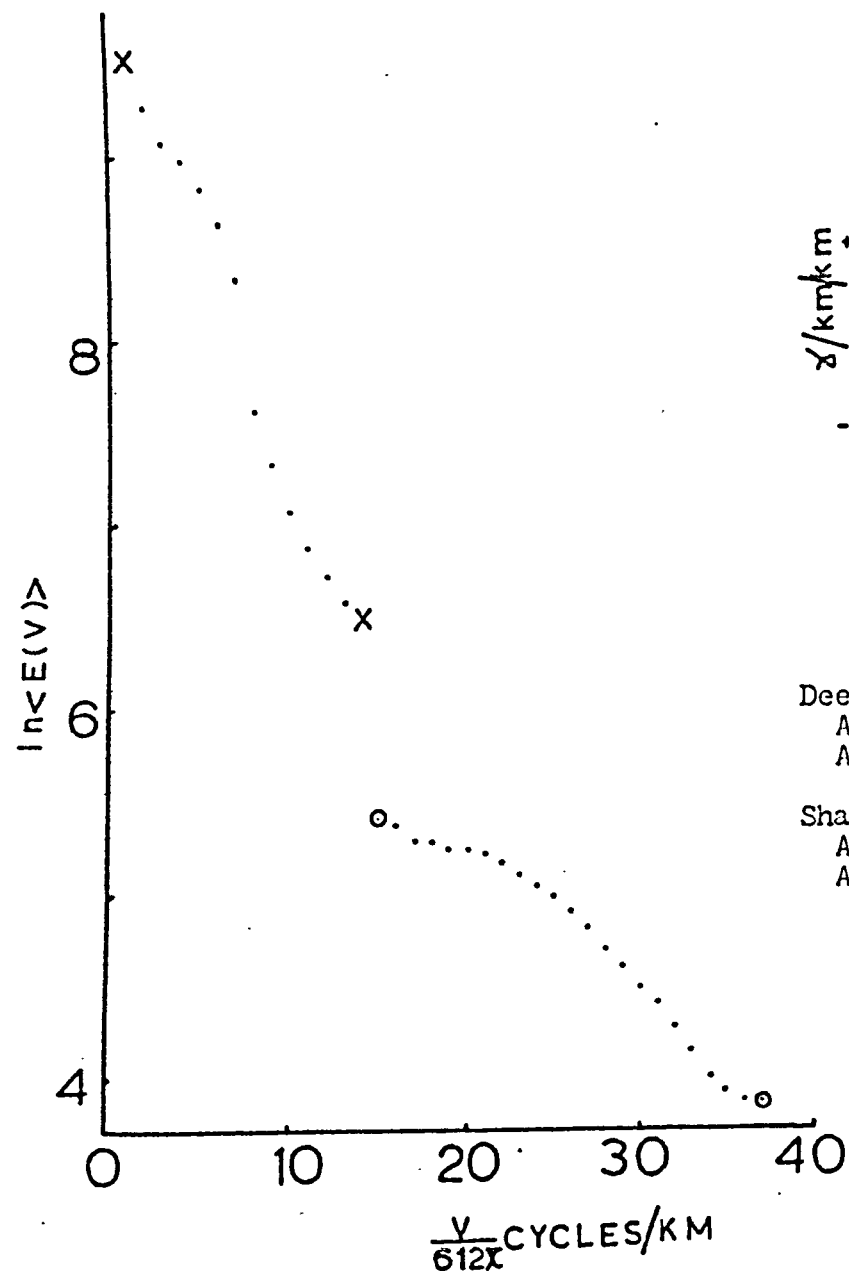
10KM.

18° 24' S.
26° 17' E.

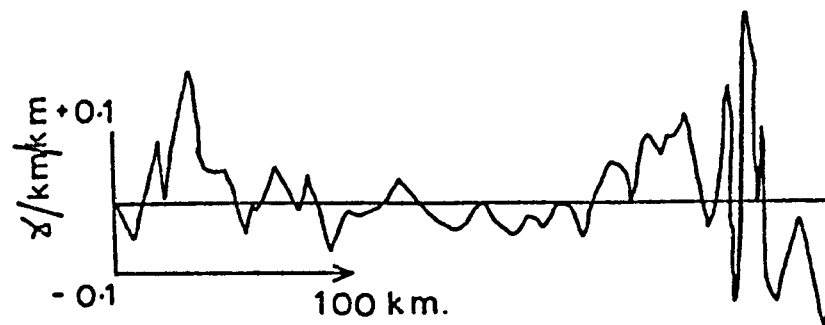
FL. 517 av. alt. 3.2 kms.

20° 02' S.
34° 45' E.





517-A



Deep Ensemble.

Average half-width = 27.0 kms.

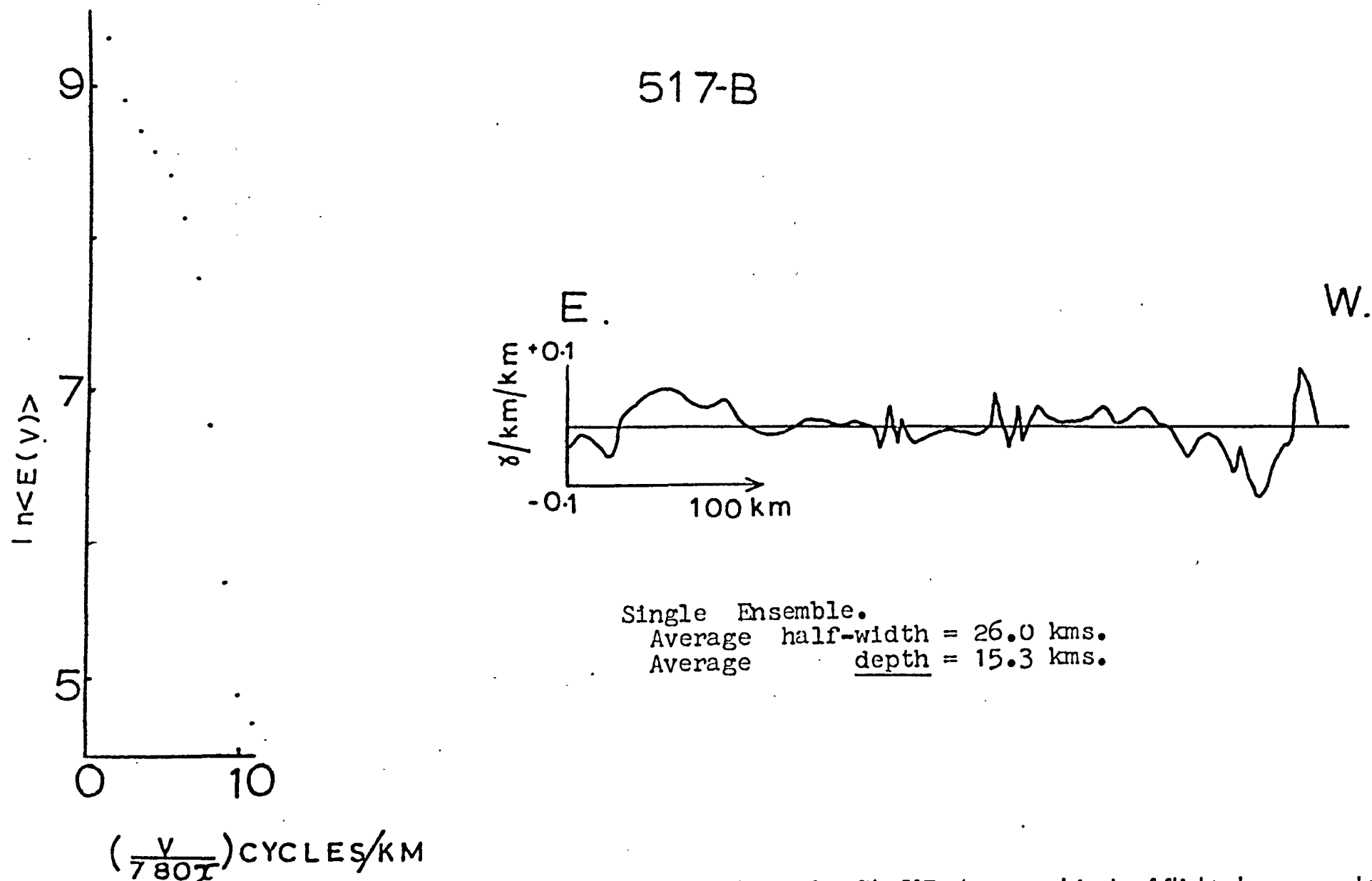
Average depth = 5.7 kms.

Shallow Ensemble.

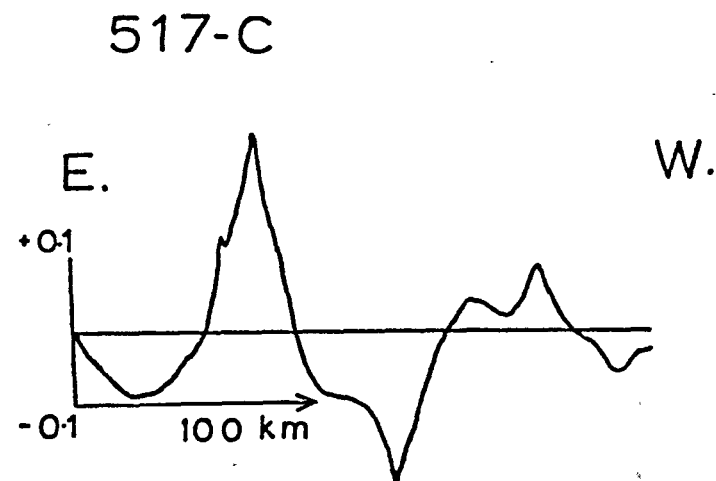
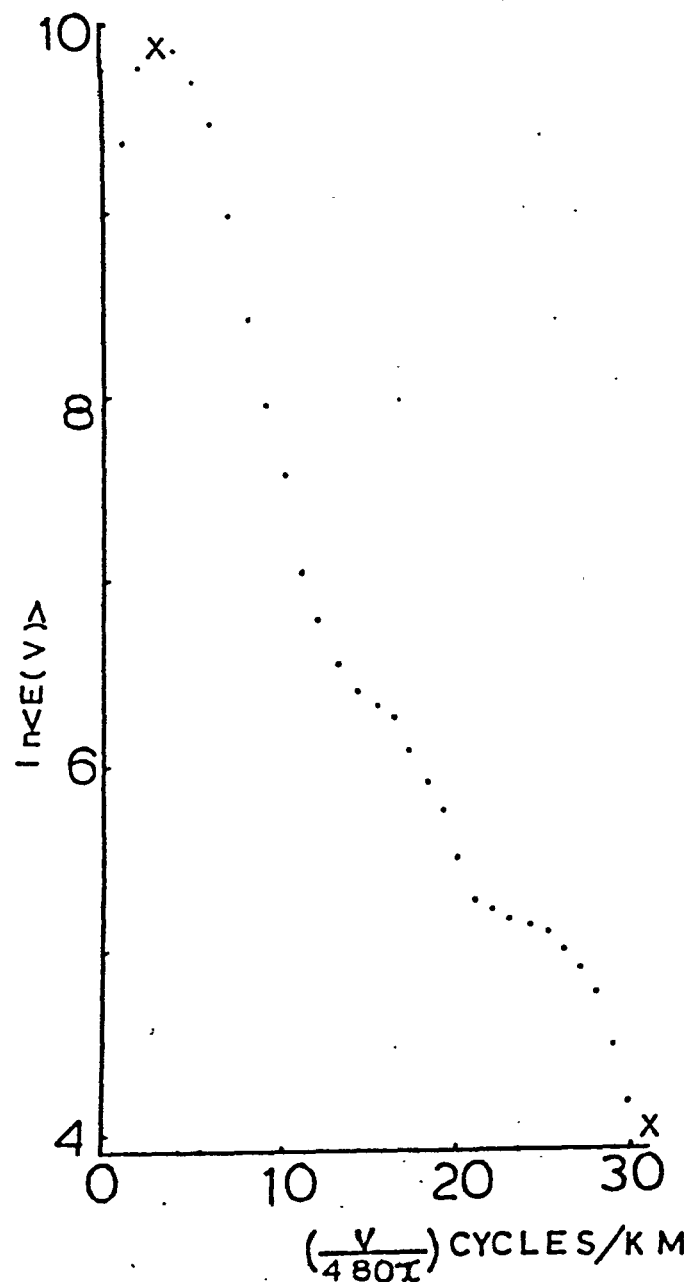
Average half-width = 6.0 kms.

Average depth = 2.0 kms.

Fig(36) Energy spectrum and second derivative curve for section a-b of profile 517. Average altitude of the flight above ground level = 2.2km. Therefore the average depths below ground level are 3.5km. and -0.2km.



Fig(37) Energy spectrum and second derivative curve for section b - d of profile 517. Average altitude of flight above ground = 2.2km. Therefore the average depth below ground level is 13.1km.



Single Ensemble.
 Average half-width = 27.0 kms.
 Average depth = 3.7 kms.

Fig(3.8) Energy spectrum and second derivative curve for section d - e of profile 517. Average altitude of flight above ground level = 2.8km.
 Therefore the average depth below ground level is 0.9km.

confirmation of the postulated contribution of the Karroo volcanic rocks to the magnetic anomaly pattern. The energy spectrum of the next 390 km. of profile (b to d in figure (35)) shows only a single ensemble of bodies at average depth 13.1 km. (figure (37)). The region in the spectrum where the anomalies of the Great Dyke would be observed was very erratic. The average half-width of this deep set of bodies is estimated to be 26.0 km. from the second derivative curve. The final 240 km. of track (d to e in figure (35)) yields only a single ensemble of bodies at an average depth of 0.9 km. with an average half-width of 27.0 km. (figure (38)). Again this shallow depth is confirmation of the postulated contribution of the Karroo volcanic rocks to the magnetic relief.

(4.4.3) Flight T225

Profile T225 has a complete transcontinental path at approximately latitude 13.5°S (figure (20)). This profile crosses successively (i) the Angola Basement, (ii) the Kalahari Basin, (iii) the Katangan Belt, (iv) the Tumbide and Irumide Belts (v) the Mozambique Belt (figure (21), figure (39)).

(4.4.3.1) The Angola Basement and Kalahari Basin Sediments

The magnetic relief observed across the Angola Basement and the Kalahari Basin is very similar, both regions contain high amplitude (150 gammas to 800 gammas), long and short wavelength magnetic anomalies (figure (39)). Within the Angola Basement the granite and granodiorite masses contribute to the observed magnetic anomalies, but the very high amplitude of some of the anomalies is indicative of higher magnetic sources. These higher magnetic bodies are most likely to be the 'Post Permian' dolerites, shown on the Angola Geological Map (1953) in the near

vicinity of the profile. De Sousa Machado (in Haughton (1963)) has assigned these dolerites to the Karroo period of magmatism. Beneath the Kalahari sediments, in this locality, the mixture of basement rocks (granite, granodiorite and gneiss) and Karroo volcanics are the most likely source of high amplitude, high wavenumber anomalies. From the energy spectrum for this section of profile (a to b in figure (39)), the average depth to the shallow ensemble of bodies is estimated to be 0.4 km. below ground level (figure (40)), while an average half-width of 8 km. is obtained from the original anomaly curve (figure (39)).

The high amplitude long wavelength anomalies, which are best observed in the upward continued curves of figure (39), are shown in the energy spectrum to have their sources at an average depth of 7.5 km. below ground level. From the second derivative curve an average half-width of 35 km. is obtained for these deep bodies. That the conditions required by the method of chapter (2) are not completely satisfied for this section of profile is demonstrated by the highly oscillating character of the energy spectrum between the two regions used in the depth analysis (figure (40)).

In the east of the region covered by Kalahari sediments the magnetic relief decreases. Exceptions to this are the anomaly near the point marked b and the double peaked anomaly near the point c in figure (39), neither of these are explained by the underlying geology. This lower magnetic activity may be related to the Katangan basement which outcrops within the sediments of this region (see below).

(4.4.3.2) The Katangan, Irumide and Tumbide Orogenic Belts

The magnetic relief observed across these orogenic belts is very low. With the exception of a single anomaly (marked d in figure (39)) the magnetic relief is less than 100 gammas for a total distance of

600 km., after which the Mozambique Orogenic Belt is encountered. The one exception to this low magnetisation is a very high amplitude (~ 900 gammas) negative anomaly situated on the ill defined border of the Katangan and Irumide Orogenic Belts. From the surface geology there is no obvious source to this anomaly, although the correlation of the anomaly with the edge of a large granite mass may be significant (figure (39)).

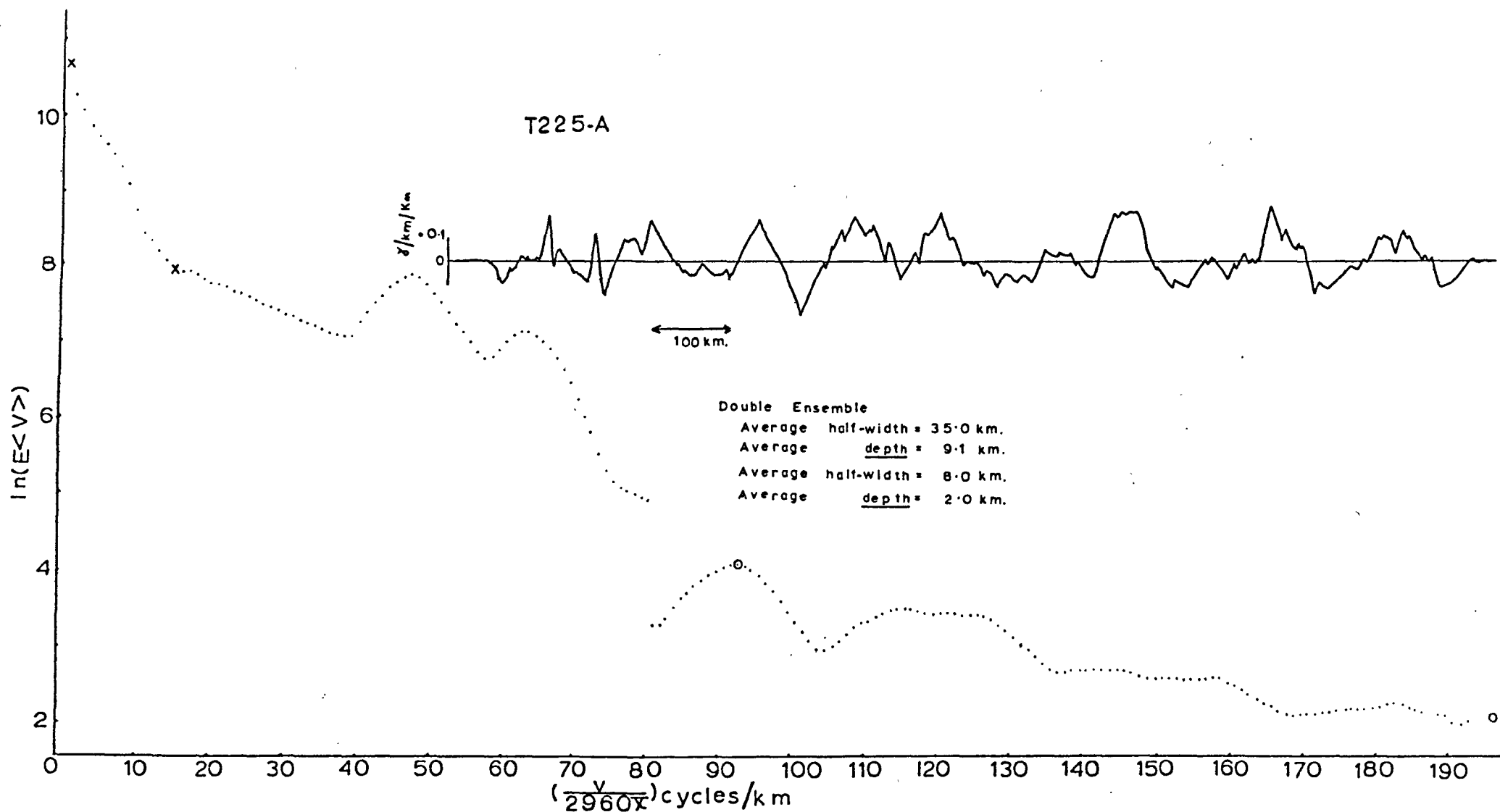
Only the Katangan Belt to the west of the point d in figure (39) is depth and width analysed. The large negative anomaly, discussed above, cannot be considered to be part of the same ensemble of bodies on either the Katangan or Irumide-Tumbide sides of the boundary. From the energy spectrum of the Katangan Belt two ensembles of magnetic bodies are revealed; a shallow set at 0.4 km. average depth and a deeper set at 16.9 km. average depth below ground level (figure (40)). The average half-widths are estimated to be respectively 8 km. and 24 km. (figure (41)).

(4.4.3.3) The Mozambique Orogenic Belt

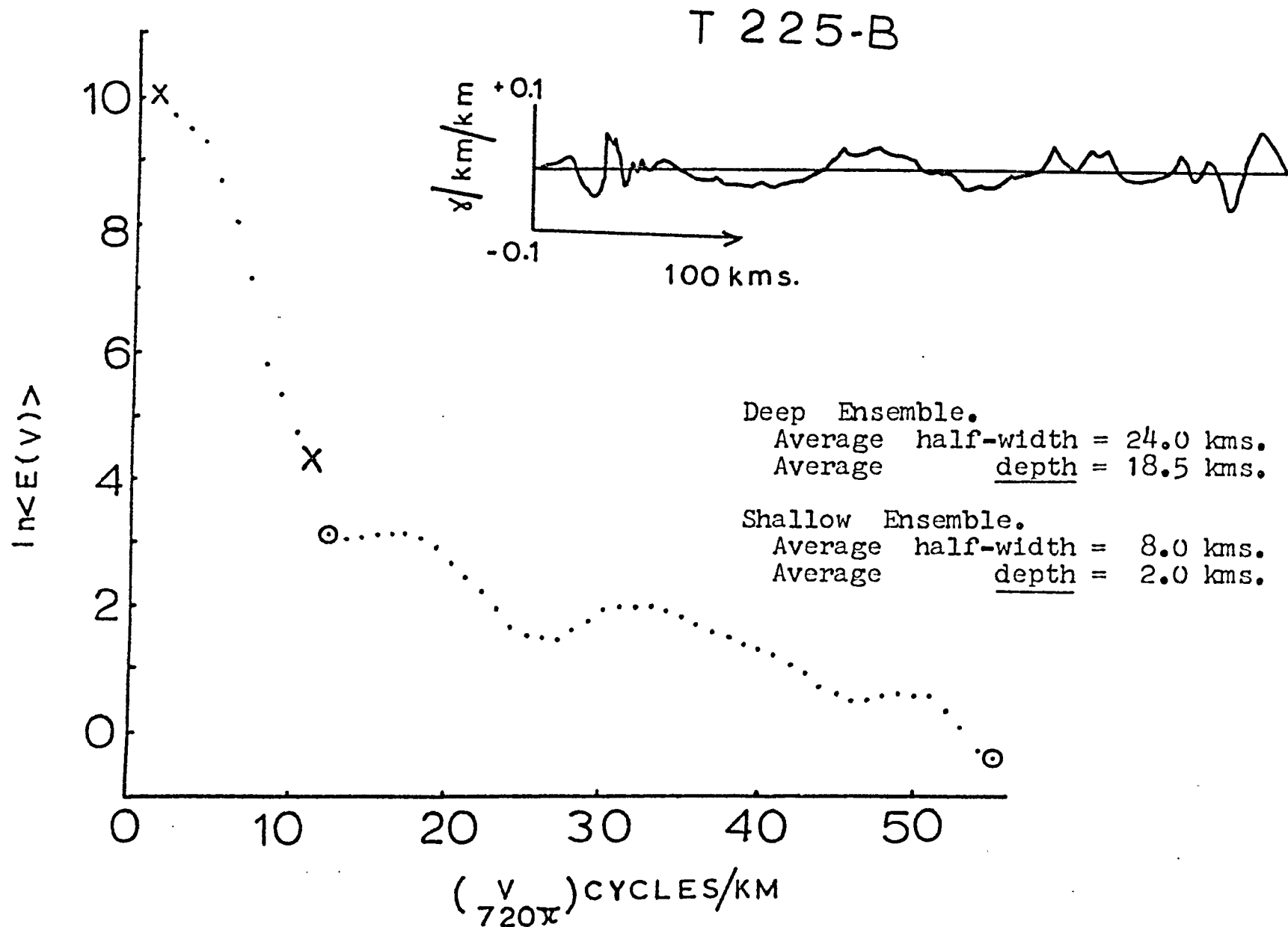
As the profile crosses from a region where the Tumbide and Irumide trends are preserved, onto the Mozambique Orogenic Belt there is a marked change in the size of the magnetic anomalies recorded (figure (39)). Although the western margin of the Mozambique Belt is concealed beneath Karroo sediments it is clear that the region of the Mozambique Belt to the west of the point marked f in figure (39) is characterised by high magnetic anomalies. The high amplitude (400 gammas peak to trough) magnetic anomaly marked e in figure (39) has a high gradient and may therefore be correlated with the large granite mass which it crosses at this point. The high wavenumber magnetic relief to the east of this point may be related to the gabbroic and doleritic intrusions found with-

in a large granitoid mass (figure (39)) shown beneath the profile. In the upward continued curves this granitoid mass is observed to be the source of a long wavelength magnetic 'hump'. After the granitoid mass the magnetic relief is low (~ 100 gammas) for approximately 100 km., at which point two large amplitude (~ 300 gammas), 45 km. wide peaks are found near to the Shire Rift (see section (1.8)) (marked recent alluvium in figure (39)). Rocks on either side of the Shire Rift are gneiss and associated rocks of the Malawi Basement (part of the Mozambique Belt) while to the north of the profile granites, syenites, basic and ultra-basic intrusives of the Lake Malawi Province (Bloomfield (1970)) outcrop and to the south similar rocks of the Chilwa Alkaline Province are observed (Woolley and Garson (1970)). Dolerite dykes of Precambrian A and Karroo age outcrop to the north of the profile on the east of Lake Malawi (Geological Map of Malawi). It is unlikely that these high amplitude anomalies are due to these geological features, but the tectonic activity in Karroo and later times thus indicated, may be a pointer to a possible source (see section (4.5.2)).

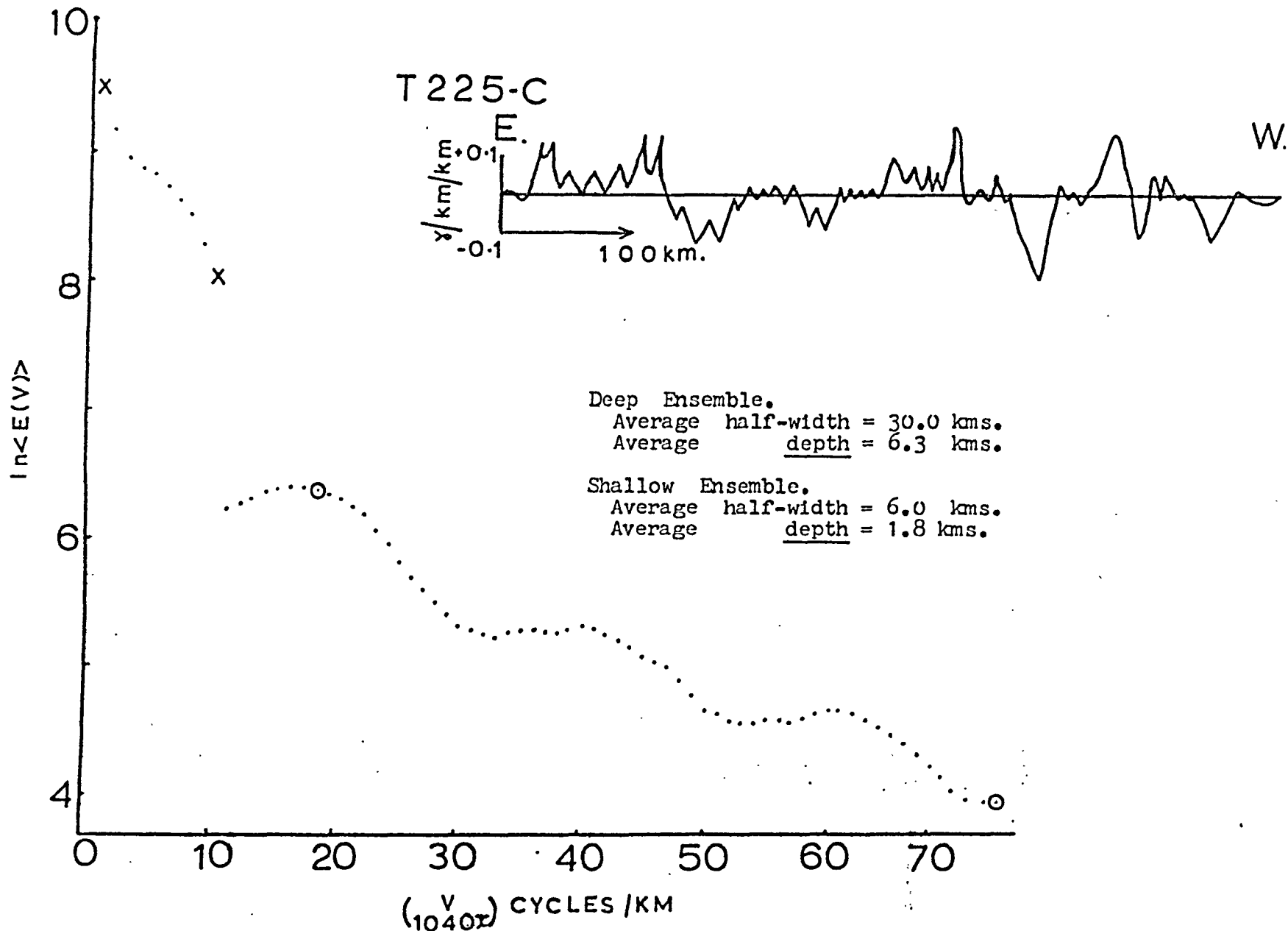
The energy spectrum of the section of profile crossing the Mozambique Belt, to the west of the point f in figure (39), confirms shallow sources (0.1 km. below ground level) for the high wavenumber magnetic relief. From the original profile the average half-width to these shallow sources is estimated to be 6 km. (figure (42)). A deeper set of sources, at 4.6 km. below ground level, is also revealed in the energy spectrum. The second derivative curve is used to obtain an estimate of 30 km. for the average half-width of this deep set of bodies. The sources to the high amplitude anomalies near to the point marked f in figure (39) are probably included in this deep ensemble of bodies.



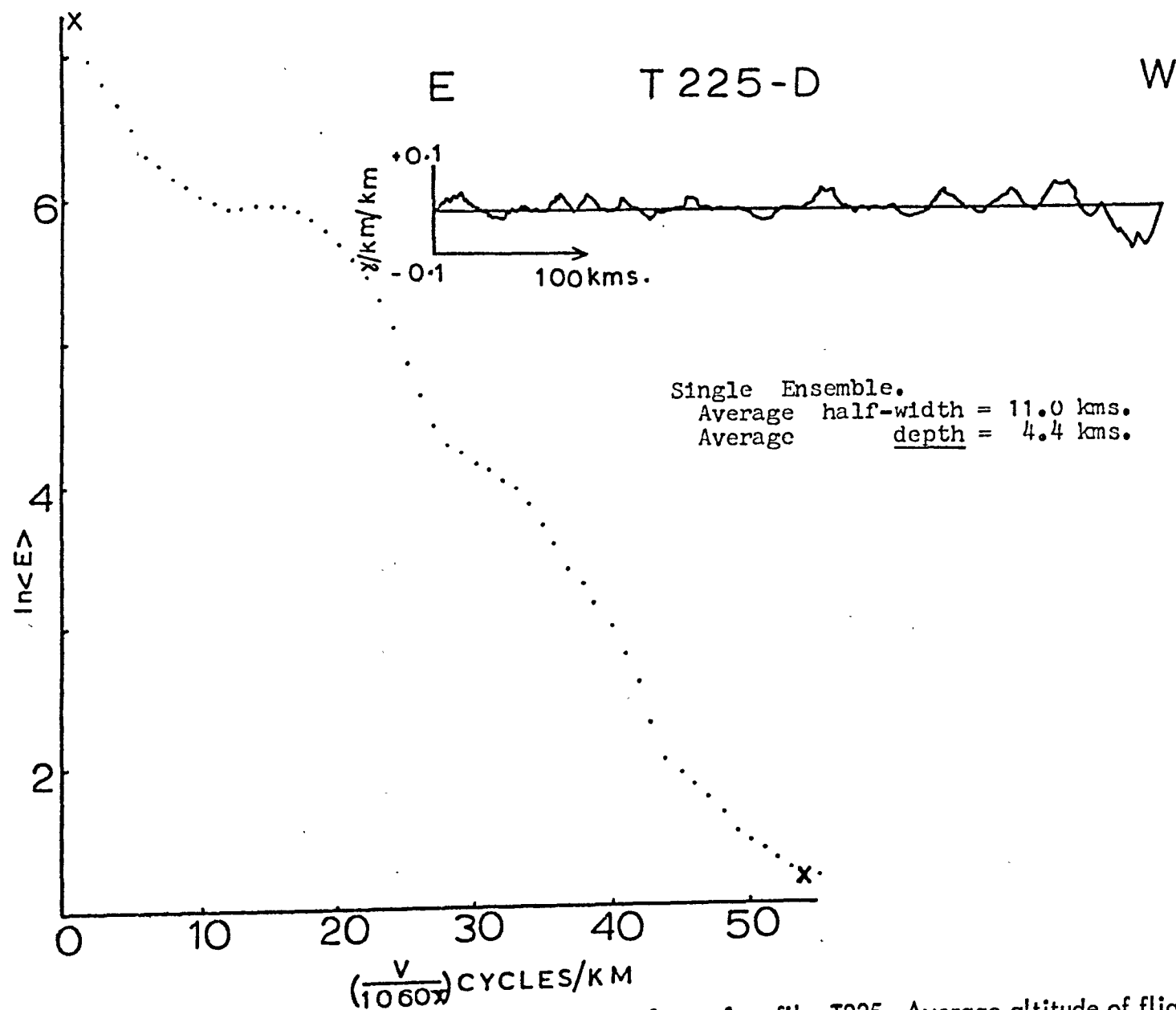
Fig(40) Energy spectrum and second derivative curve for section a - b of profile T225. Average altitude of flight above ground = 1.6km. Therefore the average depths below ground level are 7.5km. and 0.4km.



Fig(41) Energy spectrum and second derivative curve for section c - d of profile T225. Average altitude of flight above ground level = 1.6km. Therefore the average depths below ground level are 16.9km. and 0.4km.



Fig(42) Energy spectrum and second derivative curve for section e - f of profile T225. Average altitude of flight above ground = 1.7km. Therefore the average depths below ground level are 4.6km. and 0.1km.



Fig(43) Energy spectrum and second derivative curve for section f - g of profile T225. Average altitude of flight above ground = 2.2km. Therefore the average depth below ground level is 2.2km.

The amplitude of the anomalies observed to the east of the point f in figure (39) are noticeably less than to the west. Although there is considerable activity of 60 gammas amplitude, only twice over a distance of 510 km. is an anomaly greater than 100 gammas. This low magnetic relief is consistent with the underlying geology of mainly gneiss and migmatites. The energy spectrum for this region (f to g in figure (39)) yields only a single depth of 2.2 km. below ground level (figure (43)). This estimate must be viewed with caution as a very broad (400 km. wide) low gradient magnetic trough of approximately 120 gammas (this anomaly is best observed in the upward continued curves of figure (39)) may be affecting the spectrum. The magnetic trough does not constitute a complete cycle and therefore the energy associated with it, will 'leak' into the low wavenumber part of the spectrum; unfortunately the effect of this anomaly cannot be quantitatively estimated. From the second derivative curve a value of 11 km. is obtained for the average half-width of this ensemble of bodies.

(4.4.4) Flight T203

Except for a distance of 250 km. in the west of the continent, profile T203 has a transcontinental path at approximately 12.5°S. (figure 20)). This profile crosses successively (i) the Angola Basement, (ii) the Kalahari Basin in which outcrops of the Kasai Shield are observed, (iii) the Katangan Belt, (iv) the Irumide Belt, and (v) the Mozambique Belt (figure (22), figure (44)).

(4.4.4.1) The Angola Basement and Kalahari Basin Sediments (including a region of the Kasai Shield)

The pattern of continuous high amplitude magnetic anomalies from the Angola Basement to the margin of the Katangan Belt, shown in this

length of profile (a to c in figure (44)), is essentially the same as that described for profile T225 in section (4.4.3.1). The Karroo dolerites mentioned in that section are observed in several outcrops beneath the flight path of profile T203 (figure 44)). This supports the hypothesis that the Karroo volcanic rocks are the principle source to the very high amplitude short wavelength magnetic anomalies observed on both profiles. The energy spectrum of this section of profile (a to b in figure (44)) shows a shallow ensemble of bodies at an average depth below ground level of 0.7 km. (compare to 0.4 km. obtained from profile T225) while the original profile yields an average half-width of 10 km. for the short wavelength anomalies (figure (45)).

The high amplitude long wavelength anomalies, which are clearly observed on the upward continued curves of figure (44), are shown in the energy spectrum to have their sources at an average depth of 6.7 km. below ground level (figure (45)) (compare to 7.5 km. obtained from profile T225). From the second derivative curve these deep bodies have an estimated half-width of 36.0 km.

(4.4.4.2) Katangan and Irumide Orogenic Belts

In the region where Katangan rocks are observed within the Kalahari sediments (section b to c in figure (44)) the magnetic relief is generally less than 100 gammas; this low relief extends for a distance of approximately 270 km. After this distance the amplitude of the anomalies gradually increase until anomalies exceeding 200 gammas are frequently recorded. Although the majority of this magnetic relief is concentrated in the long wavelengths (note the high amplitude of the long wavelength anomalies in the upward continued curves of figure (44)) there are a number of anomalies of 200 gammas amplitude which have widths of only 12 km. The shallow depth of -0.1 km., obtained from the energy spectrum (figure (46)) of this section of profile (c to d in figure (44)),

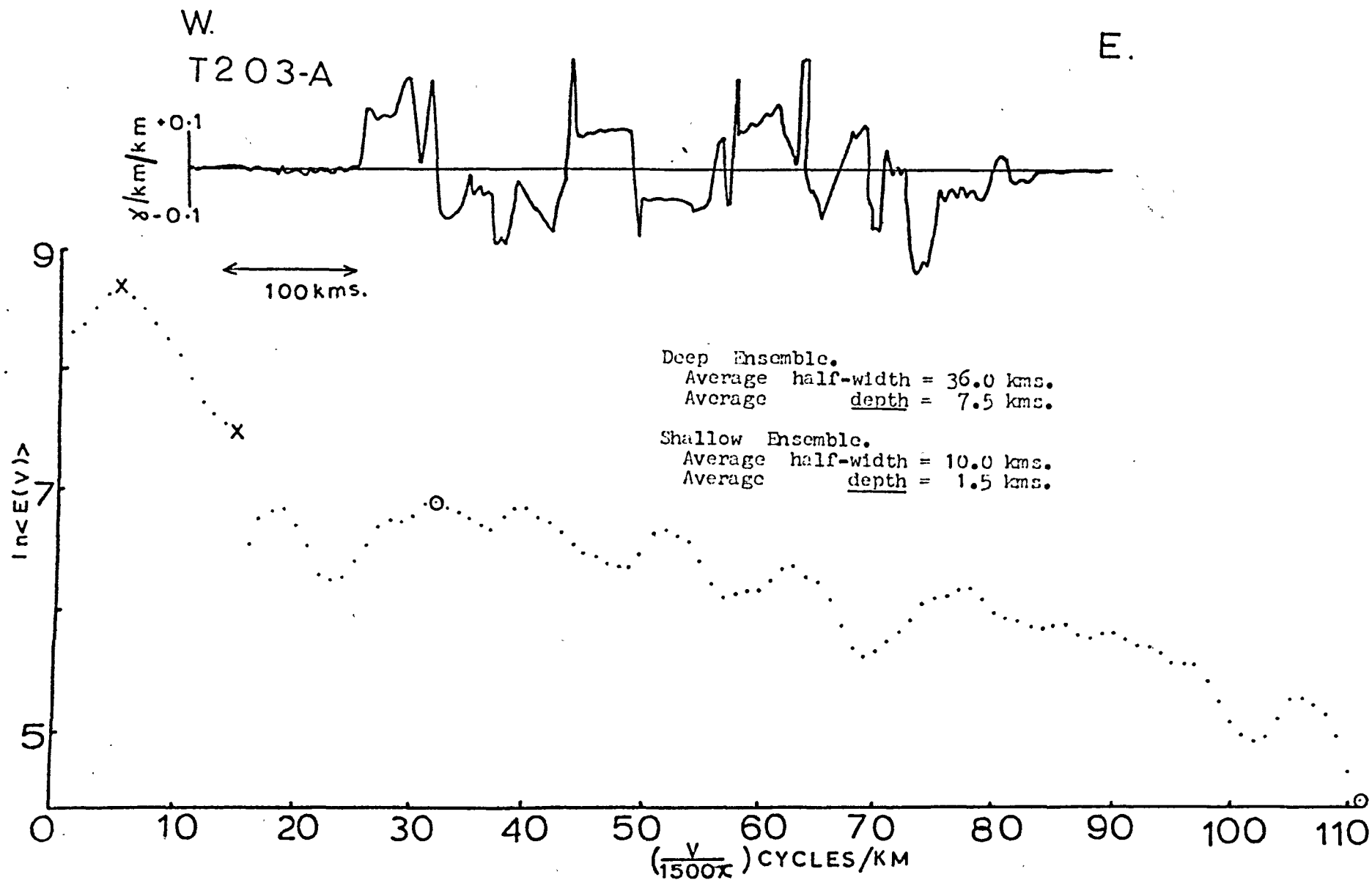
suggests that the ironstones found within the Katangan system (figure (44)) are the most probable source to these high amplitude, short wavelength anomalies. From the original profile an average half-width of 6 km. is obtained for these shallow features.

The sources to the long wavelength anomalies are shown in the energy spectrum at an average depth of 22.8 km. below ground level, while their average half-width is estimated from the second derivative curve to be 25 km. (figure (46)).

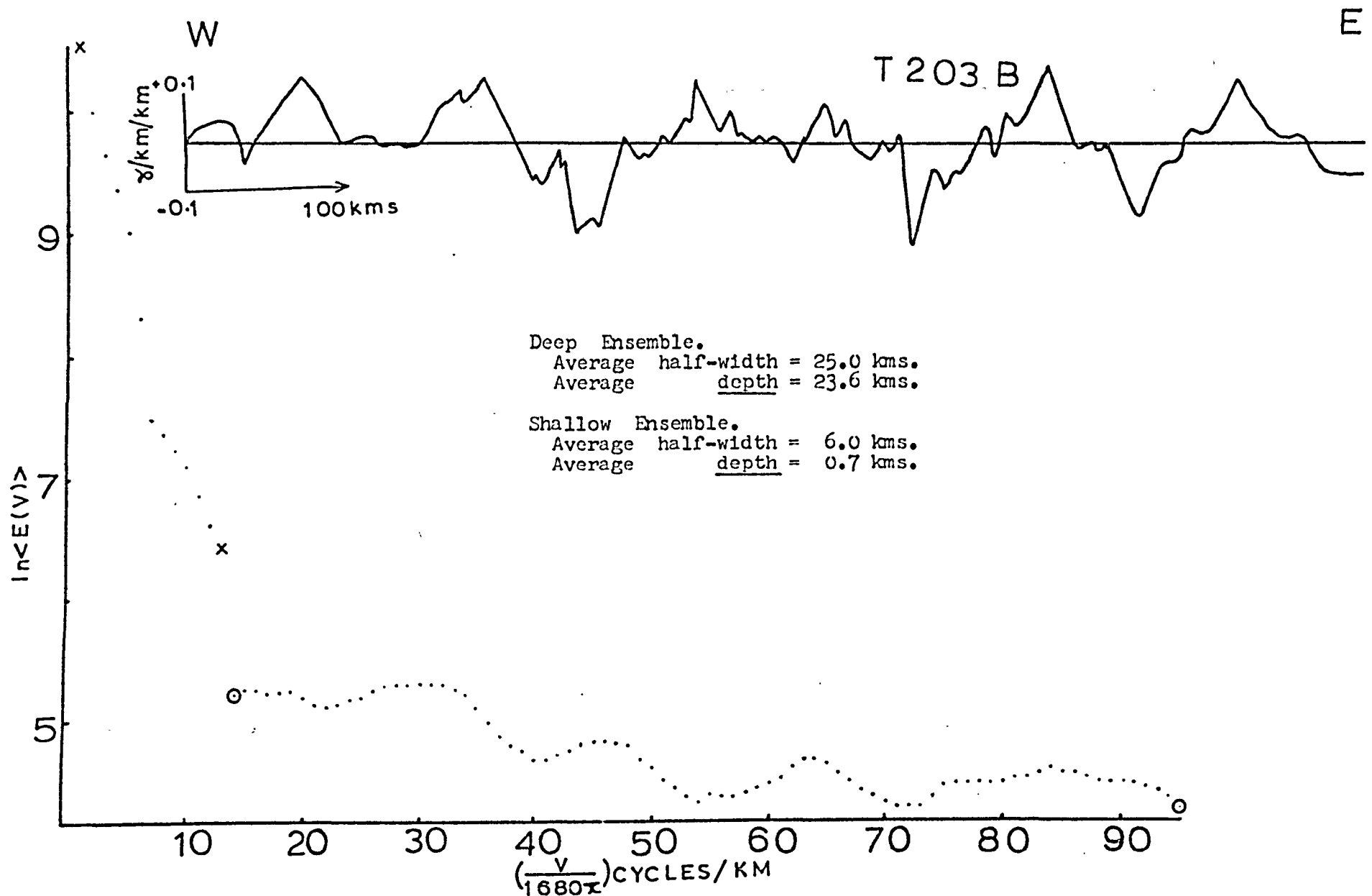
(4.4.4.3) The Mozambique Orogenic Belt

There is a marked decrease in the amplitude of the high wavenumber magnetic relief as profile T203 crosses from rocks of the Zambia Basement (affected by the Irumide Orogeny) onto those of the Mozambique Belt. Some of this change may be attributed to the 2.2 km. increase in altitude of the aeroplane (figure (44)). Between the points marked d and e in figure (44) the profile is dominated by high amplitude long wavelength anomalies. The energy spectrum of this section of profile shows that the sources to these anomalies are situated at an average depth of 5.6 km. below ground level, while the second derivative curve yields an average half-width of 48 km. (figure (47)). The source to the prominent double peak (200 gammas to 300 gammas amplitude) to the west of the point marked e in figure (44) is discussed further in section (4.5.2).

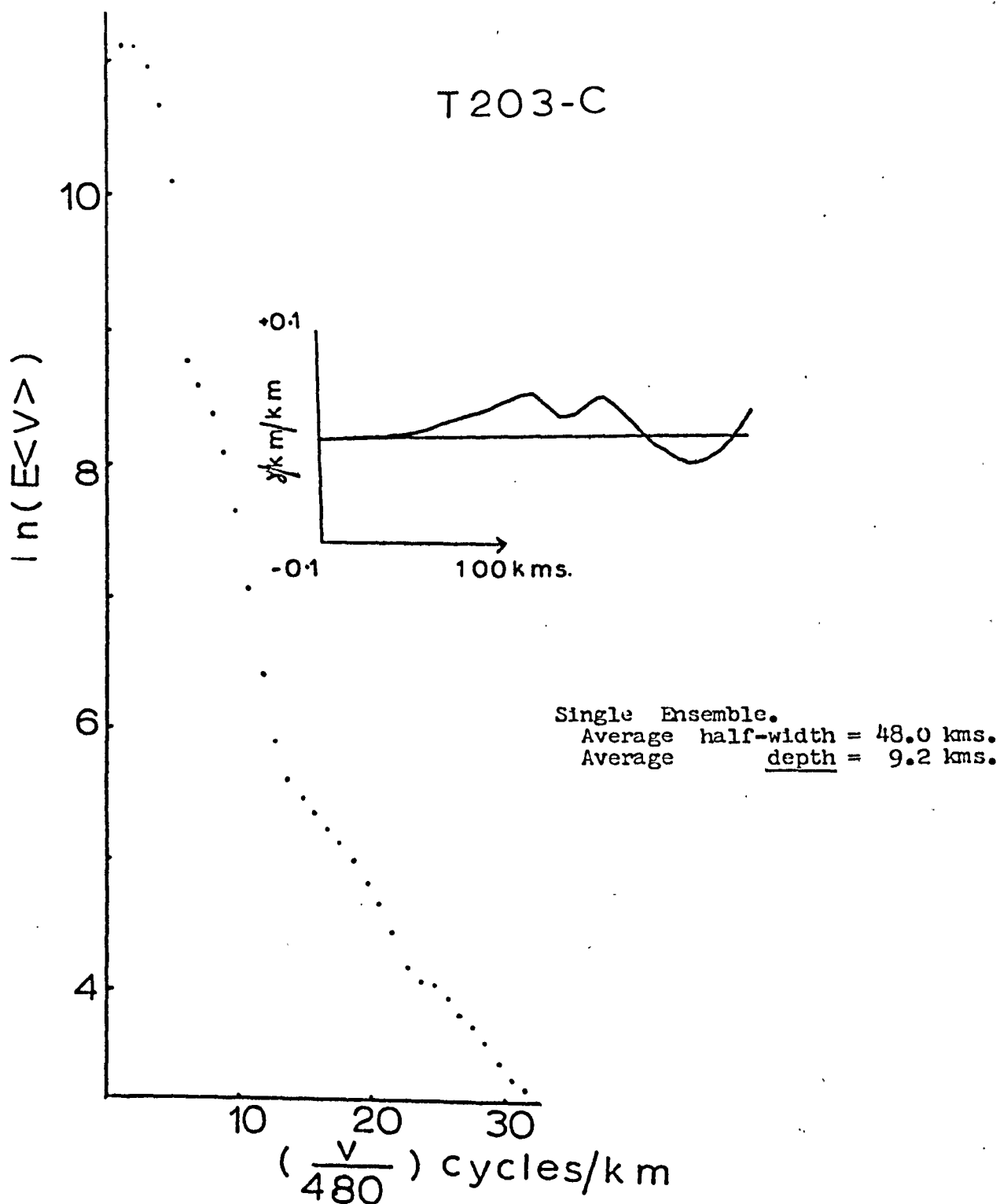
The amplitude of the anomalies observed to the east of the point e in figure (44) are noticeably less than to the west (note the equivalent situation at the point f on profile T225 (figure (39))). These low amplitude anomalies, which are mostly of 50 gammas amplitude with widths near to 16 km., are consistent with the underlying geology of mainly gneissic rocks. The shallow gradient of the energy spectrum



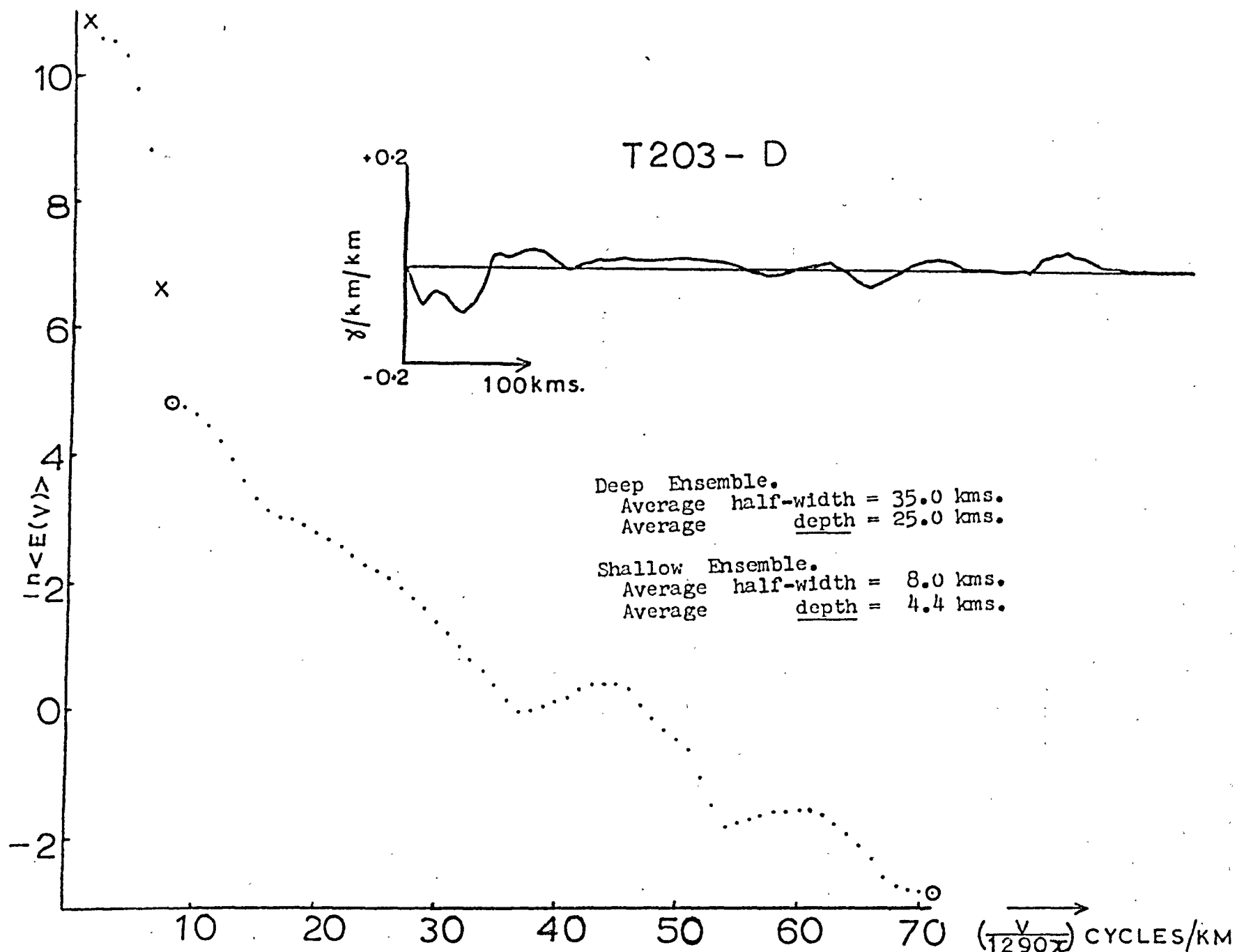
Fig(45) Energy spectrum and second derivative curve for section a - b of profile T203. Average altitude of flight above ground level = 0.8km. Therefore the average depths below ground level are 6.7km. and 0.7km.



Fig(46) Energy spectrum and second derivative curve for section c - d of profile T203 . Average altitude of flight above ground = 0.8km
Therefore the average depths below ground level are 22.8km. and -0.1km.



Fig(47) Energy spectrum and second derivative curve for section d - e of profile T203. Average altitude of flight above ground level = 3.6km. Therefore the average depth below ground level is 5.6km.



Fig(48) Energy spectrum and second derivative curve for section e - f of profile T203. Average altitude of flight above ground level = 4.0km. Therefore the average depths below ground level are 21.0km. and 0.4km.

of this section of profile (e to f in figure (44)) yields an average depth of 0.4 km. below ground level for the sources of this low amplitude relief (figure (48)). From the steep gradient of the spectrum an average depth of 21 km. is obtained for the sources to the long wavelength anomalies. These long wavelength features only appear as 40 gammas undulations in the upward continued curves of figure (44) but show up clearly in the second derivative curve (figure (48)); from the latter curve an average half-width of 35 km. is obtained.

(4.4.5) Flight T220

Except for a distance of approximately 250 km. in the west of the continent, flight T220 has a transcontinental path between latitudes 4°S. and 10°S. (figure (20)). This profile crosses successively (i) the Congo Basin Sediments (includes a region tectonically defined as the Kasai Shield), (ii) the Kibaran Orogenic Belt, (iii) the Ubendian Orogenic Belt and (iv) the Mozambique Orogenic Belt (mostly covered by Karroo sediments) (figure (21) and figure (49)).

(4.4.5.1) The Congo Basin Sediments and the Kasai Shield

High amplitude, long and short wavelength, magnetic anomalies are continuous across this section of the Congo Basin and the Kasai Shield. The tectonic classification of the Kasai Shield in figure (49) is based on the work of Cahen and Snelling (1966) and Cahen and Lepersonne (1967) in which Dibaya Migmatites (section (1.5.3)) are reported to the north of the profile, while the geology is based on the Geological Map of the Belgian Congo (1951)). The high magnetic relief of this region is also observed on a vertical component anomaly map (figure (53)), compiled by Evrard et. al. (1959). From figure (53) it is clear that the high

magnetic anomalies are restricted to south of approximately 4°S . Lack of basement outcrops in this region prevents a magnetic anomaly to geology correlation. But the inferred basement of Dibaya rocks allows a meaningful guess as to the source of the high amplitude, short wavelength anomalies. Further south within the exposed Dibaya Complex, there are two main types of rock which may yield high magnetic anomalies. These are (i) Basic to ultrabasic intrusives (mainly serpentinite, pyroxenite and dolerite lavas) (Cahen and Lepersonne (1967)) and (ii) some massive iron ore deposits (Haematite-magnetite bodies with 40% to 60% Fe content - Cahen and Lepersonne (1967)). Evrard (personal communication (1972)), who has conducted a magnetic survey over this southern region, reports only small anomalies across exposures of the former rock type, while very high magnetic anomalies (upto 16,000 gammas vertical component) are recorded across the iron ore bodies. Thus it is reasonable to infer similar iron ore sources for some of the anomalies recorded on profile T220. However it is unreasonable, on the basis of Evrard's communication alone, to disregard the possibility of a significant magnetic contribution from the igneous rocks, which may well include Karroo volcanics (Cahen and Lepersonne (1967)).

The energy spectrum of this section of profile (a to b in figure (49)) indicates two ensembles at relatively shallow depths (figure (50)). The probable igneous/iron ore sources to the high wavenumber magnetic relief is shown to be at an average depth of 0.4 km. below ground level; from the original profile the average half-width of these bodies is estimated to be 6 km. The sources to the longer wavelength anomalies are estimated to be at an average depth of 2 km., with an average half-width of 30 km. (figure (50)); the peak in the spectrum at the 9th harmonic indicates that these sources are probably thin (less than 5 km. thick).

(4.4.5.2) The Kibaran Orogenic Belt (includes an outcrop of the Bushimay Series)

The amplitude of the magnetic anomalies recorded across this section of profile (b to c in figure (49)) are very low with both boundaries of this orogenic belt being marked by distinct changes in magnetic relief (figure (49)). Although this region seems to be well-defined on the Tectonic Map of Africa (1968), more recent articles show that this region is unsurveyed (e.g. Cahen (1970)); it is therefore not possible to state the rock types crossed by this section of profile.

The magnetic relief is generally too low, with too few anomalies, to obtain a statistical depth estimate.

(4.4.5.3) The Ubendian Orogenic Belt

The section of profile which crosses this orogenic belt (c to e in figure (49)) is characterised by high amplitude, long and short wavelength, magnetic anomalies. These anomalies extend across the region marked ? on the tectonics of figure (49). This latter region was originally part of the Ubendian Belt but is now believed to have been reworked in the later Kibaran and Mozambique Orogenies (see sections (1.2.2.2), (1.3.1) and (1.4.5), and figure (21)). The pattern of high magnetic relief does not appear to have been affected by these later events. Note the excellent correspondence between the tectonic boundaries and the region of high magnetic relief observed on the original profile and the upward continued curves (figure (49)).

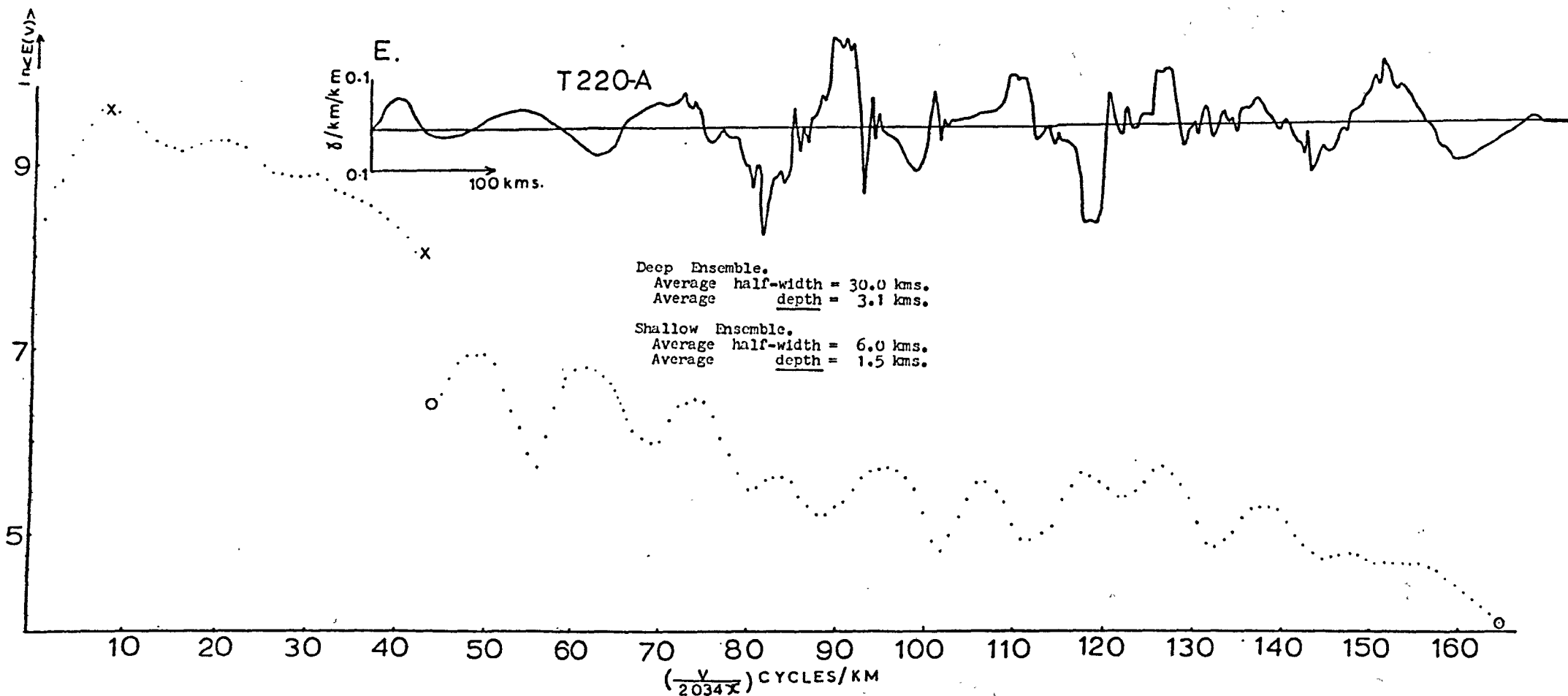
Over the section of profile c to d in figure (49) most of the high wavenumber magnetic relief may be confidently correlated (a one to one correspondence is often possible) with the surface geology of (i) large granite masses, (ii) basic intrusives and (iii) a large outcrop of 'ancient acid lavas'. The high amplitude (600 gammas) negative anomaly

east of the point marked d in figure (49) is almost certainly caused by the Rungwe volcanic cone which it crosses at this point. From the sign of the anomaly it is inferred that the major volume of the volcano is reversely magnetised. The complexity of the region to the east of the recent volcanic outcrop permits only a general correlation of the high magnetic relief with the underlying basic to ultrabasic rocks. The margin of these latter rock types is well defined by the magnetic profile, which shows an abrupt change of character near the western margin of a large outcrop of Karroo sediments (the Ruhuhu Basin).

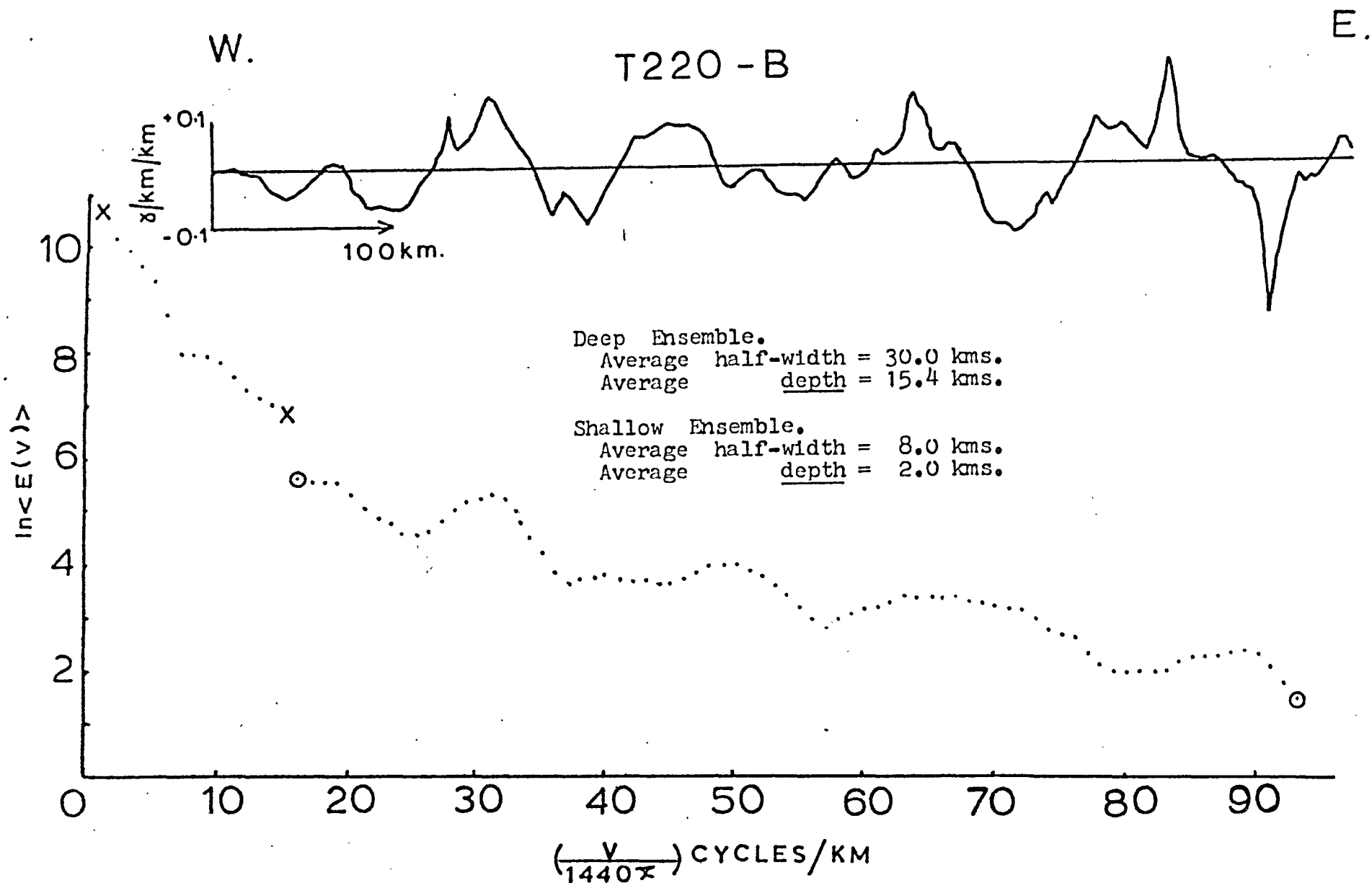
The possible effects of later orogenies (Irumide and Mozambique) and the extrusion of recent volcanic rocks in the area marked ? would not reasonably allow this region to be included as part of the Ubendian Orogenic Belt; for this reason, only the region which has remained stable since the Precambrian C is included in the average depth analysis. The shallow gradient of the energy spectrum of this section of profile (c to d in figure (49)) yields an average depth of 0.0 km. below ground level (figure (51)), confirming the correlations of the geology with the high wavenumber magnetic relief. From the original profile an average half-width of 8 km. is obtained for these shallow sources (figure (49) and figure (51)). The long wavelength magnetic anomalies, which are most clearly observed on the upward continued curves, are shown to have their sources at an average depth of 13.4 km. below ground level; an estimate of 30 km. is obtained from the second derivative curve for the average half-width for these deep sources.

(4.4.5.4) The Mozambique Orogenic Belt

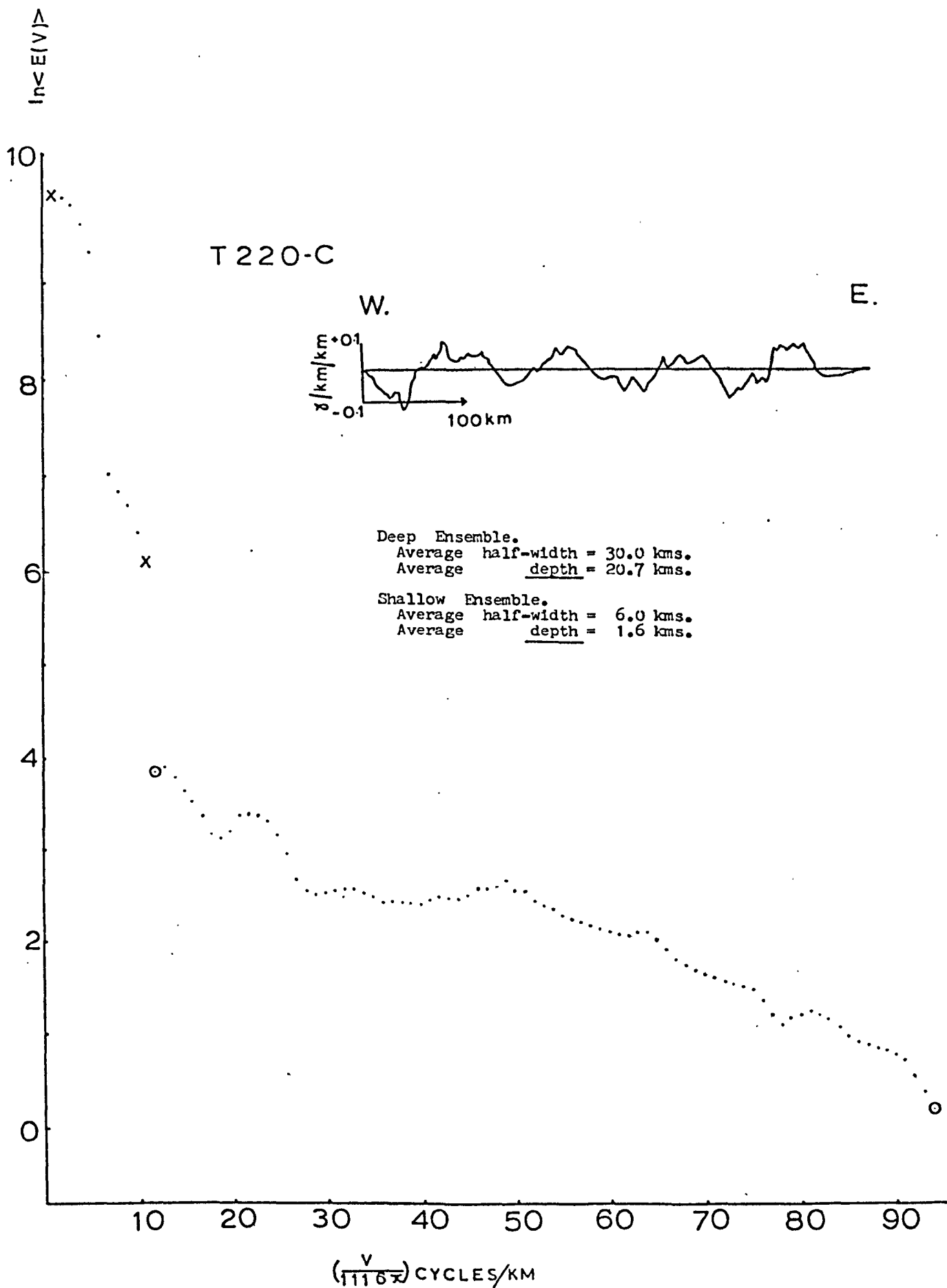
Only a small outcrop of rocks of the Mozambique Belt are observed to the east of the Ruhuhu Basin (this outcrop is shown beneath



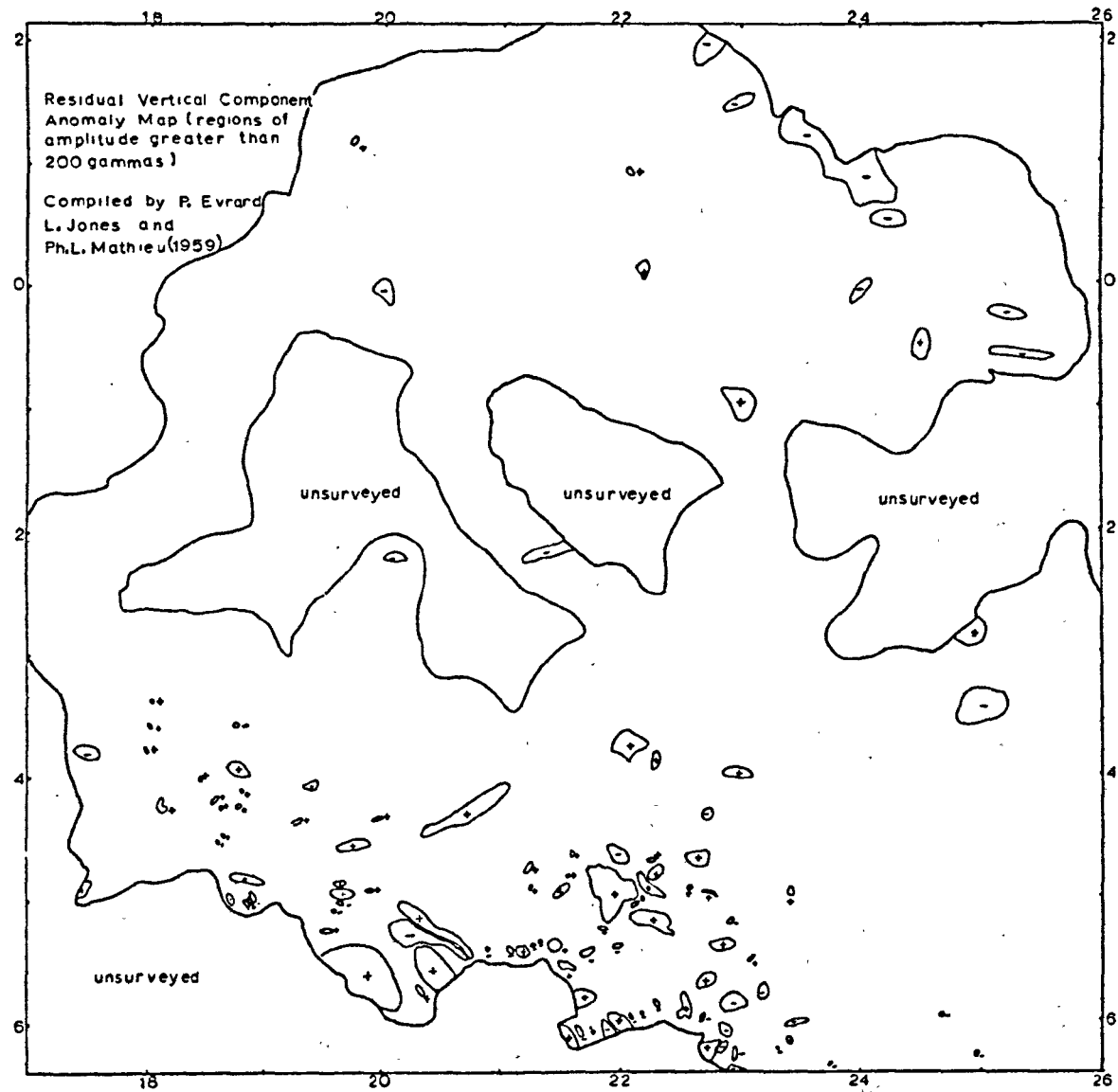
Fig(50) Energy spectrum and second derivative curve for section a - b of profile T220. Average altitude of flight above ground level = 1.1km. Therefore the average depths below ground level are 2.0km. and 0.4km.



Fig(51) Energy spectrum and second derivative curve for section c - d of profile T220. Average altitude above ground level of flight = 2.0km. Therefore the average depths below ground level are 13.4km. and 0.0km.



Fig(52) Energy spectrum and second derivative curve for section e - f of profile T220. Average altitude of flight above ground level = 1.1km. Therefore the average depths below ground level are 19.6km and 0.5km.



Fig(53)

the point marked e in figure (49)) before Karroo sediments are again encountered. The continuous low magnetic relief (mostly less than 100 gammas) which is observed from the point marked e to the coast is evidence that rocks of the Mozambique Belt are basement to the Karroo sediments. The energy spectrum of this section of profile (e to f in figure (49)) reveals a shallow source of bodies at an average depth 0.5 km. below ground level and a deep ensemble at 19.6 km. average depth (figure (52)). The magnetic effects of this deep ensemble of bodies appear as 60 km. wide undulations, of only 30 gammas to 50 gammas amplitude, in the upward continued curves of figure (49), but show up very clearly in the second derivative curve (figure (52)).

(4.4.6) Flight T219a

Except for distances of approximately 250 km. and 500 km. in the west and east respectively, flight T219a has a transcontinental path between latitudes 5°S. and 1°S. (figure (20)). The profile crosses successively (i) the Congo Basin Sediments, (ii) the Kibaran Orogenic Belt (the Burundian and Karagwe Ankolean in figure (54)), (iii) Lake Victoria and the Tanganyika Shield and (iv) the Mozambique Orogenic Belt (figure (21) and figure (54)).

(4.4.6.1) The Congo Basin Sediments

The first 800 km. to 1000 km. of this profile consists of medium amplitude (100 gammas to 250 gammas) long wavelength (50 km. to 100 km. width) magnetic anomalies (figure (54)). Very little energy is observed in the short wavelength anomalies. Deep drilling (Evrard (1960)) directly beneath the flight path at position (3°34'S., 21°24'E) has revealed a basement of Precambrian A platform sediments similar to those of the West Congolian Orogenic Belt, outcropping to the west of the

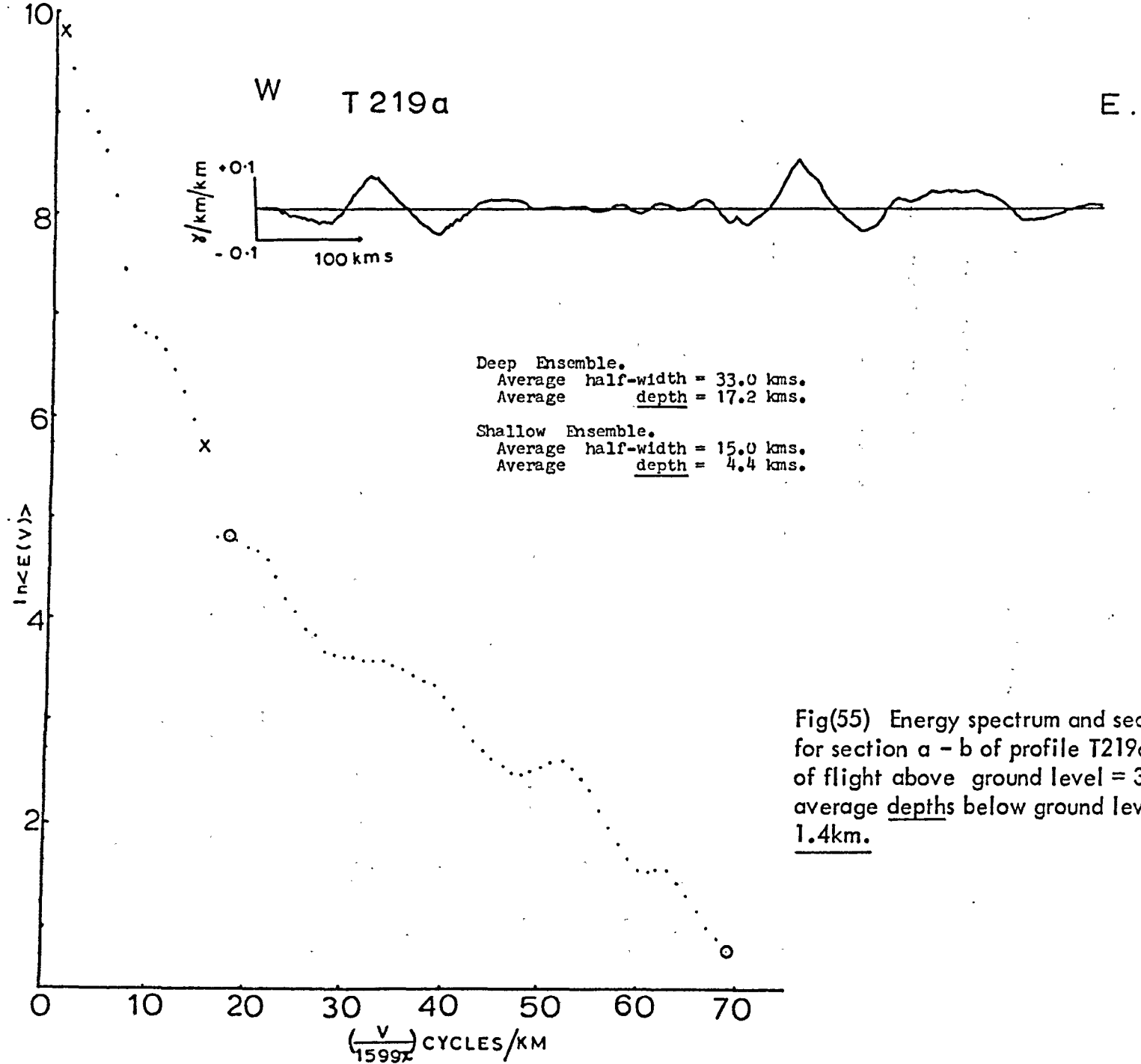
profile (figure (21)). This low magnetic basement (there is no igneous activity reported for the West Congolian Orogenic Belt (Cahen and Lepersonne (1967)) is therefore consistent with the low amplitude of the short wavelength anomalies. The 1.4 km. average depth to magnetic sources, obtained from this section of profile (a to b in figure (55)) probably indicates the depth to the 'basement' of the Precambrian A formation; this estimate is too deep to represent the depth to the Precambrian A rocks. From the original profile a value of 15 km. is obtained for the average half-width of this shallow ensemble of bodies. The steep slope of the energy spectrum yields a depth of 14.2 km. below ground level for the source of the long wavelength anomalies (see the upward continued curves in figure (54)), while the second derivative curve gives an average half-width of 33 km. (figure (55)).

East of the point marked b in figure (54) the magnetic relief is always less than 50 gammas and as this low relief is continuous into the Burundian formation on the east it is reasonable to postulate that this formation is basement to the sediments in this region.

(4.4.6.2) The Kibaran Orogenic Belt (the Burundian and Karagwe Ankolean Formations)

The section of profile crossing the Kibaran Orogenic Belt is characterized by very low magnetic relief. Except for a part of the profile which crosses a recent lava field, south of Lake Kivu (marked c in figure (44)), the magnetic anomalies are always less than 50 gammas. This low magnetic relief is consistent with the underlying geology of sediments, schists and occasional granite.

In this and subsequent sections of the profile, the magnetic relief is generally too low, with too few anomalies for a statistical depth analysis.



Fig(55) Energy spectrum and second derivative curve for section a - b of profile T219a. Average altitude of flight above ground level = 3.0km. Therefore the average depths below ground level are 14.2km. and 1.4km.

(4.4.6.3) Lake Victoria and the Tanganyika Shield

There is a small increase in the magnetic relief as the profile crosses from the Kibaran Orogenic Belt onto Lake Victoria and subsequently the Tanganyika Shield (figure (44)). In general it is not possible to correlate the low amplitude anomalies (~50 gammas) recorded across the Tanganyika Shield with specific geology, although the large amplitude negative anomaly (100 gammas to 200 gammas) observed near to the eastern margin of the shield may be associated with the granite/granodiorite mass which it straddles.

(4.4.6.4) The Mozambique Orogenic Belt

Only a small section of this profile crosses the Mozambique Belt, and for almost one half of this section the anomaly pattern is dominated by the effects of Plio-Pleistocene trachytes and associated pyroclastics (figure (44)). Within the region of exposed Mozambique Belt the magnetic relief is less than 50 gammas while across the volcanic rocks the relief is as high as 100 gammas.

(4.4.7) Flights T201 and T202

Except for a gap of approximately 130 km., flights T201 and T202 have a transcontinental path at approximately latitude $0^{\circ}30' \text{ N}$. (figure (20)). These profiles cross successively (i) the Cameroun Shield, (ii) the Congo Basin Sediments (including the Sembe Ouessou and Lindian Formations), (iii) the Kibalian Orogenic Belt, (iv) the Uganda Basement and (v) the Mozambique Orogenic Belt (figure (21), figure (56) and figure (59)).

(4.4.7.1) The Cameroun Shield

The first 200 km. of profile T202 are dominated by three high amplitude (150 gammas to 300 gammas) magnetic troughs (figure (56)).

There is difficulty in correlating these anomalies with the geology observed beneath the profile. It is unlikely that the pyroxene gneiss (charnokites?), shown in this locality, are the source to these anomalies but the correlation of the second trough with a dolerite intrusive may be significant. For the next 200 km. of track the magnetic profile is characterized by low amplitude (~ 60 gammas) short wavelength anomalies (6 km. to 15 km. wide) superimposed on a broad magnetic hump of almost 200 gammas amplitude (see the upward continued curves of figure (56)). The amphibolite-granite rocks shown on the geology for this region are consistent with the low amplitude of the short wavelength anomalies. The 0.1 km. average depth (figure (57)) obtained from the energy spectrum of this section of profile (a to b in figure (56)) confirms that these surface rocks are the source to the short wavelength magnetic anomalies. From the original profile an estimate of 5 km. is obtained for the average half-width of these bodies. The steep slope of the low 'harmonics' of the spectrum indicates the existence of a deep ensemble of magnetic bodies, but a large peak in this section of the spectrum (figure (57)) prevents a least squares depth analysis. From the second derivative curve a value of 33 km. is obtained for the half-width of the deep bodies.

(4.4.7.2) The Congo Basin Sediments (including the Sembe Ouesso and Lindian Formations)

For approximately 250 km., the pattern of low amplitude short wavelength magnetic anomalies superimposed on higher amplitude undulations (~ 100 gammas), is preserved as the profile crosses from the Cameroun Shield onto the Sembe Ouesso Formation and subsequently the Congo Basin Sediments (figure (56)). After this, for approximately 500 km., the anomalies are of generally long wavelength with low amplitudes (~ 50 gammas).

This pattern is also shown on the vertical component anomaly map of figure (53). Towards the end of profile T202 (figure (56)) and at the beginning of profile T201 (figure (59)) the magnetic relief increases to values in excess of 100 gammas.

Deep drilling, almost directly beneath the flight path of profile T202, at (0°13'N., 21°25'E.) (Evrard (1960)), has revealed a basement of Precambrian A platform sediments similar to those which outcrop to the north and west of the profile (figure (21)). This low magnetic basement is consistent with the magnetic profile data observed here. The energy spectrum of the section of profile b to c in figure (56) reveals only a deep ensemble of bodies at an average depth of 19.5 km. below ground level, while the second derivative curve yields an average half-width of 41 km.; the average depth estimate must be viewed with extreme caution as this length of profile contains a large section in which the anomalies are only 50 gammas amplitude.

(4.4.7.3) The Kibalian Orogenic Belt, the Lake Albert Rift and the Uganda Basement

From the western margin of the Kibalian Orogenic Belt to the eastern margin of the Uganda Basement, long wavelength undulations, broken up by high amplitude shorter wavelength anomalies in the region of the Lake Albert Rift, are the most significant features recorded (see original curve and upward continued curves in figure (59)).

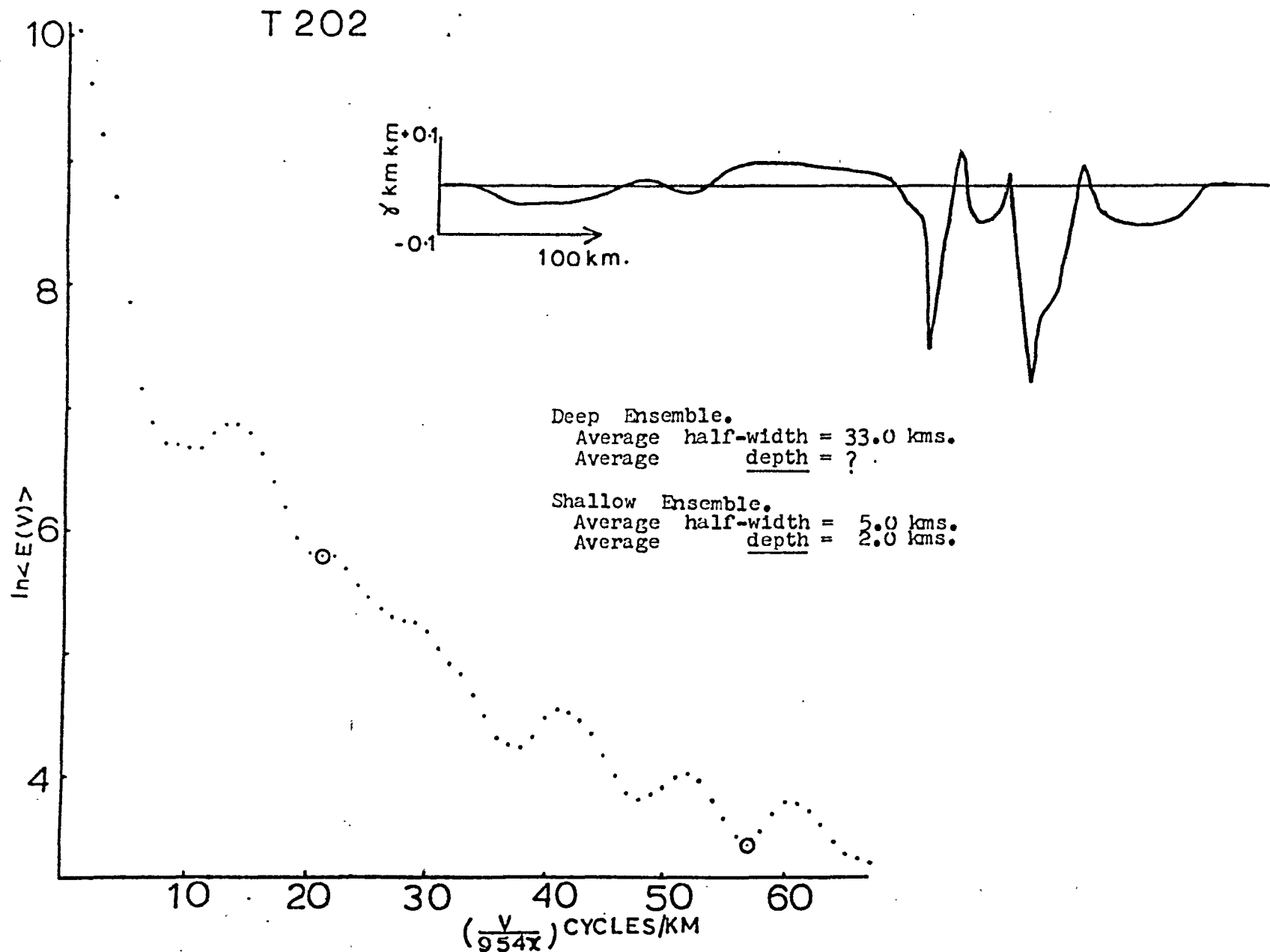
Correlation of the magnetic anomalies with specific geology is not possible. The isolated large amplitude, short wavelength anomalies prevents a meaningful depth analysis for this section of profile.

(4.4.7.4) The Mozambique Orogenic Belt

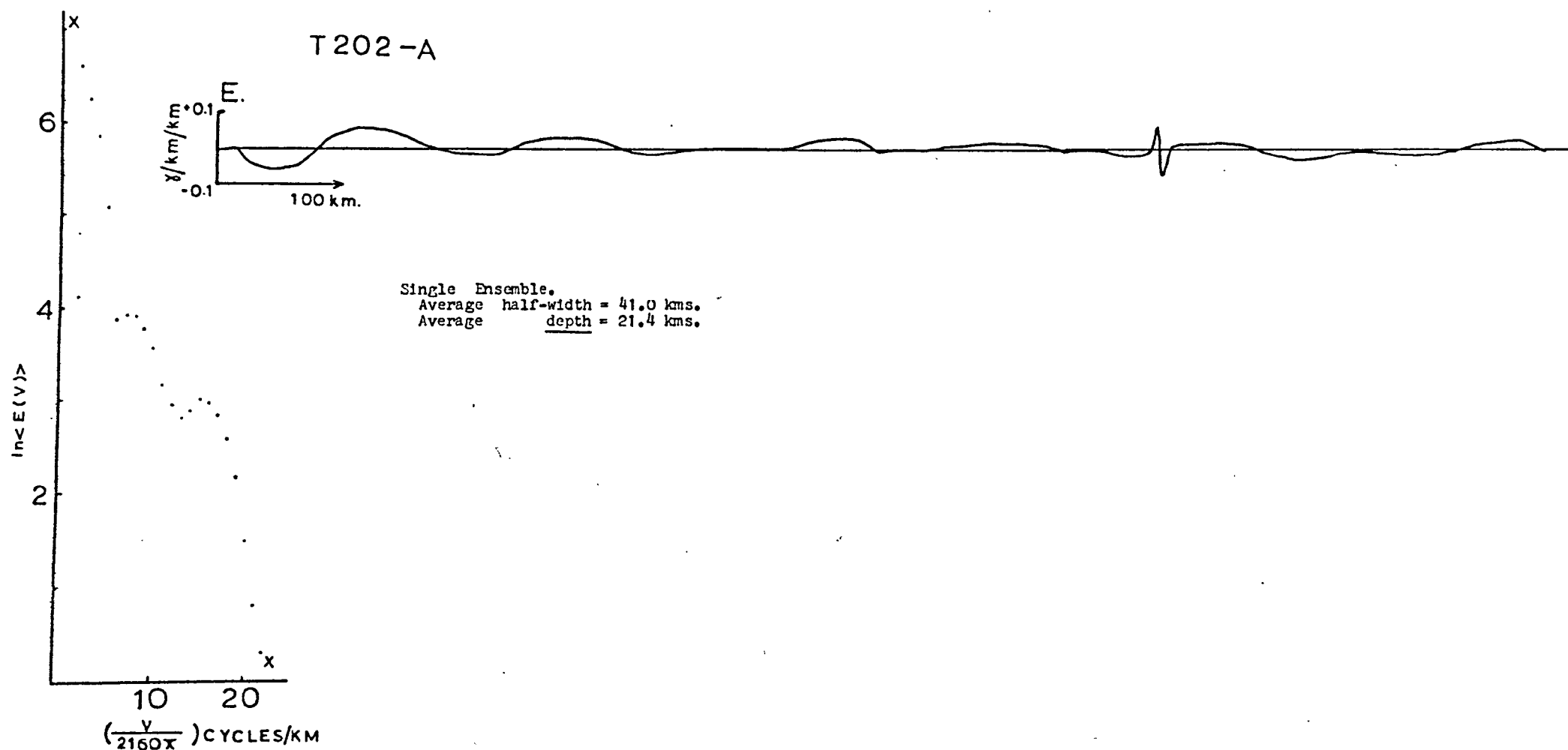
There is a noticeable change in the magnetic relief as the profile crosses from the Uganda Basement (see section (1.2.1) for a

discussion of the relationship between the Mozambique Orogenic Belt and the Uganda Basement) onto a region generally accepted as part of the Mozambique Belt (figure (59)). In contrast to the long wavelength magnetic 'hump' observed across the Uganda Basement, the section of profile crossing the Mozambique Belt is characterized by low amplitude (mostly less than 50 gammas) very short wavelength anomalies. Most of these anomalies may be directly related to the Tertiary volcanic rocks which outcrop either directly beneath the profile (note the correlation of the anomaly marked a and the anomalies between the points c and d with the underlying Tertiary volcanic rocks (figure (59)) or in the near vicinity of the profile (a large volcanic mass is observed only 2 km. from the flight path at the position of a 100 gammas negative anomaly marked e in figure (59)). The low magnetisation of the rocks of the Mozambique Belt is clearly demonstrated by the lack of magnetic expression of the massive Turkwell fault, at which point a drop in excess of 1.2 km. is shown in the topography (marked b on the topographic relief of figure (59)). The energy spectrum of the region of the Mozambique Belt not affected by Tertiary magmatism (e to f in figure (59)) shows an ensemble of bodies at an average depth of 2.7 km. below ground level (figure (60)). An average half-width of 26 km. is estimated from the second derivative curve of (figure (60)).

In the first 200 km. of profile which cross Triassic to Jurassic sediments (figure (59)) the magnetic record is almost 'flat'; the record is flat to an accuracy of 15 gammas. Towards the end of the profile, near to the east coast, the amplitude of the anomalies increases to values in excess of 50 gammas. No explanation of this change in magnetic relief is available from the geology, as the basement is hidden beneath a thick sedimentary cover. The average depth to the sources of the anomalies recorded over the section g to h in figure (59) is estimated

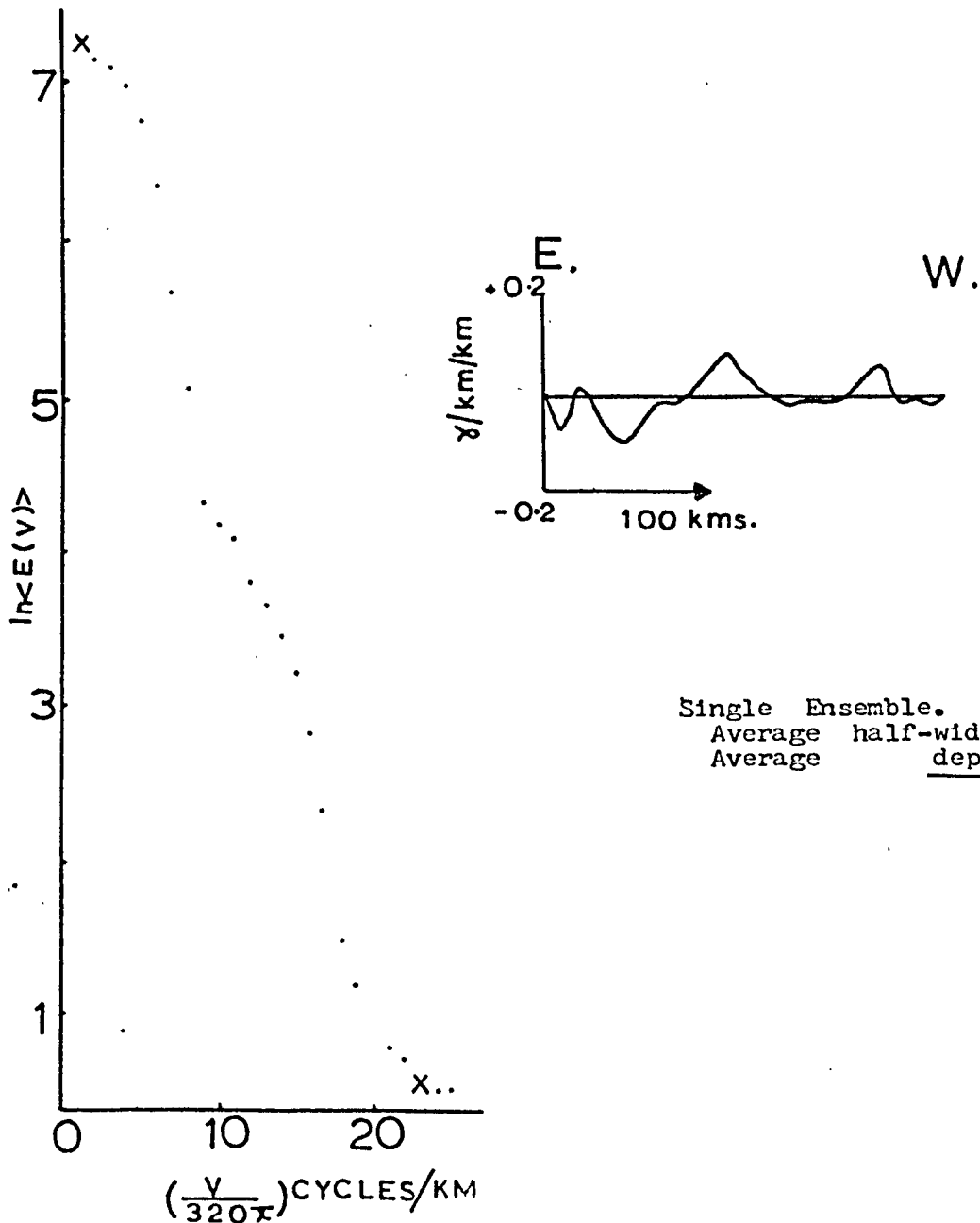


Fig(57) Energy spectrum and second derivative curve for section a - b of profile T202. Average altitude of flight above ground level = 1.9km. Therefore the average depth below ground level is 0.1km.

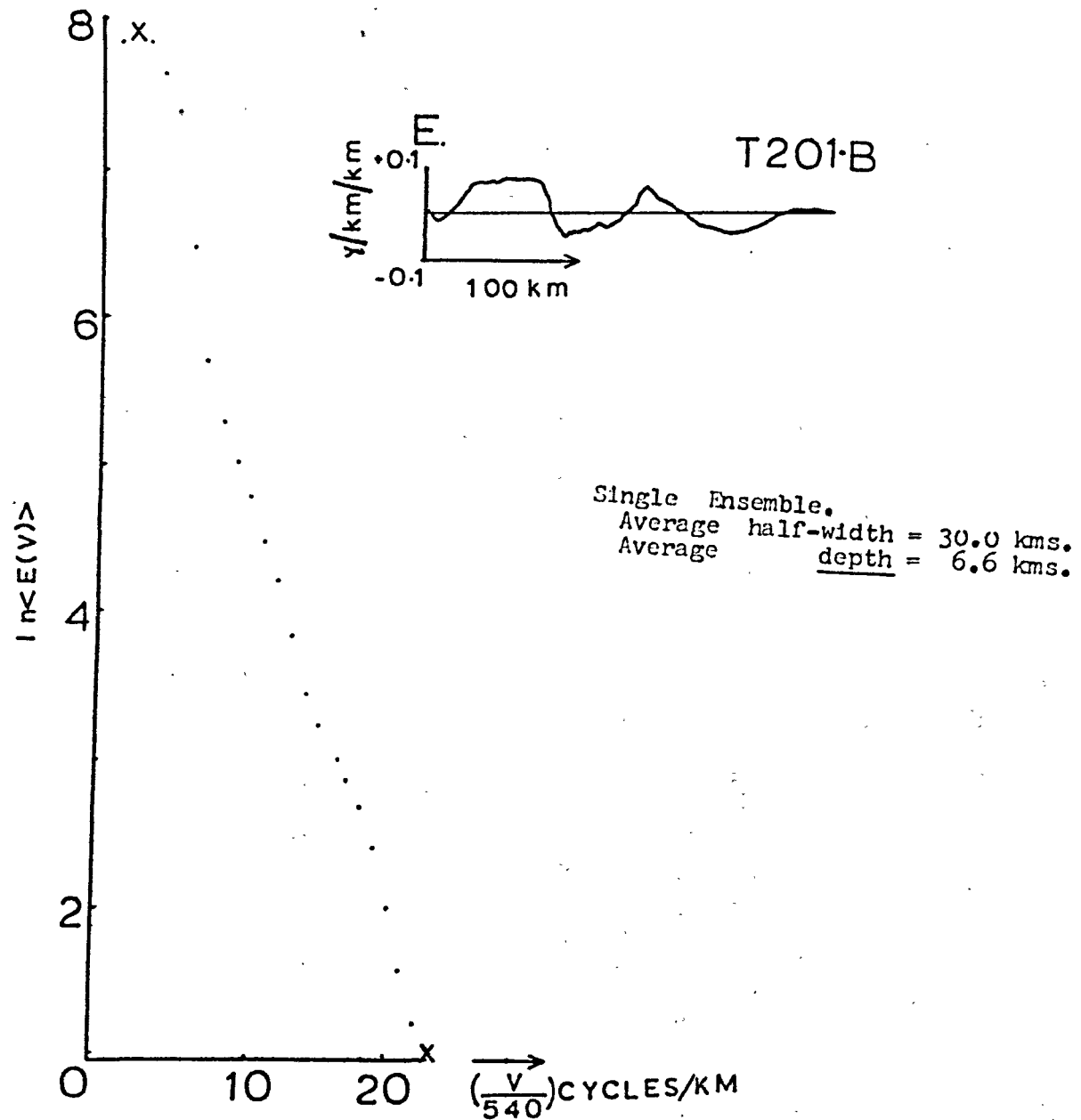


Fig(58) Energy spectrum and second derivative curve for section b - c of profile T202. Average altitude of flight above ground level = 1.9km. Therefore the average depth below ground level is 19.5km.

T201-A



Fig(60) Energy spectrum and second derivative curve for section e - f. of profile T201.
 Average altitude of flight above ground level = 2.3km. Therefore the average depth below
 ground level = 2.7km.



Fig(61) Energy spectrum and second derivative curve for section g -h of profile T201. Average altitude of flight above ground level = 1.9km. Therefore the average depth below ground level is 4.7km.

from the energy spectrum to be 4.7 km. below ground level (figure (61)) while the second derivative curve yields an average half-width of 30 km. for these bodies. The average depth estimate is in accord with the depth to basement shown in the postulated stratigraphic column of the Kenya coast, to the south of the profile (Francis et. al. (1966)).

(4.4.8) Flights T204 and T205

Except for a gap of approximately 400 km. and a section of Somalia, profiles T204 and T205 have a transcontinental path at approximately $3^{\circ}30'N$ (figure (20)). These profiles cross successively (i) the North Congo Shield (this includes the Cameroun Basement, the Congo Basin Sediments and the Liki Bembian Formation of figure (62)), (ii) the Kibalian Orogenic Belt, (iii) the Uganda Basement (this includes the West Nile Complex, the Lake Albert Rift and the Buganda-Toro Orogenic Belt in figure (62)) and (iv) the Mozambique Orogenic Belt (which includes the Tertiary volcanic rocks in figure (66)) (figure (21), figure (62), figure (66)).

(4.4.8.1) The North Congo Shield and the Kibalian Orogenic Belt

The similarity of very high amplitude negative long wavelength magnetic anomalies observed over the North Congo Shield and the Kibalian Orogenic Belt demands that these sections of profile be discussed together (figure (62)). The dominant negativity of these anomalies indicates reversely magnetised bodies while the very high amplitudes require very highly magnetic and stable sources. The high amplitude of these anomalies is even more impressive when it is remembered that this profile was recorded near to the magnetic equator. If the sources to the anomalies were moved undisturbed to latitude $20^{\circ}S.$, the amplitude of the anomalies would be almost doubled (compare figure (24) to figure (25)). The highest amplitude anomaly (between the points c and d in

figure (62)) is probably the most spectacular magnetic anomaly recorded to date. Although anomalies of similar amplitude have been reported (see for example figure (22)), none have the lateral extent of that shown in figure (62). Even when the profile is upward continued by 20 km. the anomaly maintains its high amplitude (figure (62)). The 750 km. wide anomaly between points c and d in figure (62) has an amplitude of 1200 gammas (peak to trough) at an altitude of 2.4 km. above ground level and an amplitude of 900 gammas at an altitude of 22.4 km. At satellite altitudes the anomaly is still prominent (Regan et. al. (1973)). This anomaly has been chosen from a global magnetic contour map, obtained from data recorded on the satellites Pogo and Cosmos 49, for special investigation.

The source to the high amplitude magnetic anomalies cannot be discerned from the surface geology of metamorphic and sedimentary rocks shown beneath the profile (figure (62)). These rocks may be the source of the very low amplitude short wavelength magnetic relief. Two sections of this profile have been subjected to average depth analysis. From the energy spectrum of section c to d in figure (62) a single ensemble of bodies is shown at an average depth of 29.9 km. below ground level (figure (63)); the spectrum past the last harmonic shown in figure (63) was almost perfectly 'white'. The second derivative curve yields an average half-width of 30 km. for these bodies. Two ensembles of magnetic bodies are revealed in the energy spectrum of section e to f in figure (62); a deep ensemble at an average depth of 8.4 km. with an average half-width of 38 km. (figure (64)) and a shallow ensemble at an average depth of -0.1 km. with an average half-width of 6 km. The shallow ensemble of bodies are probably the source to the low amplitude short wavelength magnetic anomalies observed over that section of profile (figure (62)).

From the average depths obtained from the energy spectrums it is reasonable to state that the source of the high amplitude magnetic relief is at 'great' depths (8.4 km. for e to f and 29.9 km. for c to d in figure (62)). The very low amplitude of the short wavelength magnetic relief supports this statement.

(4.4.8.2) The Uganda Basement (including the West Nile Complex, the Lake Albert Rift and the Buganda Toro Orogenic Belt)

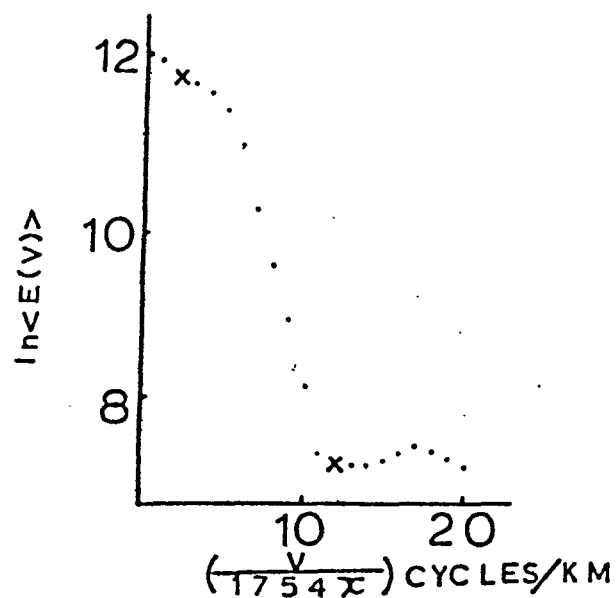
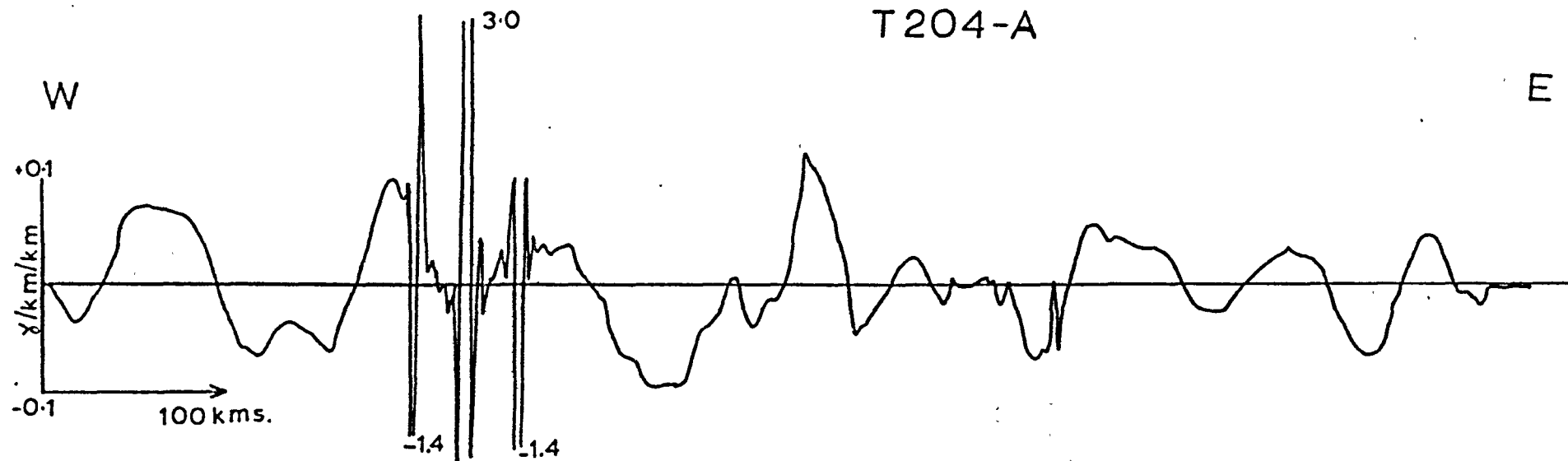
The magnetic relief is continuously low as the profile crosses from the Kibalian Orogenic Belt (the low relief to the east of the point marked f in figure (62)) onto rocks of the West Nile Complex. In the region of the Lake Albert Rift the relief changes to a series of 100 gammas amplitude anomalies of approximate width 30 km. These anomalies extend across the Uganda Basement to the boundary of the Buganda Toro Orogenic Belt. Within the Uganda Basement the tectonics or geologic boundaries which define the Western Rift, the Bunyoro Series and the Basement rocks do not appear to correlate with the recorded anomalies (figure (62)). There is insufficient data for an average depth analysis for the region g to f in figure (62), but the low gradient of the anomalies indicates sub-surface sources.

There is a marked change in the magnetic pattern of profile T204 as it crosses onto rocks of the Buganda Toro Orogenic Belt and subsequently onto Lake Victoria; the section of profile across Lake Victoria (shown dotted on figure (62)) is part of profile 508. The pattern of low amplitude short wavelength magnetic anomalies superimposed on steep sided broad anomalies is continuous from the western margin of the orogenic belt almost to the eastern shore of the lake. This very distinctive pattern (steep sided broad anomalies) would support the hypothesis of a Buganda Toro type basement for this part of Lake Victoria.

The near continuity of flight paths (T204 and 508) allows a composite average depth estimate to be made. The six points (18 km. of track) which separate the ends of the two profiles were linearly interpolated and the second derivative and energy spectrum (figure (65)) were computed in the same manner as for other profiles. The source to the long wavelength features are shown to be at the shallow average depth of 4.8 km. while the average half-width is estimated to be 52 km. The average depth to the source of the short wavelength anomalies is estimated to be 0.6 km. with an average half-width of 6 km. (figure(65)).

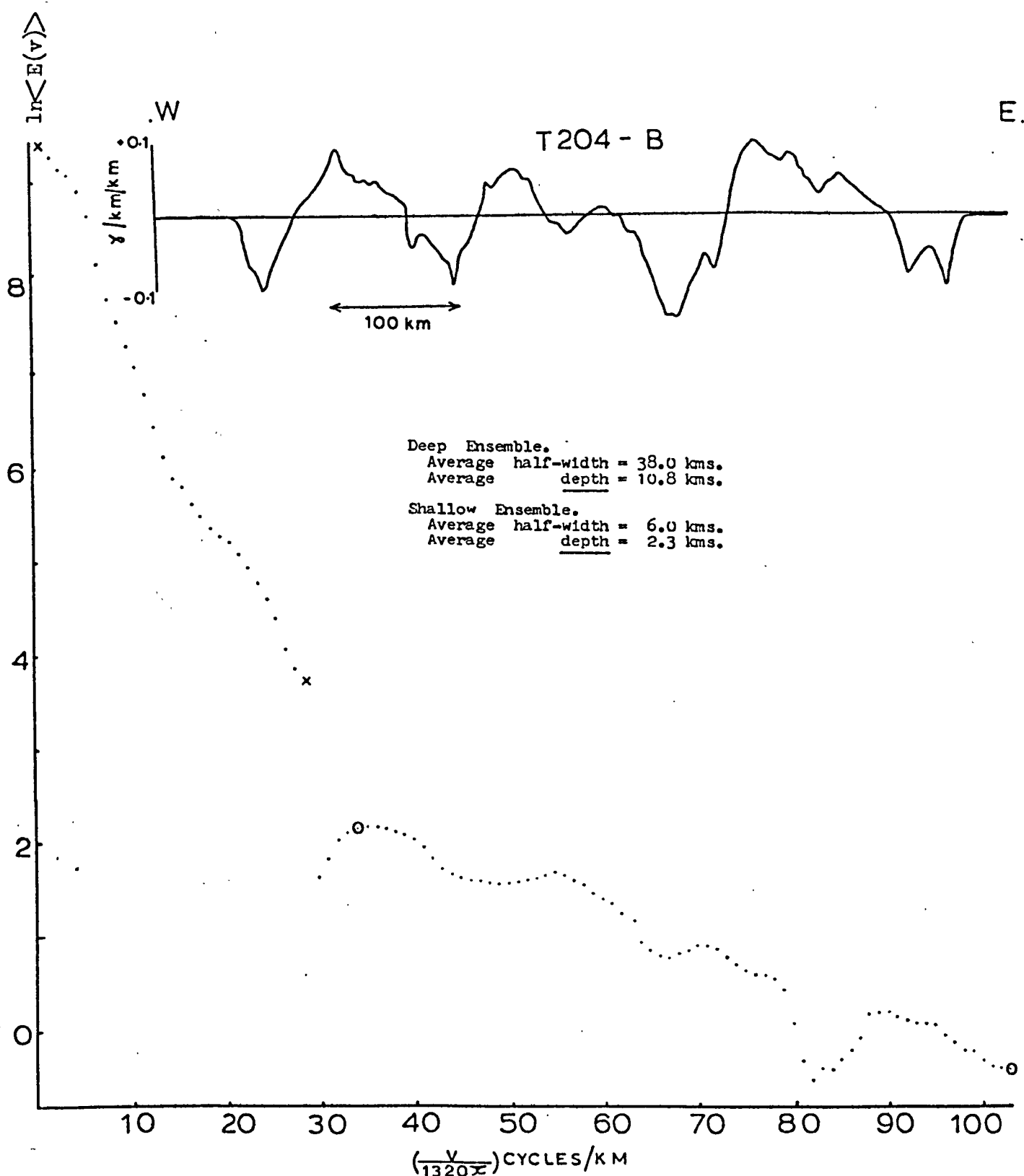
(4.4.8.3) The Mozambique Orogenic Belt (including a large area covered by Rift volcanic rocks

A large region of the Mozambique Belt crossed by profile T205 is covered by Tertiary volcanic rocks and various sedimentary formations (figure (66)). Over the complete length of profile the magnetic anomalies are significantly higher (100 gammas to 250 gammas amplitude) than other parts of the Mozambique Belt (see section (4.5.1)). This high amplitude relief is particularly noteworthy when it is remembered that the magnetic dip is very low here (-15°). Most of the energy is contained in the longer wavelength anomalies which maintain their high amplitudes in the upward continued profiles (figure (66)). Some of these anomalies may be directly related to the thick volcanics (greater than 1.0 km. in most regions here - Baker et. al. (1972)) which are mostly Miocene basalts in the west and Pliocene to Recent in other areas. The continuity of the magnetic anomalies across the Quaternary sediments may be taken to indicate the continuity of volcanic rocks beneath them. Rift tectonics and magmatism have also affected the topographic relief in this region and the correlation of the three topographic 'humps' (marked a, b, c in figure (66)) with similar magnetic features suggests

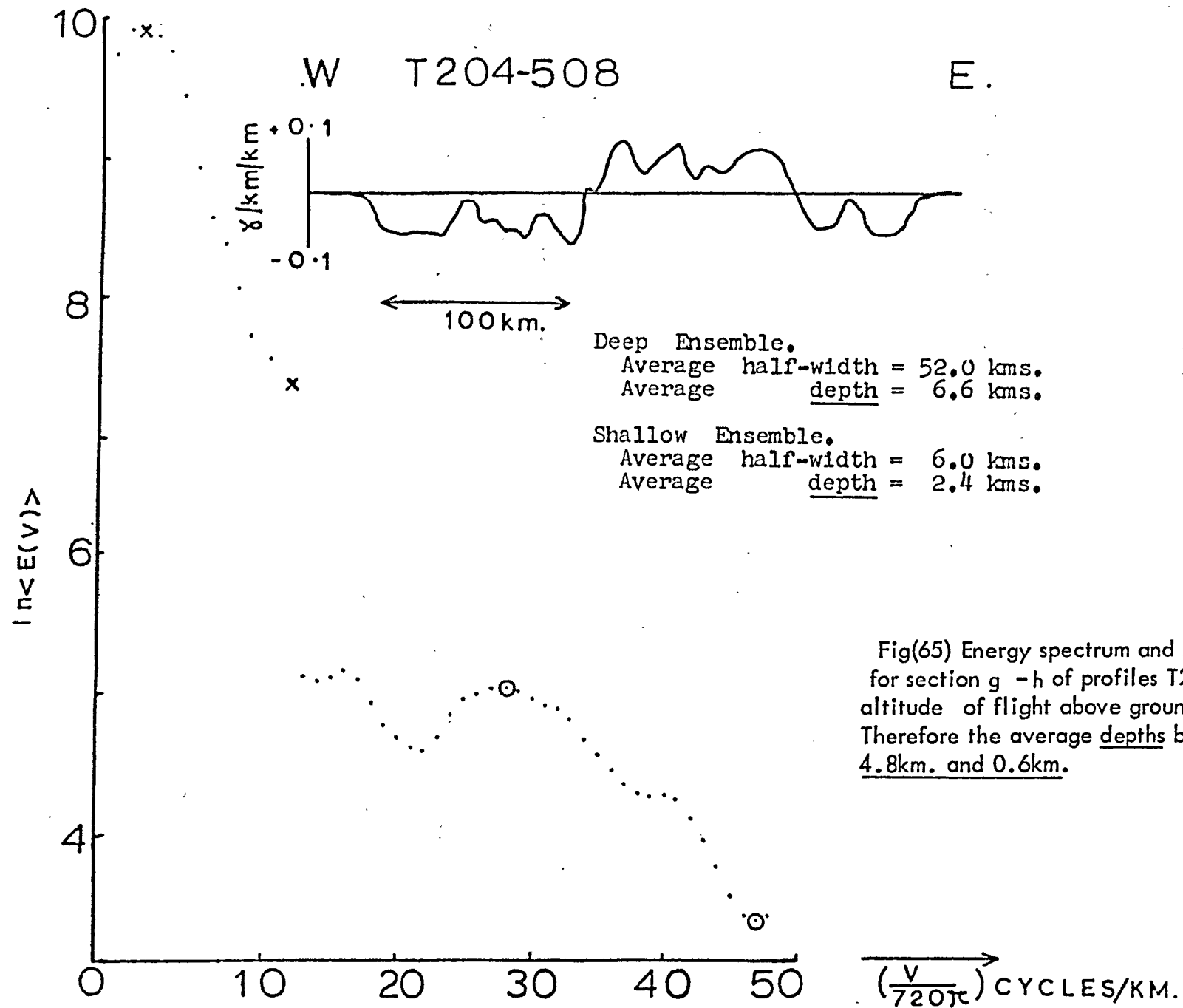


Single Ensemble.
 Average half-width = 30.0 kms.
 Average depth = 32.3 kms.

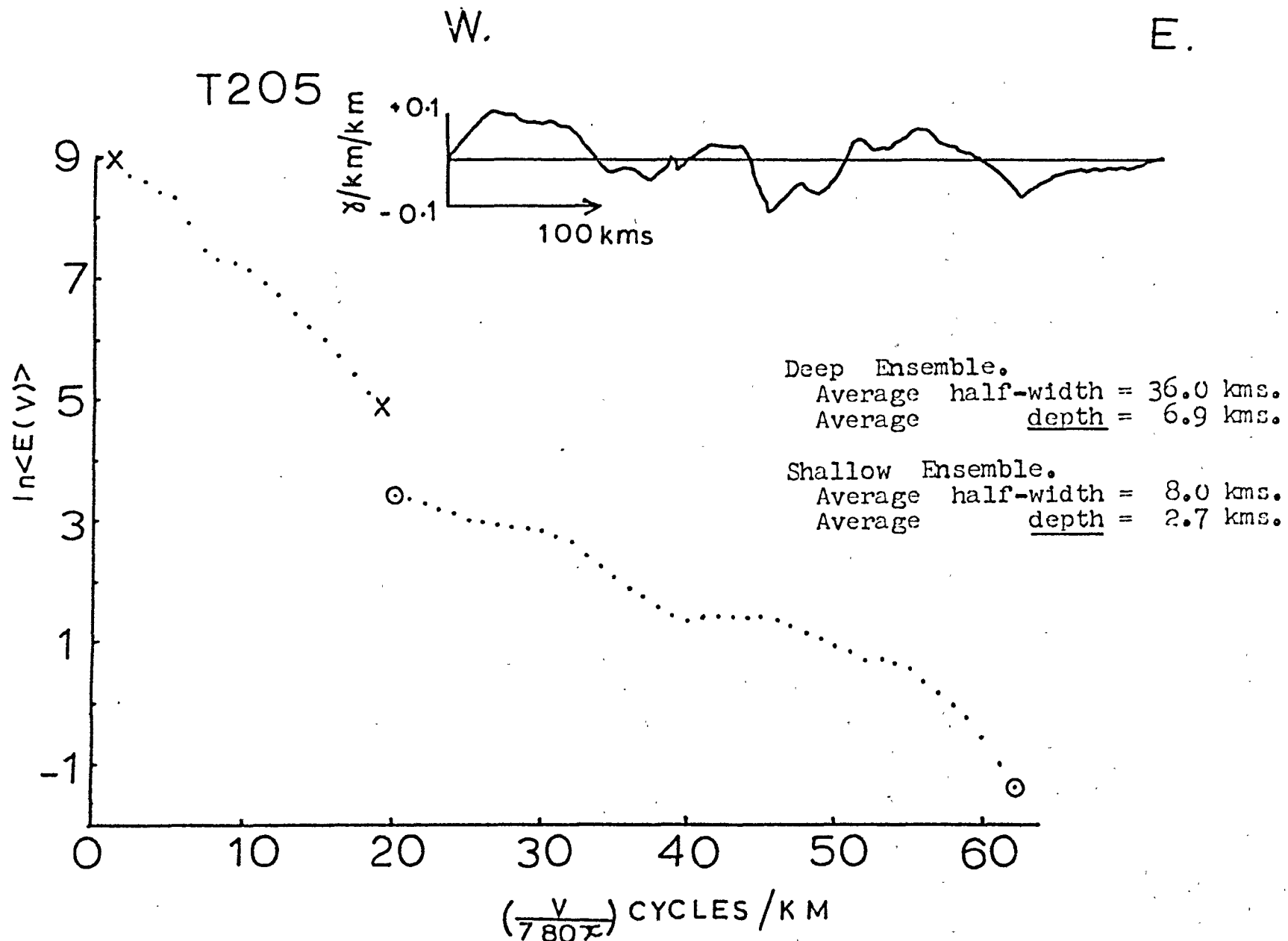
Fig(63) Energy spectrum and second derivative curve for section a - b of profile T204. Average altitude above ground level of flight = 2.4km. Therefore the average depth below ground level is 29.9km.



Fig(64) Energy spectrum and second derivative curve for section e - f of profile T204. Average altitude of flight above ground level = 2.4km. Therefore the average depths below ground level are 8.4km. and -0.1km.



Fig(65) Energy spectrum and second derivative curve for section g - h of profiles T204 and 508. Average altitude of flight above ground level = 1.8km. Therefore the average depths below ground level are 4.8km. and 0.6km.



fig(67) Energy spectrum and second derivative curve for section d - e of profile T205. Average altitude of flight above ground level = 2.5km. Therefore the average depths below ground level are 4.4km. and 0.2km.

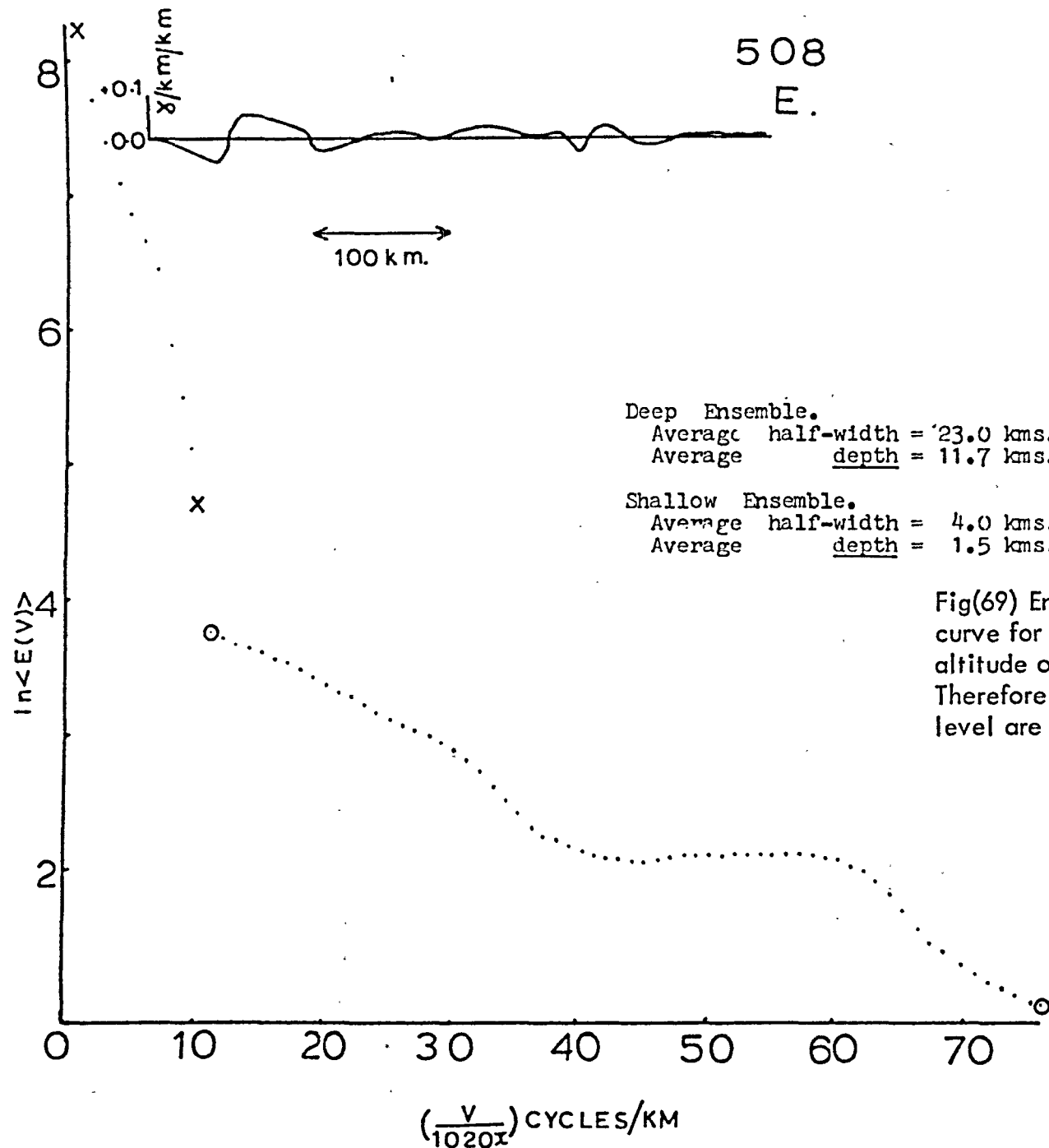
that some of the longer wavelength anomalies may also be caused by Rift volcanics. Until more data is available the topographic to magnetic correlation must remain tentative, but if it is proven then it will demonstrate that these 'northern' volcanics are highly magnetic.

Within the regions marked as Kenya Basement and Jurassic-Cretaceous sediments the magnetic anomalies are still of high amplitude. Possible sources to some of these anomalies are the various 'other intrusives' and small granite masses shown on the Kenya Geological Map for this region. However, from the low gradient and long wavelength of the anomalies it seems more reasonable that the dominant sources are at depth. The average depth of 4.4 km. obtained from the energy spectrum of section d to e of figure (66) supports the latter reasoning (figure (67)); from the second derivative curve an average half-width of 36 km. is obtained for these bodies. That the surface bodies shown on the geological map are at least having a small effect is demonstrated by the average depth of 0.2 km. obtained from the high wave-number part of the spectrum.

(4.4.9) Flight 508

From west to east profile 508 crosses successively (i) Lake Victoria, (ii) the Tanganyika Shield (includes large regions of Tertiary volcanic rocks) and (iii) the Mozambique Orogenic Belt (figure (21), figure (68)). The north western limit of this profile, which is practically continuous with profile T204 (figure (20)), is discussed in section (4.4.8.2).

Across the Tanganyika Shield the amplitude of anomalies range from 20 gammas to 100 gammas amplitude; most of the anomalies may be correlated with either the granodiorite granite masses of the shield



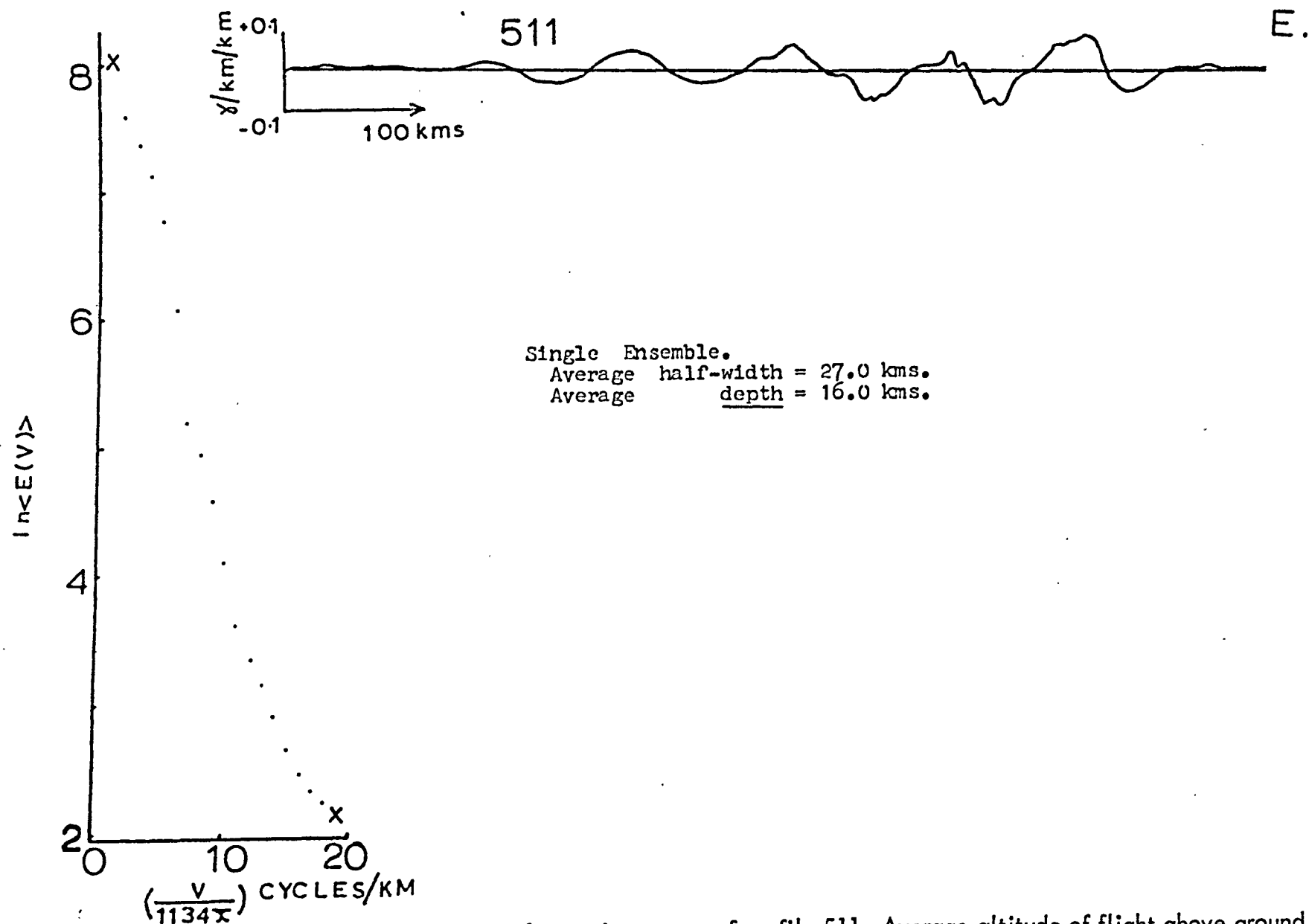
Fig(69) Energy spectrum and second derivative curve for section a - b of profile 508. Average altitude of flight above ground level = 1.0km. Therefore the average depths below ground level are 10.7km and 0.5km.

(see section (1.5.2)) or the patches of Tertiary volcanic rocks lying on the Shield (figure (68)). The eastern margin of the Shield is hidden beneath the basalt-trachyte lavas extruded from the Ngorongoro volcano (Plio-Pleistocene age). The large amplitude (~ 300 gammas) anomaly marked c in figure (68) lies directly above the central cone of the volcano. The central negative feature may indicate a reversely magnetised core.

The section of profile which crosses the metamorphic rocks (mainly gneiss and charnokites) of the Masai Plain (part of the Mozambique Belt) is characterized by a generally low magnetic relief. An exception of this, is the 'strange' shaped anomaly marked b in figure (68) which cannot be correlated with the surface geology. Only the magnetic bodies in the region to the east of the point marked b may be included in a single ensemble. Although this section of profile (a to b in figure (68)) contains only low amplitude anomalies (~ 50 gammas) two ensembles of magnetic bodies are revealed in the energy spectrum (figure (69)). The deep ensemble is at an average depth of 10.7 km. below ground level and is shown to have an average half-width of 23 km. from the second derivative curve (figure (69)). The shallow sources are estimated to be at an average depth of 0.5 km. with an average half-width of 4 km.

(4.4.10) Flight 511

This profile crosses rocks of the Mozambique Orogenic Belt, parts of which are covered by Tertiary volcanic rocks or Karroo sediments (figure (70)). The length of profile between the points a and c of figure (70) is dominated by a number of 50 gammas amplitude anomalies of average half-width 27 km. (figure (71)). Correlation of the magnetic anomalies with specific geology (i.e. the Tertiary volcanic rocks) is



Fig(71) Energy spectrum and second derivative curve for section a - c of profile 511. Average altitude of flight above ground level = 3.0km. Therefore the average depth below ground level is 13.0km.

not possible. The energy spectrum of this section of profile (a to c in figure (70)) reveals only a single ensemble of magnetic bodies at an average depth of 13 km. below ground level. The energy spectrum past the last harmonic shown in figure (71) was still decaying but was dominated by some very large amplitude peaks and is therefore unsuitable for average depth analysis.

East of the point marked a in a figure (70) the magnetic relief is very near to zero; this is consistent with the thick Karroo sediments observed here.

(4.4.11) Flight 506

This small section of profile crosses rocks of the Mozambique Orogenic Belt, most of which are covered by Quarternary sediments (figure (72)). The anomaly curve is dominated by some long wavelength anomalies (40 km. to 100 km. wide) of amplitudes 50 gammas to 80 gammas (see original and upward continued curves of figure (72)). The energy spectrum of this complete length of profile yields an average depth of 14.3 km. below ground level for the sources of these long wavelength features (figure (73)). Several 20 km. to 30 km. wide anomalies of approximately 100 gammas amplitude are superimposed on the long wavelength anomalies in the west of the profile (figure (72)). From the energy spectrum an average depth of 0.0 km. is estimated for the source to these bodies; this depth must be viewed with extreme caution as all the short wavelength features are concentrated in the west of the profile.

(4.4.12) Flight T208

After crossing rocks of the Uganda Basement, profile T208 passes onto a region of the Tanganyika Shield which is mostly covered by Tertiary and Quarternary volcanic rocks (figure (74)). Except for

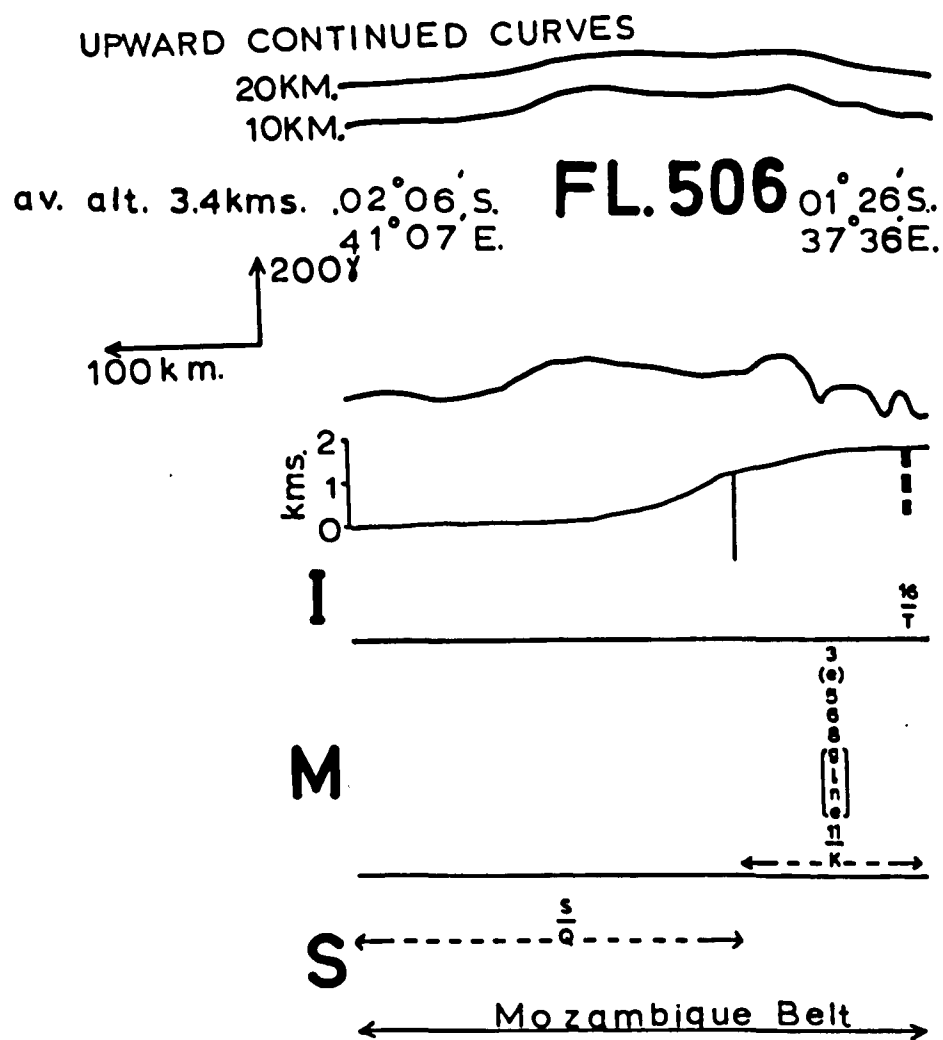
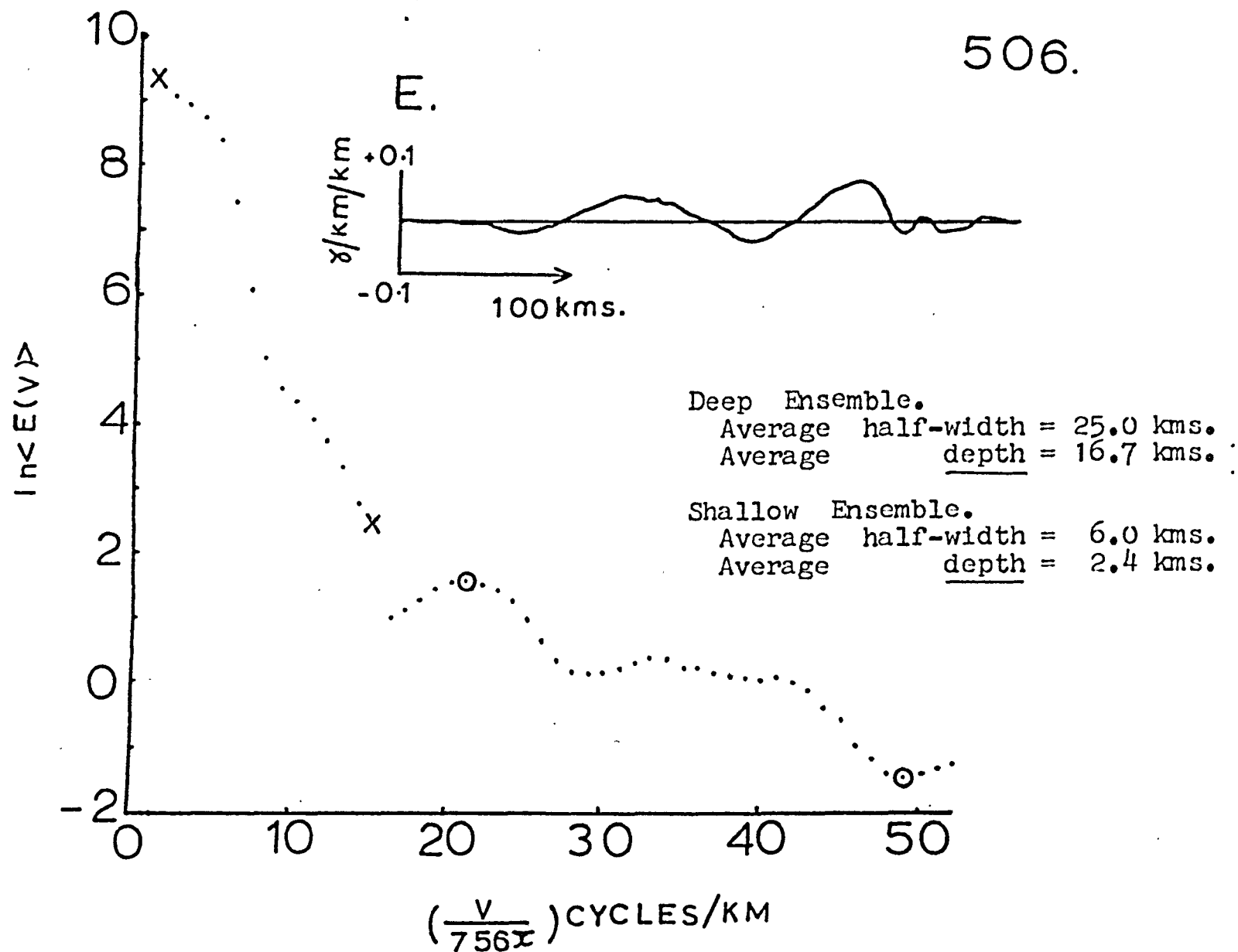


Fig (72) Tectonics, geology, topography, magnetic profile and upward continued curves for flight 506.



Fig(73) Energy spectrum and second derivative curve for profile 506. Average altitude of flight above ground level = 2.4km. Therefore the average depths below ground level are 14.3km. and 0.0km.

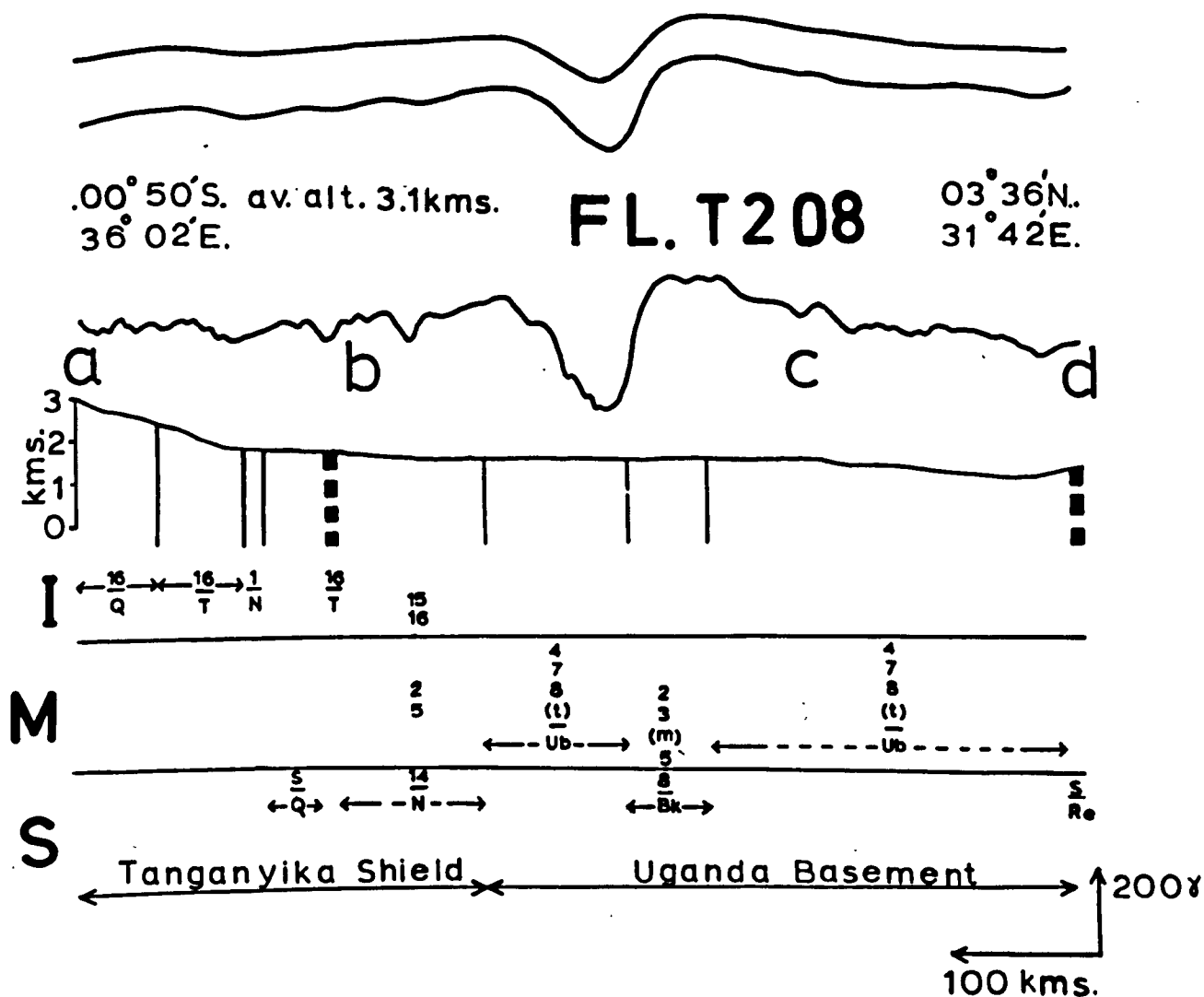
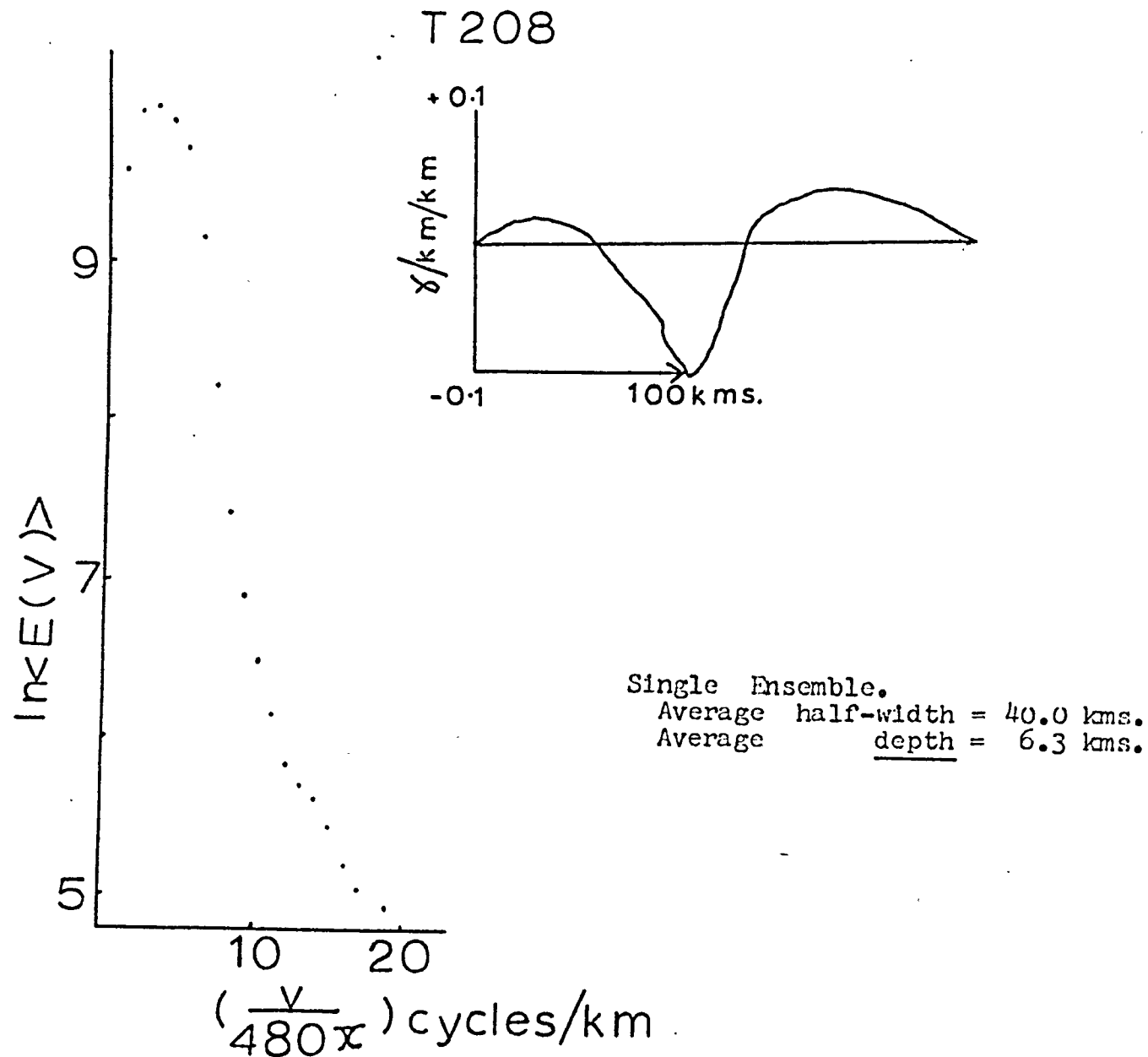


Fig (74) Tectonics, geology, topography, magnetic profile and upward continued curves for flight T208.



Fig(75) Energy spectrum and second derivative curve for section b - c of profile T208. Average altitude of flight above ground level = 1.6km. Therefore the average depth below ground level is 4.7km.

the very prominent negative anomaly between the points marked b and c in figure (74), the magnetic relief is of short wavelength (mostly of 6 km. to 21 km. width) and low amplitude (mostly less than 50 gammas). The high wavenumber nature of the anomalies is evidence that the majority of magnetic sources are near surface or surface bodies.

The anomaly (300 gammas amplitude) between the points b and c of figure (74) has been subjected to an 'average' depth analysis. The energy spectrum indicates that the source to this anomaly is at a depth of 4.7 km. below ground level (figure (75)), while the second derivative curve yields a half-width of 40 km.

(4.5) Summary and Discussion of the Magnetic Characteristics of African Tectonic Units

The average depths, average half-widths and principle magnetic characteristics of each African tectonic unit are summarized in table (12). The following is a brief discussion of some of the most important features observed in the magnetic data.

(4.5.1) The Mozambique Orogenic Belt

The most notable feature of all the magnetic data presented in this study is the 'magnetic quiet zone' observed across the Mozambique Orogenic Belt (figure (76), figure (79)). Except for an area of Malawi and Zambia, outlined in figure (76), the low magnetic relief (amplitudes mostly less than 100 gammas) is continuous across the Mozambique Belt from latitude 14°S . (profile T225) to latitude 3°N (profile T205). This is quite extraordinary when all the profiles are viewed together (figure (76)), as there are few regions where such low magnetic relief is observed; the general increase in the amplitude of anomalies from north to south is adequately explained by the increasing angle of the dip of the geomagnetic field (compare figure (24) and figure (25)).

Tectonic Unit	Flight No.	Fig.	Grad. Removed	Short Wavelength Magnetic Relief			Long Wavelength Magnetic Relief		
				Ave. Depth(km)	Ave. Width(km)		Ave. Depth(km)	Ave. Width(km)	
Mozambique Belt (excluding Malawi and Zambia)	T225 43 T203 48 T220 52 508 70 511 72 506 74 T201 60 T201 61 T205 67	43 48 52 70 72 74 60 61 67	- - 0.6 0.4 0.7 - - - -	- 0.4 0.5 0.5 - 0.0 - - -	- 8.0 6.0 4.0 - 6.0 - - -	Low amplitude consistent with the underlying geology of highly metamorphic rocks. Low magnetic relief often marked by a well defined boundary. The East African Rift has only a small effect on the magnetic pattern.	2.2 21 20 11 13 14 2.7 4.7 4.4	11 35 30 23 27 25 26 30 36	Low amplitude long wavelength undulations best observed on the upward continued and second derivative curves.
Mozambique Belt (Malawi and Zambia)	T225 42 T203 47	42 47	- -	0.1 -	6.0 -	Moderate to low amplitude relief consistent with the underlying geology.	4.6 5.6	30 48	Dominated by high amplitude double peaks possibly related to the Lake Malawi and Shire Rifts.
Uganda Basement	T201 T204 T208 76	 76	- - -	- - -	- - -	Mostly low amplitude relief consistent with the geology of highly metamorphic rocks. Some high relief observed near to the Lake Albert Rift.	- - 4.7	- - 40	Smooth long wavelength features. Large amplitude negative anomaly observed on profile T208 (unrelated to the geology).
Damaran Belt	T211 T213 37	 37	- -	- -	- -	Variable due to the influence of Karroo volcanic rocks.	- 8.6	- 48	Variable between profiles.
Katangan and Irumide Belts	T225 41 T203 46	41 46	- -	0.4 -0.1	8.0 6.0	Highly variable with little correlation with the geology. Ironstones may be the source to the high magnetic relief of profile T203.	17 23	24 25	Variable between profiles.

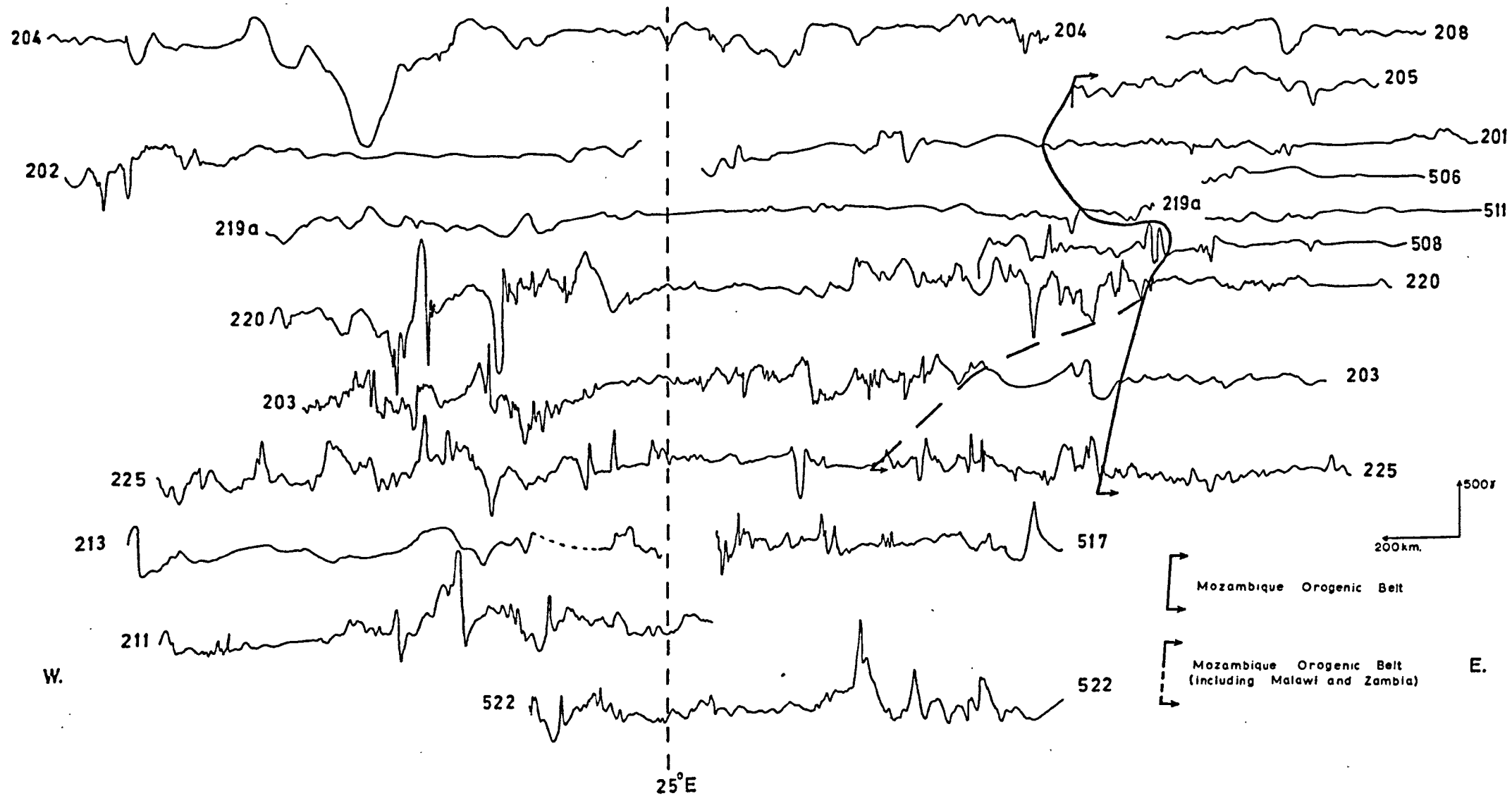
Table(12)

Tectonic Unit					Short Wavelength Magnetic Relief		Long Wavelength Magnetic Relief		
	Flight No.	Fig.	Grad. Removed	Ave. Depth(km)	Ave. Width(km)		Ave. Depth(km)	Ave. Width(km)	
Kibaran Belt	T219a T220	- -	- -	- -	- -	Very low amplitude with well boundaries .	- -	- -	Very low amplitude .
Ubendian Belt	T220	51	-	0.0	8.0	High amplitude relief confined within the tectonic boundaries. Good correlation of the anomalies with basic rocks.	13	30	High amplitude relief confined within the tectonic boundaries.
Buganda Toro Belt	T204 508	65	-	0.6	6.0	Moderate amplitude relief.	4.8	52	Distinct high amplitude anomalies with high gradient sides. The peak in the energy spectrum may indicate thin sources.
Rhodesian Shield and Limpopo Belt	522	30	-	-	-	Mostly low amplitude anomalies across the metamorphic rocks of the Shield. Very high amplitude anomalies associated with the Precambrian dykes and Karroo volcanics	6.9	26	As for the short wavelength relief .
	522	31	-	-	-		2.3	29	
	517	34	-	-	-		13	26	
	517	35	-	-	-		0.9	27	
Tanganyika Shield	T219a	-	-	-	-	Mostly low amplitude .	-	-	Mostly low amplitude .
	508	-	-	-	-		-	-	
	T208	-	-	-	-		-	-	
Cameroun Shield	T202	57	-	0.1	6.0	Variable with some high amplitude negative anomalies possibly correlated with some dolerite intrusives .	?	33	High amplitude .
North Congo Shield	T204 T204	63 64	- -	- -0.1	- 6.0	Mostly low amplitude anomalies consistent with the geology.	30 8.4	30 38	Very high amplitude negative anomalies. These anomalies require a highly magnetic and stable source with remanent magnetisation dominant.

Table(12) continued

Tectonic Unit	Flight No.	Fig.	Grad. Removed	Short Wavelength Magnetic Relief			Long Wavelength Magnetic Relief		
				Ave. Depth(km)	Ave. Width(km)		Ave. Depth(km)	Ave. Width(km)	
Kalahari Basin	T211	27	-	1.0	8.0	High amplitude anomalies related to the extensive Karroo volcanics beneath the sediments. Granodiorite and granite masses may contribute to the anomaly patterns of profiles T203 and T225.	13	33	Meridional, high amplitude positive anomaly may be traced throughout the length of the Kalahari Basin.
	522	29	-	0.8	6.0		13	30	
	T213	38	-	0.9	?		18	38	
	517	33	-	0.2	6.0		3.5	27	
	T225	40	-	0.4	8.0		7.5	35	
	T203	45	-	0.7	10.0		6.7	36	
Congo Basin	T220	50	-	0.4	6.0	Very high amplitude anomalies to the south of approximately latitude 4°S. while to the north the relief is low. The high amplitude relief is probably due to an igneous/iron ore complex which is an extension of that observed on the Kasai Shield.	2.0	20	The high amplitude anomalies of profile T220 may be related to the meridional anomaly observed in the Kalahari Basin. The other profiles have a low magnetic relief.
	T219a	55	-	1.4	15.0		14	33	
	T202	58	-	-	-		20	41	

Table(12) continued



Fig(76) Project MAGNET profiles with the boundaries of the Mozambique Orogenic Belt.

The geology of the Mozambique Belt is almost as uniform as the magnetic data, with gneisses and associated rocks dominating (see section (1.2.1.1)). In the exceptional areas of Malawi and Zambia the igneous activity of Precambrian A age (the Mozambique Orogeny) and younger times (Karoo and Cretaceous) may be the source of the high amplitude magnetic anomalies observed there (see also section (4.5.2)); the large plutonic masses observed in these areas are certainly atypical of the Mozambique Belt (see section (1.2.1.1)).

The energy spectra of the sections of profile which cross the Mozambique Belt usually reveal two ensembles of magnetic bodies: (i) Shallow with average depths between 0.0 km. and 0.5 km. and average half-widths of 4.0 km. to 8.0 km. (table (12) and figure (77)). The charnokites and small pegmatite intrusions, as well as the gneissic rocks, are the most probable sources contributing to these shallow ensembles. (ii) Deeper bodies with mean depths generally increasing from north to south (figure (78)). From profiles T201 and T205 the average depths range from 2.7 km. to 4.7 km., further south profiles 506, 508 and 511 yield average depths ranging from 11 km. to 14 km., while the two most southern profiles T220 and T203 (excluding profile T225) give average depths of 20 km. and 21 km. respectively (table (12)). The anomalies due to these deep ensembles of magnetic bodies are best observed in either the upward continued profiles of the previous sections, or more conveniently in the second derivative curves. The latter curves yield average half-widths ranging from 23 km. to 36 km. (excluding profile T225).

Several authors (Pakiser and Zietz (1965), Zietz and King (1966), Zietz et. al. (1966), Caner (1969), Haines et. al. (1971), Berry et. al. (1971)) have remarked on the low amplitude of the long wavelength magnetic anomalies recorded to the west of the Rocky Mountains in North America as

compared to those observed to the east of the mountains. Although the situation observed west of the Rockies is not quite the same as that recorded across the Mozambique Belt, only the long wavelength anomalies are of low amplitude in the former region, it is worth while to use the three proposed interpretations of the western North American 'magnetic quiet zone' as a starting point for discussion here. The three interpretations are (Caner (1969)):

- (a) The Curie point isotherm rises from approximately 40 km. depth in central and eastern North America to a value near 20 km. in the west.
- (b) The high amplitude long wavelength anomalies to the east are caused by surface and deeper structures which on the west have been broken up by orogeny.
- (c) The basement in the west contains less ferromagnetic material (unaltered) than in the east. For Africa it is useful to list the following:
 - (i) The geology of the complete length of the Mozambique Belt is remarkably uniform (except Zambia and Malawi), highly metamorphic rocks with low ferromagnetic content predominating at the surface.
 - (ii) The East African Rift has affected a large region of the Mozambique Belt and the high temperatures expected in the rift (Searle (1970)) will certainly have caused a major upwelling of the Curie point isotherm.
 - (iii) The depths to the magnetic sources of the Mozambique Belt (figure (79) and table (12)) generally increase from north to south and this corresponds to the decreasing effects of the Rift.
 - (iv) Gravity data obtained across the Tanganyika Shield (Darracott (1972), Darracott et. al. (1972)) reveal large anomalies which are

abruptly terminated at the boundary with the Mozambique Belt. Within the Belt the gravity field is practically featureless.

(v) Geomagnetic deep sounding has shown a well defined conductivity anomaly beneath the eastern Rift.

Points (ii), (iii) and (v) indicate that uprising of the Curie point isotherm at least affects the region of the Belt near to the Rift, while point (iv) supports the break-up of structure explanation and point (i) shows that the surface rocks of the Mozambique Belt have low magnetisations. It is clear from the evidence above that all three factors (a, b and c above) are affecting the amplitude of the magnetic anomalies.

(4.5.2) The East African Rift and Related Structures

One of the most surprising results of this project has been the very low magnetic expression of East African Rift volcanics. In some of the profiles a small increase in the amplitude of the anomalies may be significant, but the evidence is not good. Large magnetic anomalies are only observed when a profile crosses a volcanic centre such as Ngorongoro (profile 508 in figure (68)) and Rungwe (profile T220 in figure (49)). The magnetic anomalies recorded in the Turkana region (profile T205 in figure (66)) may indicate high magnetisation of the Tertiary volcanic rocks there, but it is emphasized that the magnetisation of the basement rocks is also high in this region. Ground magnetic surveys (Searle (1969, 1970), Sowerbutts (1972)) and a low altitude aeromagnetic survey (Wohlenberg and Batt (1972)) have also revealed a generally low magnetic relief across the Rift Volcanics. From the lack of any 'magnetic lineations' it seems reasonable to postulate that the majority of igneous rocks have been extruded from randomly orientated dykes, small cones, and large central volcanoes; Lippard (personal communication (1973))

reports that more central volcanoes are being discovered in northern Kenya with improved geological mapping. The absence of a significant magnetic anomaly across the high density intrusive body, postulated from the evidence of a detailed gravity survey of the Gregory Rift to be within 3 km. of the surface (Searle (1969, 1970)), is best explained by a combination of:

- (i) The low dip angle of the geomagnetic field in the region of the rift.
- (ii) The high heat flow expected in the rifted regions (Searle (1970)).

A Curie temperature as high as 200°C (see O'Reilly and Readman (1971) for a Curie temperature contour plot superimposed on the $\text{FeO} - \text{TiO}_2 - \text{Fe}_2\text{O}_3$ ternary diagram, and Creer (1971) for representative Curie temperatures of basalts) would allow the top of the intrusive body to be within 7 km. of the surface (assuming the temperature-depth profile of Roy et. al. (1968)) and still be completely non-magnetic (neglecting para and diamagnetism).

In contrast to the main East African Rift, there are some large magnetic anomalies associated with its postulated southern extension along the Lake Malawi - Shire Rifts (see section (1.8.2)). Across this southern rift zone three profiles show a double peaked magnetic anomaly crossing the rifted region (the parts of profiles T225, T203 and T220 to the west of the line outlining the Mozambique Belt in figure (76)). Profiles T225 and T220 both show high magnetic relief to the west of Malawi and it is therefore possible that these double peaked anomalies merely indicate the continuation of this basement into the rifted regions. If not, then the anomalies may mark the position of a very large intrusive body which attempted to break the surface in Karroo to Cretaceous times, causing the major rifts and volcanics now observed in Malawi and Mozambique

(see sections (1.6) and (1.7)). From the energy spectra for profiles T225 and T203 the depth to the top of the body would be included in the average depth estimates of between 4.5 km. and 5.6 km. with an average half-width of between 30 km. to 48 km. (figure (42) and figure (47)). Support for the intrusive body postulate comes from an impressive gravity anomaly (55 km. wide with an amplitude of 750 gravity units) observed 50 km. to the north of Lake Malawi at the junction of the eastern and western rifts (Sowerbutts (1972)). Sowerbutts (1972) has qualitatively related this gravity anomaly to a 13 km. wide 'Precambrian ultrabasic intrusive'.

There are two reasons why a large magnetic anomaly would be expected across the southern rift zone and not across the main East African Rift:

- (i) The magnetic dip is greater across the Lake Malawi - Shire Rifts (44° to 52°) than across the rift over which ground or aeromagnetic surveys have been made (15° to 35° dip).
- (ii) The temperature of a pre-Tertiary plutonic body is likely to be very much lower than the Tertiary and Recent intrusives of the East African Rift and is therefore more likely to be below the Curie temperature.

A more detailed survey of either long gravity or magnetic traverses would help to confirm or refute the intrusive body postulate for the Lake Malawi - Shire Rifts.

(4.5.3) The Kalahari and Congo Basins

Profiles which sample the Kalahari Basin (522, T211, T213, 517, T225, T203) show a consistent pattern of high magnetic relief in both long and short wavelengths (figure (76)); only profile T213 has little energy in the short wavelength anomalies, but this is probably

an instrumental effect. Extensive Karroo volcanic rocks beneath the sediments are considered to be the principle source of the short wavelength magnetic relief, with granodiorite and granite masses contributing to the anomaly pattern in the more northern profiles (T203, T225). Average depths below ground level to these shallow sources range from 0 km. to 1 km. (figure (77) and table (12)).

Across the Congo Basin, the Project MAGNET profiles (T220, T219a, T202) and a vertical component magnetic survey (Evrard et. al. (1959)) reveal two distinct magnetic regimes. To the south of approximately 4°S . there are many high amplitude long and short wavelength magnetic anomalies (figure (49), figure (53)), while to the north of this latitude the magnetic relief is very low (figure (53), figure (54), figure (56)). The source of the high amplitude short wavelength anomalies is postulated to be an extension of the large igneous/iron ore complex observed on the Kasai Shield. The low magnetic basement to the north is known, from the evidence of deep bore-holes and a seismic refraction survey (Evrard (1960)), to be similar to the Precambrian A platform sediments which outcrop around the Congo Basin (figure (1)). Average depths to the shallow ensemble of bodies in the Congo Basin range from 0.1 km. to 1.4 km. (figure (77) and table (12)).

The long wavelength magnetic structure of the Kalahari Basin and the southern part of the Congo Basin (figure (21)) shows a certain continuity of pattern (figure (79)). A series of large amplitude long wavelength magnetic anomalies may be traced from latitudes 20°S . (profile T211) to 6°S . (figure (76) and figure (79)). These features may be seen in the original profiles (figure (76)) but are best observed in the 20 km. upward continued curves (a to b in figure (79)). Average depths to the sources of these long wavelength structures generally decrease from 13 km. in the south to a minimum value of 2 km. estimated from profile

T220 (table (12) and figure (78)).

From the continuity of long wavelength magnetic pattern seen in profiles T211 to T220, it seems reasonable to suggest that a single deep structural unit underlies a major part of the Kalahari and Congo Basins; continuity of the pattern to the east and west of profiles T203 and T225 (figure (39), figure (44)) may indicate that the same deep magnetic structure lies beneath the Angola Basement and Kasai Shield. The very different anomaly pattern observed to the north of approximately 4°S . (figure (53), figure (54), figure (56)) suggest a change of structure in this region.

(4.6) Discussion of the Average Depth Estimates

In the following discussion of the average depths it is most important to remember the fundamental assumptions of the 'Statistical Models Method', that the majority of magnetic bodies belong to a limited number of ensembles (2 or 3) of 'two dimensional prisms' which have characteristic depths, thicknesses, widths and magnetisation vectors. The requirement in the theory of chapter (2) that the declinations and inclinations of the magnetic bodies should lie within $\pm 20^{\circ}$ of their mean value has been shown (section (2.5)) not to be too restrictive, as long as the anomalies of adjacent bodies with widely varying magnetisation vectors do not interfere appreciably. By only analysing each section of profile which has a consistent pattern of anomalies with similar widths and amplitudes along its length, it is hoped that the above requirements have been fulfilled. The linearity of the computed spectra is evidence that the theory is applicable to most of the Project MAGNET data across Africa.

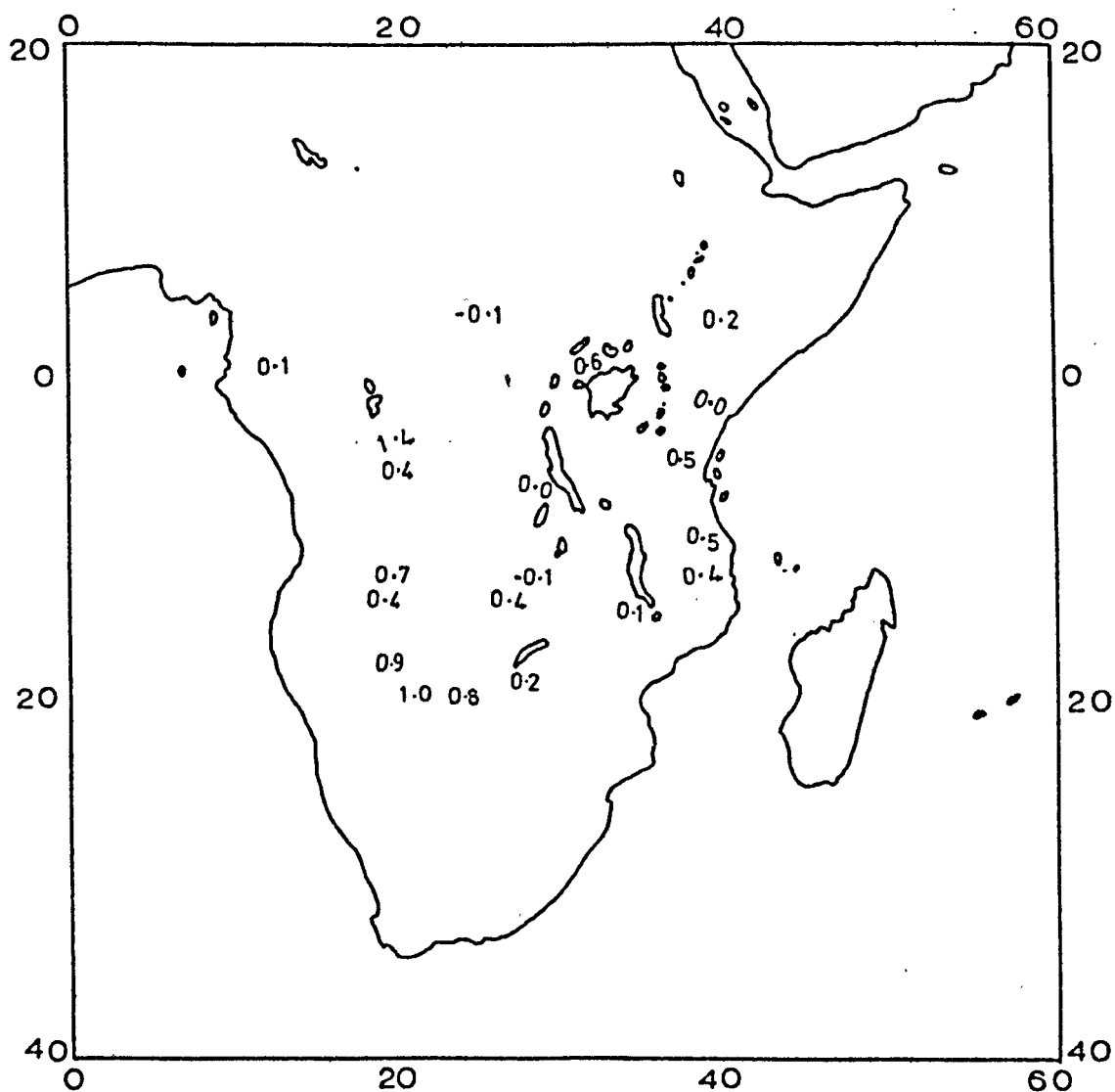
(4.6.1) Shallow Ensembles

The average depths obtained from the high wavenumber parts of the energy spectra of the previous sections are shown in figure (77). As described in chapter (2) this part of the spectrum always yields shallow average depths. Some shallow depths are also shown in figure (78), where the average depths obtained from the low wavenumber part of the spectrum are plotted. These latter shallow depths correspond to long wavelength anomalies with high gradient sides, indicating broad shallow magnetic sources.

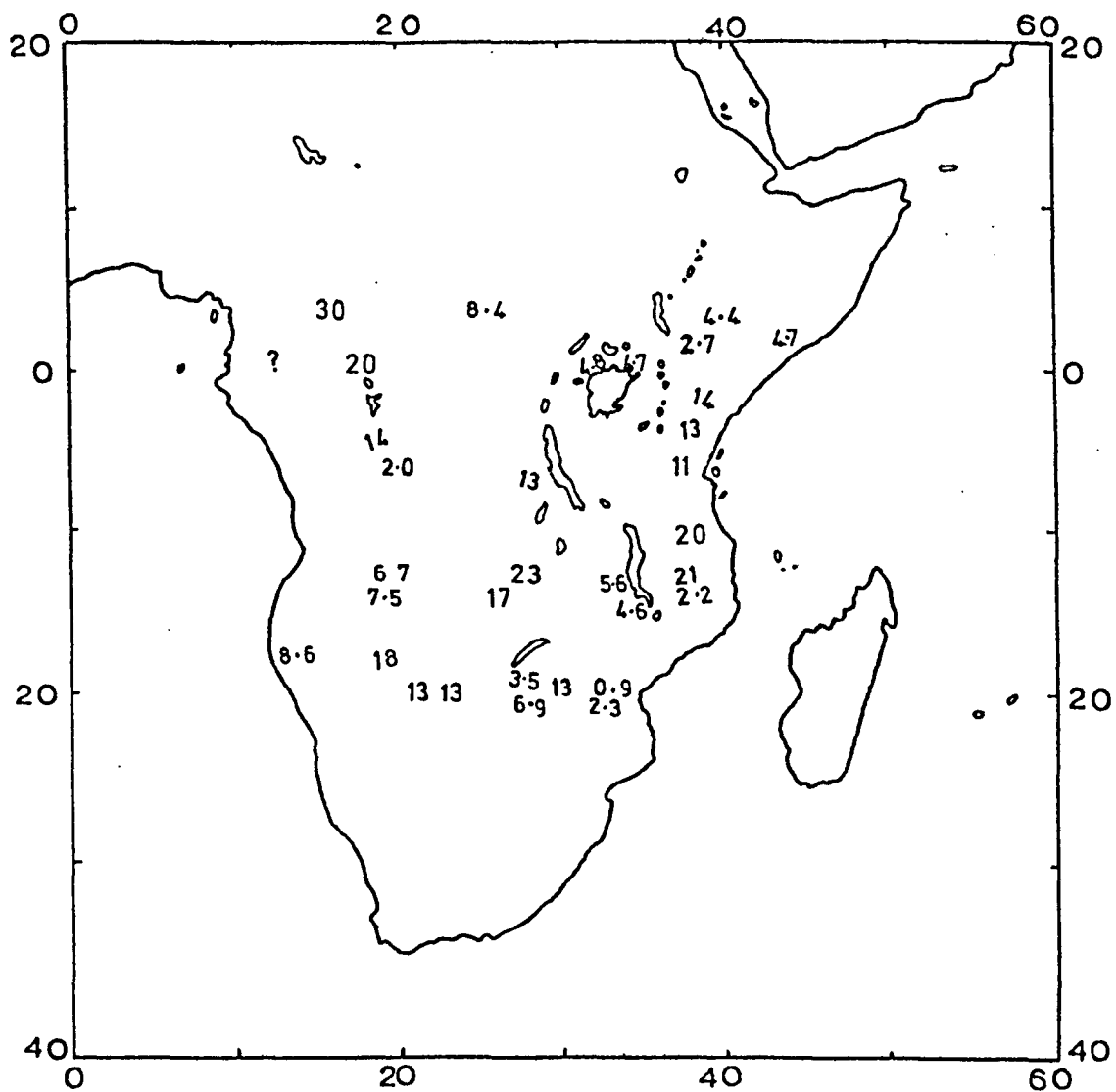
All the depths shown in figure (77) appear to be reasonable; the few negative estimates are well within the 0.3 km. probable error of the average terrain clearance of the aircraft. As expected, the mean depth to the magnetic sources beneath the thick sediments of the Kalahari and Congo Basins (0.8 km. with a standard deviation of 0.3 km.) is significantly higher than the mean depth obtained from all other regions (0.2 km. with a standard deviation of 0.2 km.).

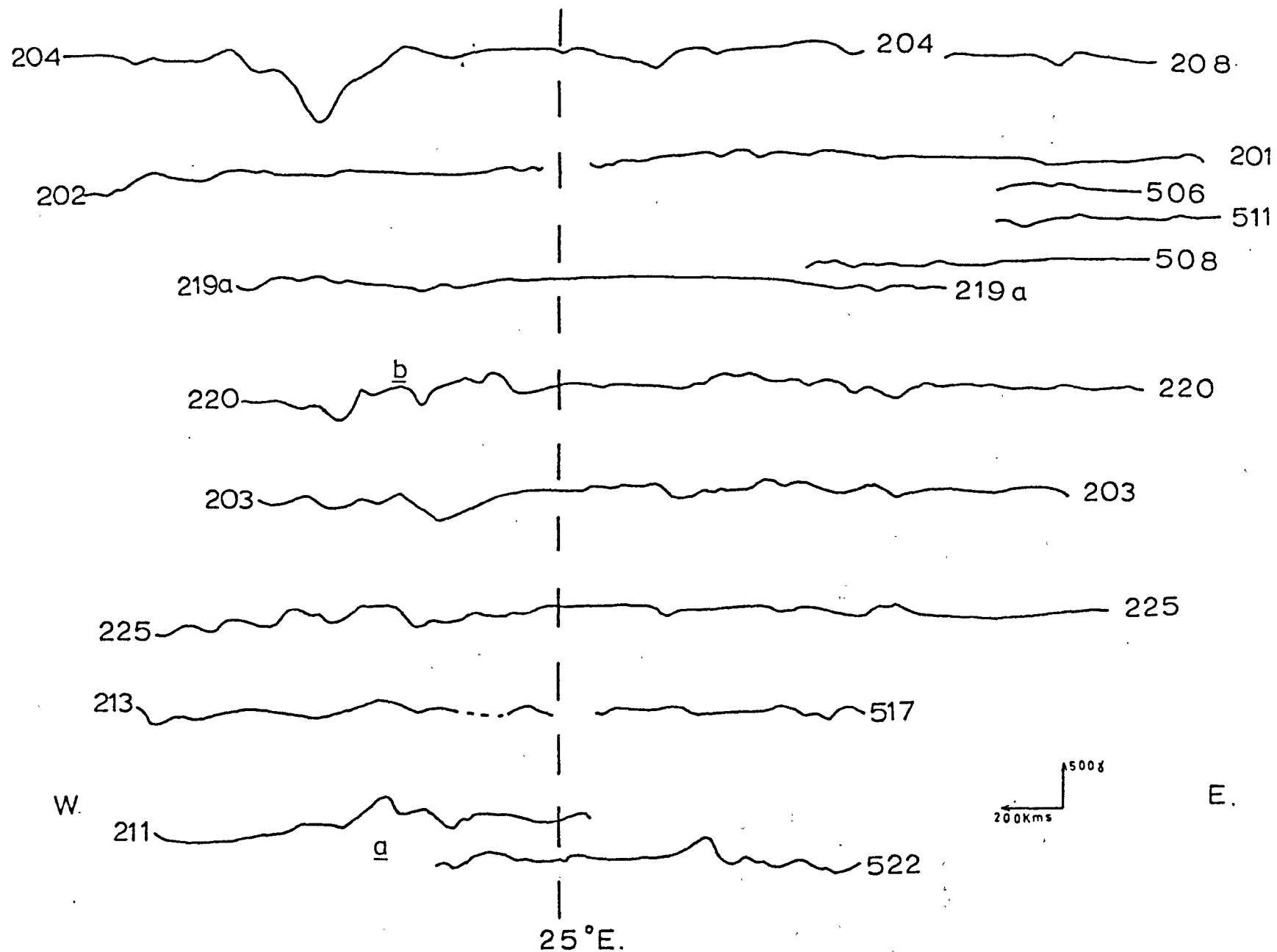
(4.6.2) Deep Ensembles

The distribution of average depths obtained from the low wavenumber part of the energy spectrum is shown in figure (78). It has already been observed that this part of the spectrum generally yields the average depth to the deeper ensembles of magnetic bodies. Average depths less than 4 km. were obtained from spectra which yielded only a single depth (except for the section of profile T220 which crosses the Congo Basin) and are considered to represent either the average depth of bodies extending from near to the surface to greater depths or the average depths to near surface broad magnetic sources. The following discussion is principally concerned with average depths greater than 4 km.



Fig(77) Average depths to the shallow magnetic sources of Africa. These depths (kms.) were obtained from the high wavenumber part of the energy spectra.





Fig(79) Project Magnet profiles upward continued 20kms.

The similarity of the average depth estimates from near neighbouring profiles (figure (78) and table (12)) gives some confirmation of both the spectral method of depth determination and the consistency of the data. Only the average depths obtained from Mozambique Orogenic Belt and the Congo and Kalahari Basins show any indication of a long distance trend or pattern. All the other tectonic or geological units are insufficiently sampled to arrive at any conclusions about the consistency or pattern of depth estimates within the given units. That there is little consistency in the magnetic patterns or discernable trend in the average depth estimates between the tectonic or geological units may be a vital clue to the history of the geological evolution of the African continent. This would be the first geophysical evidence to support that the deep structure of the continent may be considered to be composed of a number of distinct tectonic or geologic units (see chapter (1)).

(4.6.3) Comparison of the Average Depth Estimates to 'Deep' African Magnetic Sources with Estimates from Other Continents

In figure (78) the majority of average depths are greater than 4 km. (26 out of 32 estimates) and the mean value of these is found to be 11.8 km. with a standard deviation of 5.6 km. (using original unrounded values). It seems worthwhile to compare these values to those obtained from other regions of the world (table (13)). A magnetic anomaly is very much more sensitive to the depth and topography of the top of the body than the bottom and therefore the depths to the bottom of the magnetic bodies in table (13) must be viewed with caution.

As the average depths shown in figure (78) are likely to be maximum depths (see section (2.6)) it is apparent that the values obtained for the African continent are not significantly different from those

Region	Average Depth or Range of Depths to the Top of the Bodies. (km.)	Average Depth or Range of Depths to the Bottom of the Bodies. (km.)	Number of Anomalies Used.	Reference
North America		20.0	126	Vacquier and Affleck (1941)
	4.0 to 30.0	4.0 to	-	Serson and Hannaford (1957)
	4.8 to 8.0	14.4 to 25.6	85	Bhattacharyya and Morley (1965)
		40.0 to 48.0	-	McClure (1963)
	4.0 to 13.0	13.0 to 20.0	-	Hall (1968) and MacGrath Hall (1969)
Russia		Conrad Discontinuity (~15km.)	-	Bulina (1961)
		Conrad to Mohorovicic Discontinuity (15 to 35)	-	Fotiadi and Karatayev (1963)
		Above the Conrad Discontinuity	-	Puchkova and Ladynin (1966)
Germany		Above the Conrad Discontinuity	-	Mundt (1965)
Gt Britain	8.0 to 15.0	15.0 to 26.0	-	N.E.R.C. Report (70/10)
Africa	4.4 to 29.9		-	This Study

Table (13). Average depths or range of depths to the top and bottom of 'deep' magnetic sources from various studies.

obtained from other regions (table (13)). The present thesis covers the largest area analysed in a single study and consequently the depth estimates cover a larger range; but within a single tectonic unit (Mozambique Orogenic Belt, Kalahari and Congo Basins) the average depth estimates seem to show a logical trend or pattern.

Some of the authors referenced in table (13) (Vacquier and Affleck (1941), Bhattacharyya and Morley (1965), McClure (1963)) postulate that the base of their models represents the Curie point isotherm. Although undulations in Curie point isotherm may well affect the depth estimates given here, it is not possible to give an estimate of its position in the crust from these estimates. It is only reasonable to state that magnetic bodies may exist at least to a depth of 23 km. (figure (78)) and possibly to a depth of 30 km.

(4.7) Conclusions

From this study of the Project MAGNET profiles which cross the African continent the following may be concluded:

(i) A characteristic magnetic pattern is observed across many of the tectonic or geological units of Africa (chapter (1)) and the boundaries between these units is often marked by a change in magnetic relief. Of particular note is (a) the magnetic 'quiet zone' observed across the Mozambique Orogenic Belt, (b) the near absence of magnetic anomalies across the East African Rift volcanic rocks, (c) the double peaked anomalies associated with the Lake Malawi - Shire Rifts, (d) the high amplitude anomalies (short and long wavelength) recorded across the Kalahari Basin and the Congo Basin south of latitude 4°S. , (e) the high amplitude (short and long wavelength) anomalies recorded across the Precambrian dykes and Karroo lavas of the Rhodesian Shield, and (f) the very high amplitude, long wavelength, mostly negative features observed

across the North Congo Shield and Kibalian Orogenic Belts.

(ii) Application of the 'statistical models method' of chapter (2) to the Project MAGNET data generally reveals two ensembles of magnetic sources (figure (77), figure (78), table (12)). In most cases there is a good correlation between the short wavelength magnetic anomalies and the surface geology and therefore these surface rocks and deeper equivalents are interpreted as the principle members of the shallow ensemble of bodies. The nature of the deeper ensemble of magnetic Bodies is not so clear. Within a given tectonic unit (i.e. the Mozambique Orogenic Belt or the Kalahari and Congo Basins) the average depth estimates seem to show a simple pattern or trend, but there is no discernible relation between the depth estimates of separate units.

(iii) The average depths to the 'deep' magnetic sources of the African continent are not significantly different from those of other continents.

(iv) No adequate estimate of the errors in the average depth values is available from the present analysis. Trial computations with synthetic data show that the mean square difference of the computed spectra from the least squares straight line is not adequate. The best estimate of the reliability of the average depth values from real data should prove to be the repeatability of the values from near neighbouring profiles.

CHAPTER 5

PROJECT MAGNET PROFILES AND SEAFLOOR SPREADING

(5.1) The Importance of Madagascar in the Gondwanaland

Reconstructions

(5.2) Reconstructions of Madagascar with the African Mainland

(5.2.1) Madagascar against the Kenya-Tanzania Coast

(5.2.2) A Stationary Madagascar

(5.2.3) Madagascar Adjacent or Overlapping Mozambique

(5.3) New Evidence Bearing on the Relationship between

Madagascar and the African Mainland

(5.3.1) Project MAGNET Profiles North of Latitude 21°S

(5.3.2) Project MAGNET Profiles South of Latitude 21°S

(5.3.3) The Mozambique Ridge as an Extinct Spreading Centre

(5.3.4) The Malagasy Fracture Zone as a Transform Fault

(5.3.5) Geological Correspondence Between Madagascar and
the African Mainland-Evidence for a Southern
Derivation of the Island from the Mainland

(5.4) Postulated Movement of Madagascar Relative to the African

Mainland - A New Reconstruction

(5.5) Conclusions

CHAPTER 5

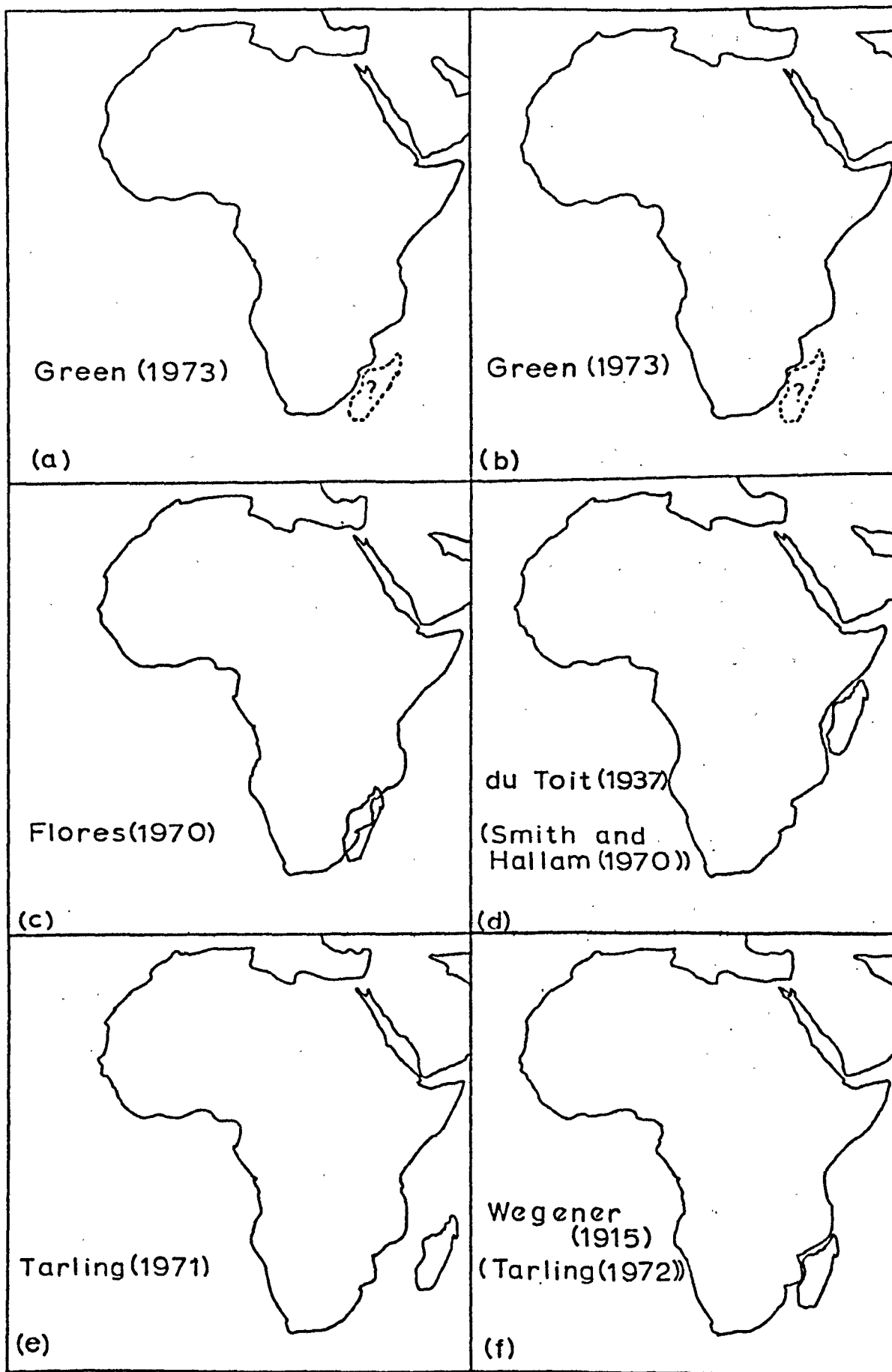
PROJECT MAGNET PROFILES AND SEA FLOOR SPREADING

(5.1) The Importance of Madagascar in the Gondwanaland Reconstructions

Recent attempts to reconstruct the southern continents into a single land mass, Gondwanaland, have emphasized the importance of the fit of Madagascar (Smith and Hallam (1970), Dietz and Holden (1970), Tarling (1971, 1972)). Madagascar has been placed in four positions relative to Africa:

- (i) adjacent to Kenya-Tanzania (du Toit (1937), King (1950), Smith and Hallam (1970), Dietz and Holden (1970)) (figure (80d)),
- (ii) in its present position (Tarling (1971), figure (80e)),
- (iii) adjacent to Mozambique (Wegener (1915), Baker (1912 to 1918) in Tarling (1971b), Tarling (1972), figure (80f)). In Flores (1970) Madagascar is allowed to overlap with parts of Mozambique (figure (80c)).
- (iv) adjacent to South Africa and Mozambique (Green (1972a), figures (80a and b)).

This chapter is concerned with the interpretation of Project MAGNET profiles across the Mozambique Channel and their importance for Gondwanaland reconstructions. The principle results of this chapter are given in Green (1972a). Since this paper, new evidence has been obtained from deep sea drilling (DSDP legs 25 and 26) in the Mozambique Channel and adjacent regions, and this supports (iv).



Fig(80) Suggested reconstructions of Madagascar and the African Continent

(5.2) Reconstructions of Madagascar with the African Mainland

(5.2.1) Madagascar against the Kenya-Tanzania Coast

Independently, Smith and Hallam (1970) and Dietz and Holden (1970) gave similar reconstructions of the southern continents using a computer to derive at least squares fit of the 500 or 1000 fathom contours with the constraint that the predrift geology be matched across the fit. The result closely resembled the classic reconstruction of du Toit (1937) as modified by King (1950), with Madagascar fitted along the Kenya-Tanzania coast. The principle arguments in favour of this fit are:

- (i) There is a close resemblance between the Jurassic rocks and fossils in Madagascar and Tanzania (du Toit (1937)).
- (ii) There is a lack of Jurassic to Late Cretaceous volcanics (Stormberg volcanics) in Madagascar and this part of the east African coast (du Toit (1937)), whereas in the south of the mainland these volcanics are extensive (see section (1.6)).
- (iii) The resultant Gondwanaland reconstruction is generally consistent with palaeomagnetic data (Briden et. al. (1971)).
- (iv) It is possible that there is a large transform fault extending from the South West Indian Ocean Ridge to the Carlsberg Ridge along which Madagascar may have moved southwards (Fisher et. al. (1968)) (unless there is an additional east-west movement this requires Madagascar to fit against Somalia) (figure (81)).

(5.2.2) Stationary Madagascar relative to Africa

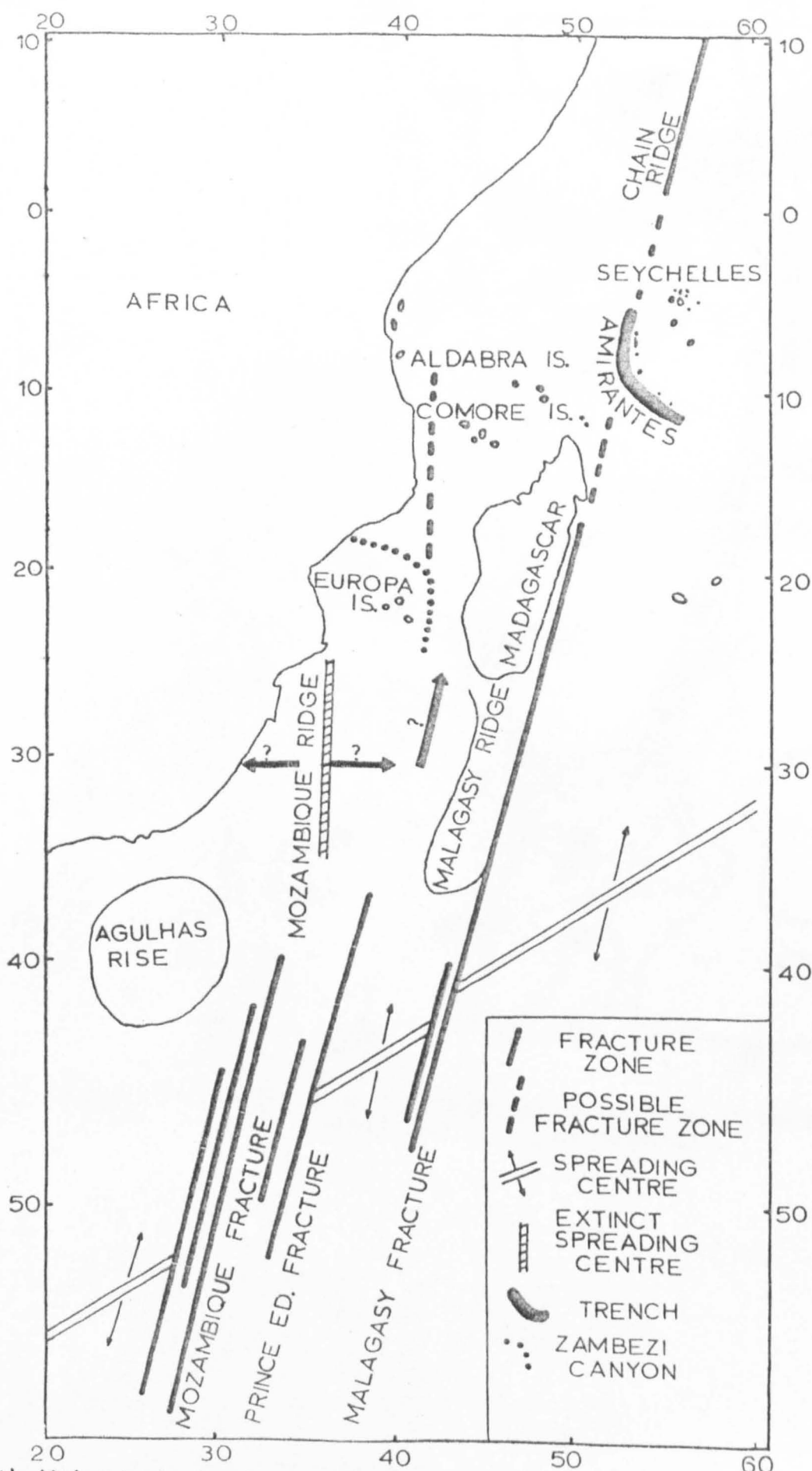
Tarling (1971) reviewed the possibility of a stationary Madagascar relative to Africa since the Permian and found several convincing lines of evidence for not allowing the island to have moved from the north since that time (Tarling did not consider an easterly or northerly movement

of the island in the 1971 publication). The principle arguments put forward by Tarling are:

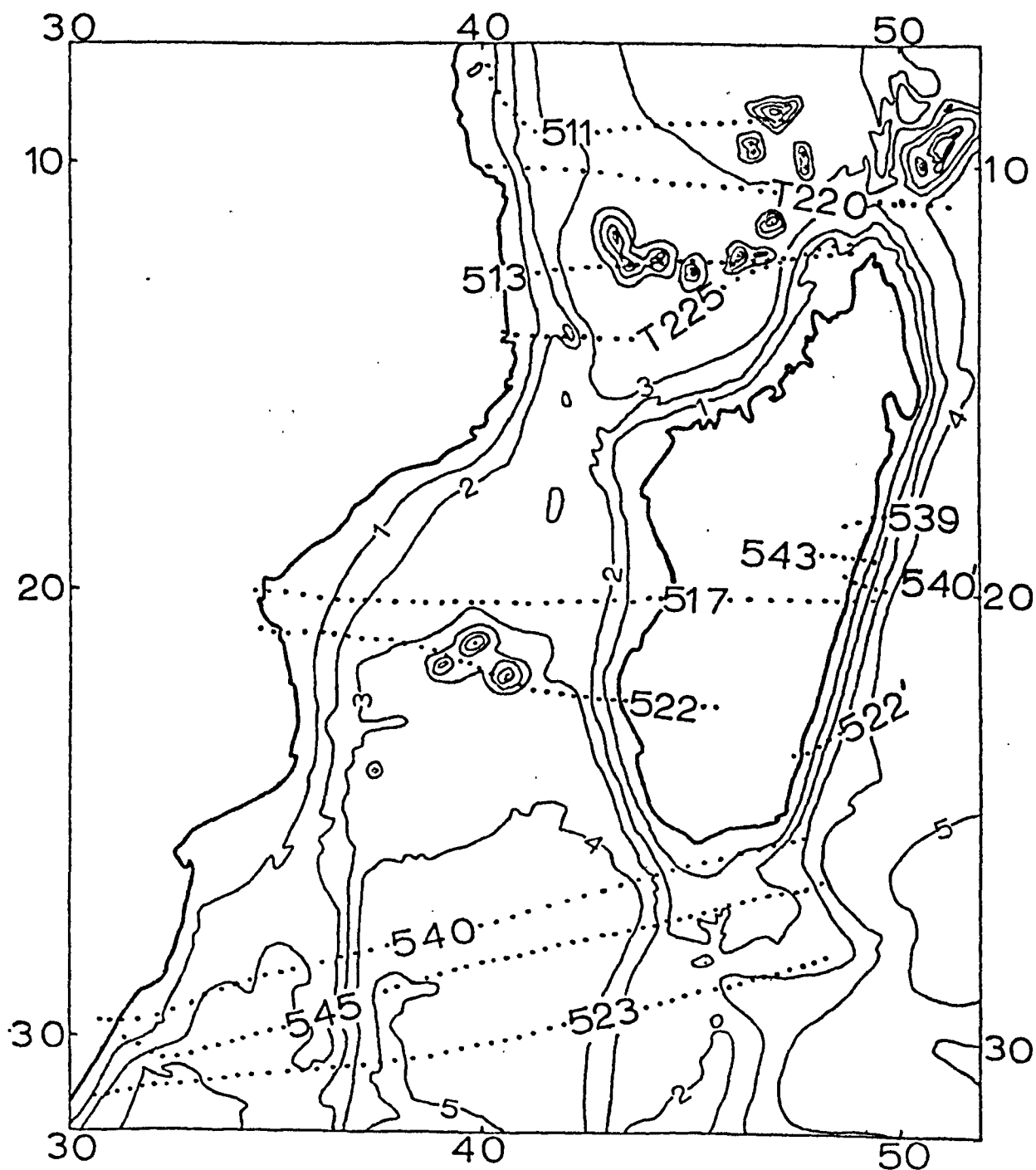
- (i) Dixey's (1960) contention that the margins of the Mozambique Channel indicate that it may be an enormous geosyncline.
- (ii) The results from seismic refraction (Francis et. al. (1966)) and reflection (Bunce et. al. (1967)) work indicates very thick sediments from the Kenya coast almost as far east as the Seychelles Islands. The correlation of the seismic refraction horizons with the postulated geologic column at Lamu (for at least shot 3 of the refraction line of Francis et. al. (1966)) has been substantiated by the results of deep drilling (DSDP 241 in figure (86) and figure (87)).
- (iii) Sandstone inclusions have been found within the volcanics of the Comores Archipelago (see figure (81) for location of the Comores) (Flower and Strong (1969)).
- (iv) The resultant Gondwanaland reconstruction is also generally consistent with the Palaeomagnetic data.

(5.2.3) Madagascar Adjacent to or Overlapping Mozambique

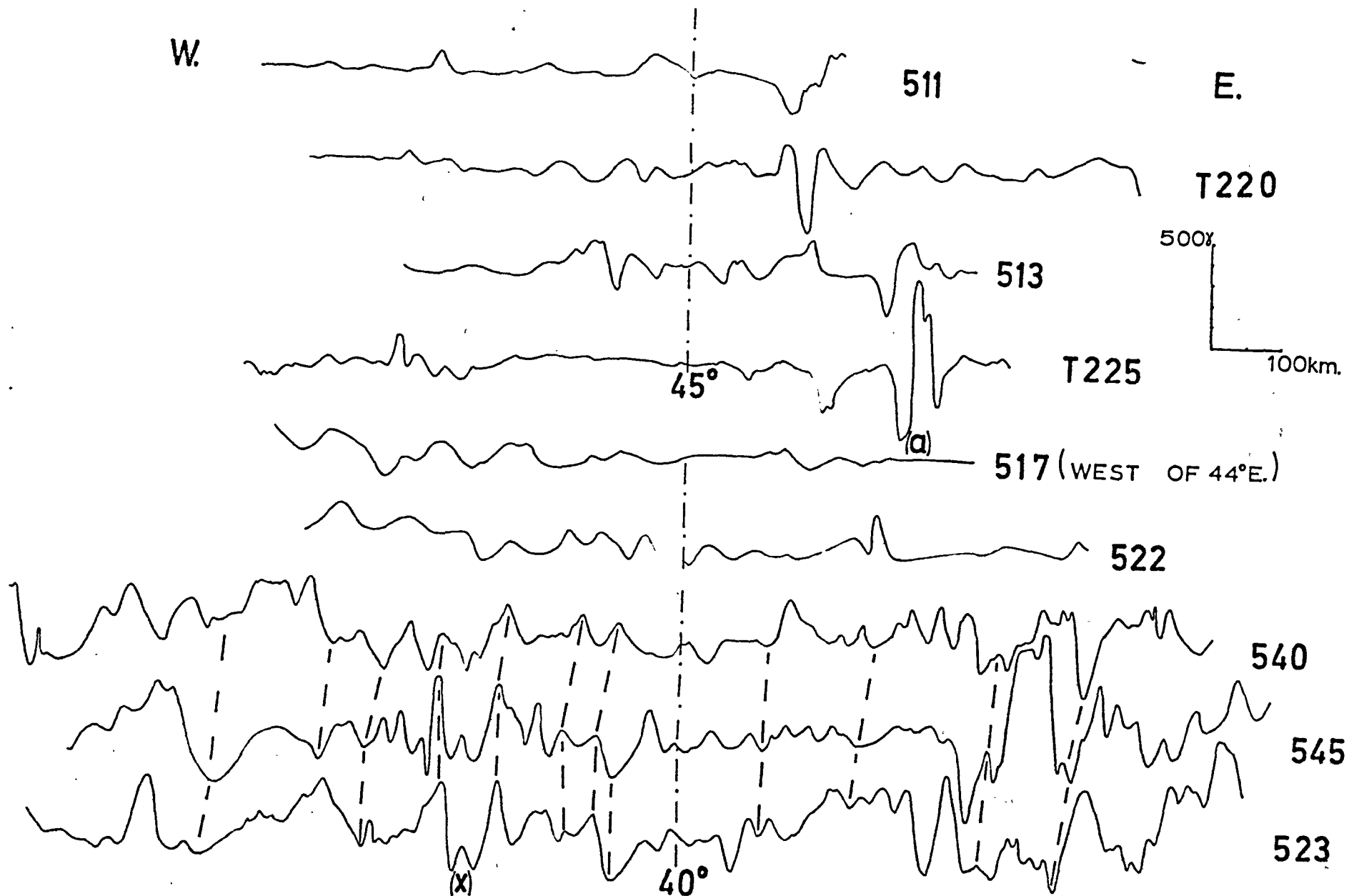
The earliest reconstructions of the southern continents placed Madagascar against the Mozambique coast (Wegener (1915), Baker (1912 to 1918) in Tarling (1971b)) but this fit has largely been neglected since du Toit (1937) argued for a northern fit of the island. New evidence from geological surveys and radiometric dating on the two land masses has deemed it necessary to revive these early reconstructions (Flores (1970), Wright and McCurry (1970)). Wright and McCurry (1970) give a similar reconstruction to Tarling (1972) with the island adjacent to the present Mozambique coast (figure (80f)), but Flores (1970) argues that the Pre-Karoo basement of the two land masses should be adjacent (figure (80e)). For the latter reconstruction it is necessary to assume that an enormous area of Mozambique now covered by young sediments is underlain by crustal material of Karroo and Post Karroo age.



FIG(61) Major tectonic features discussed in the text.



Fig(82) Map of the Mozambique Channel showing the location of the Project MAGNET profiles. The depth contours are in 1,000m intervals.



Fig(83) Project MAGNET profiles observed across the Mozambique Channel. All the profiles shown were obtained at altimeter heights from 8,000 to 11,000 feet except for profiles T225 and 513 which were flown at 4,000 feet and 15,000 feet respectively.

506

0°03' S.
46°55' E.

2°12' S.
40°00' E.

508

5°55' S.
43°12' E.

6°41' S.
39°05' E.

Fig(84) Project MAGNET profiles north of 8° S. in the Somali Basin.

The principle evidence for a Madagascar-Mozambique fit is geological and applies to the fit of Madagascar against the Mozambique-South Africa coast (figure (80a) and figure (80b)) and is discussed in section (5.3.5).

(5.3) New Evidence Bearing on the Relationship between Madagascar and the African Mainland

(5.3.1) Project MAGNET Profiles North of Latitude 21°S

West to east Project MAGNET profiles cross various parts of the Mozambique Channel (figure (82)) and the adjacent Somali Basin to the north, and the Mozambique Ridge to the south. Two profiles (figure (82) and figure (84)) north of 8°S . and west of 48°E . have already been discussed (McKenzie and Sclater (1971)), and show a lack of anomalies over the Somali Basin as found in ship surveys (Fisher et. al. (1968), Bunce et. al. (1967), Francis et. al. (1966)). Profiles between latitudes 8°S . and 21°S . are observed to be very 'quiet' except over the Comores and Aldabra islands (figure (83)). The large anomalies on profile 513 and on the east of profile T225 can be correlated with the volcanic Comores. The cross-over section of these flights, marked (a) in figure (83), permits good correlation between the profiles; the differences are due to the different altitudes and flight directions of the two profiles. On flight T220, at approximately 47°E ., there is a large negative anomaly which indicates a reversally magnetised body. The size of the anomaly suggests that the Aldabra Islands may be connected by a submarine intrusion or extrusion to the volcanic north eastern section of Madagascar and/or the Comores.

Except for the above anomaly, most of the magnetic relief outside of the islands is less than 100 gammas with wavelengths between 15km.

and 60km. This very low magnetic relief between the island and mainland north of latitude 21°S . (profiles 511 to 517 in figure (83)) suggests that the island has not moved from either the north west or the west in Post-Cretaceous times. This is supported by the age of sediments in DSDP 242 where Eocene was drilled and DSDP 241 where Cretaceous was drilled, basement was not reached in either (figure (86) and figure (87)).

(5.3.2) Project MAGNET Profiles South of Latitude 21°S .

There is a change in magnetic relief between profiles 517 and 522, the latter which crosses the Europa group of islands (figure (82) and figure (83)) contains anomalies of 120 gammas (peak to trough) with widths around 30km. Most of this magnetic activity can be attributed to the islands which are most likely volcanic. The change in magnetic relief between profile 522 and the three profiles between latitudes 25°S . and 32°S . is even more marked, the latter showing anomalies typically oceanic in amplitude and wavelength. Somewhere between the Europa group of islands and flight 540 there must be a drastic change in the age and nature of the underlying oceanic crust. It is conceivable that this group of islands is the dividing line. Unfortunately deep drilling in three key locations, i.e. DSDP 242, 243 and 244 (figure (86) and figure (87)) failed to reach basement and hence failed to substantiate this.

The large amplitude anomalies of the three profiles 540, 545 and 523 to the south of the channel extend across the thick sediments of the basin east of the Mozambique Ridge onto the Malagasy Ridge where the amplitudes become particularly high (figure (82) and figure (83)). The oceanic nature of this southern region was originally inferred from seismic refraction experiments (Ludwig et. al. (1968)) and this is now proven by the results of DSDP 248, 249 and 250 (figure (86) and figure (87)). Correlations of specific features of the profiles are indicated

in figure (83), the correspondence between lines 545 and 523, which are between 100 km. and 250km. apart, is particularly good west of longitude 40° E. The large anomalies to the east of this meridian are directly related to the Malagasy Ridge and Malagasy Fracture Zone (figure (81)).

The north-south lineations shown on these southern profiles demonstrate that seafloor spreading has occurred in an east-west direction. This is in complete contradiction to the postulated movement of Antarctica from the African mainland in a southerly direction as required by the reconstructions of Dietz and Holden (1970) and Smith and Hallam (1970).

Originally simulated sea floor spreading magnetic anomalies, using the time scale of Heirtzler et. al. (1968) and Helsly and Steiner (1969) were compared with the anomaly patterns of the three southern profiles. Although several possible regions of correlation existed the evidence was not very convincing, so it was therefore proposed that the seafloor in this region might be older than 140 My. (Green (1972)). That this is so, is adequately demonstrated by the fact that sediments of upper Lower Cretaceous (110 to 120 My.) age have been drilled from the top of the ocean floor basalts near the crest of the Mozambique Ridge at DSDP 249 in figure (86) and figure (87) .

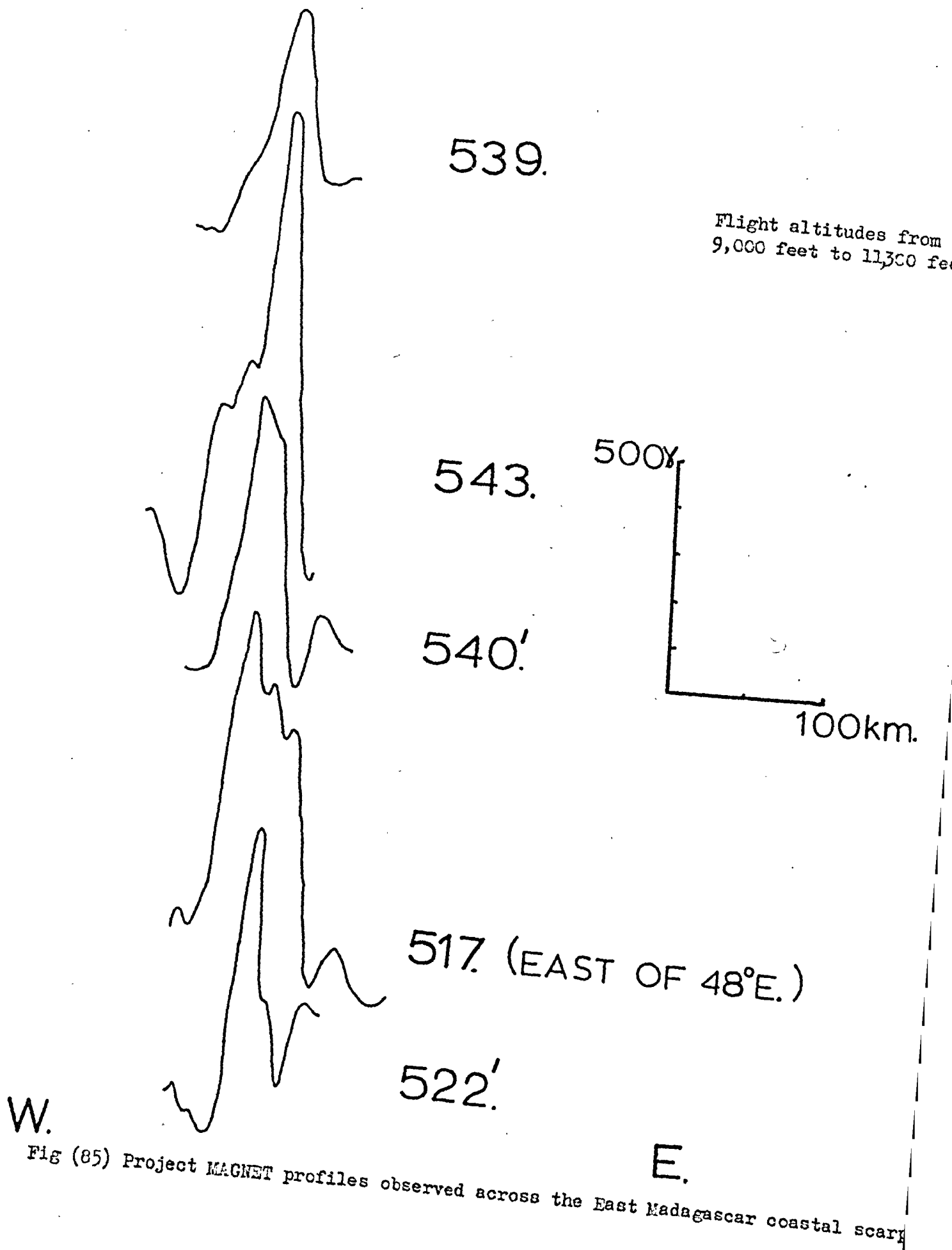
(5.3.3) The Mozambique Ridge as an Extinct Spreading Centre

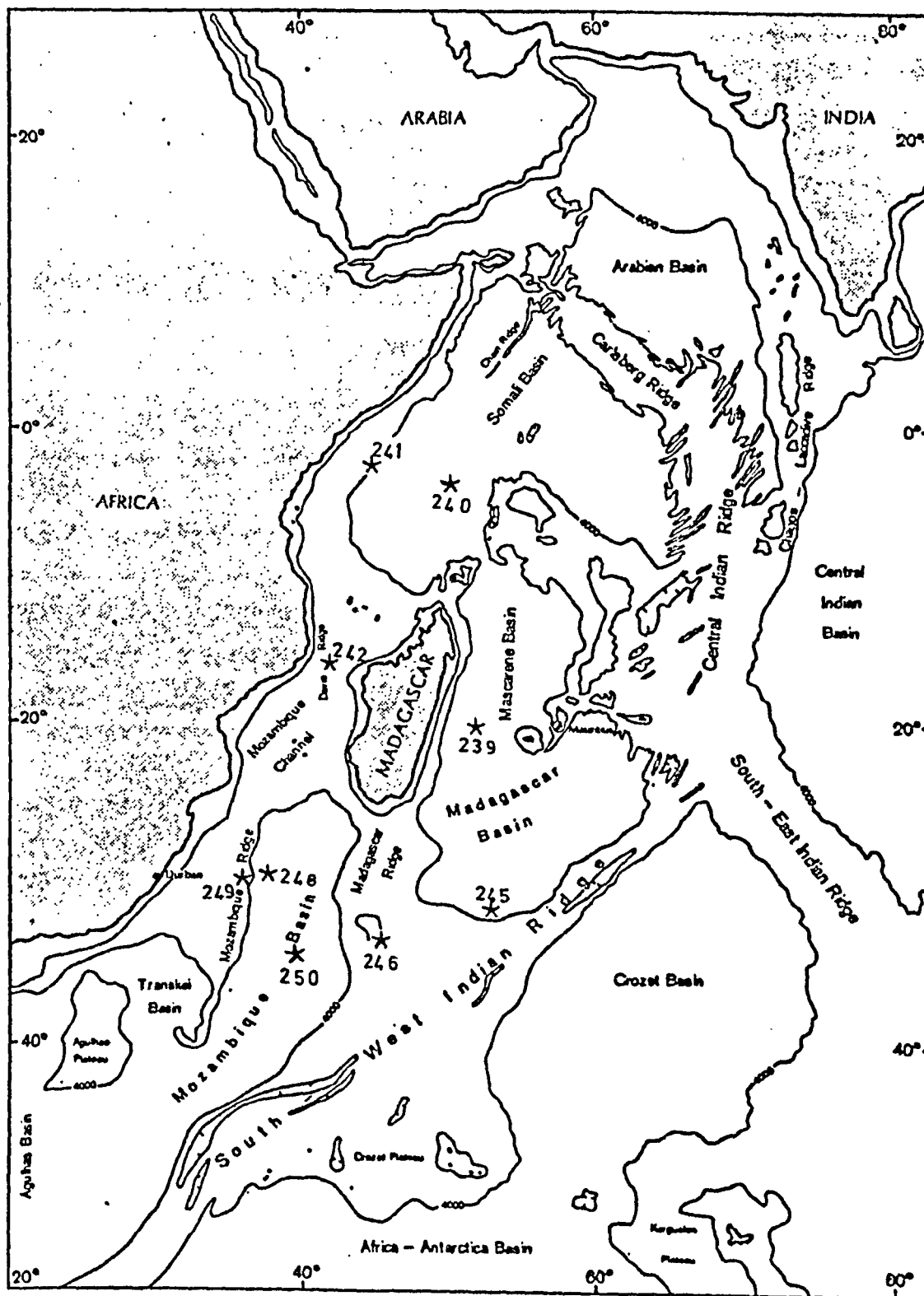
As there is no distinct central anomaly, or symmetry of pattern as is usually found on a spreading ridge, it is not possible to define the axis of spreading from the magnetic profiles alone. The bathymetry (figure (82)) suggests that the most probable axis is the Mozambique Ridge (Natal Ridge) (figure (81)) (Heezen and Tharp (1964), which has very high and distinct magnetic anomalies (x in figure (83)) coincident with its northern scarp. Additional evidence that the ridge may have been a spreading centre comes from the large free air

gravity anomaly (Vening-Meinesz (1948), Le Pichon and Talwani (1969)) observed on one side of the ridge and the high seismic activity (Fairhead and Girdler (1971)) and magnetic anomalies observed on its northern extension into the Shire-Malawi rift (chapter (4)). Apart from the lack of seismicity on the ridge and of a central positive anomaly, the 'normal' heat flow (Langseth and Taylor (1967)) on the ridge and the thick sediments of at least upper Lower Cretaceous age (DSDP 249 in figure (86) and figure (87)) found in this region are evidence that it is not spreading at present. The sediments in the west basin are particularly thick, indicating that the ridge has acted as a blockade to the transportation of sediments from the African continent (Ludwig et. al. (1968)). The magnetisation, or metamorphic effects on the underlying basalts, of these thick sediments may explain why only longer wavelengths are observed west of the very high gradient eastern scarp of the Mozambique Ridge (figure (82) and figure (83)).

(5.3.4) The Malagasy Fracture Zone as a Transform Fault

In the magnet profiles crossing the eastern coast of Madagascar (figure (82) and figure (85)) a very large positive anomaly (500 to 1000 gammas) is coincident with the sharply dipping coastal scarp (figure (82)) from at least 18°S. to 24°S. This observation plus the fact that there are abundant outcrops of volcanic material along the eastern coast of Madagascar would support the idea of a continuous 'leaky' transform fault stretching from the South West Indian Ocean Ridge along the Malagasy Fracture Zone, the Malagasy Ridge, the eastern Madagascar coastal scarp and possibly to as far north as the Amirantes (figure (81)).





Fig(86) Drilling sites for D.S.D.P. legs 25 and 26 in the Mozambique Channel.

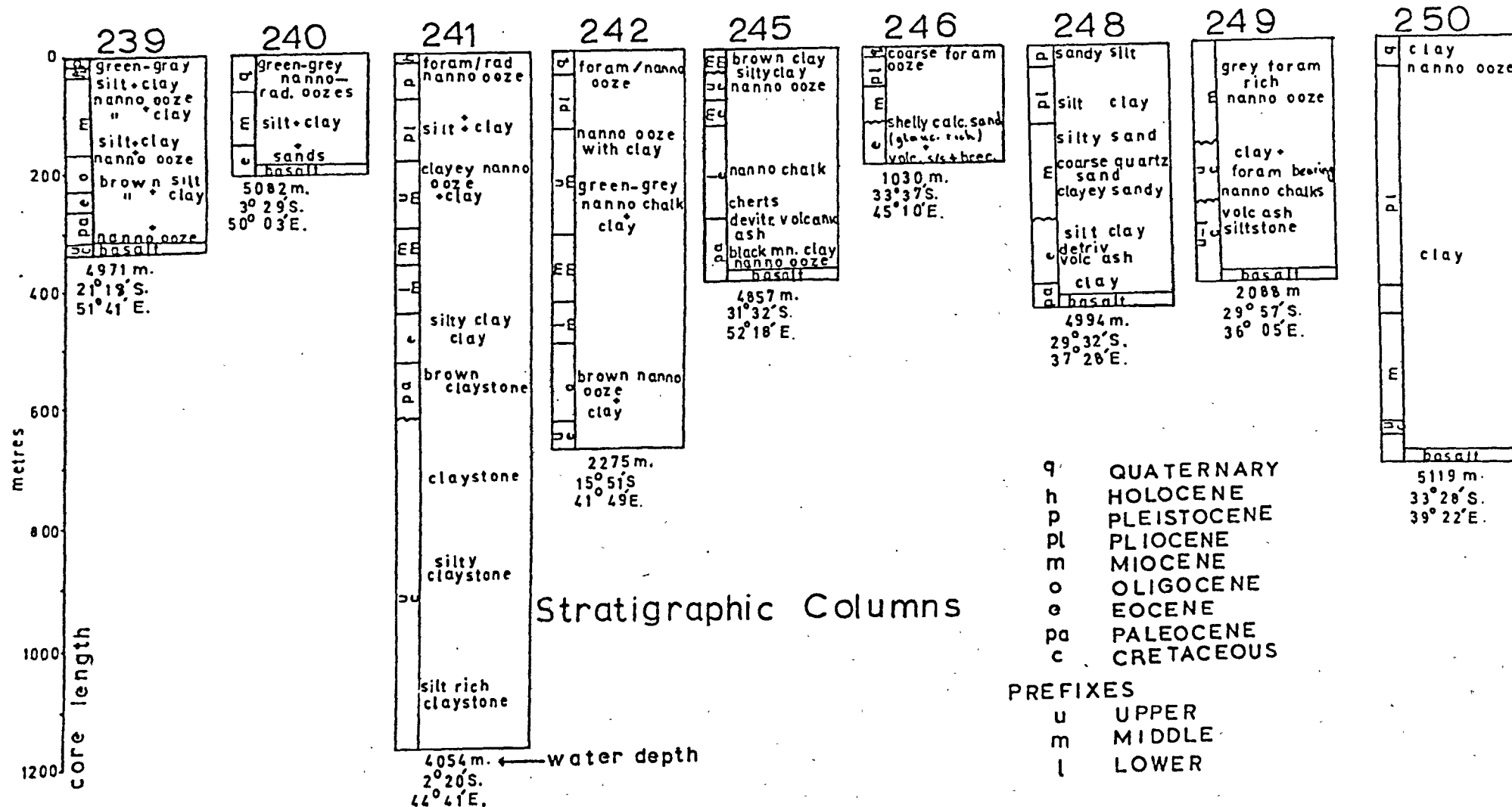


Fig (87) Stratigraphic columns obtained from the deep sea drilling holes D.S.D.P. legs 25 and 26.

(5.3.5) Geological Correspondence Between Madagascar and the African Mainland - Evidence For a Southern Derivation of the Island from the Mainland

The most comprehensive comparisons of the geology of Madagascar and the African continent have been made by du Toit (1937) and Dixey (1960). Much new evidence from the two land masses together with geophysical work in the Mozambique Channel, throw new light on the comparison. The early Precambrian orogeny which affected most of the island (Besaire (1957, 1967)) is of the same age as many of the Precambrian D formations of the mainland (see chapter (1)). It must be emphasized that correlations for the early Precambrian are highly questionable because of the small number of age determinations and their large errors. There is a significant correlation between the Late Precambrian orogeny which affected three quarters of the island and the massive Mozambique Orogeny of the mainland (chapter (1)). As well as the geological and geophysical similarities (Dixey (1960), Besaire (1957)), the age determinations of the islands orogeny (Delbos (1964)) falls within the 450 to 700 my. age range for the Mozambique Orogeny (Cahen and Snelling (1966)). A particularly striking correspondence is found between the rare earths in the pegmatites of the island and those found in the southern parts of the mainland (Von Knorring (1970), see also Petrascheck (1973)); enrichment of scandium is found only in Madagascar and Mozambique and of lithium and beryllium only in Madagascar, Mozambique and South West Africa. The pegmatites in the more northern parts of the Mozambique Orogeny are particularly deficient in the latter two elements.

More specific correlations for the younger formations indicate a possible fit of the island to the mainland. The Lower and Middle Karroo of southern Africa (27°S. to 32°S.) and south west Madagascar have

been compared by Flores (1970) in a detailed geological analysis. He demonstrates the very close resemblance between the Dwyka (tillites), Eccca (lacustrine and possibly marine deposits), Stormberg (continental sediments) series of southern Africa and the Sakoa, Sakema, Isalo (continental sediments) series of Madagascar. In addition Pallister (1971) points to the similarities for this period, of the 'local basins of deposition with intra-formational erosion and unconformities' of Malawi and those indicated from geophysical work in Madagascar (Cliquet (1957)). Although du Toit (1937) favoured a northern fit, he noted many of these Pre-Cretaceous similarities of the two land masses.

The Upper Karroo shows differences rather than similarities between Africa and Madagascar. In Madagascar there is the marine Jurassic already compared to that of coastal Tanzania (Smith and Hallam (1970), du Toit (1937), Dixey (1960)) but which is now thought to have extended the complete length of eastern Africa (Kent (1972), Dingle and Klinger (1971), Tarling (1972)). At the same time, southern Africa was involved in the spectacular Stormberg volcanicity. It is this period which is usually recognised as the initiation of the main phase of continental breakup and is the most likely time for the drift of Madagascar from the mainland. That this is so, is adequately demonstrated by the upper Lower Cretaceous sediments obtained at DSDP 249 (figure (86) and figure (87)) and the Upper Cretaceous sediments obtained at DSDP 250. That Madagascar did not completely escape the volcanic activity is shown by the Mid-Cretaceous basalt flows in the west of the island (Brasseur et. al. (1959), Flores (1970), Kent (1972)).

(5.4) Postulated Movement of Madagascar Relative to the African Mainland - A New Reconstruction

Before examining the reconstruction of Madagascar with the

mainland from the evidence presented, it is worthwhile to emphasize the difficulty that has been found in explaining the tectonics of the South West Indian Ocean. The dominant feature of this region is the South West Indian Ocean Ridge with its enormous NNE trending fracture zones (Heezen and Tharp (1964), figure (81)). Although the spreading centre appears to be well defined seismically (Stover (1966), Banghar and Sykes (1969)) the bathymetry and magnetic anomalies have defied reasonable interpretation; a recent survey near 44°S. , 38°E. shows the only anomaly that can be correlated, the central anomaly, is unrelated to the prominent bathymetric trend (Bergh (1971)). It is possible that the confusion for this south west section of the Indian Ocean Ridge is caused by a change in spreading direction (McKenzie and Sclater (1971)). Any interpretation of the movement of Madagascar must take this possible change of motion into account.

Geophysical and geological results from the Mozambique Channel and surrounding regions which give constraints on the movement of Madagascar since at least the Permian are summarised as follows:

(i) The area north of 9°S. (Somali Basin) has consolidated Jurassic sediments extending 500km. from the African coast and Cretaceous sediments extending almost as far as the Seychelles; this is shown by:

(a) Geological evidence from the east African coast which shows thick marine sediments ranging from Lower Jurassic age (possibly pre-Triassic) to present, indicating a coastal environment for the present Tanzania - Kenya - Somalia coast since that time (Kent (1972), Kent et. al. (1971), Francis et. al. (1966)).

(b) The horizons observed on seismic reflection (Bunce et. al. (1967)) and refraction (Francis et. al. (1966) records which have been confidently related to the predicted geological column of the Kenya coast.

(c) Gravity anomalies which indicate very thick sediments (up to 10km. thick) across the east African continental margin between latitudes 1°S . and 7°S (Rabinowitz (1971)).

(d) An extremely flat magnetic pattern across this northern region (figure (83), figure (84), Bunce et. al. (1967), Fisher et. al (1968), Francis et. al. (1966)) which indicates that seafloor spreading has not occurred in this area since at least mid-Cretaceous (Larson and Pitman (1972)).

(e) The results of DSDP 241 (figure (86) and figure (87)) which penetrated 1200m. of sediments without reaching basement. The oldest sediments recovered were Upper Cretaceous.

(ii) Except for the Comores, Aldabra and Europa islands, the Mozambique Channel between latitudes 9°S . and 21°S . is characterised by an extremely low magnetic relief. The sea floor in this region is at least as old as Upper Eocene (DSDP 242 in figure (86) and figure (87)), but is likely to be older as the drilling failed to reach basement.

(iii) The Mozambique Ridge was a spreading centre prior to the mid-Cretaceous (see section (5.3.3)).

(iv) The Malagasy Fracture Zone, the Malagasy Ridge and the scarp of the eastern Madagascar coast may be a transform fault (see section (5.3.4)).

Although these data place strong constraints on the movement of the island with respect to the mainland, it seems premature to attempt a detailed reconstruction of the two land masses until more details about the true pre-drift continental edges are obtained (see discussion by Flores (1970), Scrutton and du Plessis (1973), Talwani and Eldholm (1973)). For this reason the two possible reconstructions shown in figure (80a) and figure (80b) showing Madagascar at the same latitude but with slightly different orientations, must be regarded as tentative. Unfortunately, present palaeomagnetic knowledge cannot help to resolve the finer details

of the reconstruction (personal communication, Tarling and Hailwood (1972)). Determinations from Upper Cretaceous rocks in Madagascar (Andriamirado and Roche (1969)) yield a pole position between the Lower Cretaceous and Lower Tertiary poles of the mainland.

From the geological correspondences and the geophysics of the channel, it is only possible to say that the island fitted against South Africa and Mozambique with the northern tip of the island south of 21°S . (figure 80a) and figure 80b)). It is suggested that the Mozambique Ridge, with its landward extension into the Shire-Malawi Rifts, was the probable spreading centre from the Late Triassic until sometime in the Mid Cretaceous. The early stage of drifting is inferred from:

- (i) The absence of Jurassic volcanics on Madagascar which are abundant on the mainland.
 - (ii) The marine Jurassic sediments on the west coast of the island and the southern tip of the mainland (Dingle and Klinger (1971)); any evidence of this marine incursion in the south east part of the mainland has been covered by the younger volcanic and sedimentary sequences.
 - (iii) The upper Lower Cretaceous age of the sediments found near to the crest of the Mozambique Ridge (figure (86) and figure (87)).
- The correlation of the Madagascar marine Jurassic fauna with that of the Tanzania coast only implies a sea connection between the two areas and not that they were once adjacent (see Kent (1972) for a detailed discussion).

In the Cretaceous-Early Tertiary the whole region was affected by the development of the principle Indian Ocean Ridge system (McKenzie and Sclater (1971), DSDP 246 in figure (86) and figure (87)). In the South West Indian Ocean, massive faults developed to accommodate the changing stress pattern, and their evolution was possibly affected to a large extent

by the thick crust of the surrounding continental masses. But the differential spreading (faster to the east) due to the changing spreading direction, which may still be a feature of this region, may have pushed the Madagascar, Seychelles and Indian sub-continent north relative to the African mainland. West of Madagascar this difference in spreading was taken up by the right lateral Prince Edward and Mozambique fracture zones (figure 81)) with a possible extension along the eastern scarp of the Mozambique Ridge. The present seismicity of the channel (Fairhead and Girdler (1971)) may indicate an extension of the fracture zones. The Zambezi Canyon could be part of this fault system. The differential spreading which caused the northward movement of the Seychelles and Indian (McKenzie and Sclater (1971)) sub-continent relative to Madagascar, would have been taken up by the Malagasy Fracture Zone and its extension along the east Madagascar coastal scarp and possibly further north along the line of topographic features discussed by Fisher et. al. (1968). The Amirantes Trench (figure (81)) may have been a temporary subduction zone during the early phase of the development of the South West Indian Ocean Ridge and its fracture zones; basalts dredged from the Amirantes Trench yield a radiometric age of 82my. (Fisher et. al. (1968)). The present day seismic activity of the Mozambique Channel and the fracture zones may indicate that the northward movement of Madagascar relative to Africa is still in progress.

(5.5) Conclusion

We can state with a reasonable amount of confidence that a southern derivation of Madagascar relative to the African mainland helps to explain the following:

- (i) The correspondence of the Pre-Jurassic geology of the island and mainland.

- (ii) The major topographic features observed in the Mozambique Channel, Somalia Basin and surrounding regions.
- (iii) The geophysical and bore hole data in the above regions.
- (iv) Palaeomagnetic data - independently Thompson (1972) and Tarling (1972) both claim that in general the reconstructions of Gondwanaland with Madagascar in a southern position adjacent to Africa, yields a distribution of paleomagnetic poles with significantly less scatter than that obtained for the Smith and Hallam (1970) (figure (80d)) reconstruction. The conclusion of Briden et. al. (1971) that there was significant non-axial geocentric components in the pre-drift geomagnetic field (based on the Smith and Hallam (1970) reconstruction) is therefore premature (Tarling (1972)).
- (v) The discrepancy between McKenzie and Sclater's (1971) reconstruction of the southern continents (back to Late Cretaceous), obtained by progressively removing the old ocean floor as defined by sea floor magnetics, and the Gondwanaland reconstructions proposed prior to 1972. McKenzie and Sclater (1971) state 'It is difficult to understand how the fit proposed by du Toit (1937) and refined by Smith and Hallam (1970) could evolve to the Upper Cretaceous arrangement proposed in this paper (McKenzie and Sclater (1971))'. On the reconstruction proposed in this chapter, McKenzie and Sclater's Upper Cretaceous reconstruction is the natural next stage in the evolution of the South West Indian Ocean.

Clearly the major problem remaining is the detailed timing of the various events, particularly for the formation of the Amirantes, but the present data is adequate to explain the gross features of the tectonics of this region.

REFERENCES - PART I

- Ackerman, E. (1950) Ein neuer Faltengurtel in Nordrhodesian und seine tectonische Stellung in Afrikanischen Grundgebirge. Geol. Rund. 38, 24.
- Ackerman, E. & Foster, A. (1960) Grundzüge der Stratigraphie und Struktur des Irumide-orogens. C.R. XXI p.182.
- Aldredge, L.R., Van Voorhis, G.D. & Davies, T.M. (1963) Magnetic Profile Round the World. J.G.R. 68, 3679.
- Andriamirado, R. and Roche, R. (1969) C.R. 269, 16.
- Baker, B.H., Williams, L.A.J., Miller, J.A., & Fitch, F.J. (1971) Sequence and Geochronology of the Kenya Rift Volcanics. Tectonophysics 11, 191.
- Baker, B.H., Mohr, P., & Williams, L.A.J. (1972) Geology of the Eastern Rift System of Africa. Geol. Soc. of Amer. Spec. paper 136.
- Banghar, A.R. & Sykes, L.R. (1969) Focal Mechanics of Earthquakes in the Indian Ocean and Adjacent Regions. J.G.R. 75, 632.
- Bergh, H.W. (1971) Sea Floor Spreading in the South West Indian Ocean. J.G.R. 76, 6276.
- Besaire, H. (1967) The Precambrian of Madagascar. The Precambrian Vol. III, Rankama, K. (ed).
- Besaire, J.W. (1957) La Geologie de Madagascar. (Serv. Geol. Tananarive).
- Bhattacharyya, B.K. (1965) Two-dimensional Harmonic Analysis as a tool for Magnetic Interpretation. Geophys. 30, 829.
- Bhattacharyya, B.K. (1966) Continuous Spectrum of the Total Magnetic Field Anomaly due to a Rectangular Prismatic Body. Geophys. 31, 97.
- Bhattacharyya, B.K. (1966b) A Method for Computing the Total Magnetisation Vector and the Dimensions of a Rectangular Block Shaped Body from Magnetic Anomalies. Geophys. 31, 74.
- Bhattacharyya, B.K. & Morley, L.W. (1965) The Delineation of Deep Crustal Magnetic Bodies from Total-Field Aeromagnetic Anomalies. J. of Geomag. & Geoelec. 17, p.237.
- Bichan, R. (1970) The Evolution and Structural Setting of the Great Dyke, Rhodesia, in African Magmatism and Tectonics. Clifford and Gass (eds) Oliver and Boyd.

- Bingham, C., Godfrey, M.D. & Tukey, J.W. (1967) Modern Techniques in Power Spectrum Estimation. I.E.E.E. Trans. Electroacoustic. Au-15, 56.
- Bishop, D. & Van Eeden, O. (1971) The Tectonics of Southern Africa, in Tectonics of Africa, U.N.E.S.C.O. Earth Sciences no. 6 Choubert, G. and Faure-Muret, A. (eds).
- Black, D.I. (1970) Lunar and Solar Magnetic Variations at Abinger, their Detection and estimation by Spectral Analysis via Fourier Transforms. Phil. Trans. Roy. Soc. of London (A), 268, 233.
- Black, D.I. & Schollar, I. (1969) Spacial Filtering in the Wave Vector Domain. Geophys. 34, 916.
- Blakely, and Cox, (1972) Identification of Short Polarity Events by Transforming Marine Magnetic Profiles to the Pole. J.G.R. 77, 4339.
- Bloomfield, K. (1961) The Precambrian of Nyasaland (Malawi). Geol. Surv. Nyasaland, Rept. KB 145.
- Bloomfield, K. (1970) Orogenic and Post Orogenic Plutonism in Malawi, in African Magnetism and Tectonics, Clifford and Gass (eds), Oliver and Boyd.
- Bloomfield, K. & Hapgood, F. (1966) Explanatory Notes on the Structural Map of Malawi.
- Berry, M.J., Jacoby, W.R., Niblett, E.R. & Stacey, R.A. (1971) A Review of Geophysical Studies in the Canadian Cordillera. Can. J. Earth Sci. 8, 787.
- Brasseur, R., Godard, J.M., Guerin-Desjardins, B., Hindemeyer, J. and Rebilly, G. (1959) Preseconnaissance Petroliere due Bassin du Majunga (Madagascar). Inst. Franc. de Petrole.
- Briden, J.C., Smith, A.G. & Sallomy, J.T. (1971) The Geomagnetic Field in Permo-Triassic Time. Geophys. J. 23, 101.
- Brock, and Piper. (1972) Interpretation of Late Precambrian Palaeomagnetic Results from Africa. Geophys. J. 28, 139.
- Bulina, L.V. (1961) The Use of Airborne Magnetic Prospecting Data in Deep-Seated Structure of the Earth's Crust within the Siberian Platform. Sovetskaya Geologiya, no. 5, 134.
- Bullard, E.C., Hill, M.N., & Mason, C.S. (1962) Chart of the Total Force of the Earth's Magnetic Field for the North-Eastern Atlantic Ocean. Geomagnetica 185 (Servico Meteorologico Nacional, Lisbon 1962).

- Bullard, E.C. (1967) The Removal of Trend from Magnetic Surveys. Earth Planet. Sci. Lett. 2, 293.
- Bunce, E.T., Langseth, M.G., Chase, R.L. & Ewing, M. (1967) Structure of the Western Somali Basin. J.G.R. 72, 2547.
- Burlisch, R. (1967) Numerical Calculations of Sine, Cosine and Fesnal Integrals. Numerishe Mathematic 9, 380.
- Cahen, L. (1954) Geologie due Congo Belge. H. Vaillant - Carmanne, Liège.
- Cahen, L. (1970) Igneous Activity and Mineralisation Episodes of the Kibaride and Katangan Orogenic Belts of Central Africa, in African Magmatism and Tectonics, Clifford and Gass (eds), Oliver and Boyd.
- Cahen, L. & Snelling, N.J. (1966) Geochronology of Equatorial Africa, North-Holland.
- Cahen, L. & Lepersonne, J. (1967) The Precambrian of the Congo, Rwanda and Burundi, in The Precambrian vol. 3, Rankama, K. (ed).
- Caner, B. (1969) Long Aeromagnetic Profiles and Crustal Structure in Western Canada. Earth Planet. Sci. Lett. 7, 3.
- Chapman, and Bartels, (1945) Geomagnetism. Oxford Clarendon Press.
- Clifford, T.N. (1967) The Damaran Episode in the Upper Proterozoic-Lower Palaeozoic Structural History of Southern Africa. Geol. Soc. Am. Spec. Paper 92.
- Clifford, T.N. (1968) Radiometric Dating and the Pre-Silurian Geology of Africa, in Radiometric Dating for Geologists, Hamilton, E.I. and Farquhar, R.M. (eds), Interscience Publishers.
- Clifford, T.N. (1970) The Structural Framework of Africa, in African Magmatism and Tectonics, Clifford and Gass (eds), Oliver and Boyd.
- Clifford, T.N., Nicolaysen, L.O., & Burger, A.J. (1962) Petrology and Age of the Pre-Otavi Basement Granite at Franzfontain Northern South West Africa. J. Petrol., 3, 244.
- Clifford, T.N., & Snelling, N.J. (1967) Radiometric Age Data for the Urungwe and Miami Granites of Rhodesia. Earth and Planet. Sci. Lett. 2, 5.
- Cliquet, P.C. (1957) C.C.T.A Reg. Comm. Geol. second Meeting C.R., 199.
- Combe, A.D. (1932) The Geology of South West Ankole. Geol. Surv. Uganda, mem. 2.

- Cooley, J.W. & Tukey, J.W. (1965) An Algorithm for the Machine Calculations of Complex Fourier Series. Maths. Comput., 19, 297.
- Cooley, J.W., Lewis, P.A.W. & Welsh, P.D. (1967) The Fast Fourier Transform and its Applications. I.B.M. Res. Rept. RC-1743.
- Cox, K.G. (1970) Tectonics and Vulcanism of the Karroo Period and their Bearing on the Postulated Fragmentation of Gondwanaland, in African Magmatism and Tectonics, Clifford and Gass (eds), Oliver and Boyd.
- Cox, K.G. (1972) The Karroo Volcanic Cycle. J. of the Geol. Soc., 128, 311.
- Creer, K.M. (1971) Geophysical Interpretation of Remanent Magnetisation in Oxidized Basalts. Ziet für Geophys. 37, 383.
- Darracott, B.W. (1972) Gravity and Magnetic Survey of the Speke Gulf, Serengeti and Mara Regions and their Relevance to Rifting in East Africa. Ph.D. Thesis, University of Newcastle.
- Darracott, B.W., Fairhead, J.D., & Girdler, R.W., (1972) Gravity and Magnetic Surveys in Northern Tanzania and Southern Kenya. Tectonophysics 15, 131.
- Davies, K.A. (1935) A Contribution to the Study of the Kavirondo. Geol. Surv. Uganda Bull. 2, 30.
- Davies, K.A. (1956) The Geology of part of South East Uganda. Mem. Geol. Surv. Uganda, 8.
- Dawson, J.(1970) The Structural Setting of African Kimberlite Magmatism, in African Magmatism and Tectonics, Clifford and Gass (eds), Oliver and Boyd.
- Delbos, L. (1964) Mesures d'age Absols sur les Series Precambriennes de Madagascar. C.R. 258, 1853.
- De Swardt, A.M.J., Garrard, P. & Simpson, I.G. (1965) Major Zone of Transcurrent Dislocation and Superposition of Orogenic Belts in Part of Central Africa. Geol. Soc. of Am. Bull. 76, 89.
- Dietz, R.S. & Holden, J.L. (1970) Reconstruction of Pangea, Breakup and Dispersion of Continents, Permian to Present. J.G.R. 75, 4939.
- Dingle, R.V. & Klinger, H.R. (1971) Significance of Upper Jurassic Sediments in the Knysna Outlier (Cape Province) for Timing of the Breakup of Gondwanaland. Nature 232, 37.

- Dixey, F. (1960) The Geology and Geomorphology of Madagascar and a Comparison with Eastern Africa. Quart. J. Geol. (Lond.) 116, 225.
- Du Toit, A.L. (1937) Our Wandering Continents, Oliver and Boyd.
- Evans, A. Ll., Fairhead, J.D. & Mitchell, J.G. (1971) Potassium Argon Ages from the Volcanic Province of Northern Tanzania. Nature 229, 19.
- Evrard, P. (1960) Resultats Scientifiques des Missions due Syndicate pour l'etude Geologique et Miniere de la Curvette et Travaux Connexes; Seismique. Ann. de Musee Royal du Congo Belge, 33.
- Evrard, P., Jones, L. & Mathieu, P.L. (1959) Syndicat pour l'etude Geologique et Miniere de la Cuvette Congolaise. Turvuen.
- Ewing, W.M. & Heezen, B.C. (1956) Some Problems of Antarctic Submarine in Geology. Am. Geophys. Un. Mono. 1, 75.
- Ewing, W.M., Eittreim, S., Truchan, M. & Ewing, J. (1969) Sediment Distribution in the Indian Ocean. Deep Sea. Res. 16, 231.
- Fairhead, J.G. & Girdler, R.W. (1969) How Far Does the Rift System Extend through Africa. Nature 221, 1018.
- Fairhead, J.D. & Girdler, R.W. (1970) Seismicity of the Red Sea, Gulf of Aden and Afar Triangle. Phil. Trans. Roy. Soc. A267, 49.
- Fairhead, J.D. & Girdler, R.W. (1971) The Seismicity of Africa. Geophys. J.24, 271.
- Fairhead, J.D., Mitchell, J.G. & Williams, L.A.J. (1972) New K/Ar Determinations on Rift Volcanics of S. Kenya and their Bearing on Age of Rift Faulting. Nature 238, 66.
- Fisher, L.R., Engel, C.G., & Hilde, T.W.C. (1968) Basalts Dredged from the Amirante Ridge, West Indian Ocean. Deep Sea Res. 15, 521.
- Fitches, W.R. (1971) A Part of the Ubendian Orogenic Belt in Northern Malawi and Zambia. Geol. Rund. 59, 444.
- Flores, G. (1970) Suggested origin of the Mozambique Channel. Trans. Geol. Soc. of South Africa 73, 1.
- Flower, M.J.F. & Strong, D.F. (1969) The Significance of Sandstone Inclusions in Lavas of the Comores Archipelago. Earth. Planet. Sci. Lett. 7, 47.

- Fotiadi, E.E. & Karatayev, G.I. (1963) Structure of the Earth's Crust of Siberia and the Far East According to Data of Regional Geophysical Investigations. Geology and Geophysics, Siberian Section, Academy of Sciences of the U.S.S.R., no. 10.
- Francis, T.J.G., Davies, D. & Hill, M.N. (1966) Crustal Structure between Kenya and the Seychelles. Phil Trans. Roy. Soc. (Lond.) A259, 240.
- Furon, R. et. al. (1959) Esquisse Structurale Provisoire de l'Afrique a 1:10,000,000, avec Notice Explicative. Intern. Geol. Congr., Assoc. Serv. Geol. Africans, Paris.
- Gass, I. (1970) Tectonic and Magmatic Evolution of the Afro-Arabian Dome in African Magmatism and Tectonics, Clifford and Gass (eds), Oliver and Boyd.
- Girdler, R.W., Fairhead, J.D., Searle, R.C. & Sowerbutts, W.T.C. (1969) The Evolution of Rifting in Africa. Nature 224, 1178.
- Girdler, R.W. & Sowerbutts, W.T.C. (1970) Some Recent Geophysical Studies of the Rift System in East Africa. J. of Geomag. and Geoelec. 22, 153.
- Grant, F.S. (1972) Review of Data Processing and Interpretation Methods in Gravity and Magnetism 1964-1971. Geophys. 37, 647.
- Grant, F.S. & West, G.F. (1965) Interpretational Theory in Applied Geophysics, McGraw-Hill Book Co. Inc.
- Green, A.G. (1972a) Seafloor Spreading in the Mozambique Channel. Nature 236, 19.
- Green, A.G. (1972b) Magnetic Profile Analysis. Geophys. J. 30, 393.
- Green, D. (1966) The Karroo System in Bechuanaland. Geological Survey Botswana, Bull. no. 2.
- Gregory, J.W. (1920) The African Rift Valleys. Geog. J. 56, 13.
- Gregory, J.W. (1921) The Rift Valley and Geology of East Africa. Seeley and Service.
- Griffith, D.H., King, R.F., Khan, M.A. & Blundell, D.J. (1971) Seismic Refraction Line in Gregory Rift. Nature 229, 69.
- Haines, G.V., Hannaford, W. & Riddihough, J. (1971) Magnetic Anomalies over British Columbia and Adjacent Pacific Ocean. Can. J. Earth. Sci. 8, 387.
- Hall, D.H. (1968) Regional Magnetic Anomalies, Magnetic Units and Structure in the Kenora District of Ontario. Can. J. Earth Sci. 5, 1277.

- Halligan, R. (1962) The Proterozoic Rocks of Western Tanganyika. Geol. Surv. Tanganyika Bull. 34.
- Hapgood, F. (1963) The Geology of the Country West of the Shire River between Chikwawa and Chiroma. Geol. Surv. Nyasaland Bull. 14.
- Harkin, D.A. (1960) The Rungwe Volcanics at the Northern End of L. Nyasa. Geol. Surv. Tanzania Mem. 11.
- Harpum, J.R. (1954) Some Problems of Pre-Karoo Geology, in Tanganyika Proc. 19th Int. Geol. Congr., Algiers, 1952, 20, 209.
- Haughton, S.H. (1963) The Stratigraphic History of Africa, South of the Sahara. Oliver and Boyd.
- Heezen, B.C. & Tharp, M. (1964) Physiographic Diagram of the Indian Ocean. Geol. Soc. of Am.
- Heirtzler, J.R., Dickson, G.O., Herrin, E.M., Pitman, W.C. and Le Pichon, X. (1968) Marine Magnetic Anomalies, Geomagnetic Field Reversals and Motions of the Ocean Floor and Continents. J.G.R. 73, 2119.
- Henderson, R.G. (1970) On the Validity of the Use of the Upward Continuation Integral for Total Magnetic Intensity Data. Geophys. 35, 916.
- Henderson, R.G. & Zietz, I. (1949) The Computation of Second Vertical Derivatives of Geomagnetic Fields. Geophys. 14, 508.
- Henderson, R.G. & Zietz, I. (1958) Interpretation of, and Aeromagnetic Survey of Indiana. U.S. Geol. Survey Prof. Paper 316-B.
- Hepworth, J.V. (1961) Unpublished thesis, University of Leeds.
- Hepworth, J.V. (1964) Explanation of the Geology of Sheets 19, 20, 28 and 29 (Southern West Nile) Geol. Surv. Uganda Rept. 10.
- Hepworth, J.V. (1972) The Mozambique Orogenic Belt and it's Foreland in North-east Tanzania. J. Geol. Soc. (Lond.) 128, 461.
- Hepworth, J.V. & Macdonald, R. (1966) Orogenic Belts of the Northern Uganda Basement. Nature 210, 726.
- Hepworth, J.V., Kennerly, J.B. and Shackleton, R.M. (1967) Photogeologic Investigation of the Mozambique Front in Tanzania. Nature 216, 146.
- Hepworth, J.V. & Kennerly, J.B. (1970) Photogeology and Structure of the Mozambique Orogenic Front Near Kolo, North-east Tanzania. Quart. J. Geol. Soc. (Lond.) 125, 447.
- Hitchen, B. (1958) The Geology of the Kariba Area. Rep. Geol. Surv. N. Rhodesia, 3.

- Holmes, A. (1951) The Sequence of Precambrian Orogenic Belts in South and Central Africa. Proc. 18th Int. Geol. Congr. (Lond.) 194D 14, 254.
- Holmes, A. (1965) Principles of Physical Geology. Nelson.
- Holmes, A. & Cahen, L. (1955) African Geochronology. Col. Geol. and Min. Res. 5, 3.
- Holmes, A. & Cahen, L. (1957) Geochronologie Africaine 1956 Acad. Roy. Sci. Coloniales (Brussels), Classe Sci. Nat., New Ser., Mem. 5, part 1.
- Irving, E. (1964) Palaeomagnetism and it's Application to Geological and Geophysical Problems. J. Wiley and Sons.
- I.E.E.E. Transactions. Acoust. Electroacoust., Au-15, 1967. Special Issue on the Fast Fourier Transform and its Applications.
- Jenkins, G.M. & Watts, D.C. (1968) Spectral Analysis and it's Applications. Holden-Day Series.
- Jones, R.H. (1965) A Reappraisal of the Periodogram in Spectral Analysis. Technometrics 7, 531.
- Johnson, R.L. (1968) Structural History of the Western Front of the Mozambique Belt in North-East Southern Rhodesia. Geol. Soc. of Am. Bull. 79, 513.
- Johnson, R.L. & Vail, J.R. (1965) The Junction between the Mozambique and Zambezi Orogenic Belts in North-East Southern Rhodesia. Geol. Mag. 102, 489.
- Kent, P.E. (1965) An Evaporite Basin in Southern Tanzania, in Salt Basins Around Africa Symposium, Inst. of Petrol.
- Kent, P.E. (1972) Mesozoic History of the East Coast of Africa. Nature 238, 147.
- Kent, P.E., Hunt, J.A. & Johnstone, P.W. (1971) The Geology and Geophysics of Coastal Tanzania. Inst. of Geol. Sci. Geophys. paper 6.
- King, B.C. (1970) Vulcanicity and Rift Tectonics in East Africa, in African Magmatism and Tectonics, Clifford and Gass (eds), Oliver and Boyd.
- King, B.C. & Sutherland, D.S. (1966) The Carbonatite Bearing Complexes of Eastern Uganda, in Carbonatites, Wiley and Sons.
- King, B.C. & Chapman, G.R. (1972) Vulcanism of the Kenya Rift Valley. Phil. Trans. R. Soc. (Lond.) A271, 185.

- King, B.C., Le Bas, J.M. & Sutherland, D.S. (1972) The History of the Alkaline Volcanoes and Intrusive Complexes of Eastern Uganda and Western Kenya. J. of the Geol. Soc. 128, 173.
- King, L. C. (1950) Speculation Upon the Outline and the Mode of Disruption of Gondwanaland. Geol. Mag. 87, 353.
- Langseth, M.G. & Taylor, P.T. (1967) Recent Heat Flow Measurements in The Indian Ocean. J.G.R. 72, 6249.
- Lassare, M. (1964) Mesures d'ages Absolus sur les Series Precambriennes et Paleozoiques du Cameroun (Afrique Equatoriale). C.R. 258, 998.
- Lippard (1973) personal communication.
- Loney (1970) Ph.D. Abstract in 14th Ann. Rep. of the Res. Inst. of African Geology, Leeds.
- Ludwig, W.J., Nafe, J.E., Simpson, E.S.W. & Sacks, S. (1968) Seismic Refraction Measurements on the South East African Continental Margin. J.G.R. 73, 3707.
- Le Mouel, J., Galdeano, A. & Le Pichon, X. (1972) Remanent Magnetisation Vector Direction and the Statistical Properties of Magnetic Anomalies. Geophys. J. 30, 335.
- Le Pichon, X. & Talwani, M. (1969) Regional Gravity Anomalies in the Indian Ocean. Deep Sea Res. 16, 263.
- Macdonald, R. (1961) Explanation of the Geology of Sheet 36 (Nabilatuk). Geol. Surv. Uganda rep. 5.
- Macdonald, R. (1963) The Charnokite - Basement Complex in Northern West Nile District, Uganda, and its Relation to the Western Rift. Ph.D. Thesis, London University.
- Macgregor, A.M. (1947) An Outline of the Geological History of Southern Rhodesia. Geol. Surv. S. Rhod. Bull. 38.
- Macgregor, A.M. (1951a) Some Milestones in the Precambrian of Southern Rhodesia. Trans. Geol. Soc. of South Africa 54, 27.
- Macgregor, A.M. (1951b) A Comparison of the Geology of Northern Rhodesia (Zambia) and Southern Rhodesia and Adjoining Territories. Int. Geol. Cong. 18th.
- McCall, G.J.H. (1958) Geology of the Gwasi Area. Geol. Surv. Kenya rep. 45.
- McClure, D. (1963) Interpretation of Long Aeromagnetic Profiles. M.Sc. Thesis, University of Alberta.
- McConnell, R.B. (1951) Rift and Shield Structure in East Africa. Int. Geol. Cong. 18th.

- McEllinney, M.W. and Opdyke, N.D. (1964) The Palaeomagnetism of the Precambrian Dolerites of Eastern Southern Rhodesia, an Example of Geological Correlation by Rock Magnetism. *J.G.R.* 69, 2465.
- McGrath, P. & Hall, D.H. (1969) Crustal Structure in North Western Ontario: Regional Magnetic Anomalies. *Can. J. Earth Sci.* 6, 101.
- McKenzie, D.P. & Sclater, J.G. (1971) The Evolution of the Indian Ocean Since the Late Cretaceous. *Geophys. J.* 24, 437.
- Mestraud, J.L. (1971) The Tectonics of Central Africa, in *Tectonics of Africa*, U.N.E.S.C.O., Earth Sciences 6, Choubert, G. and Faure-Muret, A. (eds).
- Mundt, W. (1965) On the Statistics of Geomagnetic Anomalies in the Territory of the German Democratic Republic. *Geophysik* 74, 106.
- Oberholtzer, W.F. (1964) On the Tectonics of Mozambique (unpublished report).
- Old, R.A. & Rex, D.C. (1971) Rubidium and Strontium Age Determinations of Some Precambrian Granite Rocks of S.E. Uganda. *Geol. Mag.* 108, 353.
- O'Reilly, W. & Readman, P.W. (1971) The Preparation and Unmixing of Cation Deficient Titanomagnetites. *Zeit. für Geophys.* 37, 321.
- Page, B.G.N. (1961) The Stratigraphical and Structural Relationships of the Abercorn Sandstones, the Plateau Series and the Basement Rocks of the Kawimbe Area, Abercorn District, Northern Rhodesia (Zambia). 6th Ann. Rep. of the Res. Inst. of African Geology, Leeds.
- Pallister, J.W. (1971) The Tectonics of East Africa in *Tectonics of Africa*, U.N.E.S.C.O., Earth Sciences 6, Choubert, G. and Faure-Muret, A. (eds.)
- Pakiser, L.C. & Zietz, J. (1965) Transcontinental Crustal and Upper Mantle Structure. *Rev. of Geophys.* 3, 505.
- Petrascheck, W.E. Some Aspects of the Relations Between Continental Drift and Metallogenic Provinces, in *Continental Drift, Seafloor Spreading and Plate Tectonics*, Tarling, D.H. and Runcorn, S.K. (eds), Academic Press.
- Phillips, K.A. (1961) The Chinderei Mobil Belt. Ph.D. Thesis, University of Cape Town.
- Piper, J.D.A. (1972) A Palaeomagnetic Study of the Bukoban System, Tanzania. *Geophys. J.* 28, 111.

- Podmore, F. (1970) The Shape of the Great Dyke of Rhodesia as Revealed by Gravity Surveying. Geol. Soc. of South Africa Spec. Publ. 1, 610.
- Puchkova, L.I. & Ladynin, A.V. (1966) On the Relationship of Magnetic Anomalies to Crustal Structure in the South Eastern Part of Central Kazakhstan. Acad. Nauk SSSR. - U.S. Geol. Surv. Geophys. Abs. 238.
- Quennell, A.M., McKinlay, A.C.M. & Aitken, W.G. (1956) Summary of the Geology of Tanganyika pt. 1, Introduction and Stratigraphy. Geol. Surv. Tanganyika Mem. 1.
- Rabinowitz, P.D. (1971) Gravity Anomalies Across the East African Continental Margin. J.G.R. 76, 7107.
- Ray, G.E. (1971) Ph.D. Thesis Abstract, 15th Ann. Rep. of the Rest. Inst. of African Geology, Leeds.
- Reeves, C.V. (1972) Rifting in the Kalahari ? Nature 237, 94.
- Robertson, I.D.M. (1968) Granulite Metamorphism of the Basement Complex in the Limpopo Metamorphic Zone. Trans. Geol. Soc. of South Africa Annexure 71, 125.
- Robertson, I.D.M. & Van Breeman, O. (1970) The Satellite Dykes of the Great Dyke, Rhodesia. Geol. Soc. of South Africa Spec. Publ. 1, 621.
- Rothé, J.P. (1954) La Zone Zeismique Mediane Indo Atlantique. Proc. R. Soc. (Lond.) 121, 51.
- Roubault, M., Delafosse, R., Leutwein, F. & Sonet, J. (1965) Premieres Donnes Geochronologiques sur les Formations Granitiques et Crystattophylliennes de la Republique Centre Africaine. C.R. 260, 4787.
- Roy, R.F., Blackwell, D.D. & Birch, F. (1968) Heat Generation of Plutonic Rocks and Continental Heat Flow Provinces. Earth. Planet. Sci. Lett. 5, 1.
- Sanders, L.D. (1965) Geology of the Contact Between the Nyanza Shield and the Mozambique Belt in Western Kenya. Geol. Surv. Kenya Bull. 7.
- Saggerson, E.P. and Baker, B.H. (1965) Post Jurassic Erosion Surfaces in Eastern Kenya and their Deformation in Relation to Rift Structures. Quart. J. Geol. Soc. 121, 51.
- Schouten, J.A. (1971) A Fundamental Analysis of Magnetic Anomalies Over Oceanic Ridges. Mar. Geophys. Res. 1, 1.
- Schouten, J.A. & McCamey (1972) Filtering Marine Magnetic Anomalies. J.G.R. 35, 7089.

- Scrutton, R.A. & du Plessis, A. (1973) Possible Marginal Fracture Ridge South of South Africa. *Nature* 22, 1973.
- Searle, R.C. (1969) Barometric Hypsometry and a Geophysical Study of Part of the Gregory Rift Valley in Kenya. Ph.D. Thesis, University of Newcastle upon Tyne.
- Searle, R.C. (1970) Evidence from Gravity Anomalies from Thinning of the Lithosphere Beneath the Rift Valley in Kenya. *Geophys. J.* 21, 13.
- Serson, P.H. and Hannerford, W.L.W. (1957) A Statistical Analysis of Magnetic Profiles. *J.G.R.* 62, 1.
- Shackleton, R.M. (1946) Geology of the Migori Gold Belt. *Geol. Surv. Kenya Rep.* 10.
- Shackleton, R.M., Vail, J.R. & Wood, D.S. (1966) Preliminary Report on the Origin and Significance of the Urungwe Klippe, Rhodesia. 10th Ann. Rep. of the Rest. Inst. of African Geology, Leeds.
- Simpson, E.S.W. The Anorthosite of Southern Angola: A Review of Present Data, in *African Magmatism and Tectonics*, Clifford and Gass (eds), Oliver and Boyd.
- Smith, A.G. & Hallam, A. (1970) The Fit of the Southern Continents. *Nature* 223, 139.
- Snelling, N.J., Hamilton, E.I., Rex, D., Horung, G., Johnson, R.L. Slater, D. & Vail, J.R. (1964) Age Determinations from the Mozambique and Zambezi Orogenic Belts, Central Africa. *Nature* 201, 463.
- Sowerbutts (1972) Long Gravity and Magnetic Profiles over the East African Rift System and their Interpretation. Ph.D. Thesis, University of Newcastle upon Tyne.
- Spector, A. (1968) Spectral Analysis of Aeromagnetic Data. Ph.D. Thesis, University of Toronto.
- Spector, A. & Grant, F.S. (1970) Statistical Models for Interpretating Aeromagnetic Data. *Geophys.* 35, 293.
- Spooner, C.M., Hepworth, J.V. & Fairbairn, H.W. (1970) Whole Rock Rb-Sr Isotopic Investigation of Some East African Granulites. *Geol. Mag.* 107, 511.
- Stagman, J.G. (1962) The Geology of the Southern Urungwe District. *Geol. Surv. S. Rhodesia. Bull.* 55.
- Stover, C.W. (1966) Seismicity of the Indian Ocean. *J.G.R.* 71, 2575.
- Sutton, J., Watson, J. & James, T.C. (1954) A Study of the Metamorphic Rocks of Karema and Kungwe Bay, Western Tanganyika. *Geol. Surv. Tanganyika Bull.* 22.

- Talwani, M. & Heirtzler, J.R. (1964) Computation of Magnetic Anomalies Caused by Two Dimensional Structures of Any Shape, in Computers in the Mineral Industries, Parks, G.A. (ed), Stanford University.
- Talwani, M. & Eldholm, O. (1973) Boundary Between Continental and Oceanic Crust at the Margins of Rifted Continents. Nature 241, 325.
- Tarling, D.H. (1971) Gondwanaland, Palaeomagnetism and Continental Drift. Nature 229, 17.
- Tarling, D.H. (1971b) Continental Drift, Bell.
- Tarling, D.H. (1972) Another Gondwanaland, Nature 238, 92.
- Tarling, D.H. (1972b) Principles and Applications of Palaeomagnetism, Chapman and Hall.
- Tavener-Smith, R. (1960) The Karroo System and Coal Resources of the Gwembe District, South Western Section. Geol. Surv. S. Rhodesia Bull. 40.
- Thatcher, E.C. (1970) Preliminary Report on the Geology of the Nyika Area, N. Malawi. 14th Ann. Rep. of the Res. Inst. of African Geology, Leeds.
- Thompson, R. (1972) Palaeomagnetic Results from the Paganzo Basin of N.W. Argentina. Earth and Planet. Sci. Lett. 15, 145.
- Trietal, S., Clement, W.G. & Kaul, R.K. (1971) The Spectral Determination of Depths to Buried Magnetic Basement Rocks. Geophys. J. 14, 415.
- Tukey, J.W. (1961) Discussion Emphasizing the Connection Between the Analysis of Variance and Spectrum Analysis. Technometrics 3, 191.
- U.N.E.S.C.O., (1968) International Tectonic Map of Africa at 1:5,000,000.
- Vacquier, V. & Affleck, J. (1941) Computation of the Depth to the Bottom of the Earth's Magnetic Crust. Trans. Am. Geophys. Un. 446.
- Vacquier, V., Steenland, N.C., Henderson, R.G. & Zietz, I. (1951) Interpretation of Aeromagnetic Maps. Geol. Soc. Am. Mem. 47.
- Vail, J.R. (1966) Zones of Progressive Regional Metamorphism Across the Western Margin of the Mozambique Belt in Rhodesia and Mozambique. Geol. Mag. 103, 231.
- Vail, J.R. (1968) The Southern Extension of the East African Rift System and Related Igneous Activity. Geol. Rdsch. 57, 601.
- Vail, J.R. (1968b) The Significance of the Tectonic Pattern of Southern Africa. Tectonophysics 6, 403.

- Vail, J.R. (1970) Dykes and Related Irruptives in Eastern Africa, in African Magmatism and Tectonics, Clifford and Gass (eds), Oliver and Boyd.
- Vail, J.R., Snelling, N.J. & Rex, D.C. (1968) Pre-Katangan Geochronology of Zambia and Adjacent Parts of Central Africa. Can. J. Earth Sci. 5, 621.
- Vail, J.R. & Dodson, M.H. (1970) Geochronology of Rhodesia. Geol. Soc. of South Africa, Trans. and Proc. 72, 79.
- Vail, J.R. & Snelling, N.J. (1971) Isotopic Age Measurements for the Zambezi Orogenic Belt and the Urungwe Klippe, Rhodesia. Geol. Rdsch. 60, 619.
- Van Breeman, O. (1970) Geochronology of the Limpopo Belt, Southern Africa. Leeds J. of Earth Sci. 8, 57.
- Van Breeman, O., Dodson, M.H. & Vail, J.R. (1966) Isotopic Age Measurements on the Limpopo Orogenic Belt, S. Africa. Earth and Planet. Sci. Lett. 1, 401.
- Van Breeman, O. & Dodson, M.H. (1972) Metamorphic Chronology of the Limpopo Orogenic Belt. Southern Africa. Geol. Soc. of Am. Bull. 83, 2005.
- Vening Meinesz, F.A. (1948) Gravity Expeditions at Sea 1923 - 1938. Publ. Netherlands, Geodet. Comm. 4, 233.
- Vine, F.J. (1966) Spreading of the Ocean Floor, New Evidence. Science 154, 1405.
- Vine, F.J. & Matthews, D.H. (1963) Magnetic Anomalies over Oceanic Ridges. Nature 199, 947.
- Von Knorring, O. (1970) Mineralogical and Geochemical Aspects of Pegmatites from Orogenic Belts of Equatorial and Southern Africa, in African Magmatism and Tectonics, Clifford and Gass (eds), Oliver and Boyd.
- Wegener, A. (1915) Die Entstehung der Kontinente und Ozeane, Vieweg, Braunschweig.
- Welsh, P.D. (1967) The Use of the FFT for Estimation of Spectra - A Method Based on Time Averaging over Short Modified Periodograms. I.E.E.E., Trans. Audio Electroacoust., Au-15, 70.
- Williams, L.A.J. (1970) The Volcanoes of the Gregory Rift Valley, East Africa. Volcanol. 34, 439.
- Wohlenberg, J. & Bhatt, N.V. (1972) Report on an Aeromagnetic Survey of Two Areas in the Kenya Rift Valley, Tectonophysics 15, 143.

- Woolley, A.R. & Garson, M.S. (1970) Petrochemical and Tectonic Relationship of the Malawi Carbonatite-Alkaline Province and the Lupata-Lebombo Volcanics, in African Magmatism and Tectonics, Clifford and Gass (eds), Oliver and Boyd.
- Worst, B.G. (1960) The Great Dyke of Southern Rhodesia. Geol. Surv. S. Rhodesia Bull. 47.
- Wright, J.B. & McCurry, P. (1970) The Significance of Sandstone Inclusions in Lavas of the Comores Archipelago. Earth. and Planet. Sci. Lett. 8, 267.
- Zietz, I. & King, E.R. (1966) Crustal Study along the Transcontinental Great Circle from Washington D.C. to San Francisco, Calif., in Continental Margins and Island Arcs, Int. Upper Mantle Comm. Symp. Ottawa, Can. Geol. Surv. paper 66, 445.
- Zietz, I., King, E.R., Geddes, W. & Lidiak, E.G. (1966) Crustal Study of a Continental Strip from the Atlantic Ocean to the Rocky Mountains. Geol. Soc. of Am. Bull. 77, 1427.

A P P E N D I X A

An Algol computer program to linearly interpolate distance time data.

Input

- 1 initial time in hours and minutes.
- 2, 3 etc. the latitude and longitude of the beginning of each five minute interval of flight.

Output

The output is the times in hours and minutes of the equi-distant (3 km.) points.

Appendix (A) Algol Computer Program for Interpolation of Distance - Time Data

```

begin
comment to linearly interpolate between 5min navigation points
so the times for consecutive 3km position are found
input data consists of latitude longitude of all navigation
points- output is times of equidistant points;
real excessd, pi, rad, timex, latx, longx, timey, laty, longy, del, osined, dist,
vel, d, timez;
integer n, i, f1, f2, f3, hr;
open(20); open(30);
f1:=format([sddd;]); f2:=format([sdd;]);
f3:=format([nddd.dddddddc]);
excessd:=0; pi:=3.14159; rad:=6378.16;
n:=read(20); timex:=read(20)+read(20)/60;
latx:=(read(20)+read(20)/60)*pi/180;
longx:=(read(20)+read(20)/60)*pi/180;
for i:=1 step 1 until n-1 do
begin
timey:=read(20)+read(20)/60;
laty:=(read(20)+read(20)/60)*pi/180;
longy:=(read(20)+read(20)/60)*pi/180;
if longy<longx then del:= longx-longy else goto finnish;
osined:=cos(latx)*cos(laty)*cos(del) +sin(latx)*sin(laty);
dist:=rad*arctan(((1-osined**2)**0.5)/osined);
writetext(30,[dist*eq[sss]]); write(30,f3,dist);
vel:=dist*12;
d:=excessd+dist;
if d>5 then begin
d:=d-5;
timez:=timex+(5-excessd)/vel;
hr:=entier(timez);
write(30,f2,hr); writetext(30,[hr]);
write(30,f1,entier((timez-hr)*600+0.5));
writetext(30,[min[ss]]);
step1: if d>5 then begin
timez:=timez+5/vel;
d:=d-5;
hr:=entier(timez); write(30,f2,hr);
writetext(30,[hr]);
write(30,f1,entier((timez-hr)*600+0.5));
writetext(30,[min[ss]]);
goto step1
end;
end;
excessd:=d; timex:=timey; latx:=laty; longx:=longy;
end; writetext(30,[c]excessd**equals[ss]);
write(30,format([sdc],d));
finnish: close(30); close(20);
end→

```

A P P E N D I X B

Program 1

A Fortran computer program to find the thickness of magnetic bodies using the 'statistical models method' of Chapter (2). Given the average depth to the top of the bodies and the peak in the spectrum the program solves equation (25) by iteration to give the average thickness of the causative bodies.

Input

1 h, v, fac with format 3F8.4

where h = average depth to the top of the bodies.

v = the integer harmonic of the peak in the spectrum.

fac = constant to convert integer harmonic to equivalent wavelength.

Output

The output is the average thickness of the bodies, the final value of equation (25) (should be near to zero), the final value of the derivative of equation (25) and an error code message.

Program 2

A Fortran computer program to check the results of Program 1.

Input

1 h, t, fac with format 3F8.4

where h and fac are as for program 1 and t is the estimated average thickness of the bodies.

Output

The output is the values of the energy spectrum at integer harmonics.

Program 3

A Fortran computer program to :

- (i) Remove a specified linear gradient from the original profile.
- (ii) Smooth the original profile with a specified filter set.

- (iii) Calls a Fast Fourier Transform subroutine to give the set of 'raw Fourier coefficients'.
 - (iv) For the energy spectrum the 'raw Fourier coefficients' are Hanned (i.e. a $(-\frac{1}{4}, \frac{1}{4}, -\frac{1}{4})$ filter set applied).
 - (v) For the energy spectrum the values $\underline{a}^2 + \underline{b}^2$ are computed, where the \underline{a} 's and \underline{b} 's are the set of Hanned coefficients, and smoothed with either:
 - (a) a $(+\frac{1}{4}, +\frac{1}{4}, +\frac{1}{4})$ filter set (Hanning window)
 - (b) any specified symmetrical filter set.
- This is then taken as an estimate of the energy spectrum.
- (vi) Calculated the upward continued version of the profile (uses the 'raw Fourier coefficients').
 - (vii) Calculates the second vertical derivative of the profile.
 - (viii) Low pass filters the original profile by truncating the set of 'raw Fourier coefficients' and reforming.
 - (ix) Removes the effect of the average width of the body, by subtracting values computed by the expression (2) from each of the energy spectrum.
 - (x) Computes the gradient of specified parts of the spectrum by least squares fitting a straight line.
 - (xi) Plots the energy spectrum, upward continued curve, etc.

Input - Device No. 3

All the instructions to the program are fed in on this device.

1 NUMB, WORD(M) with format 15, 17A4

where NUMB = number of data points.

 WORD(M) contains useful text - for users convenience.

IK(M) (M = 1, 9), IKJ, AINT, WID, CONT, GRAD with format
912, 14, 4F8.2

where IK(M) - this defines whether or not the operations (i) to (xi) are performed. For the operation to be performed the value of IK(M) is set to 1, if not then it is set to 0.

IK(1) gives the energy spectrum. This will need to be set to 1 if any of the values of IK(2) to IK(4) are set to 1.

IK(2) gives the energy spectrum using the Hanning window.

IK(3) gives the energy spectrum with any specified symmetrical filtering.

IK(4) subtracts the width factor from the energy spectrum with the specified symmetrical filter.

IK(5) set to 1 if any of the operations defined by IK(6) to IK(9) are required.

IK(6) gives the second vertical derivative profile.

IK(7) gives the upward continued profile.

IK(8) low pass filters the original data.

IK(9) smooths the original data by convolving with a specified set of filters.

IKJ is the number of 'raw Fourier coefficients' to be retained if IK(8) is set to 1.

AINT is the interval between the given data points of the profile (in km. say).

WID is the average half - width of the deep ensemble of magnetic bodies.

CONT is the extra height to which the profile is to be continued.

GRAD is the difference in gammas between the first and last point of the linear gradient term which may be removed from the original profile. If no gradient is to be removed then set to 0.

If either IK(3) or IK(9) are set to 1 then the following will be required:

3 M with format 15

where 2M-1 is the number of filter coefficients for the smoothing of either the spectrum or the original profile respectively.

4 W(I) with format 20F4.1

where W(I) are the filter coefficients.

If IK(4) is set to 1 then the following will be required:

5 IPP, IP, IQ, WID2 with format 315, F8.2

where for a single ensemble of bodies IP and WID2 are set to 0 and IPP and IQ are the first and last harmonics in the least squares fit. For two ensembles of magnetic bodies IPP and IP-1 are the first and last harmonics in the least squares fit for the deep ensemble of magnetic bodies, IP and IQ are the first and last harmonics in the least squares fit for the shallow ensemble of magnetic bodies and WID2 is the average half - width of the shallow ensemble.

Input - Device 5

All the data is fed in on device 5 with format 10F7.1.

Output

The output consists of :

- (a) Original profile
- (b) The unsmoothed spectrum (first 200 values of NUMB/2 values which ever is less) with and without the application of the Hanning coefficients to the 'raw Fourier coefficients'.

- (c) The smoothed spectrum with the Hanning applied to the series $\underline{a}^2 + \underline{b}^2$
- (d) The smoothed spectrum which has been smoothed with the specified filter set.
- (e) The estimate of the depths of the two ensembles of magnetic bodies.
- (f) The second vertical derivative profile.
- (g) The upward continued profile.
- (h) The smoothed profile using the low pass truncation filter.

EXTERNAL FCT

C PROGRAM TO FIND VALUES OF THICKNESS OF CAUSATIVE BODIES BY ITERATION
 C INPUT
 C H IS THE DEPTH TO THE TOP OF THE BODY, V IS THE INTEGER HARMONIC AT
 C WHICH THE PEAK IN THE SPECTRUM IS TO BE FOUND, FAC IS THE CONSTANT
 C TO CONVERT INTEGER HARMONIC TO WAVELENGTH
 C OUTPUT
 C RETURNS THE THICKNESS OF THE BODY, THE VALUE OF THE EQUATION (4.2)
 C OF GREEN, A.G., (1972)-MAGNETIC PROFILE ANALYSIS, GEOPHYSICAL J. OF
 C ROY. ASTR. SOC. VOL 30, ITS DERIVATIVE AND AN ERROR CODE
 C THIS PROGRAM FIRST FINDS THE TWO VALUES ON EITHER SIDE OF THE STATIONARY
 C POINT OF EQUATION (4.2) AND THEN CALLS THE SSP SUBROUTINE RTNI
 C WHICH GIVES THE FINAL VALUE OF THE THICKNESS BY NEWTON'S
 C ITERATION SCHEME (SEE HILDEBRAND, F.B., INTRODUCTION TO NUMERICAL
 C ANALYSIS MAGRAW HILL NY. (1956))

READ(5,1)H,V,FAC
 WRITE(6,1)H,V,FAC
 COMMON H,V

1 FORMAT(3F8.4)
 V=V*8.0*ATAN(1.0E+00)
 X=FAC
 P=1.0-EXP(-2.0*X*V)
 Q=P/(4.0*X*V-(2+P)*P)
 F2=-2.0*H-1.0/V+4.0*X*Q*P
 DO 3 I=2,300
 X=FLOAT(I)*FAC
 P=1.0-EXP(-2.0*X*V)
 Q=P/(4.0*X*V-(2+P)*P)
 F1=-2.0*H-1.0/V+4.0*X*Q*P
 M=(ABS(F1)/F1)
 N=(ABS(F2)/F2)
 IF(N.EQ.M) GO TO 3
 J=I
 GO TO 4
 3 F2=F1
 WRITE(6,5)
 5 FORMAT('NO SOLUTION')
 GO TO 8

PROGRAM 1

CONFIDENTIAL

RECEIVED - 1967

THE UNIVERSITY OF CHICAGO

4 WRITE(6,6)

```
6  FORMAT('SOLUTION')
```

$$XST = X - FAC$$
$$EPS = FAC$$

```

IEND=100

```

C CALLS THE RTNI SUBROUTINE

```
CALL RTNI(X,F,DERF,FCT,XST,EPS,IEND,IER)
```

```
WRITE(6,2)X,F,DERF,IER
```

```
2  FORMAT(3E12.4,I4)
```

8 STCP

END

SUBROUTINE FCT(X,F,DERF)

C SUBROUTINE TO GIVE VALUES OF EQUATION (4.2) AND ITS DERIVATIVE

C THIS IS REQUIRED FOR THE NEWTON'S ITERATION SCHEME

COMMON H,V

$$P=1.0-\exp(-2.0 * X * V)$$
$$Q=P/(4.0*X*V-(2+P)*P)$$
$$F = -2.0 * H - 1.0 / V + 4.0 * X * Q * P$$
$$DERF=4.0*P*Q+16.0*X*V*(Q-Q*Q*P*P)$$

RETURN

END

FILE

```

      IMPLICIT REAL*8(A-H,O-Z)
C PROGRAM TO CHECK PROGRAM (1) - VALUES OF H,T(THICKNESS),FAC
C ARE FED IN AND INTEGER VALUE OF HARMONIC RETURNED
C DIMENSIONY(1000)
C READ(5,1)H,T,FAC
C IF WRITE(6,1)H,T,FAC
C J=0
4 DO 2 I=1,40
  V=DFLOAT(I)*FAC*0.8D+01*DATAN(0.1D+01)
  Y(I)=-2.0*H*V
  IF(J.EQ.0) GO TO 2
  Y(I)=Y(I)+DLOG(0.1D+01-(0.3D+01-DEXP(-2.0*T*V))*(0.1D+01
1-DEXP(-2.0*T*V)))/(4.0*T*V))
2 CONTINUE
C WRITE(6,3)(Y(JJ),JJ=1,40)
3 PD- FORMAT(10E10.3)
1 PD- FORMAT(3F8.4)
C IF(J.EQ.1) GO TO 5
C J=1
C GO TO 4
5 STOP
END

```

PROGRAM 2

FILE

```

      IMPLICIT REAL*8(A-H,O-Y)
C INPUT:AD(5,2) (ZATI(M),ZY4(M),ZD(2000))
C NUMB=1 IS THE NUMBER OF POINTS. THE ARRAY WORD MAY CONTAIN SCRIPT
C FOR DESCRIPTION PURPOSES
C IF IK(4)=1 THEN THE REQUIRED CALCULATION WILL BE PERFORMED
C 1-POWER SPECTRUM(UNMODIFIED) 2-HANNED 3-TRIANGULAR 4-AS 3-WIDTH FAC
C 5- THEN CONTINUATION OR SECOND DERIV OR LOW PASS FILTER ETC.
C 6-2ND DERIVATIVE 7-UPWARD CONTINUATION 8-CUT OFF(NO 2ND DER)
C 9-GIVES SMOOTHING OF ORIGINAL DATA BEFORE ANY OF ABOVE CALCULATIONS
C IK(4)=1 THE WIDTH FACTOR IS ALSO REMOVED
C IKJ=HARMONICS TO BE LEFT NUMB=NO OF POINTS NP=NP OF HARMONICS
C THIS IS SET IN THE PROGRAM TO BE<200. AINT=INT BETWEEN POINTS
C WID IS THE HALF-WIDTH OF THE BODIES 1, 2
C CONT IS THE VALUE TO WHICH THE DATA IS TO BE CONTINUED
C IPP=1 FIRST HARMONIC FOR LEAST SQUARES FIT(FIRST ENSEMBLE)
C IP= FIRST HARMONIC FOR LEAST SQUARES FIT(SECOND ENSEMBLE)
C FOR DOUBLE ENSEMBLE CASE LAST HARMONIC FOR FIRST ENSEMBLE IS
C TAKEN AS (IP-1); FOR SECOND ENSEMBLE LAST HARMONIC IS IQ
C AND THE HALF WIDTH FOR THIS SECOND ENSEMBLE IS WID2
C FOR A SINGLE ENSEMBLE IP=0, IQ IS THE LAST HARMONIC FOR
C LEAST SQUARES, WID2=0
C CALLS ON SUBROUTINES SMOOTH(FOR SMOOTHING DATA IN WAVENUMBER
C DOMAIN OR SPACIAL DOMAIN), LES(FINDS LEAST SQUARES FIT OF STRAIGHT
C LINE TO LINEAR PARTS OF WAVENUMBER CURVE), FFT(FAST FOURIER
C TRANSFORM(WRITTEN BY SINGLETON TO TRANSFORM MULTIVARIATE DATA
C OF ALMOST ANY NUMBER IE. DOES NOT HAVE TO BE FACTORED BY ONLY 2),
C SICI(CALCULATES SINE AND COSINE INTEGRALS-PROVIDED BY SSP ),
C ALPL(PLOTTING ROUTINE FOR NUMAC PLOTTING FACILITIES)
      DIMENSION WORD(18)
      DIMENSION DAT(2000),B1(2000),B2(2000),X(2000)
1, ZC(2000),ZATI(2000),ZY4(2000),ZD(2000),IK(20)
      READ(3,1) NUMB, (WORD(M), M=1, 17)
      WRITE(6,1) NUMB, (WORD(M), M=1, 17)
1   FORMAT(I5,17A4)
      WRITE(4,232) (DAT(M), M=1, NUMB), (B1(M), M=1, NUMB), (B2(M), M=1, NUMB),
232  FORMAT(' WRITE IN THE ARRAY VALUES OF IK UP TO 9 ETC.')
      READ(3,9) (IK(M), M=1, 9), IKJ, AINT, WID, CONT, GRAD
      WRITE(6,9) (IK(M), M=1, 9), IKJ, AINT, WID, CONT, GRAD

```

PROGRAM 3

```

191 IFORMAT(9I2,I4,4F8.2)
READ(5,2)(ZATI(M),M=1,NUMB)
WRITE(6,2)(ZATI(M),M=1,NUMB)
2 DFORMAT(10F7.1)
AS=NUMB*(1+(NP-1)*0.5)
NP=200
IF(NP.GT.NUMB/2)NP=NUMB/2
IF(IK(9).EQ.1)CALL(SMOOTH(ZATI,NUMB)
87 DO 4 K=1,NUMB
DAT(K)=ZATI(K)-DFLOAT(K)*GRAD/DFLOAT(NUMB)
B1(K)=0.0
4 CONTINUE
CALL FFT(DAT,B1,NUMB,NUMB,NUMB,-1,IERR)
10 IF(IERR.EQ.0)GOTO 88
NUMB=NUMB-1
AS=DFLOAT(NUMB)
15 GOTO 87
88 DO 30 K=1,NUMB
DAT(K)=DAT(K)/AS
102 X(K)=DAT(K)
B1(K)=B1(K)/AS
B2(K)=B1(K)*B1(K)
30 CONTINUE
WRITE(6,2)(DAT(K),K=1,NUMB)
WRITE(6,2)(B1(K),K=1,NUMB)
IF(IK(1).EQ.0)GO TO 103
DO 5 K=2,NP
ZC(K)=DABS(DAT(K)*DAT(K)+B1(K)*B1(K))*4.0
5 CONTINUE
ZC(1)=DABS(DAT(1)*DAT(1))
ZATI(1)=0.0
GO TO(101)
100 DO 6 K=1,NP,3
I=K+2
WRITE(6,7)(ZC(M),M=K,I),(ZATI(M),M=K,I),(ZD(M),M=K,I),(ZY4(M),
IM=K,I)
7 FORMAT(3F10.2,3F6.2,3F10.2,3F6.2)
6 CONTINUE
CALL ALPL(ZATI,NP,0.25)
GO TO (102,104,108,103),ICOUNT

```

```

101 ICOUNT=1.0000000000000000
C WILL NOT HAVE TO TAKE PRECAUTIONS TO TAKE LAST VALUE AS AM
C USING TRUNCATED SERIES
DO 11 K=2, NP(ZD(K))
C ZD(K)=((-B1(K-1)+2.0*B1(K)-B1(K+1))*2+(-DAT(K-1)
1+DAT(K)*2.0-DAT(K+1))*2)/4.0
5 ZD(K)=ZD(K)*8.0/3.0
ZY4(K)=ALOG(ABS(ZD(K)))
ZATI(K)=ALOG(ABS(ZC(K)))
11 CONTINUE
17 ZD(1)=(DAT(1)-DAT(2))*2
ZY4(1)=0.0
WRITE(6,10)
101 FORMAT('THESE ARE THE HANNED AND NON-HANNED COEF -HANNED TO
1 PREVENT LEAKAGE FROM INTERMEDIATE SPECTRAL ESTIMATES')
WRITE(6,15)
15 FORMAT(10X,'NON-HANNED',12X,'LOG(NON-HANNED',17X,'HANNED',16X,
1 LOG(HANNED'))
GO TO 100
102 ICOUNT=2.0000000000000000
IF(1K(2).EQ.0)GO TO 104
C WILL NOW COMPARE THE MODIFIED PERIODOGRAM WITH THE SMOOTHED VERSION
C USING AGAIN THE HANNING COEF BUT NOW AS WE HAVE A SYMMETRICAL
C FUNCTION WE USE THE +1/4 ETC
ZC(1)=(ZD(1)+ZD(2))/2.0
ZATI(1)=0.0
NP=NP-1
DO 12 K=2, NP
ZC(K)=ABS(ZD(K-1)+ZD(K)*2.0+ZD(K+1))/4.0
ZATI(K)=ALOG(ZC(K))
12 CONTINUE
WRITE(6,13)
13 FORMAT('NOW COMPARISON OF THE ONCE SMOOTHED MODIFIED PERIODOGRAM
1 WITH MODIFIED PERIODOGRAM ')
WRITE(6,16)
16 FORMAT(5X,'HAN MOD PERIODOGRAM',3X,'LOG HAN MOD PERIODOGRAM',
18X,'MOD PERIODOGRAM',8X,'LOG MOD PERIODOGRAM')
GO TO 100
104 CONTINUE
NP=NP-1

```

```

IF(IK(3).EQ.0)GO TO 108
103 CALL SMOOTH(ZD,NP)
DO(900)K=2,NP
900 ZATI(K)=ALOG(ZD(K))
C C1 AND ZATI REMAIN THE SAME AS FOR HANNING
WRITE(6,501)
501 FORMAT('NOW COMPARISON OF TRIANGULAR WINDOWED PERIODOGRAM
1 WITH (MODIFIED PERIODOGRAM)')
11 COUNT=3
WRITE(6,17)
17 FORMAT(5X,'TRIANGMOD PERIODOGRAM',3X,'LOG TRI MOD PERIODOGRAM',
18X,'MOD PERIODOGRAM',8X,'LOG MOD PERIODOGRAM')
GO TO(1000,2,4,6,8,10,12,14,16,18,20,22,24,26,28,30,32,34,36,38,40,42,44,46,48,50,52,54,56,58,60,62,64,66,68,70,72,74,76,78,80,82,84,86,88,90,92,94,96,98,100)K
108 COUNT=4
IF(IK(4).EQ.0)GO TO 103
WRITE(4,345)
345 FORMAT('WRITE IN THE VALUES OF IPP,IP,IQ,WID2')
READ(3,245)IPP,IP,IQ,WID2
245 FORMAT(3I5,F8.2)
IF(WID.LT.0.00001)GO TO 599
2432 NP=NP-1
DO(502)K=2,NP
502 IF(K.EQ.IP)WID=WID2
VV=8.0*DATAN(1.0D+00)*DFLOAT(K-1)/(AINT*AS)
XX=4.0*VV*WID
CALL SICI(SI,CI,XX)
XX=XX/2.0
VV=DSIN(XX)*DSIN(XX)/(XX*XX)
VV=-VV+(2.0*DATAN(1.0D+00)+SI)/(XX)
ZATI(K)=ALOG(ZD(K))-DLOG(VV)
502 CONTINUE
599 CONTINUE
ZATI(1)=0.0
ZA=FLOAT(NUMB-1)*AINT
IF(IP.NE.0)CALL LES(ZA,ZATI,IPP,IP-1)
IF(IP.EQ.0)IP=IPP
CALL LES(ZA,ZATI,IP,IQ)
WRITE(6,504)
504 FORMAT(' HAVE SUBTRACTED THE WIDTH FACTOR FROM TRIANGULAR
1 SMOOTHED FUNCTION')

```

```

      GO TO 100
103  K=0
      IF(IK(5).EQ.0) GO TO 41
105  CALL FFT(DAT,B1,NUMB,NUMB,NUMB,+1,IERR)
      WRITE(6,2)(DAT(M),M=1,NUMB)
      WRITE(6,2)(B1(M),M=1,NUMB)
      DO 29 JK=1,NUMB
        ZATI(JK)=DAT(JK)
29   IF(K.EQ.1.AND.(JK.LE.8.OR.JK.GT.(NUMB-8))) ZATI(JK)=0.0
      IF(K.GT.0) CALL ALPL(ZATI,NUMB,0.1)
      IF(IK(6).EQ.0.AND.K.EQ.0.AND.IK(8).EQ.0) K=1
      IF(K.EQ.2) GO TO 41
      IF(IK(7).EQ.0.AND.K.EQ.1) GO TO 41
      N=NUMB/2+1
      A=8.0*DATAN(1.0D+00)
      DAT(1)=X(1)*B1(1)
      B1(1)=B2(1)
      IF(K.EQ.0) DAT(1)=0.0
      DO 40 I=2,NUMB
        B=A*DFLOAT(I-1)/(AINT*AS)
        IF(K.EQ.1) B=DEXP(-B*CONT)
        IF(K.EQ.0) B=B*B
        IF(K.EQ.0.AND.IK(8).EQ.1.AND.I.GT.IKJ) B=0.0
        IF(K.EQ.0.AND.IK(8).EQ.1.AND.I.LE.IKJ) B=1.0
        DAT(I)=X(I)*B
        DAT(NUMB-I+2)=DAT(I)
        B1(I)=B2(I)*B
        B1(NUMB-I+2)=-B1(I)
40   CONTINUE
      K=K+1
      GO TO 105
41   CONTINUE
      STOP
      END

```

SUBROUTINE LES(ZA,Y,NP1,NP2)
 C TO FIND A LEAST SQUARES FIT OF A STRAIGHT LINE TO LINEAR PARTS
 C OF THE SPECTRUM RETURNS THE DEPTH, THE STANDARD DEVIATION OF THE
 C VALUES FROM THE DEPTH ESTIMATE AND THE INTERCEPT OF THE
 C STRAIGHT LINE WITH THE ENERGY SPECTRUM AXIS

```

1  DIMENSION Y(1)
   AN=FLOAT(NP2-NP1)+1.0
   PI=4.0*ATAN(1.0)
   SX=0.0
   SY=0.0
   SXX=0.0
   SXY=0.0
   DO 1 K=NP1,NP2
     SX=SX+FLOAT(K)
     SY=SY+Y(K)
     SXX=SXX+FLOAT(K)**2
     SXY=SXY+Y(K)*FLOAT(K)
1  CONTINUE
   A=(AN*SXY-SX*SY)/(AN*SXX-SX*SX)
   B=(SY*SXX-SX*SXY)/(AN*SXX-SX*SX)
   SDD=0.0
   DO 2 K=NP1,NP2
     DD=(A*FLOAT(K)+B-Y(K))**2
     SDD=SDD+DD
2  CONTINUE
   ALA=SQRT(SDD/(AN-2.0))*SQRT(AN/(AN*SXX-SX*SX))
   ALB=SQRT(SDD/(AN-2.0))*SQRT(SXX/(AN*SXX-SX*SX))
   A=A*ZA/(4.0*PI)
   ALA=ALA*ZA/(4.0*PI)
   WRITE(6,3)A,B,ALA,ALB
3  FORMAT(4E12.4)
   RETURN
   END
   SUBROUTINE SMOOTH(A,N)
     DIMENSION A(2000),B(2000),W(40)
C   SMOOTHS A SET OF VALUES A(N) OVER (2M-1) VALUES WITH COEF W(M)
C   WHERE THE MTH VALUE IS THE CENTRE OF THE FILTER COEF AND THE
C   SMOOTHING FUNCTION IS SYMMETRICAL
     WRITE(4,46)
46    FORMAT('WRITE IN THE NUMBER OF FILTER COEF')
     READ(3,34)M
34    FORMAT(I5)
     IF(M.EQ.0)RETURN
     WRITE(4,33)M
33    FORMAT('WRITE IN THE',I5,' FILTER COEF')

```

```

1  READ(3,1)(W(I),I=1,M)
   FORMAT(20F4.1)
   KM=M-1
   AA=0.0
   DO 2 I=1,KM
2  AA=2.0*W(I)+AA
   AA=AA+W(M)
   NM=N-KM
   DO 3 K=M,NM
   B(K)=0.0
   DO 4 KK=1,KM
4  B(K)=(A(K-KK)+A(K+KK))*W(KM-KK+1)+B(K)
   B(K)=(B(K)+A(K)*W(M))/AA
3  CONTINUE
   DO 5 K=2,KM
   B(N-K+1)=0.0
   B(K)=0.0
   C=0.0
   KKK=K-1
   DO 6 KK=1,KKK
   C=2.0*W(KM-KK+1)+C
   B(K)=B(K)+(A(K-KK)+A(K+KK))*W(KM-KK+1)
   B(N-K+1)=B(N-K+1)+(A(N-K-KK+1)+A(N-K+KK+1))*W(KM-KK+1)
6  CONTINUE
   C=C+W(M)
   B(K)=(A(K)*W(M)+B(K))/C
   B(N-K+1)=(A(N-K+1)*W(M)+B(N-K+1))/C
5  CONTINUE
   N=N-1
   DO 7 K=2,N
7  A(K)=B(K)
   N=N+1
   RETURN
   END

```

Appendix(c) List of Geological Maps Used in the Magnetic Profile -
Geology Interpretation

Map	Scale	Year of Publication
Esboco Geologico de Angola	1 : 2 x 10 ⁶	1954
Provisional Geological Map of Botswana	1 : 2 x 10 ⁶	1971
Carte Geologique du Cameroun	1 : 1 x 10 ⁶	1956
Carte Geologique du Congo Belge et du Ruanda - Urundi	1 : 2 x 10 ⁶	1951
Carte Geologique de L'Afrique Equatoriale Francaise	1 : 2 x 10 ⁶	1958
Kenya Geological Map	1 : 3 x 10 ⁶	1962
Geological Map of Malawi	1 : 1 x 10 ⁶	1966
Geological Map of Mozambique	1 : 2 x 10 ⁶	1968
Geological Map of Rhodesia	1 : 1 x 10 ⁶	1971
Geological Map of South West Africa	1 : 1 x 10 ⁶	1963
Geological Map of Tanzania	1 : 3 x 10 ⁶	1967
Geological Map of Tanganyika	1 : 2 x 10 ⁶	1959
Geological Map of Uganda	1 : 1.25 x 10 ⁶	1961
Geological Map of Uganda	1 : 1.50 x 10 ⁶	1966
Geological Map of Northern Rhodesia (Zambia)	1 : 1 x 10 ⁶	1961
Geological Map of Africa	1 : 5 x 10 ⁶	1963

P A R T I I

C H A P T E R 1

BASIC PRINCIPLES AND COMPUTATIONAL DETAILS

(1.1) Basic Principles

(1.2) Three Dimensional Analysis

(1.2.1) Ray Equations in Rectangular Coordinates

(1.2.2) Ray Equations in Spherical Coordinates

(1.2.3) Equations for Reflection and Refraction
at Velocity Discontinuities.

(1.2.4) Relative Intensity Equations (geometrical spreading)

(1.3) Two Dimensional Analysis

(1.3.1) Ray Path Equations in circular coordinates

(1.3.2) Relative Intensity Equations (geometrical spreading)

(1.3.3) Initial Values

(1.3.4) Reflection and Refraction - Energy Partitioning of
a Plane Wave Incident at a Plane Interface.

(1.4) Interpolation of the Velocity Data

(1.4.1) Spline Interpolation

(1.4.2) Spline Smoothing

(1.4.3) Spline Interpolation on a Plane

(1.5) Integration Procedure

(1.6) Computer Programs

(1.6.1) Three Dimensional Program

(1.6.2) Two Dimensional Program

(1.7) Summary

C H A P T E R I

BASIC PRINCIPLES AND COMPUTATIONAL DETAILS

(1.1) Basic Principles

Given the following assumptions:-

- (i) the displacement is infinitesimal,
- (ii) the components of strain are linear functions of the components of stress (Hooke's Law in three dimensions),
- (iii) the media is isotropic,
- (iv) the variations of the Lamé elastic parameters, λ_0 and μ_0 , in space are small relative to their magnitudes,
- (v) the body forces (e.g. gravitational) are negligible,

then the equation of the motion of a disturbance travelling through a material medium can be shown to be (see for example Bullen (1965)):

$$\rho \frac{\partial^2 u}{\partial t^2} = (\lambda_0 + 2\mu_0) \text{grad}(\text{div}(u)) - \mu_0 \text{curl}(\text{curl}(u)) \quad (1)$$

where t is the time,

ρ is the density of the medium

and u is the displacement vector (arbitrary coordinates).

Condition (i) applies if:

$$\text{div } u \gg \nabla^2 u \text{ and higher derivatives.}$$

If this condition is not applicable then finite strain theory must be invoked and this may involve violations of condition (ii). It is clear that equation (1) will not apply to the motions in the very near region of the source of the disturbance.

Operating on both sides of equation (1) with the divergence operator and substituting $e_0 = \text{div } u$ gives

$$\rho \frac{\partial^2 e_0}{\partial t^2} = (\lambda_0 + 2\mu_0) \nabla^2 e_0 \quad (2)$$

Similarly operating with the rotational operator gives

$$\rho \frac{\partial^2}{\partial t^2} (\text{curl } u) = \mu_0 \nabla^2 (\text{curl } u) \quad (3)$$

These equations (2 and 3) are both forms of the wave equation:-

$$\frac{\partial^2 \phi}{\partial t^2} = c^2 \nabla^2 \phi \quad (4)$$

where c is the propagation speed. Thus equation (2) represents the wave motion of dilatational disturbance (ϕ) with speed given by

$$\alpha = \left(\frac{\lambda_0 + 2\mu_0}{\rho} \right)^{\frac{1}{2}} \quad (5)$$

and equation (3) represents the wave motion of rotational disturbance ($\text{curl } u$) with speed given by

$$\beta = \left(\frac{\mu_0}{\rho} \right)^{\frac{1}{2}} \quad (6)$$

The dilatational disturbance approaches longitudinal motion at distance from source and is known as the P wave while the rotational disturbance approaches transverse motion and is known as the S wave.

(1.2) Three Dimensional Analysis

(1.2.1) Ray Equations in Rectangular Coordinates.

For a rectangular coordinate system (x_1, x_2, x_3) Officer (1958) demonstrates that if

$$\delta c \ll \frac{c}{\lambda} \quad (7)$$

where λ is the wavelength and δc is the fractional change of speed over a single wavelength then the time independent part of the solution of equation (4) is also a solution of the Eikonal Equation:-

$$\frac{\partial W}{\partial x_i} \frac{\partial W}{\partial x_i} = \left(\frac{c_0}{c} \right)^2 = n^2 \quad (8)$$

where c_0 is a constant reference speed, $n(x_i)$ is the corresponding refractive index of the material with speed $c(x_i)$ and W is related to the general solution of equation (4) ϕ , by

$$\phi(x_i, t) = W(x_i, t) - c_0 t \quad (9)$$

The solutions of the Eikonal equation are

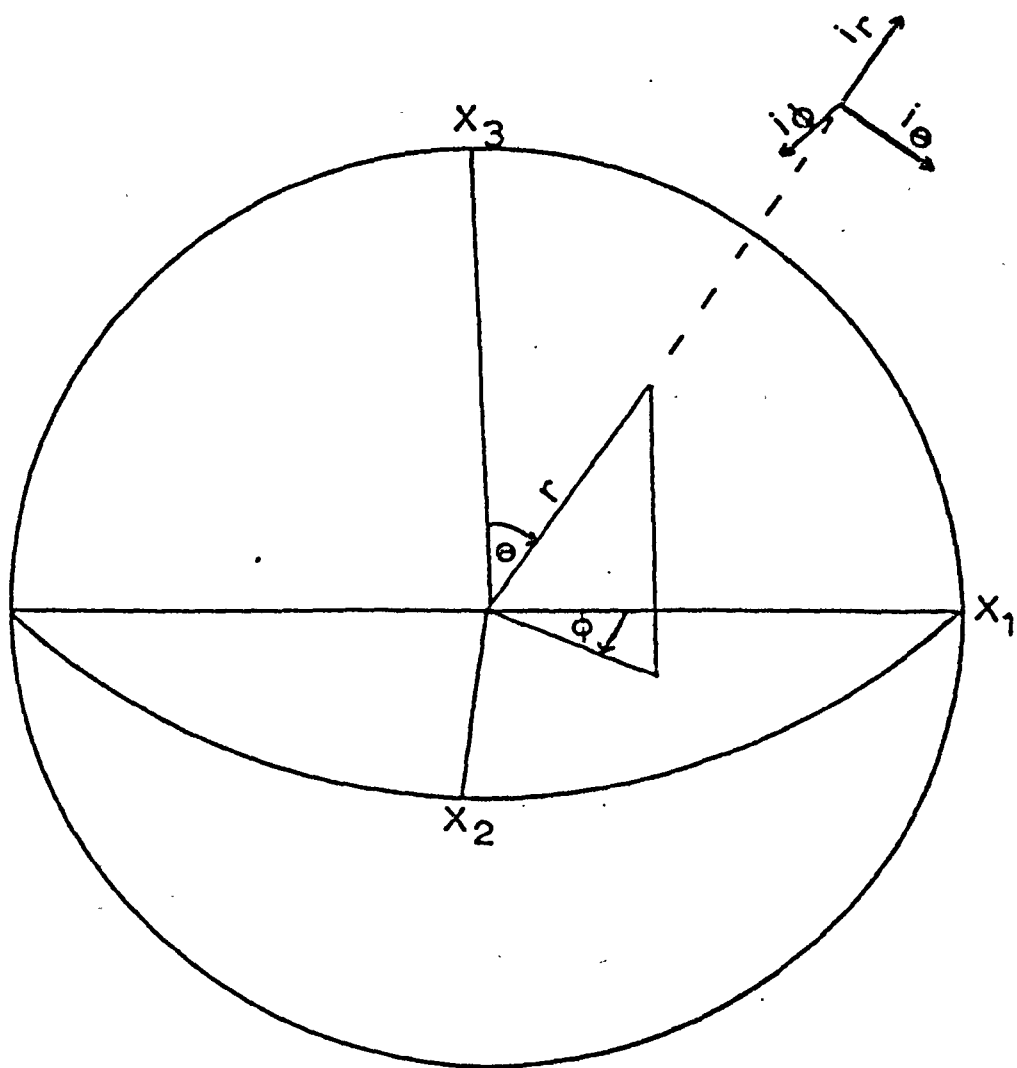
$$W(x_i) = \text{constant} \quad (10)$$

which represents surfaces in three dimensional space. For a given value of W at a given instant of time the phase of ϕ in (9) will be constant and therefore all points along the surface defined by (10) will be 'in phase.' This surface is referred to as the wave front and the normals to the surface define the direction of propagation and are called the ray paths. It is readily shown that the rays define the direction of energy propagation, so that the energy in a narrow bundle of rays is confined to that bundle throughout space (Officer (1958)). The ray solution is then a complete solution to any problem for which the Eikonal equation is a good approximation. Officer (1958) shows that the ray equations

$$\frac{d}{ds} \left(n \frac{dx_i}{ds} \right) = \frac{\partial n}{\partial x_i} \quad i = 1 \text{ to } 3 \quad (11)$$

are derivable from the Eikonal equation where ds is an element of length of the ray path. These ray equations may also be obtained in a more straightforward manner (although physically less revealing) by using either:-

- 1) Huygen's Principle which states that the disturbance at time $t + \delta t$ can be obtained by considering the effect produced on the wave surface at time t , acting as a secondary source (Officer (1958)).
- or



Fig(1)

Spherical coordinate system used in chapter (1)

2) Fermat's Principle of stationary time of travel between two points (may be either a maximum or a minimum) (Chernov (1960), Officer (1958)). Both of these routes to the final equations of the ray are shown in Officer (1958) for a rectangular coordinate system. Various authors have applied these equations to problems in acoustics (Ugincius (1965), Eliseevnin (1964), Eby (1967, 1969)).

Problems in seismology are best solved in spherical coordinates. Julian (1970) and Jacob (1970) both use Fermat's Principle to obtain the ray equations in spherical coordinates, while Wesson (1970) uses the Eikonal equation to obtain the solution in vector form (no indication of the coordinate system is given). Julian obtains five linear first order differential equations using first principles of variational calculus (Goldstein (1960), Lanzos (1949), Leech (1965)). Julian only gives the initial and final equations with one or two intermediate steps indicated, so the complete derivation of these equations is given here for the general three dimensional case. It will then be a relatively simple matter to contract these equations to those applicable to the two dimensional problem.

(1.2.2) Ray Equations in Spherical Coordinates

From the geometry of fig. (1) the following is derived (Julian (1970)):

$$\frac{1}{\cos(i_r)} \frac{dr}{dt} = c \quad (12)$$

$$\frac{r}{\cos(i_\theta)} \frac{d\theta}{dt} = c \quad (13)$$

$$\frac{r \sin(\theta)}{\cos(i_\phi)} \frac{d\phi}{dt} = c \quad (14)$$

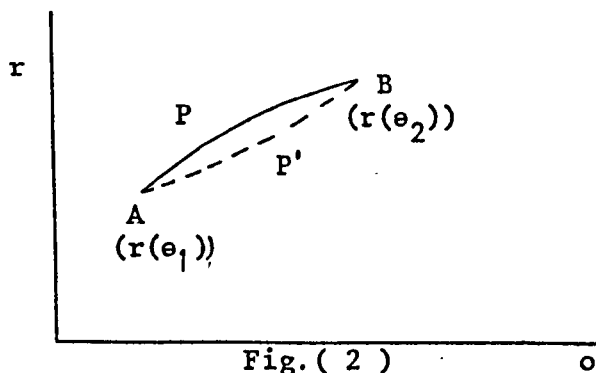
where r = radial coordinate
 θ = colatitude
 ϕ = longitude
 c = ray speed

and i_r , i_θ and i_ϕ are the base vectors which describe the direction of the ray relative to the coordinates r , θ and ϕ (fig. (1)).

Following Julian (1970) let θ be the parameter of integration for the ray path specified by $r(\theta)$ and $\phi(\theta)$. The travel time of a ray between the two points $\theta = \theta_1$ and $\theta = \theta_2$ is given by

$$T = \int_{\text{path}}^{\text{total}} \frac{ds}{c} = \int_{\theta_2}^{\theta_1} \frac{r d\theta}{c \cos(i_\theta)} \quad (15)$$

where ds is again an element of length along the ray path. Let the path APB in figure (2) be the stationary path and AP'B a small variation from it, the two end points remaining fixed.



A similar diagram applies to the variation in the ϕ direction.

The variation in travel time is then given by:

$$\delta T = \int_{\theta_2}^{\theta_1} \delta \left(\frac{r}{c \cos(i_\theta)} \right) d\theta$$

where ' δ ' is the variation of the parameters and is an operator for small variations with similar properties to the 'd' (differential)

operator. Expanding gives:

$$\begin{aligned} \delta T = & \int_{\theta_1}^{\theta_2} \frac{\delta r}{c \cos(i_\theta)} d\theta + \int_{\theta_1}^{\theta_2} \delta\left(\frac{1}{c}\right) \frac{r}{c \cos(i_\theta)} d\theta \\ & + \int_{\theta_1}^{\theta_2} \delta\left(\frac{1}{\cos(i_\theta)}\right) \frac{r}{c} d\theta \end{aligned}$$

where it must be remembered that $c = c(r, \theta, \phi)$.

$$\begin{aligned} \therefore \delta T = & \int_{\theta_1}^{\theta_2} \left[\left\{ \frac{1}{c \cos(i_\theta)} - \frac{\partial c}{\partial r} \left(\frac{r}{c^2 \cos(i_\theta)} \right) \right. \right. \\ & \left. \left. - \frac{\partial}{\partial r} \left(\frac{1}{\cos(i_\theta)} \right) \frac{r}{c} \right\} \delta r \right. \\ & \left. - \left\{ \frac{\partial c}{\partial \phi} \left(\frac{r}{c^2 \cos(i_\theta)} \right) + \frac{\partial}{\partial \phi} \left(\frac{1}{\cos(i_\theta)} \right) \frac{r}{c} \right\} \delta \phi \right] d\theta \quad (16) \end{aligned}$$

To obtain more convenient expressions for the underlined parts of (16) the following relation:

$$ds^2 = (dr^2 + r^2 d\theta^2 + r^2 \sin^2(\theta) d\phi^2)^{\frac{1}{2}}$$

gives

$$\frac{1}{r} \frac{ds}{d\theta} = \left[\frac{1}{r^2} \left(\frac{dr}{d\theta} \right)^2 + 1 + \sin^2(\theta) \left(\frac{d\phi}{d\theta} \right)^2 \right]^{\frac{1}{2}} = X^{\frac{1}{2}} \text{ say } (17)$$

Also from the geometry of the ray and coordinate system

$$\frac{1}{\cos(i_\theta)} = \frac{1}{r} \frac{ds}{d\theta} = X^{\frac{1}{2}}$$

$$\begin{aligned} \therefore \frac{\partial}{\partial r} \left(\frac{1}{\cos(i_\theta)} \right) \frac{r}{c} &= \frac{\partial}{\partial r} \left(x^{\frac{1}{2}} \right) \frac{r}{c} \\ &= x^{\frac{1}{2}} \left[- \left(\frac{\partial r}{\partial \theta} \right)^2 \frac{1}{r^3} + \frac{1}{r^2} \frac{dr}{d\theta} \frac{\partial}{\partial r} \left(\frac{dr}{d\theta} \right) \right] \frac{r}{c} \quad (18) \end{aligned}$$

Integrating the latter part of equation (18) by parts and using the condition of fixed end points gives:-

$$\begin{aligned} \int_{\theta_1}^{\theta_2} \frac{\partial}{\partial r} \left(\frac{1}{\cos(i_\theta)} \right) \frac{r}{c} \delta r d\theta &= \int_{\theta_1}^{\theta_2} \left[\left(\frac{dr}{d\theta} \right)^2 \frac{\cos(i_\theta)}{rc} \right. \\ &\quad \left. - \frac{d}{d\theta} \left(\frac{\cos(i_\theta)}{rc} \frac{dr}{d\theta} \right) \right] \delta r d\theta \quad (19) \end{aligned}$$

Following very similar arguments it can be shown that:

$$\begin{aligned} \int_{\theta_1}^{\theta_2} \frac{\partial}{\partial \phi} \left(\frac{1}{\cos(i_\theta)} \right) \frac{r}{c} \delta \phi d\theta &= \int_{\theta_1}^{\theta_2} \left[- \frac{d}{d\theta} \left(\frac{r \cos(i_\theta) \sin^2(\theta)}{c} \frac{d\phi}{d\theta} \right) \right] \delta \phi d\theta \\ &\quad (20) \end{aligned}$$

Substituting (19) and (20) into equation (16) yields the next equation given by Julian (1970):

$$\begin{aligned} \delta T &= \int_{\theta_1}^{\theta_2} \left[\left(\frac{1}{c \cos(i_\theta)} - \frac{r}{c^2 \cos(i_\theta)} \frac{\partial c}{\partial r} - \frac{\cos(i_\theta)}{c r^2} \left(\frac{dr}{d\theta} \right)^2 \right. \right. \\ &\quad \left. \left. - \frac{d}{d\theta} \left(\frac{\cos(i_\theta)}{r c} \frac{dr}{d\theta} \right) \right) \delta r + \left(\frac{-r}{c^2 \cos(i_\theta)} \frac{\partial c}{\partial \phi} - \right. \right. \\ &\quad \left. \left. \frac{d}{d\theta} \left(\frac{r \cos(i_\theta)}{c} \sin^2(\theta) \frac{d\phi}{d\theta} \right) \right) \delta \phi \right] d\theta \quad (21) \end{aligned}$$

It is important to note that $\frac{\partial c}{\partial r}$ etc. are derivatives with respect to position not derivatives along the ray.

The coordinate system is orthogonal and therefore variations along the r and ϕ directions are independent of each other. It is therefore possible to set each of the coefficients of δr and $\delta \phi$ in equation (21) equal to zero to give the required condition of stationary time of travel T .

From the δr coefficients

$$\begin{aligned} \frac{1}{c \cos(i_e)} - \frac{r}{c^2 \cos(i_e)} \left(\frac{\partial c}{\partial r} \right) - \left(\frac{dr}{d\theta} \right)^2 \frac{\cos(i_e)}{r^2 c} - \frac{d}{d\theta} \left(\frac{\cos(i_e)}{r c} \frac{dr}{d\theta} \right) \\ = 0 \end{aligned} \quad (22)$$

From equations (12) to (14)

$$\frac{dr}{d\theta} = \frac{r \cos(i_r)}{\cos(i_e)} \quad \text{and} \quad \frac{d\phi}{d\theta} = \frac{\cos(i_\phi)}{\sin(\theta) \cos(i_e)}$$

Substituting these into equation (22) gives:

$$\begin{aligned} \frac{1}{c \cos(i_e)} - \frac{r}{c^2 \cos(i_e)} \left(\frac{\partial c}{\partial r} \right) - \frac{\cos(i_e)}{c r^2} \left(\frac{r^2 \cos^2(i_r)}{\cos^2(i_e)} \right) \\ - \frac{d}{d\theta} \left(\frac{\cos(i_e)}{r c} \times \frac{r \cos(i_r)}{\cos(i_e)} \right) = 0 \end{aligned} \quad (23)$$

Taking the last term in this equation

$$\frac{d}{d\theta} \left(\frac{\cos(i_r)}{c} \right) = - \frac{di_r}{d\theta} \frac{\sin(i_r)}{c} - \frac{\cos(i_r)}{c^2} \frac{\partial c}{\partial \theta} \quad (24)$$

but

$$\begin{aligned} \frac{dc}{d\epsilon} &= \frac{\partial c}{\partial r} \frac{dr}{d\epsilon} + \frac{\partial c}{\partial \theta} + \frac{\partial c}{\partial \phi} \frac{d\phi}{d\epsilon} \\ &= \frac{\partial c}{\partial r} \frac{r \cos(i_r)}{\cos(i_e)} + \frac{\partial c}{\partial \theta} + \frac{\partial c}{\partial \phi} \frac{\cos(i_\phi)}{\sin(\epsilon) \cos(i_e)} \end{aligned} \quad (25)$$

Substituting (25) into (23) and rearranging gives:

$$\begin{aligned} \left(\frac{c}{r} - \frac{\partial c}{\partial r} \right) \sin(i_r) + \frac{\partial i_r}{\partial \theta} \cos(i_e) \frac{c}{r} + \frac{\partial c}{\partial \theta} \frac{\cot(i_r) \cos(i_e)}{r} \\ + \frac{\partial c}{\partial \phi} \left(\frac{\cot(i_r) \cos(i_\phi)}{r \sin(\epsilon)} \right) = 0 \end{aligned} \quad (26)$$

Following a similar procedure for the $\delta\phi$ coefficient yields

$$\begin{aligned} \frac{c}{r} \cos(i_e) \frac{di_\phi}{d\epsilon} + \cot(i_\phi) \cos(i_r) \left(\frac{\partial c}{\partial r} - \frac{c}{r} \right) + \frac{\cot(i_\phi) \cos(i_e)}{r} \frac{\partial c}{\partial \theta} \\ - c \cot(i_\phi) \cot(\epsilon) - \left(\frac{\sin(i_\phi)}{r \sin(\epsilon)} \right) \frac{\partial c}{\partial \phi} = 0 \end{aligned} \quad (27)$$

The total differentials of equation (26) and (27), $\frac{di_r}{d\epsilon}$ and $\frac{di_\phi}{d\epsilon}$, may be converted to differentials with respect to time, $\frac{di_r}{dt}$ and $\frac{di_\phi}{dt}$, by using equation (13). The system of equations is unique because the $\frac{di_e}{dt}$

variation can be obtained from:

$$\cos^2(i_r) + \cos^2(i_e) + \cos^2(i_\phi) = 1.$$

To obtain the final set of equations given by Julian (1970) the angle ϵ , defined as the angle between the vertical plane tangent to the ray

(the plane defined by the centre of the Earth and the ray path) and the meridional plane, is introduced. This is given by

$$\cos(e) = \frac{\cos(i_e)}{\sin(i_r)} \quad \text{or} \quad \sin(e) = \frac{\cos(i_\phi)}{\sin(i_r)} \quad (28)$$

from which the following is obtained

$$\cos(e) \frac{de}{dt} = \frac{-\sin(i_\phi)}{\sin(i_r)} \frac{di_\phi}{dt} - \frac{\cos(i_\phi) \cos(i_r)}{\sin^2(i_r)} \frac{di_r}{dt} \quad (29)$$

Therefore from equations (12) to (14) and equations (26) to (29) the final equations as given by Julian are obtained:-

$$\frac{dr}{dt} = c \cos(i_r) \quad (30)$$

$$\frac{de}{dt} = \frac{c}{r} \sin(i_r) \cos(e) \quad (31)$$

$$\frac{d\phi}{dt} = \frac{c \sin(i_r) \sin(e)}{r \sin(e)} \quad (32)$$

$$\frac{di_r}{dt} = \sin(i_r) \left(\frac{\partial c}{\partial r} - \frac{c}{r} \right) - \frac{\cos(i_r)}{r} \left[\cos(e) \frac{\partial c}{\partial e} + \frac{\sin(e)}{\sin(e)} \frac{\partial c}{\partial \phi} \right] \quad (33)$$

$$\begin{aligned} \frac{de}{dt} = & \frac{\sin(e)}{r \sin(i_r)} \frac{\partial c}{\partial e} - \frac{\cos(e)}{\sin(i_r)} \times \frac{1}{r \sin(e)} \frac{\partial c}{\partial \phi} \\ & - \frac{c}{r} \sin(i_r) \sin(e) \cot(e) \end{aligned} \quad (34)$$

To allow for reflections and refractions at finite velocity discontinuities (e.g. Moho., dipping plate boundary), harmonic solutions of the wave equation with the boundary conditions (i.e. continuity of displacement and stress) yields the familiar Snell's laws. Again this result may be obtained from Fermat's Principle of least time (Bullen (1965)). The situation is not identical to the optical equivalent because an incident longitudinal wave or an incident transverse wave

produces reflected and refracted waves of both longitudinal and transverse types. The equations which allow reflection and/or refraction of a seismic ray at a velocity discontinuity in three dimensional space were derived independently by the present author and Sorrells et. al. (1971). The derivation presented here applies Snell's Laws to the ray vector whereas Sorrells et. al. resolve the ray into a normal and a tangential component relative to the normal of the discontinuity and apply Snell's Laws to each component.

(1.2.3) Equations for Reflection and Refraction at Velocity Discontinuities.

(1.2.3.1) Planar Discontinuity

In the computer programs described later, a seismic ray is traced (step-wise time integrated) until it encounters a velocity discontinuity. Whether or not a ray has encountered a discontinuity must be defined by a 'closeness of approach criteria'.

Define some distance z say, such that if a ray comes within this distance then finite reflection or refraction occurs. To obtain the distance between the ray at position x'_1 and the plane of discontinuity assuming the ray is to continue along its presently defined path (defined by i_r , i_e , and i_ϕ) the following procedure was adopted:-

First the spherical coordinates are converted to rectangular coordinates, x'_1 , (it is easier to reflect and refract in a rectangular coordinate system than in a spherical system) with the direction of the ray now defined by:

$$\begin{aligned} B_1 &= \sin(\theta) \cos(\phi) \cos(i_r) + \cos(\theta) \cos(\phi) \cos(i_e) - \sin(\theta) \cos(i_\phi) \\ B_2 &= \sin(\theta) \sin(\phi) \cos(i_r) + \cos(\theta) \sin(\phi) \cos(i_e) + \cos(\theta) \cos(i_\phi) \\ B_3 &= \cos(\theta) \cos(i_r) - \sin(\theta) \cos(i_e) \end{aligned} \tag{35}$$

The vector defining the ray is then

$$\frac{x_2 - x_2'}{B_2} = \frac{x_1 - x_1'}{B_1} \quad \text{or} \quad x_2 = \frac{B_2}{B_1} (x_1 - x_1') + x_2' \quad (36)$$

and

$$\frac{x_3 - x_3'}{B_3} = \frac{x_1 - x_1'}{B_1} \quad \text{or} \quad x_3 = \frac{B_3}{B_1} (x_1 - x_1') + x_3' \quad (37)$$

Let

$$A_i x_i = D \quad (38)$$

define the plane of discontinuity. The coefficients A_i and D may be obtained if any three points within the plane are given. Substitution of (36) and (37) into equation (38) yields a value of x_1 which with equations (36) and (37) will give all the coordinates of the point of intersection of the vector defining the ray at the point x_1' with the plane of discontinuity. The distance the ray must travel to reach the plane is then simply given by

$$((x_1' - x_i) (x_1' - x_i))^{\frac{1}{2}}.$$

(i) Reflection Equations

Let the vectors:

A_i define the perpendicular to the plane of discontinuity

B_i define the incident ray (unit vector)

B_i' define the reflected ray (unit vector).

Snell's Laws of reflection in vector form are then:

$$B \cdot A = -B' \cdot A \quad (39)$$

$$B \wedge A = B' \wedge A \quad (40)$$

For rectangular coordinates solving (39) and (40) simultaneously gives

$$B_2' = \frac{A_1 B_2 - B_1 A_2 + B_1' A_2}{A_1}$$

$$B'_3 = \frac{A_1 B_3 - B_1 A_3 + B'_1 A_3}{A_1}$$

where B'_1 is given by

$$B'_1 = \frac{(A_2^2 + B_3^2 - A_1^2) B_1 - 2A_1 A_2 B_2 - 2A_1 A_3 B_3}{(A_1^2 + A_2^2 + A_3^2)}$$

(ii) Refraction Equations

Using the same notation as above, except that B'_i now defines the refracted ray and n the relative refractive index of the two media, Snell's Laws of refraction can be stated in a single equation in vector form

$$B \wedge A = n B' \wedge A. \quad (41)$$

That B' is a unit vector is used as the extra constraint required to give a unique solution to equation (41),

$$\text{i.e.} \quad B' \cdot B' = 1. \quad (42)$$

From (41)

$$B'_2 = \frac{1}{A_1} \left(\frac{1}{n} (A_1 B_2 - B_1 A_2) + B'_1 A_2 \right) \quad (43)$$

$$B'_3 = \frac{1}{A_1} \left(\frac{1}{n} (A_1 B_3 - B_1 A_3) + B'_1 A_3 \right) \quad (44)$$

Substituting (43) and (44) into (42) gives after considerable rearrangement

$$B'_1 = \frac{B_1}{n} - \frac{(B \cdot A) A_1}{n(B \cdot B)} \pm \frac{A_1 ((B \cdot A) - (B \cdot B) (n^2 - 1))^{\frac{1}{2}}}{n(B \cdot B)} \quad (45)$$

Consideration of the ray geometry shows that the positive root is taken when $(B \cdot A)$ is positive and the negative root is taken for $(B \cdot A)$ negative.

After reflection or refraction the vector B' is transformed to spherical coordinates using the inverse of equations (35) and the integration scheme restarted (for refraction the ray is allowed to migrate

across the plane of discontinuity, the extra travel time and distance being accounted for).

(1.2.3.2) Spherical Discontinuity

Essentially the same procedure is adopted for a spherical discontinuity as for a planar one. The distance the ray must travel to reach the spherical discontinuity is simply given by

$$\left| \frac{R - r}{\cos(i_r)} \right| \quad \text{where } R \text{ is the radius of the discontinuity}$$

and r is the radial coordinate of the ray. Reflection is simulated by reversing the angle i_r (i.e. set $i'_r = 180^\circ - i_r$). In the programs, refraction follows essentially the same course as for a planar discontinuity except that the vector A is replaced by the radial vector.

(1.2.4) Relative Intensity Equations (Geometrical Spreading).

The equations describing geometrical spreading of rays in a generally heterogeneous media were first derived for problems in acoustics and were obtained for a rectangular coordinate system (Eby and Einstein (1965), Ugincius (1968a and 1968b)). Julian (1970) was the first to derive the intensity equations for a three dimensional structure using spherical coordinates. Wesson (1970) also derives intensity equations which may be applicable to three dimensional models, but these need conversion from vectors to a practical coordinate system. The equations amount to ten extra first order partial differential equations which must be time integrated simultaneously with the ray path equations (30) to (34) to obtain the geometrical spreading effect. The time required to integrate these fifteen partial differential equations prohibits this type of analysis on the presently available computer (360/67) and therefore the intensity equations have not been incorporated in the three dimensional computer program.

(1.3) Two Dimensional Analysis

(1.3.1) Ray Path Equation

The difference between a two dimensional and a three dimensional analysis, is that in the former no velocity gradients are allowed perpendicular to the plane of the ray, i.e. any ray is constrained to remain in the plane of the source, receiver and centre of the Earth. The two dimensional ray path equations may be derived in an analagous manner to the three dimensional equations (section (1.2.2)), or they may be obtained by contracting the three dimensional equations. The contraction of equations (30) to (34) leads to only three differential equations if the plane of the ray is transferred to the 'equatorial plane'; i.e. by allowing the ray plane to be defined in spherical coordinates by either:

$$(i) \quad i_{\theta} = 90^{\circ}, \theta = 90^{\circ} \text{ and } \frac{\partial c}{\partial \theta} = 0$$

or

$$(ii) \quad i_{\phi} = 90^{\circ}, \phi = 90^{\circ} \text{ and } \frac{\partial c}{\partial \phi} = 0$$

the ray equations (30 to 34) contract to:

$$\frac{dr}{dt} = c \cos(i_r) \quad (46)$$

$$\frac{d\theta}{dt} = \frac{c}{r} \sin(i_r) \quad (47)$$

$$\frac{di_r}{dt} = \sin(i_r) \left(\frac{\partial c}{\partial r} - \frac{c}{r} \right) - \frac{\cos(i_r)}{r} \frac{\partial c}{\partial \theta} \quad (48)$$

These three first order linear differential equations allow the ray paths and various associated parameters ($dt/d\theta$ etc.) to be obtained. Within the computer program of Appendix (A) the 'equatorial' coordinates are transferred to the standard latitude and longitude of the Earth in which the source and expected receiver coordinates have been defined. Thus throughout the analysis, the geographic coordinates of the ray may be obtained.

(1.3.2) Relative Intensity Equations (Geometrical Spreading)

Most other works on relative intensities have assumed either

(i) the velocity is a function of only one variable; in seismology this is usually the radial coordinate (Jeffreys (1971), Bullen (1965), Julian and Anderson (1968), Shimshoni and Ben Menaham (1970), Chapman (1971), Wesson (1970)).

or

(ii) the velocity is a function of all three coordinates (Eby and Einstein (1965), Ugincius (1968b), Wesson (1970), Julian (1970)). Although the necessary equations have been derived for the three dimensional case no application of these equations has yet been published, presumably because of the large amount of computer time required to integrate these equations and the very difficult problem of three dimensional interpolation of the velocity data (see section (1.4) for a discussion of the sensitivity of the relative intensity estimates to the interpolation). To contract efficiently the ten differential equations given by Julian (1970), for the relative intensity of seismic rays in structures where the velocity is a function of three dimensions to a similar set of equations applicable to the two dimensional problem is difficult. Julian (1970) claims that a reduction of only two equations from the original ten is possible for the two dimensional case. By treating the problem from first principles a total reduction of seven equations is obtained, leaving only three relative intensity equations to be time integrated with the three ray path equations.

Continuing with the ray solution to the wave equation, the energy contained within a narrow ray bundle is constrained to that bundle throughout all space. The variation of the intensity (neglecting anelastic attenuation for the present discussion) is then

directly proportional to the surface area of the wavefront. Take the infinitesimal ray bundle contained within the area $dd'e'e$ shown in figure (3) at a unit distance from the source and trace the rays to some greater distance defined by the wavefront $aa'c'c$. The ratio of the intensity at this greater distance (at time T) to the value of a unit distance is given by:

$$\frac{I}{I'} = \frac{ac \times cc'}{de \times ee'} \quad (49)$$

A single plane contains the complete length of the rays $a'd'$ and $c'e'$ in exactly the same way as the equatorial plane of the coordinate system contains the rays ad and ce . The velocity structure in these two planes, both which contain the x_1 axis, are identical to each other; it is this condition which is difficult to incorporate into the three dimensional relative intensity equations for contraction to a two dimensional problem. From the geometry of fig. (3) therefore:

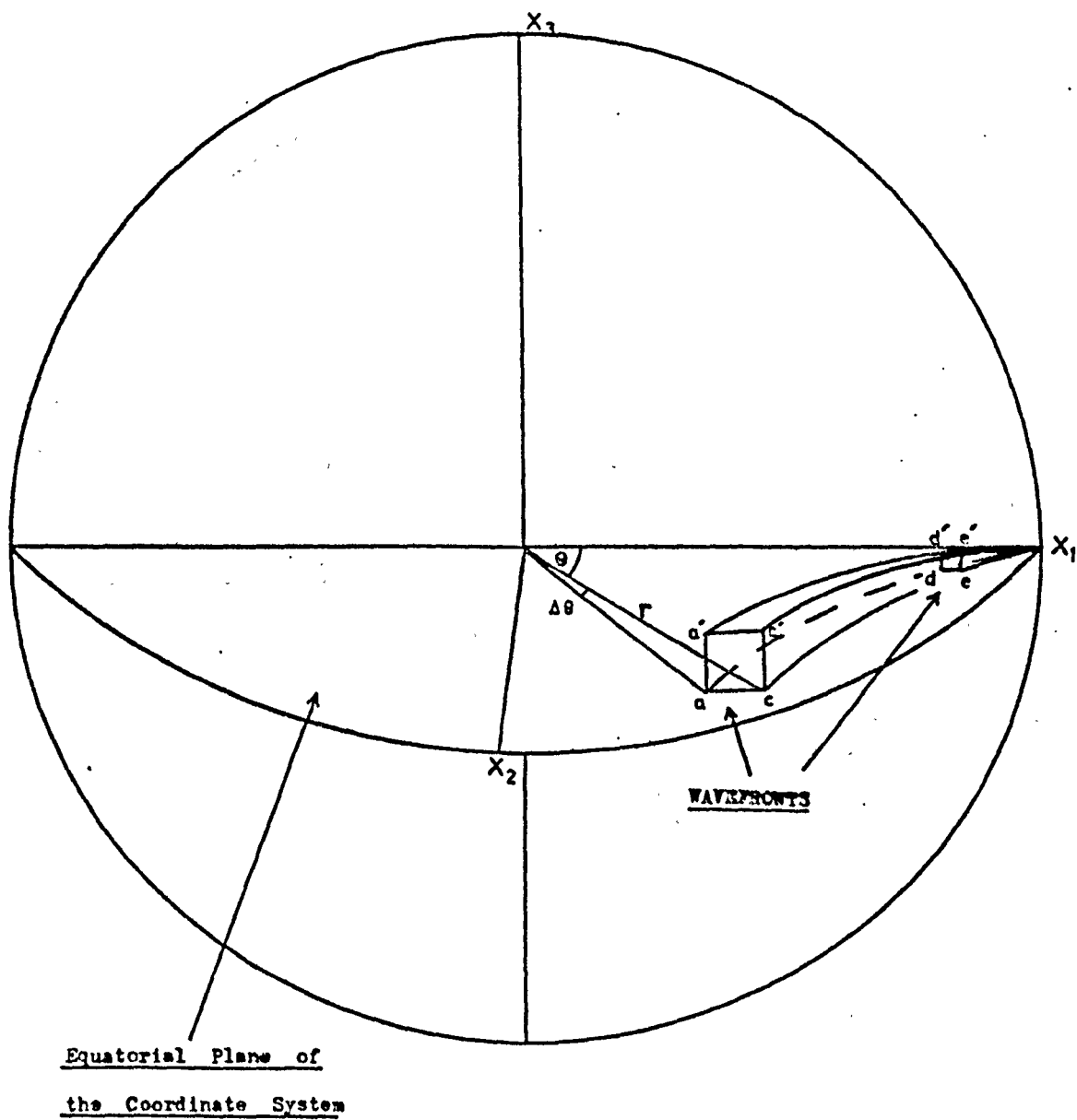
$$\frac{cc'}{ee'} = \frac{r \sin(\theta)}{(\sin(\pi - i'_r))} \quad (50)$$

where r and θ are defined in figure (3) and i'_r is the initial angle between the ray and the radial coordinate (see figure (4)).

From figure (4) which is the plan view of figure (3),

$$\begin{aligned} de &= \Delta i'_r \\ ac &= (ab^2 + bc^2)^{\frac{1}{2}} \quad (\text{for an infinitesimal wavefront}) \\ &= \left[\left(\frac{\partial r}{\partial i'_r} \right)^2 + r^2 \left(\frac{\partial \theta}{\partial i'_r} \right)^2 \right]^{\frac{1}{2}}_{t=T} \Delta i'_r \\ \therefore \frac{ac}{de} &= \left[\left(\frac{\partial r}{\partial i'_r} \right)^2 + r^2 \left(\frac{\partial \theta}{\partial i'_r} \right)^2 \right]^{\frac{1}{2}}_{t=T} \end{aligned} \quad (51)$$

Equations for $\left(\frac{\partial r}{\partial i'_r} \right)$ and $\left(\frac{\partial \theta}{\partial i'_r} \right)$ at a constant phase (i.e. on a wavefront)



Fig(3)Diagram to illustrate the geometrical spreading of seismic rays.



Fig(4) Plan view of fig(3).

may be obtained by differentiating equations (46) to (48) with respect to i_r' and interchanging the order of integration to give:

$$\frac{d}{dt} \left(\frac{\partial r}{\partial i_r'} \right) = \left(\frac{\partial c}{\partial r} \frac{\partial r}{\partial i_r'} + \frac{\partial c}{\partial \theta} \frac{\partial \theta}{\partial i_r'} \right) \cos(i_r) - c \sin(i_r) \frac{\partial i_r}{\partial i_r'} \quad (52)$$

$$\begin{aligned} \frac{d}{dt} \left(\frac{\partial \theta}{\partial i_r'} \right) &= \left(\frac{\partial c}{\partial r} \frac{\partial r}{\partial i_r'} + \frac{\partial c}{\partial \theta} \frac{\partial \theta}{\partial i_r'} \right) \frac{\sin(i_r)}{r} - \frac{c}{r^2} \sin(i_r) \frac{\partial r}{\partial i_r'} \\ &+ \frac{c}{r} \cos(i_r) \frac{\partial i_r}{\partial i_r'} \end{aligned} \quad (53)$$

$$\begin{aligned} \frac{d}{dt} \left(\frac{\partial i_r}{\partial i_r'} \right) &= \left[\frac{\partial r}{\partial i_r'} \frac{\partial^2 c}{\partial r^2} + \frac{\partial \theta}{\partial i_r'} \frac{\partial^2 c}{\partial r \partial \theta} - \right. \\ &\left. \frac{1}{r} \frac{\partial c}{\partial r} \frac{\partial r}{\partial i_r'} - \frac{1}{r} \frac{\partial c}{\partial \theta} \frac{\partial \theta}{\partial i_r'} + \frac{c}{r^2} \frac{\partial r}{\partial i_r'} \right] \sin(i_r) + \\ &\left(\frac{\partial c}{\partial r} - \frac{c}{r} \right) \cos(i_r) \frac{\partial i_r}{\partial i_r'} + \frac{\cos(i_r)}{r^2} \frac{\partial c}{\partial \theta} \frac{\partial r}{\partial i_r'} + \frac{\sin(i_r)}{r} \times \\ &\frac{\partial c}{\partial \theta} \frac{\partial i_r}{\partial i_r'} - \frac{\cos(i_r)}{r} \left[\frac{\partial r}{\partial i_r'} \frac{\partial c^2}{\partial \theta \partial r} + \frac{\partial \theta}{\partial i_r'} \frac{\partial c^2}{\partial \theta^2} \right] \end{aligned} \quad (54)$$

It is important to note that second differentials of the velocity with respect to the coordinates are now required (see section (14) for the method of interpolation). To obtain the values of $\frac{\partial r}{\partial i_r'}$ and $\frac{\partial \theta}{\partial i_r'}$

required in equation (51), the equations (46) to (48) and equations (52) to (54) must be simultaneously integrated to give the required values at constant phase.

Substituting (50) and (51) into (49) gives:

$$\frac{I}{I'} = \left[\left(\frac{\partial r}{\partial i'_r} \right)^2 + r^2 \left(\frac{\partial \theta}{\partial i'_r} \right)^2 \right]^{\frac{1}{2}} \frac{r \sin(\theta)}{\sin(\pi - i'_r)} \quad (55)$$

In conclusion the fifteen partial differential equations required for three dimensional analysis (ray path and geometrical spreading effect) have been reduced to a manageable six equations for two dimensional analysis. This is half the number given by Julian (1970).

To account for the possibility of attenuation of the ray energy due to anelastic effects a further equation of the form (see for example Julian (1970))

$$-w \int \frac{dt}{Q} \quad (56)$$

e

is required, where Q is the intrinsic quality factor (the reciprocal of the attenuation coefficient) and w is the angular frequency of the waves.

(1.3.3) Initial Values

The initial values of r , θ , and i_r are specified in the input parameters and may take any reasonable value (i.e. r must be less than or equal to the radius of the Earth). If these parameters are set to:

$$r = r' \quad (57)$$

$$\theta = \theta' \quad (58)$$

$$i_r = i'_r \quad (59)$$

then differentiating (57) to (59) with respect to i'_r yields the initial conditions:

$$\frac{\partial r}{\partial i'_r} = 0 \quad (60)$$

$$\frac{\partial e}{\partial i'_r} = 0 \quad (61)$$

$$\frac{\partial i'_r}{\partial i'_r} = 1 \quad (62)$$

(1.3.4) Reflection and Refraction - Energy Partitioning of a Plane Wave Incident at a Plane Interface.

As with the three dimensional analysis, reflection and/or refraction of the rays at velocity discontinuities are incorporated in the two dimensional analysis. The required ray path equations are essentially the same as given in section (1.2.3) with one of the coordinates set to zero. In the two dimensional scheme relative intensities are also computed and therefore the effect of energy partitioning at the velocity discontinuities must be accounted for. The general equations for the energy partitioning of a plane wave incident at a plane interface between two semi-infinite media have been given by Zoeppritz (1919); these equations are obtained by taking the simple harmonic plane wave solution of equation (1) and applying the continuity of stress and displacement conditions at the boundary. In matrix form these equations may be written as follows (Richter (1958), Singh et. al. (1970)):-

For an Incident P Wave

$$\begin{bmatrix}
 -\sin(i_a) & \cos(i_b) & -\sin(i_e) & \cos(i_f) \\
 \cos(i_a) & \sin(i_b) & -\cos(i_e) & -\sin(i_f) \\
 -\sin(2 i_a) & \frac{C_{p1}}{C_{s1}} \cos(2 i_b) & \left(\frac{C_{s2}}{C_{s1}}\right)^2 \frac{C_{p1}}{C_{p2}} \frac{\rho_2}{\rho_1} \sin(2 i_e) & -\left(\frac{C_{s2}}{C_{s1}}\right)^2 \frac{C_{p1}}{C_{s2}} \frac{\rho_2}{\rho_1} \cos(2 i_f) \\
 \cos(2 i_b) & \frac{C_{s1}}{C_{p1}} \sin(2 i_b) & \frac{C_{p2}}{C_{p1}} \frac{\rho_2}{\rho_1} \cos(2 i_f) & \frac{C_{s2}}{C_{p1}} \frac{\rho_2}{\rho_1} \sin(2 i_f)
 \end{bmatrix}
 \begin{bmatrix}
 C \\
 D \\
 E \\
 F
 \end{bmatrix}
 = A
 \begin{bmatrix}
 -\sin(i_a) \\
 -\cos(i_a) \\
 \sin(2 i_a) \\
 \cos(2 i_b)
 \end{bmatrix}
 \quad (64)$$

For an Incident S Wave

$$\begin{bmatrix}
 \cos(i_a) & \sin(i_b) & -\cos(i_e) & -\sin(i_f) \\
 \sin(i_a) & -\cos(i_b) & \sin(i_e) & -\cos(i_f) \\
 -\frac{C_{s1}}{C_{p1}} \sin(2 i_a) & \cos(2 i_b) & \frac{C_{s2}^2}{C_{s1} C_{p2}} \frac{\rho_2}{\rho_1} & -\frac{C_{s2}}{C_{s1}} \frac{\rho_2}{\rho_1} \cos(2 i_f) \\
 \frac{C_{p1}}{C_{s1}} \cos(2 i_b) & \sin(2 i_b) & \frac{C_{p2}}{C_{s2}} \frac{\rho_2}{\rho_1} \cos(2 i_f) & \frac{C_{s2}}{C_{s1}} \frac{\rho_2}{\rho_1} \sin(2 i_f)
 \end{bmatrix}
 \begin{bmatrix}
 C \\
 D \\
 E \\
 F
 \end{bmatrix}
 = A
 \begin{bmatrix}
 -\sin(i_b) \\
 -\cos(i_b) \\
 -\cos(2 i_b) \\
 \sin(2 i_b)
 \end{bmatrix}
 \quad (65)$$

where ρ_2 and ρ_1 are the densities of the upper and lower mediums (see fig. (5)) and the other symbols are defined in fig. (5) and table (1).

<u>Wave Type</u>	<u>Velocity</u>	<u>Amplitude</u>	<u>Phase</u>	<u>Angle with Normal</u>
Incident P	C_{p1}	A	$\phi(A)$	i_a
Incident SV	C_{s1}	B	$\phi(B)$	i_b
Reflected P	C_{p1}	C	$\phi(C)$	i_a
Reflected SV	C_{s1}	D	$\phi(D)$	i_b
Refracted P	C_{p2}	E	$\phi(E)$	i_e
Refracted SV	C_{s2}	F	$\phi(F)$	i_f

Table (1)

Following Singh et. al. (1970), a single arrow indicates the direction of propagation of a wave in fig. (5), while a double arrow indicates the positive direction of displacement. The expressions for the phase factors ϕ , for both real and imaginary angles i_a , i_e , and i_f may be obtained from the paper by Singh et. al. (1970). These authors give the correct expressions for the phases and point out that many previous authors have used incorrect expressions (e.g. Jeffreys in fourth edition of The Earth, McCamy et. al. (1962) and Costain et. al. (1965)).

Although equations (64) and (65) strictly apply only to plane boundaries they may also be applied to other low curvature surfaces (e.g. the 'M' discontinuity). As stated at the beginning of this section the equations were derived for two infinite media in contact; therefore for

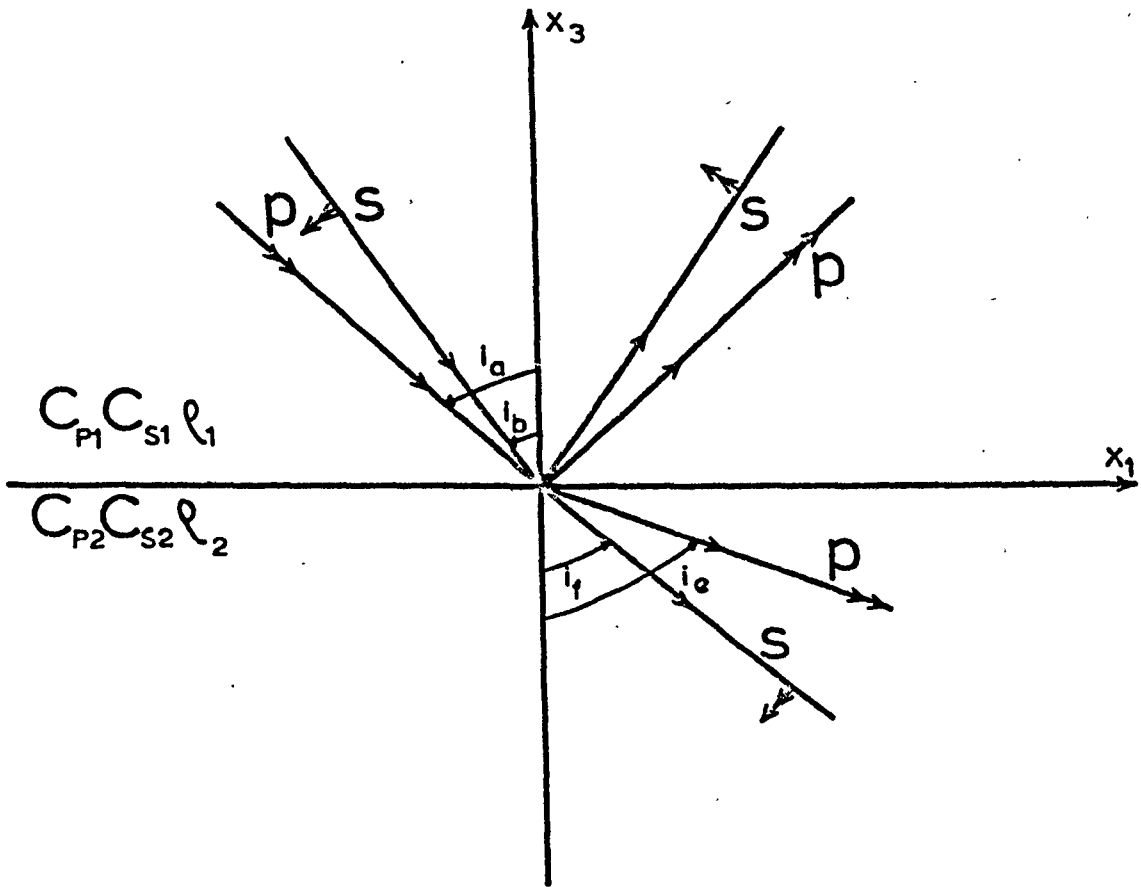


Figure (5) Convention used for reflection and refraction of a plane wave incident at a plane interface between two semi-infinite elastic solids. Single arrow indicates the direction of propagation of a wave , while a double arrow shows the positive direction of its displacement.

more than one boundary (e.g. the Conrad and 'M' discontinuities) these equations will only be fair approximations if the distance between the boundaries is greater than the wavelength of the disturbance, otherwise multiple reflections and interference phenomena will have to be included in the analysis.

The matrices (64) and (65) may easily be extended to include the situation of a linear velocity transition layer between the two media rather than a finite velocity boundary. The appropriate mathematics have been given by Gupta (1966), who shows that 8×8 matrices are required for this situation. As the thickness of the transition layer decreases to zero the solution approaches that of (64) and (65) (Gupta (1966)). In the program given in Appendix (A) only the finite velocity boundary is treated, but it would be a relatively simple proposition to include the more general situation in the program if the accuracy of the data should warrant such a refinement.

(1.4) Interpolation of the Velocity Data

To compute the ray paths and relative intensities of seismic rays it is necessary to have estimates of the velocity and the first and second derivatives of the velocity with respect to the space coordinates (see equations (46) to (48) and (52) to (54)). The velocity is defined at discrete points within a given Earth model (e.g. Gutenberg model, Jeffrey's model etc.) and it is therefore necessary to devise an interpolation procedure which will give estimates of the above quantities at any intermediate point. It will be apparent that the velocity and derivatives must be continuous across the data points (unless there is a defined discontinuity) and this requirement places strong constraints on the forms of interpolation that may be used. Landisman et. al. (1966) and Julian and Anderson (1968) when attempting to find relative amplitudes

of seismic rays travelling through an Earth model composed of spherical shells (velocity a function of radius only) used the Bullen equation,

$$v = \underline{a} r_i^{\underline{b}} \quad (63)$$

to determine the velocity throughout the i_{th} shell. The constants \underline{a} and \underline{b} are determined by the condition of continuous velocity across shell boundaries, but no restraint of continuous derivatives can be included. Discontinuous derivatives lead to amplitude (or intensity) curves with false caustics and zeros, which are only a function of the interpolation scheme used (see Landisman et. al. (1966) Julian and Anderson (1968), Shimshoni and Ben-Menahem (1970), Wesson (1970)). Wesson (1970) uses a number of polynomials of degrees two to five to represent the velocity profile and thus obtains a smoother and more realistic intensity - distance curve for the Gutenberg Earth model. The fitting of high order polynomials to long lengths of data is very time consuming on even the largest computer and to fit m pieces of data exactly would require a m_{th} degree polynomial. Wesson overcomes this problem by only fitting the data approximately and fits different polynomials to subjectively chosen lengths of data. This form of interpolation would be extremely difficult to apply to a large set of Earth models and is almost impossible to apply to Earth models for which the velocity is a function of two variables. Archambeau et. al. (1969) fit their data exactly with rational polynomials $\left(\sum_{k=0}^n a_k r^k / \sum_{k=0}^n b_k r^k \right)$ but again this is a time consuming process.

Independently, Moler and Solomon (1970), Julian (1970), Shimshoni and Ben-Menahem (1970) and Chapman (1971) advocate the use of cubic splines for the interpolation problem. Julian makes only a passing reference to the use of splines while Shimshoni and Ben-Menahem analyse the travel time tables and only deal with models of full spherical

symmetry. Chapman (1971) is again concerned with models with full spherical symmetry but now the velocity depth profile is analysed. The cubic spline algorithm advocated by Chapman (1971) is similar to that used by the present author in the early stages of the development of the ray tracing program of Appendix (A) (see section (1.4.1)).

Before proceeding it is necessary to give a description of the method of spline interpolation. The ray path and relative intensity equations derived earlier in the chapter apply to two dimensional and three dimensional structures and therefore require interpolation in two and three dimensions respectively. For reasons of clarity the procedure for interpolation in a single dimension is first described, and it is then shown how this has been adapted for interpolation on a plane. The procedure for interpolation in three dimensions then follows logically.

(1.4.1) Spline Interpolation

This form of interpolation is named after the tool used by draughtsmen to draw a continuous curve between points. Mathematically the general spline procedure involves fitting an n_{th} degree polynomial function between pairs of consecutive data points such that the function values and the first $(n-1)$ derivatives are continuous across data points. The continuity constraints plus two extra conditions to be applied to the curves which pass through the end points is sufficient to determine the polynomials exactly and uniquely. The resultant curve represented by this set of functions (usually polynomials of degree three) is unlikely to contain false oscillations between data points which are a feature of single high degree polynomial fits and the computation of the spline coefficients is an extremely rapid process. The derivation

of the formulae required to obtain the spline coefficients using polynomials of n_{th} order has been given by Anselone and Laurent (1968) using methods of functional analysis and by Woodford (1970) using a Lagrangian parameter. Woodford (1970) also gives an efficient computer program to solve this problem.

In the program used for computations in this thesis only third order polynomials have been used in the spline fit. The use of the 'cubic spline' as opposed to the n_{th} degree polynomial spline is particularly efficient both in computer time and computer space. A fourth order spline (de Boor - personal communication of fourth order spline program) was considered at one stage in the development of the ray tracing program. This would have yielded continuous third derivatives of velocity with respect to the space coordinates and thus smoother second derivatives would be obtained. It was soon realised that the standard velocity models of the Earth were insufficiently defined to warrant such refinement. Even Herrin's (1968) velocity - depth profile, which is quoted to four decimal places is not 'smooth' when viewed in the second derivative domain (see figure (6)).

If the data is defined at the points (x_j, y_j) $j = 1, m$ and x_j is monotonically increasing (the case for confluent abscissae has not yet been treated, but Reinsh (1967) claims that it can be solved) then the value of y at the position x where $x_i < x < x_{i+1}$ is given by:-

$$y = D_i(x-x_i)^3 + C_i(x-x_i)^2 + B_i(x-x_i) + y_i \quad (64)$$

where B_i , C_i , and D_i are the cubic spline coefficients. With m pieces of information there must only be m independent variables so that the $3(m-1)$ spline coefficients are interrelated. The relationship between

the coefficients may be obtained by twice differentiating (64) and inserting the conditions of continuity of the data and first and second derivatives. This leads to $(m-2)$ equations in the m unknowns (Pennington (1965), see also the extensive reference list on the use of splines given by Schultz and Varga (1967)). The two extra conditions which must be specified in order to determine these quantities completely is usually given in the form of some restraints on the cubics which pass through the first and last points. Either a zero second derivative or a continuous third derivative (i.e. a linearly extrapolated second derivative from succeeding or preceding points) is assumed for the curves at the end points.

The m unknowns can be obtained from the final m equations by any of the standard matrix inversion schemes. The inversion is particularly simple since only three of the unknowns appear in each equation. A computer program which calculates the spline coefficients was obtained from M. Richards of the Scripps Institute of Oceanography (1971) and used in the initial stages of the development of the ray tracing program. This spline procedure used the condition of zero second derivative at the end points. A second program was written using the algorithm given by Pennington (1965) which allows a continuous third derivative at the end points (this is the same algorithm as that used by Chapman (1971)). The present author's version is considerably more efficient in computer time and space than that given by Pennington. As expected the two algorithms (continuous third derivative and zero second derivative algorithms) produce identical results except at the end points. Both algorithms were tested by interpolating between function values of an exponential and a sine curve and comparing the function values and the exact first and second

derivatives at intermediate points with those obtained by spline interpolation. With only ten points defining a complete sine cycle the interpolated values were accurate to at least the first four decimal places.

The results of the spline interpolation when compared to the exact function values are extremely good and give confidence to the general applicability of this scheme. Since the spline interpolation procedure was introduced into the Newcastle School of Physics it has found application to a large number of data sets with a good deal of success on even the most variable data.

(1.4.2) Spline Smoothing

The values of the exponential and sine function quoted above were read into the computer with an accuracy of 16 decimal places, the maximum accuracy of the computer. If instead, the function values are rounded to n decimal places (four say) then it has been shown (Reinsh (1967), Woodford (1970)) that improved estimates of the function and derivatives may be obtained if certain smoothing conditions are applied to the input data. The smoothing required depends on the accuracy of the data and the number of data points used. Using the same notation as for the spline interpolation (here on cubic splines applied to unsmoothed data will be termed interpolation splines while those applied to data which are smoothed will be termed smoothing splines) we wish to find function $g(x)$ such that the following function of its second derivative is minimised:-

$$\sum_{x_1}^{x_m} \left(\frac{\partial^2 g(x)}{\partial x^2} \right)^2 dx \quad (65)$$

subject to the constraint

$$\sum_{i=1}^m \frac{g(x_i) - y_i}{\delta y_i} \leq s \quad (66)$$

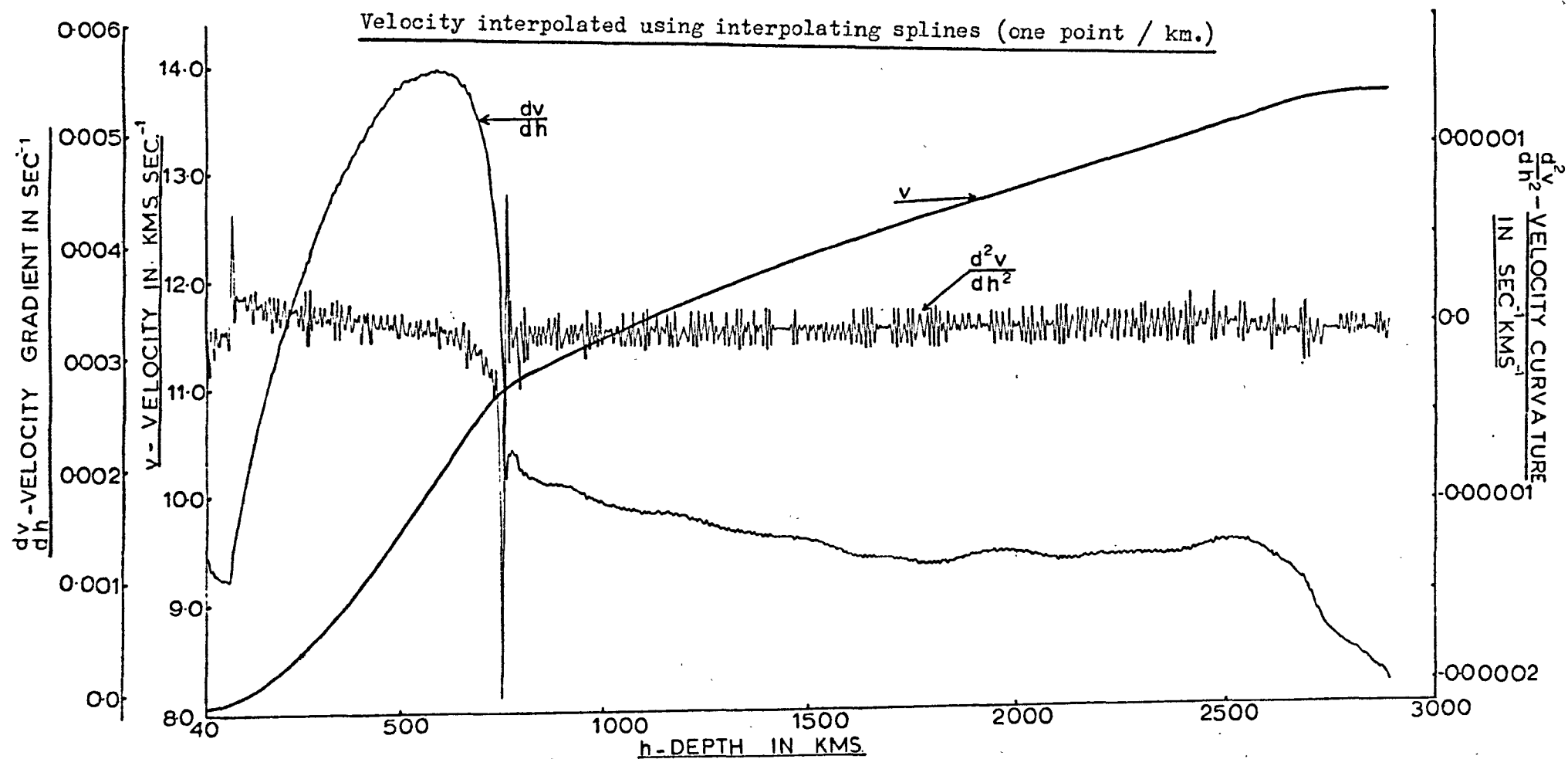
where $\delta y_i > 0$ ($i = 1$ to m) and $S \geq 0$. The quantities δy_i control the amount of smoothing to be applied to each point and ideally should be an estimate of the standard deviation of the ordinates y_i (some other estimate of the accuracy of the data will often do). If the standard deviation is used then the value of S (a quantity which may be used to escalate the overall smoothing) should be set to the number of data points (Reinsh (1967)). Equations (65) and (66) may be solved by the standard method of the calculus of variations if Lagrange's method of combining these conditions is applied. Reinsh (1967) has shown that solutions to these equations may be cubic splines. Effectively we have adjusted or smoothed the data to obey the conditions (65) and (66) and fitted a cubic spline to the resulting data. It is important to note that if S is set to zero then the data remains unchanged and the process that follows is the same as for spline interpolation.

Table (2) shows the results of representing the data set obtained from $\sin(x)$ where $x = 0^\circ(1^\circ)180^\circ$ rounded to four decimal places (from Reinsh (1967)). In the table the mean square errors are shown which have been obtained from comparison with the true values for the function and the first three derivatives from (i) difference quotients, (ii) spline interpolation, (iii) spline smoothing. It is clear that the smoothing spline produces superior results by one and two orders of magnitude for the first and second derivatives respectively. The improvement in the estimate of the third derivative is particularly impressive.

For the problem at hand the smoothing spline is again found to be superior to the interpolating spline. Figures (6) and (7) show the results of interpolating Herrin's (1968) velocity depth curve with

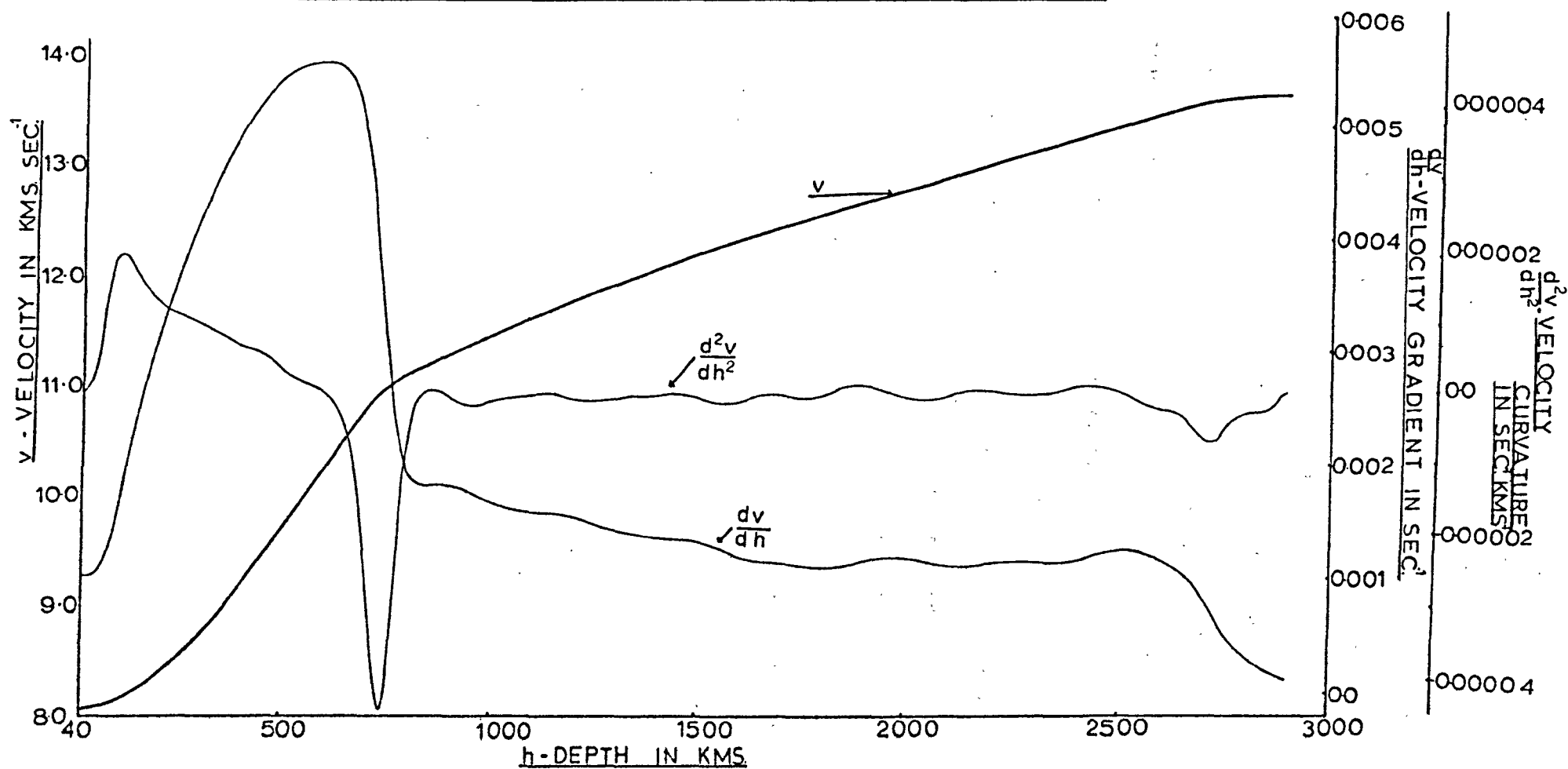
Order of Differentiation	Difference Quotients (interpolation)	Cubic Spline S = 0 (interpolation)	Cubic Spline S = 180 (smoothing)
0	3.0×10^{-5}	3.0×10^{-5}	1.3×10^{-5}
1	2.6×10^{-3}	3.4×10^{-3}	0.21×10^{-3}
2	0.26	0.67	0.42×10^{-3}
3	28	74	0.16

Table (2) Mean square error of numerical derivatives of $\sin(x)$ computed by difference quotients, cubic spline interpolation and cubic spline smoothing.



Fig(6) Velocity and first and second derivatives of velocity with respect to depth for the Herrin(1968) Earth model.

Velocity interpolated using smoothing splines (one point / km.)



Fig(7) Velocity and first and second derivatives of velocity with respect to depth for the Herrin (1968)

Earth model.

interpolating and smoothing splines respectively. In both sets of curves the velocity data is given at 5km. intervals and the velocity and first and second derivatives interpolated at 1km. intervals. Cubic polynomials represent the velocity data, quadratics represent the first derivative and straight lines the second derivatives. In figure (6) the interpolating splines give smooth curves for both the velocity and first derivative curves, although the latter contains a large number of small ripples. These ripples are 'magnified' in the second derivative curve which is very erratic, almost random. The erratic nature of this latter curve and the ripples in the first derivative curve are almost entirely due to the small variations in the data which are observed in the third and fourth decimal places. Figure (7) shows the result of smoothing the velocity - depth profile with a value of $\delta y_i = 0.001$ (for all i). The velocity values ($\sim 10\text{km./sec.}$) are altered by a maximum of 0.008 km./sec. with the vast majority of data points (over 70%) being altered by $0(0.0001)$. With this very small change of the data, which is well within the accuracy quoted, the resultant first and second derivative curves show quite dramatic changes. The ripples have now disappeared from the former curve to leave only the longer wavelength more 'significant' oscillations. The second derivative curve shown in figure (7) is still composed of straight lines but is now observed to be extremely smooth (the third derivative is now slowly changing). It must be pointed out that the scale of the second derivative curve of figure (7) is approximately one half that of figure (6).

The results of applying equations ((46) to (48)) to the problem of ray tracing is not affected to the accuracy of 0.01 sec. when the interpolating and smoothing splines are used. It is in the

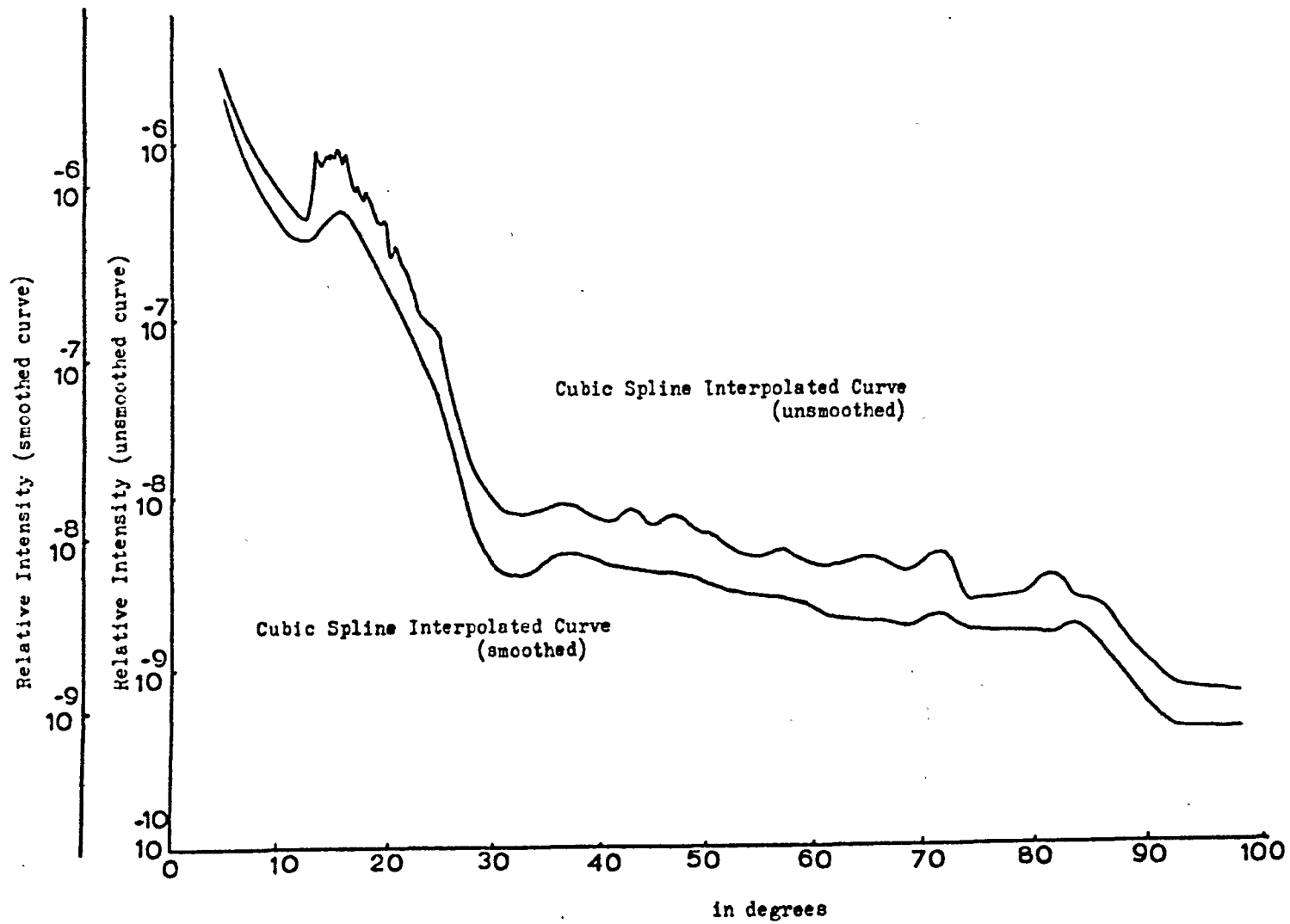
amplitude equations (52 to 54) where the superiority of smoothing splines is clearly seen. The relative intensity curves (geometrical spreading effect) obtained from the velocity and derivative curves of figures (6) and (7) are shown in figure (8) for comparison. The small ripples in the first derivative and the erratic nature of the second derivative curve of figure (6) are the cause of the erratic 'humps' of the corresponding relative intensity curve of figure (8). In the relative intensity curve obtained from the smoothed spline profile of figure (7) most of these erratic 'humps' have disappeared. The remaining humps may be significant (see chapter (2)).

Finally it is worth pointing out that the smoothing splines have the very great advantage of being an objective method of curve fitting. The only subjectivity that might arise is if an estimate of the standard deviation is not available ; a subjective estimate of the smoothing must then be chosen. Other spline procedures (e.g. Powell (1970)) also yield smooth second derivatives but the number of data points retained is dependent on the variability of the data; it is more convenient in the present problem to retain all the data points

Reinsh's procedure is extremely flexible and may be a superior alternative to fitting subjectively chosen polynomials to give data sets. Only if the data is expected on physical grounds to obey polynomial law is the latter method recommended.

(1.4.3) Spline Interpolation on a Plane

De Boor (1962) has given the necessary equations for spline interpolation on a plane (bi-cubic interpolation) and Bhattacharyya (1969) has written a computer program to find the spline coefficients. This program was tested with a function defined by sine curves in the x and y directions and found to require a prohibitive amount of computer time



Figure(8) Relative Intensity Curve of the Herrin Earth Model for smoothed and unsmoothed velocity profiles.

and space (16 coefficients are required to define each point on the plane). A more efficient (in computer time and space) quasi bi-cubic spline procedure was devised by the present author using the uni-cubic spline as the basic interpolating element. If the data set is defined at the points (x_i, y_i) ($i = 1$ to m , $j = 1$ to n) with values at each point given by $z(x_i, y_i)$ and estimates of all the first and second derivatives are required, then the uni-cubic spline is used to interpolate $z(x_i, y_i)$ in the y direction to give:

$$z(x_i, y), \quad \frac{\partial z(x_i, y)}{\partial y}, \quad \frac{\partial^2 z(x_i, y)}{\partial y^2} \quad (i = 1 \text{ to } m)$$

then interpolate the values $z(x_i, y)$ in the x direction to give:

$$z(x, y), \quad \frac{\partial z(x, y)}{\partial x}, \quad \frac{\partial^2 z(x, y)}{\partial x^2}$$

and the values $\frac{\partial z(x_i, y)}{\partial y}$ and $\frac{\partial^2 z(x_i, y)}{\partial y^2}$ in the x direction to give:

$$\frac{\partial z(x, y)}{\partial y}, \quad \frac{\partial^2 z(x, y)}{\partial y \partial x}, \quad \frac{\partial^2 z(x, y)}{\partial y^2} .$$

Thus by progressive use of the very efficient uni-cubic spline it is possible to obtain all the information required to time integrate equations (46) to (48) and (52) to (54). To check the routine, data were interpolated over a surface on which discrete values of the function defined by sine waves in the x and y directions were given. The results of representing a half cycle defined by 10 points in each direction (i.e. a total of 100 points) and interpolating the values of z and the various derivatives is shown in table (3). All the values are obtained with extremely satisfactory accuracy when compared with the

VALUES OF A SIN(X)*SIN(Y) SURFACE INTERPOLATED COMPARED TO TRUE VALUE

Table (3)

Y= 25.0 DEGREES X= 25.0 DEGREES							INTERPOLATED TRUE VALUES	VALUES
Z	DZ/DX	DZ2/DX2	DZ/DY	DZ2/DY2	DZ2/DXDY			
0.1786D 00	0.3830D 00	-0.1784D 00	0.3830D 00	-0.1784D 00	0.8214D 00			
0.1786D 00	0.3830D 00	-0.1786D 00	0.3830D 00	-0.1786D 00	0.8214D 00			
Y= 25.0 DEGREES X= 45.0 DEGREES							INTERPOLATED TRUE VALUES	VALUES
Z	DZ/DX	DZ2/DX2	DZ/DY	DZ2/DY2	DZ2/DXDY			
0.2988D 00	0.2988D 00	-0.2985D 00	0.6409D 00	-0.2985D 00	0.6409D 00			
0.2988D 00	0.2988D 00	-0.2988D 00	0.6409D 00	-0.2988D 00	0.6409D 00			
Y= 25.0 DEGREES X= 65.0 DEGREES							INTERPOLATED TRUE VALUES	VALUES
Z	DZ/DX	DZ2/DX2	DZ/DY	DZ2/DY2	DZ2/DXDY			
0.3830D 00	0.1786D 00	-0.3825D 00	0.8214D 00	-0.3825D 00	0.3830D 00			
0.3830D 00	0.1786D 00	-0.3830D 00	0.8214D 00	-0.3830D 00	0.3830D 00			
Y= 25.0 DEGREES X= 85.0 DEGREES							INTERPOLATED TRUE VALUES	VALUES
Z	DZ/DX	DZ2/DX2	DZ/DY	DZ2/DY2	DZ2/DXDY			
0.4210D 00	0.3683D-01	-0.4205D 00	0.9029D 00	-0.4205D 00	0.7899D-01			
0.4210D 00	0.3683D-01	-0.4210D 00	0.9029D 00	-0.4210D 00	0.7899D-01			
Y= 25.0 DEGREES X=105.0 DEGREES							INTERPOLATED TRUE VALUES	VALUES
Z	DZ/DX	DZ2/DX2	DZ/DY	DZ2/DY2	DZ2/DXDY			
0.4082D 00	-0.1094D 00	-0.4077D 00	0.8754D 00	-0.4077D 00	-0.2346D 00			
0.4082D 00	-0.1094D 00	-0.4082D 00	0.8754D 00	-0.4082D 00	-0.2346D 00			
Y= 25.0 DEGREES X=125.0 DEGREES							INTERPOLATED TRUE VALUES	VALUES
Z	DZ/DX	DZ2/DX2	DZ/DY	DZ2/DY2	DZ2/DXDY			
0.3462D 00	-0.2424D 00	-0.3457D 00	0.7424D 00	-0.3457D 00	-0.5198D 00			
0.3462D 00	-0.2424D 00	-0.3462D 00	0.7424D 00	-0.3462D 00	-0.5198D 00			
Y= 25.0 DEGREES X=145.0 DEGREES							INTERPOLATED TRUE VALUES	VALUES
Z	DZ/DX	DZ2/DX2	DZ/DY	DZ2/DY2	DZ2/DXDY			
0.2424D 00	-0.3462D 00	-0.2421D 00	0.5198D 00	-0.2421D 00	-0.7424D 00			
0.2424D 00	-0.3462D 00	-0.2424D 00	0.5198D 00	-0.2424D 00	-0.7424D 00			
Y= 25.0 DEGREES X=165.0 DEGREES							INTERPOLATED TRUE VALUES	VALUES
Z	DZ/DX	DZ2/DX2	DZ/DY	DZ2/DY2	DZ2/DXDY			
0.1094D 00	-0.4082D 00	-0.1092D 00	0.2346D 00	-0.1092D 00	-0.8754D 00			
0.1094D 00	-0.4082D 00	-0.1094D 00	0.2346D 00	-0.1094D 00	-0.8754D 00			

VALUES OF A SIN(X)*SIN(Y) SURFACE INTERPOLATED COMPARED TO TRUE VALUE

Y= 45.0 DEGREES X= 25.0 DEGREES

Z	DZ/DX	DZ2/DX2	DZ/DY	DZ2/DY2	DZ2/DXDY
0.2988D 00	0.6409D 00	-0.2985D 00	0.2988D 00	-0.2985D 00	0.6409D 00
0.2988D 00	0.6409D 00	-0.2988D 00	0.2988D 00	-0.2988D 00	0.6409D 00

INTERPOLATED VALUES
TRUE VALUES

Y= 45.0 DEGREES X= 45.0 DEGREES

Z	DZ/DX	DZ2/DX2	DZ/DY	DZ2/DY2	DZ2/DXDY
0.5000D 00	0.5000D 00	-0.4994D 00	0.5000D 00	-0.4994D 00	0.5000D 00
0.5000D 00	0.5000D 00	-0.5000D 00	0.5000D 00	-0.5000D 00	0.5000D 00

INTERPOLATED VALUES
TRUE VALUES

Y= 45.0 DEGREES X= 65.0 DEGREES

Z	DZ/DX	DZ2/DX2	DZ/DY	DZ2/DY2	DZ2/DXDY
0.6409D 00	0.2988D 00	-0.6400D 00	0.6409D 00	-0.6400D 00	0.2988D 00
0.6409D 00	0.2988D 00	-0.6409D 00	0.6409D 00	-0.6409D 00	0.2988D 00

INTERPOLATED VALUES
TRUE VALUES

Y= 45.0 DEGREES X= 85.0 DEGREES

Z	DZ/DX	DZ2/DX2	DZ/DY	DZ2/DY2	DZ2/DXDY
0.7044D 00	0.6163D-01	-0.7035D 00	0.7044D 00	-0.7035D 00	0.6163D-01
0.7044D 00	0.6163D-01	-0.7044D 00	0.7044D 00	-0.7044D 00	0.6163D-01

INTERPOLATED VALUES
TRUE VALUES

Y= 45.0 DEGREES X=105.0 DEGREES

Z	DZ/DX	DZ2/DX2	DZ/DY	DZ2/DY2	DZ2/DXDY
0.6830D 00	-0.1830D 00	-0.6821D 00	0.6830D 00	-0.6821D 00	-0.1830D 00
0.6830D 00	-0.1830D 00	-0.6830D 00	0.6830D 00	-0.6830D 00	-0.1830D 00

INTERPOLATED VALUES
TRUE VALUES

Y= 45.0 DEGREES X=125.0 DEGREES

Z	DZ/DX	DZ2/DX2	DZ/DY	DZ2/DY2	DZ2/DXDY
0.5792D 00	-0.4056D 00	-0.5785D 00	0.5792D 00	-0.5785D 00	-0.4056D 00
0.5792D 00	-0.4056D 00	-0.5792D 00	0.5792D 00	-0.5792D 00	-0.4056D 00

INTERPOLATED VALUES
TRUE VALUES

Y= 45.0 DEGREES X=145.0 DEGREES

Z	DZ/DX	DZ2/DX2	DZ/DY	DZ2/DY2	DZ2/DXDY
0.4056D 00	-0.5792D 00	-0.4051D 00	0.4056D 00	-0.4051D 00	-0.5792D 00
0.4056D 00	-0.5792D 00	-0.4056D 00	0.4056D 00	-0.4056D 00	-0.5792D 00

INTERPOLATED VALUES
TRUE VALUES

Y= 45.0 DEGREES X=165.0 DEGREES

Z	DZ/DX	DZ2/DX2	DZ/DY	DZ2/DY2	DZ2/DXDY
0.1830D 00	-0.6830D 00	-0.1828D 00	0.1830D 00	-0.1828D 00	-0.6830D 00
0.1830D 00	-0.6830D 00	-0.1830D 00	0.1830D 00	-0.1830D 00	-0.6830D 00

INTERPOLATED VALUES
TRUE VALUES

VALUES OF A SIN(X)*SIN(Y) SURFACE INTERPOLATED COMPARED TO TRUE VALUE

Y= 65.0 DEGREES X= 25.0 DEGREES

Z	DZ/DX	DZ2/DX2	DZ/DY	DZ2/DY2	DZ2/DXDY
0.3830D 00	0.8214D 00	-0.3825D 00	0.1786D -00	-0.3825D 00	0.3830D -00
0.3830D 00	0.8214D 00	-0.3830D 00	0.1786D -00	-0.3830D 00	0.3830D -00

INTERPOLATED VALUES
TRUE VALUES

Y= 65.0 DEGREES X= 45.0 DEGREES

Z	DZ/DX	DZ2/DX2	DZ/DY	DZ2/DY2	DZ2/DXDY
0.6409D 00	0.6409D 00	-0.6400D 00	0.2988D 00	-0.6400D 00	0.2988D 00
0.6409D 00	0.6409D 00	-0.6409D 00	0.2988D -00	-0.6409D 00	0.2988D -00

INTERPOLATED VALUES
TRUE VALUES

Y= 65.0 DEGREES X= 65.0 DEGREES

Z	DZ/DX	DZ2/DX2	DZ/DY	DZ2/DY2	DZ2/DXDY
0.8214D 00	0.3830D 00	-0.8203D 00	0.3830D -00	-0.8203D 00	0.1786D -00
0.8214D 00	0.3830D 00	-0.8214D 00	0.3830D -00	-0.8214D 00	0.1786D -00

INTERPOLATED VALUES
TRUE VALUES

Y= 65.0 DEGREES X= 85.0 DEGREES

Z	DZ/DX	DZ2/DX2	DZ/DY	DZ2/DY2	DZ2/DXDY
0.9029D 00	0.7899D -01	-0.9017D 00	0.4210D -00	-0.9017D 00	0.3683D -01
0.9029D 00	0.7899D -01	-0.9029D 00	0.4210D -00	-0.9029D 00	0.3683D -01

INTERPOLATED VALUES
TRUE VALUES

Y= 65.0 DEGREES X=105.0 DEGREES

Z	DZ/DX	DZ2/DX2	DZ/DY	DZ2/DY2	DZ2/DXDY
0.8754D 00	-0.2346D 00	-0.8743D 00	0.4082D -00	-0.8743D 00	-0.1094D -00
0.8754D 00	-0.2346D 00	-0.8754D 00	0.4082D -00	-0.8754D 00	-0.1094D -00

INTERPOLATED VALUES
TRUE VALUES

Y= 65.0 DEGREES X=125.0 DEGREES

Z	DZ/DX	DZ2/DX2	DZ/DY	DZ2/DY2	DZ2/DXDY
0.7424D 00	-0.5198D 00	-0.7415D 00	0.3462D -00	-0.7415D 00	-0.2424D 00
0.7424D 00	-0.5198D 00	-0.7424D 00	0.3462D -00	-0.7424D 00	-0.2424D -00

INTERPOLATED VALUES
TRUE VALUES

Y= 65.0 DEGREES X=145.0 DEGREES

Z	DZ/DX	DZ2/DX2	DZ/DY	DZ2/DY2	DZ2/DXDY
0.5198D 00	-0.7424D 00	-0.5192D 00	0.2424D -00	-0.5192D 00	-0.3462D -00
0.5198D 00	-0.7424D 00	-0.5198D 00	0.2424D -00	-0.5198D 00	-0.3462D 00

INTERPOLATED VALUES
TRUE VALUES

Y= 65.0 DEGREES X=165.0 DEGREES

Z	DZ/DX	DZ2/DX2	DZ/DY	DZ2/DY2	DZ2/DXDY
0.2346D 00	-0.8754D 00	-0.2343D 00	0.1094D -00	-0.2343D 00	-0.4082D 00
0.2346D 00	-0.8754D 00	-0.2346D 00	0.1094D -00	-0.2346D 00	-0.4082D 00

INTERPOLATED VALUES
TRUE VALUES

VALUES OF A SIN(X)*SIN(Y) SURFACE INTERPOLATED COMPARED TO TRUE VALUE

Y=185.0 DEGREES X= 25.0 DEGREES

Z	DZ/DX	DZ2/DX2	DZ/DY	DZ2/DY2	DZ2/DXDY
0.4210D 00	0.9029D 00	-0.4205D 00	0.3683D-01	-0.4205D 00	0.7899D-01
0.4210D 00	0.9029D 00	-0.4210D 00	0.3683D-01	-0.4210D 00	0.7899D-01

INTERPOLATED VALUES
TRUE VALUES

Y=185.0 DEGREES X= 45.0 DEGREES

Z	DZ/DX	DZ2/DX2	DZ/DY	DZ2/DY2	DZ2/DXDY
0.7044D 00	0.7044D 00	-0.7035D 00	0.6163D-01	-0.7035D 00	0.6163D-01
0.7044D 00	0.7044D 00	-0.7044D 00	0.6163D-01	-0.7044D 00	0.6163D-01

INTERPOLATED VALUES
TRUE VALUES

Y=185.0 DEGREES X= 65.0 DEGREES

Z	DZ/DX	DZ2/DX2	DZ/DY	DZ2/DY2	DZ2/DXDY
0.9029D 00	0.4210D 00	-0.9017D 00	0.7899D-01	-0.9017D 00	0.3683D-01
0.9029D 00	0.4210D 00	-0.9029D 00	0.7899D-01	-0.9029D 00	0.3683D-01

INTERPOLATED VALUES
TRUE VALUES

Y=185.0 DEGREES X= 85.0 DEGREES

Z	DZ/DX	DZ2/DX2	DZ/DY	DZ2/DY2	DZ2/DXDY
0.9924D 00	0.8682D-01	-0.9911D 00	0.8682D-01	-0.9911D 00	0.7596D-02
0.9924D 00	0.8682D-01	-0.9924D 00	0.8682D-01	-0.9924D 00	0.7596D-02

INTERPOLATED VALUES
TRUE VALUES

Y=185.0 DEGREES X=105.0 DEGREES

Z	DZ/DX	DZ2/DX2	DZ/DY	DZ2/DY2	DZ2/DXDY
0.9622D 00	-0.2578D 00	-0.9610D 00	0.8419D-01	-0.9610D 00	-0.2256D-01
0.9623D 00	-0.2578D 00	-0.9623D 00	0.8419D-01	-0.9623D 00	-0.2256D-01

INTERPOLATED VALUES
TRUE VALUES

Y=185.0 DEGREES X=125.0 DEGREES

Z	DZ/DX	DZ2/DX2	DZ/DY	DZ2/DY2	DZ2/DXDY
0.8160D 00	-0.5714D 00	-0.8150D 00	0.7139D-01	-0.8150D 00	-0.4999D-01
0.8160D 00	-0.5714D 00	-0.8160D 00	0.7139D-01	-0.8160D 00	-0.4999D-01

INTERPOLATED VALUES
TRUE VALUES

Y=185.0 DEGREES X=145.0 DEGREES

Z	DZ/DX	DZ2/DX2	DZ/DY	DZ2/DY2	DZ2/DXDY
0.5714D 00	-0.8160D 00	-0.5707D 00	0.4999D-01	-0.5707D 00	-0.7139D-01
0.5714D 00	-0.8160D 00	-0.5714D 00	0.4999D-01	-0.5714D 00	-0.7139D-01

INTERPOLATED VALUES
TRUE VALUES

Y=185.0 DEGREES X=165.0 DEGREES

Z	DZ/DX	DZ2/DX2	DZ/DY	DZ2/DY2	DZ2/DXDY
0.2578D 00	-0.9622D 00	-0.2575D 00	0.2256D-01	-0.2575D 00	-0.8419D-01
0.2578D 00	-0.9623D 00	-0.2578D 00	0.2256D-01	-0.2578D 00	-0.8419D-01

INTERPOLATED VALUES
TRUE VALUES

VALUES OF A SIN(X)*SIN(Y) SURFACE INTERPOLATED COMPARED TO TRUE VALUE

Y=105.0 DEGREES X= 25.0 DEGREES

Z	DZ/DX	DZ2/DX2	DZ/DY	DZ2/DY2	DZ2/DXDY
0.4082D 00	0.8754D 00	-0.4077D 00	-0.1094D 00	-0.4077D 00	-0.2346D 00
0.4082D 00	0.8754D 00	-0.4082D 00	-0.1094D 00	-0.4082D 00	-0.2346D 00

INTERPOLATED VALUES
TRUE VALUES

Y=105.0 DEGREES X= 45.0 DEGREES

Z	DZ/DX	DZ2/DX2	DZ/DY	DZ2/DY2	DZ2/DXDY
0.6830D 00	0.6830D 00	-0.6821D 00	-0.1830D 00	-0.6821D 00	-0.1830D 00
0.6830D 00	0.6830D 00	-0.6830D 00	-0.1830D 00	-0.6830D 00	-0.1830D 00

INTERPOLATED VALUES
TRUE VALUES

Y=105.0 DEGREES X= 65.0 DEGREES

Z	DZ/DX	DZ2/DX2	DZ/DY	DZ2/DY2	DZ2/DXDY
0.8754D 00	0.4082D 00	-0.8743D 00	-0.2346D 00	-0.8743D 00	-0.1094D 00
0.8754D 00	0.4082D 00	-0.8754D 00	-0.2346D 00	-0.8754D 00	-0.1094D 00

INTERPOLATED VALUES
TRUE VALUES

Y=105.0 DEGREES X= 85.0 DEGREES

Z	DZ/DX	DZ2/DX2	DZ/DY	DZ2/DY2	DZ2/DXDY
0.9622D 00	0.8419D-01	-0.9610D 00	-0.2578D 00	-0.9610D 00	-0.2256D-01
0.9623D 00	0.8419D-01	-0.9623D 00	-0.2578D 00	-0.9623D 00	-0.2256D-01

INTERPOLATED VALUES
TRUE VALUES

Y=105.0 DEGREES X=105.0 DEGREES

Z	DZ/DX	DZ2/DX2	DZ/DY	DZ2/DY2	DZ2/DXDY
0.9330D 00	-0.2500D 00	-0.9318D 00	-0.2500D 00	-0.9318D 00	0.6699D-01
0.9330D 00	-0.2500D 00	-0.9330D 00	-0.2500D 00	-0.9330D 00	0.6699D-01

INTERPOLATED VALUES
TRUE VALUES

Y=105.0 DEGREES X=125.0 DEGREES

Z	DZ/DX	DZ2/DX2	DZ/DY	DZ2/DY2	DZ2/DXDY
0.7912D 00	-0.5540D 00	-0.7902D 00	-0.2120D 00	-0.7902D 00	0.1485D 00
0.7912D 00	-0.5540D 00	-0.7912D 00	-0.2120D 00	-0.7912D 00	0.1485D 00

INTERPOLATED VALUES
TRUE VALUES

Y=105.0 DEGREES X=145.0 DEGREES

Z	DZ/DX	DZ2/DX2	DZ/DY	DZ2/DY2	DZ2/DXDY
0.5540D 00	-0.7912D 00	-0.5533D 00	-0.1485D 00	-0.5533D 00	0.2120D 00
0.5540D 00	-0.7912D 00	-0.5540D 00	-0.1485D 00	-0.5540D 00	0.2120D 00

INTERPOLATED VALUES
TRUE VALUES

Y=105.0 DEGREES X=165.0 DEGREES

Z	DZ/DX	DZ2/DX2	DZ/DY	DZ2/DY2	DZ2/DXDY
0.2500D 00	-0.9330D 00	-0.2497D 00	-0.6699D-01	-0.2497D 00	0.2500D 00
0.2500D 00	-0.9330D 00	-0.2500D 00	-0.6699D-01	-0.2500D 00	0.2500D 00

INTERPOLATED VALUES
TRUE VALUES

VALUES OF A SIN(X)*SIN(Y) SURFACE INTERPOLATED COMPARED TO TRUE VALUE

Y=125.0 DEGREES X= 25.0 DEGREES

Z	DZ/DX	DZ2/DX2	DZ/DY	DZ2/DY2	DZ2/DXDY
0.3462D 00	0.7424D 00	-0.3457D 00	-0.2424D 00	-0.3457D 00	-0.5198D 00
0.3462D 00	0.7424D 00	-0.3462D 00	-0.2424D 00	-0.3462D 00	-0.5198D 00

INTERPOLATED VALUES
TRUE VALUES

Y=125.0 DEGREES X= 45.0 DEGREES

Z	DZ/DX	DZ2/DX2	DZ/DY	DZ2/DY2	DZ2/DXDY
0.5792D 00	0.5792D 00	-0.5785D 00	-0.4056D 00	-0.5785D 00	-0.4056D 00
0.5792D 00	0.5792D 00	-0.5792D 00	-0.4056D 00	-0.5792D 00	-0.4056D 00

INTERPOLATED VALUES
TRUE VALUES

Y=125.0 DEGREES X= 65.0 DEGREES

Z	DZ/DX	DZ2/DX2	DZ/DY	DZ2/DY2	DZ2/DXDY
0.7424D 00	0.3462D 00	-0.7415D 00	-0.5198D 00	-0.7415D 00	-0.2424D 00
0.7424D 00	0.3462D 00	-0.7424D 00	-0.5198D 00	-0.7424D 00	-0.2424D 00

INTERPOLATED VALUES
TRUE VALUES

Y=125.0 DEGREES X= 85.0 DEGREES

Z	DZ/DX	DZ2/DX2	DZ/DY	DZ2/DY2	DZ2/DXDY
0.8160D 00	0.7139D-01	-0.8150D 00	-0.5714D 00	-0.8150D 00	-0.4999D-01
0.8160D 00	0.7139D-01	-0.8160D 00	-0.5714D 00	-0.8160D 00	-0.4999D-01

INTERPOLATED VALUES
TRUE VALUES

Y=125.0 DEGREES X=105.0 DEGREES

Z	DZ/DX	DZ2/DX2	DZ/DY	DZ2/DY2	DZ2/DXDY
0.7912D 00	-0.2120D 00	-0.7902D 00	-0.5540D 00	-0.7902D 00	0.1485D 00
0.7912D 00	-0.2120D 00	-0.7912D 00	-0.5540D 00	-0.7912D 00	0.1485D 00

INTERPOLATED VALUES
TRUE VALUES

Y=125.0 DEGREES X=125.0 DEGREES

Z	DZ/DX	DZ2/DX2	DZ/DY	DZ2/DY2	DZ2/DXDY
0.6710D 00	-0.4698D 00	-0.6702D 00	-0.4698D 00	-0.6702D 00	0.3290D 00
0.6710D 00	-0.4698D 00	-0.6710D 00	-0.4698D 00	-0.6710D 00	0.3290D 00

INTERPOLATED VALUES
TRUE VALUES

Y=125.0 DEGREES X=145.0 DEGREES

Z	DZ/DX	DZ2/DX2	DZ/DY	DZ2/DY2	DZ2/DXDY
0.4698D 00	-0.6710D 00	-0.4692D 00	-0.3290D 00	-0.4692D 00	0.4698D 00
0.4698D 00	-0.6710D 00	-0.4698D 00	-0.3290D 00	-0.4698D 00	0.4698D 00

INTERPOLATED VALUES
TRUE VALUES

Y=125.0 DEGREES X=165.0 DEGREES

Z	DZ/DX	DZ2/DX2	DZ/DY	DZ2/DY2	DZ2/DXDY
0.2120D 00	-0.7912D 00	-0.2117D 00	-0.1485D 00	-0.2117D 00	0.5540D 00
0.2120D 00	-0.7912D 00	-0.2120D 00	-0.1485D 00	-0.2120D 00	0.5540D 00

INTERPOLATED VALUES
TRUE VALUES

VALUES OF A SIN(X)*SIN(Y) SURFACE INTERPOLATED COMPARED TO TRUE VALUE

Y=145.0 DEGREES X= 25.0 DEGREES

	DZ/DX	DZ/DY	DZ2/DX2	DZ2/DY2	DZ2/DXDY
INTERPOLATED	0.2424D 00	0.5198D 00	-0.2421D 00	-0.3462D 00	-0.2421D 00
TRUE VALUES	0.2424D 00	0.5198D 00	-0.2424D 00	-0.3462D 00	-0.2424D 00

Y=145.0 DEGREES X= 45.0 DEGREES

	DZ/DX	DZ/DY	DZ2/DX2	DZ2/DY2	DZ2/DXDY
INTERPOLATED	0.4056D 00	0.4056D 00	-0.4051D 00	-0.5792D 00	-0.4051D 00
TRUE VALUES	0.4056D 00	0.4056D 00	-0.4056D 00	-0.5792D 00	-0.4056D 00

Y=145.0 DEGREES X= 65.0 DEGREES

	DZ/DX	DZ/DY	DZ2/DX2	DZ2/DY2	DZ2/DXDY
INTERPOLATED	0.5198D 00	0.2424D 00	-0.5192D 00	-0.7424D 00	-0.5192D 00
TRUE VALUES	0.5198D 00	0.2424D 00	-0.5198D 00	-0.7424D 00	-0.5198D 00

Y=145.0 DEGREES X= 85.0 DEGREES

	DZ/DX	DZ/DY	DZ2/DX2	DZ2/DY2	DZ2/DXDY
INTERPOLATED	0.5714D 00	0.4999D 01	-0.5707D 00	-0.8160D 00	-0.5707D 00
TRUE VALUES	0.5714D 00	0.4999D 01	-0.5714D 00	-0.8160D 00	-0.5714D 00

Y=145.0 DEGREES X= 105.0 DEGREES

	DZ/DX	DZ/DY	DZ2/DX2	DZ2/DY2	DZ2/DXDY
INTERPOLATED	0.5540D 00	-0.1485D 00	-0.5533D 00	-0.7912D 00	-0.5533D 00
TRUE VALUES	0.5540D 00	-0.1485D 00	-0.5540D 00	-0.7912D 00	-0.5540D 00

Y=145.0 DEGREES X= 125.0 DEGREES

	DZ/DX	DZ/DY	DZ2/DX2	DZ2/DY2	DZ2/DXDY
INTERPOLATED	0.4698D 00	-0.3290D 00	-0.4692D 00	-0.6710D 00	-0.4692D 00
TRUE VALUES	0.4698D 00	-0.3290D 00	-0.4698D 00	-0.6710D 00	-0.4698D 00

Y=145.0 DEGREES X= 145.0 DEGREES

	DZ/DX	DZ/DY	DZ2/DX2	DZ2/DY2	DZ2/DXDY
INTERPOLATED	0.3290D 00	-0.4698D 00	-0.3286D 00	-0.4698D 00	-0.3286D 00
TRUE VALUES	0.3290D 00	-0.4698D 00	-0.3290D 00	-0.4698D 00	-0.3290D 00

Y=145.0 DEGREES X= 165.0 DEGREES

	DZ/DX	DZ/DY	DZ2/DX2	DZ2/DY2	DZ2/DXDY
INTERPOLATED	0.1485D 00	-0.5540D 00	-0.1483D 00	-0.2120D 00	-0.1483D 00
TRUE VALUES	0.1485D 00	-0.5540D 00	-0.1485D 00	-0.2120D 00	-0.1485D 00

INTERPOLATED
TRUE VALUES

INTERPOLATED
TRUE VALUES

INTERPOLATED
TRUE VALUES

INTERPOLATED
TRUE VALUES

INTERPOLATED
TRUE VALUES

INTERPOLATED
TRUE VALUES

INTERPOLATED
TRUE VALUES

INTERPOLATED
TRUE VALUES

VALUES OF A SIN(X)*SIN(Y) SURFACE INTERPOLATED COMPARED TO TRUE VALUE

Y=165.0 DEGREES X= 25.0 DEGREES

Z	DZ/DX	DZ2/DX2	DZ/DY	DZ2/DY2	DZ2/DXDY
0.1094D 00	0.2346D 00	-0.1092D 00	-0.4082D 00	-0.1092D 00	-0.8754D 00
0.1094D 00	0.2346D 00	-0.1094D 00	-0.4082D 00	-0.1094D 00	-0.8754D 00

INTERPOLATED VALUES
TRUE VALUES

Y=165.0 DEGREES X= 45.0 DEGREES

Z	DZ/DX	DZ2/DX2	DZ/DY	DZ2/DY2	DZ2/DXDY
0.1830D 00	0.1830D 00	-0.1828D 00	-0.6830D 00	-0.1828D 00	-0.6830D 00
0.1830D 00	0.1830D 00	-0.1830D 00	-0.6830D 00	-0.1830D 00	-0.6830D 00

INTERPOLATED VALUES
TRUE VALUES

Y=165.0 DEGREES X= 65.0 DEGREES

Z	DZ/DX	DZ2/DX2	DZ/DY	DZ2/DY2	DZ2/DXDY
0.2346D 00	0.1094D 00	-0.2343D 00	-0.8754D 00	-0.2343D 00	-0.4082D 00
0.2346D 00	0.1094D 00	-0.2346D 00	-0.8754D 00	-0.2346D 00	-0.4082D 00

INTERPOLATED VALUES
TRUE VALUES

Y=165.0 DEGREES X= 85.0 DEGREES

Z	DZ/DX	DZ2/DX2	DZ/DY	DZ2/DY2	DZ2/DXDY
0.2578D 00	0.2256D-01	-0.2575D 00	-0.9622D 00	-0.2575D 00	-0.8419D-01
0.2578D 00	0.2256D-01	-0.2578D 00	-0.9623D 00	-0.2578D 00	-0.8419D-01

INTERPOLATED VALUES
TRUE VALUES

Y=165.0 DEGREES X=105.0 DEGREES

Z	DZ/DX	DZ2/DX2	DZ/DY	DZ2/DY2	DZ2/DXDY
0.2500D 00	-0.6699D-01	-0.2497D 00	-0.9330D 00	-0.2497D 00	0.2500D 00
0.2500D 00	-0.6699D-01	-0.2500D 00	-0.9330D 00	-0.2500D 00	0.2500D 00

INTERPOLATED VALUES
TRUE VALUES

Y=165.0 DEGREES X=125.0 DEGREES

Z	DZ/DX	DZ2/DX2	DZ/DY	DZ2/DY2	DZ2/DXDY
0.2120D 00	-0.1485D 00	-0.2117D 00	-0.7912D 00	-0.2117D 00	0.5540D 00
0.2120D 00	-0.1485D 00	-0.2120D 00	-0.7912D 00	-0.2120D 00	0.5540D 00

INTERPOLATED VALUES
TRUE VALUES

Y=165.0 DEGREES X=145.0 DEGREES

Z	DZ/DX	DZ2/DX2	DZ/DY	DZ2/DY2	DZ2/DXDY
0.1485D 00	-0.2120D 00	-0.1483D 00	-0.5540D 00	-0.1483D 00	0.7912D 00
0.1485D 00	-0.2120D 00	-0.1485D 00	-0.5540D 00	-0.1485D 00	0.7912D 00

INTERPOLATED VALUES
TRUE VALUES

Y=165.0 DEGREES X=165.0 DEGREES

Z	DZ/DX	DZ2/DX2	DZ/DY	DZ2/DY2	DZ2/DXDY
0.6699D-01	-0.2500D 00	-0.6690D-01	-0.2500D 00	-0.6690D-01	0.9330D 00
0.6699D-01	-0.2500D 00	-0.6699D-01	-0.2500D 00	-0.6699D-01	0.9330D 00

INTERPOLATED VALUES
TRUE VALUESSTOP 0
EXECUTION TERMINATED

known function values and derivatives. This form of interpolation is easily extended to three dimensions and was successfully used in the three dimensional program written by the author.

For consistency, smoothing splines are applied in the radial direction while interpolating splines ($S = 0.0$) are used for interpolation in the transverse direction. In the program given in Appendix (A) all the spline coefficients for interpolation in the radial direction are computed near to the beginning of the program and stored. It is at this stage that the velocity profile for each set of data along a single radial vector is smoothed (no smoothing is needed if relative intensities are not required). The amount of smoothing in any part of the data may be controlled by assigning different estimates of δy_i to that region; thus the smoothing is governed by the confidence of the data.

The decision to interpolate along all the radial vectors and store the coefficients was taken so that time on the computer would be conserved, but this of course means that more space is used in the computer. Throughout the development of the ray tracing programs the 'trade off' between time and space on the computer was found to require important consideration.

(1.5) Integration Procedure

Integration methods of initial value differential equations are well known (see for example Ralston and Wilf (1960)) and therefore this topic will only be discussed briefly. There are a large number of numerical schemes available which might be used to integrate equations (46) to (48) and (52) to (54). The Hamming-Milne Predictor Corrector method of step-wise integration was chosen for the following reasons:-

1) It is accurate to the fourth order of differentiation and thus accurate to $O(h^5)$ (if a function is represented by a Taylor series then the accuracy of computation is governed by the number of terms of the series retained. So that if terms upto $\frac{h^n \partial^n y(x_0)}{n! \partial x^n}$ are retained then the accuracy is $O(h^{n+1})$).

2) The method is stable i.e. given a suitable step size the integration converges to a solution.

3) Only two estimates of the right hand side of the given differential equations are required for each step and thus the method is computationally rapid. This point is particularly important for large systems of complex equations which require an extensive amount of computer time to evaluate (see equations (46 to 48) and (52 to 54)). The more familiar Runge-Kutta method of integration requires four evaluations of the right hand side of the given equations per step.

4) After each step an estimate of the local truncation error (this will also include part of the round off error) is readily available with only a small amount of extra computer time.

5) The computer program which performs the integration is readily available as part of the standard IBM Science Subroutine Package.

The principle disadvantage of this scheme is that it is not self starting and therefore a hybrid of the Runge-Kutta method is used to generate the first few sets of values.

Given a set of first order differential equations :

$$y'_i = \frac{dy_i}{dx} = f_i(x, y_1, y_2, y_3, \dots, y_n) \quad (67)$$

where $i = 1$ to n

with initial values $y_i(x_0) = y_{i0}$ and using vector notation

$$Y' = \frac{dY}{dx} = F(x, Y), Y(x_0) = Y_0 \quad (68)$$

where capital letters indicate column vectors with n components the solution at Y_{j+1} follows from the solution at previous values (i.e. Y_j, Y_{j-1} etc.) thus:-

$$\text{(PREDICTOR)} \quad P_{j+1} = Y_{j-3} + \frac{4h}{3}(2Y'_j - Y'_{j-1} + 2Y'_{j-2}) \quad (69)$$

$$\text{(MODIFIER)} \quad M_{j+1} = P_{j+1} - \frac{112}{121}(P_j - C_j) \quad (70)$$

$$M'_{j+1} = F(x_{j+1}, M_{j+1}) \quad (71)$$

$$\text{(CORRECTOR)} \quad C_{j+1} = \frac{1}{8}(9Y_j - Y_{j-2} + 3h(M'_{j+1} + 2Y'_j - Y'_{j-1})) \quad (72)$$

$$\text{(FINAL VALUE)} \quad Y_{j+1} = C_{j+1} + \frac{9}{121}(P_{j+1} - C_{j+1}) \quad (73)$$

where P, M, M', and C are all column vectors. It has been shown that the components of the vector $P_{j+1} - C_{j+1}$ is a measure of the truncation error in the vector Y_{j+1} and therefore control of the accuracy and adjustment of the step size h can be attained by generating the following test value:-

$$\delta = \sum_{i=1}^n a_i |P_{j+1} - C_{j+1}|_i \quad (74)$$

where a_i are a system of relative weights given to each equation. If δ is greater than a given tolerance the increment h may be halved and the procedure rerun (in the S.S.P. package a sixth order interpolation formula is used instead of the complete rerun). After each numerical step the integrating procedure returns to an output subroutine (written by the present author) which allows reflection, refraction, termination of the program etc.

(1.6) Computer Programs

(1.6.1) Three Dimensional Program

A computer program has been written by the present author to trace rays through models in which the velocity is a function of the three spherical coordinates. The velocity may be continuously varying and/or defined by a series of blocks which are bounded by finite velocity changes. Comparison with analytic solutions to certain laterally homogeneous velocity models demonstrates that the program yields correct travel times, azimuths and phase velocities. Tests have also been applied which confirm that the reflection and refraction conditions are adhered to. Some parameter changes within the program (e.g. dimensions of the array stores, input and output procedures etc.) are required before any realistic Earth models may be treated. The development of the three dimensional program was terminated at this stage in favour of the two dimensional approach for several reasons:

- (i) Computer storage and time for the three dimensional analysis is very much larger than for a two dimensional one. If only ten points are required at each level to define the velocity variation in the direction perpendicular to the ray path, then almost ten times as much computer storage is required than that needed for the two dimensional analysis. An analytic function used to describe the transverse variation of velocity would obviously cut the space required.
- (ii) The lower number of equations needed for two dimensional analysis (six instead of the fifteen required for three dimensional structures) allows intensity estimates to be obtained in addition to the ray path information.
- (iii) It is intuitively difficult to 'model' three dimensional structures.

(iv) Most known tectonic or geological structures (continental-oceanic boundary, subduction zones, rifts, and faults) can be allowed for in the two dimensional scheme. Any deviation from the great circle path, which these structures may cause, may be modelled by allowing finite reflection or refraction at the tectonic feature. This would involve using equations (39) to (45) to redefine the plane of the ray path as well as the refractive or reflective effects within the plane. Most of the recent papers utilizing three dimensional ray tracing (Jacob (1970, 1972), Julian (1970), Davies and Julian (1972)) have assumed essentially two dimensional structures (dipping plates) and the third dimension has only been required to allow for the deflection of the ray from the great circle path at the tectonic feature. A two dimensional scheme allowing for a finite change of the plane of the ray path would have been just as adequate; perhaps more realistic, for both sets of authors require possible finite discontinuities to be smoothed out to allow the infinitesimal theory to be applied.

(v) The evidence for substantial deviations of the ray from the great circle path connecting the source and receiver, caused by structures at depth (i.e. the lower mantle) is at present only qualitative (Davies and Sheppard (1972), Kanasewich et. al. (1972)). If better estimates of these possible deviations can be obtained then the three dimensional program will certainly be useful. The two dimensional program may still be used for the initial modelling and the three dimensional program used to refine the models.

(1.6.2) Two Dimensional Program

The two dimensional ray tracing program, given in Appendix (A), has been developed to the stage where practically any two dimensional velocity structure may be modelled (see chapter (3) for ray tracing applied to models of the East African Rift). The principle computations

of this program are described in the flow diagram of figure (9) while all the information about input and output parameters etc. is given in Appendix (A).

(1.7) Summary

The following is a summary of the novel features contained in this chapter and the computer program of Appendix (A).

(i) The equations describing the reflection and refraction of a ray at a plane or spherical interface have been derived from the vector equivalents of Snell's Laws. In the two dimensional program the ray intensity is partitioned at each velocity discontinuity according to the equations derived by Zoeppritz (1919). The subroutine which partitions the intensity (subroutine Zo in Appendix (A)) is extremely versatile, it may be applied to any of the following situations:

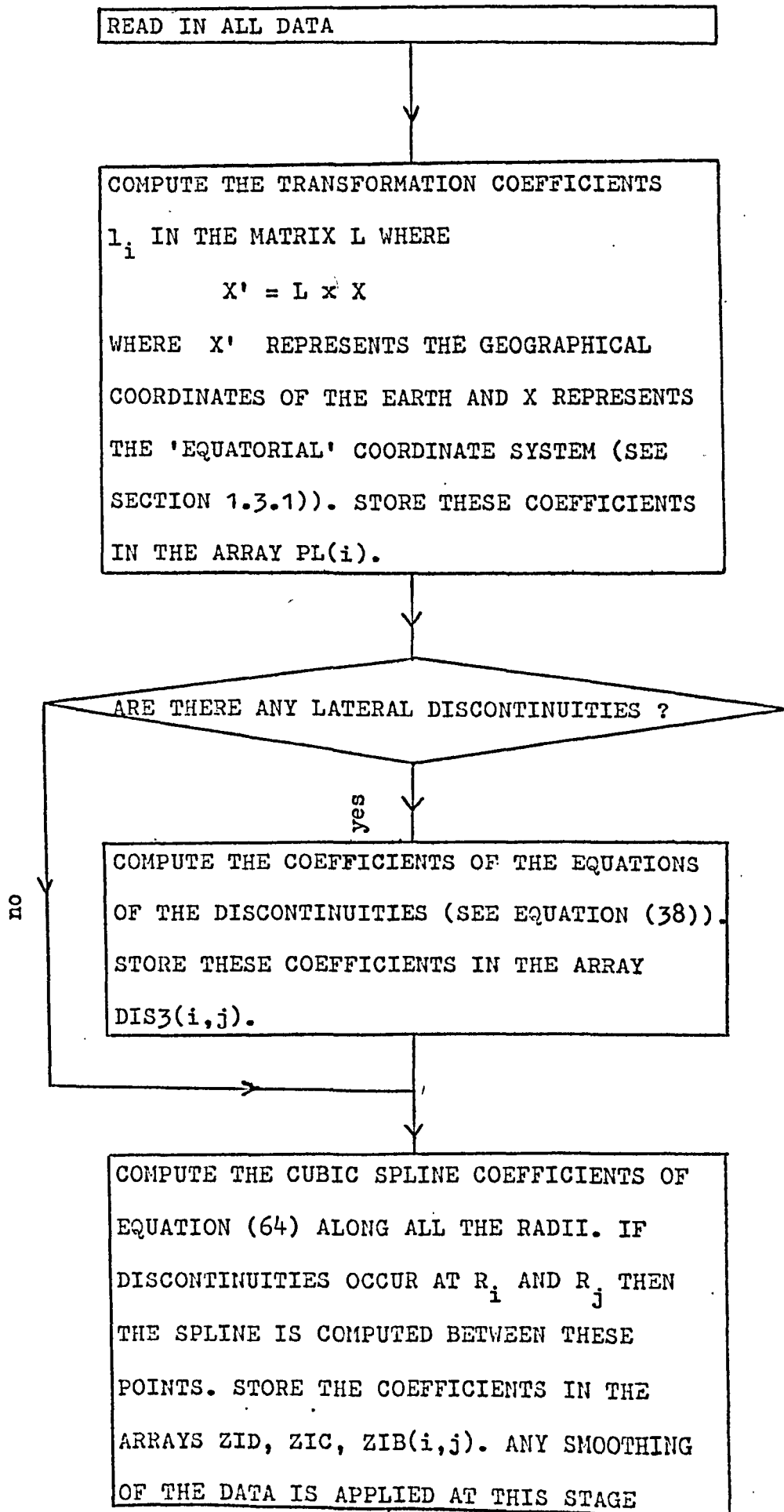
(a) P wave or S wave incident at a boundary between two solid media in welded contact.

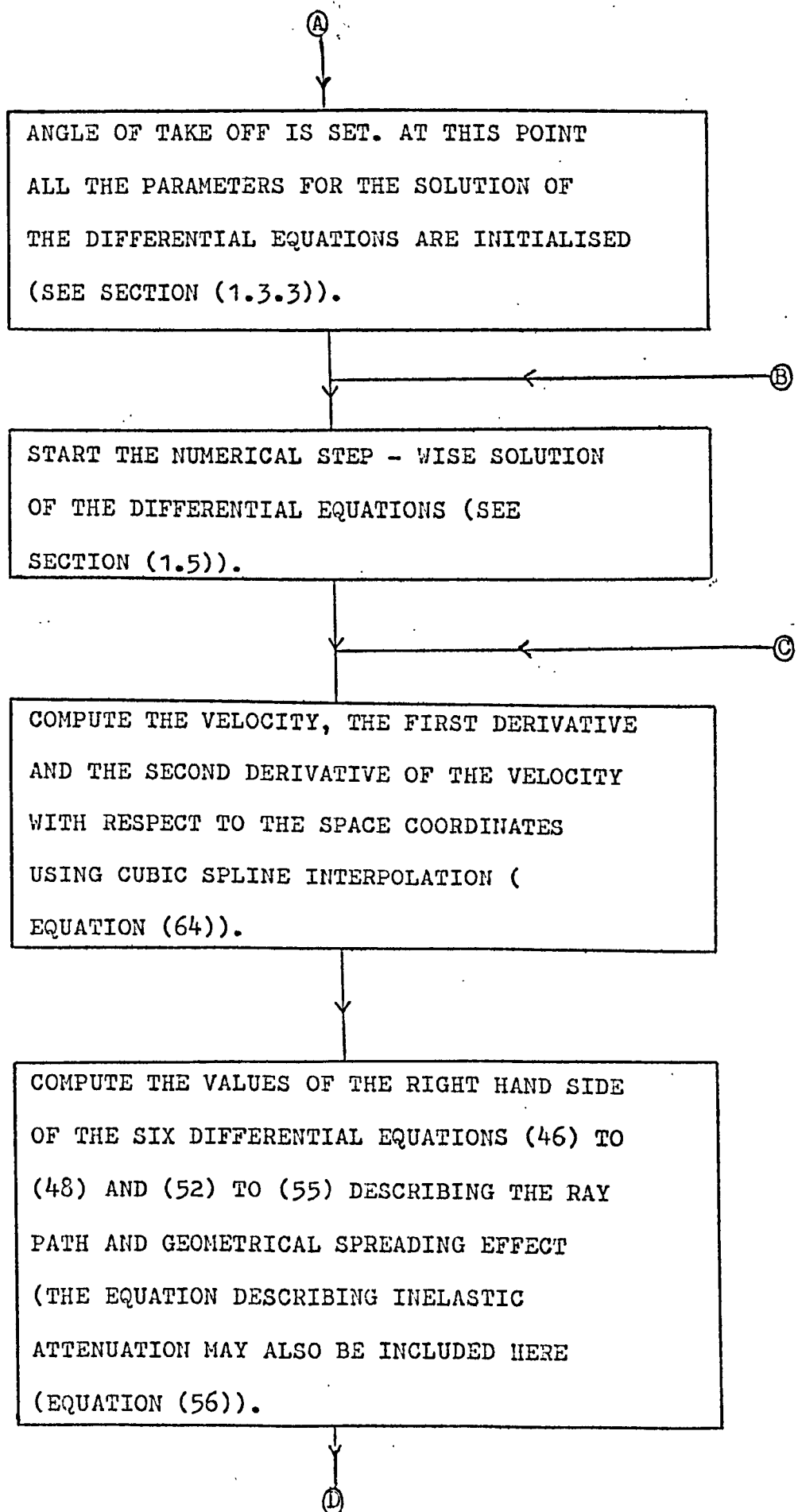
(b) P wave or S wave incident at a boundary between a solid and fluid media (e.g. earth-air boundary).

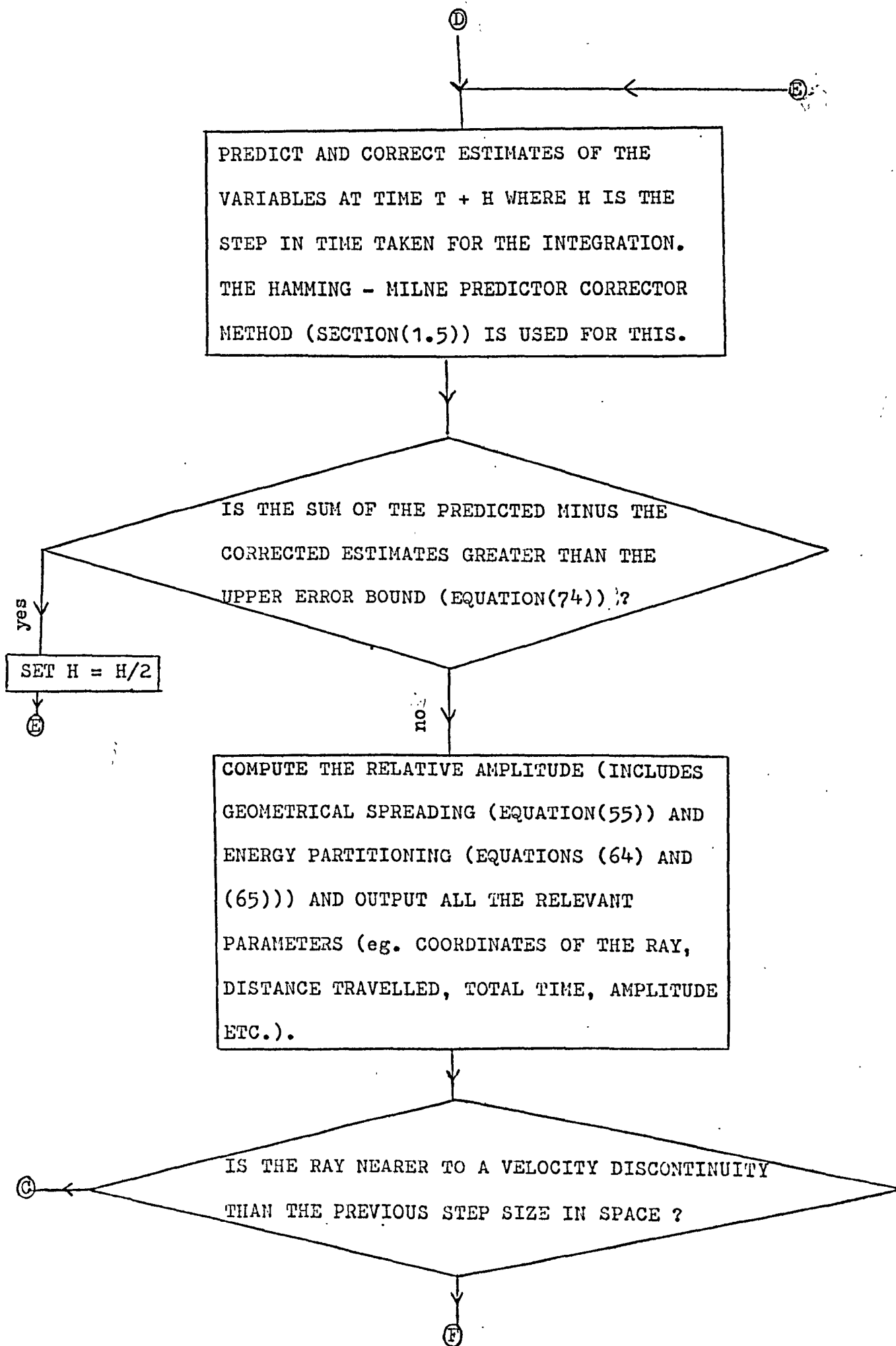
This subroutine has been checked against the results of several papers, each of which solve Zoeppritz's equations for only one or two of the above situations (McCamey et al. (1962), Costain et. al. (1963), Tooley et. al. (1965), and Koefoed (1962)).

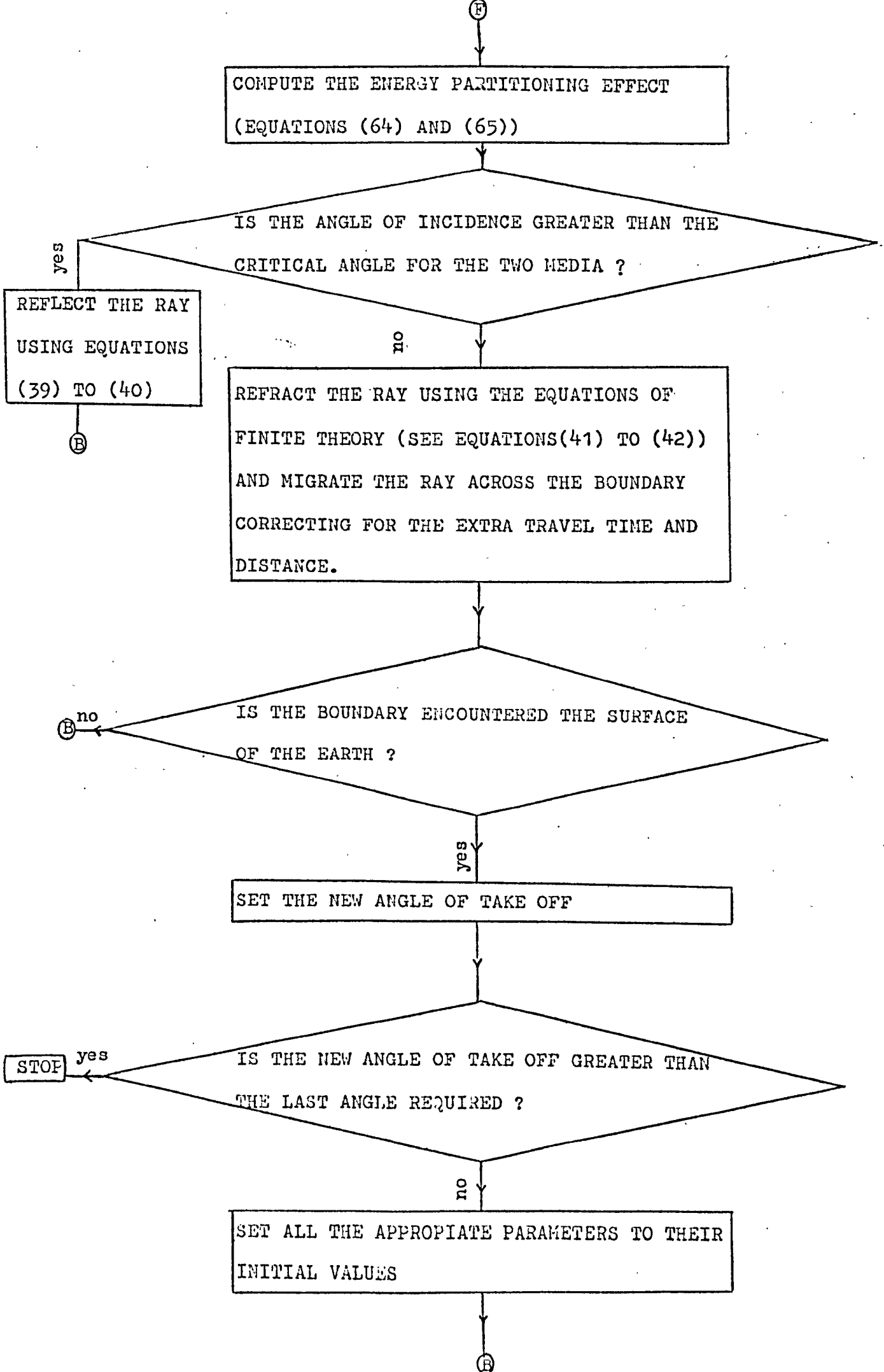
(ii) The five equations describing the path of a ray in a three dimensional continuum (Julian (1970)) have been contracted for the two dimensional case. By transferring the ray plane to the equator and setting the latitudinal terms to zero the contraction results in only three ray path equations; Julian (1970) claims a reduction to four equations but probably does not transfer the ray plane. It is important to emphasize that the same three ray path equations could be obtained by treating the two dimensional problem from first principles (i.e. by using circular coordinates).

FIG(9)

FLOW DIAGRAM FOR THE TWO DIMENSIONAL RAY TRACING COMPUTER PROGRAM







- (iii) The relative intensity equations (geometrical spreading effect) for velocity structures which are a function of two dimensions have been derived from first principles. This formulation only applies to three dimensional velocity structures (geometrical spreading is essentially a three dimensional problem) in which there is an axial symmetry about one of the radial vectors (see figure (3) and section (1.3.2)). To obtain the relative intensity, the three equations (52) to (54) must be simultaneously time integrated with the three ray path equations (46) to (48). The resultant six differential equations required for the ray path and relative intensity is half the number quoted by Julian for two dimensional velocity structures (Julian (1970)).
- (iv) Smoothing splines are used for interpolation of the velocity depth profiles. This form of interpolation produces a much smoother relative intensity versus distance curve (see for example figure (8)) than the previously suggested interpolating splines (Chapman (1971)).
- (v) Successive use of the efficient uni-cubic spline (smoothing and interpolating) is used to interpolate data in two and three dimensions. The excellent results obtained by interpolating the data and first and second derivatives of the data, defined on a plane by a sine wave in the x and y directions, is confirmation of the validity of this technique.

C H A P T E R 2

APPLICATION OF RAY TRACING TO SPHERICALLY SYMMETRIC EARTH MODELS

(2.1) Travel Times and Ray Paths - Integration Step Size

(2.2) Relative Intensities (geometrical spreading) -
Integration Step Size

(2.3) Relative Intensities (or relative amplitudes) of Rays
Traced Through Some Standard Earth Models

(2.3.1) Gutenberg Earth Model

(2.3.2) Jeffreys-Bullen Earth Model

(2.3.3) Herrin Earth Model

(2.3.4) The effect of Energy Partitioning at the
Conrad and Mohorovicic Discontinuities -
Herrin Earth Model

(2.3.5) Comparison of Theoretical (Herrin Earth
Model) and Experimental Relative Amplitude
Curves

APPLICATION OF RAY TRACING TO SPHERICALLY SYMMETRIC EARTH MODELS

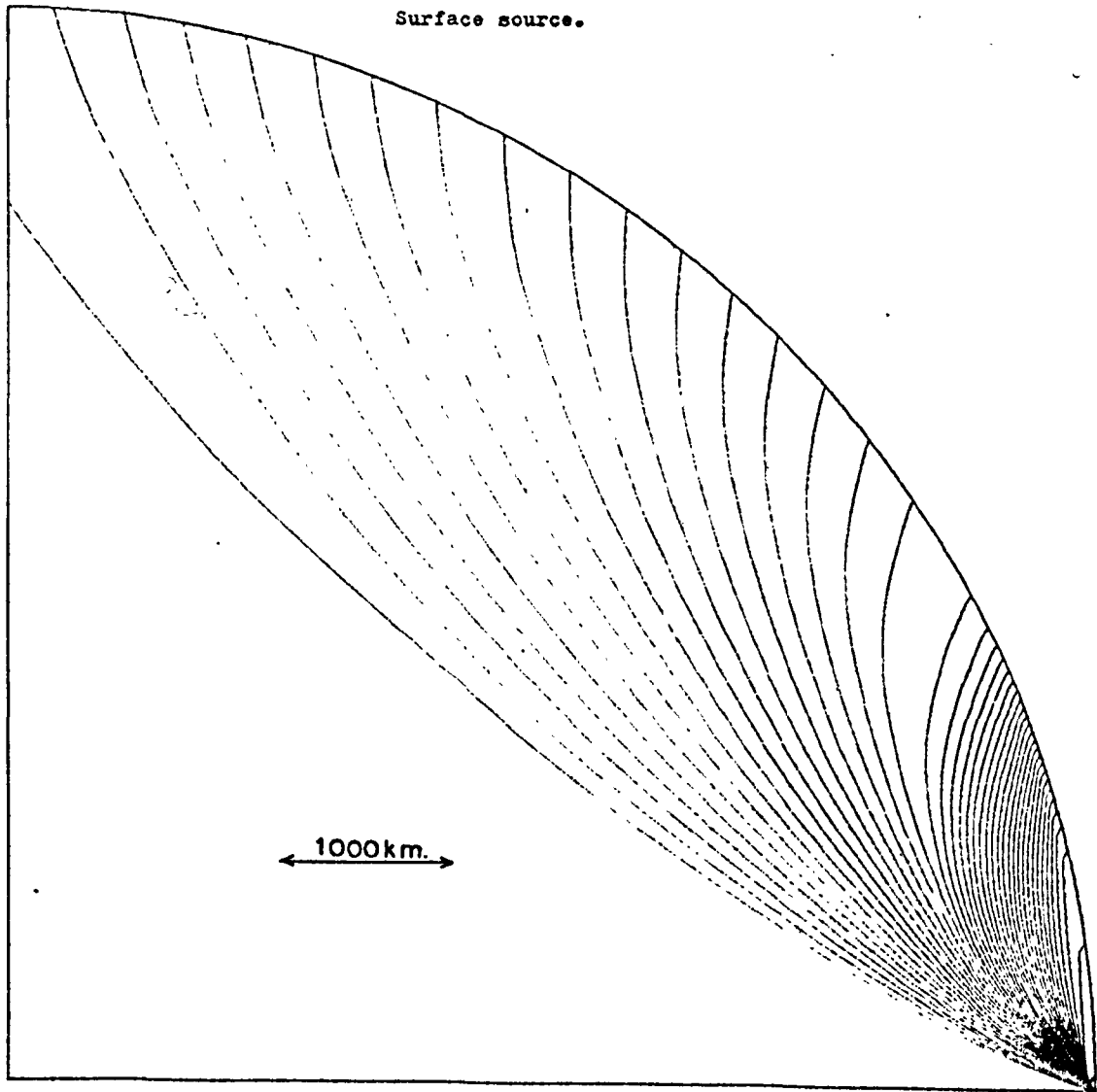
The first sections of the chapter are concerned with the determination of a suitable step size for the numerical integration of equations (46) to (48) and equations (52) to (54). The relative intensity estimates obtained from the application of the computer program of Appendix (A) to some 'standard' Earth models is then compared to those obtained by others. Results obtained from the program of Appendix (A) are referred to as RAY traced.

(2.1) Travel Times and Ray Paths - Integration Step Size

In order to find a satisfactory step size for the numerical integration of the ray path equations (46) to (48) RAY tracing was applied to the velocity depth profile of Herrin (1968). In the Herrin model the velocity is defined at five kilometer intervals from the Earth's surface to the core-mantle boundary. Herrin's travel time - distance curve was reproduced to an accuracy ~ 0.01 seconds using a time step of 0.02 seconds (space step ~ 0.16 km.) and to ~ 0.05 seconds using a time step of 0.2 seconds (space step ~ 1.6 km.). Seismograms can only be read to 0.1 seconds so the latter step interval was considered sufficiently accurate for the ray path calculations. If a strong velocity gradient is encountered along the ray path (other than a defined velocity discontinuity) then the program decreases the step size.

Figure (10) shows the paths of rays traced through the Herrin Earth model using the integration time step of 0.2 seconds, while figure (10a) shows the travel time, phase velocity at the surface and maximum depth attained by the ray for $0^\circ < \Delta < 100^\circ$. These latter parameters are found to be identical to the values given by Herrin (1968).

FIG(10) Ray paths for the Herrin(1968) Earth model.
Surface source.



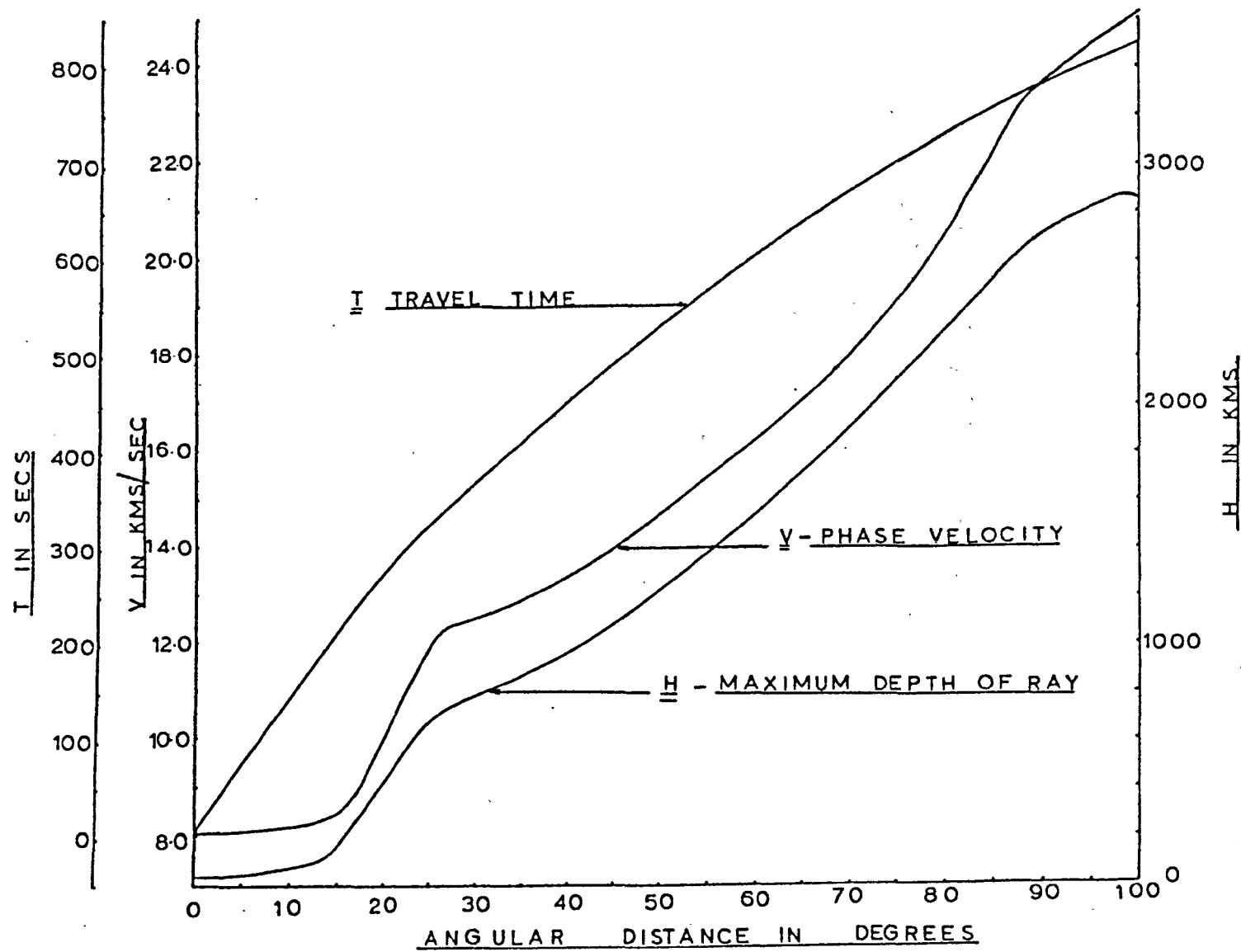


FIG (10a)

(2.2) Relative Intensities (geometrical spreading) - Integration Step Size

There is no standard relative intensity curve with which to compare the RAY traced estimates. Therefore to find a satisfactory step size for the numerical integration of equations (52) to (54) the program was applied to a hypothetical earth model for which an analytic solution exists. For a velocity depth profile defined by the equation:

$$v = a - b r^2 \quad (75)$$

where v is the velocity, r is the radial coordinate, a and b are constants, then it is easily shown (Bullen (1965)) that all the ray paths are circles of radius $2.b.p$, where

$$p = \frac{r \sin(i_r)}{v} \quad (76)$$

and i_r is the angle between the ray and the radial vector. From the geometry of the rays Bullen (1965) shows that

$$\tan\left(\frac{\Delta}{2}\right) = \frac{v' \cot(i_r')}{(2a - v')} \quad (77)$$

where the apostrophe sign refers to quantities at the surface.

$$\therefore d\Delta = \frac{2 v' \operatorname{cosec}^2(i_r') di_r'}{\sec^2\left(\frac{\Delta}{2}\right) (2a - v')} \quad (78)$$

From (76)

$$dp = \frac{r'}{v'} \cos(i_r') di_r' \quad (79)$$

Substituting (78) and (79) into the relative intensity equations of Bullen (1965) leads to

$$\frac{I}{I'} = \frac{\sin^3(i_r') (2a - v')}{2 v' R^2 \cos^2\left(\frac{\Delta}{2}\right) \sin(\Delta) \cos(i_r')} \quad (80)$$

R is the radius of the Earth for a ray which has its source and receiver at the surface.

Velocities calculated from equation (75), with $a = 11.24717$ and $b = 8.0 \times 10^{-8}$ (Wesson (1970)), were fed into the RAY tracing program at digitised values (one value per five kilometers) and the relative intensities computed by the method described in chapter (1). The resultant values, obtained with a time step of 0.2 seconds, are compared with the analytic solutions in table (4). The maximum difference occurs in the smallest epicentral distance where the difference is 2.6%. After approximately $\Delta = 13^\circ$ the difference is always less than 0.16%. Considering the uncertainty introduced by the interpolation of the data (see following sections) this step size is considered satisfactory.

(2.3) Relative Intensities (or Relative Amplitudes) of Rays Traced Through Some Standard Earth Models.

Relative intensity values are extremely sensitive to the scheme used to interpolate the discrete velocity data. In comparison the travel time is insensitive to the interpolation. In the following sections the relative intensity (or relative amplitude) curves obtained by applying RAY tracing to the velocity depth profiles of Gutenberg, Jeffreys-Bullen and Herrin are compared to those obtained by others. Unless stated otherwise, the relative intensities (or relative amplitudes) plotted in the following sections have been obtained by only considering geometrical spreading (the papers referenced do not consider the effect of energy partitioning at the crustal velocity boundaries).

Some of the authors referenced give the relative intensity curve while others give the relative amplitude curve. In order to compare the RAY traced curves with other estimates some of the diagrams in the following sections are of relative intensity (e.g. those of Gutenberg in figure (11) to figure (14)) and some are of relative amplitude

(e.g. those of Jeffreys-Bullen in figure (15) and Herrin figure (16) to figure (20)). In the following, the 'relative amplitude' is simply the square root of the relative intensity.

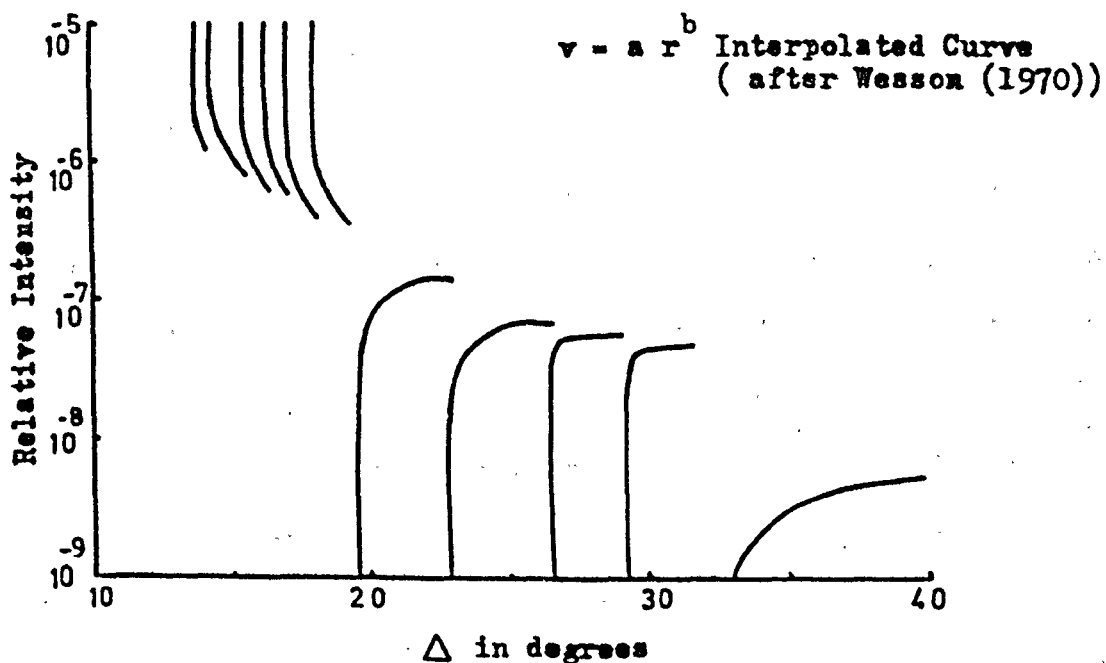
(2.3.1.) Gutenberg Earth Model

Julian and Anderson (1968) were the first to utilize ray tracing to obtain relative amplitudes for P waves travelling through various Earth models. As already stated these authors interpolate the data by means of the Bullen equation ($v = a r^b$) and thus allow discontinuous derivatives at the data points (see chapter (1)). The relative amplitude curve they obtain is very similar in shape to the relative intensity curve of figure (11) taken from Wesson (1970), which was obtained for a source and receiver at the base of the crust, whereas Julian and Anderson (1968) have their source and receiver at the top of the crust. Wesson (1970) has shown that the zeros and anomalous lows of figure (11) are caused by $d\Delta/dp$ diverging to infinity at the data points, while the infinite values are obtained when $d\Delta/dp$ in addition to tending to infinity changes sign at the data point. The rays that approach the bottom of a velocity shell may be significant (see Pedersen (1961)) and thus the true values of figure (11) are likely to be those at the top of the 'hooks'.

In an attempt to obtain a continuous relative intensity curve, Wesson (1970) interpolates the data by fitting a set of polynomials ranging from degree two to degree five to the discrete velocity depth profile. The polynomials are matched at the data points to give continuous first and second derivatives (four polynomials were fitted to twenty data points). A certain amount of smoothing has been incorporated into the polynomials as the data points are not fitted exactly. This latter scheme is similar in theory to the smoothing

Take off Angle	Distance	Relative Intensity	Relative Intensity
	Travelled	From the Analytical	From Ray Tracing
(degrees)	(degrees)	Solution ($\times 10^{-6}$)	($\times 10^{-6}$)
4.0	4.55	3.793	3.897
8.0	8.94	0.9939	1.0010
12.0	13.44	0.4357	0.4369
16.0	18.04	0.2374	0.2378
20.0	22.77	0.1453	0.1455
24.0	27.67	0.09547	0.09552
28.0	32.77	0.06566	0.06568
32.0	38.12	0.04657	0.04658
36.0	43.77	0.03376	0.03376
40.0	49.77	0.02485	0.02485
44.0	56.19	0.01850	0.01850
48.0	63.10	0.01390	0.01390

Table(4). Comparison of ray traced relative intensities with an analytic solution. Velocity model used $\rightarrow v = 11.24717 - 8.0 \times 10^{-8} r^2$



fig(11) Relative Intensity curve for the Gutenberg Earth model.

Interpolation using Bullen equation (after Wesson(1970)).

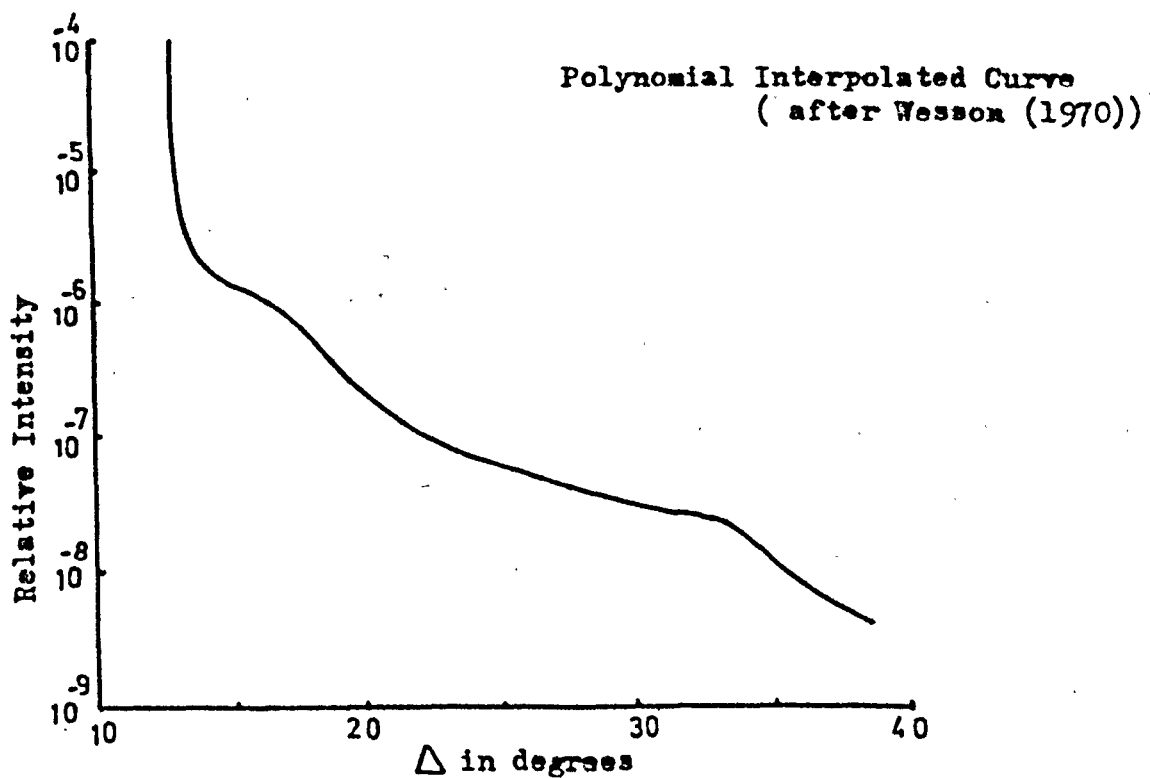


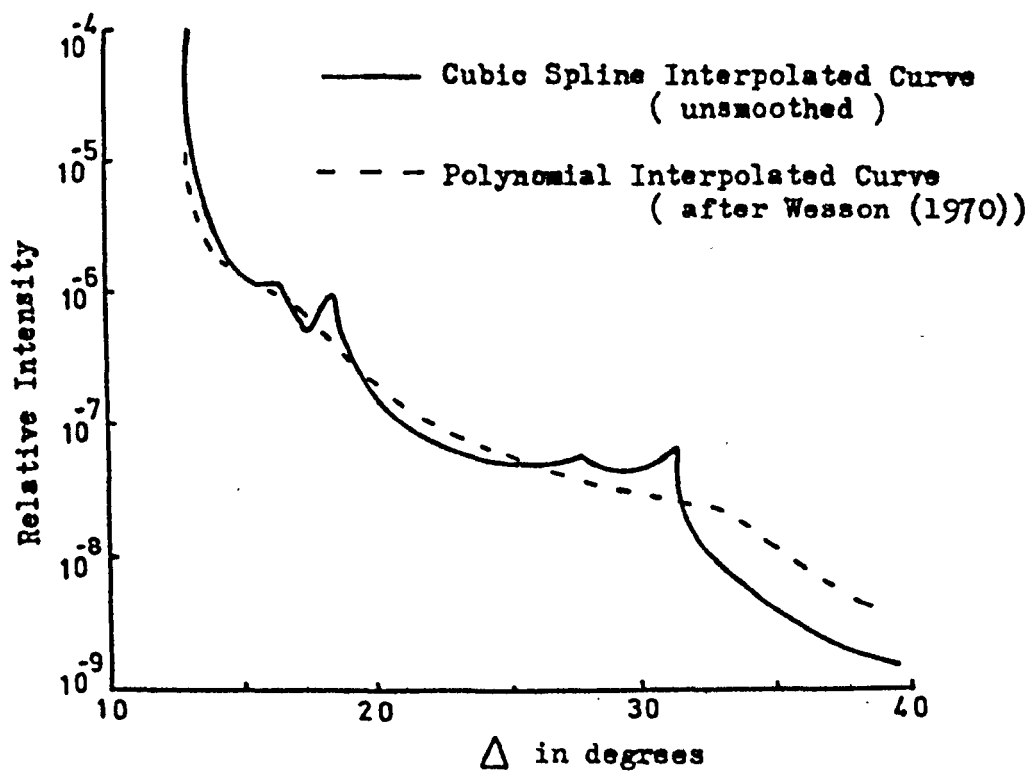
figure (12) Relative Intensity of the Gutenberg Earth Model .

Interpolation using piecewise fitted polynomials (after Wesson(1970)).

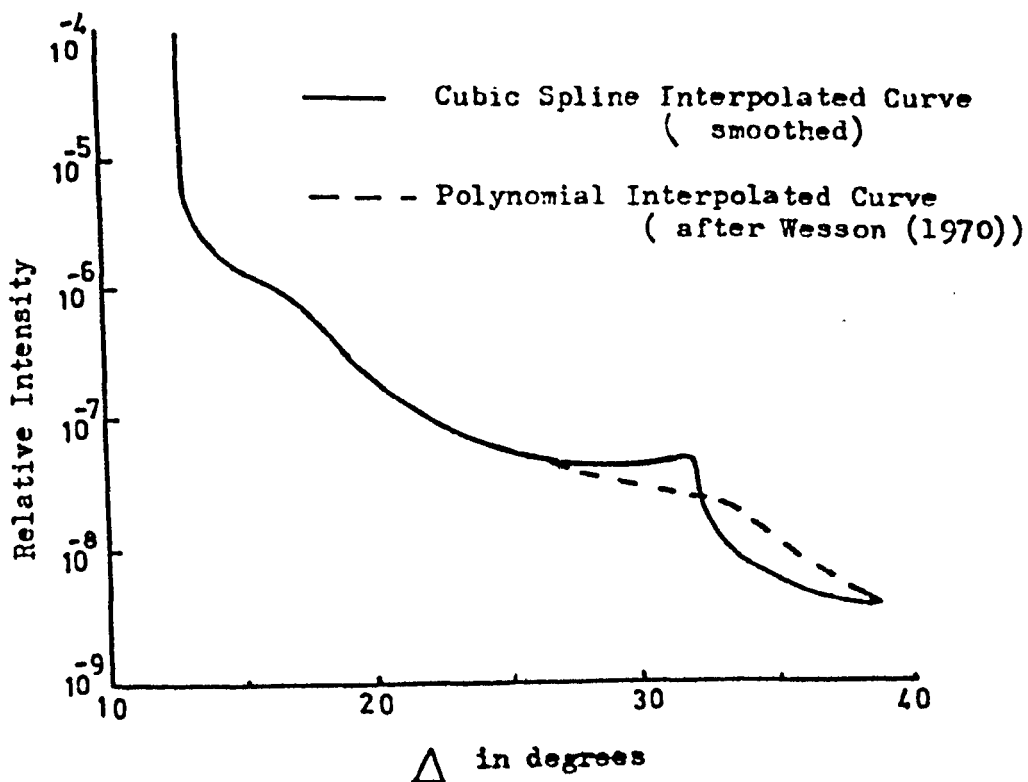
spline fits (chapter 1)) but is computationally more complex and time consuming and in addition requires a higher degree of subjectivity. The resultant relative intensity curve, which is shown in figure (12), is clearly more meaningful.

Figure (13) shows the RAY traced relative intensity curve obtained by using interpolating splines (no smoothing, so that an exact fit is obtained between the spline and the given data points - see chapter (1)). The solution obtained by Wesson (1970) using the polynomial interpolation is shown for comparison. The general shapes of the two curves are similar but there are two regions where they notably differ. In the first region, near $\Delta = 16^\circ$, the interpolating spline curve contains more 'fine structure' than shown on Wesson's curve. Only a single hump appears on the latter curve while on the spline curve two narrow peaks are observed. The second difference occurs for $28^\circ < \Delta < 40^\circ$. It is in this region that the rays pass through the strong velocity gradient between 900km. and 1000km. depth (table (5)). In the interpolated spline curve a small peak is observed at approximately $\Delta = 28^\circ$ and a more pronounced peak is shown at approximately $\Delta = 31.4^\circ$, while in the polynomial interpolated curve a smaller change in gradient is seen at approximately $\Delta = 34^\circ$.

If instead of fitting the tabulated data exactly, a small amount of smoothing is allowed (this corresponds, in Wesson (1970), to only fitting the data approximately) a much improved correlation between the RAY traced curve and Wesson's curve is obtained. The resultant velocity values after smoothing are shown in the fourth column of table (5) so that these values may be compared, both to the original velocity profile and the profile obtained by using the polynomials of Wesson (1970). In the smoothing spline profile, no smoothing was allowed in



(figure(13)) Relative Intensity curve for the Gutenberg Earth model. Interpolation using interpolating splines.



(Figure(14)) Relative Intensity Curve of the Gutenberg Earth model. Interpolation using smoothing splines.

Depth (km)	Tabulated Velocity (km/sec)*	Computed Velocity Using Polynomials of Wesson(1970)	Computed Velocity Using Smoothing Splines (chapter 8)
		(km/sec)	(km/sec)
40.0	8.08	8.081	8.080
60.0	7.87	7.863	7.870
80.0	7.80	7.805	7.800
100.0	7.83	7.825	7.830
120.0	7.89	7.880	7.890
140.0	7.94	7.942	7.940
160.0	8.00	8.000	8.000
180.0	8.06	8.059	8.060
200.0	8.12	8.121	8.123
250.0	8.30	8.298	8.302
300.0	8.51	8.509	8.513
350.0	8.75	8.753	8.752
400.0	9.00	9.021	9.017
500.0	9.60	9.589	9.579
600.0	10.10	10.114	10.084
700.0	10.50	10.560	10.506
800.0	10.90	10.942	10.894
875.0	11.20 *	-	11.200
900.0	11.30	11.280	11.300
1000.0	11.40	11.390	11.483

* Velocities above 400km. from Gutenberg(1959), below 400km. from Press(1966).

* Velocity interpolated to continue linear gradient from 600km. to 900km.

Table(5)

the regions of the low velocity channel or the strong velocity gradient near 900km. depth (an extra point has been inserted at 875km. depth to ensure the linear velocity increase is maintained between 600 km. and 900km. depth). The mean square variation of the smoothed spline profile from the original profile is 3.99×10^{-4} Km/sec which is to be compared with 3.46×10^{-4} Km/sec obtained from the Wesson profile.

The resultant relative intensity curve is now an almost exact match with that obtained by Wesson, except in the region at approximately $\Delta > 28^\circ$. Even in this latter region the fit between the polynomial interpolated curve and the spline interpolated curve is improved when smoothing is allowed. It is emphasized that the remaining difference between the two curves is solely a function of the interpolation used; the relative intensity curve given by Wesson has been reproduced exactly by RAY tracing, when the polynomials given by Wesson (1970) are used to interpolate the velocity data (the a_4 coefficient for the region between 160 and 550 kms. given in Wesson's table (2) requires a minus sign). It is not possible to say which of the two curves (polynomial or smoothing spline interpolated) is the 'true curve'. On the contrary the difference between these two curves serves to emphasise the uncertainty of relative intensity computations due to the uncertainty of the interpolation of the discrete velocity data.

(2.3.2) Jeffreys-Bullen Earth Model

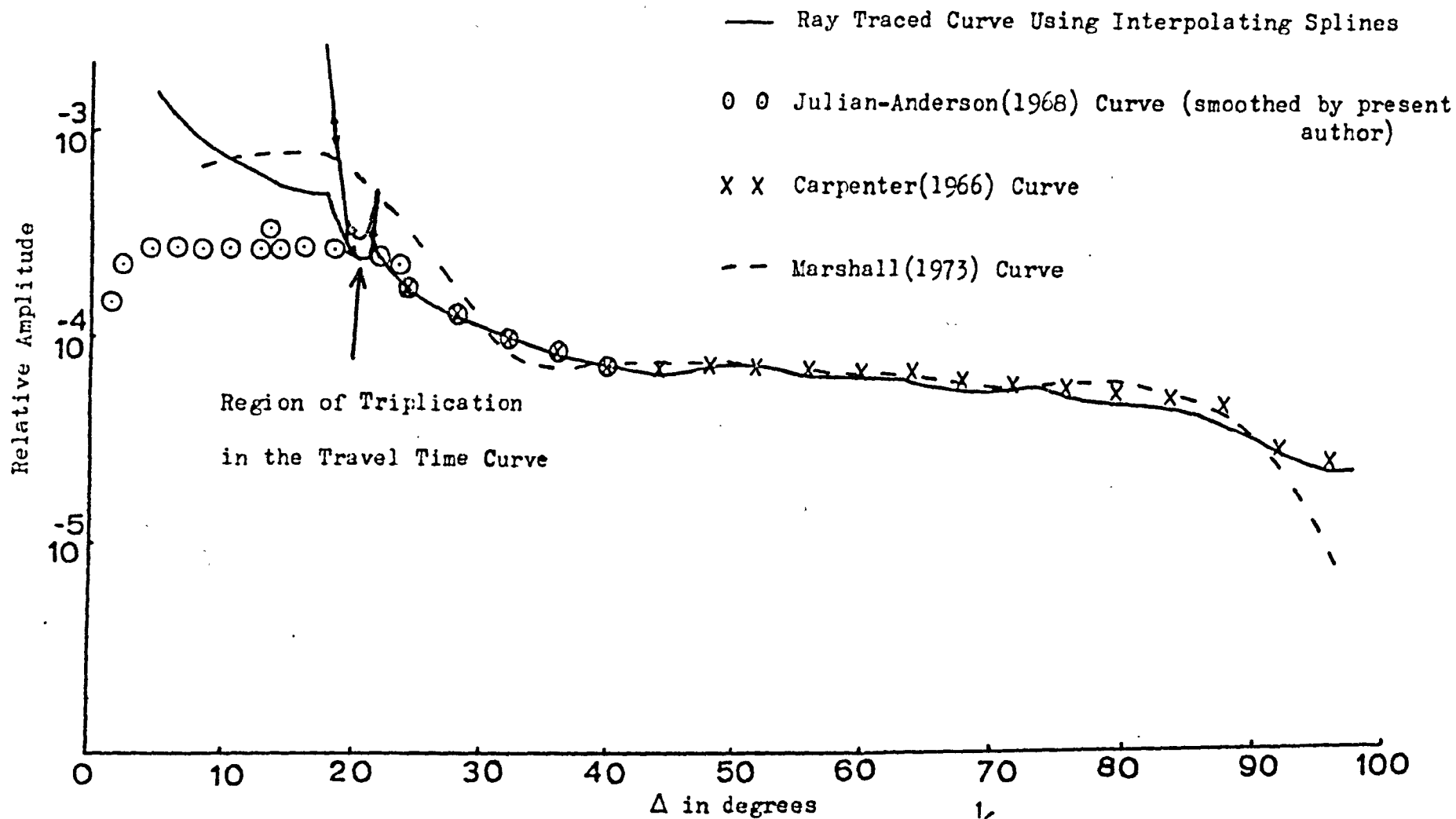
A number of authors (Carpenter (1966), Julian and Anderson (1968), Shimshoni and Ben-Menahem (1970), Marshall (1973)) have attempted to obtain relative amplitude curves for the Jeffreys-Bullen Earth Model (Bullen (1965), Jeffreys (1959, 1971)). Some of these have used the Jeffreys-Bullen travel time tables as the data (see Bullen (1965) and

Carpenter (1966) for the required formula for this computation), while others have used the velocity depth profiles of either Jeffreys (1959, 1971) or Bullen (1965).

Carpenter's curve, as shown in figure (15), was obtained from the travel time tables for distances greater than 24° epicentral distance. This author does not state how the derivatives of the travel time table were calculated (the first and second derivative of the data are again required) but Marshall (personal communication (1973)) believes that a third or fourth order difference scheme was used. Julian and Anderson (1968) use ray tracing, in an analagous manner to that described for the Gutenberg model (section (2.3.1)), on the velocity depth profile of Jeffreys (1959). Extra data points were generated by four point Lagrangian interpolation in the region from 380 km. to 1014km depth before the Bullen equation was used (see Shimshoni and Ben-Menaham (1970)). The values plotted in figure (15) for the Julian and Anderson curve corresponds to the top of the hooks of their original relative amplitude curve.

Shimshoni and Ben-Menaham (1970) use the travel times for their computation and their result corresponds extremely well with that obtained by Julian and Anderson (1968) for $0^{\circ} < \Delta < 40^{\circ}$. These authors obtain the derivatives by using Powell's least squares cubic spline routine (Powell (1970)). Because of the very close similarity of the Shimshoni and Ben-Menaham curve with the Julian and Anderson curve only the latter is plotted in figure (15). Marshall's (1973) curve was obtained in a similar manner to that of Carpenter using a fourth order difference routine and is in part an attempt to reproduce the results of Carpenter (1966).

The RAY traced relative intensity curve shown in figure (15) was obtained using only the tabulated velocity depth profile given by

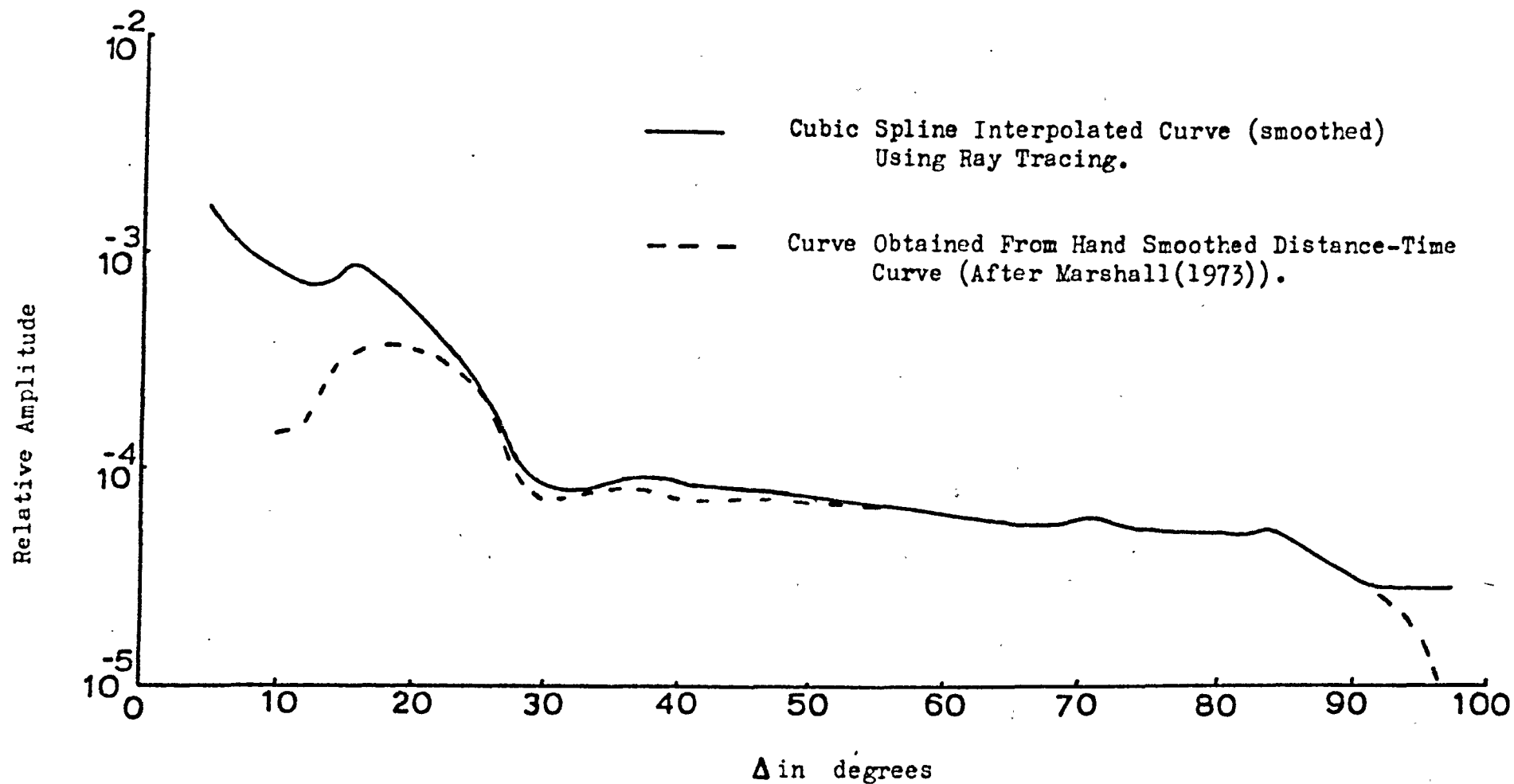


Jeffreys (1959) and applying interpolating splines. The relative amplitude curve obtained is sufficiently smooth and therefore no smoothing of the velocity profile was necessary. For distances greater than 21° the relative intensity curves of Carpenter (1966), Julian and Anderson (1968) (and therefore Shimshoni and Ben-Menaham (1970)), and that obtained from RAY tracing are very close. Marshall's curve is not so close but is still very similar to the rest (some of the curves have been adjusted to the scale shown by a constant term). Below $\Delta = 21^{\circ}$ the match between the curves is poor. The difference between the curves is puzzling but may be explained by the different interpolation schemes used.

In the RAY traced curve the relative amplitude across the triplication region of 19° to 21° has been obtained. The actual values in this region must be viewed with caution as the spline interpolation forces continuity of the first and second derivatives and therefore the intended second order discontinuity at approximately 400km. depth has been smoothed. However the RAY traced estimate may be used as at least a qualitative guide to the shape of the intensity curve in this region for the Jeffreys-Bullen Earth Model.

(2.3.3) Herrin Earth Model

Marshall (personal communication (1973)) has obtained a relative amplitude curve (figure (16)) from the Herrin travel time tables (Herrin (1968)) using similar techniques to that applied to the Jeffreys-Bullen tables. A moderate amount of smoothing was applied to the travel time tables in order to obtain reasonable estimates of the second derivative of the travel time with respect to distance (Marshall, personal communication (1973)). The RAY traced relative amplitude curve using smoothing splines is shown for comparison in figure (16) (see figure



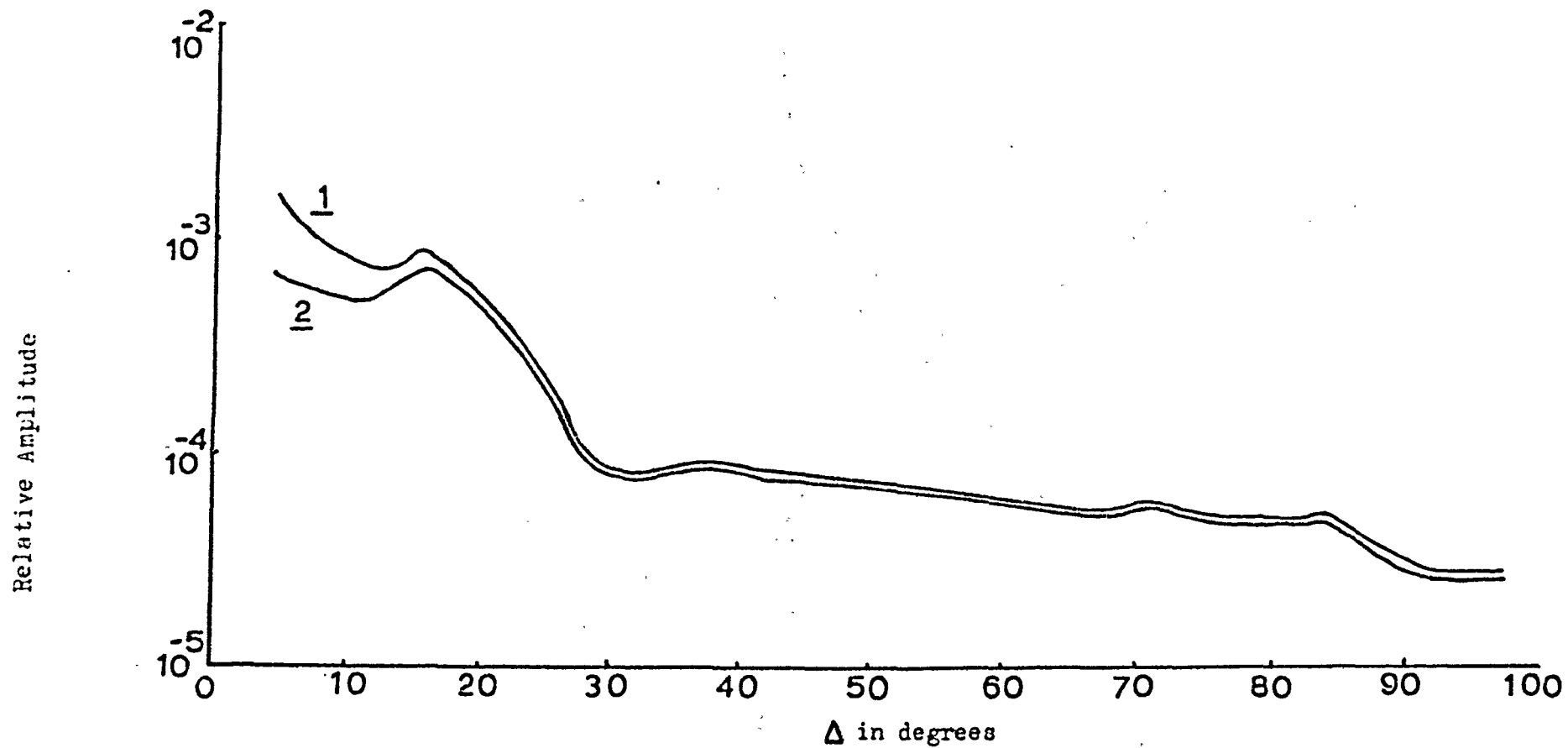
Figure(16) Relative Amplitude Curve of the Herrin Earth Model
(Relative Intensity)^{1/2}

(8) for a comparison of relative intensities using interpolating and smoothing splines). As with the Jeffreys-Bullen earth model there is very good agreement between the curves for distances greater than approximately 21° but below this distance the correspondence is poor. Again this may be explained as due to the different methods of obtaining the derivatives of the data (hand smoothed fourth order difference scheme for Marshall's curve and smoothing splines for the RAY traced curve).

(2.3.4) The Effect of Energy Partitioning at the Crustal Discontinuities - Herrin Earth Model

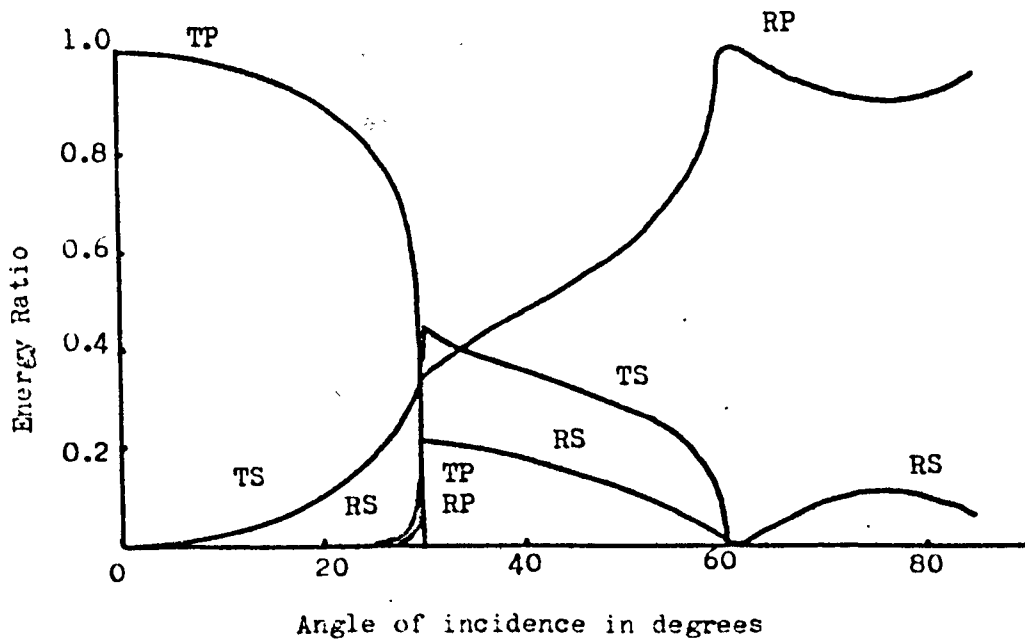
Up to this point the effect of energy partitioning at the Mohorovicic and Conrad discontinuities (these are set at 40km. and 15km. depth in the Herrin Earth model) has not been taken into account. To show this effect the relative amplitude curves for the Herrin Earth model, with and without the energy partitioning is given in figure (17). Clearly the effect of energy partitioning on the gradient of the amplitude curve is negligible for $\Delta > 15^{\circ}$. For shorter distances, the angle of incidence between the ray and the normal to the discontinuities increases, so that the amount of energy partitioned into phases other than the transmitted P wave increases. At the critical angle of incidence, according to first order ray theory, no energy is permitted in the 'refracted P phase'. The form of the energy partitioning for a particular set of parameter ratios is shown in figure (18) taken from Tooley et. al. Although the velocity ratio of 2:1 is not applicable to the Conrad or Mohorovicic discontinuities, the curves demonstrate the complex nature of energy partitioning.

It is clear from figure (17), that energy partitioning is an important factor in considerations of amplitude or magnitude estimates for near source epicentral distances (Δ less than 15°).



Fig(17) Relative Amplitude Curves (Relative Intensity $\frac{1}{2}$) of the Herrin Earth Model.

Curve 1 allows for geometrical spreading only, while curve 2 allows for both geometrical spreading and energy partitioning at the Conrad and Mohorovicic discontinuities.



Fig(18) Energy coefficients for a P wave incident at a plane boundary.

TP - Transmitted P wave , TS - Transmitted S wave , RP - Reflected P wave, RS - Reflected S wave.

Velocity ratio between the two media = 2:1
 Density ratio between the two media = 1:2
 Poisson's ratio for medium 1 = 0.3
 Poisson's ratio for medium 2 = 0.25

(2.3.5) Comparison of Theoretical (Herrin Earth Model) and
Experimental Relative Amplitude Curves

At this stage it is useful to compare the relative amplitude curve obtained experimentally with that predicted from considerations of geometrical spreading and energy partitioning using RAY tracing. Booth and Marshall (to be published) have already compared the Jeffreys-Bullen and Herrin relative amplitude curves, obtained by Marshall, with the experimental data shown here from Booth (1972).

In general the amplitude of a signal recorded at a seismic station is dependent on a number of factors:

- (i) Source function,
- (ii) Geometrical Spreading,
- (iii) Energy partitioning at finite velocity boundaries,
- (iv) Interference effects caused by finite velocity boundaries,
- (v) Inelastic attenuation,
- (vi) Instrumental effects.

For observations from the same type of instrument (i.e. identical response functions for each instrument) the last effect may be discounted in considerations of relative amplitudes. Only points (ii) and (iii) are considered in this section.

There are a number of studies which have obtained relative amplitude information from earthquakes (Gutenberg (1945a and 1945b), Gutenberg and Richter (1956), Cleary (1967), Vanek (1966, 1967, 1968a and b, 1969a, b and c), Vanek and Radu (1968), Vanek and Christoskov (1971), Willey et. al. (1970), Booth (1972)) and explosions (Carpenter et. al. (1967), Kaila (1970), Veith and Clawson (1972), Nuttli (1972)). The data shown here (figure (19)) are taken from Booth (1972). These data are preferred for several reasons:

- (i) The amplitudes from short period (pass band 0.1 to 4 seconds)

and long period (pass band 14 to 40 seconds) records were measured at the same set of stations for the same set of events. The Long Range Seismic Measurements (LRSM) Network of stations were used in this work (Booth (1972)).

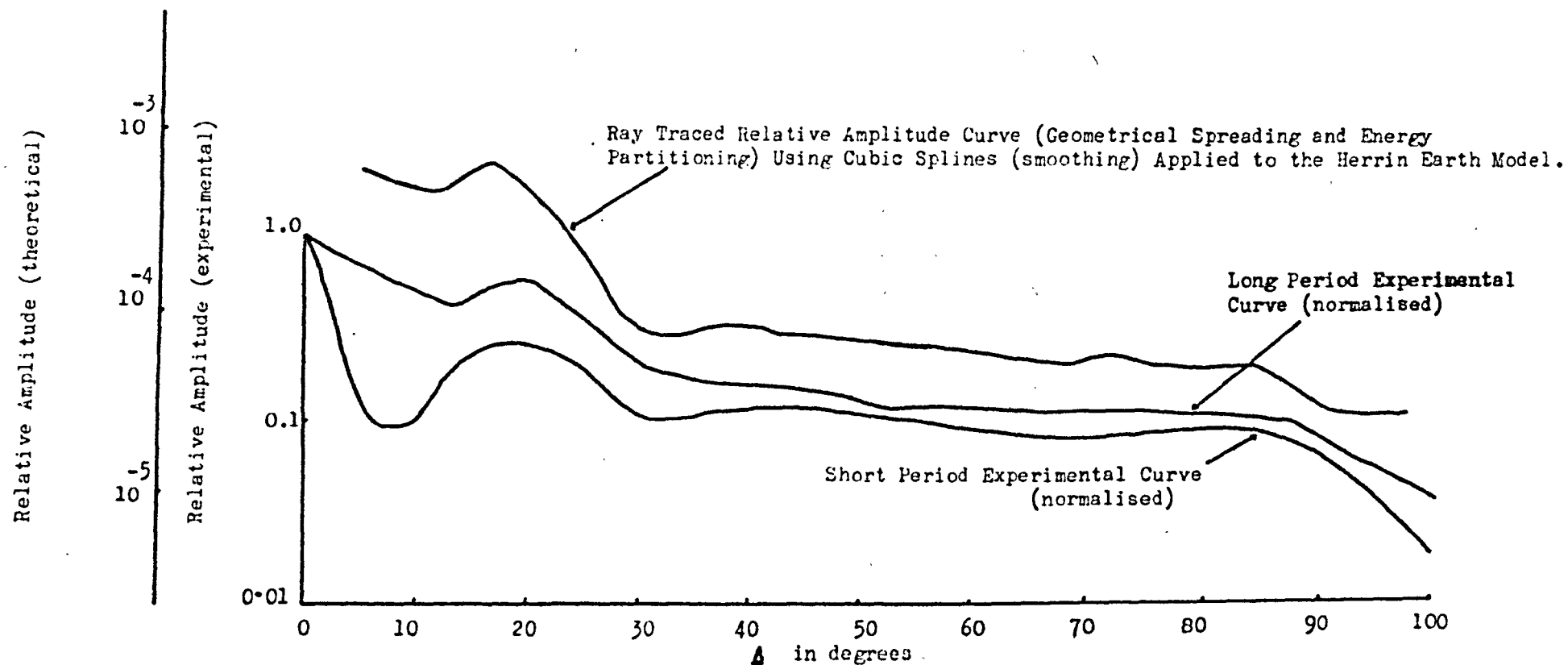
(ii) The largest number of observations were used in this compilation. A total of 4000 observations from 1474 earthquakes recorded at 39 stations across North America were used.

(iii) A complete statistical study has been made on the data (Booth (1972)). The method described by Carpenter et. al. (1967) was used. Only significant features are shown in figures (19) and (20); many of the peaks and bumps reported from less extensive studies are shown not to exist in Booth's study.

Figure (19) shows the long and short period relative amplitude curves obtained by Booth (1972) compared to the relative amplitude curve obtained from the Herrin velocity depth profile using RAY tracing considering geometrical spreading and energy partitioning at the crustal discontinuities. It is readily observed that most of the features of the experimental curves are seen in the theoretical curve. The correspondence between the long period experimental curve and the RAY traced curve is particularly impressive. Any differences which remain between the experimental and theoretical curves may be explained by:

- (i) Inaccurate velocity depth profile,
- (ii) Inaccurate representation of the energy partitioning at the velocity discontinuities,
- (iii) Inelastic attenuation.

Only the latter two points can explain the difference between the two experimental curves.



Figure(19) Theoretical and Experimental Relative Amplitude Curves (Relative Intensity) ^{$\frac{1}{2}$} . Experimental curves after Booth. Theoretical curve includes the effect of energy partitioning at finite velocity boundaries.

C H A P T E R 3

RAY TRACING APPLIED TO AFRICA

- (3.1) An Average Velocity-Depth Profile for East/Southern Africa
 - (3.1.1) Travel Time-Distance Curve for East/Southern Africa
 - (3.1.2) 'Smoothed' Travel Times and Average Velocity Depth Profiles
 - (3.1.3) Predicted Relative Amplitude ((Relative Intensity)¹) Curve for East/Southern Africa
- (3.2) Application of RAY Tracing to Models of the East African Rift
 - (3.2.1) Gravity Profiles
 - (3.2.2) Standard Velocity Depth Profiles
 - (3.2.3) Estimation of Seismic Velocity from Density
 - (3.2.4) RAY Diagrams
 - (3.2.5) Girdler et. al. (1969) Model Using the Herrin (1968) Velocity Depth Profile for the Standard Earth
 - (3.2.5.1) Eastern Rift Source above the Crustal Intrusive - East West Rays
 - (3.2.5.2) Western Rift Source - East West Rays
 - (3.2.5.3) Rays Travelling North South
 - (3.2.5.4) Mid-Atlantic Ridge Source
 - (3.2.6) Girdler et. al. (1969) Model Using the Anderson and Kovach (1969) Velocity Depth Profile for the Standard Earth
 - (3.2.6.1) Girdler et. al. (1969) Model (3) with an Eastern Rift Source above the Crustal Intrusive - East West Rays

- (3.2.6.2) Girdler et. al. (1969) Model (4) with
an Eastern Rift Source - East West Rays
- (3.2.6.3) Girdler et. al. (1969) Model (3) with a
Western Rift Source - East West Rays
- (3.2.6.4) Rays Travelling North South
- (3.2.7) Sowerbutt's (1972) Model (4) Using the Herrin (1968)
Velocity Depth Profile for the Standard Earth
 - (3.2.7.1) Eastern Rift Source Above the Crustal
Intrusive - East West Rays
 - (3.2.7.2) Western Rift Source - East West Rays
 - (3.2.7.3) Mid-Atlantic Ridge Source
 - (3.2.7.4) Rays Travelling North South
- (3.2.8) Sowerbutt's (1972) Models (1), (2) and (3) Using
the Herrin (1968) Velocity Depth Profile for the
Standard Earth
 - (3.2.8.1) Sowerbutt's (1972) Model (1) with a
Western Rift Source - East West Rays
 - (3.2.8.2) Sowerbutt's (1972) Model (2) with an
Eastern Rift Source - East West Rays
 - (3.2.8.3) Sowerbutt's (1972) Model (3) with an
Eastern Rift Source - East West Rays
 - (3.2.8.4) Sowerbutt's (1972) Models (1), (2) and
(3) with a Mid-Atlantic Ridge Source
 - (3.2.8.5) Sowerbutt's (1972) Models - Rays
Travelling North South
- (3.2.9) Darracott et. al. (1972) Model Using the Anderson
and Kovach Velocity Depth Profile for the Standard
Earth

(3.2.10) Comparison of the Observed and RAY Traced Travel
Time 'Corrections' For Events in the North Western
Rift and Central Tanzania

(3.2.10.1) Observed Travel Time 'Corrections'

(3.2.10.2) RAY Traced Travel Time 'Corrections'

(3.2.10.3) Comparison of the RAY Traced Estimates
with the Observed Travel Time
'Corrections'

(3.2.10.4) Conclusions and Future Use of RAY
Tracing to Africa.

C H A P T E R 3

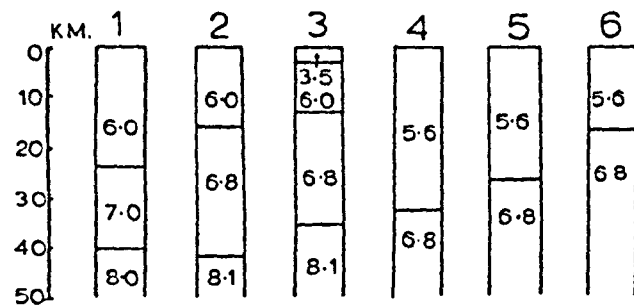
RAY TRACING APPLIED TO AFRICA

In the first section of this chapter RAY tracing is used to obtain a spherically symmetric velocity depth model which represents the average velocity beneath east and southern Africa. The vast majority of earthquakes used in this section are situated in the Red Sea, the Gulf of Aden and the East African Rift, while most of the receiver stations are situated on the Precambrian Shield of Africa. It is well known that positive travel time corrections are associated with tectonically active regions, such as mid-ocean ridge type structures, whereas negative corrections tend to be associated with stable shield regions (Herrin and Taggart (1968), Lilwall and Douglas (1970)). Africa is no exception to these rules and therefore any laterally homogeneous model will represent the average velocity beneath a young rift structure and a stable continental shield.

In the second section of this chapter RAY tracing is used to test some models which have been obtained from interpretations of gravity data. The travel time anomalies predicated from these models are compared to the observed anomalies discussed by Fairhead and Girdler (1971).

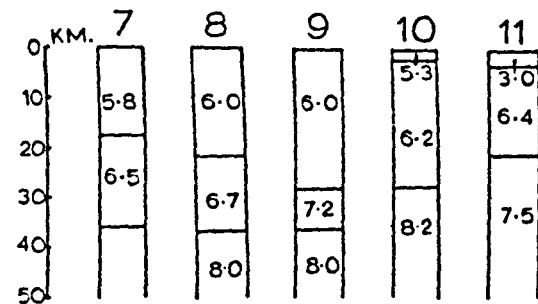
(3.1) An Average Velocity-Depth Profile for East/Southern Africa

Most velocity-depth profiles for Africa have been obtained from either near source refraction surveys or long path surface wave dispersion analysis. The results and locations of the refraction surveys are shown in figure (20) and those of the surface wave dispersion analysis are shown in figure (21). The near source refraction data



1, 2, 3 Bonjer et.al. (1970)

4, 5, 6 Dopp (1964)

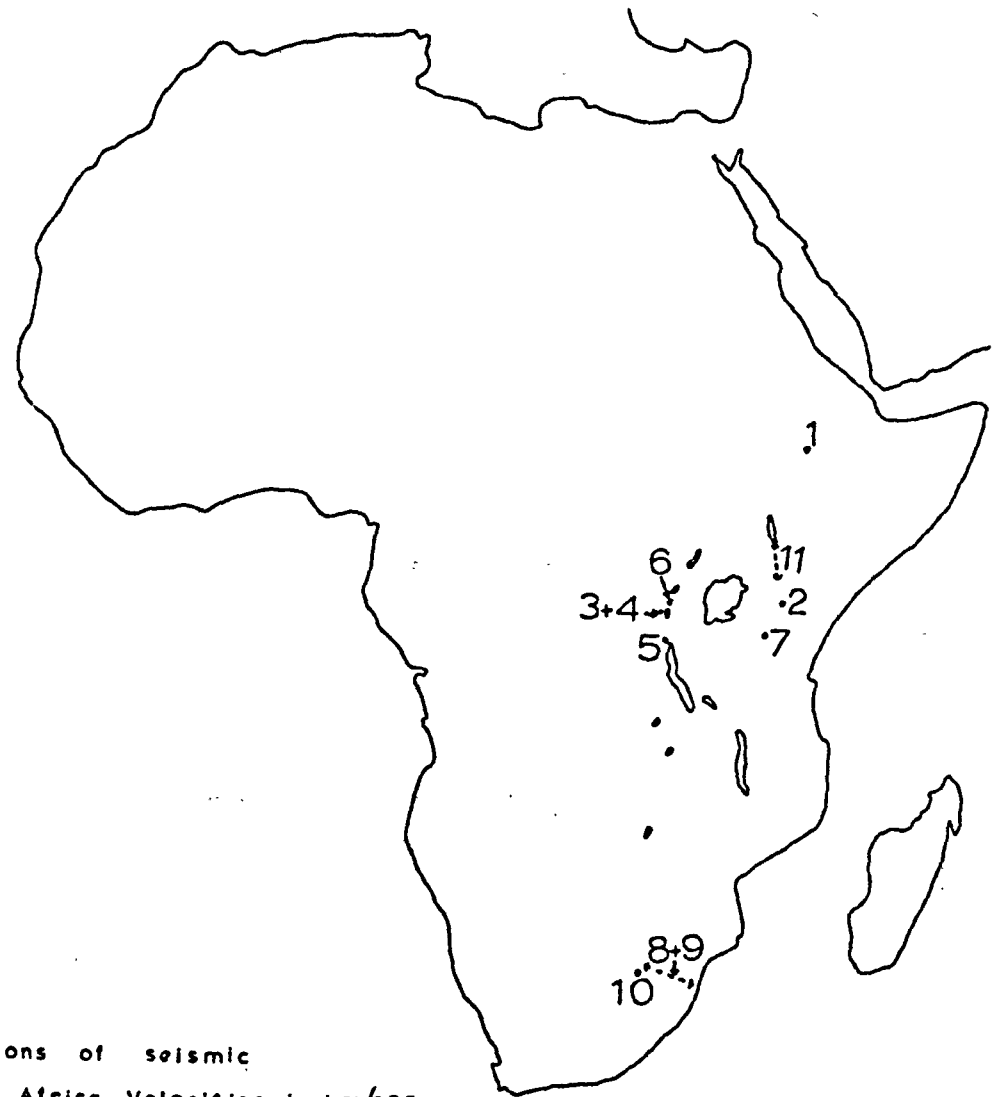


7 Rykounov et.al.(1972)

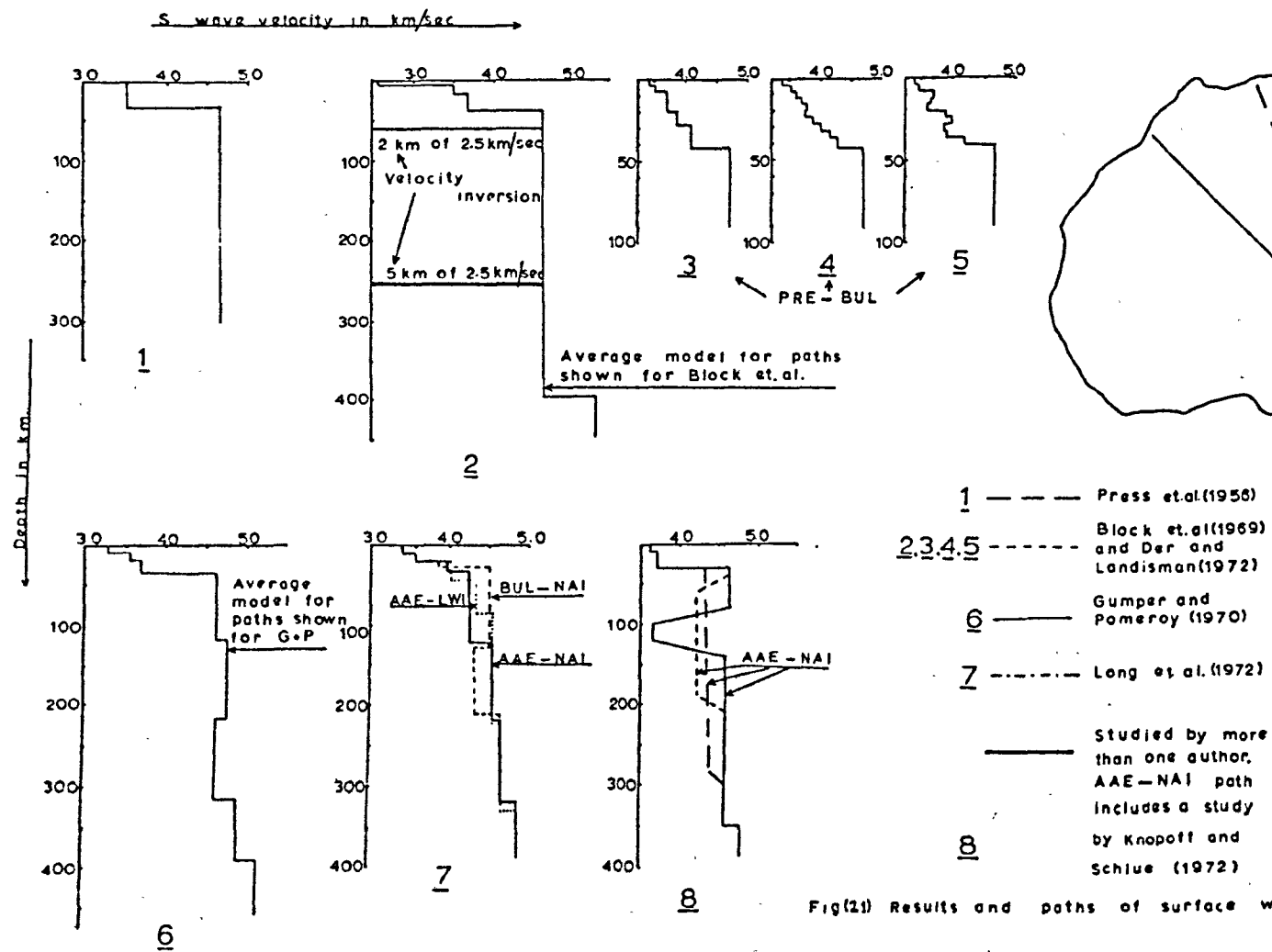
8, 9 Hales and Sacks(1959)

10 Gane et.al. (1956)

11 Griffith et.al.(1971)



Fig(20) Results and locations of seismic refraction experiments in Africa. Velocities in km/sec. (Bonjer et.al. used a spectral response technique)



Fig(21) Results and paths of surface wave dispersion analysis of Africa

only yield information about the crust and top most mantle (i.e. from the surface to approximately 40 km.) while the surface wave dispersion gives information of the gross structure of the top 300 to 400 km. To obtain information about the fine structure of the upper mantle body wave data must be used.

(3.1.1) Travel Time-Distance Curve for East/Southern Africa

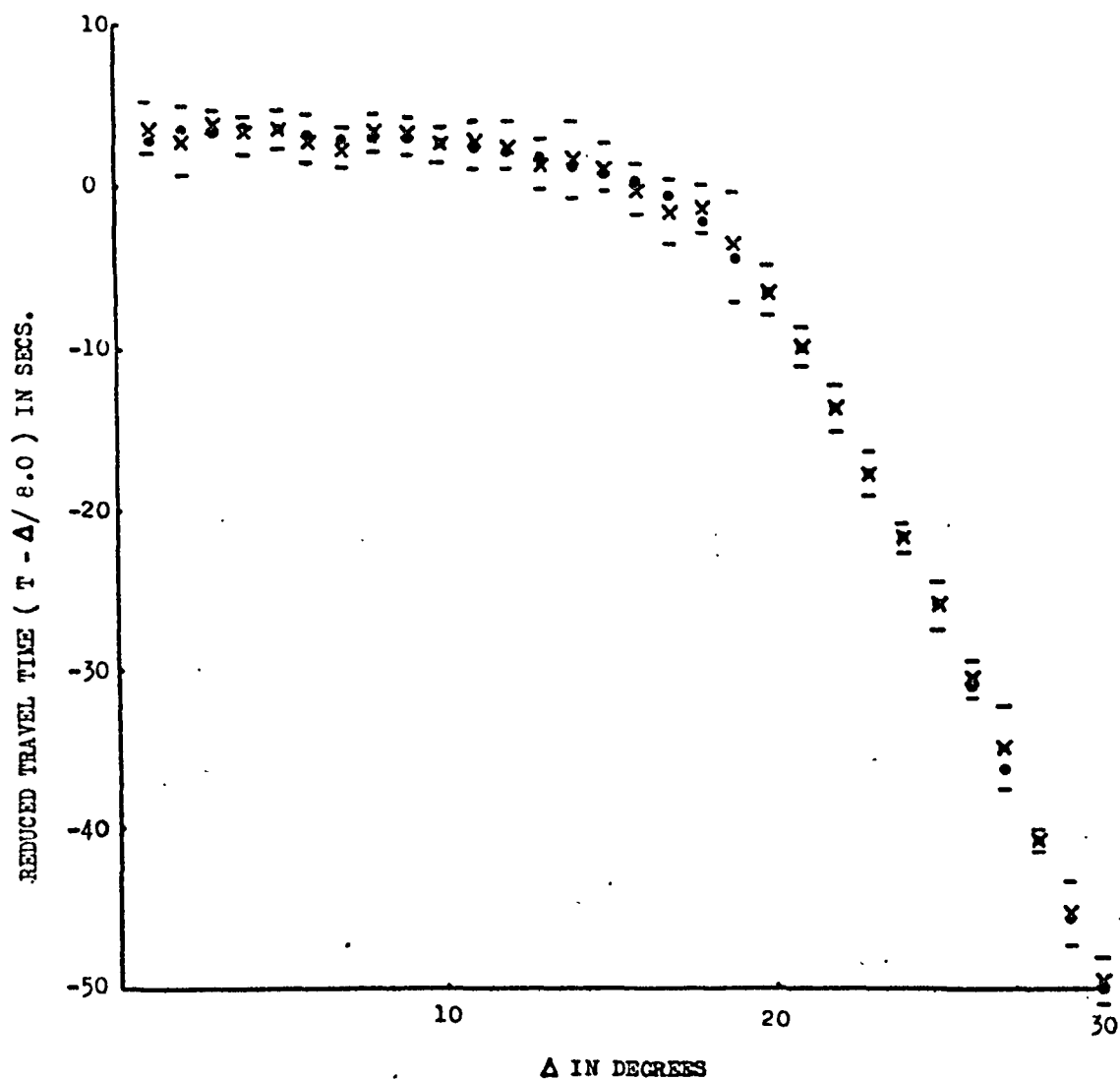
Nuclear explosion data, with well defined epicentre and origin time is the best source of information for near source ($\Delta < 30^\circ$) travel times, but unfortunately this data is not available for east and southern Africa. However there are a large number of earthquakes which have been accurately located by Fairhead (Fairhead and Girdler (1969, 1970, 1971)) using the joint epicentre determination (JED) technique of Douglas (Douglas (1967), Lilwall and Douglas (1970)). This technique has shown its worth by locating the known epicentres of the Longshot (Douglas (1967)), Nevada (Blamey and Gibbs (1968)), Bikini and Eniwetok (Lilwall and Douglas (1970)) explosions all more accurately than the standard method. When this technique is applied to African earthquakes a much improved correlation between the epicentre and mapped faults is obtained (Fairhead and Girdler (1969, 1970, 1971)). Fairhead and Girdler (1969) claim that the locations may be accurate to ± 2 km. using far and near stations for the epicentre determination. Using these new epicentres Fairhead (1968) has obtained an average travel time curve for sources and receivers in Africa. This has been updated by the present author using the more recent events given in Fairhead and Girdler (1970) for the Red Sea and Gulf of Aden. Each data point on the reduced travel time curve (figure (22)) represents the average travel time for distances within $\pm \frac{1}{2}^\circ$ of the centre point. This curve must be viewed as a preliminary travel time curve, as it only represents the first

stage of the normal procedure for obtaining a standard travel time curve (Herrin and Taggart (1968)). The next stage would involve the relocation of all the events using the new travel time curve, and this process would then be repeated until satisfactory convergence was obtained.

(3.1.2) 'Smoothed' Travel Times and Average Velocity Depth Profiles

A large number of velocity-depth profiles were fed into the RAY tracing program to see if it was possible to obtain a reasonable model which would fit the travel time data of figure (22) to within the standard error of the mean (the standard deviation is shown in figure (22)). It was not possible to fit the data to this accuracy because of the jumps in the travel time in the regions $5^{\circ} < \Delta < 8^{\circ}$ and $16^{\circ} < \Delta < 20^{\circ}$. The data were therefore smoothed with smoothing splines (chapter (1) and Curtis and Simshoni (1970)). The final smoothed travel time curve of figure (23) represents the least smoothed curve (i.e. the lowest value of S in the expression (66)) for which a plausible velocity depth profile could be obtained. It is pertinent to point out that the classical Weichert-Herglotz method of inverting travel time data (see Bullen (1965)) requires monotonically decreasing values of $dt/d\Delta$ with distance and therefore could not be used to obtain a velocity depth profile from the data of figure (22). Additional smoothing would be required before this technique could be applied.

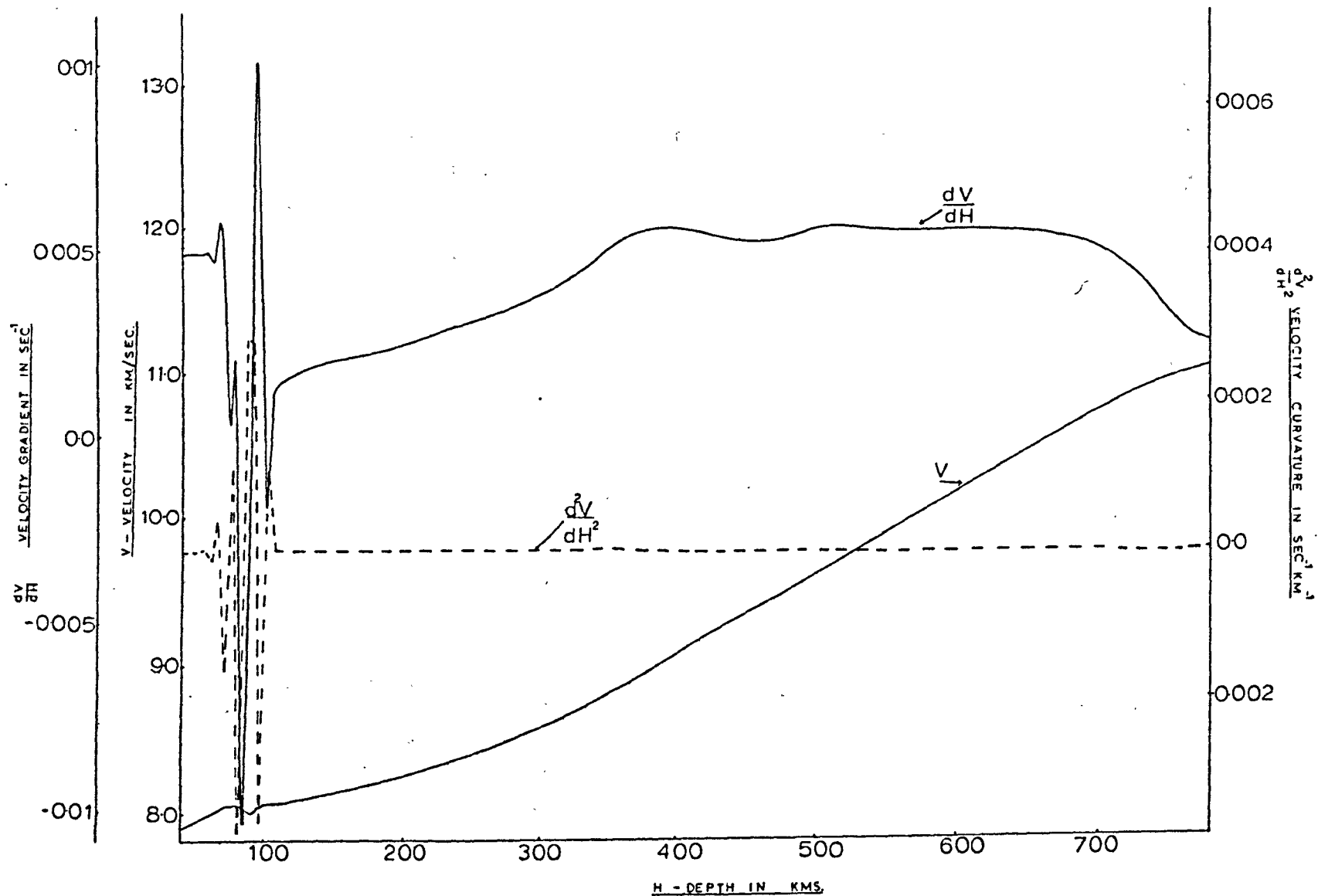
A velocity depth profile obtained by trial and error from RAY tracing which produces travel times consistent with the smoothed travel times of figure (22) is shown in figure (23). Only the region below 35 km. depth is shown in figure (23), the crustal model of Gumper and Pomeroy (figure (21)) was used above this depth. In figure (24)



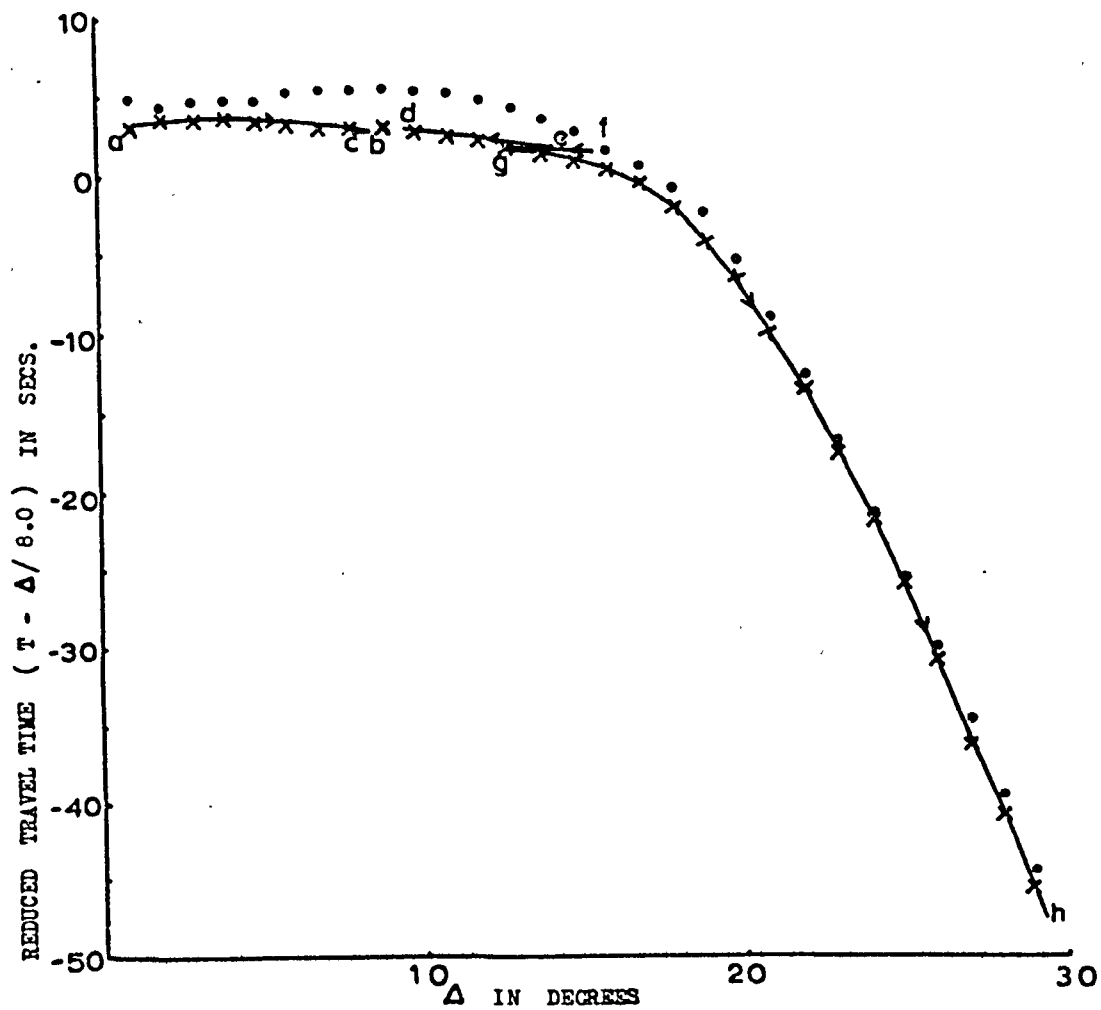
FIG(22) Experimental African travel time curve from Fairhead(1968) . Smoothed travel time curve obtained by applying smoothing splines to Fairhead's data (see chapter(1)).

$\bar{x} \pm \bar{s}$ average travel times from Fairhead(1968). Each data point represents the average travel time for data obtained within one half degree of the centre point. The bars indicate the standard deviation.

• • • smoothed data obtained with smoothing splines.



FIG(23) VELOCITY AND FIRST AND SECOND DERIVATIVE OF VELOCITY WITH RESPECT TO DEPTH FOR FAIRHEAD'S (1968) EAST AFRICAN TRAVEL TIME - DISTANCE CURVE, OBTAINED BY RAY TRACING



FIG(24) Comparison of experimental and theoretical travel time curves for East Africa.

—— theoretical curve obtained by trial and error using the ray tracing program described in Appendix(A). The resultant velocity versus depth profile is shown in fig(23).

x x x experimental travel time curve of Fairhead (1960) smoothed with smoothing splines (see chapter(1) and Curtis and Shimshoni(1970)).

• • • Jeffreys - Bullen travel time curve.

Arrows indicate the direction of increasing angle of incidence of the ray with the Earth's surface.

Depth (km.)	African Body Wave Model (km/sec)	Herrin Model (km/sec)	J-B Model (km/sec)	Depth (km.)	African Body Wave Model (km/sec)	Herrin Model (km/sec)	J-B Model (km/sec)
0.0	5.9000	5.0000	5.5700	165.0	8.1622	8.2332	8.3300
5.0	5.9000	5.0000	5.5700	170.0	8.1736	8.2454	
10.0	6.1500	6.0000	5.5700	175.0	8.1851	8.2580	
15.0	6.1500	6.0000	5.5700	180.0	8.1968	8.2710	
20.0	6.6000	6.7500	6.5000	185.0	8.2088	8.2843	
25.0	6.6000	6.7500	6.5000	190.0	8.2210	8.2980	
30.0	6.6000	6.7500	6.5000	195.0	8.2335	8.3120	
35.0	6.6000	6.7500	6.5000	200.0	8.2462	8.3264	
40.0	7.8875	8.0491	7.7500	205.0	8.2593	8.3410	
45.0	7.9125	8.0582		210.0	8.2726	8.3560	
50.0	7.9375	8.0642		215.0	8.2862	8.3713	
55.0	7.9625	8.0698		220.0	8.3001	8.3870	
60.0	7.9875	8.0753		225.0	8.3143	8.4029	
65.0	8.0125	8.0806		230.0	8.3288	8.4191	
70.0	8.0375	8.0859		235.0	8.3436	8.4357	
75.0	8.0425	8.0911		240.0	8.3587	8.4525	
80.0	8.0440	8.0962		245.0	8.3741	8.4696	
85.0	8.0000	8.1013		250.0	8.3897	8.4870	
90.0	8.0000	8.1064		255.0	8.4057	8.5047	
95.0	8.0440	8.1115	7.9400	260.0	8.4220	8.5227	
100.0	8.0440	8.1165		265.0	8.4386	8.5410	
105.0	8.0465	8.1219		270.0	8.4555	8.5595	
110.0	8.0539	8.1285		275.0	8.4728	8.5783	
115.0	8.0618	8.1356		280.0	8.4904	8.5973	
120.0	8.0704	8.1432		285.0	8.5084	8.6167	
125.0	8.0794	8.1513		290.0	8.5268	8.6362	
130.0	8.0888	8.1599		295.0	8.5456	8.6561	
135.0	8.0985	8.1690		300.0	8.5649	8.6762	
140.0	8.1086	8.1786		305.0	8.5846	8.6966	
145.0	8.1189	8.1886		310.0	8.6049	8.7172	
150.0	8.1294	8.1991		315.0	8.6258	8.7380	
155.0	8.1401	8.2101	8.1300	320.0	8.6472	8.7591	
160.0	8.1511	8.2214		325.0	8.6693	8.7804	

Table (6) African Body Wave Velocity Model compared to the standard Jeffreys-Bullen (J-B) and Herrin Velocity Models.

Depth (km.)	African Body Wave Model (km/sec)	Herrin Model (km./sec)	J-B Model (km/sec)	Depth (km.)	African Body Wave Model (km/sec)	Herrin Model (km/sec)	J-B Model (km/sec)
325.0	8.6693	8.7804	8.7500	485.0	9.5242	9.5626	9.9100
330.0	8.6921	8.8020		490.0	9.5517	9.5895	
335.0	8.7156	8.8238		495.0	9.5794	9.6165	
340.0	8.7397	8.8458		500.0	9.6073	9.6437	
345.0	8.7647	8.8680		505.0	9.6355	9.6709	
350.0	8.7903	8.8905		510.0	9.6637	9.6981	
355.0	8.8166	8.9131		515.0	9.6921	9.7255	
360.0	8.8433	8.9360		520.0	9.7204	9.7530	
365.0	8.8705	8.9590		525.0	9.7486	9.7805	
370.0	8.8981	8.9823		530.0	9.7768	9.8080	
375.0	8.9259	9.0058		535.0	9.8049	9.8356	
380.0	8.9539	9.0294		540.0	9.8329	9.8632	
385.0	8.9820	9.0532		545.0	9.8608	9.8908	
390.0	9.0102	9.0773		550.0	9.8887	9.9185	
395.0	9.0383	9.1015	8.9700	555.0	9.9165	9.9462	
400.0	9.0664	9.1258		560.0	9.9443	9.9740	
405.0	9.0943	9.1503		565.0	9.9721	10.0018	
410.0	9.1221	9.1750		570.0	9.9999	10.0296	
415.0	9.1498	9.1999		575.0	10.0277	10.0574	
420.0	9.1772	9.2248		580.0	10.0556	10.0853	
425.0	9.2044	9.2499		585.0	10.0834	10.1132	
430.0	9.2314	9.2752		590.0	10.1113	10.1411	
435.0	9.2582	9.3007		595.0	10.1392	10.1690	
440.0	9.2848	9.3262		600.0	10.1671	10.1970	
445.0	9.3112	9.3519		605.0	10.1950	10.2249	10.26
450.0	9.3376	9.3778		610.0	10.2229	10.2528	
455.0	9.2640	9.4038		615.0	10.2508	10.2807	
460.0	9.3903	9.4299		620.0	10.2787	10.3086	
465.0	9.4168	9.4562		625.0	10.3065	10.3364	
470.0	9.4434	9.4826		630.0	10.3343	10.3642	
475.0	9.4701	9.5091		635.0	10.3621	10.3920	
480.0	9.4970	9.5358	9.5000	640.0	10.3899	10.4197	

Table (6) (cont.)

Depth (km.)	African Body Wave Model (km/sec)	Herrin Model (km/sec)	J-B Model (km/sec)
640.0	10.3899	10.4197	10.55
645.0	10.4176	10.4474	
650.0	10.4452	10.4750	
655.0	10.4727	10.5024	
660.0	10.5001	10.5297	
665.0	10.5274	10.5570	
670.0	10.5545	10.5840	
675.0	10.5815	10.6109	
680.0	10.6082	10.6375	
685.0	10.6348	10.6638	
690.0	10.6610	10.6899	
695.0	10.6869	10.7157	
700.0	10.7125	10.7412	
705.0	10.7376	10.7664	
710.0	10.7621	10.7911	
715.0	10.7861	10.8154	
720.0	10.8093	10.8392	
725.0	10.8317	10.8624	
730.0	10.8532	10.8850	
735.0	10.8736	10.9068	
740.0	10.8930	10.9279	
745.0	10.9112	10.9479	
750.0	10.9282	10.9663	
755.0	10.9441	10.9819	
760.0	10.9590	10.9933	
765.0	10.9730	11.0029	
770.0	10.9864	11.0134	
775.0	10.9994	11.0240	
780.0	11.0122	11.0348	
785.0	11.0248	11.0455	

Table(6) (cont.)

the reduced travel time curves for (a) the velocity depth profile of figure (23), (b) the smoothed travel time data for east/southern Africa and (c) the Jeffreys - Bullen travel times are shown for comparison. The important feature of this figure is that it demonstrates how first arrivals predicted by the model of figure (23) coincide extremely well with the smoothed observed data.

The digitised velocity data of figure (23) are given in table (6) along with the standard Jeffreys-Bullen (1940) and Herrin (1968) Earth models. From figure (23) and table (6) the following should be noted:-

- (i) All the velocities are lower than the corresponding Herrin velocities. At some depths the velocities are also lower than the Jeffreys-Bullen values while at other depths the velocities are slightly higher.
- (ii) There is a low velocity channel between 80 km. and 90 km. depth. Although there is an inherent non-uniqueness in the inversion of travel time data which allows velocity inversions (see for example Gerver and Markushevich (1966, 1967) and Johnson (1967)), it was not possible to obtain a model to fit the smoothed data of figure (22) without a low velocity channel. However it cannot be stated with any certainty that the low velocity channel is a significant feature, for the smoothing criteria applied to the original averaged data of figure (22) was that of 'least smoothing' which would give a reasonable velocity depth profile. If the smoothing is increased then the requirement of a low velocity channel disappears. To confirm that a low velocity channel exists, later P phases must be analysed.
- (iii) Above the low velocity channel the velocity gradient is high (0.005 sec^{-1}) while below it, the velocity gradient is at first low.

From the low velocity channel downwards the velocity gradient gradually increases (except over small sections of depth) so that the velocity depth curve approaches the Herrin (1968) curve. At 600 km. depth the difference between figure (23) and the Herrin curve is only 0.03 km/sec.

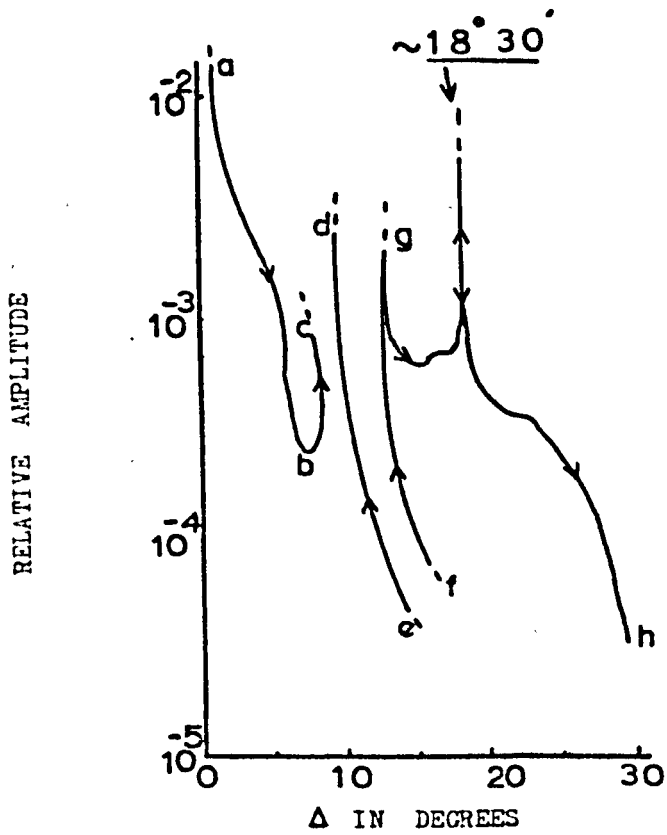
(iv) The very small velocity inversion shown just below the main velocity inversion, best observed on the first derivative curve (figure (23)), is caused by the spline procedure in its attempt to obtain continuity of the first and second derivatives. This inversion is the cause of the small retrograde branch (f-g) of the travel time curve of figure (24).

(3.1.3) Predicted Relative Amplitude ((Relative Intensity)^{1/2}) Curve
for East/Southern Africa

The relative amplitude curve, due to geometrical spreading, for the velocity depth profile of figure (23) is shown in figure (25). In this figure the letters a to h indicate the corresponding section of travel time curve of figure (24). Smoothing splines were used to obtain the final velocity depth profile shown in figure (23) so that each branch of the relative amplitude curve is smooth.

There are several important features to be noted from figure (25):

- (i) The retrograde branches of the travel time curve produce amplitude curves which rise very sharply with increasing angle of incidence (and therefore decreasing epicentral distance).
- (ii) The peak shown at $\Delta = 18^{\circ} 30'$ is produced by the rays that bottom near to the velocity gradient 'hump' between 300 km. and 420 km. depth (figure (23)).



fig(25) Relative amplitude $((\text{Relative intensity})^{\frac{1}{2}})$ curve due to geometrical spreading for the East African velocity versus depth profile (fig(23)). Arrows indicate the direction of increasing angle of incidence of the rays with respect to the Earth's surface. Letters a to h indicate the corresponding sections of travel time curve shown in fig(24).

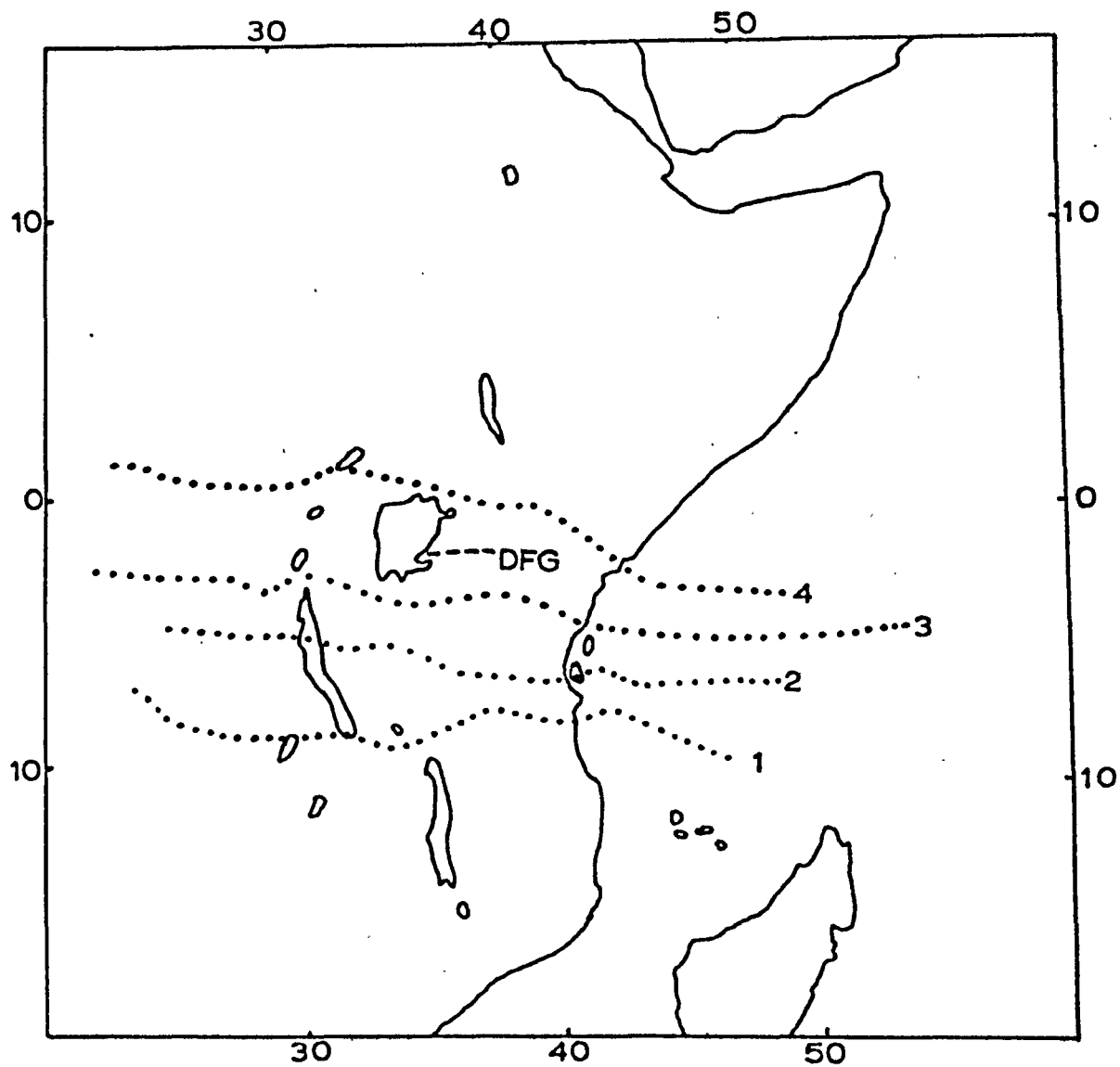
(iii) For Δ greater than approximately 16° the relative amplitude curve of figure (25) follows very closely the relative amplitude derived from the Herrin velocity depth model (figure 16)). Between $\Delta = 22^\circ$ and $\Delta = 27^\circ$ there is almost a perfect match. There is very little correlation between the Jeffrey-Bullen relative amplitude curve (figure (15)) and figure (25) except in terms of 'orders of magnitude'.

Unfortunately the amplitude data available from African events recorded in Africa is very poor. To check the curve in figure (25) against real data would require a suite of well distributed earthquakes. To obtain an average amplitude curve, each amplitude estimate would have to be normalised, so that all the amplitudes refer to a single magnitude event (magnitude 5 say, (see Nuttli (1972))).

(3.2) Application of RAY Tracing to Models of the East African Rift

(3.2.1) Gravity Profiles

Sowerbutts (1969, 1972) has compiled four long (> 2500 km.) gravity profiles crossing the East African Rift between latitudes 1°N. and 10°S. (figure (26)). All the profiles (figure (27), (47), (51) and (55)) show a long wavelength (~ 1000 km. wide) shallow gradient negative Bouguer anomaly across the East African Plateau, the maximum amplitude of which increases from 500 g.u. on profile (1) to 1500 g.u. on profile (4). Detailed gravity surveys (Searle (1969, 1970), Darracott et. al. (1972)) between latitudes 0.25°N. to 4°S. have revealed a 40 km. to 80 km. wide positive Bouguer anomaly of 300 g.u. to 600 g.u. amplitude coincident with the axial trough of the eastern rift. This anomaly is observed north of approximately 2°S. and is therefore superimposed on the long wavelength negative anomaly of profile (4) (e.g. figure



FIG(26) Location of gravity profiles. Lines 1, 2, 3, 4 are taken from Sowerbutts (1972) and line marked DFG is from Darracott et.al.(1972).

(27)). In the following all the gravity anomalies are Bouguer anomalies.

A number of authors have analysed the gravity field across the East African Plateau. Of these Baker and Wohlenberg (1971) and Khan and Mansfield (1971) do not interpret the complete negative anomaly and are therefore not discussed further here. The remaining interpretations based on the model of Girdler et. al. (1969) (e.g. Girdler and Sowerbutts (1970), Searle (1969, 1970), and Darracott et. al. (1972)) and the revised interpretations of Sowerbutts (1972) are fundamentally different from each other. The models of Girdler et. al. (1969) and Darracott et. al. (1972) take the source of the long wavelength negative anomaly to be a low density asthenolith which has thinned and partly replaced the continental lithosphere beneath East Africa (see figure (27) and figure (60)). In these models the low density material is situated above 100 km. depth. The axial positive anomaly is taken to be a crustal intrusion which is continuous with the asthenolith (Searle (1969), 1970)).

The revised models of Sowerbutts (1972) take the source of the long wavelength negative anomaly to be a body of low density material situated between 95 km. and 140 km. depth (see figure (47)). To account for the axial positive anomaly Sowerbutts (1972) allows a relatively thin 'plume' of low density material to extend to and intrude the lower density crust of the eastern rift (figure (42)).

In sections (3.2.5) to (3.2.9) RAY tracing is applied to the models of Girdler et. al. (1969) (including the interpretation of the axial positive anomaly of Searle (1969, 1970)), Sowerbutts (1972) and Darracott et. al. (1969) to show the different ray patterns, travel time anomalies and relative amplitudes that would be produced by these models.

(3.2.2) Standard Velocity Depth Profiles

Before applying RAY tracing to laterally heterogeneous velocity models it is necessary to choose a 'standard' velocity depth profile to represent the 'normal' mantle and crust (i.e. mantle and crust unperturbed by rifting etc). From figure (20) and figure (21) it is readily observed that there is no generally accepted velocity depth profile for Africa away from the rifting. The velocity depth profile derived in section (3.1) used earthquakes situated in the rifted regions of Africa and therefore cannot be used to represent the 'normal' mantle and crust beneath Africa. For this reason most of the RAY tracings in the following sections have used the velocity depth profile of Herrin (1968). The gravity models of Girdler et. al. (1969) and Darracott et. al. (1972) require a high density lithosphere overlying a low density and presumably a low velocity asthenosphere; to accommodate this interpretation a smoothed hybrid of the velocity depth profile of Anderson and Kovach (1969) (table (7)) is used as the base model for some of the RAY tracings. The top 100 km. of the Anderson and Kovach (1969) velocity depth profile, which is primarily an oceanic model, has been altered so that the crustal model of Herrin (1968) overlies an upper mantle in which the velocity increases linearly with depth (table (7)); below 100 km. the Anderson and Kovach model has been smoothed with smoothing splines (section (1.4.2)). Only rays which have their maximum depth above 350 km. in the Anderson and Kovach (1969) model are utilised. Below this depth there are several second order discontinuities which produce a multiplicity of arrivals over a wide range of Δ . This multiplicity would obscure the perturbations of the ray paths due to the rift models.

Depth (km)	Anderson and Kovach (1969) Earth Model (km/sec)	Herrin(1968) Earth Model (km/sec)	Depth (km)	Anderson and Kovach (1969) Earth Model (km/sec)	Herrin(1968) Earth Model (km/sec)
0.0	6.0	6.0	135.0	7.5402	8.1690
15.0	6.0	6.0	140.0	7.5566	8.1786
15.0	6.75	6.75	145.0	7.5803	8.1886
40.0	6.75	6.75	150.0	7.6114	8.1991
			155.0	7.6501	8.2101
40.0	8.0154	8.0491	160.0	7.6964	8.2214
45.0	8.0231	8.0582	165.0	7.7500	8.2332
50.0	8.0377	8.0642	170.0	7.8101	8.2454
55.0	8.0385	8.0698	175.0	7.8752	8.2580
60.0	8.0462	8.0753	180.0	7.9435	8.2710
65.0	8.0538	8.0806	185.0	8.0125	8.2843
70.0	8.0615	8.0859	190.0	8.0796	8.2980
75.0	8.0692	8.0911	195.0	8.1424	8.3120
80.0	8.0769	8.0962	200.0	8.1989	8.3264
85.0	8.0846	8.1013	205.0	8.2476	8.3410
90.0	8.0923	8.1064	210.0	8.2880	8.3560
95.0	8.1000	8.1115	215.0	8.3203	8.3713
100.0	8.1077	8.1165	220.0	8.3457	8.3870
			225.0	8.3655	8.4029
100.0	7.5792	8.1165	230.0	8.3812	8.4191
105.0	7.5644	8.1219	235.0	8.3942	8.4357
110.0	7.5505	8.1285	240.0	8.4056	8.4525
115.0	7.5389	8.1356	245.0	8.4162	8.4696
120.0	7.5309	8.1432	250.0	8.4264	8.4870
125.0	7.5279	8.1513	255.0	8.4364	8.5047
130.0	7.5307	8.1599			

Table(7) Anderson and Kovach velocity depth profile compared to the Herrin curve.

Depth (km)	Anderson and Kovach (1969) Earth Model (km/sec)	Herrin(1968) Earth Model (km/sec)
255.0	8.4364	8.5047
260.0	8.4466	8.5227
265.0	8.4569	8.5410
270.0	8.4669	8.5595
275.0	8.4771	8.5783
280.0	8.4872	8.5973
290.0	8.4973	8.6167
295.0	8.5072	8.6362
300.0	8.5170	8.6561
305.0	8.5267	8.6762
310.0	8.5363	8.7172
315.0	8.5459	8.7380
320.0	8.5557	8.7591
325.0	8.5657	8.7804
330.0	8.5763	8.8020
335.0	8.5876	8.8238
340.0	8.6000	8.8458
345.0	8.6141	8.8680
350.0	8.6305	8.8905

Table(7) Anderson and Kovach velocity depth profile compared to the Herrin(1968)
(continued)

(3.2.3) Estimation of Seismic Velocity from Density

There is no generally accepted formulation for estimating the seismic velocity of a rock from its density. The modified Nafe-Drake curve (Ludwig et. al.(1971)) is based on a large number of experimental data and is generally consistent with the theoretical models of Birch (1961, 1964). Therefore this curve is used to estimate the seismic velocity contrasts from the inferred density contrasts.

In all the models the velocity within an anomalous region is altered by a constant value from the standard Earth (except at the edges of some of the models where the velocity is allowed to grade linearly to standard Earth values) so that the velocity gradients within these regions are the same as for the standard Earth at the same depth.

(3.2.4) RAY Diagrams

For each of the rift models which have the Herrin (1968) velocity depth profile for the standard mantle and crust the following RAY diagrams (i.e. ray paths, travel time residuals and relative amplitudes) are constructed:

(a) For short epicentral distances ($\Delta < 20^\circ$) the source is placed in the eastern and/or the western rift and rays are traced perpendicular (east and west) and parallel to the rift with 0.25° increments of i_r (e.g. figure (28)), starting with the lowest value of i_r (to the nearest 0.25°) which allows the ray to penetrate into the mantle (i.e. the first ray not reflected at the M discontinuity). The analysis for the easterly trending rays is terminated at the first value of i_r which allows the ray to cross the zero of the model; in most cases the zero of the model corresponds to the East African coast. This often means that only one or two rays are traced in an easterly direction, so that most of the following will be concerned with westerly trending rays.

(b) For long epicentral distances the source is placed in the eastern rift (except model (1) of Sowerbutts (1972) where the source is placed in the western rift) and rays traced in a westerly direction perpendicular to the rift with 1.0° increments of i_r to a maximum value of $i_r = 70^{\circ}$ so that information for $0^{\circ} < \Delta < 80^{\circ}$ is obtained. Due to the symmetry of most of the models, the analysis of the westerly propagating rays for $16^{\circ} < \Delta < 80^{\circ}$ also applies to rays propagating to the east.

(c) For the effect of the rift on rays received in and near to the rift from an event outside of Africa, a source is placed at an epicentral distance corresponding to a mid-Atlantic Ridge event and rays are traced with 0.25° increments of i_r into the region of the rift.

For those rift models which have the Anderson and Kovach (1969) velocity depth profile for the standard mantle and crust only RAY diagrams corresponding to (i) are constructed (for reasons see section (3.2.2)).

Estimates of focal depths for African events are few and of poor quality but do indicate relatively shallow sources (Dopp (1964), Wohlenberg (1969), Tobin et. al. (1969), Rykounov et. al. (1972)). Therefore the focal depth is taken at 15 km. in all the RAY diagrams.

Before examining the RAY diagrams it is worthwhile to note:-

- (i) Thinning and replacing the crust by mantle material (e.g. figure (27)) will in general produce a positive travel time anomaly. The travel time anomaly or travel time residual is the difference between the time of travel in the standard Earth and the time of travel in the perturbed Earth. Simple calculation shows that the anomalies will be positive even allowing for the fact that for a given Δ a ray will not penetrate as deep as it would in a standard Earth.
- (ii) Replacing the standard crust by a higher velocity crustal intrusive (e.g. figure (27)) will also produce positive travel time anomaly.

(iii) Replacing the standard mantle by lower velocity material will produce a negative travel time anomaly.

In the following discussion it will be convenient to refer to the above three effects.

(3.2.5) Girdler et. al. (1969) Model using the Herrin (1968) Velocity Depth Profile for the Standard Earth

In the first two attempts to velocity model the Girdler et. al. (1969) interpretation of gravity profile (4) (figure (26) and figure (27)), the low density low velocity material (-0.4 km/sec contrast with the standard mantle) extends from beneath a thinned crust to 120 km. depth. At the outer boundaries of the model the low velocity material grades linearly into normal mantle material. Between the eastern and western rifts the interpretation of Girdler et. al. (1969) requires an enclave of normal mantle material just below the crust (figure (27)). How this enclave is represented in the velocity models distinguishes between the models referred to here as Girdler et. al. models (1) and (2). In model (1) the enclave is surrounded by velocity discontinuities, while in model (2) the low velocity material grades linearly into the normal mantle. The high density crustal intrusive mentioned in section (3.2.1) is represented in both velocity models by a region of relatively high velocity (+0.58 km/sec contrast with the standard crust) material surrounded by velocity discontinuities.

(3.2.5.1.) Eastern Rift Source above the Crustal Intrusive - East West Rays

$$\Delta < 7^{\circ}$$

=====

From the RAY diagrams (figure (28) to figure (31)) it is clear that the enclave of normal mantle material is most important for $3.1^{\circ} < \Delta < 7^{\circ}$ (Pn rays). Rays of varying travel time residuals are predicted by model (1) (figure (28)), whereas in model (2) (figure (30)) this region is devoid

of rays due to the refractive effects (rays refracted downwards) of the high lateral velocity gradients near the edges of the enclave. In model (1) the travel time residuals change from small positive values for $\Delta < 5^\circ$ to small negative values for $5^\circ < \Delta < 7^\circ$. It is clear that effects (i) and (ii) dominate for $\Delta < 5^\circ$ and that for $\Delta > 5^\circ$ the rays are in the low velocity material for a sufficient length of their path for (iii) to become dominant.

$7^\circ < \Delta < 16^\circ$

The RAY diagrams of models (1) and (2) for $7^\circ < \Delta < 16^\circ$ are very similar, only the Pn rays differ, while for $\Delta > 16^\circ$ they are identical. The following discussion will therefore apply to both models. For $7^\circ < \Delta < 12^\circ$ (ray at $\Delta = 12^\circ$ is marked (a) in figure (28) and figure (29)) the rays are in the anomalous mantle material for between 600 km. and 800 km. of their total path. The first arrivals have negative travel time residuals of 3 sec. to 5.1 sec. Included in these are the rays which are refracted upwards by the high velocity gradient at the base of the anomalous mantle material. These high amplitude rays have a focus in the region $7^\circ < \Delta < 8^\circ$ and are observed intermingled with the lower amplitude Pn rays which have similar travel time residuals in this distance range.

In the region $12^\circ < \Delta < 16^\circ$ the first arrivals correspond to rays which have penetrated the high velocity gradient at the base of the anomalous mantle (figure (29)). These rays have negative travel time residuals from 0.4 sec. to 0.8 sec. In this same region a number of lower amplitude Pn rays arrive 3 sec. to 4 sec. later than the first arrivals; compare the rays past the point marked (a) in figure (28) and figure (29)).

$$\underline{\underline{\Delta > 16^\circ}}$$

For $\Delta > 16^\circ$ all the rays have travelled in mostly normal mantle material (figure (29) and figure (31)). The amplitude of the rays are nearly equal to the standard Earth values while the travel time residuals are from 0.05 sec. to 0.4 sec.; thus demonstrating that effect (iii) is almost compensated for by (i) and (ii) in this distance range. The shadow zone shown at approximately $18^\circ > \Delta > 21^\circ$ is somewhat artificial. If a ray approaches within approximately 2 km. (the integration step size) of two boundaries of velocity discontinuity, then the computer is programmed to terminate the ray and return that 'diffraction is required'. In this case the rays which would be expected at $18^\circ > \Delta > 21^\circ$ approach within 2 km. of the 'M' discontinuity and the western boundary defining the extent of the high velocity material of the crustal intrusive. If the position of the source were to be shifted by only 10 km. then the apparent shadow zone may be shifted by up to 10° .

(3.2.5.2) Western Rift Source - East West Rays

The RAY diagram for the western rift source is relatively simple (figure (32)). The rays travelling west of the rift (this is the same for models (1) and (2)) are in the low velocity mantle material for less than 250 km. of their path. Therefore effect (ii) dominates yielding positive travel time residuals for most of the arrivals. Rays received in the region $3^\circ > \Delta > 6^\circ$ are exceptions to this. These rays would normally correspond to the Pn phase travelling at mantle velocities below the crust mantle boundary. In this model the mantle ray path is interrupted by the vertical boundary connecting the base of the normal and thinned crust (figure (27) and figure (32)). The ray is refracted into the normal crust and continues along its path (only a small change

of i_r is observed as the ray is almost normal to the boundary, figure (32)) but now the ray is travelling at the crustal velocity. This leads to travel time delays of up to 9 sec. in this region. It must be emphasized that a completely different pattern would be obtained if the boundary between the normal and thinned crust was altered.

The first easterly trending ray to penetrate the crust appears to be 'channelled' by the various high velocity gradients of this model (model (2)). This ray would cross the zero of the model (figure (32)) and therefore the computer run was terminated at this stage (see section (3.2.4)). However information about the rays which travel between the eastern and western rifts is given in section (3.2.5.1).

(3.2.5.3) Rays Travelling North South

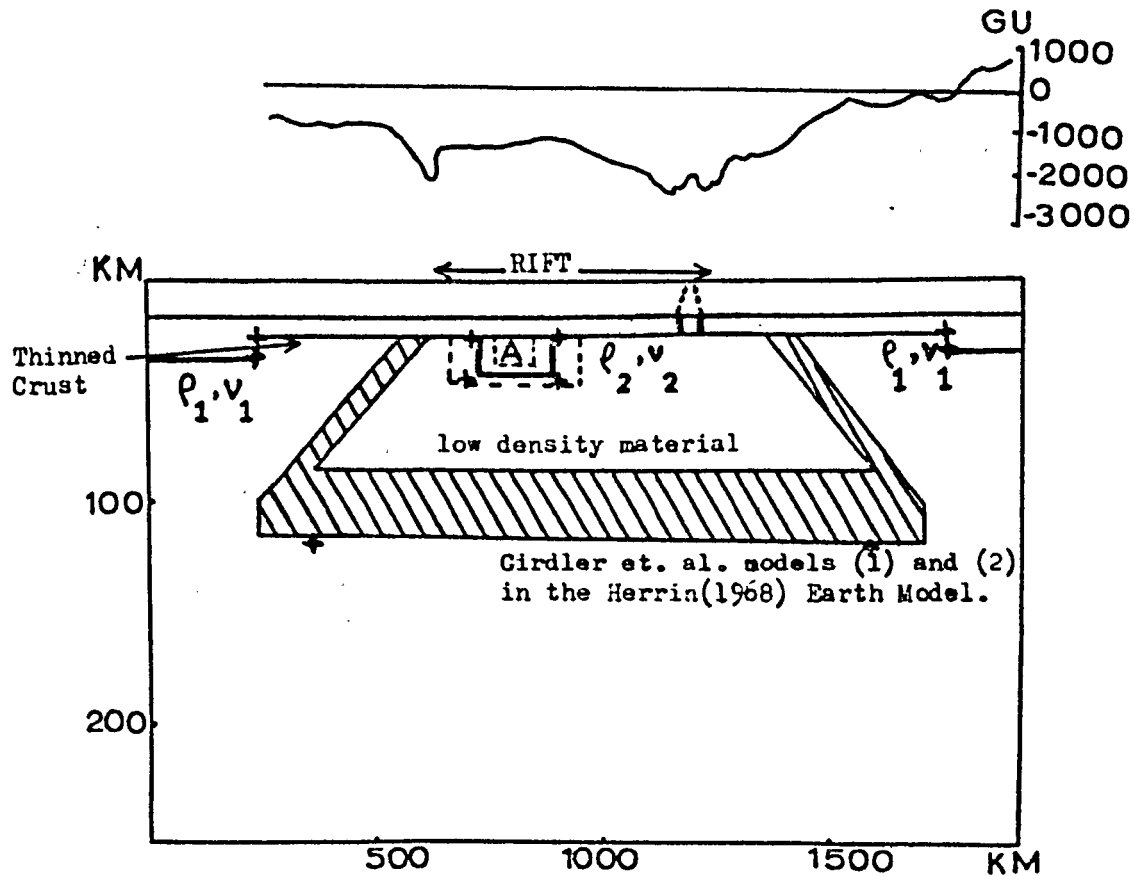
In the RAY diagram of figure (33) both the source and receivers are situated in the Rift. No crustal intrusive is included. This situation corresponds to a ray travelling from any event in the East African Rift except those in the trough of the eastern rift and those above the enclave of normal mantle material. The only effects which need to be considered for this diagram are (i) and (iii).

$$\underline{\underline{\Delta < 7^\circ}}$$

Although only a single ray is plotted for $\Delta < 7^\circ$ it is clear that for approximately $\Delta < 3.5^\circ$ (the ray at 3.57° has a 0.04 sec. negative travel time residual) effect (i) will dominate producing positive travel time residuals, while for $\Delta > 3.5^\circ$ the rays are in the low velocity material for a sufficient length of their path for effect (iii) to become dominant.

$$\underline{\underline{7^\circ < \Delta < 10^\circ}}$$

For $\Delta > 7^\circ$ all the travel time residuals in figure (33) are negative and greater than 0.7 sec. indicating the dominance of effect (iii)



FIG(27) Gravity profile(4) and representative model of Girdler et.al.(1969) and Searle(1970).



- ▨ Marks the extent of the low density asthenolith. In the region of the dashed lines the data values change to normal mantle values linearly. Normal mantle material is assumed for the region marked A. In the model named here as Girdler et.al. model(1) the region A is separated from the low density material by discontinuities (defined by the thick lines) while in the model(2) the low density material grades into the normal material(defined by the dashed lines).
- || Marks the extent of the region of anomalous velocity and density in the crust. This boundary is treated as a discontinuity.
- + Mark the corresponding + shown in fig(28)to fig(34).

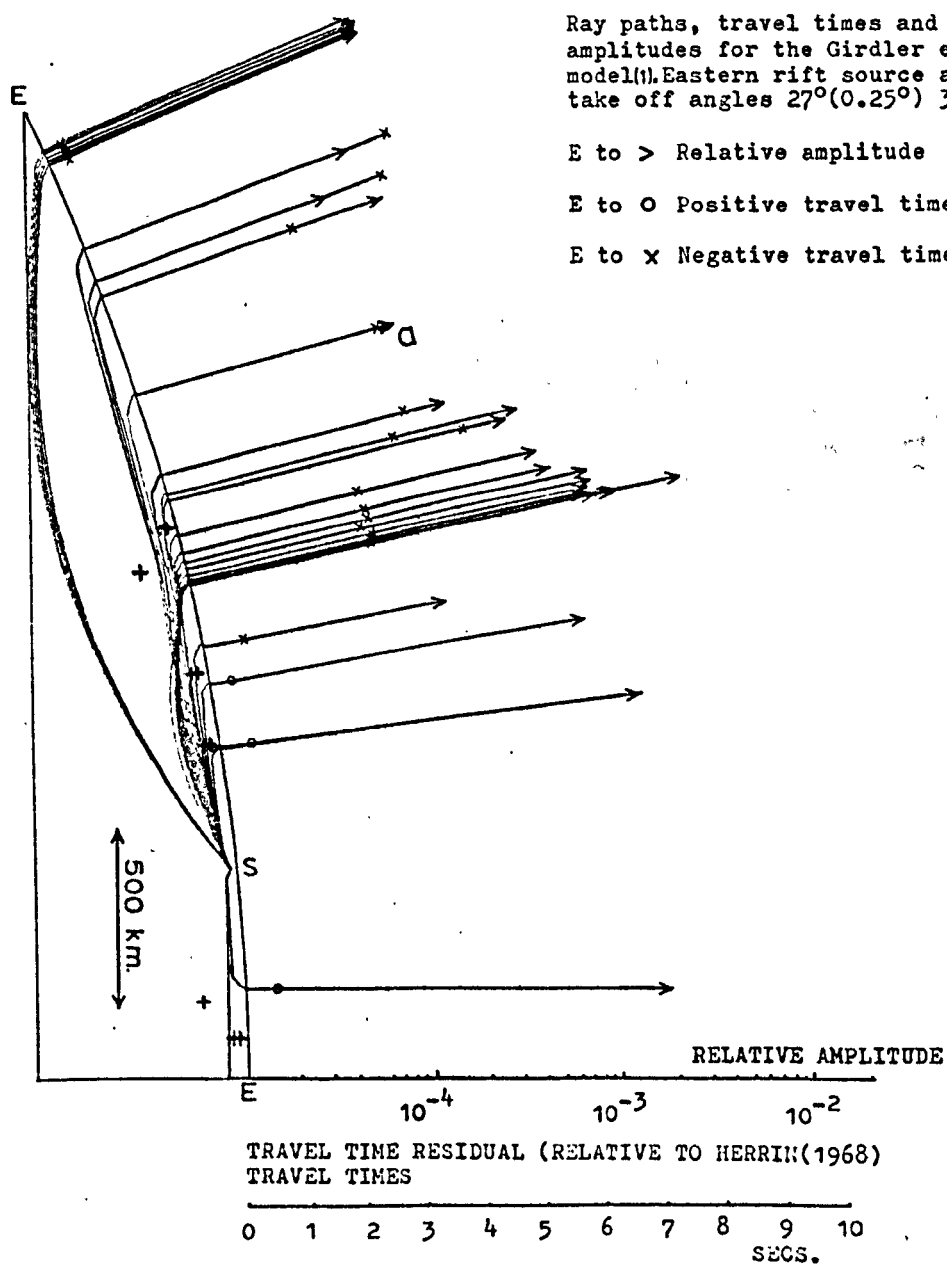
$$\text{s.g. difference} = \rho_2 - \rho_1 = 3.22 - 3.34 = -0.12$$

$$\text{corresponding velocity difference} = -0.4 \text{ km/sec}$$

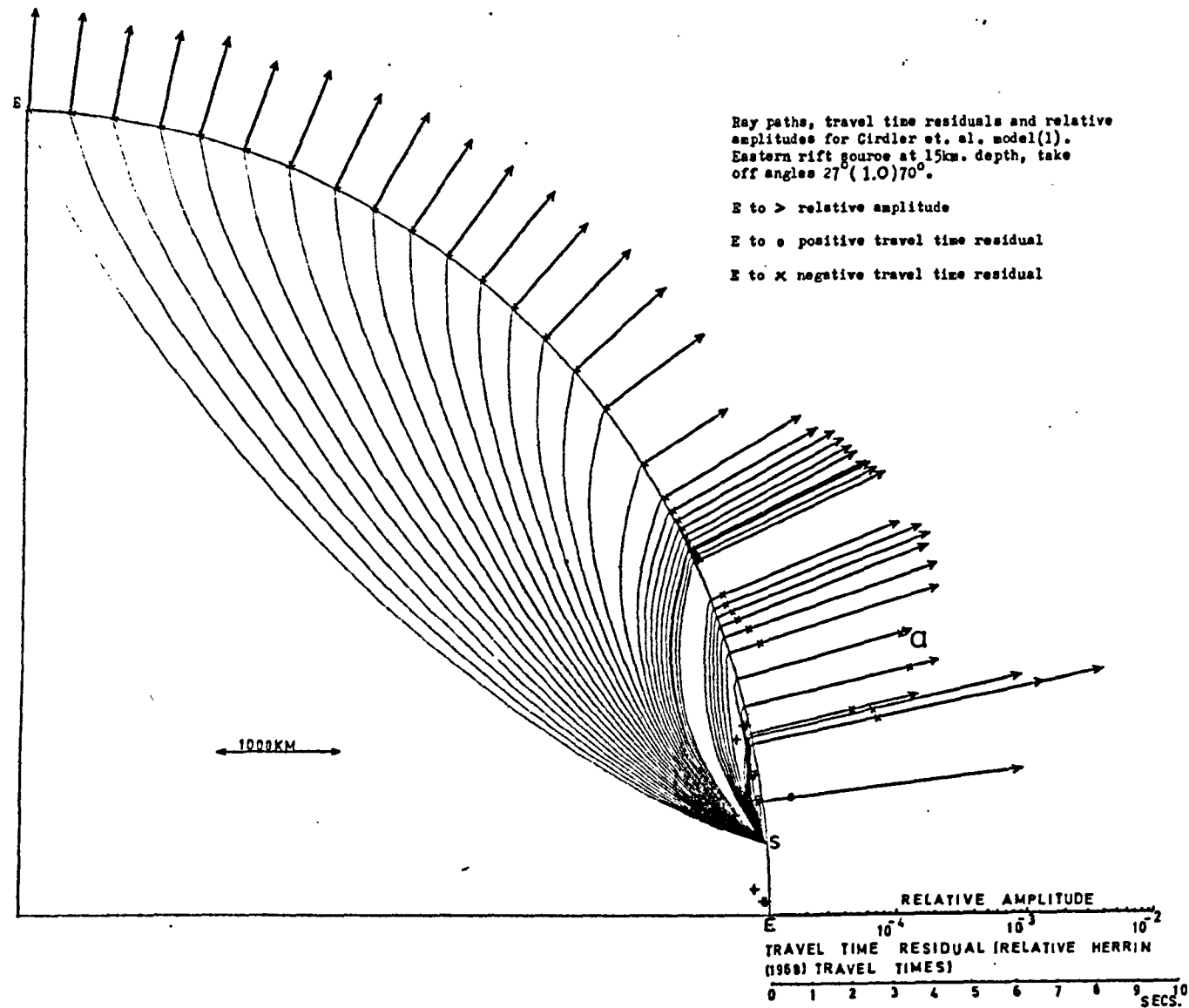
$$\text{s.g. difference in the crust} = 2.9 - 2.77 = 0.13$$

$$\text{corresponding velocity difference} = 0.58 \text{ km/sec.}$$

$$\text{vertical exaggeration } 5 : 1$$



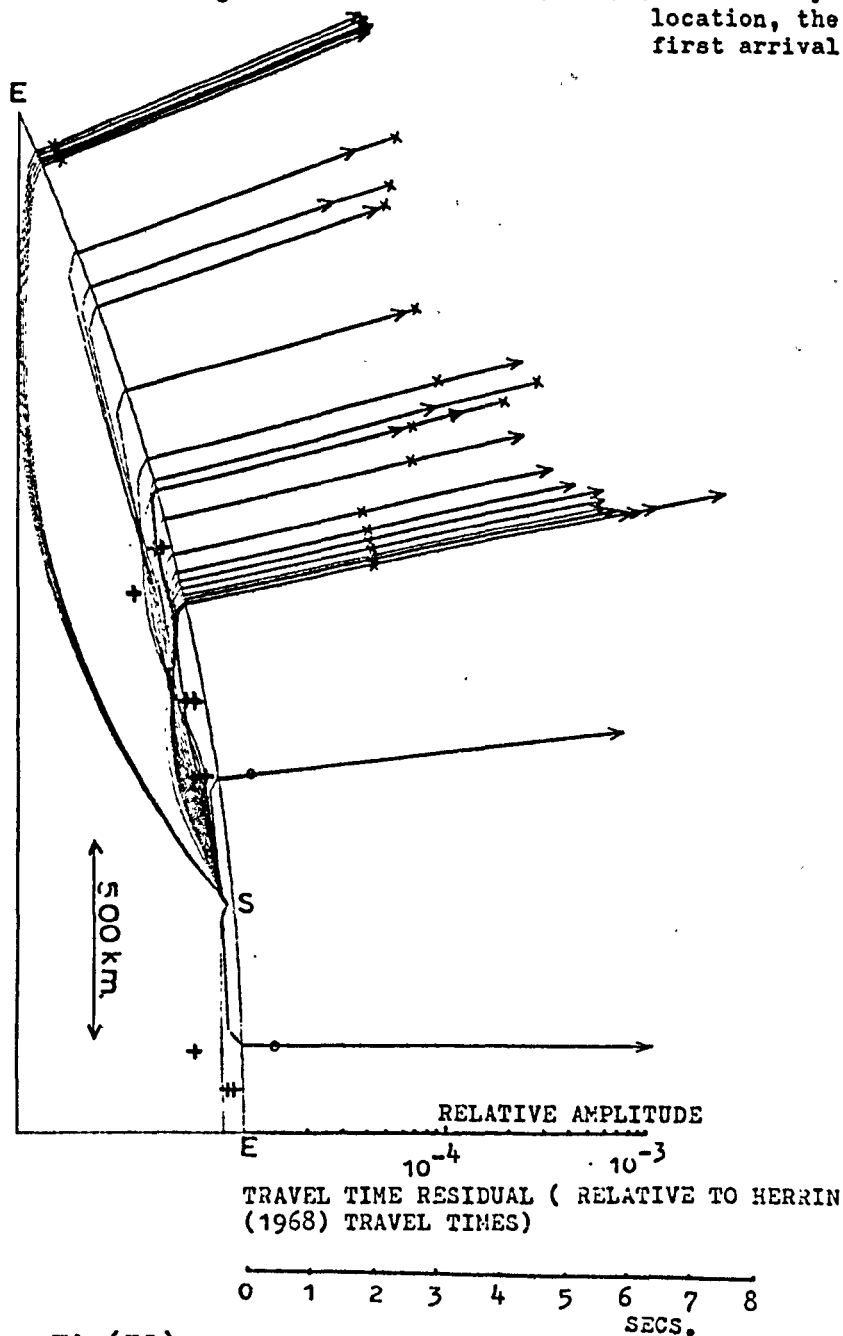
Fig(28)



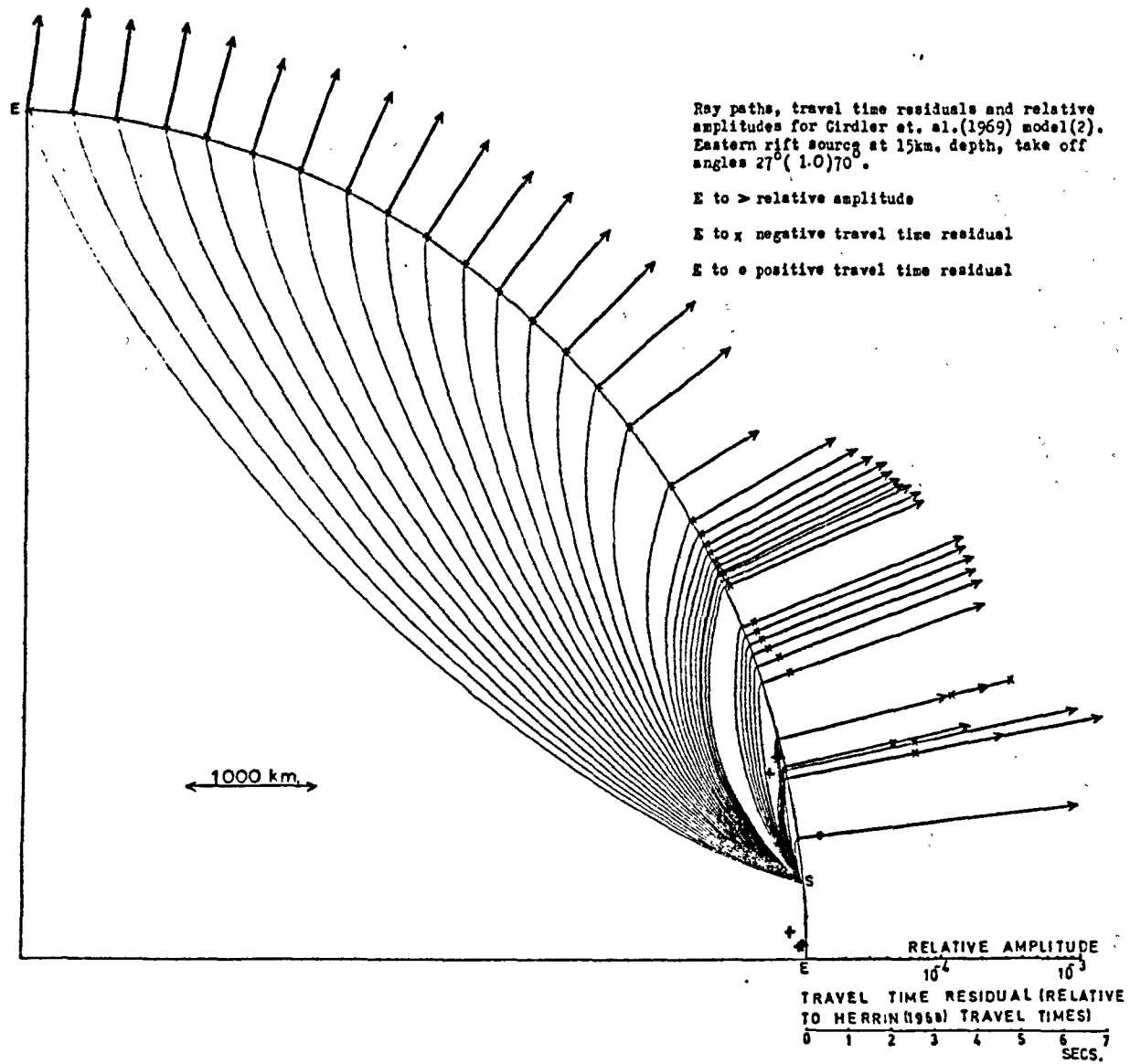
FIG(29)

Ray paths, travel time residuals and relative amplitudes for Girdler et. al. (1969) model (2). Eastern rift source at 15km. depth, take off angles $27^{\circ}(0.25^{\circ})33^{\circ}$.

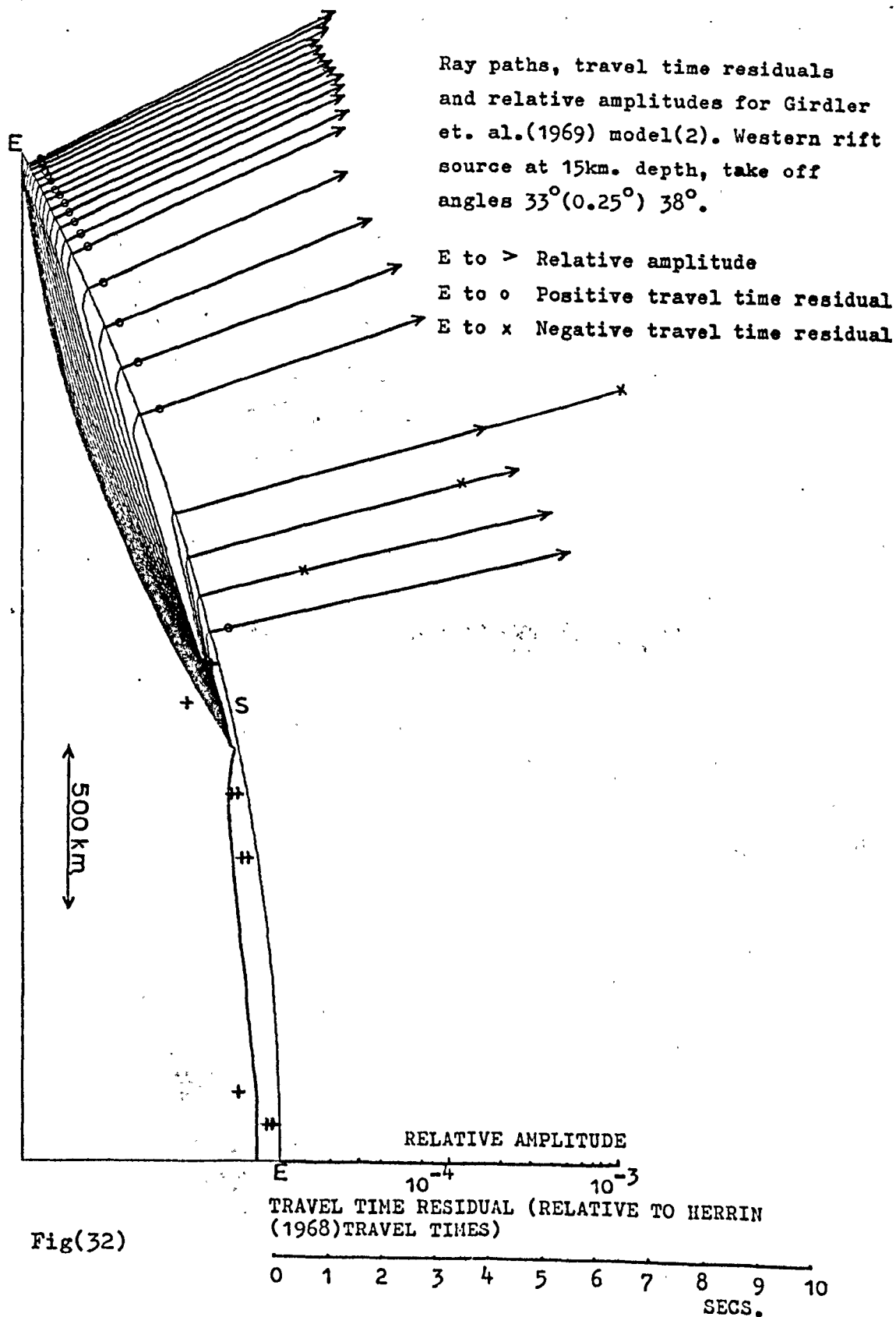
E to > Relative amplitude, E to o Positive travel time residual,
E to x Negative travel time residual. (When two rays occur at a single location, the amplitude of the first arrival is marked >)

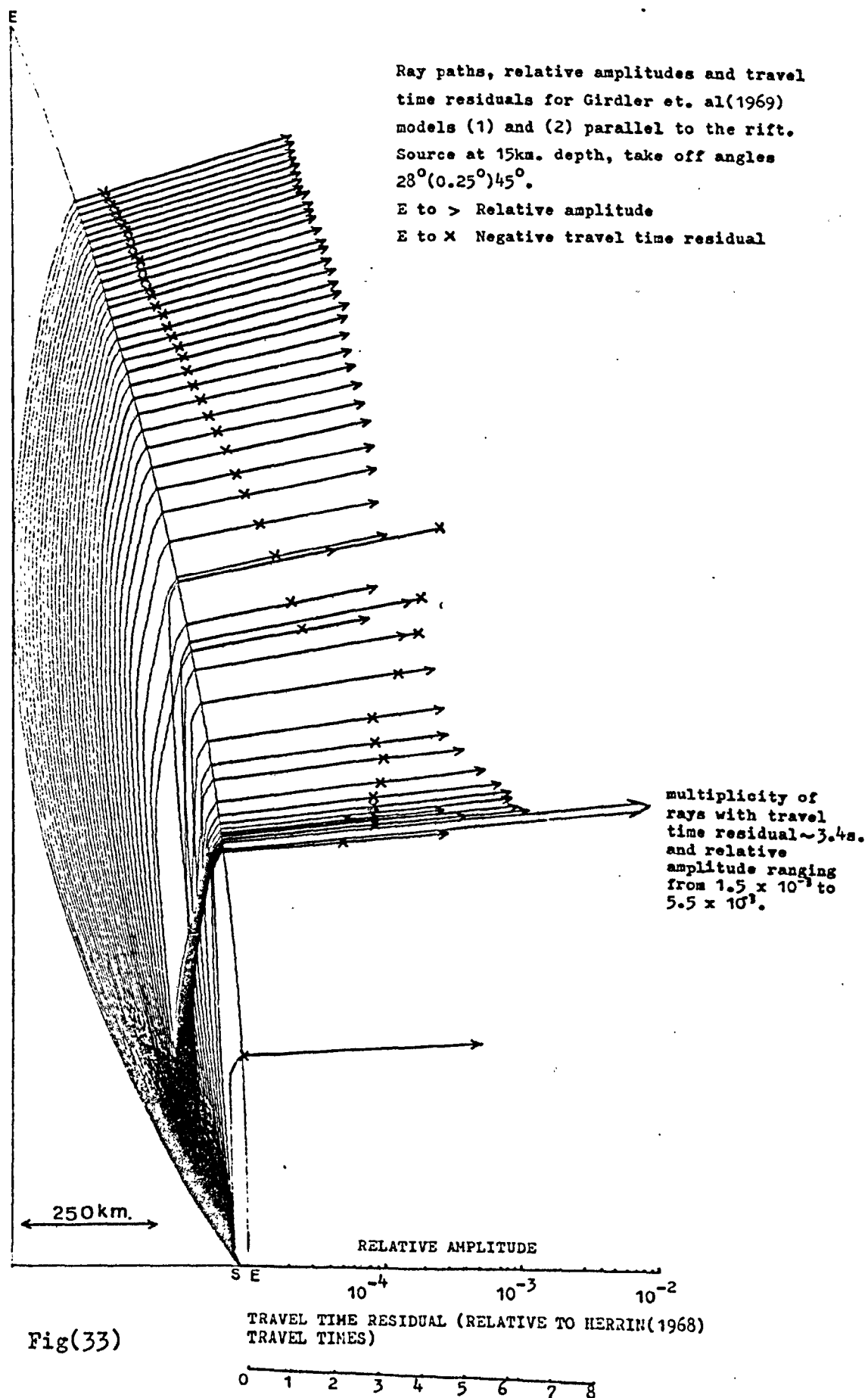


Fig(30)



FIG(31)

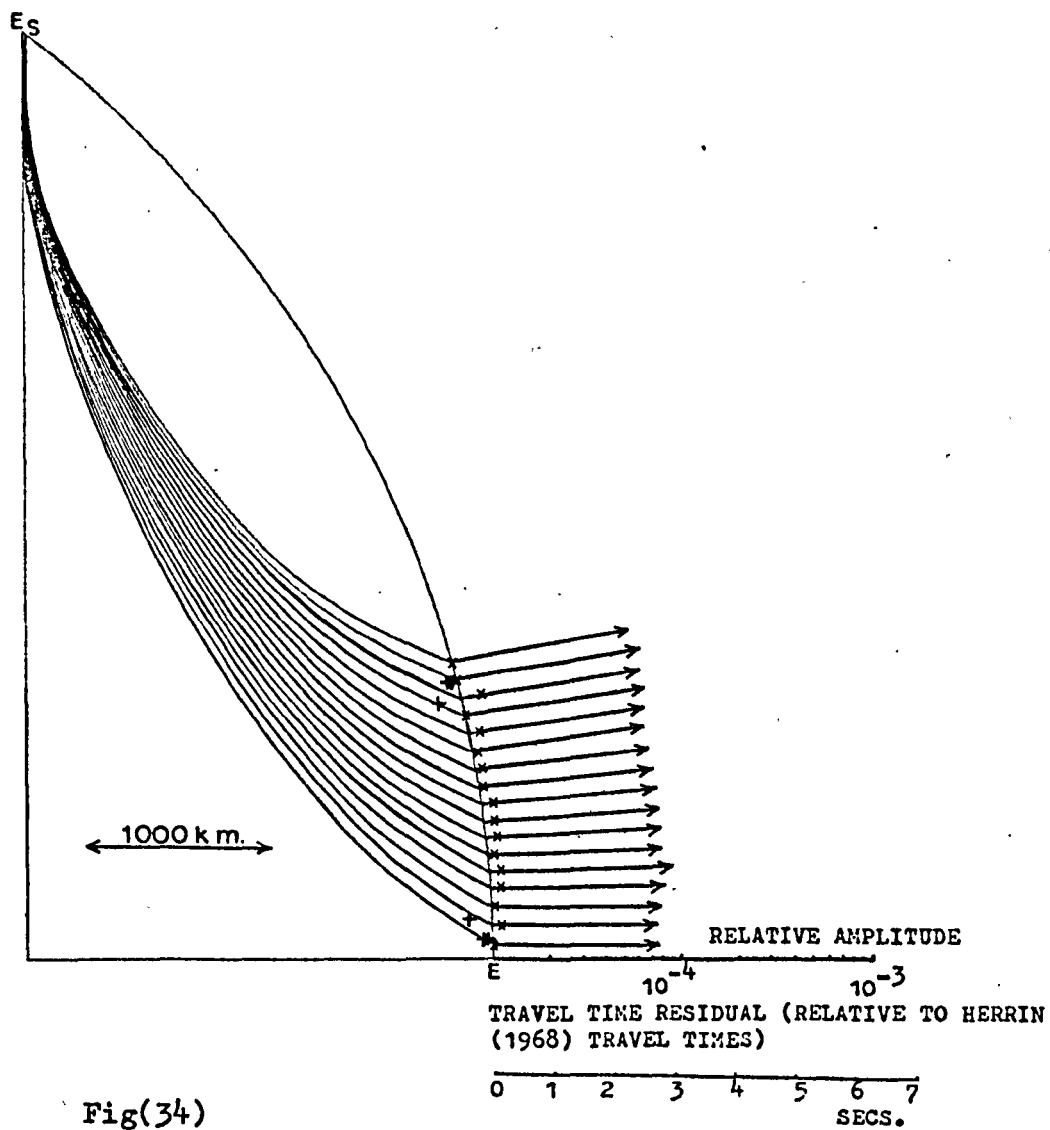




Fig(33)

Ray paths, travel times and relative amplitudes for the Girdler et. al.
 (1969) model (2). Atlantic source at 15km. depth, take off angles $59^{\circ}(0.25^{\circ})63^{\circ}$

E to > Relative amplitude, E to x Negative travel time residual



Fig(34)

for this region. In the range $7^{\circ} < \Delta < 10^{\circ}$ the low amplitude Pn rays are observed intermingled with the high amplitude rays which have been refracted upwards by the high velocity gradient at the base of the anomalous mantle. For $7^{\circ} < \Delta < 8^{\circ}$ the Pn rays arrive first with negative travel time residuals of 2.7 sec. to 3 sec. and these are followed 0.7 sec. later by the 'refracted' rays which tend to focus in this region (figure (33)). For $8^{\circ} < \Delta < 10^{\circ}$ the Pn and 'refracted' rays arrive at approximately the same time with negative travel time residuals ~ 4 sec.

$\Delta > 10^{\circ}$

For $\Delta > 10^{\circ}$ the first arrivals correspond to rays which have penetrated the high gradient at the base of the anomalous mantle; the negative travel time residuals for these rays range from 0.7 sec. to 2.2 sec. (figure (33)). In the region $10^{\circ} < \Delta < 11.7^{\circ}$ these first arrivals are followed 3 sec. to 4 sec. later by lower amplitude Pn rays.

(3.2.5.4) Mid-Atlantic Ridge Source

The rift structure of the Girdler et. al. model (2) (also of model (1)) has little effect on the paths, travel times and relative amplitudes of the rays from the mid-Atlantic Ridge event (figure (34)). The travel time residuals are either zero or small negative. Within the rifted region, the minimum travel time delays are observed over the enclave of normal mantle material with values of 0.1 sec. while in other regions of the rift, the values range from 0.2 sec. to 0.3 sec.

(3.2.6) Girdler et. al. (1969) Model using the Anderson and Kovach (1969) Velocity Depth Profile for the Standard Earth

In the modified version of the Anderson and Kovach (1969) velocity depth profile (table (7)) a velocity discontinuity separates the lithosphere (crust and mantle above 100 km) from the low velocity

asthenosphere. For the models referred to here as Girdler et. al. models (3) and (4), the low velocity material is allowed to extend to the base of a thinned crust by reducing the velocity in the defined region by 0.4 km/sec. (figure (35)). The boundaries separating the low velocity material of the asthenosphere from the high velocity lithosphere are defined by velocity discontinuities. All other features of model (3) (e.g. the enclave of normal mantle material and the crustal intrusive) are similar to model (1) (section (3.2.5)), while model (4) is the same as model (3) without the crustal intrusive.

All the travel time residuals shown for models (3) and (4) are with reference to the predicted travel times (RAY traced) of the modified Anderson and Kovach velocity depth profile (table (7)). These travel times are shown relative to the Herrin (1968) travel times in figure (36) and the ray paths and relative amplitudes are shown in figure (37).

(3.2.6.1) Girdler et. al. (1969) Model (3) with an Eastern Rift

Source above the Crustal Intrusive - East West Rays

$$\underline{\underline{\Delta < 6.2^{\circ}}}$$

Rays received here follow a similar pattern to those observed in model (1) (section (3.2.5.1)). For $\Delta < 5^{\circ}$ effects (i) and (ii) are dominant resulting in small positive travel time residuals (figure (38)), while for $5^{\circ} < \Delta < 6.2^{\circ}$ the rays are in the low velocity material for a sufficient length of their path for (iii) to become dominant, with the result that small negative travel time residuals are predicted.

$$\underline{\underline{6.2^{\circ} < \Delta < 10.2^{\circ}}}$$

The shadow zone at $6.2^{\circ} < \Delta < 10.2^{\circ}$ is not a significant feature of the RAY diagram of figure (38). Rays which are most likely to be received in this region approach within 2 km. of the M discontinuity

and the western boundary which defines the high velocity crustal intrusion and were therefore terminated (see section (3.2.5.1)). It must be pointed out that a similar shadow zone is observed for model (4) in figure (39). In this figure it is shown that the western boundary of the low velocity mantle material reflects or refracts the rays away from the surface. A similar effect would be expected for rays 'diffracted' into the equivalent region of model (3).

$$\underline{\underline{10.2^{\circ} < \Delta < 11.5^{\circ}}}$$

The rays received here have been greatly influenced by the high velocity gradient at the base of the low velocity channel of the Anderson and Kovach (1969) velocity depth profile (table (7)). The focus of very high amplitude arrivals near to $\Delta = 10.2^{\circ}$ is particularly noteworthy; compare to a similar focus in figure (37). The 2.8 sec. to 3.4 sec. negative travel time residuals are the result of comparing the 'deep' refracted rays of this model with the Pn rays of the Anderson and Kovach velocity depth profile (see travel time curve of figure (36) and compare RAY diagram of figure (37) with that of figure (38)).

$$\underline{\underline{\Delta > 11.5^{\circ}}}$$

The ray paths and relative amplitudes for $\Delta > 11.5^{\circ}$ (figure (38)) are similar to those of the Anderson and Kovach velocity depth profile. The jump in the values of the travel time residuals at $\Delta = 11.5^{\circ}$ is due to a similar jump in the travel time curve of figure (36). Travel time residuals for $\Delta > 11.5^{\circ}$ range from 0.2 sec. to 0.4 sec.

(3.2.6.2) Girdler et. al. (1969) Model (4) with an Eastern Rift Source -

East West Rays

The RAY diagram of figure (39) shows the effect of removing the high velocity crustal intrusive from the Girdler et. al. model (3).

The general features of this diagram may be used as representative of the 'Girdler et. al. (1969) type of model' for the three southern gravity profiles (i.e. profiles (1) to (3) in figure (26)).

$$\underline{\underline{\Delta < 8^{\circ}}}$$

Rays received here follow a similar pattern to the region $\Delta < 6.2^{\circ}$ for model (4) (figure (38)). Only the effects (i) and (iii) need be considered in the discussion of the travel time residuals. From the RAY diagram it is seen that the dominance of effect (iii) over effect (i) takes places somewhere between $\Delta = 2.6^{\circ}$ and $\Delta = 4.4^{\circ}$. For $\Delta < 2.6^{\circ}$ there are small positive travel time residuals and for $\Delta > 4.4^{\circ}$ there are small to large negative travel time residuals.

$$\underline{\underline{8^{\circ} < \Delta < 10.2^{\circ}}}$$

In this region there is a well defined shadow zone caused by the reflective and refractive effects (rays diverted away from the surface) of the western boundary of the low velocity material (figure (35) and figure (39)).

$$\underline{\underline{\Delta > 10.2^{\circ}}}$$

The rays received here are a combination of:

- (a) Rays reflected or refracted from the western boundary of the low velocity material.
- (b) Rays refracted upwards by the high velocity gradient at the base of the low velocity channel.
- (c) Rays which penetrate the region of high velocity gradient and travel in mostly normal mantle.

Rays of type (a) have the maximum negative travel time residuals of up to 12.6 sec. and are therefore secondary arrivals with moderate to high

relative amplitudes. Most of the high amplitude type (b) rays are received in the region $10.2^{\circ} < \Delta < 11.5^{\circ}$ and have a focus near to 10.2° which is to be compared to a similar focus in figure (38). The difference between the travel time residuals in this region (figure (39)), which range from 7.9 sec. to 8.8 sec., and those of figure (38) is not necessarily a measure of the travel time anomaly due to the high velocity crustal intrusive, instead it is mostly a measure of the effect of the very large $dt/d\Delta$ values of the Anderson and Kovach travel times (figure (36)).

For $\Delta > 11.5^{\circ}$ the ray paths and relative amplitudes are similar to those of figure (37) with the travel time residuals ranging from 0.3 sec. to 0.9 sec. Again the jump in the values of the travel time residuals at $\Delta = 11.5^{\circ}$ is due to the jump in the travel time curve of figure (36).

(3.2.6.3) Girdler et. al. (1969) Model (3) with a Western Rift Source -
East West Rays

$\Delta < 10.8^{\circ}$

This region is devoid of rays due to the reflective effects of the western boundary of the low velocity material (figure (40)). All the rays which approach this boundary from the region of the western rift are at a greater angle of incidence than the critical angle.

$10.8^{\circ} < \Delta < 12.9^{\circ}$

In this region there is a mixture of rays which have been reflected from the western boundary of the low velocity material with the rays refracted upwards by the high velocity gradient at the base of the low velocity channel (figure (40)). The first type of ray has negative

travel time residuals ~ 1.6 sec. and small relative amplitudes (much of the energy is transferred to the S wave at the boundary) while the second type of ray has negative travel time residuals ranging from 0.8 sec. to 3.4 sec with high relative amplitudes. The latter rays have a focus in the region of 10.8° .

$\Delta > 12.9^\circ$

The rays here have travelled in mostly normal mantle and therefore their ray paths and relative amplitudes are similar to figure (37) with travel time residuals ranging from 0.35 sec. to 0.8 secs. There is a single very low amplitude secondary arrival at $\Delta = 16.2^\circ$ (figure (40)) which has been reflected at the western boundary of the low velocity material.

Easterly Trending Rays

$\Delta < 6.1^\circ$

The easterly trending rays follow a similar pattern to that described for the near epicentre arrivals of previous figures. The dominance of effect (iii) over effect (i) takes place somewhere between $\Delta = 2.6^\circ$ and $\Delta = 4.7^\circ$. For $\Delta < 2.6^\circ$ there are small positive travel time residuals and for $\Delta > 4.7^\circ$ there are small to large negative travel time residuals.

$\Delta > 6.1^\circ$

The rays plotted for this region require reflection at the 100 km. velocity discontinuity. The RAY tracing program was terminated at this stage as first order ray theory will not allow the ray to penetrate the lithosphere-asthenosphere boundary.

(3.2.6.4) Rays Travelling North South

As with models (1) and (2), the model used for the north south rays does not include the crustal intrusive or the enclave of normal mantle material.

$$\underline{\underline{\Delta < 9.7^{\circ}}}$$

Rays received here follow a similar pattern to those of previous figures with effect (iii) overtaking effect (i) somewhere between $\Delta = 3^{\circ}$ and $\Delta = 4.7^{\circ}$ (figure (41)). Small positive travel time residuals are shown for $\Delta < 3^{\circ}$ and small to large negative travel time residuals are shown for $\Delta > 4.7^{\circ}$. The negative travel time residuals range from 1.1 sec. to 5.3 sec.

$$\underline{\underline{9.7^{\circ} < \Delta < 11.5^{\circ}}}$$

The Pn rays are the first arrivals with travel time residuals between 5.5 sec. to 6.7 sec. (figure (41)). These are followed 3 sec. to 4 sec. later by higher amplitude rays which have been refracted upwards by the high velocity gradient at the base of the low velocity channel.

$$\underline{\underline{\Delta > 11.5^{\circ}}}$$

The first arrivals here are low amplitude rays which have travelled in mostly normal mantle and have travel time residuals of 1.0 sec. to 1.3 sec. These are followed 1.2 sec. to 7.9 sec. later by high amplitude rays which have been refracted upwards by the high velocity gradient at the base of the low velocity material. The jump in the travel time residuals at 11.5° (figure (41)) is due to the jump in the travel time curve in figure (36).

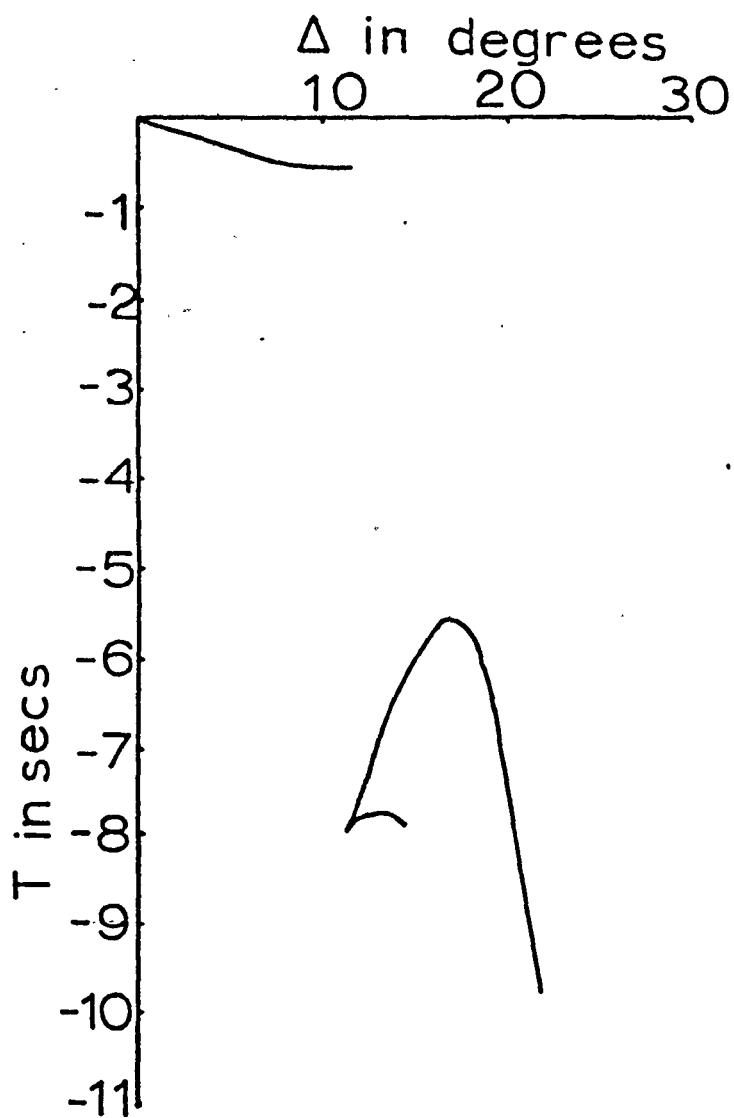
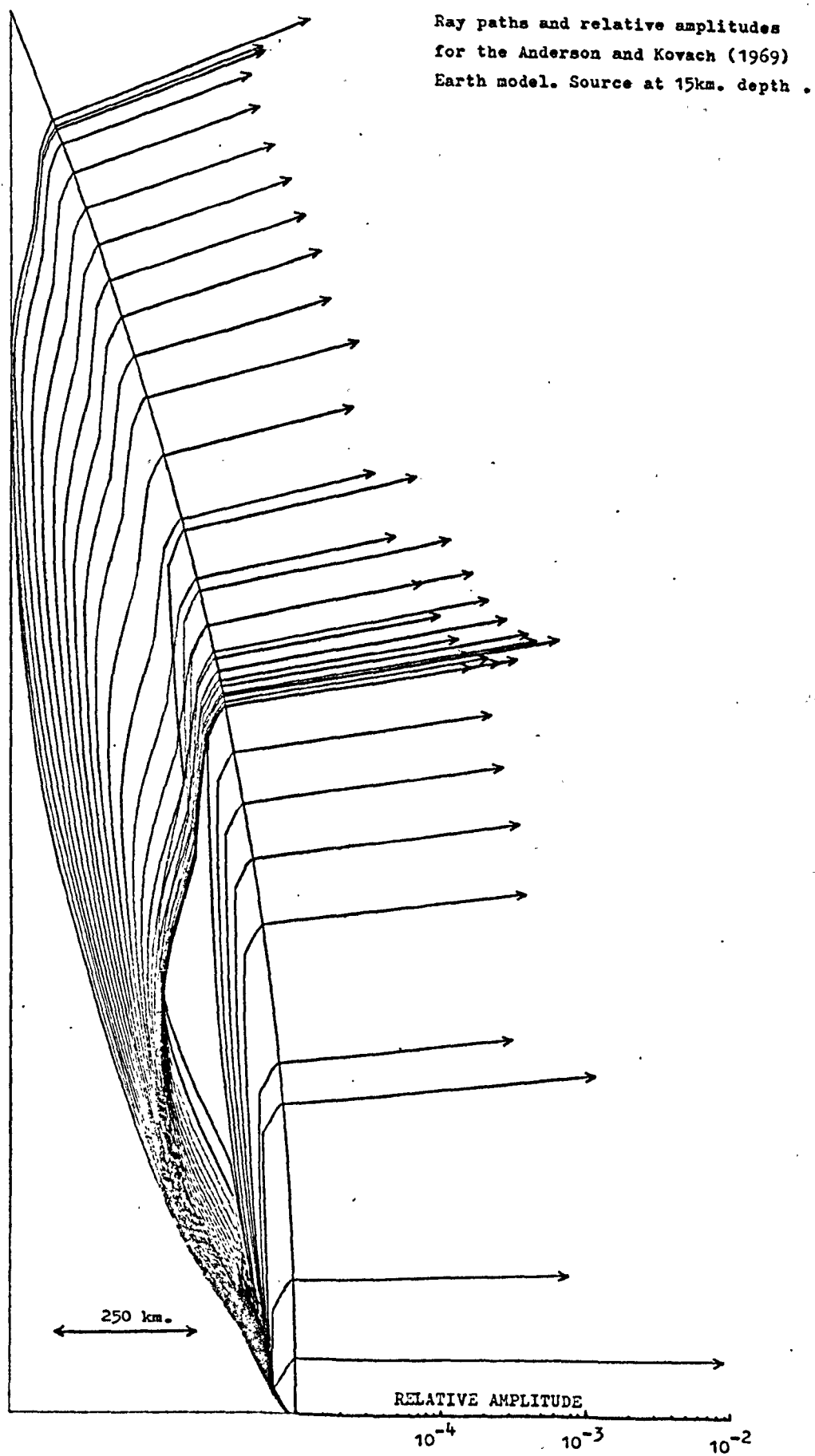
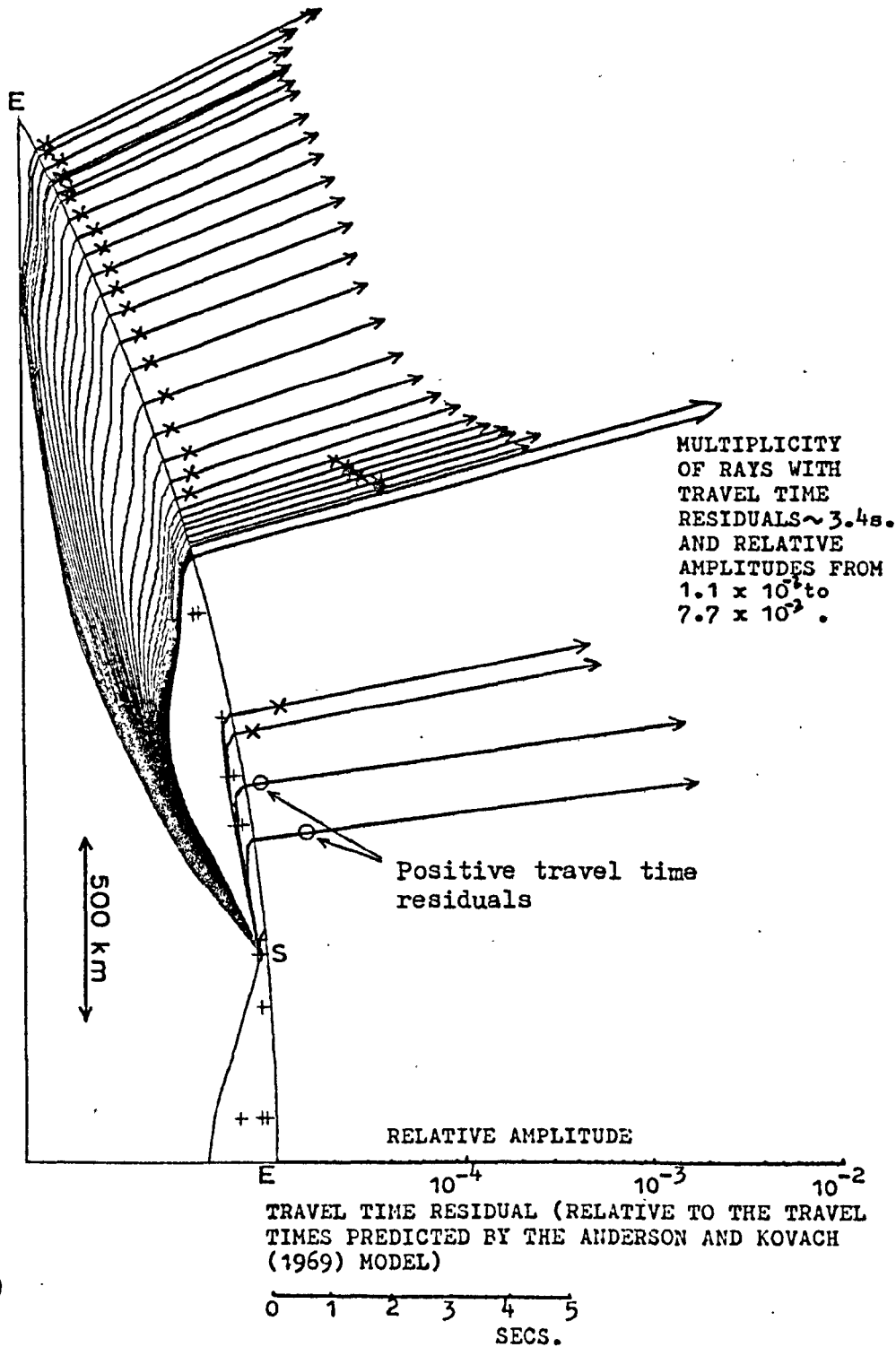


Fig (36) Predicted travel times of the Anderson and Kovach(1969) velocity depth profile. Travel times relative to the Herrin(1968) tables (Herrin(1968) times - Anderson and Kovach(1969) times)

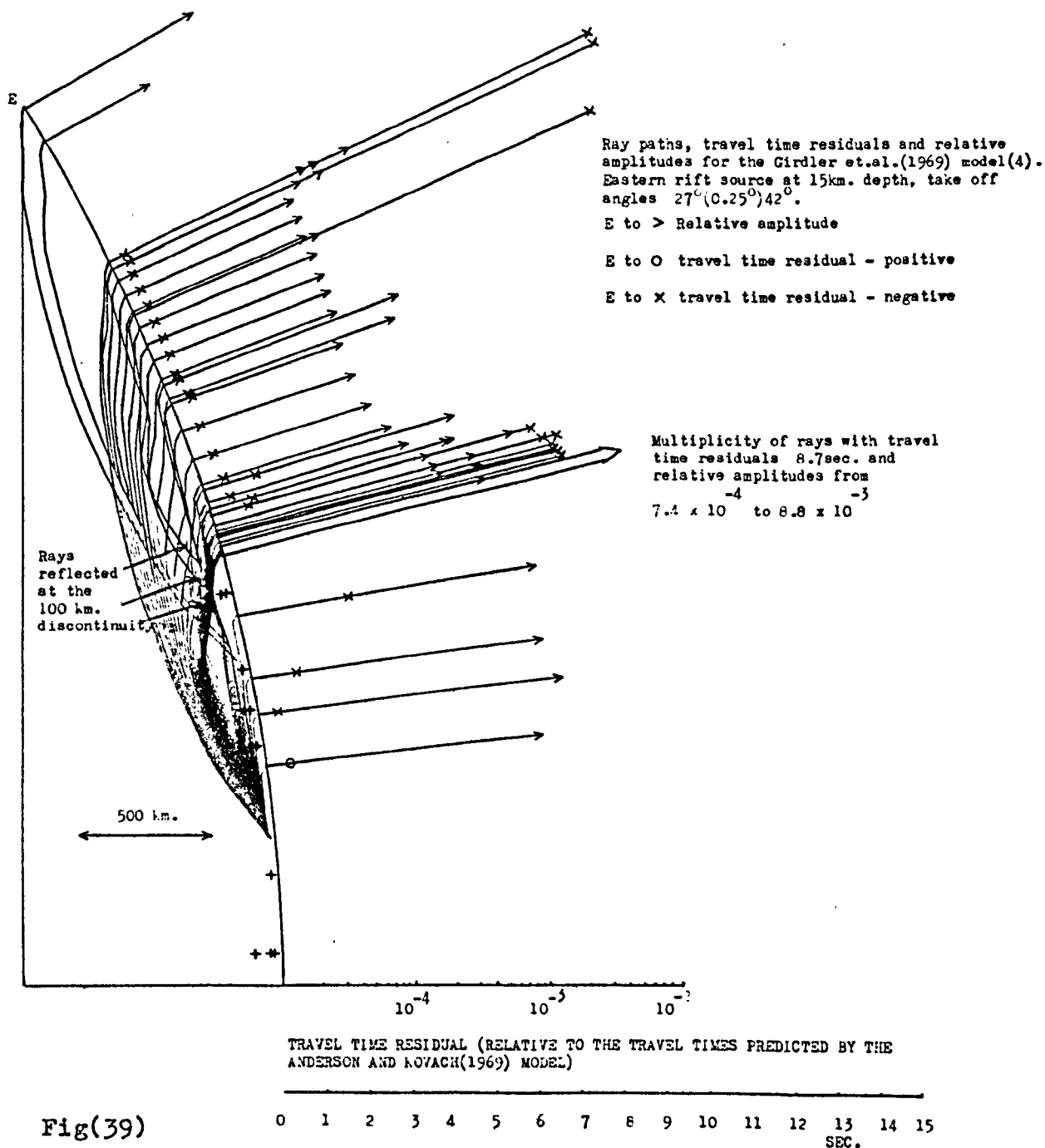


Fig(37)

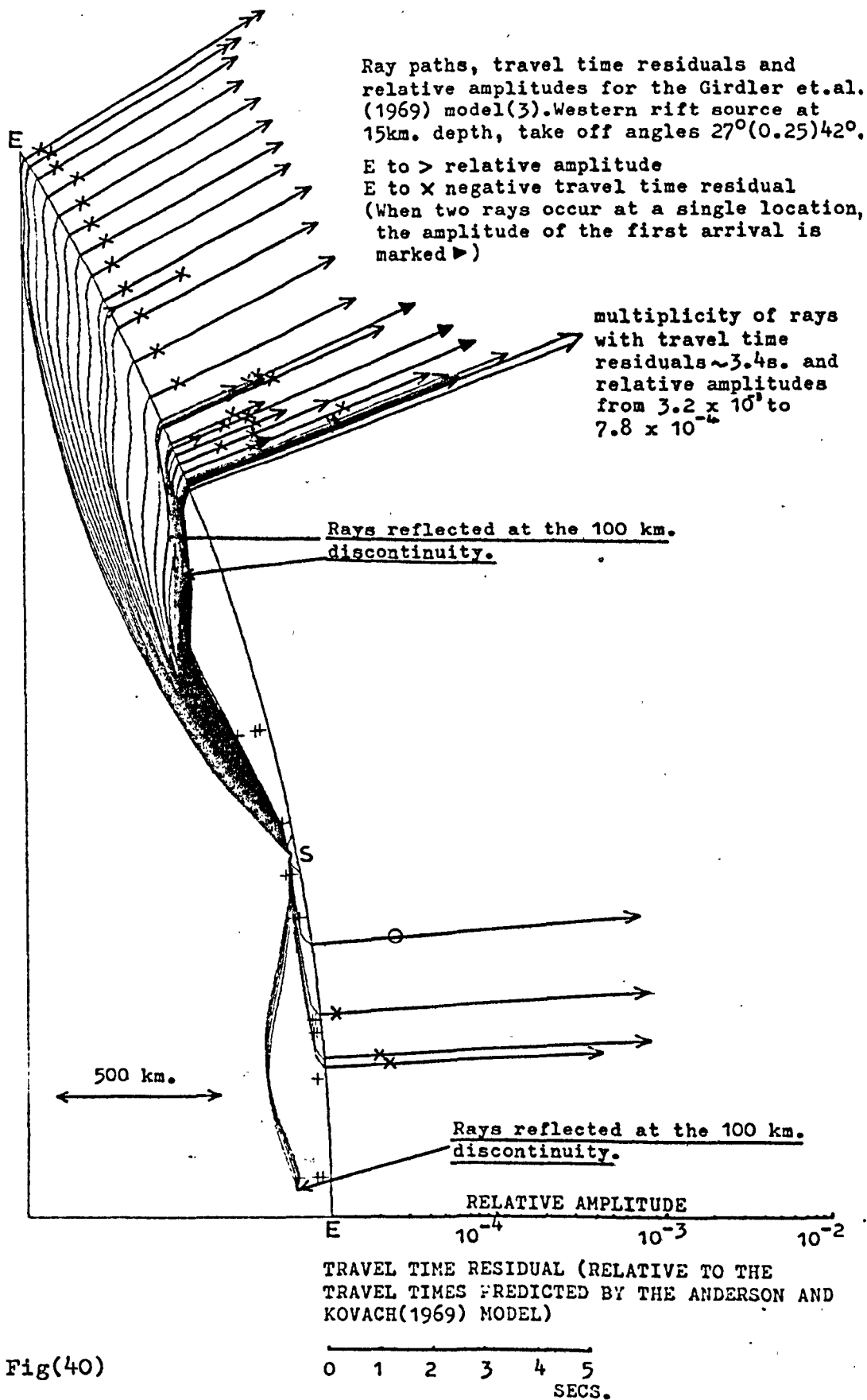
Ray paths, travel time residuals and relative amplitudes for Girdler et. al. (1969) model (3). Eastern rift source at 15km. depth, take off angles $27^{\circ}(0.25^{\circ})37^{\circ}$.
 E to > relative amplitude, E to X negative travel time residual.



Fig(38)



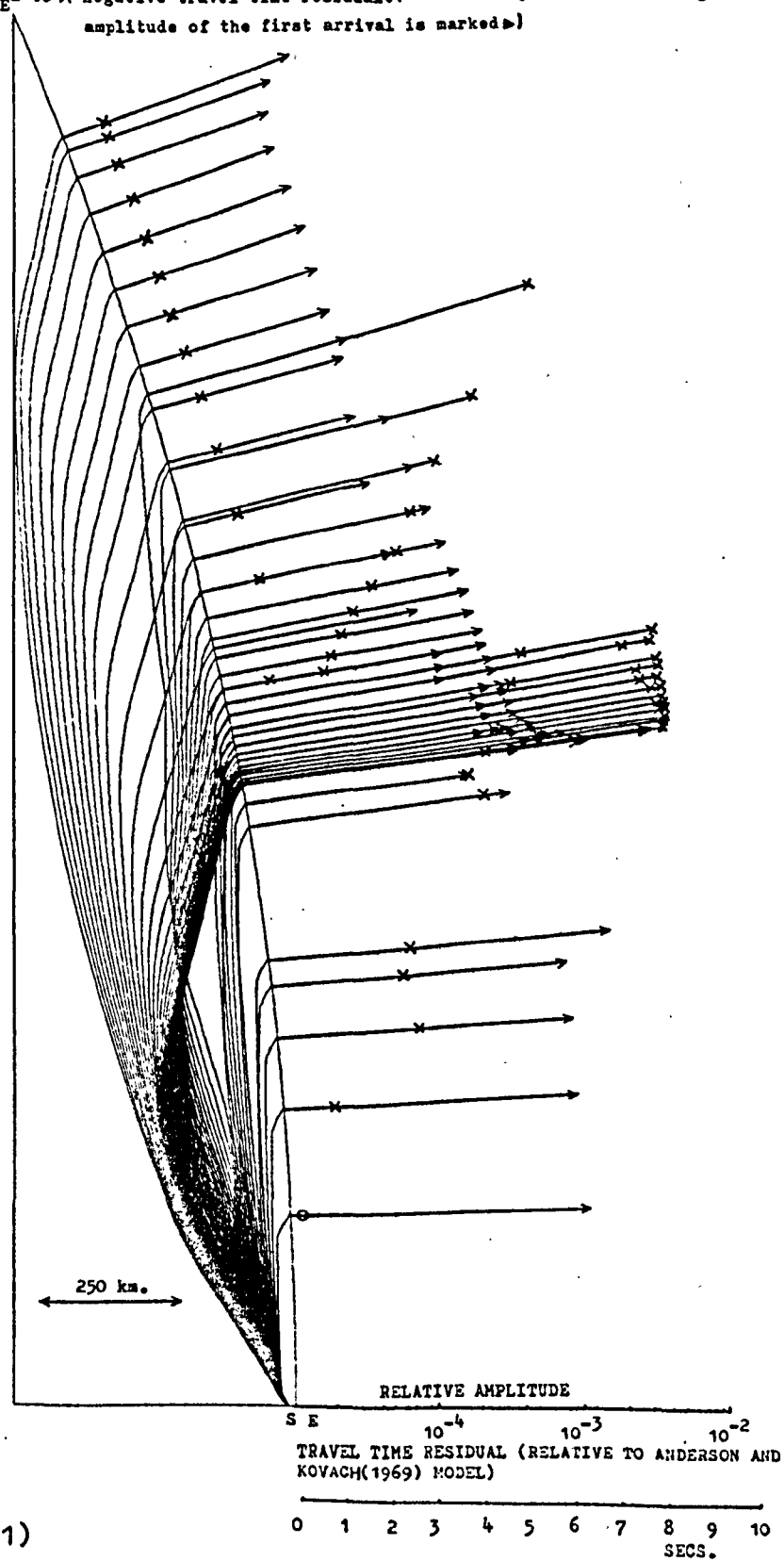
Fig(39)



Fig(40)

Ray paths, travel time residuals and relative amplitudes for Girdler et. al(1969) model(3), rays are parallel to the rift. Source at 15km. depth, take off angles $27^{\circ}(0.25^{\circ})42^{\circ}$.

E to > relative amplitude, E to O positive travel time residual, E to X negative travel time residual.(When two rays occur at a single location, the amplitude of the first arrival is marked)



Fig(41)

(3.2.7) Sowerbutt's Model (4) using the Herrin (1968) Velocity
Depth Profile for the Standard Earth

In an attempt to model Sowerbutt's (1972) interpretation of gravity profile (4), the low density, low velocity material is concentrated between approximately 80 km. and 150 km. depth (figure (42)). To account for the increased amplitude of the negative anomaly across the eastern rift and the axial positive anomaly, the low velocity mantle material is allowed to extend to and intrude the lower velocity crust of this region (figure (42)). In the mantle the low velocity material grades linearly into normal mantle material, while the relatively high velocity crustal intrusive is bounded by velocity discontinuities.

(3.2.7.1) Eastern Rift Source above the Crustal Intrusive - East
West Rays

$$\underline{\underline{\Delta < 10^{\circ}}}$$

Rays received in this region (figure (43)) do not enter the low velocity mantle material and therefore effect (ii) is dominant. This results in Pn rays with near normal amplitudes and positive travel time residuals ~ 0.8 sec.

$$\underline{\underline{10^{\circ} < \Delta < 11.6^{\circ}}}$$

Rays received here (figure (42) and figure (43)) are in the low velocity material for a sufficient length of their path for effect (iii) to become dominant, resulting in negative travel time residuals of 1.2 sec. to 1.5 sec.

$$\underline{\underline{\Delta > 11.6^{\circ}}}$$

There is a well defined shadow zone in the region $11.6^{\circ} < \Delta < 16.5^{\circ}$. Rays which would ordinarily be received in this region are refracted down-

wards by the high velocity gradient at the side of the 'plume' of low velocity material which extends from the crust (figure (42) and figure (43)). These rays which focus in the region $16.5^{\circ} < \Delta < 17^{\circ}$, have variable amplitudes and near zero travel time residuals indicating that effects (ii) and (iii) are almost equal (section (3.2.5.1)). For $\Delta > 18^{\circ}$ effect (ii) begins to dominate again, resulting in small (0.2 sec) positive travel time residuals (figure (44)).

(3.2.7.2) Western Rift Source - East West Rays

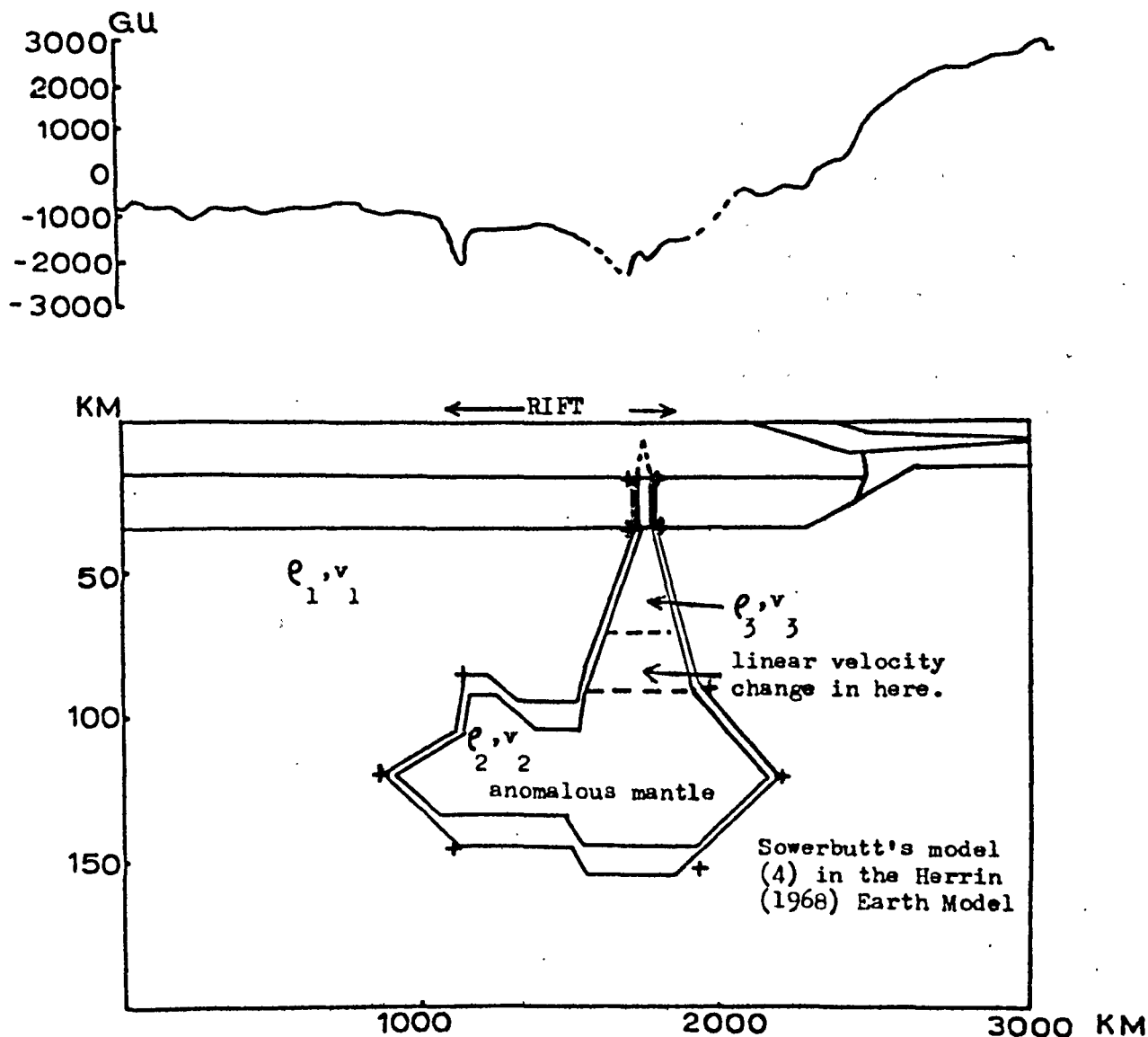
It is clear from figure (45) that rays received in the region $\Delta < 16^{\circ}$ are not affected by the features defined by Sowerbutt's model (4). For $16^{\circ} < \Delta < 17^{\circ}$ there is a small shadow zone as the rays enter the low velocity material between 80 km. and 150 km. depth. For greater values of Δ the RAY diagram will closely resemble that obtained for Sowerbutt's model (1) (figure (48) and figure (49)).

(3.2.7.3) Mid-Atlantic Ridge Source

The paths, travel times and relative amplitudes of the rays received from a mid-Atlantic event are little affected by the rift structures of the Sowerbutt's model (4) (figure (46)). The size of the negative travel time residual (0 to 0.3 sec) is directly related to the thickness of low velocity material which the ray must traverse. An exception to this is the ray which travels through the high velocity crustal intrusive, this shows a near zero travel time residual.

(3.2.7.4) Rays travelling North South

The discussion of the rays travelling north south, parallel to the strike of the Rift System, applies to Sowerbutt's models (1) to (3) and is therefore included in section (3.2.8.5).



FIG(42) Gravity profile(4) and Sowerbutt's(1972) computed model.

— Marks the extent of the region of anomalous velocity and density in the mantle. In the region between the inner and outer lines the data values change linearly to normal mantle values.

— Marks the extent of the region of anomalous velocity and density in the crust. This boundary is treated as a discontinuity.

+ Mark the corresponding + shown in fig(43) to fig(46)..

$$\text{s.g. difference} = \rho_2 - \rho_1 = 3.25 - 3.3 = -0.05$$

$$\text{corresponding velocity difference} = 0.12 \text{ km/sec.}$$

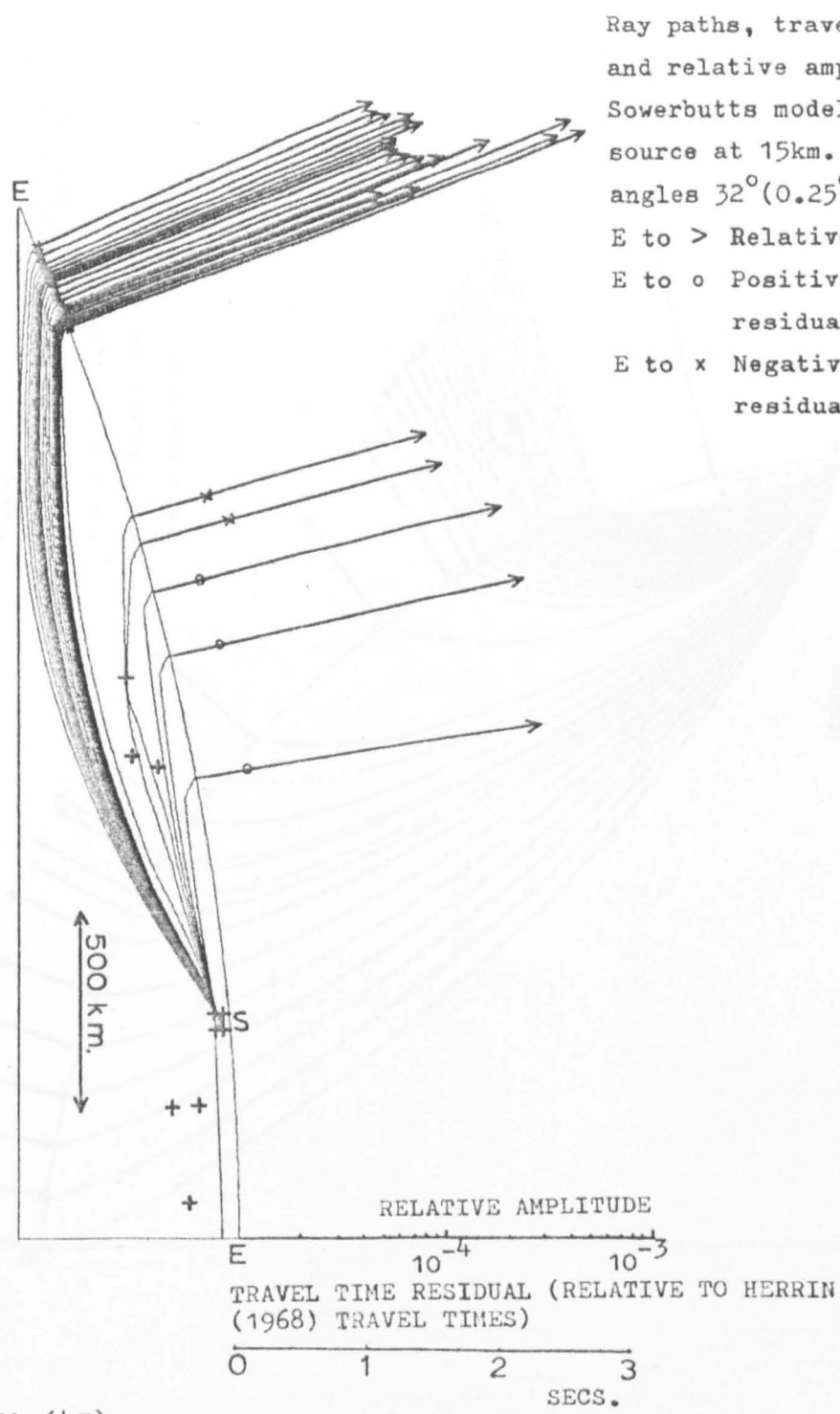
$$\text{s.g. difference} = \rho_3 - \rho_1 = 3.24 - 3.3 = -0.06$$

$$\text{corresponding velocity difference} = 0.15 \text{ km/sec.}$$

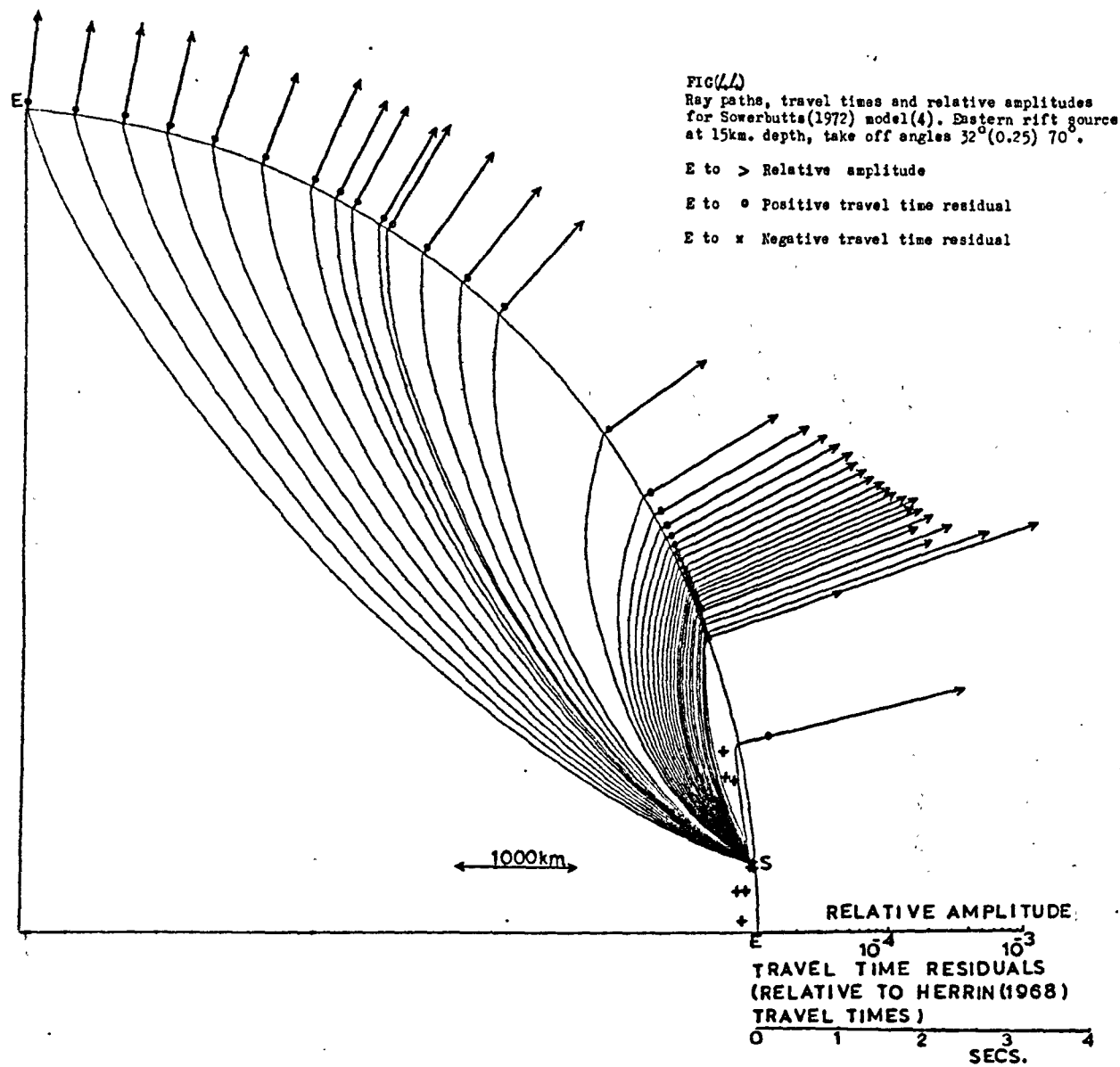
$$\text{s.g. difference in the crust} = 3.03 - 2.89 = +0.14$$

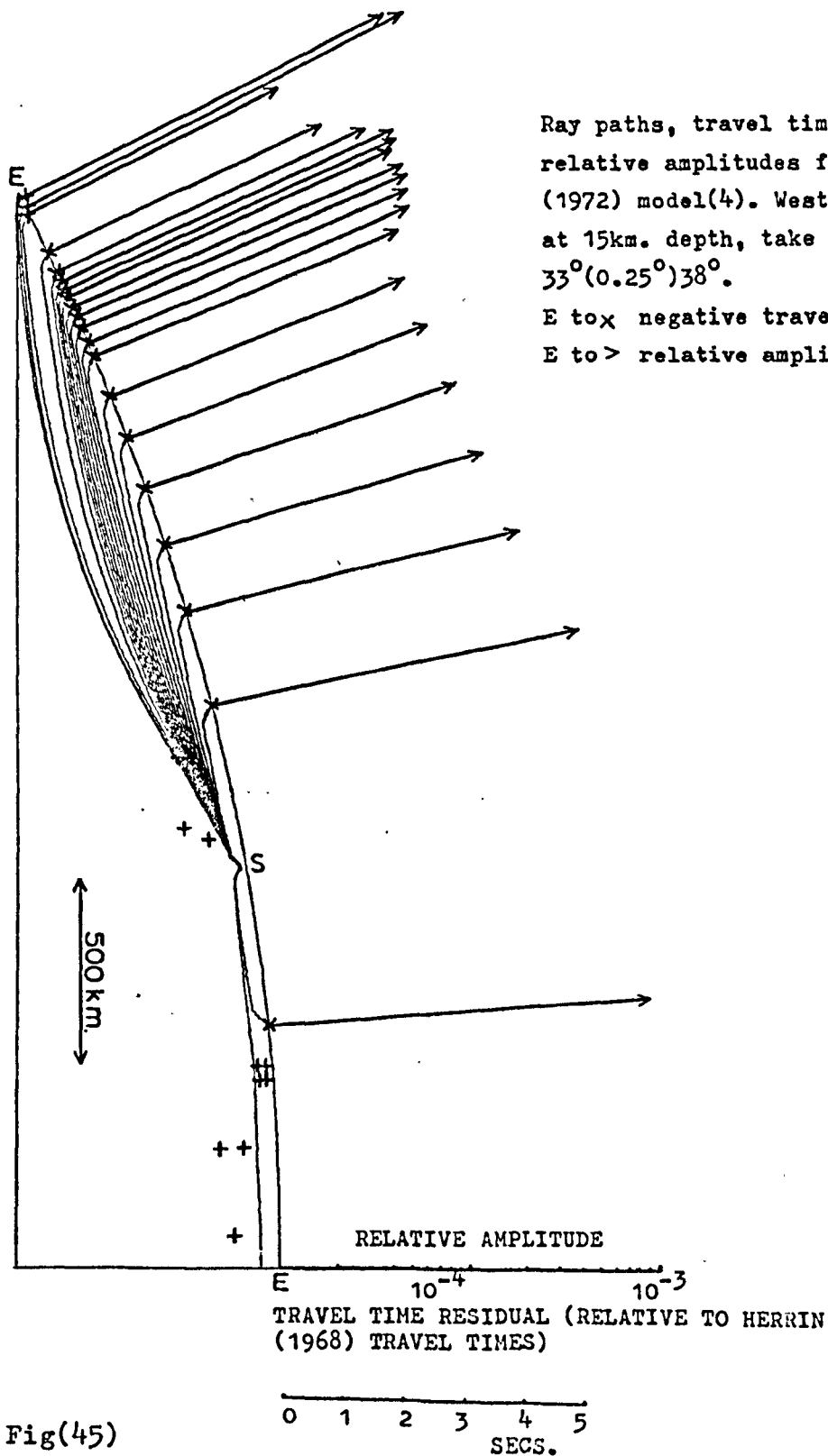
$$\text{corresponding velocity difference} = 0.65 \text{ km/sec.}$$

Vertical exaggeration 10 : 1



Fig(43)



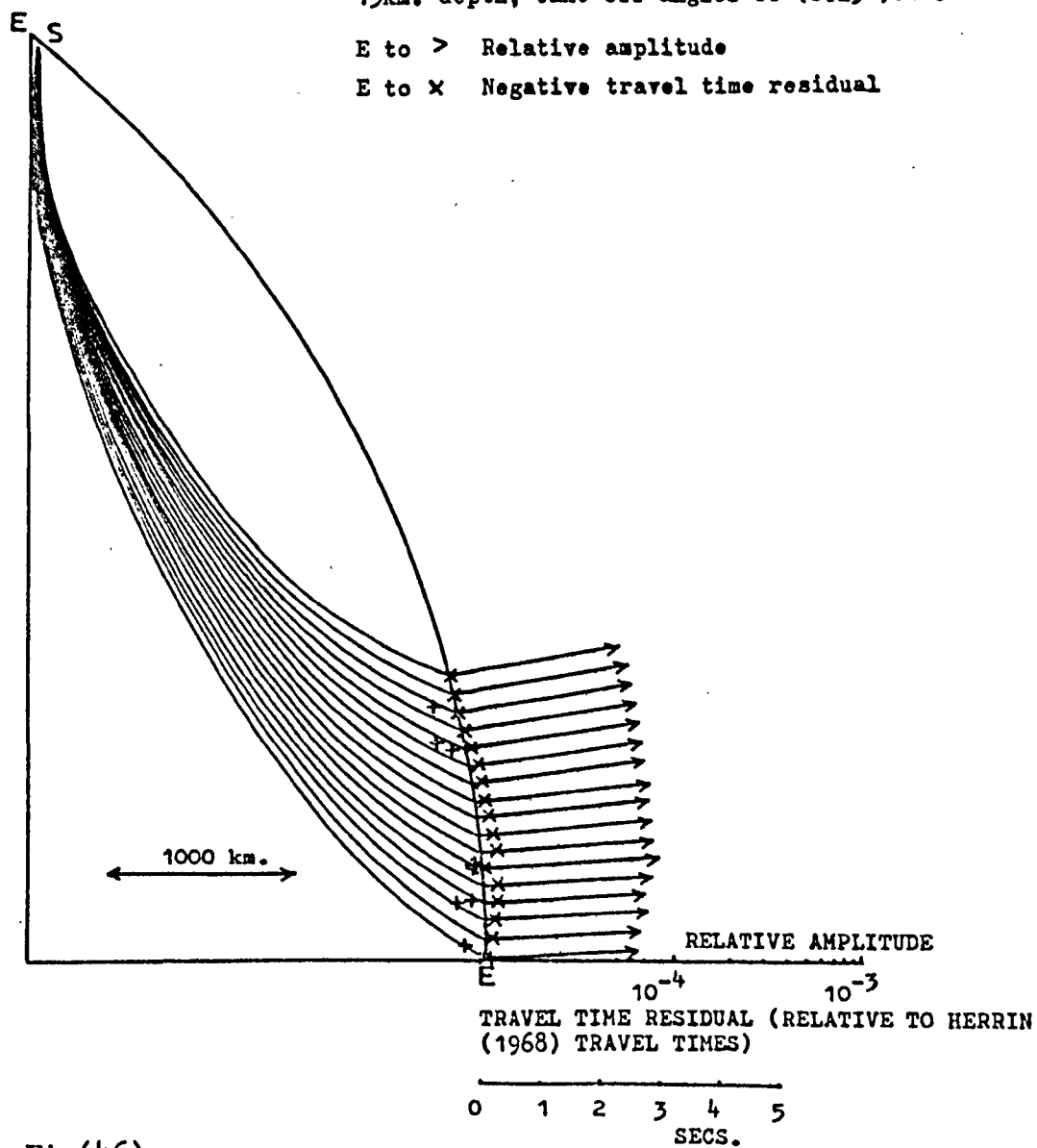


Fig(45)

Ray paths, travel time residuals and relative amplitudes
for Sowerbutt's(1972) model(4). Atlantic source at
15km. depth, take off angles $60^{\circ}(0.25^{\circ})64^{\circ}$.

E to > Relative amplitude

E to x Negative travel time residual



Fig(46)

(3.2.8) Sowerbutt's Models (1), (2) and (3) using the Herrin
(1968) Velocity Depth Profile for the Standard Earth

Sowerbutt's (1972) interpretation of gravity profiles (1) to (3) (figure (26)) are very similar to each other (figure (47), figure (51), figure (55)). As with Sowerbutt's model (4) (section (3.2.7)) the low velocity material is concentrated between approximately 80 km. and 150 km. depth, but in models (1) to (3) there are no 'plumes' of low velocity material extending upwards. Models (1) to (3) differ from each other only in the shape of the region of anomalous mantle material. In all three models the low velocity material grades linearly into normal mantle.

Profiles (2) and (3) cross a region of intense seismicity (Fairhead and Girdler (1971)) in the area around Lake Manyara, therefore an eastern rift source is taken for the east west rays of these two velocity models. The most intense seismicity in the location of profile (1) (figure (26)) is situated near to Lake Tanganyika, therefore a western rift source is taken for this velocity model. Due to the similarity of models (1) to (3) most of the features of the RAY diagrams for an eastern rift source in models (2) and (3) will apply to model (1) and most of the features of the RAY diagrams for the western rift source in model (1) will apply to models (2) and (3). All three profiles are analysed for a mid-Atlantic Ridge event.

In the following, only effect (iii) need be considered in the discussion of the travel time residuals.

(3.2.8.1) Sowerbutt's (1972) Model (1) with a Western Rift Source -
East West Rays

$$\Delta < 12.2^\circ$$

=====

Rays received here do not enter the lower velocity mantle material, therefore normal relative amplitudes and travel times are

predicted for this region (figure (48)).

$$\underline{\underline{\Delta > 12.2^\circ}}$$

In the region $12.2^\circ < \Delta < 14^\circ$ there is a small shadow zone as the rays cross the sloping boundary of the low velocity material. These rays are refracted into the region $14^\circ < \Delta < 15.6^\circ$ where a multiplicity of rays are received with travel time residuals ~ 0.4 sec. (figure (48) and figure (49)). For $\Delta > 15.7^\circ$ the ray paths and relative amplitudes are similar to those of the unperturbed Herrin velocity profile while the travel time residuals range from 0.4 sec. to 0.1 sec. (figure (49)).

(3.2.8.2) Sowerbutt's (1972) Model (2) with an Eastern Rift Source -
East West Rays

$$\underline{\underline{\Delta < 10^\circ}}$$

Rays received here do not enter the low velocity material, therefore normal relative amplitudes and travel times are predicted (figure (52)).

$$\underline{\underline{\Delta > 10^\circ}}$$

There are no shadow zones for this model. The rays refracted upwards by the high velocity gradient at the base of the model (figure (51) and figure (52)) fill the 'gap' in the RAY diagram caused by the low velocity material (see Dowling and Nuttli (1964) for a discussion of this effect). In the region $10^\circ < \Delta < 13^\circ$ there is a multiplicity of arrivals with negative travel time residuals of between 0.7 sec. and 1.8 sec. For $\Delta > 13^\circ$ the ray paths and relative amplitudes are similar to those of the Herrin velocity depth profile

while the travel time residuals range from 0.6 sec. to 0.1 sec. (figure (52) and figure (53)).

(3.2.8.3) Sowerbutt's (1972) Model (3) with an Eastern Rift Source -
East West Rays

$$\underline{\underline{\Delta < 9.3^{\circ}}}$$

Rays received here do not enter the low velocity material, therefore normal relative amplitudes and travel times are predicted (figure (56)).

$$\underline{\underline{9.3^{\circ} < \Delta < 16.3^{\circ}}}$$

The paths of the rays received here are to a large extent governed by the shape of the low velocity material (figure (55) and figure (56)). For $9.3^{\circ} < \Delta < 10.6^{\circ}$ the Pn phase which has not entered any of the low velocity material is the first arrival. This is followed 1.9 sec. later by mostly higher amplitude rays which have been refracted upwards by the high velocity gradient at the base of the low amplitude arrivals with negative travel time residuals of between 1.0 sec. and 1.1 sec. and these are followed by a shadow zone out to $\Delta = 14.3^{\circ}$. Between $\Delta = 14.3^{\circ}$ and $\Delta = 16.3^{\circ}$ there is a multiplicity of variable amplitude arrivals with negative travel time residuals ranging from 0.3 sec. to 1.3 sec.

$$\underline{\underline{\Delta > 16.3^{\circ}}}$$

In this region (figure (57)) the ray paths and relative amplitudes are similar to those of the Herrin velocity depth profile while the travel time residuals range from 0.35 sec. to 0.1 sec.

(3.2.8.4) Sowerbutt's Models (1), (2) and (3) with a mid-Atlantic

Ridge Source

The paths, travel times and relative amplitudes of the rays received from a mid-Atlantic Ridge event are little affected by the rift structures of the Sowerbutt's models (1) to (3) (figure (50), figure (54), figure (58)). All the travel time residuals are negative with magnitude ~ 0.2 sec.

(3.2.8.5) Sowerbutt's Models - Rays Travelling North South

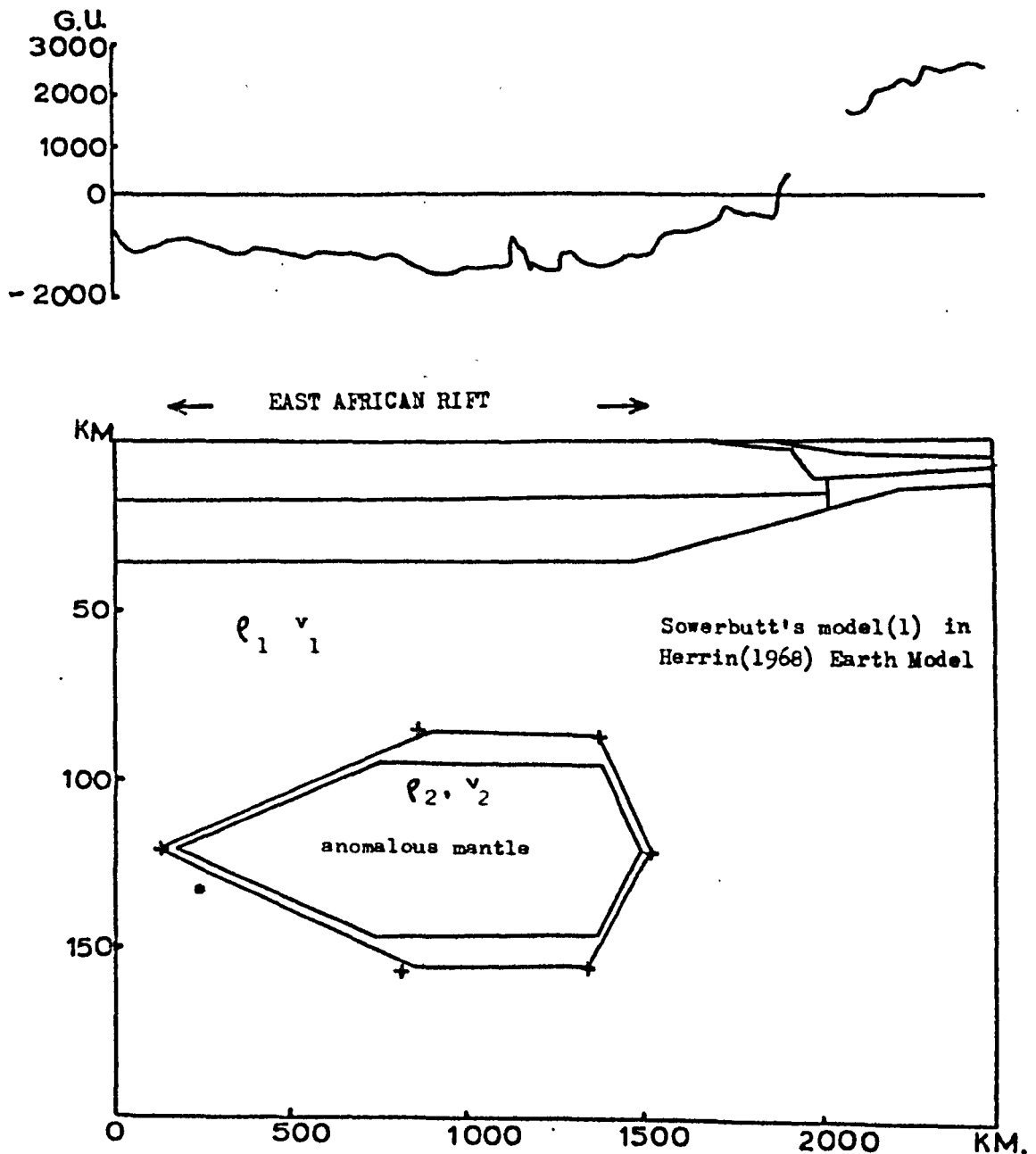
In the RAY diagram of figure (59) both the source and receivers are situated above low velocity material which is placed between 80 km. and 150 km. depth. No thin 'plume' of low velocity material extends to the crust (section (3.2.7)) and no crustal intrusives are accounted for. This corresponds to a ray travelling from any event in the East African Rift except those in the axial trough of the northern part of the eastern rift.

$$\underline{\underline{\Delta < 9.7^\circ}}$$

Rays received here do not enter the low velocity material, therefore normal relative amplitudes and travel times are predicted (figure (59)).

$$\underline{\underline{9.7^\circ < \Delta < 18.6^\circ}}$$

There is a small shadow zone between $\Delta = 9.7^\circ$ and $\Delta = 11^\circ$ which is followed by a region of duplication to $\Delta = 18.6^\circ$. The first arrivals correspond to rays which bottom beneath the low velocity material and have negative travel time residuals of 0.5 sec. to 2.0 sec. The higher travel time residuals are for the shortest epicentral distances. These are followed by rays which are refracted upwards by the high velocity



FIG(47) Gravity profile (1) and Sowerbutt's(1972) computed model.

== Marks the extent of the region of anomalous velocity and density. In the region between the inner and outer lines the data values change linearly to normal mantle values.

+ Mark the corresponding + shown in fig(48) to fig(50)

$$\text{s.g. difference} = \rho_1 - \rho_2 = 3.3 - 3.25 = 0.05$$

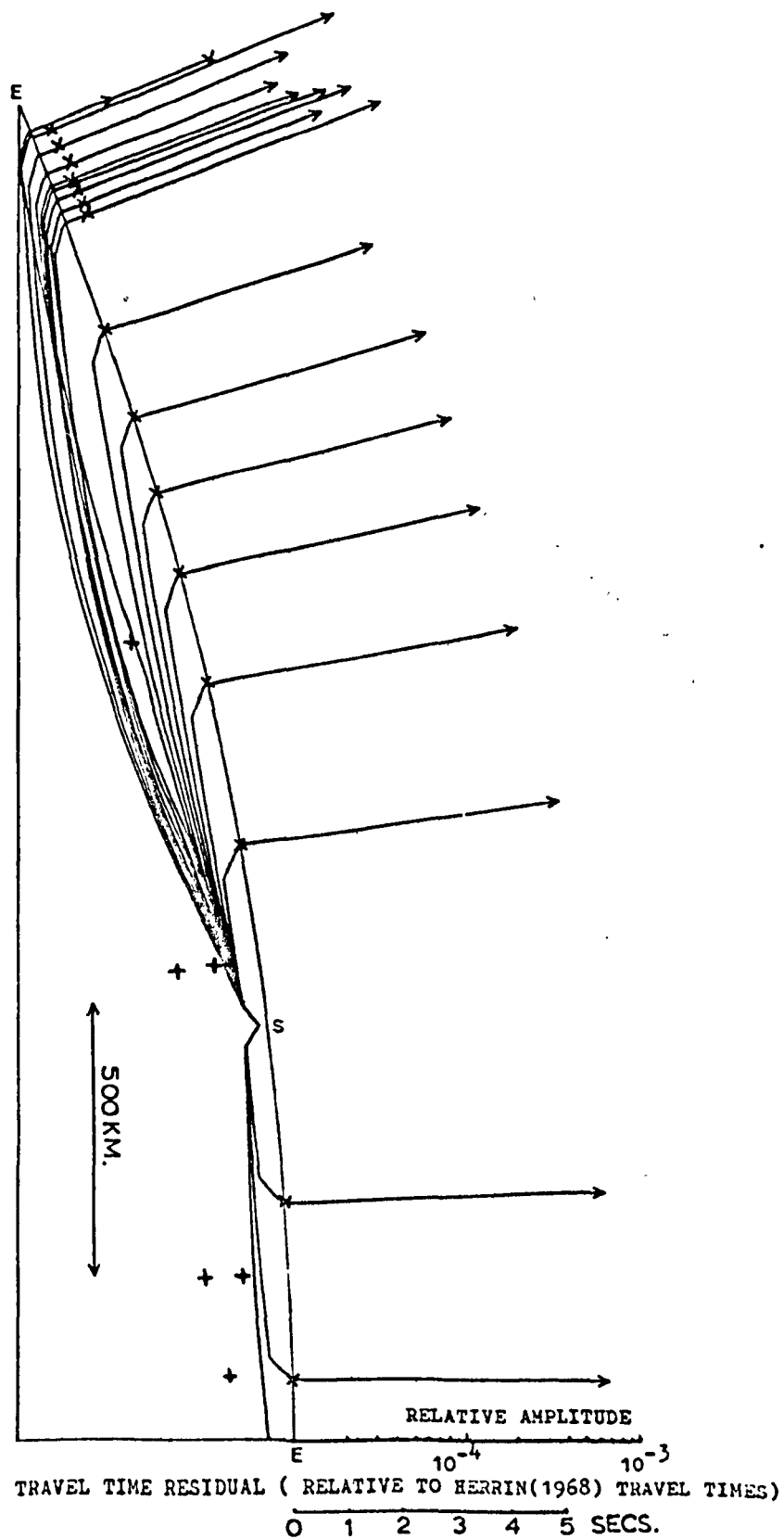
$$\text{corresponding velocity difference} = 0.12 \text{ km/sec.}$$

vertical exaggeration 10 : 1

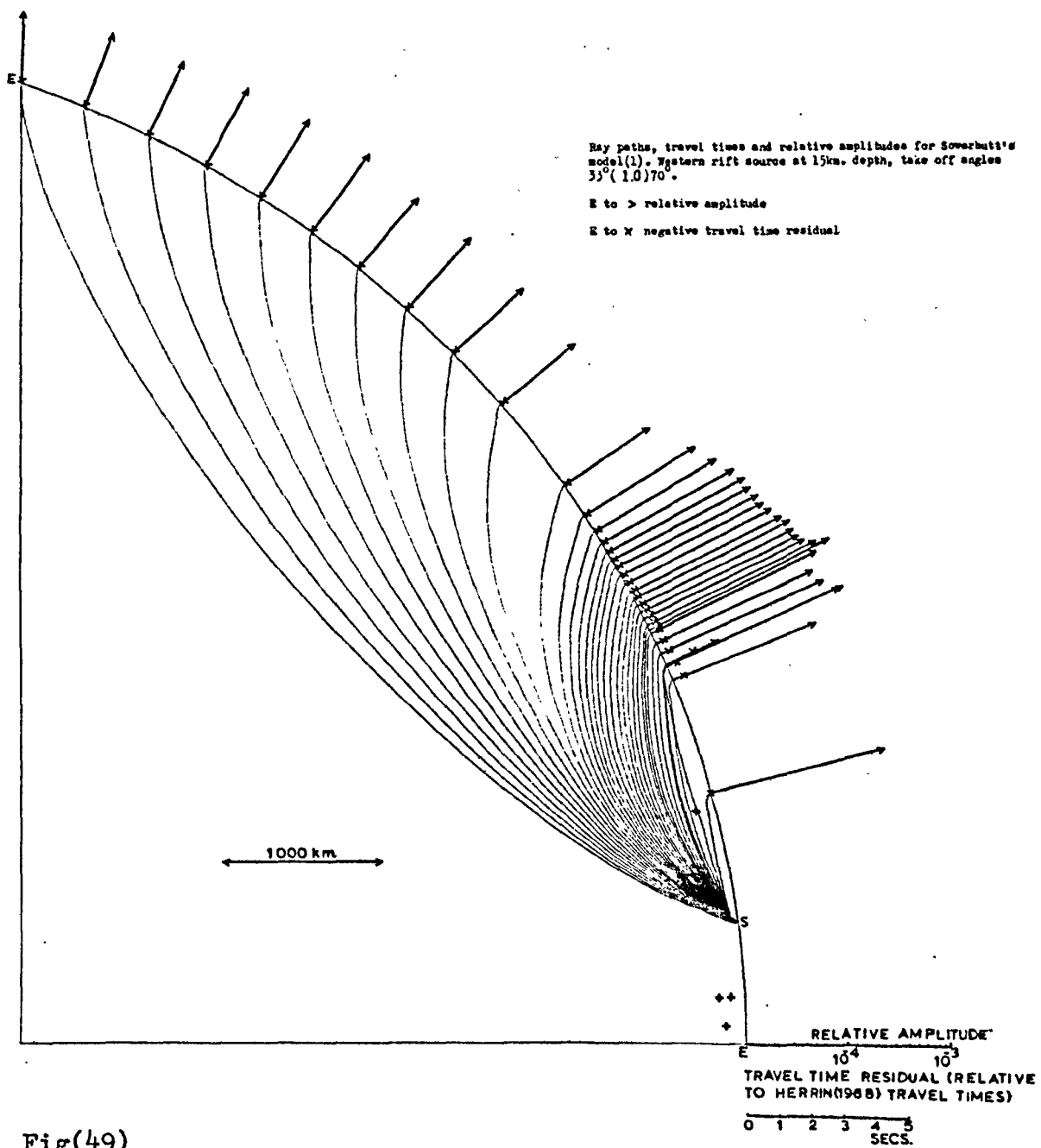
Ray paths, travel time residuals and relative amplitudes for
 Sowerbutts(1972) model (1). Western rift source at 15km. depth
 take off angles $33^{\circ}(0.25)37^{\circ}$

E to > Relative amplitude

E to x Negative travel time residual



FIG(48)



Fig(49)

E S

Ray paths, travel time residuals and relative amplitudes
for the Sowerbutts(1972) model(1). Atlantic source at
15km. depth, take off angles 60° (0.25°) 64° .

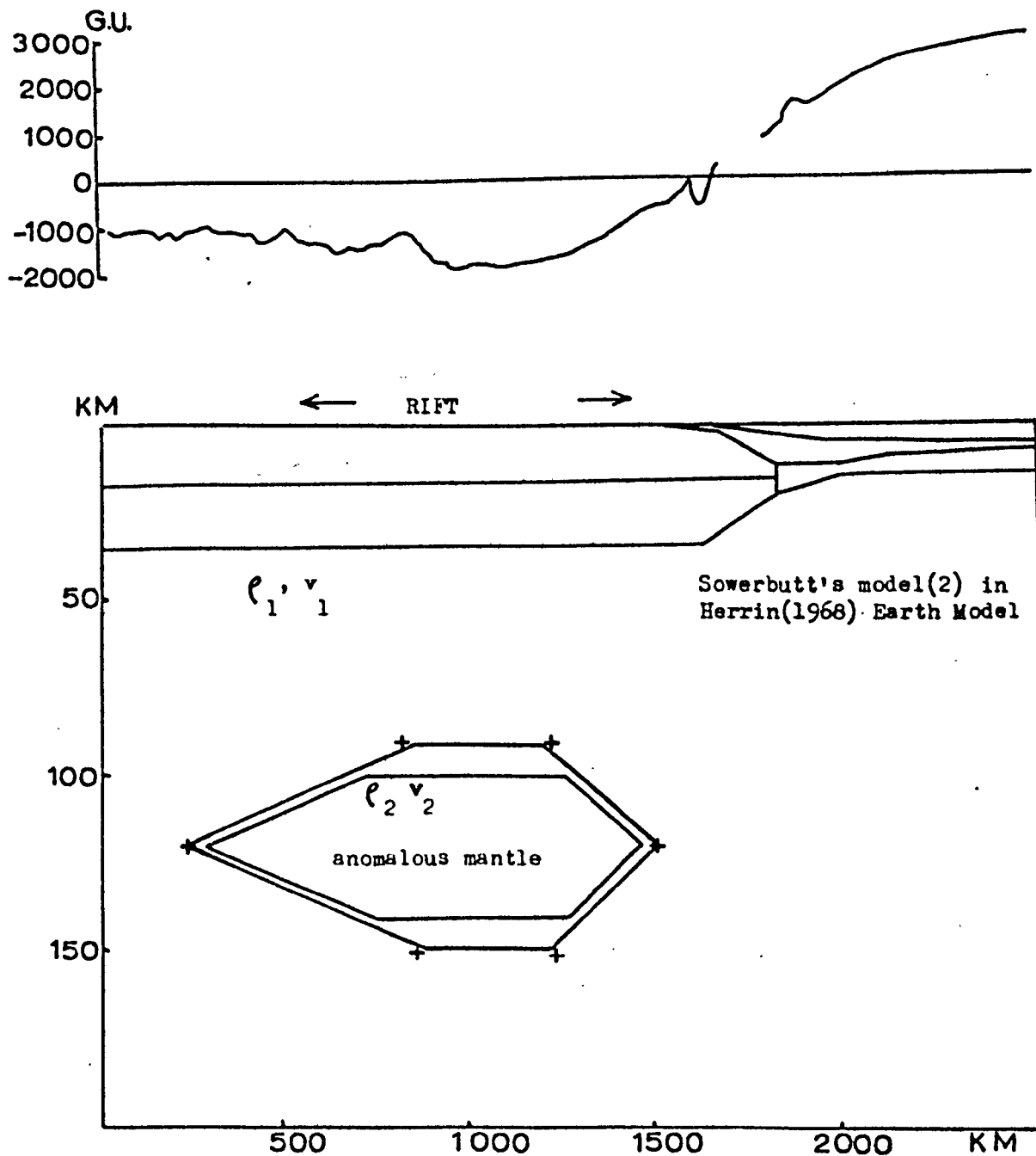
E to > Relative amplitude

E to X Negative travel time residual

1000km.

RELATIVE AMPLITUDE
E 10^{-4} 10^{-3}
TRAVEL TIME RESIDUAL (RELATIVE TO HERRIN
(1968) TRAVEL TIMES)
0 1 2 3 4 5 SECS.

Fig(50)



FIG(51) Gravity profile (2) and Sowerbutt's(1972) computed model

==== Marks the extent of the region of anomalous velocity and density.
In the region between the inner and outer lines the data values change linearly to normal mantle values.

+ Mark the corresponding + shown in fig(52) to fig(54)

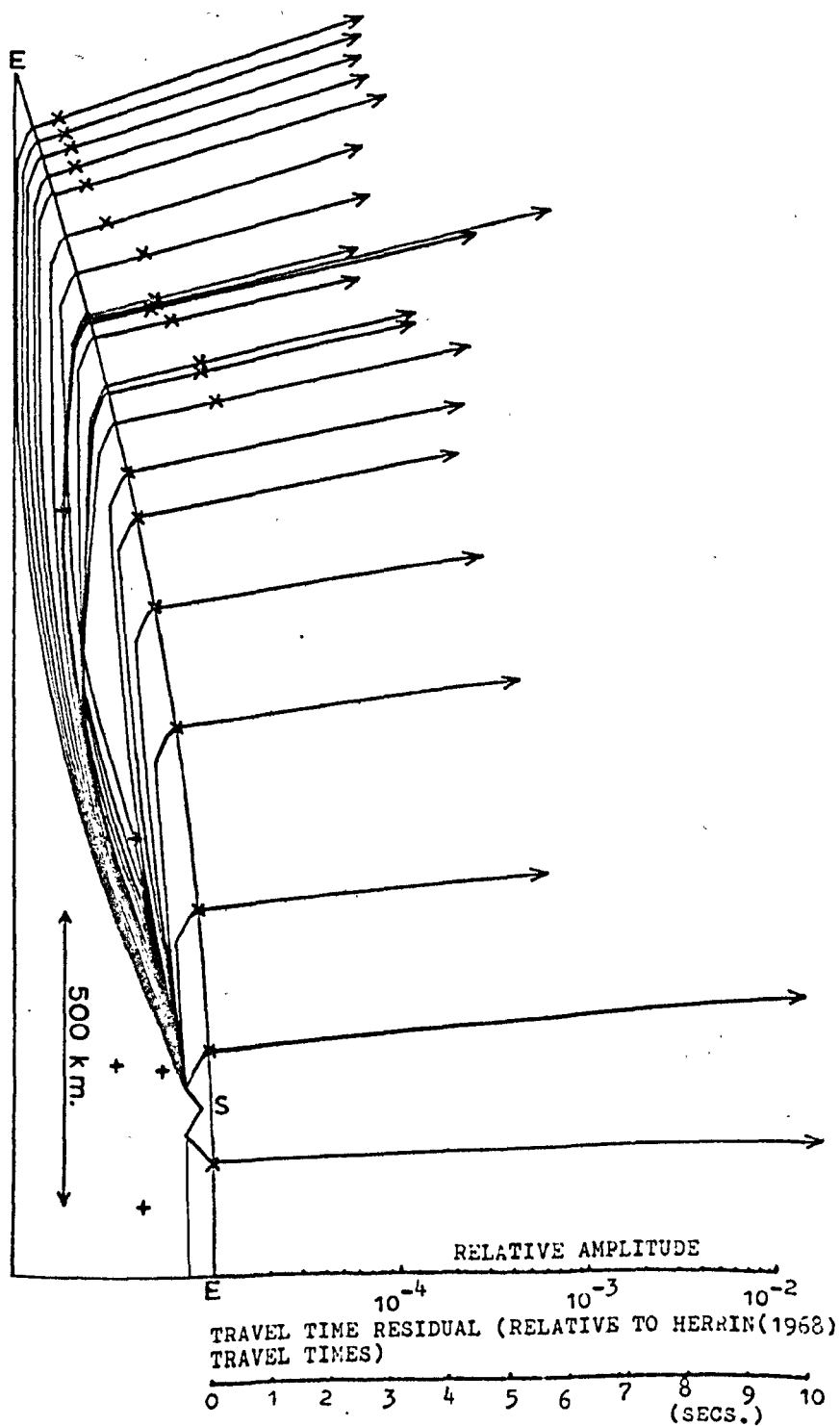
$$\text{s.g. difference} = \rho_1 - \rho_2 = 3.3 - 3.25 = 0.05$$

corresponding velocity difference = 0.12km/sec.
vertical exaggeration 10 : 1

Fig(52) Ray path, travel time residual and relative amplitude for Sowerbutt's model (2). Eastern rift source at 15km. depth, take off angles 33° (0.25°) 38° .

E to > Relative amplitude

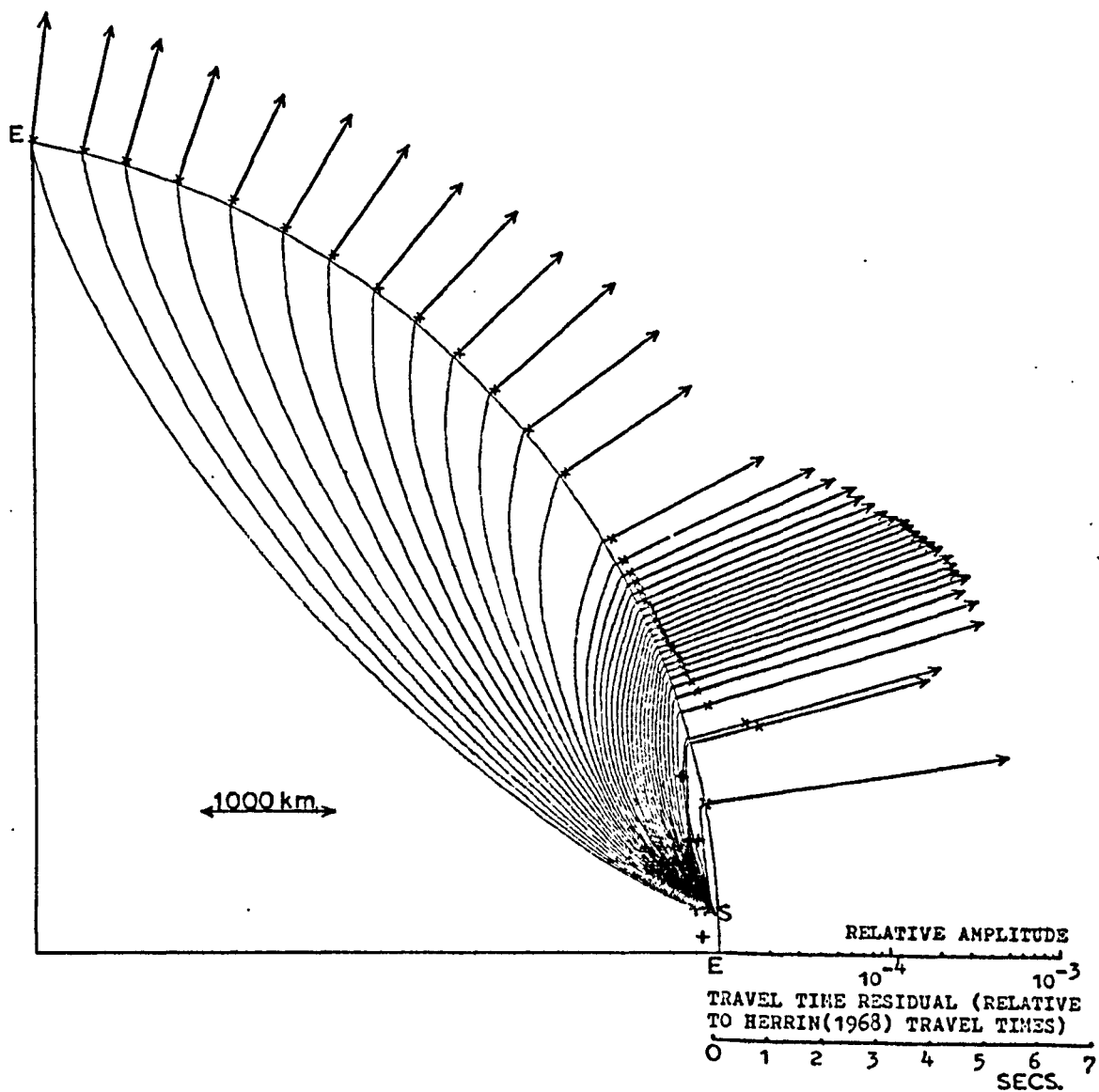
E to x Negative travel time residual



Fig(53) Ray paths, travel times and relative amplitudes for the Sowerbutt's model (2). Eastern rift source at 15km. depth, take off angles 34° (1.0°) 70° .

E to > Relative amplitude

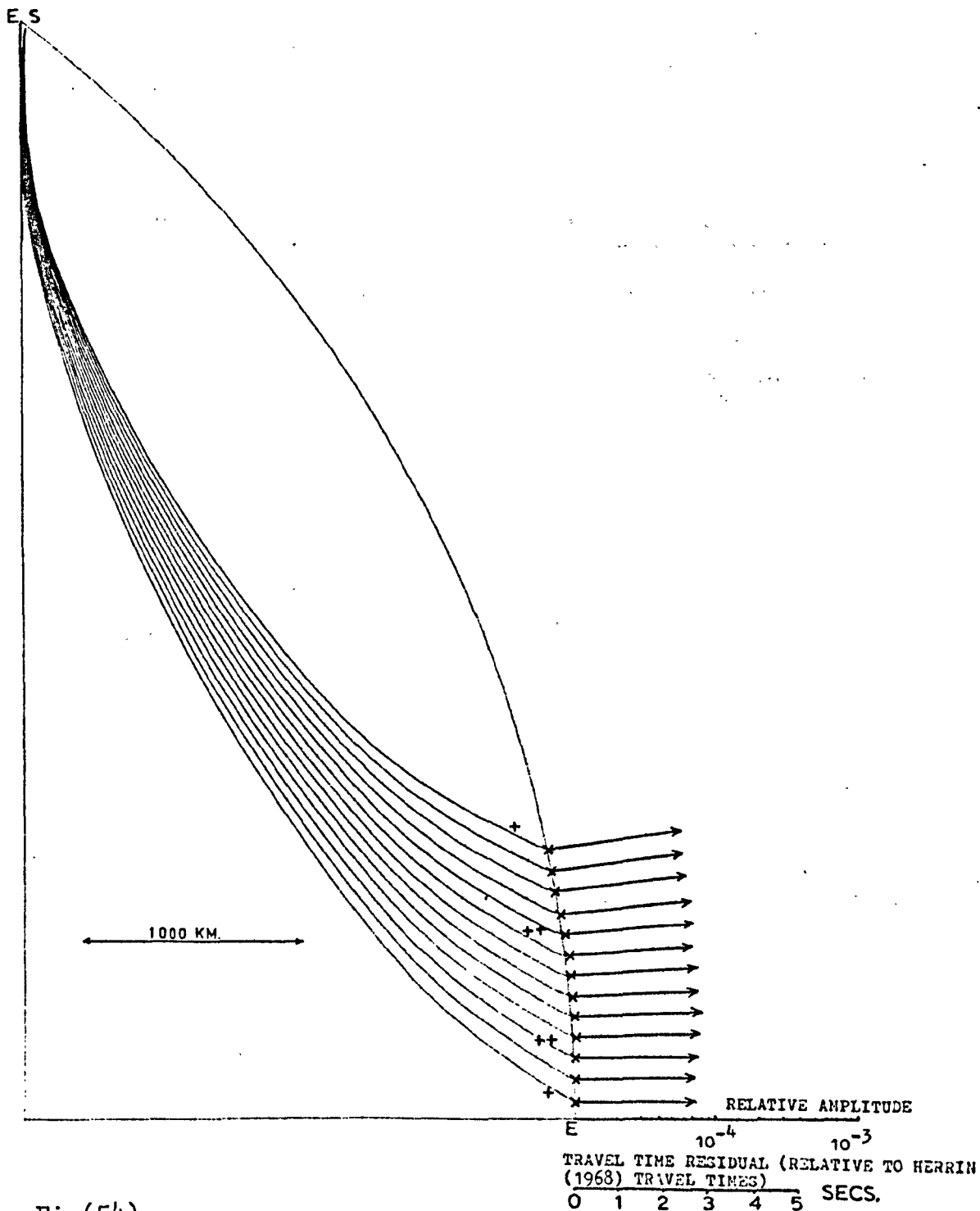
E to X Negative travel time residual



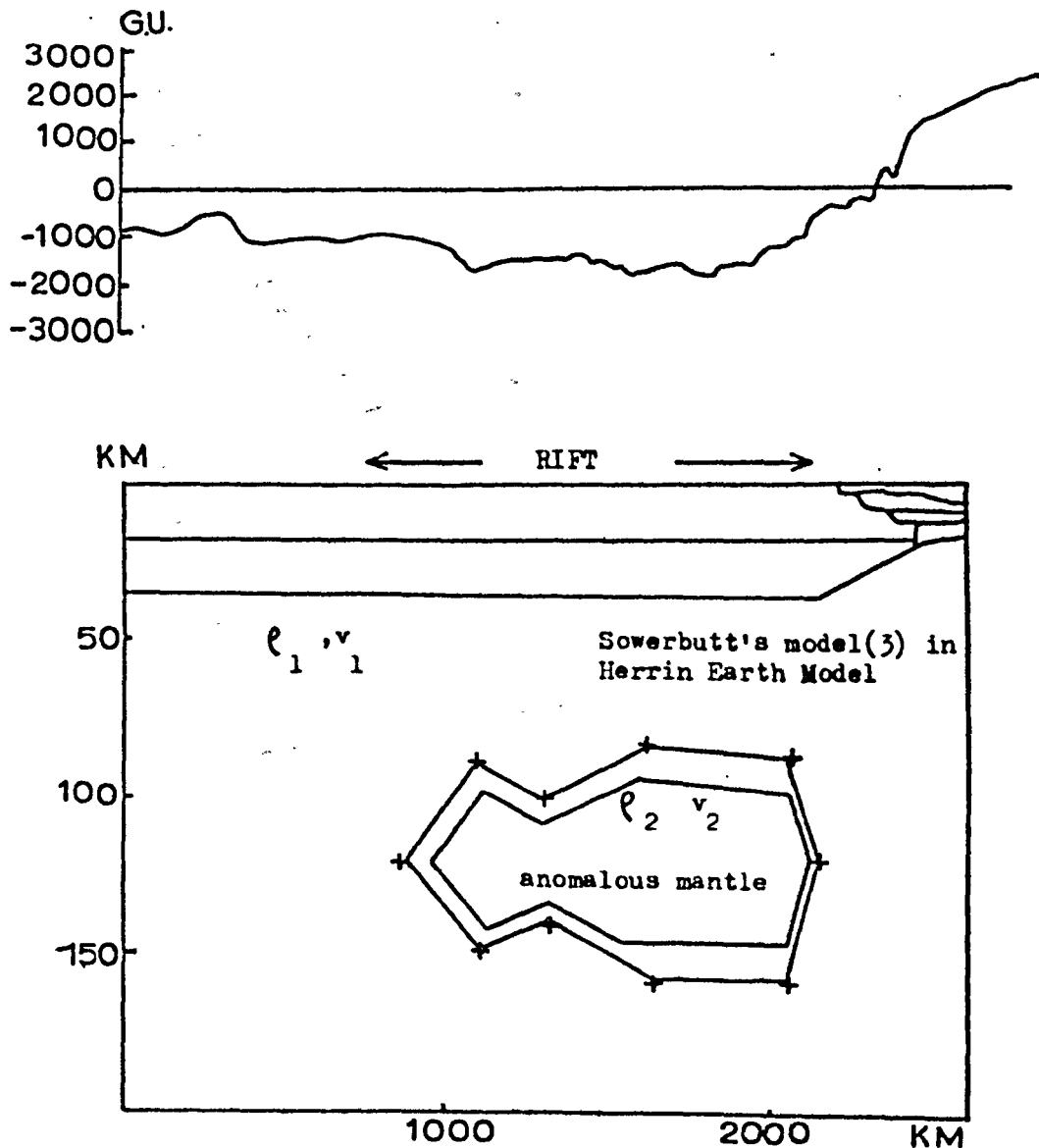
Ray paths, travel times and relative amplitudes for the Sowerbutt's model (2).
 Atlantic source at 15km. depth, take off angles 60° (0.25°) 63° .

E to > Relative amplitude

E to x Negative travel time residual



Fig(54)



FIG(55) Gravity profile (3) and Sowerbutt's(1972) computed model.

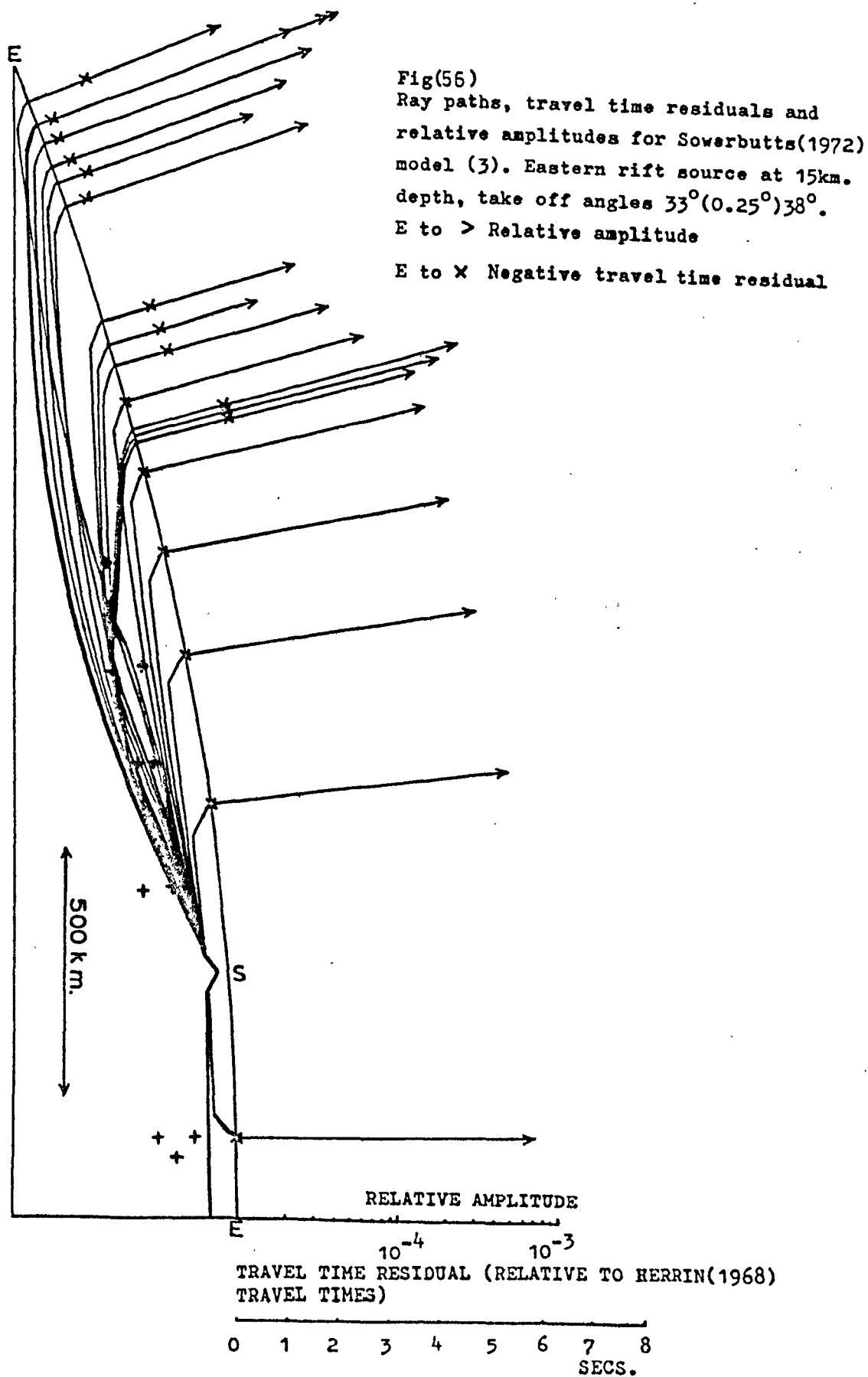
==== Marks the extent of the region of anomalous velocity and density.
In the region between the inner and outer lines the data values
change linearly to normal mantle values.

+ Mark the corresponding + shown in fig(56) to fig(58)

s.g. difference = $\rho_1 - \rho_2 = 3.3 - 3.25 = 0.05$

corresponding velocity difference = 0.12km/sec.

vertical exaggeration 10 : 1



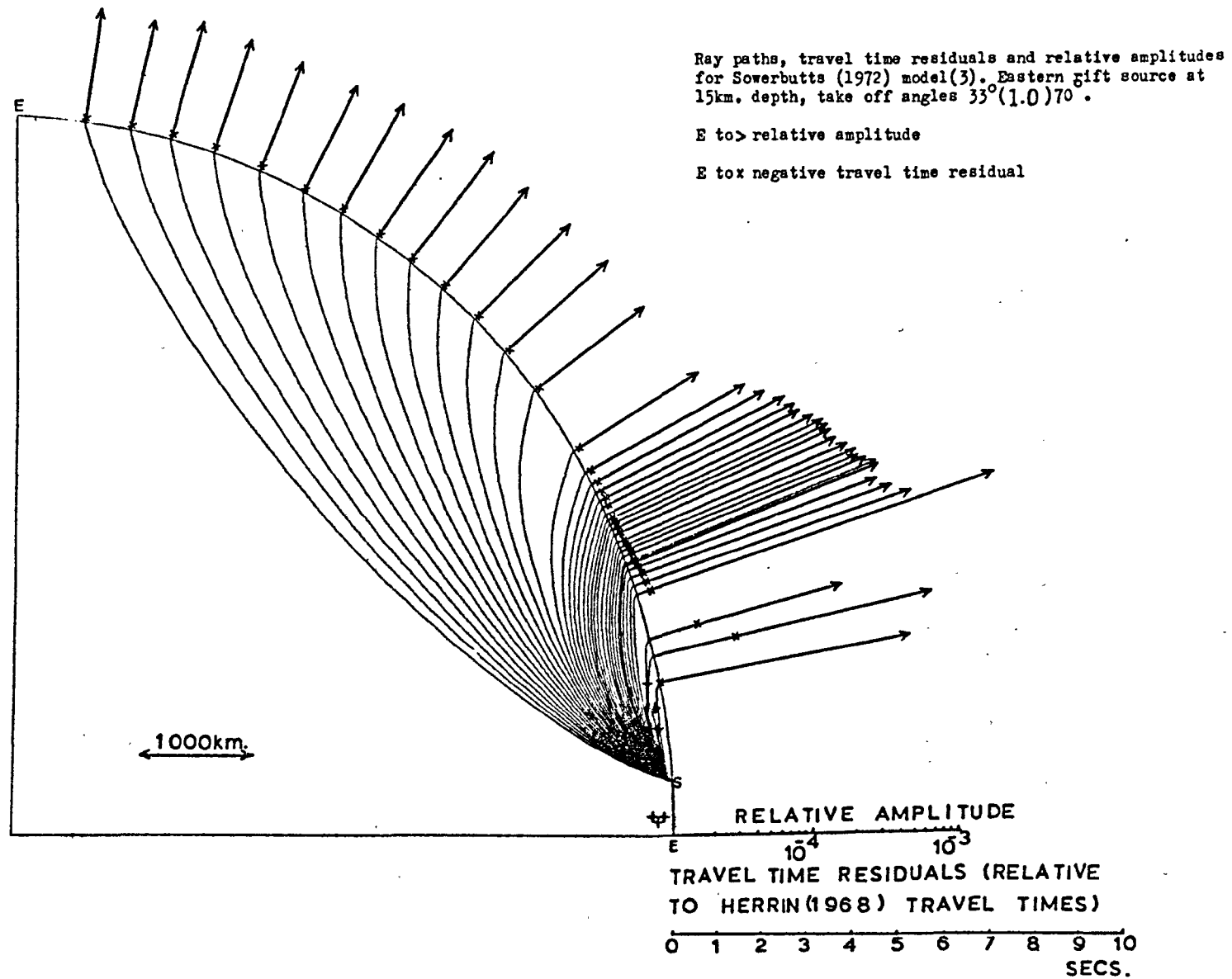
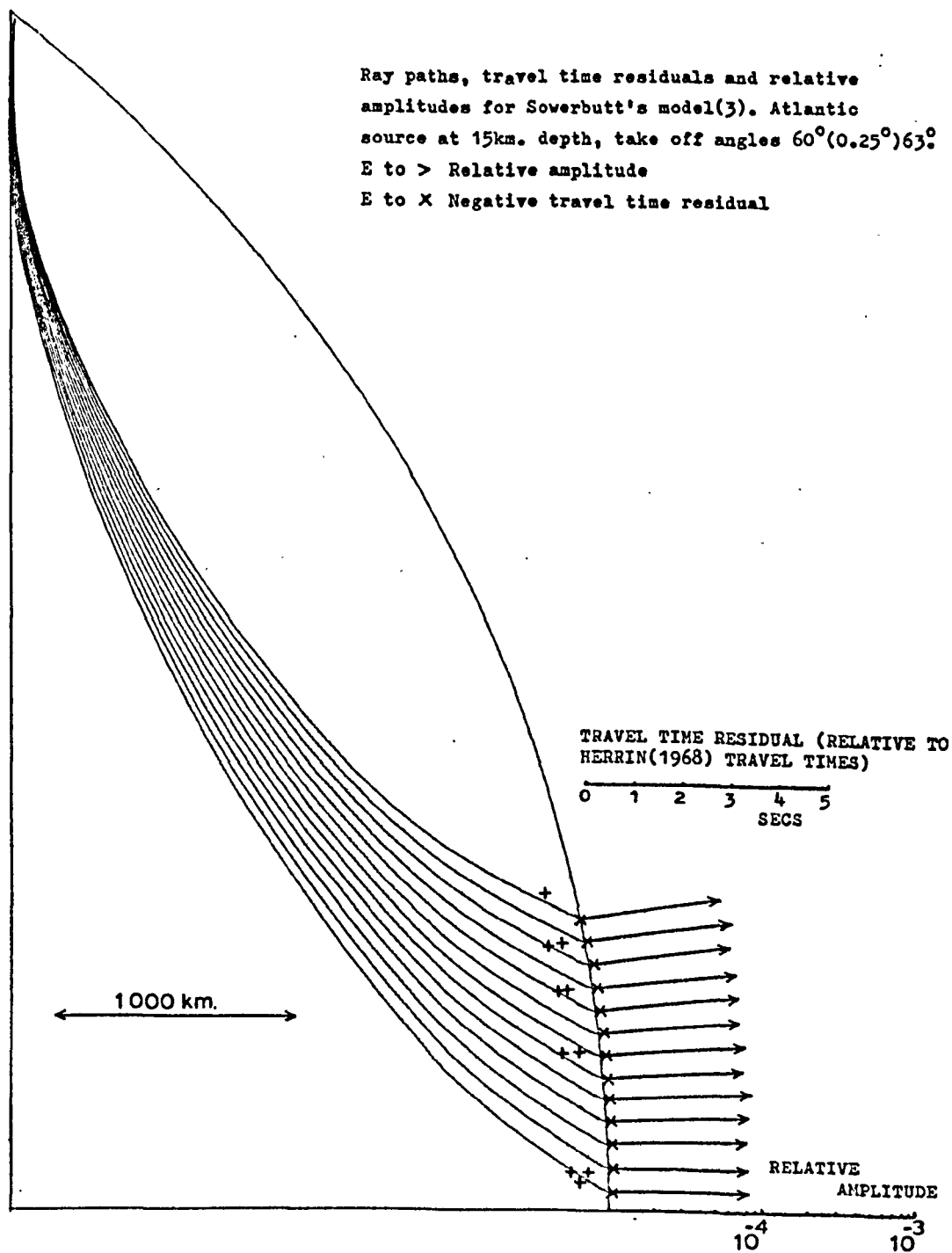


FIG (57)



Fig(58)

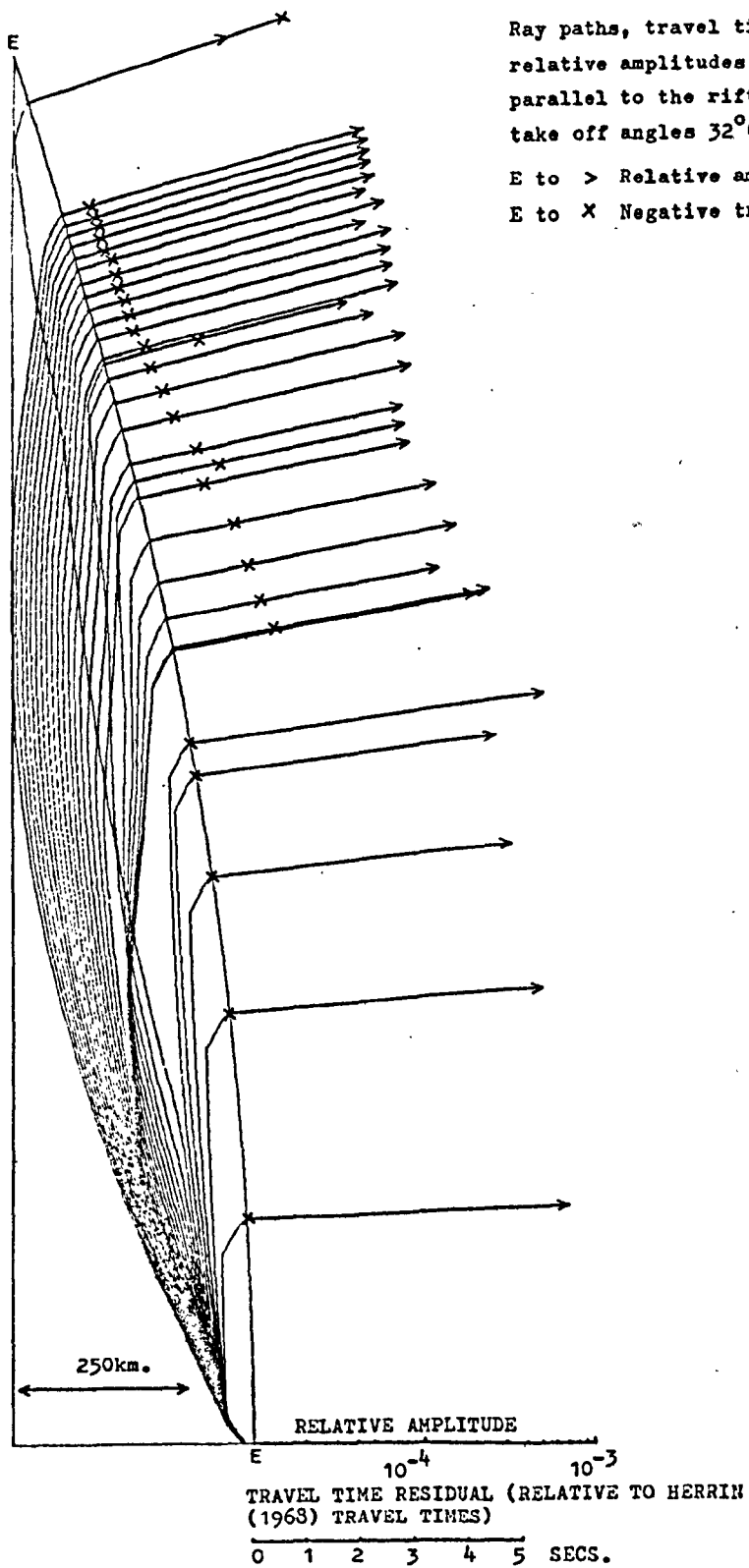


Fig (59)

gradient at the base of the low velocity material and have negative travel time residuals of between 2.0 sec. and 5.1 sec. In this case the higher travel time residuals are for the longer epicentral distances (figure (59)).

$$\Delta > 18.6^\circ$$

The RAY diagram for $\Delta > 18.6^\circ$ will correspond very closely to that obtained for the east west rays of models (2) and (3) (sections (3.2.8.2) and (3.2.8.3)) except the travel time residuals will be approximately doubled.

(3.2.9) Darracott et. al. (1972) Model using the Anderson and Kovach
Velocity Depth Profile for the Standard Earth - Eastern
Rift Source

The interpretation of gravity profile DFG (figure (26) and figure (60)) by Darracott et. al. (1972) is based on similar ideas to the model of Girdler et. al. (1969) and Searle (1969, 1970). This profile, which lies between profiles (3) and (4) crosses 450 km. of the eastern rift. Due to the relative shortness of this profile the very broad regional negative anomaly (figure (27) and figure (55)) is not accounted for in this analysis, only the axial positive anomaly and that part of the negative anomaly concentrated across the eastern rift is interpreted (figure (60)).

In this velocity model (figure (60)) the low velocity asthenolith approaches the base of a normal (unthinned) crust to within 15 km., except in the region of the axial trough where a 'plume' of low velocity material extends to and intrudes the crust. The velocity of this 'plume' decreases as it approaches the surface such that there is no velocity contrast between the mantle material which intrudes the crust and the lower crustal layer (figure (60)). All the boundaries shown in figure (60) are defined by velocity discontinuities. The Anderson and

Kovach velocity depth profile is used for the standard Earth and therefore the travel time residuals of figure (61) are relative to the travel times of figure (36).

There is no crustal thinning or positive velocity contrast in the lower crustal layer, in which the source is placed, so only effect (iii) need be considered in the following analysis.

$$\underline{\underline{\Delta < 5.7^\circ}}$$

Rays received here do not enter the low velocity material, therefore normal relative amplitudes and travel times are predicted (figure (61)).

$$\underline{\underline{5.7^\circ < \Delta < 12.3^\circ}}$$

This region is devoid of rays due to the refractive effects (rays refracted upwards) of the western boundary of the low velocity material (figure (61)).

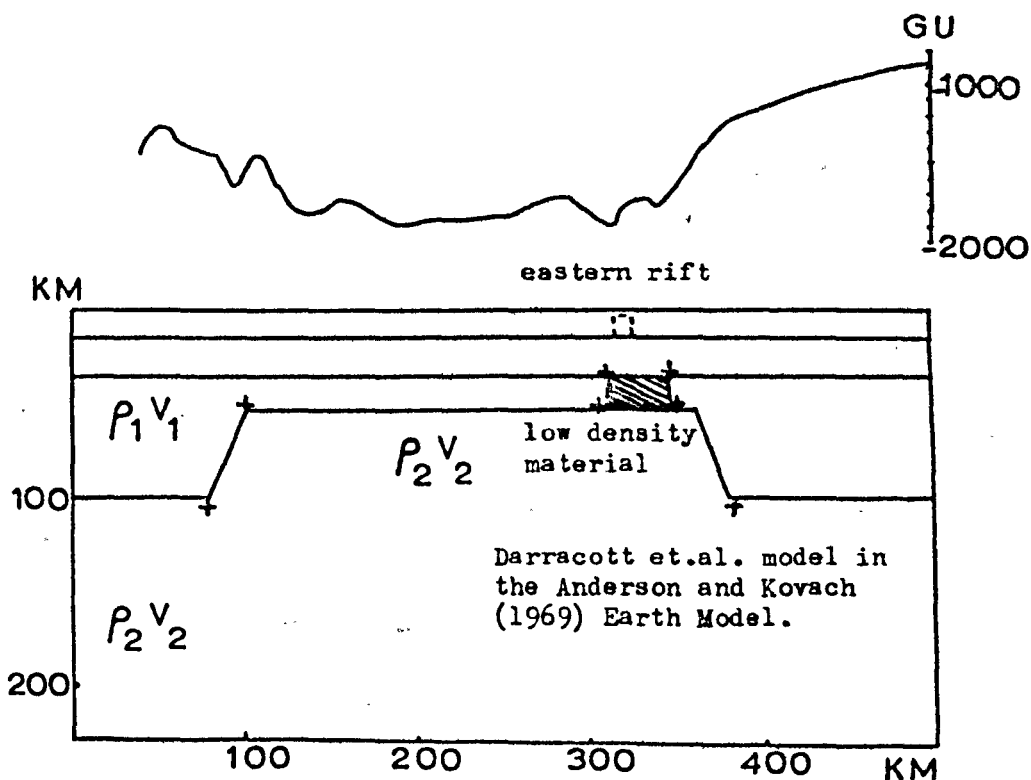
$$\underline{\underline{\Delta > 12.3^\circ}}$$

Arrivals in the region $12.3^\circ < \Delta < 12.6^\circ$ correspond to a mixture of rays whose paths are either:

(a) crust \rightarrow refraction at radial discontinuity into normal mantle \rightarrow refraction at radial discontinuity into low velocity mantle \rightarrow refraction downwards at the sloping western boundary of the low velocity material into normal mantle \rightarrow refraction at radial discontinuity into the crust.

or

(b) crust \rightarrow refraction at radial discontinuity into low velocity mantle \rightarrow refraction downwards at the vertical western boundary of the low velocity material into normal mantle \rightarrow refraction at radial discontinuity into low velocity mantle which grades into normal mantle \rightarrow refraction at radial discontinuity into the crust.



FIG(60) Gravity profile of Darracott et.al.(1972) and their interpretation For this model the velocity depth profile of Anderson and Kovach(1969) is taken for the normal mantle.

All the lines on this diagram represent discontinuities.

+ Marks the corresponding + shown on fig(61)

$$\text{s.g. difference} = \rho_2 - \rho_1 = 3.24 - 3.34 = -0.1$$

$$\text{corresponding velocity difference} = -0.32 \text{ km/sec.}$$

$$\text{s.g. difference of dashed region} = 3.20 - 3.34 = -0.14$$

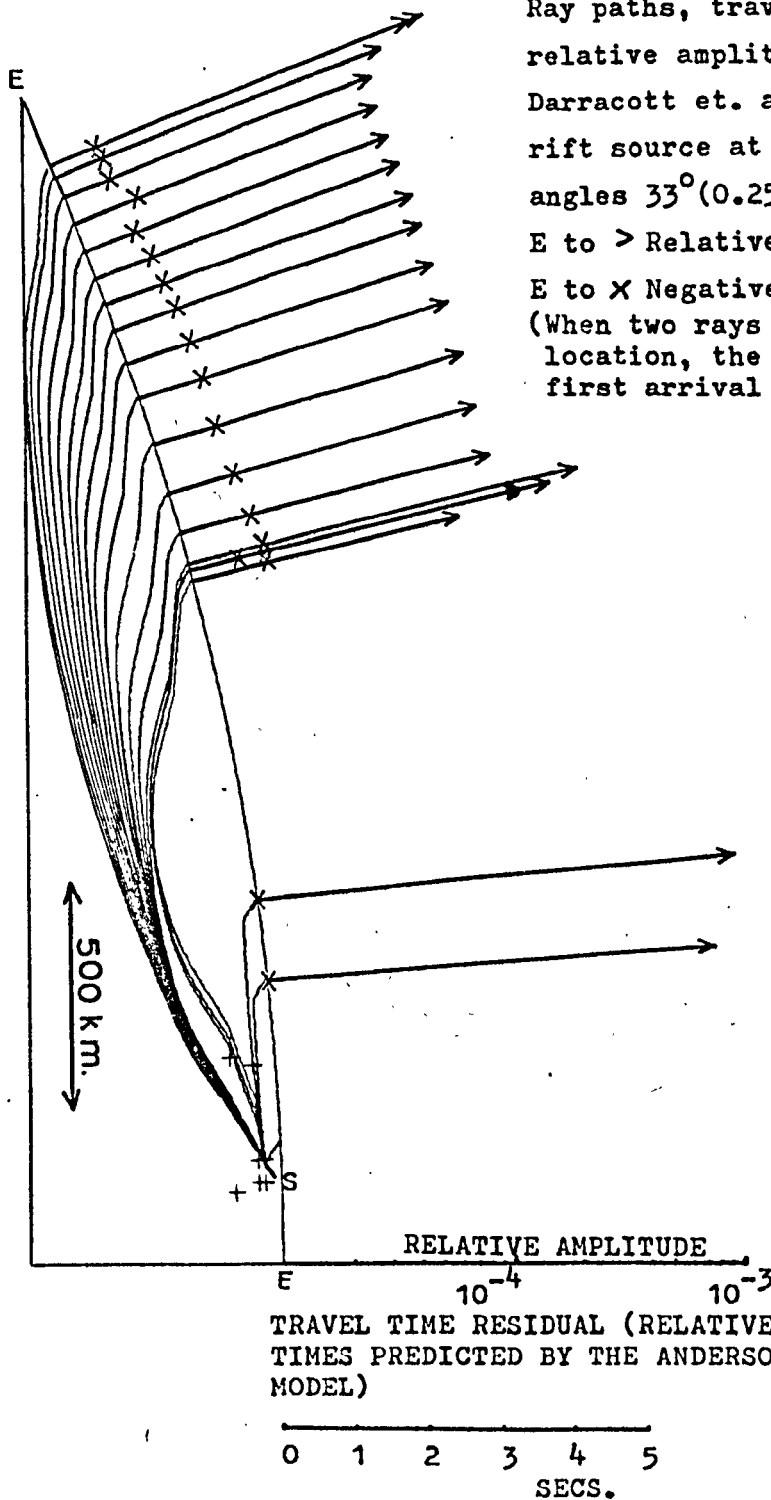
$$\text{corresponding velocity difference} = 0.42 \text{ km/sec.}$$

Fig(61)

Ray paths, travel time residuals and relative amplitudes for the Darracott et. al.(1972) model. East rift source at 15km. depth, take off angles 33° (0.25°) 38° .

E to > Relative amplitude

E to X Negative travel time residual
(When two rays occur at a single location, the amplitude of the first arrival is marked ►)



TRAVEL TIME RESIDUAL (RELATIVE TO THE TRAVEL TIMES PREDICTED BY THE ANDERSON AND KOVACH(1969) MODEL)

Type (a) rays arrive first with negative travel time residuals ~ 0.8 sec. and these are followed 0.3 sec. to 0.4 sec. later by type (b) rays (figure (61)). Type (a) rays show a progressive increase in amplitude with distance in this region.

For $\Delta > 12.6^\circ$ all the rays are of type (b) with travel time residuals from 0.5 sec. to 0.9 sec.

(3.2.10) Comparison of the Observed and RAY Traced Travel Time
'Corrections' for Events in the North Western Rift and
Central Tanzania

(3.2.10.1) Observed Travel Time Corrections

In a study of the seismicity of Africa, Fairhead and Girdler (1971) obtained average travel time 'corrections' for a number of ray paths. These 'corrections' are the difference between the recorded time of arrival and the estimated time of arrival using the JED (see section (3.1)) located epicentres and the Herrin (1961) travel times. Each average 'correction' is the mean for a number of near neighbouring events. The four 'average' events which are of interest here are those of the north western rift and central Tanzania for pre-1963 (locations 1 and 3 in figure (62)) and post-1963 (locations 2 and 4 in figure (62)).

The travel time 'corrections' (TC1) are shown in table (8) (personal communication from Girdler (1972)) together with the station corrections (TC0) of Lilwall and Douglas (1970). The station corrections of Lilwall and Douglas (1970) are preferred in this study as an estimate for each of the African stations is available. Herrin and Taggart (1968) only give corrections for seven out of the sixteen stations of figure (62) but the pattern of their corrections is similar

to that of Lilwall and Douglas (1970). In general the station corrections are azimuthally dependent and may be represented in the form $A + B \sin (\theta + \phi)$ where θ is the azimuth and A, B and ϕ are constants. The azimuthal term is included in the corrections for the stations for which it is available, otherwise only the constant term A is used (table (8)).

If the travel time 'corrections' are split into three components:

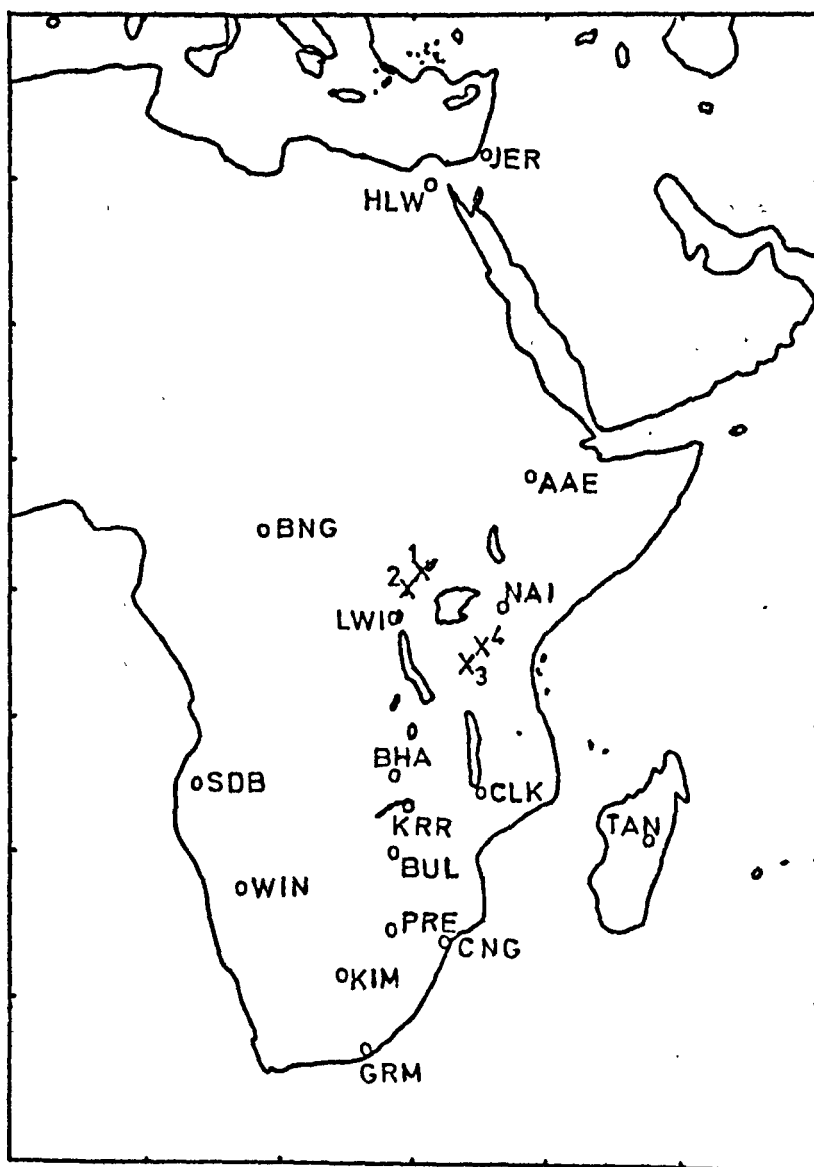
- (a) near source component (effect of the crust and uppermost mantle near to the source),
- (b) ray path component (effect of the mantle away from the source and receiver),
- (c) near receiver component (effect of the crust and uppermost mantle near to the receiver),

it is clear that for events and stations in the rift the velocity models should account for all three components, while for events in the rift and stations away from the rift the velocity models will only account for (a) and part of (b). By subtracting the station correction from the travel time 'correction' it is hoped that most of (c) will be eliminated. In most cases the TC1 values to stations outside of the rift are large negative (table (8)) while most of the modified travel time 'corrections', TC2 (table (8)), are much smaller in magnitude. For comparison with the RAY traced estimates, TC1 will be used for paths to stations in the rift while TC2 will be used for paths to stations away from the rift.

It must be emphasized that relative travel time 'corrections' are important in this study. If different tables (e.g. Herrin (1968)) are used for the reference travel times then some of the smaller magnitude

	WESTERN RIFT 1				WESTERN RIFT 2				TANZANIA 1				TANZANIA 2			
	N	TC0	TC1	TC2	N	TC0	TC1	TC2	N	TC0	TC1	TC2	N	TC0	TC1	TC2
AAE	3	2.3	0.2		21	2.3	2.2		4	2.5	0.6		8	2.6	2.5	
* BHA	10	-0.1	-0.2	-0.1	16	-0.1	0.2	0.3	7	-0.1	-2.0	-1.9	13	-0.1	-1.2	-1.1
BNG	10	-0.5	1.7	2.2	17	-0.4	0.7	1.1	4	-0.4	-3.9	-3.5	11	-0.4	-1.3	-0.9
BUL	16	-1.1	-1.8	-0.7	30	-1.1	-1.6	-0.5	7	-1.1	-3.2	-2.1	11	-1.1	-3.7	-2.6
* CLK	9	0.4	-2.5	-2.9	9	0.4	-2.3	-2.7					12	0.4	-0.4	-0.8
* CNG	3	-0.5	-1.1	-0.6									6	-0.5	-1.0	-0.5
* HLW	2	-0.7	-0.5		3	-0.7	-0.4		7	-0.7	-1.0					
JER	3	1.2	-0.2		3	1.2	-0.1		5	1.2	-0.3		2	1.2	-0.1	
* KIM	2	-0.8	-1.4	-0.6					10	-0.8	-1.9	-1.1				
* KRR	6	-1.0	-2.2	-1.2	2	-1.0	-1.8	-0.8					6	-1.0	-1.4	-0.4
LWI	15	0.3	1.0		32	0.3	1.0		12	1.4	-1.1		10	1.2	0.8	
NAI	17	1.9	-1.1		30	2.0	-0.2						19	2.7	0.3	
PRE					11	0.4	0.1	-0.3	11	0.4	-1.8	-2.2	6	0.4	0.6	0.2
SDB					19	0.1	-0.4	-0.5					8	0.4	0.6	0.2
WIN					2	0.6	0.8	0.2	9	0.7	0.4	-0.3	3	0.6	0.5	-0.5

Table (8) Travel time ' corrections ' of paths from four East African average events to African seismic stations (TC1). Station 'corrections ' (TC0) after Lilwall and Douglas (1970). N is the number of events , $TC2 = TC1 - TC0$ represents the travel time ' correction ' associated with the ray path away from the receiver station.



Fig(62) Map of Seismograph stations in Africa and the 4 'average' events used in this study.

'corrections' would change sign, but the relative values within a given set of 'corrections' would not be expected to change very much (see Jacob (1972)).

In their discussion of the travel time 'corrections', with magnitudes greater than 1 sec., Fairhead and Girdler (1971) conclude that rays travelling along paths beneath the shield regions are speeded up, whilst rays travelling beneath the East African Rift System are slowed down. When all the travel time 'corrections' are studied, regardless of magnitude, the same general pattern is observed. Possible inconsistencies and interesting features of these data, which have not been mentioned before are:

- (i) The rays to AAE from the pre-1963 events 1 and 3 are approximately 1.8 sec. faster than the near neighbouring post-1963 events 2 and 4 (table (8)). Only three and four events respectively were used in the averaging for the pre-1963 events so these estimates must be viewed with caution.
- (ii) Three of the four paths which sample the uppermost part of the mantle beneath the Tanganyika Shield (see Part 1, chapter (1)) have small to moderate negative 'corrections' (table (8)) but the fourth path (4 to LWI) has a 0.8 sec. positive 'correction'.
- (iii) The travel time 'corrections' for rays to BNG from the western rift are large positive while the rays from the eastern rift have large negative 'corrections' (table (8)). This indicates that the mantle at approximately 300 km. beneath the Tanganyika Shield and the Congo Basin is speeding up the rays. How much of the speeding up takes place beneath the Tanganyika Shield is difficult to estimate as the rays from the western rift travel 50 km. to 100 km. higher in the mantle than

the rays from the eastern rift. It is therefore possible that the speeding up is due to a large radial increase in velocity between 200 km. and 300 km. depth.

Neither the inconsistencies in the data nor the variation in travel time 'corrections' to BNG are explained by the velocity models but these features should be kept in mind in the following discussion.

(3.2.10.2) RAY Traced Travel Time 'Corrections'

The RAY traced travel time 'corrections', which are the travel time residuals of sections (3.2.5) to (3.2.9) with the sign reversed, are estimated from the RAY diagrams using the following criteria:

(i) The stations AAE, HLW, JER, LWI and NAI are situated above low velocity mantle material, all other stations are above normal mantle.

(ii) For events 1 and 2 to (a) AAE, HLW, JER and LWI the RAY diagrams for north south rays are used,

(b) BHA, BNG, BUL, CLK, CNG, GRM, KIM, KRR, NAI, PRE, SDB and WIN the RAY diagrams for east west rays are used.

(iii) For events 3 and 4 to (a) AAE, HLW, JER and NAI the RAY diagrams for north south rays are used,

(b) BHA, BNG, BUL, CLK, CNG, GRM, KIM, KRR, LWI, PRE, SDB and WIN the RAY diagrams for east west rays are used.

(iv) There is no well defined axial positive anomaly in the region of the central Tanzania events. Therefore between 0.1 sec. and 0.4 sec has been removed from each RAY traced estimate of the Girdler et. al. models (1) and (2) to compensate for this. Girdler et. al. model (4) and Sowerbutts models (2) and (3) are used for the other RAY traced estimates of these events.

(v) Due to the restriction that rays must bottom above 350 km.

in the standard Earth defined by the Anderson and Kovach velocity depth profile (section (3.2.2)), only data for $\Delta < 21^\circ$ are available from the Girdler et. al. models (3) and (4).

The use of the east west RAY diagrams for the estimation of the travel time 'corrections' for the southern stations is fully justified by the fact that rays which reach these stations are only affected by the vertical extent of the low velocity material. That is, for $\Delta > 16^\circ$ (in most cases $\Delta > 12^\circ$) the travel times obtained from the given two dimensional velocity models are independent of azimuth.

(3.2.10.3) Comparison of the RAY Traced Estimates with the Observed Travel Time 'Corrections'

In figure (63) to figure (66) the ray paths across the surface of the Earth are plotted for the observed data and the various velocity models according to the sign and magnitude of the travel time 'corrections'.

Western Rift Events (1 and 2) to NAI

Girdler et. al. models show moderate positive 'corrections' (~ 0.8 sec.) while the Sowerbutts models show moderate negative 'corrections' (~ -0.8 sec.). The latter are consistent with the event 1 path (~ -1.1 sec.) (table (8) and figure (63)). The event 2 path has a small negative 'correction' (~ -0.2 sec.) (figure (64)).

Western Rift Events (1 and 2) to AAE

All models show large positive 'corrections' consistent with the event 2 path (figure (64)). The magnitudes of the 'corrections' from the Girdler et. al. models (~ 2.0 sec.) are nearer to the observed (~ 2.1 sec.) than the estimates from the Sowerbutts models (~ 1.1 sec.).

Event 1 path has a small positive 'correction' (~ 0.2 sec.) (table (8) and figure (63)) but is based on only 3 observations.

Western Rift Events (1 and 2) to BNG

The predicted travel times from all the models, are too small by at least 0.6 sec. for this path.

Western Rift Events (1 and 2) to LWI

Girdler et. al. models correctly predict travel time 'corrections' ~ 1.0 sec. for both events (figure (63) and figure (64)), while the Sowerbutts models have a zero 'correction'.

Western Rifts Events (1 and 2) to JER and HLW

From the Girdler et. al. models (1) and (2) small negative travel time 'corrections' are correctly predicted for both events (figure (63) and figure (64)). The Sowerbutts models show small positive 'corrections'.

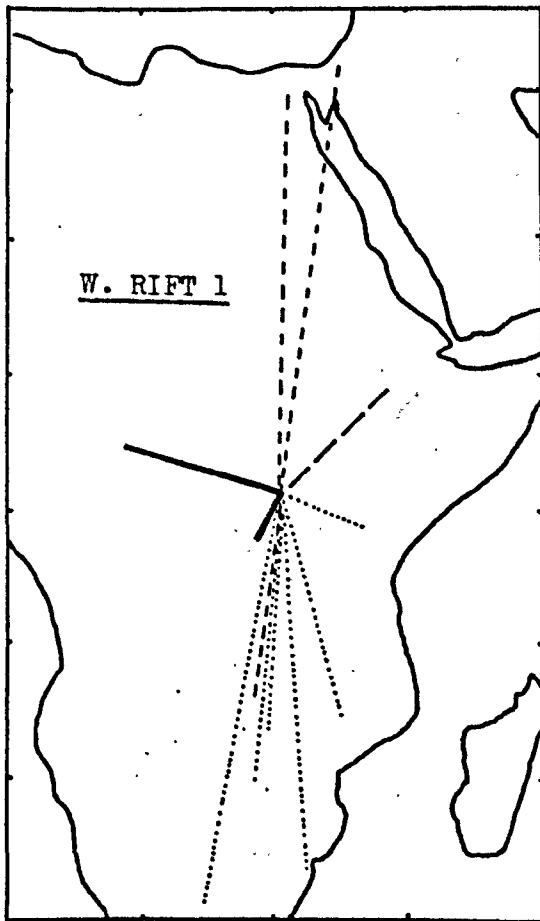
Western Rift Events (1 and 2) to Stations in the South

The rays through all the models are too slow for most of the paths to stations in the south (figure (63) and figure (64)). The very small negative 'corrections' of the Girdler et. al. models are nearest to the observed data, but even these are mostly 0.5 sec. too slow.

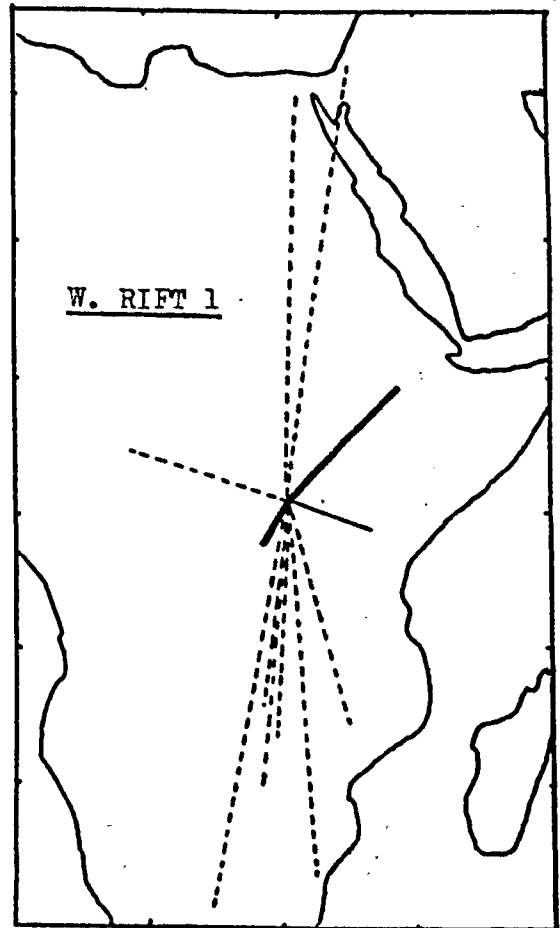
Tanzania Event (4) to NAI

The Girdler et. al. models show large positive 'corrections' (1.1 sec. to 1.5 sec.) while the Sowerbutts models have a zero correction. These must be compared to the observed 0.3 sec. positive 'correction' (table (8) and figure (66)).

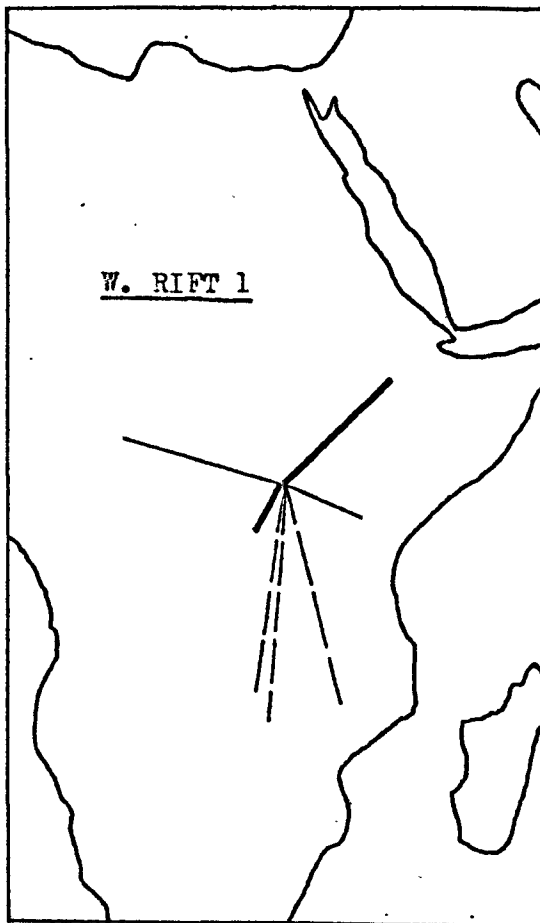
(a) Observed



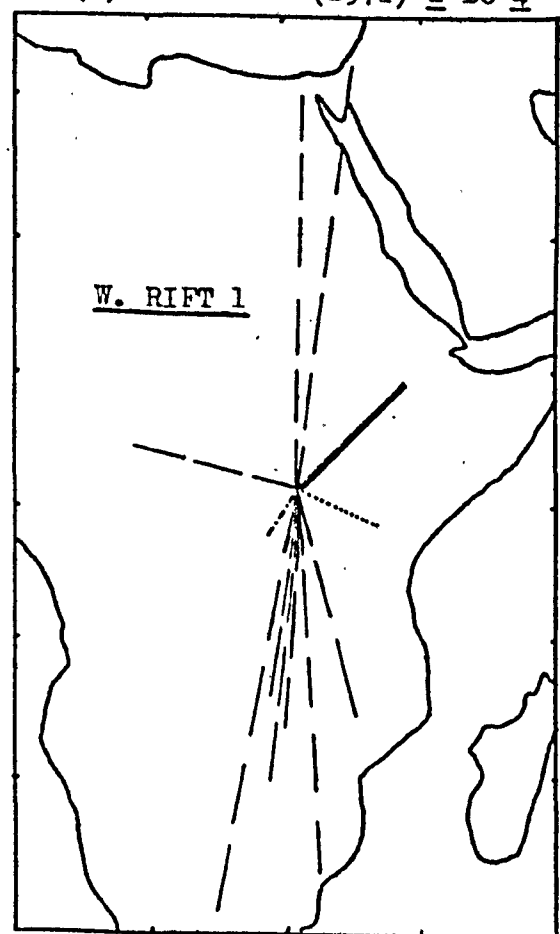
(b) Girdler et.al.(1969) 1 and 2



(c) Girdler et.al.(1969) 3 and 4

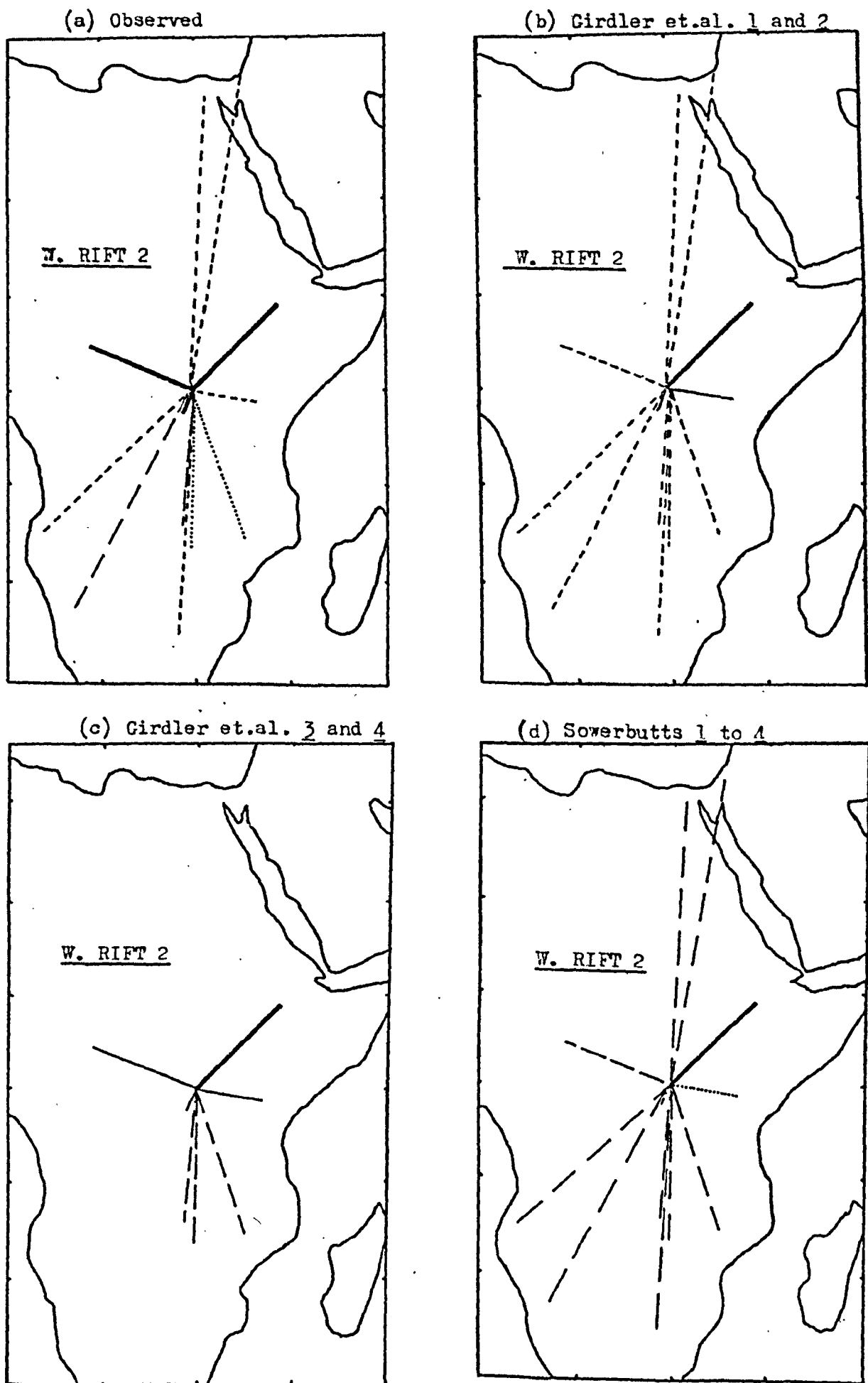


(d) Sowerbutts(1972) 1 to 4



Fig(63) Comparison of observed travel time 'corrections' with those predicted from RAY tracing. correction ≤ -0.5 (sec),

--- $-0.5 \leq \text{correction} < 0.0$, - - - - - 0 = correction, ——— $0.0 < \text{correction} \leq 0.5$
0.5 < correction < 1.0, ——— $1.0 \leq \text{correction}$



Fig(64) Comparison of observed travel time 'corrections' with those predicted from RAY tracing.

.....	correction < -0.5 sec.	----	$-0.5 \leq \text{correction} < 0.0$
-----	0 = correction	— — —	$0.0 < \text{correction} \leq 0.5$
———	$0.5 < \text{correction} < 1.0$	————	$1.0 \leq \text{correction}$

Tanzania Events (3 and 4) to AAE

The Girdler et. al. models show large positive corrections (1.1 sec. to 1.5 sec.) consistent with the event 4 path (figure (66)), whereas the Sowerbutts models have moderate positive corrections (~ 0.6 sec.) consistent with the event 3 path (figure (65)). It is emphasized that the event 3 'correction' is based on only four observations.

Tanzania Events (3 and 4) to HLW and JER

The predicted travel times from all the models are too large for these paths (rays are 0.3 sec. to 1.0 sec. too slow).

Tanzania Events (3 and 4) to BNG

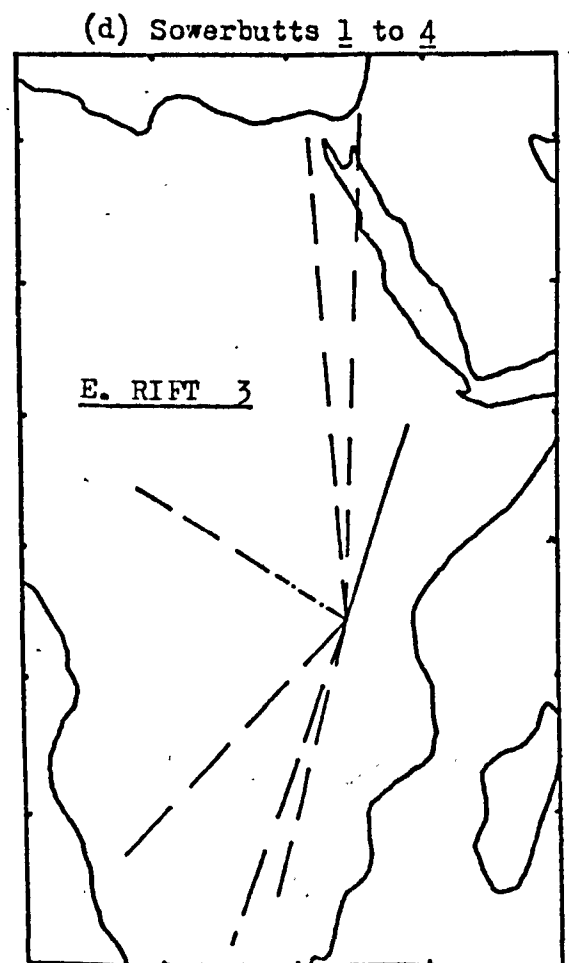
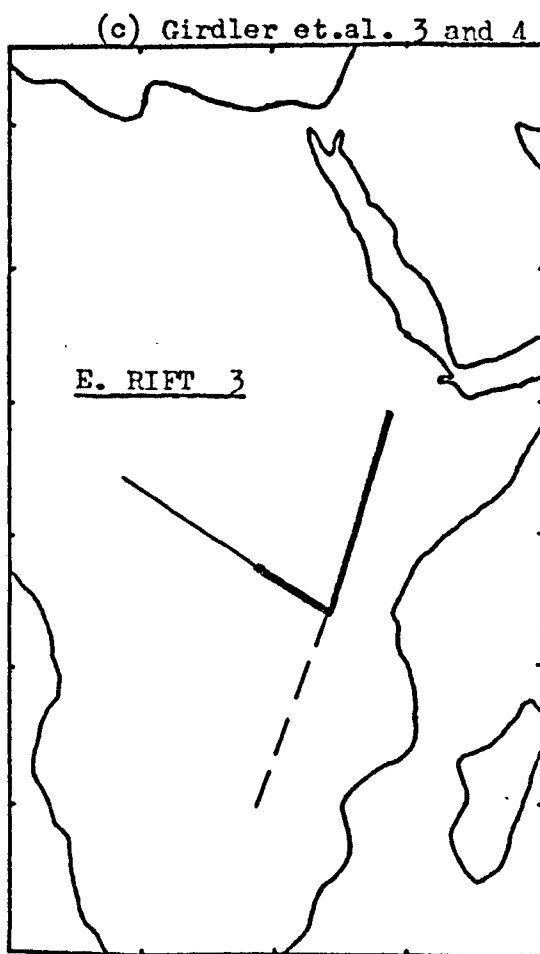
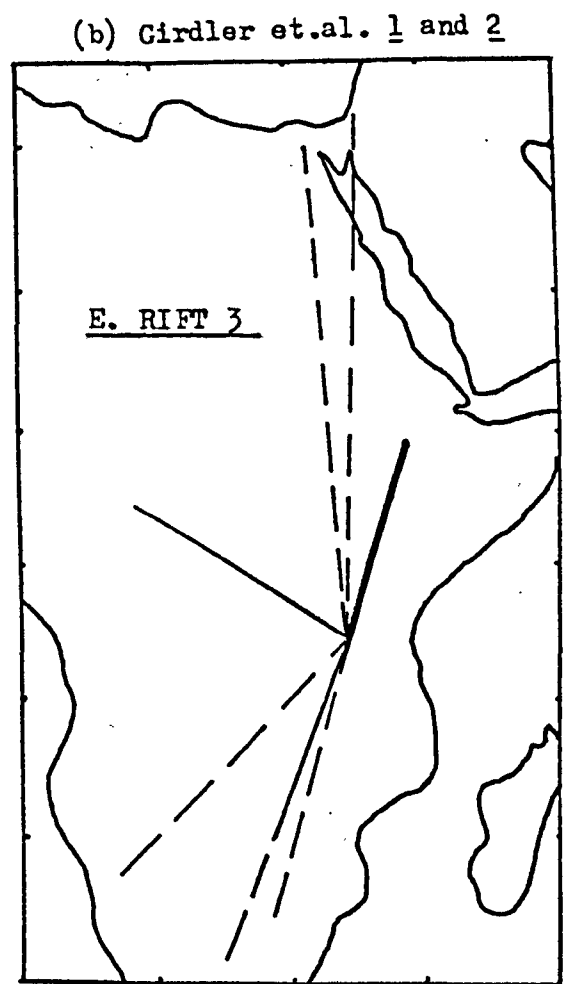
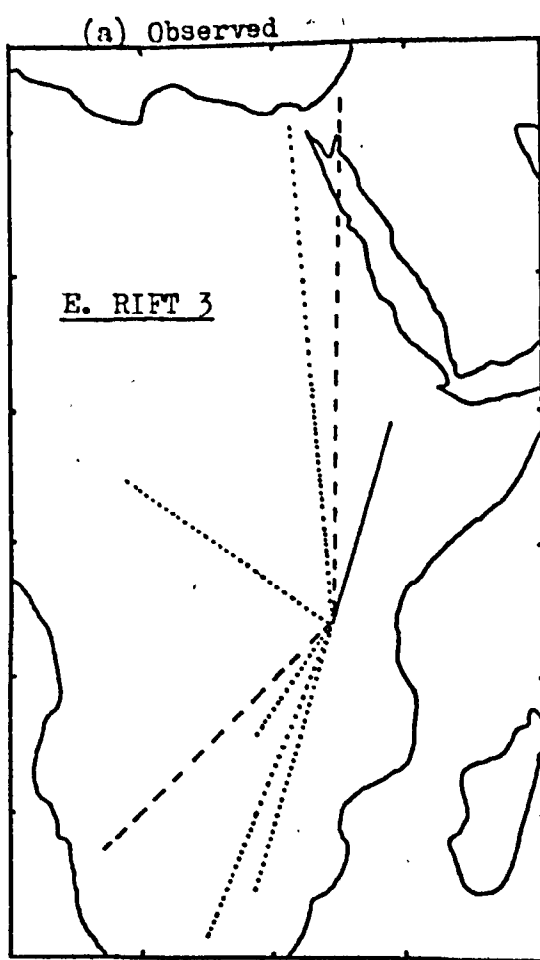
The predicted travel times from all the models are too large for these paths (rays are 1.3 sec. to 4.2 sec. too slow) (figure (65) and figure (66)).

Tanzania Events (3 and 4) to LWI

The Girdler et. al. models show moderate (0.8 sec. to 1.0 sec.) positive 'corrections' which are consistent with the event 4 path (0.8 sec.) while the Sowerbutts models show a zero correction. The event 3 path has a -1.1 sec. travel time 'correction'.

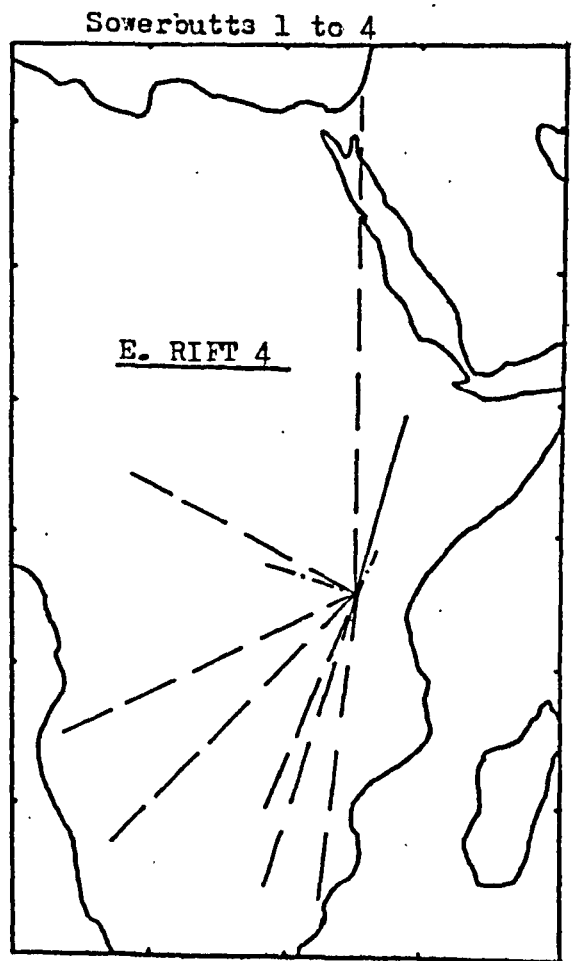
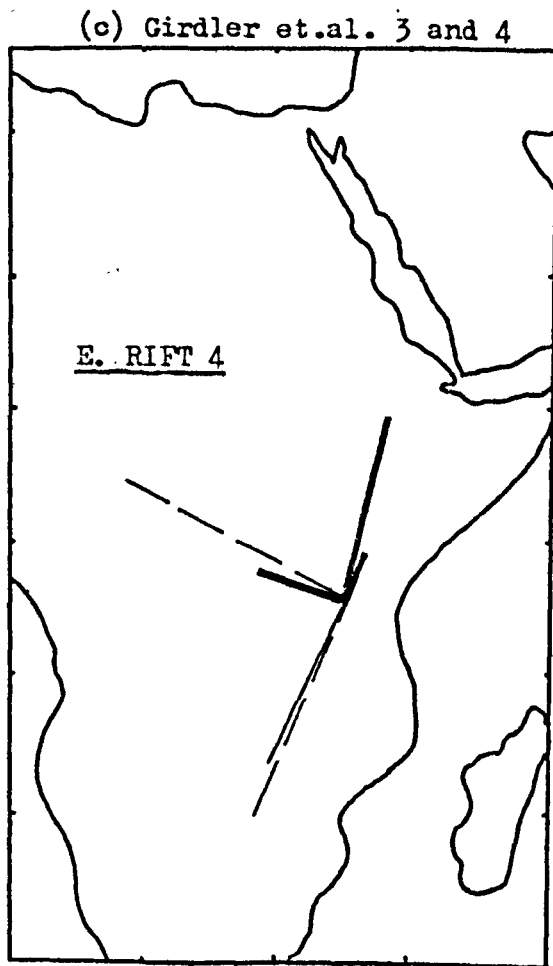
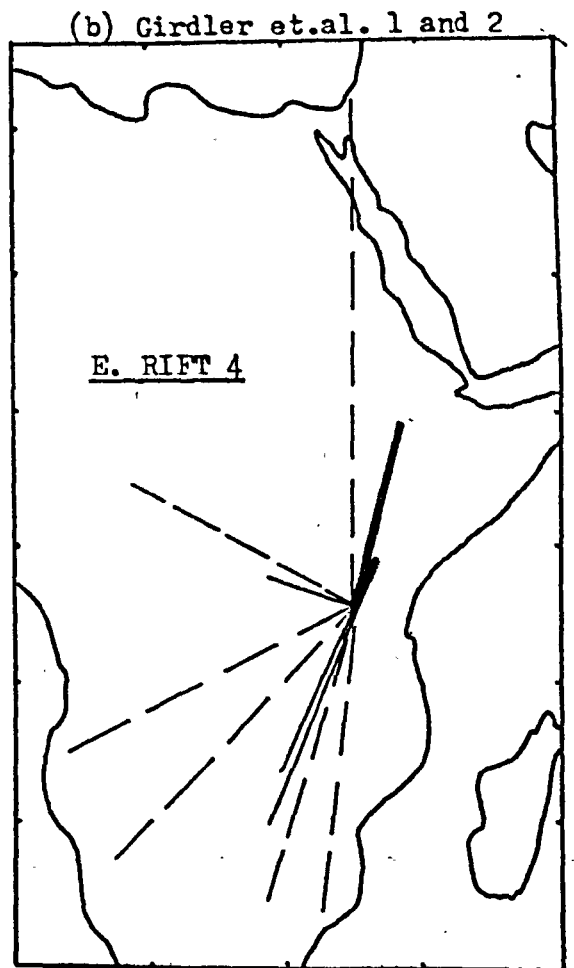
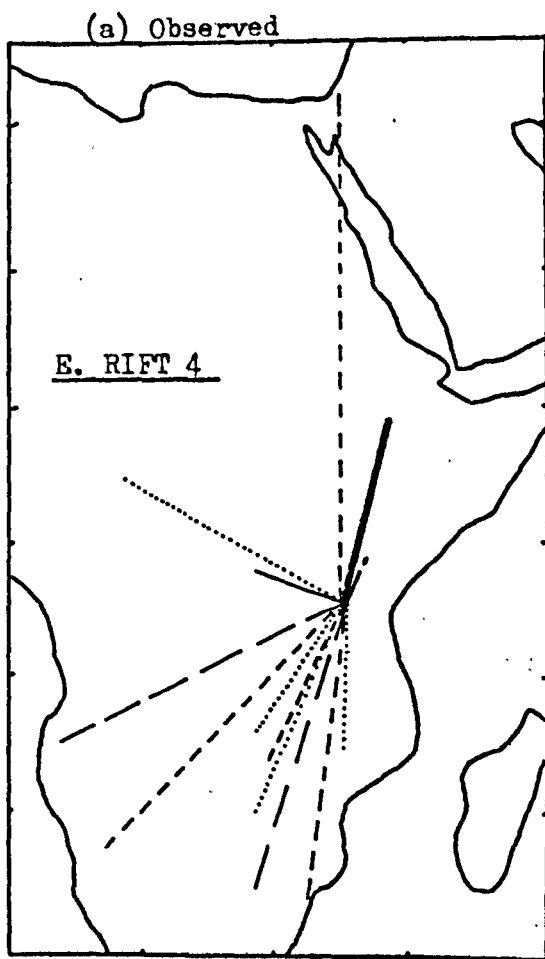
Tanzania Events (3 and 4) to Stations in the South

Most of the observed 'corrections' are small to large negative (figure (65) and figure (66)), whereas all the predicted 'corrections' are small to moderate positive. Exceptions in the observed data are the paths from event 4 to SDB and PRE which show small positive 'corrections'.



Fig(65) Comparison of observed travel time 'corrections' with those predicted from RAY tracing.

-----	-0.5 ≤ correction < 0.0	correction < -0.5 (sec.)	----	0 = correction	—	0.0 < correction ≤ 0.5
—	0.5 < correction < 1.0	—	1.0 ≤ correction				



Fig(66) Comparison of observed travel time 'corrections' with those predicted from RAY tracing.

-----	$-0.5 \leq \text{correction} < 0.0$	correction < -0.5 (sec.)	—	$0.0 < \text{correction} \leq 0.5$
———	$0.5 < \text{correction} < 1.0$	- . - . - .	$0 = \text{correction}$	———	$1.0 \leq \text{correction}$

(3.2.10.4) Conclusions and the Future Use of RAY Tracing to Africa

From the above analysis the following may be concluded:

- (i) The predicted 'corrections' for stations in the rift are in broad agreement with the observed data.
- (ii) The predicted travel times from the Girdler et. al. models (1) and (2) and the Girdler et. al. models (3) and (4) are very similar to each other for the ray paths discussed above. The travel times from these models to stations in the rift are marginally better correlated with the observed data than those obtained from the Sowerbutts models.
- (iii) The predicted travel times from all models of rays to stations in the south are generally too large. A constant 0.7 sec. baseline shift of the observed data in this region (i.e. 0.7 sec. added to the observed travel times) will produce a much improved correlation with the RAY traced estimates.
- (iv) The pattern of travel time 'corrections' for paths to BNG are not explained by any of the models. It is relevant at this stage to point out that BNG is situated directly above the very large amplitude broad negative magnetic anomaly discussed in section (4.4.8) of Part I. It is conceivable that the peculiar travel time 'corrections' observed at this station are a local effect.

It must be emphasized that RAY tracing has not been used to its fullest capacity in this study. With an improved data set, RAY tracing could be used to systematically 'scan' for plausible velocity models rather than just test existing ones. The data obtained from the Kaptagat array in Kenya (Long et. al. (1972)) would be particularly good material to use with the RAY tracing program. Apart from the travel time data, the independent $dT/d\Delta$ and amplitude estimates would offer strong constraints on the possible models.

- Anderson, D.L. & Kovach, R.L. (1969) Universal Dispersion Tables 111. Free Oscillation Variational Parameter. B.S.S.A. 59, 1667.
- Anselone, P.M. & Laurent, P.J. (1968) A General Method for the Construction of Interpolating or Smoothing Spline Functions. Num. Math. 12, 66.
- Archambeau, C.B., Flinn, E.A. & Lambert D.G. (1969) Fine Structure of the Upper Mantle. J.G.R. 74, 5825.
- Baker, B.H. & Wohlenberg, J. (1971) Structure and Evolution of the Kenya Rift Valley. Nature 229, 538.
- Bhattacharyya, (1969) Bicubic Spline Interpolation as a Method for Treatment of Potential Field Data. Geophys. 34, 402.
- Birch, F. (1961) The Velocity of Compressional Waves in Rocks to 10 kilobars, 2. J.G.R. 66, 2199.
- Birch, F. (1964) Density and Composition of Mantle and Core. J.G.R. 69, 4377.
- Blamey, C. & Gibbs, P.G. (1968) The Epicentres and Origin Times of some large Explosions. Geophys. J. 16, 1.
- Bloch, S., Hales, A.L. & Landisman, M. (1966) Velocities in the Crust and Upper Mantle of Southern Africa from Surface Wave Dispersion. B.S.S.A. 59, 1599.
- Bonjer, K.P., Fuchs, K. & Wohlenberg, J. (1970) Crustal Structure of the East African Rift System from Spectral Response Ratios of Long-Period Body Waves. Zeit. fur Geophys. 36, 287.
- Booth, D.C. Interpretation of Long and Short Period P Wave Amplitude Distance Curves and Station Residuals. M.Sc. Thesis, University of Durham.
- Bullen, K.E. (1965) An Introduction to the Theory of Seismology. Cambridge University Press.
- Carpenter, E.W. (1966) A Quantitative Evaluation of Teleseismic Explosion Records. Proc. R. Soc. (Lond.) A, 290, 396.
- Carpenter, E.W., Marshall, P.D. and Douglas, A. (1967) The Amplitude-Distance Curve for Short Period Teleseismic P-Waves. Geophys. J. 13, 61.
- Chapman, C.H. (1971) On the Computation of Seismic Ray Travel Times and Amplitudes. B.S.S.A. 61, 1267.
- Chernov, L.A. (1960) Wave Propagation in a Random Medium. McGraw-Hill Book Company.

- Cleary, J. (1967) Analysis of the Amplitudes of Short-Period P Waves Recorded by Long Range Seismic Measurement Stations in the Distance Range 30° to 102° . J.G.R. 72, 4705.
- Costain, J.K., Cook, K.L. & Algermissen, S.T. (1963) Amplitude, Energy, and Phase Angles of Plane SV Waves and their Application to Earth Crustal Studies. B.S.S.A. 53, 1039.
- Costain, J.K., Cook, K.L. & Algermissen, S.T. (1965) Corrigendum: Amplitude, Energy, and Phase Angles of Plane SV Waves and their Application to Earth Crustal Studies. B.S.S.A. 55, 567.
- Curtis, A.R. & Shimshoni, M. (1970) The Smoothing of Seismological Travel-Time Tables Using Cubic Splines. B.S.S.A. 60, 1077.
- Darracott, B.W., Fairhead, J.D. & Girdler, R.W. (1972) Gravity and Magnetic Surveys in Northern Tanzania and Southern Kenya. Tectonophysics, 15, 131.
- Davies, D. & Julian, B.R. (1972) A Study of Short Period P-Wave Signals from Longshot. Geophys. J. 29, 185.
- Davies, D. & Sheppard, M. (1972) Lateral Heterogeneity in the Earth's Mantle. Nature 239, 318.
- De Boor, C. (1962) Bicubic Spline Interpolation. J. Math. and Phys. 41, 212.
- Der, Z.A. & Landisman, M. (1972) Theory for Errors, Resolution, and Separation of Unknown Variables in Inverse Problems, with Application to the Mantle and the Crust in Southern Africa and Scandinavia. Geophys. J. 27, 137.
- Dopp, S. (1964) Preliminary Note on a Refracted P Phase in the Western Rift Valley of Africa. J.G.R. 69, 3027.
- Douglas, A. (1967) Joint Epicentre Determination. Nature 215, 47.
- Eby, E.S. (1967) Frenet Formulation of Three-Dimensional Ray Tracing. J. Acoust. Soc. Am. 42, 1287.
- Eby, E.S. (1969) Geometric Theory of Ray Tracing. J. Acoust. Soc. Am. 47, 273.
- Eby, E.S. & Einstein, L.T. (1965) Geometrical Spreading Loss Expression. J. Acoust. Soc. Am. 37, 933.
- Eliseevnin, V.A. (1965) Analysis of Waves Propagating in an Inhomogeneous Medium. Soviet Physics-Acoustics 10, 242.
- Fairhead, J.D. (1968) The Seismicity of the East African Rift System. 1965-1968. Unpubl. M.Sc. Dissertation, University of Newcastle upon Tyne.

- Fairhead, J.D. & Girdler, R.W. (1969) How Far Does the Rift System Extend through Africa? *Nature*, 221, 1018.
- Fairhead, J.D. & Girdler, R.W. (1970) The Seismicity of the Red Sea, Gulf of Aden and Afar Triangle. *Phil. Trans. R. Soc. (Lond.)* A267, 49.
- Fairhead, J.D. & Girdler, R.W. (1971) The Seismicity of Africa. *Geophys. J.* 24, 271.
- Gerver, M. & Markushevich, V. (1966) Determination of a Seismic Wave Velocity from the Travel-Time Curve. *Geophys. J.* 11, 165.
- Gerver, M. & Markushevich, V. (1967) On the Characteristic Properties of Travel Time Curves. *Geophys. J.* 13, 241.
- Girdler, R.W., Fairhead, J.D., Searle, R.C. & Sowerbutts, W.T.C. (1969) Evolution of Rifting in Africa. *Nature* 224, 1178.
- Girdler, R.W. & Sowerbutts, W.T.C. (1970) Some Recent Geophysical Studies of the Rift System in East Africa. *J. Geomag. and Geoelect.* 22, 153.
- Goldstein, M. (1960) *Classical Mechanics*. Addison-Wesley Series in Advanced Physics.
- Griffiths, D.H., King, R.F., Khan, M.A. & Blundell, D.J. (1971) Seismic Refraction Line in the Gregory Rift. *Nature* 229, 69.
- Gumper, F. & Pomeroy, P.W. (1970) Seismic Wave Velocities and Earth Structure on the African Continents. *B.S.S.A.* 60, 651.
- Gupta, R.N. (1966) Reflection of Elastic Waves from a Linear Transition Layer. *B.S.S.A.* 56, 511.
- Gutenberg, B. (1945a) Magnitude Determination for Deep-Focus Earthquakes. *B.S.S.A.* 35, 117.
- Gutenberg, B. (1945b) Amplitudes of P, PP, S and Magnitude of Shallow Earthquakes. *B.S.S.A.* 35, 57.
- Gutenberg, B. & Richter, C.F. (1956) Magnitude and Energy of Earthquakes. *Ann. Geof. (Rome)* 9, 1.
- Hales, A.L. and Sacks, I.S. (1959) Evidence for an Intermediate Layer from Crustal Structure in the Eastern Transvaal. *Geophys. J.* 15, 15.
- Herrin, E. (1961) Rep. Revision of Hypo Travel Times and Time Derivative Tables, Dallas Seism. Obs.
- Herrin, E. (1968) Introduction to "1968 Seismological Tables for P Phases". *B.S.S.A.* 58, 1193.

- Herrin, E. & Taggart, J. (1968) Regional Variations in P Travel Times. B.S.S.A. 58, 1325.
- Jacob, K. (1970) Three-Dimensional Seismic Ray Tracing in a Laterally Heterogeneous Spherical Earth. J.G.R. 75, 6675.
- Jacob, K. (1972) Global Tectonic Implications of Anomalous Seismic P Travel Times from the Nuclear Explosion Longshot. J.G.R. 77, 2556.
- Jeffreys, M. (1959) The Earth (4th Edition), Cambridge University Press.
- Jeffreys, M. (1971) The Earth (5th Edition), Cambridge University Press.
- Johnson, L. (1967) Array Measurements of P Velocities in the Upper Mantle. J.G.R. 72, 6309.
- Johnson, L. (1969) Array Measurements of P Velocities in the Lower Mantle. B.S.S.A. 59, 937.
- Julian, B.R. (1970) Ray Tracing in Arbitrary Heterogeneous Media. Tech. Note 1970-45, Lincoln Lab., Cambridge, Mass.
- Julian, B.R. & Anderson, D.L. (1968) Travel Times, Apparent Velocities and Amplitudes of Body Waves. B.S.S.A. 58, 339.
- Kaila, K.L. (1970) Decay Rate of P-Wave Amplitudes from Nuclear Explosions and the Magnitude Relations in the Epicentral Distance Range 1° to 98° . B.S.S.A. 60, 447.
- Kanasewich, E.R., Ellis, R.M., Chapman, C.H. & Gutowski, P.R. (1972) Teleseismic Array Evidence for Inhomogeneities in the Lower Mantle and the Origin of the Hawaiian Islands. Nature 239, 99.
- Khan, M.A. & Mansfield, J. (1971) Gravity Measurements in the Gregory Rift. Nature 229, 72.
- Knopoff, L. & Schlue, J.W. (1972) Rayleigh Wave Phase Velocities for the Path Addis Ababa - Nairobi. Tectonophysics 15, 157.
- Koefoed, O. (1962) Reflection and Transmission Coefficients for Plane Longitudinal Incident Waves. Geophys. Prosp. 10, 304.
- Landisman, M., Saito, Y. & Usami, T. (1966) Propagation of Disturbances in a Gutenberg-Bullen A' Spherical Earth Model: Travel Times and Amplitudes of S Waves. Am. Geophys. Union Monograph 10, The Earth Beneath the Continents. J.S. Steinhardt & T.J. Smith (eds.).
- Lanzos, C. (1964) The Variational Principles of Mechanics, University of Toronto Press.
- Leech, J.W. (1965) Classical Mechanics. Methuen's Monograph on Physical Subjects.

- Lilwall, R.C. & Douglas, A. (1970) Estimation of P-Wave Travel Times Using the Joint Epicentre Method. *Geophys. J.* 19, 165.
- Long, R.E., Backhouse, R.W., Maguire, P.K.H. & Sundaralingam, K. (1972) The Structure of East Africa Using Surface Wave Dispersion and Durham Seismic Array Data. *Tectonophysics* 15, 165.
- Ludwig, W.J., Nafe, J.E. & Drake, C.L. (1971) Seismic Refraction, in *The Sea*. Maxwell (ed.) John Wiley and Sons.
- Marshall, P.D. (1973) personal communication.
- McCamy, K., Meyer, R.P. & Smith, T.J. (1962) Generally Applicable Solutions of Zoeppritz Amplitude Equations. *B.S.S.A.* 52, 923.
- Moler, C.B. & Sololmon, L.P. (1970) Use of Splines and Numerical Integration in Geometric Acoustics. *J. Acoust. Soc. Am.* 42, 739.
- Nuttli, O.W. (1972) The Amplitudes of Teleseismic P Waves. *B.S.S.A.* 62, 343.
- Officer, C.B. (1958) An Introduction to the Theory of Sound Transmission. McGraw-Hill Book Company.
- Pederson, M.A. (1961) Acoustic Intensity Anomalies Introduced by Constant Velocity Gradients. *J. Acoust. Soc. Am.* 33, 465.
- Pennington, R.H. (1965) Introductory Computer Methods and Numerical Analysis. Macmillan Co.
- Powell, M.J.D. (1970) Curve Fitting by Cubic Splines, in *Proc. I.M.A. Conference at Canterbury on Numerical Approximation to Functions and Data*, Hayes, J.G. (ed.), Athlone Press.
- Press, F., Ewing, M. & Oliver, J. (1956) Crustal Structure and Surface-Wave Dispersion in Africa. *B.S.S.A.* 46, 97.
- Ralston, A. & Wilf, H.S. (1960) Mathematical Methods for Digital Computers. Wiley.
- Reinsch, C.H. (1967) Smoothing by Spline Functions. *Num. Math.* 10, 177.
- Richter, C.F. (1958) Elementary Seismology. W.H. Freeman and Co.
- Rykounov, L.N., Sedov, V.V., Savrina, L.A. and Bourmin, V.J.U. (1972) *Tectonophysics* 15, 123.
- Schultz, M.H. & Varga, R.S. (1967) Numerical Methods of High-Order Accuracy for Nonlinear Boundary Value Problems. *Num. Math.* 10, 394.
- Searle, R.C. (1969) Barometric Hypsometry and a Geophysical Study of Part of the Gregory Rift Valley in Kenya. Ph.D. Thesis, University of Newcastle upon Tyne.

- Searle, R.C. (1970) Evidence from Gravity Anomalies for Thinning of the Lithosphere beneath the Rift Valley in Kenya. *Geophys. J.* 21, 13.
- Shimshoni, M. & Ben-Menahem, A. (1970) Computation of the Divergence Coefficient for Seismic Phases. *Geophys. J.* 21, 285.
- Singh, S.J., Ben-Menahem, A. & Shimshoni, M. (1970) Comments on Papers by Costain et. al. and McCamy et. al. on the Solution of Zoeppritz' Amplitude Equations. *B.S.S.A.* 60, 277.
- Sorrells, G.G., Crowley, J.B. & Veith, K.F. (1971) Methods for Computing Ray Paths in Complex Geological Structures. *B.S.S.A.* 61, 27.
- Sowerbutts, W.T.C. (1969) Crustal Structure of the East African Plateau and Rift Valleys from Gravity Measurements. *Nature* 223, 143.
- Sowerbutts, W.T.C. (1972) Long Gravity and Magnetic Profiles over the East African Rift System and their Interpretation. Ph.D. Thesis, University of Newcastle upon Tyne.
- Tobin, D.G., Ward, P.L. & Drake, C.L. (1969) Microearthquakes in the Rift Valley of Kenya. *Geol. Soc. of Am. Bull.* 80, 2043.
- Tooley, R.D., Spencer, T.W. & Sagoci, H.F. (1965) Reflection and Transmission of Plane Compressional Waves. *Geophys.* 30, 552.
- Ugincius, P. (1965) Acoustic-Ray Equations for a Moving, Inhomogeneous Medium. *J. Acoust. Soc. Am.* 37, 476.
- Ugincius, P. (1968a) Intensity Equations in Ray Acoustics. 1. *J. Acoust. Soc. Am.* 45, 193.
- Ugincius, P. (1968b) Intensity Equations in Ray Acoustics. 2. *J. Acoust. Soc. Am.* 45, 206.
- Vanek, J. (1966) Amplitude Curves of Seismic Body Waves for the Region of Asia Minor. *Travaux Inst. Geophys. Acad. Tchecosl. Sci.* No. 246, *Geofysikalni Sbornik* 14, 215.
- Vanek, J. (1967) Three-Dimensional Seismic Models of the Upper Mantle. *Studia Geoph. et Geod.* 11, 337.
- Vanek, J. (1968a) Amplitude Curves of Seismic Body Waves Between 5° and 25°. *B.S.S.A.* 58, 1035.
- Vanek, J. (1968b) Amplitude Curves of Seismic Body Waves and the Structure of the Upper Mantle in Europe. *Tectonophysics*, 5, 235.
- Vanek, J. (1969a) Fitting the Amplitude Curves of Seismic Waves by Numerical Methods. *Studia Geoph. et Geod.* 13, 267.
- Vanek, J. Upper Mantle Structure and Velocity Distribution in Eurasia. *Geophys. Mono.* 13, *The Earth's Crust and Upper Mantle*, Hart, P.J. (ed.), *Am. Geophys. Un.*

- Vanek, J. (1969c) Revised Amplitude Curves of Seismic Body Waves for the Region of South-Eastern Europe. *Studia Geoph. et Geod.* 13, 173.
- Vanek, J. & Radu, C. (1968) Amplitude Curves of Seismic Body Waves at Distances Smaller than 12° . *Proc., 8th Ass. of ESC, Akademiai Kiado, Budapest.*
- Vanek, J. & Christoskov, L. (1971) Amplitude Curves of P and S Waves at Short Epicentral Distances. *Bull. of Int. Inst. of Seismology and Earthquake Engineering*, 8, 161.
- Veith, K.F. & Clawson, G.E. (1972) Magnitude from Short Period P Wave Data. *B.S.S.A.* 6, 435.
- Wesson, R.L. (1970) A Time Integration Method for Computation of the Intensities of Seismic Rays. *B.S.S.A.* 60, 307.
- Willey, G., Cleary, J.R. & Marshall, P.D. (1970) Comparison of Least Squares Analyses of Long and Short Period P Waves Amplitude. *Geophys. J.* 19, 439.
- Wohlenberg, J. (1967) Seismizität der Osafrikanischen Grabenzonen Zwischen 4°N und 12°S sowie 23°E und 40°E . Thesis, University of Ludwig - Maximilian.
- Wohlenberg, J. (1969) Remarks on the Seismicity of East Africa Between 4°N - 12°S . and 23°E - 40°E . *Tectonophysics*, 8, 567.
- Woodford, C.H. (1970) An Algorithm for Data Smoothing Using Spline Functions. *BIT* 10, 501.
- Zoeppritz, K. (1919) Erdbebenwellen VIIb, über Reflection and Durchgang Seismischer Wellen Durch Unstetigkeitsflächen, *Göttinger Nachrichten*, 1, 66.

APPENDIX A

A Fortran computer program to trace seismic rays through two dimensional structures. The flow diagram of the program is given in fig(9). This program calls the IBM science subroutine DHPCG and a user supplied subroutine CHANGE.

The velocity data which is defined at discrete knots is contained in the array ZAR (I, J). The I coordinate refers to variations in the radial direction (r) and the J coordinate refers to variations in the transverse direction (θ).

Input - Device 5

1 KM, N, TN, IQ, ITT, IFF, SSIG, AAAA, SSS with format 12, 14, F8.3, 13 214, F5.1, 2F7.1

where KM = 1

N = the number of knots in the transverse direction.

IQ = twice the number of lateral discontinuities.

ITT and IFF = the first and last velocity knots in the transverse direction which contain lateral variations of velocity.

SSIG = 1 for θ increasing rays .

= -1 for θ decreasing rays.

AAAA = average standard deviation of all the velocity values or some other estimate of the confidence of the data.

SSS = smoothing parameter. If amplitude estimates are required then set to the number of data points (see Reinch (1967)). For travel time information only, set to 0.

2 A(1), T(1), P(1), A(2), T(2), P(2) with format F7.1, 2F5.1, F7.1, 2F5.1

where A(1), T(1) and P(1) are the radial coordinate, the latitude and the longitude of the seismic source. A(2), T(2) and P(2) are the same for the receiver.

3 RAD, RRR6, R6, RRR, R, NNN, ZKM, DRAD with format F7.1, 12, 16, 12, 214, F4.1, F7.1

where RAD = radius of the Earth

RRR6 = number of radial discontinuities beneath DRAD .

R6 = number of knots in the radial direction below DRAD .

RRR = number of radial discontinuities above DRAD .

R = number of knots in the radial direction above DRAD .

NNN = number of integration steps between each set of output .

ZKM = the change in velocity between adjacent knots which defines a discontinuity.

DRAD = defines the line between a spherically symmetric Earth and the laterally varying Earth. In the region above DRAD + 30km. the velocity is allowed to vary laterally.

4 (PRMT(J), J = 1, 5), (DER(J), J = 1, 3) with format F4.1, F9.1, F5.2, F14.9,
4F4.1

where PRMT(1) = initial time (set = 0) .

PRMT(2) = maximum time the ray is allowed to travel in sec.

PRMT(3) = integration step size in sec.

PRMT(4) = δ in expression (74).

PRMT(5) = an error code. Used in the program as a control parameter (set = 0).

(DER(J), J = 1, 3) = weighting applied to the ray path equations for estimation of the truncation error. In present version of the program zero weight is given to the amplitude equations. Set the values of DER to 0.3, 0.3, 0.4 respectively.

5 to 4 + IQ (DIS1(I, J), J = 1, 3) with format 2F5.1, F16.9

where DIS1 contains all the information defining the lateral discontinuities.

I goes from 1 to IQ. I = n, n + 1 (for n even) defines a single discontinuity.

DIS1(I, 1) = radial coordinate of the knot of discontinuity.

DIS1(I, 2) = transverse coordinate of the knot of discontinuity.

DIS1(I, 3) = for I even set to ratio of the density across the discontinuity
(1.0)

- 5 + IQ (DIS2(K, 1), K = 1, IRRR) with format 10F7.1 - defines the knot positions of the radial discontinuities (IRRR = RRR + RRR6).
- 6 + IQ (DIS2(K, 2), K = 1, IRRR) with format 10F12.10 - defines the ratio of the density across the discontinuity(1.0).
- 7 + IQ (DIS2(K, 3), K = 1, IRRR) and (DIS2(K, 4), K = 1, IRRR) - for DIS2(K, 3)
and
8 + IQ DIS2(K, 4) allows the Kth radial discontinuity to be confined within the knots DIS2(K, 3) and DIS2(K, 4).
- for DIS2(K, 3)
DIS2(K, 4) allows the Kth radial discontinuity to be absent from the region between the knots DIS2(K, 3) and DIS2(K, 4).
- for the discontinuity
to be global then DIS2(K, 3) = DIS2(K, 4) = 0.
- 9 + IQ YNIT, FIN, ANG, STEP with format 3F5.1, F8.4
where YNIT and FIN are the initial and final angles of take off of the ray.
ANG is the value of θ which the ray starts at (the latitudes and longitudes will only be correct if ANG = 0). STEP is the step size of the take off angles.

Input - Device 7

- 1 to 11 (ZAR(I, 1), I = 1, R) with format 10F8.4 - contains the standard velocity depth profile above DRAD. All ZAR(I, J) (for J = 2, N) are set to ZAR(I, 1). The subroutine CHANGE is a user supplied subroutine which may alter the values of ZAR(I, J) to that of a laterally heterogeneous model.
- 12 to ((ZAR(I, J), I = 1, 100), J = N + 1, N + 12) with format 10F8.4 - contains
end of file the velocity depth profile beneath DRAD.

Output - Device 6

The original data and a few other ' diagnostic ' parameters are returned from the main program before ray tracing . This is followed by the information from subroutines

OUTP and VELOC :

RADIUS	radial coordinate of the ray.
THETA	latitude of the ray.
PHI	longitude of the ray.
TIME	time of travel of the ray in sec.
DISTANCE	distance along the ray path in km.
T	distance travelled along the surface of the Earth in degrees.
P	classical ray parameter ($d(\text{TIME}) / d T$ in the notation used here).
EMERG ANG	angle between the ray and the radial vector in radians.
AMPLITUDE	amplitude of the ray considering geometrical spreading only.
IHLF	number of times the integration step size has been halved. (max value IHLF = 10).
AMPLITUDE2	amplitude of the ray considering geometrical spreading and energy partitioning at velocity discontinuities.
R1	radial coordinate of the knot that defines the velocity unit in which the ray is travelling.
T1	transverse coordinate of this knot.
VE	velocity of the ray.
DVR	$d(VE) / dr$.
DVT	$d(VE) / dt$.
DVRR	$d^2(VE) / dr^2$.
DVRT	$d^2(VE) / dr dt$.
DVTT	$d^2(VE) / dt^2$.
JJA	shows if the ray is near to a lateral discontinuity.

When reflection or refraction takes place at a velocity discontinuity then the following additional information is given :

INCID ANG	incident angle between the ray and the normal to the discontinuity.
REF ANG	refraction or reflection angle.
VELOCITY 1	velocity of the medium for the incident ray.
VELOCITY 2	velocity of the medium for the reflected or refracted ray.
DISTANCE 1	distance between the ray and the discontinuity at the time of refraction or reflection.
DISTANCE 2	distance the ray travelled at the last integration step.

```

C     YX(1) CORRESPONDES TO ORIGINAL POSITION OF POINT+1000
C     PL=26 J=1,2
C     PROGRAM AUTO READ THE DATA INTO THE COMPUTER AND ADJUST
C     THE PARAMETERS ETC. AND THEN COMPUTE THE SPLINE COEF
C     IMPLICIT REAL*8(A-H,O-Y)
C     COMMON ZAR(102,106),ZID(102,106),ZIC(102,106),ZIB(102,106)
C     1,DIS1(32,3),DIS2(10,4),DIS3(4,32)
C     DIMENSION YX(4,4),RID(102),ROD(102),LOD(102),
C     1D(1400),A(102),P(5),T(5),DERIV(7),Y(7),DER(7),AUX(16,7)
C     DIMENSION VV(1400),C(1400),B(1400),PRMT(5)
C     DIMENSION X(1400)
C     COMMON/AS/RAD,DDRAD,DRAD,RRR6,R6,R,RRR,IQ/AE/PRMT5,PI,XXY,RESO,ZKM
C     COMMON/AG/KM,IRRR,ITT,IFF,IAA,IAB
C     COMMON/AP/TN,DDS,XK,JAL,NNN,JJA,N/AK/PL(5,5),YXZ(10,10),SSIG,
C     1JCOU
C     COMMON/HG/IHLF
C     INTEGER R,RRR6,R6,RRR,
C     PI=4.0*DATAN(0.1D+01)/0.18D 03-YX(1,1)*YXZ(1,1)
C     READ(5,1) KM,N,TN,IQ,ITT,IFF,SSIG,AAAA,SSS
C     WRITE(6,1) KM,N,TN,IQ,ITT,IFF,SSIG,AAAA,SSS
C     SSSIG=SSIG*1/JJA(1)
C     1* FORMAT(I2,I4,F8.3,I3,2I4,F5.1,2F7.4)(X(12,2)
C     READ(5,27)A(1),T(1),P(1),A(2),T(2),P(2)
C     WRITE(6,27)A(1),T(1),P(1),A(2),T(2),P(2)
C     TN=PI*TN/DFLOAT(N-1)
C     TN DEFINES FIRST THE NO OF DEGREES EQUIVALENT TO N
C     AND IS THEN CONVERTED TO A CONVERSION FACTOR CHANGING THE INTEGER
C     INTO AN ANGLE IN RADIANS
C     ITT AND IFF DEFINE THE FIRST AND LAST VALUES NOT
C     INCLUDED IN HERRIN TABLES(1,2)
C     THE FIRST VALUE CORRESPONDES TO THETA=0
C     DO 29 J=1,2
C     T(J)=T(J)*PI/X(1,1)
C     P(J)=P(J)*PI
C     29 CONTINUE
C     27 FORMAT(F7.1,2F5.1,F7.1,2F5.1)

```

C

```

C      NM=N+1
C      YX(A) CORRESPONDES TO ORIGINAL POSITION OF SOURCE+RECIEVER
      DO 261 J=1,2
      YX(J,1)=A(J)*DSIN(T(J))*DCOS(P(J))
      YX(J,2)=A(J)*DSIN(T(J))*DSIN(P(J))
212  YX(J,3)=A(J)*DCOS(T(J))
26  YX(J,3)=A(J)*DCOS(T(J))
C      YXZ(1) CORRESPONDS TO NEW POSITION OF SOURCE AND RECIEVER
C      YXZ(1,1)=A(1)*DSIN(T(1))*DCOS(P(1))
922 YXZ(1,2)=0.0D000
      YXZ(1,3)=0.0D000/DCOS(T(1))
      YXZ(2,1)=0.0D 00
      DO 251 J=1,3
25  YXZ(2,1)=YXZ(2,1)+YX(2,J)*YX(1,J)/A(1)
C      DO 204 I=1,IC
C      READ(5,3) (DIS1(I,J),J=1,3)
C      THIS IS THE SAME, SIGUAS, USED IN DIRECTIONS
      YXZ(2,2)=SSIG*DSQRT(A(2)*A(2)-YXZ(2,1)*YXZ(2,1))
      YXZ(2,3)=0.0D100,1)*DRAD*(DRAL-DRAL)
      DO 241 J=1,3 DIS1(I,2)-1)*TV
204 PL(J,1)=YX(1,J)/A(1)
241 PL(J,2)=(YX(2,J)-PL(J,1)*YXZ(2,1))/YXZ(2,2)
C      READ(5,4) (DIS2(I,1),I=1,IRRR)
C      WRITE(6,4) (DIS2(I,1),I=1,IRRR)
C      YPL(I) CORRESPONDES TO ROTATION FACTORS FOR COORD TRANSFORMATION
C      (SEE NOTE-1 FOR COORD) TRANSFORMATION-FOR DIRECTION
C      THE POSITION OF THE SOURCE HAS EFFECTIVELY BEEN TRANS
C      LATED TO THETA=0; THEREFORE NEED THETA>0
      READ(5,28) RAD,RRR6,R6,RRR,R,NNN,ZKM,DRAD
      READ(7,22) (ZAR(I,1),I=1,R)
2738 DO 107 J=2,NC,10
      DO 107 I=1,R,1
107  ZAR(I,J)=ZAR(I,1)
      NM=N+1

```

```

MN=N+11240) GO TO 1201
READ(7,22)((ZAR(I,J),I=1,100),J=NM,MN)
MN=N+1244=1,IQ=1
READ(7,22)(ZAR(I,MN),I=1,90)
212 11 FORMAT(2I4,F8.4)
22 11 FORMAT(10F8.4)
WRITE(6,28)RAD,RRR6,R6,RRR,R,NNN,ZKM,DRAD
28 11 FORMAT(F7.1,I2,I6,I2,2I4,F4.1,F7.1)
READ(5,922)(PRMT(J),J=1,5),(DER(J),J=1,3)
WRITE(6,922)(PRMT(J),J=1,5),(DER(J),J=1,3)
922 11 FORMAT(F4.1,F9.1,F5.2,F14.9,4F4.1)
CDRAD=(RAD-DRAD)/DFLOAT(R-1)
BAC=PRMT(4)
ABC=PRMT(3)
IF(IQ.EQ.0)GO TO 1241
DO 204 I=1,IQ
READ(5,3)(DIS1(I,J),J=1,3)
WRITE(6,3)(DIS1(I,J),J=1,3)
3 11 FORMAT(2F5.1,F16.9)
DIS1(I,1)=DIS1(I,1)*DDRAD+(DRAD-DDRAD)
DIS1(I,2)=(DIS1(I,2)-1)*TN
204 CONTINUE
241 11 IRRR=RRR+RRR6
READ(5,4)(DIS2(K,1),K=1,IRRR)
WRITE(6,4)(DIS2(K,1),K=1,IRRR)
READ(5,366)(DIS2(K,2),K=1,IRRR)
WRITE(6,366)(DIS2(K,2),K=1,IRRR)
READ(5,4)(DIS2(K,3),K=1,IRRR)
READ(5,4)(DIS2(K,4),K=1,IRRR)
WRITE(6,4)(DIS2(K,3),K=1,IRRR)
WRITE(6,4)(DIS2(K,4),K=1,IRRR)
366 11 FORMAT(10F12.10)
4 11 FORMAT(10F7.1)
IDIS2=DIS2(RRR,1)
J=0

```

```

      ZAR(I;J)=1;ZAR(I;J)=1
      IF(IQ.EQ.0)GO(TOP1101
      IQQ=IQ-1;47IC(IPQ;J)
      DO 244 JJ=1;IQQ;2
      DO 239 I=1,2
      II=JJ+I-1
      YX(1,I)=DIS1(II,1)*DCOS(DIS1(II,2))
      YX(2,I)=DIS1(II,1)*DSIN(DIS1(II,2))
      J=J+1
      DIS3(1,J)=(YX(2,1)-YX(2,2))/(YX(1,1)-YX(1,2))
      DIS3(2,J)=YX(2,1)-DIS3(1,J)*YX(1,1)
      IF(DABS(DIS3(2,J)).LT.0.1D-07)DIS3(2,J)=0.0D 00
      BB=DSQRT((YX(2,1)-YX(2,2))**2+(YX(1,1)-YX(1,2))**2)
      DIS3(3,J)=(YX(2,1)-YX(2,2))/BB
      DIS3(4,J)=-(YX(1,1)-YX(1,2))/BB
      244 CONTINUE
      C THE IPQ=IQ/2POSS IS TO HAVE SURE IS THE SAME AS THE Y
      C REM WRITE(6,3343)((DIS3(I,J),I=1,4),J=1,IPQ)
      3343 FORMAT(4E15:6)) GO TO 752
      C 1101 CORRES TO A 2 CORRES TO B IN Y=AX+B
      C 1103 CORRES TO A AND 4 CORRES TO B IN VECTOR EQU OF THE PERPENDICULAR
      C 798*****
      C 794 FORMATT(717,112,0)
      C 1101 COR TO 752
      C SUBROUTINE(CHANGE,IS,USER)SUPPLIED(SUBROUTINE TO ALTER THE VALUES IN
      C ZAR(I;J)=1
      1101 CALL CHANGE
      1100 NIP1=1;NIP2=1;NIP3=1;NIP4=1;NIP5=1;NIP6=1;NIP7=1;NIP8=1;NIP9=1;NIP10=1;NIP11=1;NIP12=1;NIP13=1;NIP14=1;NIP15=1;NIP16=1;NIP17=1;NIP18=1;NIP19=1;NIP20=1;NIP21=1;NIP22=1;NIP23=1;NIP24=1;NIP25=1;NIP26=1;NIP27=1;NIP28=1;NIP29=1;NIP30=1;NIP31=1;NIP32=1;NIP33=1;NIP34=1;NIP35=1;NIP36=1;NIP37=1;NIP38=1;NIP39=1;NIP40=1;NIP41=1;NIP42=1;NIP43=1;NIP44=1;NIP45=1;NIP46=1;NIP47=1;NIP48=1;NIP49=1;NIP50=1;NIP51=1;NIP52=1;NIP53=1;NIP54=1;NIP55=1;NIP56=1;NIP57=1;NIP58=1;NIP59=1;NIP60=1;NIP61=1;NIP62=1;NIP63=1;NIP64=1;NIP65=1;NIP66=1;NIP67=1;NIP68=1;NIP69=1;NIP70=1;NIP71=1;NIP72=1;NIP73=1;NIP74=1;NIP75=1;NIP76=1;NIP77=1;NIP78=1;NIP79=1;NIP80=1;NIP81=1;NIP82=1;NIP83=1;NIP84=1;NIP85=1;NIP86=1;NIP87=1;NIP88=1;NIP89=1;NIP90=1;NIP91=1;NIP92=1;NIP93=1;NIP94=1;NIP95=1;NIP96=1;NIP97=1;NIP98=1;NIP99=1;NIP100=1;NIP101=1;NIP102=1;NIP103=1;NIP104=1;NIP105=1;NIP106=1;NIP107=1;NIP108=1;NIP109=1;NIP110=1;NIP111=1;NIP112=1;NIP113=1;NIP114=1;NIP115=1;NIP116=1;NIP117=1;NIP118=1;NIP119=1;NIP120=1;NIP121=1;NIP122=1;NIP123=1;NIP124=1;NIP125=1;NIP126=1;NIP127=1;NIP128=1;NIP129=1;NIP130=1;NIP131=1;NIP132=1;NIP133=1;NIP134=1;NIP135=1;NIP136=1;NIP137=1;NIP138=1;NIP139=1;NIP140=1;NIP141=1;NIP142=1;NIP143=1;NIP144=1;NIP145=1;NIP146=1;NIP147=1;NIP148=1;NIP149=1;NIP150=1;NIP151=1;NIP152=1;NIP153=1;NIP154=1;NIP155=1;NIP156=1;NIP157=1;NIP158=1;NIP159=1;NIP160=1;NIP161=1;NIP162=1;NIP163=1;NIP164=1;NIP165=1;NIP166=1;NIP167=1;NIP168=1;NIP169=1;NIP170=1;NIP171=1;NIP172=1;NIP173=1;NIP174=1;NIP175=1;NIP176=1;NIP177=1;NIP178=1;NIP179=1;NIP180=1;NIP181=1;NIP182=1;NIP183=1;NIP184=1;NIP185=1;NIP186=1;NIP187=1;NIP188=1;NIP189=1;NIP190=1;NIP191=1;NIP192=1;NIP193=1;NIP194=1;NIP195=1;NIP196=1;NIP197=1;NIP198=1;NIP199=1;NIP200=1;NIP201=1;NIP202=1;NIP203=1;NIP204=1;NIP205=1;NIP206=1;NIP207=1;NIP208=1;NIP209=1;NIP210=1;NIP211=1;NIP212=1;NIP213=1;NIP214=1;NIP215=1;NIP216=1;NIP217=1;NIP218=1;NIP219=1;NIP220=1;NIP221=1;NIP222=1;NIP223=1;NIP224=1;NIP225=1;NIP226=1;NIP227=1;NIP228=1;NIP229=1;NIP230=1;NIP231=1;NIP232=1;NIP233=1;NIP234=1;NIP235=1;NIP236=1;NIP237=1;NIP238=1;NIP239=1;NIP240=1;NIP241=1;NIP242=1;NIP243=1;NIP244=1;NIP245=1;NIP246=1;NIP247=1;NIP248=1;NIP249=1;NIP250=1;NIP251=1;NIP252=1;NIP253=1;NIP254=1;NIP255=1;NIP256=1;NIP257=1;NIP258=1;NIP259=1;NIP260=1;NIP261=1;NIP262=1;NIP263=1;NIP264=1;NIP265=1;NIP266=1;NIP267=1;NIP268=1;NIP269=1;NIP270=1;NIP271=1;NIP272=1;NIP273=1;NIP274=1;NIP275=1;NIP276=1;NIP277=1;NIP278=1;NIP279=1;NIP280=1;NIP281=1;NIP282=1;NIP283=1;NIP284=1;NIP285=1;NIP286=1;NIP287=1;NIP288=1;NIP289=1;NIP290=1;NIP291=1;NIP292=1;NIP293=1;NIP294=1;NIP295=1;NIP296=1;NIP297=1;NIP298=1;NIP299=1;NIP300=1;NIP301=1;NIP302=1;NIP303=1;NIP304=1;NIP305=1;NIP306=1;NIP307=1;NIP308=1;NIP309=1;NIP310=1;NIP311=1;NIP312=1;NIP313=1;NIP314=1;NIP315=1;NIP316=1;NIP317=1;NIP318=1;NIP319=1;NIP320=1;NIP321=1;NIP322=1;NIP323=1;NIP324=1;NIP325=1;NIP326=1;NIP327=1;NIP328=1;NIP329=1;NIP330=1;NIP331=1;NIP332=1;NIP333=1;NIP334=1;NIP335=1;NIP336=1;NIP337=1;NIP338=1;NIP339=1;NIP340=1;NIP341=1;NIP342=1;NIP343=1;NIP344=1;NIP345=1;NIP346=1;NIP347=1;NIP348=1;NIP349=1;NIP350=1;NIP351=1;NIP352=1;NIP353=1;NIP354=1;NIP355=1;NIP356=1;NIP357=1;NIP358=1;NIP359=1;NIP360=1;NIP361=1;NIP362=1;NIP363=1;NIP364=1;NIP365=1;NIP366=1;NIP367=1;NIP368=1;NIP369=1;NIP370=1;NIP371=1;NIP372=1;NIP373=1;NIP374=1;NIP375=1;NIP376=1;NIP377=1;NIP378=1;NIP379=1;NIP380=1;NIP381=1;NIP382=1;NIP383=1;NIP384=1;NIP385=1;NIP386=1;NIP387=1;NIP388=1;NIP389=1;NIP390=1;NIP391=1;NIP392=1;NIP393=1;NIP394=1;NIP395=1;NIP396=1;NIP397=1;NIP398=1;NIP399=1;NIP400=1;NIP401=1;NIP402=1;NIP403=1;NIP404=1;NIP405=1;NIP406=1;NIP407=1;NIP408=1;NIP409=1;NIP410=1;NIP411=1;NIP412=1;NIP413=1;NIP414=1;NIP415=1;NIP416=1;NIP417=1;NIP418=1;NIP419=1;NIP420=1;NIP421=1;NIP422=1;NIP423=1;NIP424=1;NIP425=1;NIP426=1;NIP427=1;NIP428=1;NIP429=1;NIP430=1;NIP431=1;NIP432=1;NIP433=1;NIP434=1;NIP435=1;NIP436=1;NIP437=1;NIP438=1;NIP439=1;NIP440=1;NIP441=1;NIP442=1;NIP443=1;NIP444=1;NIP445=1;NIP446=1;NIP447=1;NIP448=1;NIP449=1;NIP450=1;NIP451=1;NIP452=1;NIP453=1;NIP454=1;NIP455=1;NIP4
```

7070 CONTINUE

7070 ZAR(IPP,I)=ZAR(IPP,N)
ZIB(IPP,I)=ZIB(IPP,N)
ZIC(IPP,I)=ZIC(IPP,N)
ZID(IPP,I)=ZID(IPP,N)

1444 CONTINUE

7070 GO TO 7980

222 ANG1=(I-1)*TN

L1=1

IF(IQ.EQ.0) GO TO 7070

DO 707 JL=1,IQ,2

JOE=0

IF(ANG1.LT.DMIN1(DIS1(JL,2),DIS1(JL+1,2)).OR.ANG1.GT.DMAX1(
1DIS1(JL,2),DIS1(JL+1,2))) GO TO 707

C IF (IPQ.NE.(I-1)) GO TO 752

C

C FINDS IF THE VALUE IS AT THE START OF A DISCONTINUITY

IPQ=DIS1(JL,2)/TN+0.1

C THE 0.1 IN ABOVE IS TO MAKE SURE IS THE SAME AS THE VALUE OF DIS

C READ IN -1.0

IF(IPQ.NE.(I-1)) GO TO 752

752 RID(L1)=(DIS1(JL,1)-DRAD+DDRAD)/DDRAD

122 L1=L1+1

7070 JOE=1

752 IPQ=DIS1(JL+1,2)/TN+0.1

934 FORMAT(2I7,F12.4)*1

IF(IPQ.NE.(I-1)) GO TO 753

RID(L1)=(DIS1(JL+1,1)-DRAD+DDRAD)/DDRAD

711 L1=L1+1

JOE=1

753 IF(JOE.EQ.1) GO TO 707

IF(DABS(DIS3(2,(JL+1)/2)).LT.0.1D-07)WRITE(6,313)

313 FORMAT('BOOB IN MAIN')

837 RID(L1)=DIS3(2,(JL+1)/2)/(DCOS(ANG1)*DIS3(1,(JL+1)/2)-DSIN(ANG1))

RID(L1)=(-RID(L1)-DRAD+DDRAD)/DDRAD+1.

L1=L1+1

```

707 CONTINUE
7070 CONTINUE
      K1=11.00.0000 TO 154
      L4=0.00.0000
      L1=L1-1.00.0000
722   L4=L4+1.00.0000
7952 IF(DIS2(K1,3).LT.0.1) GO TO 7954
      IPQ=K1.00.0000
      L5=DIS2(K1,3)+0.10-04
      L6=DIS2(K1,4)+0.10-04
      IF((L5.LT.L6).AND.(I.LT.L5.OR.I.GT.L6))K1=K1+1
      IF((L5.GT.L6).AND.(I.GT.L6.AND.I.LT.L5))K1=K1+1
      IF(IPQ.EQ.K1) GO TO 7954
      GO TO 7952
7954 ROD(L4)=DIS2(K1,1)+0.10-09
      L5=0.00.0000
      IF(L1.EQ.0) GO TO 708
      DO 703, L2=1, L1
702   IF(RID(L2).GT.ROD(L4)) GO TO 703
703   ROD(L4)=RID(L2)
704   L5=L2.00.0000
703 CONTINUE
122   FORMAT(I5,10F12.4)
708 CONTINUE
      IF(L5.NE.0)RID(L5)=0.80 05
      IF(L5.EQ.0) K1=K1+1
      IF(K1.GT.RRR) GO TO 711
      GO TO 722
711   L5=L4
      WRITE(6,122)I,(ROD(L2),L2=1,L4)
      L3=1.00.0000
      L1=1.00.0000
      L2=2.00.0000
333   L1L=ROD(L3)
      IF(L1L.EQ.L1) GO TO 700
      L1L=L1L+1.00.0000
      L1=L1L

```

```

      L2=L1L-1
      IF(L1.NE.L2)GO TO 754
      ZIB(L1,I)=0.0
      ZIC(L1,I)=0.0
      ZID(L1,I)=0.0
      GO TO 1700
754   DO 799 L4=L1,L2
      X(L4)=L4
      VV(L4)=ZAR(L4,I)
      X(L2+1)=L2+1
      VV(L2+1)=2.0*VV(L2)-VV(L2-1)
      SSS=DFLOAT(L2-L1+1)
      CALL SPLINE(L1,L2+1,X,VV,B,C,D,SSS,AAAA)
      DO 702 L4=L1,L2
      ZAR(L4,I)=VV(L4)
      ZIB(L4,I)=B(L4)
      ZIC(L4,I)=C(L4)
      ZID(L4,I)=D(L4)
700   L1=L2+1
783   L3=L3+1
      IF(L1.EQ.IDIS2)GO TO 798
      GO TO 333
798   CONTINUE
796   CONTINUE
77   I=1
      L1=1
      L2=DIS2(RRR+I,1)-1
      I=I+1
      DO 401 K=L1,L2
      AA=DFLOAT(K)
      J=AA/100
      JELLY=K-J*100
      J=J+N+1
      IF(JELLY.NE.0)GO TO 300
      JELLY=100
      J=J-I

```

```

300 VV(K)=ZAR(JELLY,J)
401 X(K)=DFLOAT(K)
      X(L2+1)=DFLOAT(L2+1)
      VV(L2+1)=VV(L2)*2.0-VV(L2-1)
      SSS=DFLOAT(L2+1-L1)
      CALL SPLINE(L1,L2+1,X,VV,B,C,D,SSS,AAAA)
      DO 402 K=L1,L2
      AA=DFLOAT(K)
      J=AA/100
      JELLY=K-J*100
      J=J+N+1
      IF(JELLY.NE.0) GO TO 301
      JELLY=100
      J=J-1
301 ZIB(JELLY,J)=B(K)
      ZIC(JELLY,J)=C(K)
      ZID(JELLY,J)=D(K)
      ZAR(JELLY,J)=VV(K)
402 CONTINUE
      IF(RRR+1-1.EQ.IRRR) GO TO 403
      L1=L2+1
      GO TO 400
403 CONTINUE
83  FORMAT(15)
      READ(5,91)YNIT,FIN,ANG,STEP
      WRITE(6,92)YNIT,FIN,STEP,ANG
91  FORMAT(3F5.1,F8.4)
92  FORMAT('ANGLES GO FROM',F5.1,' TO ',F5.1,' IN STEPS OF ',F8.4,F5.1)
      PDP=((FIN-YNIT)/STEP+1.)
      ISTEP=PDP+0.1D-04
      WRITE(3,83)ISTEP
      DO 123 IK=1,ISTEP
      PDP=DFLOAT(IK-1)*STEP+YNIT
      WRITE(6,99)PDP
99  FORMAT('THIS IS THE RAY PATH FOR ANGLE ',F6.2)

```

```

10 30 123
JAL=10.45
IDT=0.0D100.1 ANGLE
NDIM=7.00
SSIG=SSSIG
17 DDS=0.0D100 WLA
XXY=0.0D.00
XK=0.0D.00
IAA=4
Y(1)=A(1)
IAB=4
Y(2)=(ANG-1)*TN
Y(3)=PI*(90.0+PDP)
Y(4)=0.0D.00
Y(5)=0.0D.00
Y(6)=0.0D.00
Y(7)=1.0
2 DO 7 J=1,3
DERIV(J+4)=0.0D.00
7 DERIV(J)=DER(J)
JCOU=NNN-1
IF(JAL.NE.1)JAL=7
PRMT(1)=XXY
PRMT(3)=ABC
PRMT(4)=BAC
PRMT(5)=0.0
PRMT5=0.0D.00
EXTERNAL FCT,OUTP
CALL DHPG(PRMT,Y,DERIV,NDIM,IHLF,FCT,OUTP,AUX)
WRITE(6,1964)IHLF,PRMT(5),Y(1),Y(2)
1964 FORMAT('IHLF=',I5,' PRMT(5)=',F5.1,' RAD=',F6.1,' ANG=',F6.4)
IF(PRMT(5).EQ.0) GO TO 123
IPRMT=PRMT(5)
GO TO(44,33,2,46,46,49),IPRMT
33 WRITE(6,34)

```

```
34 FORMAT('DIFF REQD')  
GO TO 123  
44 WRITE(6,45)  
45 FORMAT('NEXT ANGLE')  
GO TO 123  
46 WRITE(6,47)  
47 FORMAT('TOO WEAK!')  
GO TO 123  
49 WRITE(6,48)  
48 FORMAT('HEAD WAVE')  
123 CONTINUE
```

```
I=0  
WRITE(3,83)I  
STOP  
END
```

FILE

```

SUBROUTINE VELOC(VE,DVR,DVT,DVRR,DVRT,DVTT,A,THET)
  IMPLICIT REAL*8(A-H,O-Y)
C THIS SUBROUTINE COMPUTES THE VELOCITY INSIDE THE EARTH MODEL
C THE ORIGINAL SPLINE COEF COMPUTED IN THE MAIN ARE USED FOR THE
C RADIAL DIRECTION      SPLINE IS CALLED AGAIN FOR INTERPOLATION IN THE
C THETA DIRECTION
  LOGICAL L2,L1
  INTEGER R,RRR,RRR6,R6,R1,T1
  COMMON/AG/KM,IRRR,ITT,IFF,IAA,IAB
102 COMMON/SOS/DRR(102),V(102),DV(102),X(102),B(102),C(102),D(102)
  COMMON ZAR(102,106),ZID(102,106),ZIC(102,106),ZIB(102,106)
  1,DIS1(32,3),DIS2(10,4),DIS3(4,32)
103 COMMON/AS/RAD,DDRAD,DRAD,RRR6,R6,R,RRR,IQ/AE/PRMT5,PI,XXY,RESO,ZKM
  COMMON/AP/TN,DDS,XK,JAL,NNN,JJA,N
  COMMON/AK/PL(5,5),YXZ(10,10),SSIG,JCOU
  COMMON/HG/IHLF
  IF(A.LT.(DRAD+30.0)) GO TO 299
  CALL BERT(A,THET,PP,FF,R1,T1)
C IF THE RAY IS NOT NEAR TO A LATERAL DISCONTINUITY THEN BETWEEN
C HERE AND LABEL 135 ANY OTHER INTERPOLATION SCHEME MAY BE
C INCORPORATED INTO THE PROGRAM.
C EG. IF THE VELOCITY IN THE CRUST IS A CONSTANT VALUE THEN
C THE FOLLOWING WOULD APPLY
C IF(A.LT.6331.0) GO TO 135
C VE=ZAR(R1,1)
C DVR=0.0D100
C ETC.
C RETURN
135 R1=DFLOAT(R1)
  TT1=DFLOAT(T1)
  IF(JCOU.LT.NNN-1) JOY=1
  IF(R1.LE.R) GO TO 100
  WRITE(6,13) R1,T1,VE,DVR,DVRR,DVRT,DVTT,DVT,A,THET
1013 FORMAT(' OUT OF BOUNDS',2I5,10E12.4)
  STOP

```

```

1000 DIS3(1,(J+1)/2)=DIS3(1,(J+1)/2)+DIS3(1,(J+1)/2).GO TO 1912
1001 IF (T1.GE.1) GO TO 1002
WRITE(6,13) R1,T1,VE,DVR,DVRR,DVRT,DVTI,DVT,A,THET
PRMT5=1.
RETURN 32
1002 IF (R1.NE.R) GO TO 1003
PRMT5=131
GO TO (104*ZID(01,J1)+ZID(01,J1)+1,1003)
1003 JJA=0R1,J1
HH=PP-R1*PP+D*ZID(01,J1)+1.G*ZID(01,J1)+1
IF (IQ.EQ.0.OR.T1.EQ.(N-1)).GO TO (78,1)
IQ=IQ-1
H1=RR1*DDRAD+DRAD-DDRAD
DIST4=DSQRT(((H1+2.*DDRAD)*DCOS(2.*TN)-H1)**2+((H1+2.*
DDRAD)*DSIN(2.*TN))**2)
SDDD=DIST4
DO 77 J=1,IQQ,2
IF ((T1+1)*TN.LT.DMIN1(DIS1(J,2),DIS1(J+1,2)).OR.(T1+1)*
1(T1-3)*TN.GT.DMAX1(DIS1(J,2),DIS1(J+1,2))) GO TO 77
IF (A.GT.DMAX1(DIS1(J,1),DIS1(J+1,1)).OR.A.LT.DMIN1(
1DIS1(J,1),DIS1(J+1,1))) GO TO 77
IF (DABS(DIS3(1,(J+1)/2)).LT.0.1D-13) GO TO 1912
C ABOVE LINE IS TO STOP DIVISION BY ZERO
X11=(H1*DSIN((T1-1)*TN)-DIS3(2,(J+1)/2))/
1DIS3(1,(J+1)/2)
DIST3=X11-H1*DCOS((T1-1)*TN).GO TO 622
DIST3=DABS(DIST3*DSIN(DABS(DATAN(DIS3(1,(J+1)/2))))))
GO TO 1911
1912 DIST3=DABS(DIS3(2,(J+1)/2)-H1*DSIN((T1-1)*TN))
1911 IF (DIST3.GT.DIST4) GO TO 77
DIST4=DIST3
JJA=(J+1)/2
77 CONTINUE
C THE .GE. FOR THE NEXT LINE SHOWS WHICH VALUES ARE TAKEN ALONG THE LINE OF
C THE DISCONTINUITY
78 IF (JJA.EQ.0) GO TO 660

```

```

622 L1=(A*DSIN(THET)-DIS3(1,JJA)*A*DCOS(THET)).GE.DIS3(2,JJA)
      IPQ=0
753 DO 632 I=1,5
      X(I)=I-2
      J1=I1+I-3
      ANG=(J1-1)*TN
      D2=DSIN(ANG)-DIS3(1,JJA)*DCOS(ANG)
      L2=A*D2.GE.DIS3(2,JJA)
      IF((L1.AND.L2).OR.(.NOT.L1.AND..NOT.L2)) GO TO 642
      V(I)=0.0D 00
      GO TO 632
642 IF((ABS(ZAR(R1,J1)-ZAR(R1+1,J1)).GT.ZKM))
      IGO TO 631
634 V(I)=((HH*ZID(R1,J1)+ZIC(R1,J1))*HH+ZIB(R1,J1))*HH
      I+ZAR(R1,J1)
      DV(I)=(HH*3.0*ZID(R1,J1)+2.0*ZIC(R1,J1))*HH+ZIB(R1,J1)
      DRR(I)=6.0*HH*ZID(R1,J1)+2.0*ZIC(R1,J1)
      GO TO 632
631 RADI=DIS3(2,JJA)/D2
      IF(DABS(DIS3(2,JJA)).LT.1.0D-10) GO TO 634
      IF(A.LT.RADI.OR.H1.GT.RADI) GO TO 634
      V(I)=0.0D 00
      IF(IPQ.EQ.0) GO TO 632
      IF(ABS(ZAR(R1+2,J1)-ZAR(R1+1,J1)).LT.ZKM) V(I)=ZAR(R1+1,J1)-
      IZAR(R1+2,J1)
      V(I)=((ZID(R1+1,J1)*HH+ZIC(R1+1,J1))*HH+ZIB(R1+1,J1))*H
      I+ZAR(R1+1,J1)+V(I)
      DV(I)=ZIB(R1+1,J1)
      DRR(I)=2.0*ZIC(R1+1,J1)
632 CONTINUE
639 CONTINUE
      IF(V(1).GT.0.0.AND.V(2).GT.0.0) GO TO 622
      IF(V(4).GT.0.0.AND.V(5).GT.0.0) GO TO 623
      IPQ=1
      GO TO 753

```

```

622 DO 614 I=3,5
    IF(V(I).GT.0.0) GO TO 614
    V(I)=2.0*V(I-1)-V(I-2)
    DV(I)=2.0*DV(I-1)-DV(I-2)
    DRR(I)=2.0*DRR(I-1)-DRR(I-2)
614 CONTINUE
    GO TO 641
623 I=4
    DO 615 II=1,3
        I=I-1
        IF(V(I).GT.0.0) GO TO 615
        V(I)=2.0*V(I+1)-V(I+2)
        DV(I)=2.0*DV(I+1)-DV(I+2)
        DRR(I)=2.0*DRR(I+1)-DRR(I+2)
615 CONTINUE
    GO TO 641
660 JKL=0
    DO 661 I=1,5
        X(I)=DFLOAT(I)
        I1=I+T1-3
        IF(I1.LT.1.OR.I1.GT.N) GO TO 7000
        V(I)=((HH*ZID(R1,I1)+ZIC(R1,I1))*HH+ZIB(R1,I1))*HH
        1+ZAR(R1,I1)
        DV(I)=(3.0*HH*ZID(R1,I1)+2.0*ZIC(R1,I1))*HH+ZIB(R1,I1)
        DRR(I)=6.0*ZID(R1,I1)*HH+2.0*ZIC(R1,I1)
        GO TO 661
7000 V(I)=0.0D 00
        JKL=1+DFLOAT(I1)
661 CONTINUE
    IF(T1.LT.((ITT-4).OR.T1.GT.((IFF+4).OR.ITT.EQ.0) GO TO 800
    IF(T1.EQ.(N-1)) GO TO 800
    IF(JKL.EQ.1) GO TO 639
641 CALL SPLINE(1,5,X,V,B,C,D,0.0D 00,0.1D 01)
    HH=FF-T1*ZID(R1,I1)+ZIC(R1,I1)

```

```

VE=((HH*D(3)+C(3))*HH+B(3))*HH+V(3)
DVT=(3.0*HH*D(3)+2.0*C(3))*HH+B(3)
DVT=DVT/TN
DVTT=(6.0*HH*D(3)+2.0*C(3))/(TN*TN)
CALL SPLINE(1,5,X,DV,B,C,D,0.0D 00,0.1D 01)
DVR=((HH*D(3)+C(3))*HH+B(3))*HH+DV(3)*HH+ZIB(R1,T1)
DVR=DVR/DDRAD
CALL SPLINE(1,5,X,DRR,B,C,D,0.0D 00,0.1D 01)
DVRR=((D(3)*HH+C(3))*HH+B(3))*HH+DRR(3)
DVRT=(3.0*D(3)*HH+2.0*C(3))*HH+B(3)
DVRR=DVRR/(DDRAD*CDRAD)
DVRT=DVRT/(DDRAD*TN)
GO TO 300
C FINDS THE VELOCITY FOR REGION IN WHICH V=F(RADIUS)
800 DVT=0.0D 00
DVTT=0.0D 00
DVRT=0.0D 00
DVRR=DRR(3)/(DDRAD*DDRAD)
DVR=DV(3)/DDRAD
VE=V(3)
GO TO 300
299 DVT=0.0D 00
DVRT=0.0D 00
DVTT=0.0D 00
IF(JCOU.LT.NNN-1)JOY=1
PP=DFLOAT(R6)*(A-1.0)/(DRAD+9.0)
T1=PP
HH=PP-DFLOAT(T1)
T1=PP/0.1D 03
R1=PP-DFLOAT(T1)*0.1D 03
T1=T1+H+1
IF(R1.NE.0) GO TO 193
R1=100
T1=T1-1
193 CONTINUE
VE=((HH*ZID(R1,T1)+ZIC(R1,T1))*HH+ZIB(R1,T1))

```

```

1*HH+ZAR(R1,T1)
DVR=(3.0*HH*ZID(R1,T1)+2.0*ZIC(R1,T1))*HH+ZIB(R1,T1)
DVR=DVR*DFLOAT(R6)/(DRAD+9.0)
DVRR=6.0*HH*ZID(R1,T1)+2.0*ZIC(R1,T1)
DVRR=DVRR*DFLOAT(R6*R6)/(((DRAD+9.0)**2),1.0/AD*ZVT*PI*PI*ZVT*PI*PI)
IF(JCOU.LT.NNN-1)JOY=1
300 CONTINUE
355 IF(JCOU.LT.NNN-1.OR.JOY.NE.1) GO TO 104
JOY=0
301 WRITE(6,12)
12 FORMAT(4X,'R1',4X,'T1',4X,'VELOCITY',8X,'DVR',8X,'DVT',
18X,'DVRR',7X,'DVRT',7X,'DVTT',6X,'JJA')
WRITE(6,2313)R1,T1,VE,DVR,DVT,DVRR,DVRT,DVTT,JJA
2313 FORMAT(2I6,6E12.3,I6)
104 RETURN
END

```

FILE

SUBROUTINE BERT(A,THET,AA,TTHET,AI,THETA1)

IMPLICIT REAL*8(A-H,O-Y)

INTEGER R,R6,RRR6,RRR,THETA1,AI

COMMON/AS/RAD,DDRAD,DRAD,RRR6,R6,R,RRR,IQ/AE/PRMT5,PI,XXY,RESO,ZKM

COMMON/AP/TN,DDS,XK,JAL,NNN,JJA,N

AA=(A-DRAD+DDRAD)/DDRAD

AI=AA

TTHET=THET/TN+1.0

THETA1=TTHET

IF(THETA1.GE.N)THETA1=N-1

RETURN

END

FILE

```

SUBROUTINE FCT(X,Y,DERIV)IV,FILE,NDIM,PRMT
  IMPLICIT REAL*8(A-H,O-Y)
  C THIS SUBROUTINE COMPUTES THE VALUES OF THE RIGHT HAND SIDE OF THE
  C DIFFERENTIAL EQUATIONS FOR RAY PATH AND GEOMETRICAL SPREADING EFFECT
  COMMON/AK/PL(5,5),YXZ(10,10),SSIG,JCOU
  DIMENSION Y(7),DERIV(7)
  COMMON/AE/PRMT5,PI,XXY,RESO,ZKM
  COMMON/DOO/VE,ZIC(102,100),ZIC(102,100)
3  CALL VELOC(VE,DVR,DVT,DVRR,DVRT,DVTT,Y(1),Y(2))
5  CONTINUE
  IF(Y(3).GT.0.1D-04) GO TO 1
  WRITE(6,2)('RAY, GOING ROUND, IN CIRCLES')
2  FORMAT('RAY, GOING ROUND, IN CIRCLES')
  PRMT5=1.
  RETURN
1  AB=DVR*Y(5)+DVT*Y(6)
  AS=DSIN(Y(3))
  AC=DCOS(Y(3))
  DERIV(1)=VE*AC
  DERIV(2)=VE*AS/Y(1)*SSIG
  DERIV(3)=AS*(DVR-VE/Y(1))-SSIG*AC*DVT/Y(1)
  DERIV(4)=VE*DERIV(1)
  DERIV(5)=AB*AC-VE*AS*Y(7)
  DERIV(6)=(AB*AS-VE*(AS*Y(5)/Y(1)-AC*Y(7)))/Y(1)*SSIG
  DERIV(7)=(Y(5)*DVRR+Y(6)*DVRT-(AB-VE*Y(5)/Y(1))/Y(1))*AS
  1+ (DVR-VE/Y(1))*AC*Y(7)+((AC*Y(5)/Y(1)+AS*Y(7))*DVT-AC*(Y(5)*
  1DVRT+Y(6)*DVTT))/Y(1)*SSIG
  RETURN
  END

```

FILE

```

SUBROUTINE OUTP(XX,YY,DERIV,IHLF,NDIM,PRMT)
  IMPLICIT REAL*8(A-H,O-Y)
C THIS SUBROUTINE OUTPUTS ALL THE NECESSARY DATA AND REFLECTS OR
C REFRACTS THE RAY AT THE RADIAL AND LATERAL DISCONTINUITIES
  INTEGER R,RRR,RRR6,R6
  LOGICAL L1,L2
  DIMENSION YY(7),DERIV(7),PRMT(5),IZA(32),IZB(32)
  COMMON ZAR(102,106),ZID(102,106),ZIC(102,106),ZIB(102,106)
  1,DIS1(32,3),DIS2(10,4),DIS3(4,32)
  COMMON/DOO/VEOP(AMPL)
  DIMENSION XOUT(10)
  COMMON/AG/KM,IRRR,ITT,IFF,IAA,IAB
  COMMON/AP/TN,DDS,XXY,JAL,NNN,JA,N/AK/PL(5,5),YXZ(10,10),SSIG,
  1JCOU
  COMMON/AS/RAD,DDRAD,DRAD,RRR6,R6,R,RRR,IQ/AE/PRMT5,PI,XXYY,
  1DS,ZKM
C FINDS IF RAY IS NEAR TO THE BOTTOM OF ITS PATH
  IF(YY(1).GT.A.AND.JJJ.EQ.0.AND.JAL.NE.1)WRITE(6,2000)A
  IF(YY(1).GT.A.AND.JJJ.EQ.0.AND.JAL.NE.1)JCOU=NNN-1
2000 FORMAT('THE RAY BOTTOMS AT ',F12.4)
  IF(YY(1).GT.A)JJJ=1
  IF(YY(1).LT.RAD.AND.PRMT5.LT.1.0) GO TO 10
  JCOU=NNN-1
  PRMT5=1
10 A=YY(1)
  T=YY(2)
  SA=YY(3)
  JJA=JA
  IF(JAL.NE.1) GO TO 4261
  VEP1=DCOS(YY(3)-0.9D 02*PI)
  I=0
  WRITE(3,89)I
  AMPL0=1.
  T2=YY(2)
  JJJ=0

```

42612 CONTINUE(611)

C COMPUTES THE AMPLITUDE (SQRT OF THE INTENSITY) - INCLUDES GEOMETRICAL
C SPREADING AND ENERGY PARTITIONING

AMPL=DSQRT(YY(5)*YY(5)+YY(1)*YY(1)*YY(6)*YY(6))

C TT=T-T2 (SEE COMMENTS TO P. 4)

IF(DABS(AMPL).GT.0.001) AMPL=DSQRT(DABS(VEP1)/(DSIN(DABS(TT))

1*AMPL))

C AMPL2=AMPL*DSQRT(AMPLO)*DSQRT(0.2D+01/0.557D+01)/(360.*PI)

AMPL2=AMPL*DSQRT(AMPLO)

IF(JAL.EQ.7.AND.ICOUNT.LT.4) GO TO 1999

DA=A-BA

DT=T-BT

DS=DSQRT(DA*DA+(A*DT)**2)

IF(JAL.EQ.1) DS=0.0D 00

DDS=DDS+DS

DS=DS*(2.0**IHLF)*1.01

DA=DA*(2.0**IHLF)*1.01

DT=DT*(2.0**IHLF)*1.01

1999 AM=A+DA

TM=T+DT

XXYY=XX+XXY

JCOU=JCOU+1

IF(JCOU.LT.NNN) GO TO 11

C OUTPUT OF ALL DATA - DEVISE 3 TAKES THE X AND Y COORDS FOR PLOTTING (

C NUMBER OF VALUES READ OUT DEPENDS ON NNN) DEVISE 5 TAKES ALL OTHER DATA

91 X=DCOS(T)*A

Y=A*DSIN(T)

JCOU=0

11 IF(JAL.EQ.1) JOCK=0

JOCK=JOCK+1

IZA(JOCK)=(X*0.1D 02)

IZB(JOCK)=(Y*0.1D 02)

IF(JOCK.NE.16.AND.JAL.NE.5) GO TO 88

107 WRITE(3,89)(IZA(K),K=1,JOCK)

WRITE(3,89)(IZB(K),K=1,JOCK)

```

311 CALL BERT(AA, TM, AAM, TEM, IAM, ITM)
89 FORMAT(16I5)T,AA,IT,IA,IT)
JOCK=0
88 TT=T/PI.EQ.IAM GO TO 127
C IF(JAL.NE.1.AND.JAL.NE.5)GO TO 1130
C ABOVE LINE MAY BE INSERTED TO FEED OUT JUST THE INITIAL AND FINAL VALUE
ROUT=0.DF.7)ICRNT=0
DO 12 J=1,3
XOUT(J)=PL(J,1)*X+PL(J,2)*Y
12 ROUT=ROUT+XOUT(J)*XOUT(J).ITHD=.01.FAK-... TO 142
ROUT=DSQRT(ROUT)
TOUT=DARCOS(XOUT(3)/ROUT)/PI
PP=ROUT*DSIN(SA)/VE-JA(IAM,3))G1ZK... ASSIGMENT
C FOR LAT BELOW THE EQUATOR MUST PUT COLAT=LAT+90 TO GIVE -Z
POUT=DABS(DATAN(XOUT(2)/XOUT(1)))/PI
IF(X.GE.0.0.AND.Y.GE.0.0)GO TO 1101
IF(X.GE.0.0)POUT=0.36D.03-POUT
IF(Y.GE.0.0)POUT=0.18D.03-POUT
IF(X.LT.0.0.AND.Y.LT.0.0)POUT=0.18D.03+POUT
C HAVE HAD TO PUT CONDITIONS TO ACCOUNT FOR ALL POSSIBLE POSITIONS OF
C SOURCE AND RECIEVER ON GLOBE
1101 WRITE(6,3366)
3366 FORMAT(4X,'RADIUS',8X,'THETA',8X,'PHI',6X,
1'TIME',6X,'DISTANCE',7X,T,11X,P,8X,'EMERG ANG',2X,'AMPL'
/1 2,'ITUDE',3X,'IHLF',3X,'AMPLITUDE2')
C TO PRINT WRITE(6,14)ROUT,TOUT,POUT,XXYY,DDS,TT,PP,SA,AMPL,IHLF,AMPL2
14 FORMAT(8F12.4,F12.8,15,F12.8)
IF(ROUT.GT.6370.0)WRITE(6,44)IAM,ITM
44 FORMAT(2I7)=XFI
11 IF(JAL.EQ.1)GO TO 500
IF(JAL.EQ.5)GO TO 1212 TO 7154
IF(A.LT.RAD.AND.PRMT5.LT.1.0)GO TO 707
LPRMT(5)=14)D.03-14
GO TO 501.LST.3D.14P.LT.LS.AB.ITD.G1V...
707 IF(A.LT.(DRAD+30.0))GO TO 400D.14P.LT.LS...
IO=1

```

```

7954 IDIS=DIS2(K,1)+.1D-4
311 2CALL IBERT(AM, TM, AAM, TTM, IAM, ITM)
CALL IBERT(A, T, AA, TT, IA, IT)
IDIS=RC.LC.IAM) GO TO 35
IF(IDIS.EQ.IAM) GO TO 127
IF(IAM.EQ.IA.AND.ITM.EQ.IT) GO TO 300
C DO I NOT WANT TO REFRACT YET
12 IF(JAL.NE.7) ICOUNT=0
IAB=4A.EQ.3) GO TO 500
IAA=4
IF(ABS(ZAR(IA, IT)-ZAR(IAM, ITM)).GT.ZKM) GO TO 242
35 I=IAM+1
J=ITM+1
IF(ABS(ZAR(IAM, ITM)-ZAR(IAM, J)).GT.ZKM.OR.ABS(ZAR(IAM,
1ITM)-ZAR(I, ITM)).GT.ZKM.OR.ABS(ZAR(I, J)
1-1-ZAR(I, ITM)).GT.ZKM) GO TO 242
GO TO 500
300 IF(IAA.EQ.4.AND.JJA.EQ.0) GO TO 500
IF(IAA.EQ.4.AND.(IAB.EQ.3.OR.IAB.EQ.5)) ICOUNT=3
242 Y=A*DSIN(T)
X=A*DCOS(T)
IF(ICOUNT.EQ.3) GO TO 50
IF(IAM.EQ.IA.AND.IAA.EQ.4.AND.(ICOUNT.EQ.2.OR.ICOUNT.EQ.5
OR 1)) GO TO 81
C TO IF(ICOUNT.EQ.1.OR.ICOUNT.EQ.4) GO TO 181
71 IK=0
C TO FIND HOW NEAR THE RAY IS TO A SPHERICAL DISCONTINUITY
IF(AM.LT.A) K=RRR+1
DO 72 I=1, RRR
IF(AM.GE.A) K=K+1
IF(AM.LT.A) K=K-1
72 IF(DIS2(K,3).LT.0.1) GO TO 7954
L5=DIS2(K,3)+0.1D-04
L6=DIS2(K,4)+0.1D-04
IF((L5.LT.L6).AND.(ITM.LT.L5.OR.ITM.GT.L6)) GO TO 72
IF((L5.GT.L6).AND.(ITM.GT.L6.AND.ITM.LT.L5)) GO TO 72

```

```

50 GR=DIAM(T-54-35)/2
7954 IDIS=DIS2(K,1)+0.1D-04).01.0.1D-04) GO TO 72
      ZRAT=DIS2(K,2)
      IF(IAM.LT.1A.AND.IDIS.EQ.1A) GO TO 35
      IF(IDIS.EQ.1A) GO TO 35
      IF(AM.LT.A) GO TO 72
82 IIAM=IAM+12,JJA)+GR*X-Y)/(DIS3(1,2)+GR)
      IF(IDIS.EQ.IIAM) GO TO 35(JJA)
72 CONTINUE V(Y2/X2)
      IF(1AA.EQ.3) GO TO 500 GO TO 1A
      1AA=400+11(Y2-Y1)*(Y2-Y1+(1A2-X)*(1A2-X)
      GO TO 81(1A2-05) GO TO 79
35 1*RR=DFLOAT(IDIS)*DDRAD+DRAD-DDRAD
      IF(RR.GT.DABS(A*DSIN(SA))) GO TO 73
      1AA=5
      GO TO 81(1A2-05,1A2-10,1A2-15) GO TO 79
73 SSA=3.14159-SA
      CB1=DABS(DABS(A*DCOS(SSA))-DABS(DSQRT(RR*RR-(A*DSIN(SSA))**
      12)))/A(1A2-05,1A2-10,1A2-15)
      IF(CB1.LT.DS) GO TO 40
      1AA=3
      GO TO 81
40 1AA=6
      GO TO 81(1A2-15,1A2-20,1A2-25) GO TO 79
1008 GO TO 81(1A2-25,1A2-30,1A2-35) GO TO 79
80 1AA=400
C TO FIND HOW NEAR THE RAY IS TO A LATERAL DISCONTINUITY
81 IF(ICOUNT.EQ.2.OR.ICOUNT.EQ.5) GO TO 95
      CALL VELOC(VEE,DVR,DVT,DVRR,DVRT,DVTT,AM,TM)
      IF(DABS(VE-VEE).LT.ZKM) GO TO 500
      IF(JJA.NE.0.OR.JA.NE.0) GO TO 50
      IF(1AA.EQ.4) GO TO 2060
      GO TO 95
2060 1IAB=4*TS OR REFRACTS AT A SPHERICAL DISCONTINUITY
C FOR WRITE(6,90) ICOUNT,IAM,IA,IT,ITM,JJA,ZAR(IA,IT),ZAR(IAM,ITM)
190 1FORMAT('NON-DEFINED DISCONTINUITY',6I5,2F12.6)
      STOP

```

```

      IAA=4
50  GR=DTAN(T+SA*SSIG)
      IF(DABS(DIS3(1,JJA)-GR).GT.0.1D-04) GO TO 82
C  ABOVE IAB=50 ENSURES THAT THE RAY IS REFLECTED AT THE
      IF(JA.EQ.0.OR.JA.EQ.JJA) GO TO (95,127)
      JJA=JADD 00
      GO TO 50.1.57080) SSA=1.0
82  X2=-(DIS3(2,JJA)+GR*X-Y)/(DIS3(1,JJA)-GR)
      Y2=DIS3(1,JJA)*X2+DIS3(2,JJA)
      DDTT=DATAN(Y2/X2) IA,IT),ZAR(1,4,ITM),,DT,Z,ZA)
      IF((DDTT-T)/DT.LT.0.0D+00) GO TO 99
120  CB2=DSQRT((Y2-Y)*(Y2-Y)+(X2-X)*(X2-X))
      IF(CB2.GT.DS) GO TO 99
      IAB=6(6,0972)
      GO TO (95,2345) ZH,SA,ZAR(IA,IT),ZAR(IAB,IT),ZAR(1,4,ITM),,DT,Z,ZA)
99  IAB=3Y**
2345 IF(JA.EQ.0.OR.JA.EQ.JJA) GO TO A95A RADIAL VELOCITY
134  JJA=JA+04
      GO TO 501
195  IF(IAA+IAB.NE.12) GO TO 64
      PRMT(5)=2(8Y***)
      GO TO A501.0.1)SA+PI*0.100 0D-04
64  CONTINUE
      IF(IAB.NE.4.AND.IQ.EQ.0) WRITE(6,1008)
1008  FORMAT('IAB*NOT*(EQ 4 WHEN IQ EQ 0')
      L1=(IAA.EQ.4.OR. IAA.EQ.5)
      L2=(IAB.EQ.4.OR. IAB.EQ.5)
3477 IF(L1.AND.L2) GO TO 500REF AND VELOCITY VELOCITY 2*
      IF((IAA.EQ.3.OR.L1).AND.IAB.EQ.6) GO TO 124
      IF((IAB.EQ.3.OR.L2).AND. IAA.EQ.6) GO TO 127
3450 /GO TO (5002.6,* DE FRACTION AT A RADIAL VELOCITY 1
C  GO TO 121
C  ST*GR-DARSIN(4+DSIN(SA)/6371.0)
C  BELOW-REFLECTS OR REFRACTS AT A SPHERICAL DISC - CALLS SUBROUTINE ZO
C  FOR SOLUTION OF ENERGY PARTITIONING EQUATIONS
127  ICOUNT=1

```

```

100SSA=1.0-PI*(1.-ZAR(IA,IT))
IAA=471.2405194-1.7E-11*ZAR(IA,IT)
IF(IDIS.EQ.R) GO TO 8
IF(IDIS.EQ.695) GO TO 126
C ABOVE LINE ENSURES THAT THE RAY IS REFLECTED AT THE CORE MANTLE BOUNDARY
SYNR=DSIN(SA)*ZAR(IAM,ITM)/ZAR(IA,IT)
SSA=0.0D 00
C BELOW LINE ASSUMES A REFRACTION INDEX OF 1.0 FOR THE CORE MANTLE BOUNDARY
IF(SA.GT.1.57080)RSSA=1.0 A=1.0-PI*(1.-ZAR(IA,IT))
124 ZH=SAOS(T+SSIG*SA)
IF(SSA.LT.0.1)ZRAT=1./ZRAT
CALL/ZO(1,ZH,ZAR(IA,IT),ZAR(IAM,ITM),ZRAT,ZZ,ZZZ)
IF(SYNR=1.0)125,154;126*PI*3.141592653589793
126 SSA=3.14159-SAS
AMPL0=AMPL0*ZZZ
WRITE(6,3972)
WRITE(6,2345)ZH,SA,ZAR(IA,IT),ZAR(IAM,ITM),CB1,DS
ICOUNT=41-ICOUNT
2345 FORMAT(6F12.6,' REFLECTION AT A RADIAL DISCONTINUITY')
154 PRMT(5)=6(1,2)
GO TO C501.NEUTRAL=1./ZRAT
125 AMPLO=AMPL0*ZZ
SA=DARSIN(SYNR)
IF(SSA.GT.0.1)SA=PI*0.18D 03-SA
A=AMS(6,3972)
T=TM ZO(1,ZH,ZV1,ZV2,ZRAT,ZZ,ZZZ)
XXY=XXY+1.1*PRMT(3);123
123 DDS=DS*1.1+DDS;124*PI*3.141592653589793
WRITE(6,3972)A,CROSS=PI*3.141592653589793
3972 FORMAT('INCIDENCE ANGLE',REF,ANGLE,VELOCITY 1 VELOCITY 2'
1;'DISTANCE 1 DISTANCE 2')
3457 WRITE(6,3456)ZH,SA,ZAR(IA,IT),ZAR(IAM,ITM),CB1,DS
3456 FORMAT(6F12.6,' REFRACTION AT A RADIAL DISCONTINUITY')
GO TO 121
189 TOT=SA-DARSIN(A*DSIN(SA)/6371.0)CB2,03
3458 A=6371.0*12.6,' REFRACTION AT A RADIAL DISCONTINUITY'

```

```

T=T+OT
IF(SSIG.LT.1.)T=T-2.*OT
OT=6371.0*DSIN(OT)/DSIN(SA)
DDS=DDS+OT.1*PRMT(3)
XXYY=XXYY+OT/VE
JAL=51.0
PRMT(5)=1.0.0) SIG=1.0
GO TO 9

```

C BELOW REFLECTS OR REFRACTS AT A LATERAL DISC - CALLS SUBROUTINE ZO

```

C124 AA=DCOS(T+SSIG*SA)
BB=DSIN(T+SSIG*SA)
1 DOT=AA*DIS3(3,JJA)+BB*DIS3(4,JJA)
CROSS=BB*DIS3(3,JJA)-AA*DIS3(4,JJA)
122 SYNI=DABS(CROSS)*DSIN(T)
RN=VEE/VES(T)-A1*DSIN(T)
IAB=47+315X-275Y
ICOUNT=275-315Y
SYNR=SYNI*RN
I=JJA*2-1
ZRAT=DIS1(I,3)
IF(VEE.LT.VE)ZRAT=1./ZRAT
ZH=SYNI
ZVE=VEE
ZVEE=VEE
WRITE(6,3972)
CALL ZO(1,ZH,ZVE,ZVEE,ZRAT,ZZ,ZZZ)
IF(SYNR-1.0)129,154,123
123 A1=-(DIS3(3,JJA)*DOT+DIS3(4,JJA)*CROSS)
B1=(DIS3(3,JJA)*CROSS-DIS3(4,JJA)*DOT)
WRITE(6,3457)SYNI,SYNR,ZVE,ZVEE,CB2,DS
ICOUNT=5
3457 FORMAT(6F12.6,' REFLECTION AT A LATERAL DISCONTINUITY')
C DELAMPLO=AMPLO*ZZZ
C IN TGO TO 122 IF SPECIFICALLY SYMMETRIC CASE
129 WRITE(6,3458)SYNI,SYNR,ZVE,ZVEE,CB2,DS
3458 FORMAT(6F12.6,' REFRACTION AT A LATERAL DISCONTINUITY')

```

AMPLO=AMPLO*ZZ

A=AM

T=TM

XXY=XXY+1.1*PRMT(3)

DDS=DDS+1.1*DS

SIG=-1.0.0) GO TO 402

IF(DOT.GE.0.0)SIG=1.0

C IF(DABS((URAD+9.0)*DIS3(3,JJA)-DIS3(4,JJA))>1.0)GO TO 1061

C 1) GO TO 401

C ID=0

A1=RN*(AA-DOT*DIS3(3,JJA)+SIG*DIS3(3,JJA)*DSQRT(DOT

1**2+(RN**(-2)-1.0))) / (URAD+9.0)

B1=((DIS3(3,JJA)*BB-AA*DIS3(4,JJA))*RN+A1*DIS3(4,JJA))/DIS3(3,JJA)

122 SA=A1*DCOS(T)+B1*DSIN(T)

ST=B1*DCOS(T)-A1*DSIN(T)

CROSS2=B1*X-A1*YU 302

CROSS=BB*X-AA*Y

IF(CROSS/CROSS2.GE.0.0)GO TO 1060

302 SSIG=-SSIG*(1+DT/URAD)/(URAD+9.0)

WRITE(6,1061)

1061 FORMAT('RAY HAS CHANGED DIRECTION')

1060 SA=DARCOS(SA)GO TO 201

C BELOW RESETS THE PARAMETERS

121 PRMT(5)=3

1212 YY(1)=AA+1

YY(2)=T27

401 YY(3)=SAUF

500 BA=AD 500

402 IBT=T

BIA=SA500

501 JAL=2XX

GOTTO 1501

C BELOW ALLOWS REFLECTION OR REFRACTION AT A SPHERICAL DISCONTINUITY

1) IN THE REGION OF SPHERICALLY SYMMETRIC EARTH

400 I=RRR+1

```

      IF(10.EQ.0) GO TO 402
      IDO(401,K)=I,IRRR
      IF(DABS((DRAD+9.0)*DIS2(K,1)/DFLOAT(R6)+2.0-A).GT.DABS(DA)

```

```

11) GO TO 401

```

```

      BID=0

```

```

      BIDIS=DIS2(K,1)+0.1

```

```

2123 A1=(A-1.0)*DFLOAT(R6)/(DRAD+9.0)

```

```

      IT=A1/0.1D 03

```

```

      IA=A1-0.1D 03*DFLOAT(IT)

```

```

      IT=IT+N+1

```

```

      IF(IA.NE.0) GO TO 302

```

```

      IA=100

```

```

      IT=IT-1

```

```

302 A1=(A-1.0+DA)*DFLOAT(R6)/(DRAD+9.0)

```

```

      ITM=A1/0.1D 03

```

```

      IAM=A1-0.1D 03*DFLOAT(ITM)

```

```

      IF(IAM.NE.0) GO TO 301

```

```

      IAM=100

```

```

      ITM=ITM-1

```

```

301 ITM=ITM+N+1

```

```

      GO TO 127

```

```

401 CONTINUE

```

```

      GO TO 500

```

```

402 IO=1

```

```

      GO TO 500

```

```

501 CXXYY=XX

```

```

      RETURN

```

```

      END

```

```

LE P=(Y(I+1)-Y(I))

```

```

      A(I)=P-1

```

```

      T(I)=2.*(C+P)

```

```

      T(I)=1/3.

```

```

      P2(I)=DY(I)-1/2

```

```

      P(I)=DY(I+1)

```

```

      P(I)=DY(I)/C-1/2

```

```

      CONTINUE

```

```

SUBROUTINE SPLINE(N1,N2,X,Y,B,C,D,S,AAAA)
IMPLICIT REAL*8(A-H,O-Z)
DIMENSION X(1);Y(1),B(1),C(1),D(1),R(2000),R1(2000),
1R2(2000);T(2000);T1(2000),U(2000),V(2000),A(2000)
DIMENSION DY(2000)
2 DO 21230 II=N1,N2
2123 DY(II)=AAAA
R1(N2)=0.
50 M1=N2+2-M1,M2
M2=N2+1-R1(I-1)*F
R(M1)=0.
R(N1)=0.
R2(N2)=0.
R2(M2)=0.0
U(M1)=0.
U(N1)=0.
U(N2)=0.
U(M2)=0.
3 P=0.
M1=N1+1
M2=N2-1
H=X(M1)-X(N1)
F=(Y(M1)-Y(N1))/H
4 Q(I)=R(I)/H
DO 1 I=M1,M2
G=H.
H=X(I+1)-X(I)
E=F
F=(Y(I+1)-Y(I))/H
A(I)=F-E
T(I)=2.*(G+H)/3.
T1(I)=H/3.
R2(I)=DY(I-1)/G
R(I)=DY(I+1)/H
R1(I)=-DY(I)/G-DY(I)/H
1 CONTINUE

```

```

      F2=F2
      F2=(F2+R(I)**2+R(I+1)**2+R(I+2)**2)/3
      DO 12 I=M1,M2
      B(I)=R(I)**2+R(I+1)**2+R(I+2)**2
      C(I)=R(I)*R(I+1)+R(I+1)*R(I+2)
      D(I)=R(I)*R(I+2)
2     CONTINUE
      F2=-S(I+1)-T(I)/X(I+1)-F(I)
      KK=I-2
56    DO 13 I=M1,M2
      R1(I-1)=R(I-1)*F(I-1)-C(I-1)*X(I-1)
      KK=I-2
      IF(KK.LT.N1)KK=N2+2
      R2(KK)=G*R(KK)
      R(I)=1.0/(P*B(I)+T(I)-F*R1(I-1)-G*R2(KK))
      U(I)=A(I)-R1(I-1)*U(I-1)-R2(KK)*U(KK)
      F=P*C(I)+T1(I)-H*R1(I-1)
      G=H*(I-1)
      H=D(I)*P/(X(I)-X(I-1))
3     CONTINUE
      IJ=M2+1
      DO 14 I=M1,M2
      IJ=IJ-1
4     U(IJ)=R(IJ)*U(IJ)-R1(IJ)*U(IJ+1)-R2(IJ)*U(IJ+2)
      E=0.5*(U(IJ)+U(IJ+1))
      H=0.5*(C(IJ+1)+C(IJ+2))/X(IJ+1)
      DO 15 I=N1,M2
      G=H*(I-IJ)
      H=(U(IJ+1)-U(IJ))/(X(IJ+1)-X(IJ))
      V(I)=(H-G)*DY(I)**2
54    E=E+V(I)*(H-G)
      FORMAT('DGT OF SPL')
      G=-H*DY(N2)**2
      V(N2)=G
      E=E-G*H

```

```

G=F2
F2=E*P*P.NE ZD(JJJ,A1,C11,C31,(Y41,A11,M2))
C=PRIR(F2,GE,S,OR,F2,LE,G)S GO TO 55 IF AL1=0 AND 1=0
C THIF=0.0ROUTINE SETS UP ZD FOR 17'S FROM 1'S AND 2'S
C H=(V(M1)-V(N1))/(X(M1)-X(N1))P,RE
C JJJ DO 16 I=M1,M2,1)P=PWV1,C(2,1)=SWV1,C(3,1)=PW7,C(4,1)=PW8
C JJJ G=H*4---C(1,1)=SWV1,C(1,1)=PWV1,C(3,1)=PW7,C(4,1)=PW8
C ALPH=(V(I+1)-V(I))/(X(I+1)-X(I)) JJJ OR 2 3 4 5 6 7 8 9 10 11 12 13 14 15 16 17 18 19 20 21 22 23 24 25 26 27 28 29 30 31 32 33 34 35 36 37 38 39 40 41 42 43 44 45 46 47 48 49 50 51 52 53 54 55 56 57 58 59 60 61 62 63 64 65 66 67 68 69 70 71 72 73 74 75 76 77 78 79 80 81 82 83 84 85 86 87 88 89 90 91 92 93 94 95 96 97 98 99 100
C B1KK=I-2 I--AMPLITUDE, J=I--PHASE, J=I--EMISSIVITY, J=I--
C B1I,IF(KK.LT.N1)KK=N2+21S FOR 1 COORDINATE OF 1 ONLY
C RH1 G=H-G-R1(I-1)*R(I-1)-R2(KK)*R(KK) MEDIA
F=F+G*R(1)*G(5,12),G(5,12)=C(5,5)
R(I)=G*X ALPH C3S, LTRG, 34CF, 7
6 CONTINUE, P12/51.395779+1309,612831353077
CORRFX1=STRT(1.-X)
16 FORMAT('TTTT')X=1.)
H=E-P*F,Y)=2.*X*Y
IF(H.LE.0.)GO TO 55
P=P+(S-F2)/((DSQRT(S/E)+P)*H)
GO TO 56
C 55 DO 7 I=N1,N2
C CCA(I)=Y(I)-P*V(I) IS VALIDITY AND DENSITY SETS
C(I)=U(I)/I
7 CONTINUE
DO 8 I=N1,M2
H=X(I+1)-X(I) ALPH=P12/240-ALPH
D(I)=(C(I+1)-C(I))/(3.0*H)
B(I)=(A(I+1)-A(I))/H-(H*D(I)+C(I))*H
8 CONTINUE LK10., .)
DO 456 I=N1,N2
456 Y(I)=A(I)SIP
44 FORMAT(10E14.6)
1111 FORMAT('OUT OF SMO')
RETURN, EC, 2, OR, JJJ, EC, 4) GO TO 75
END 1=C(1,1)
SWV1=C(2,1)

```

```

SUBROUTINE ZO(JJJ,AI,C11,C31,DRAT,AL1,AL2)
C PRODUCES THE SAME RESULTS AS SINGH ET AL. CLAIM ARE CORRECT
C THIS SUBROUTINE SETS UP ZOEPPRITZ'S EQUATIONS AND SOLVES
C SUBROUTINE ZO(JJJ,B,C,AIP,RH2,RH1)
C JJJ=1 OR 3---C(1,1)=PWV1,C(2,1)=SWV1,C(3,1)=PWV2,C(4,1)=SWV2
C JJJ=2 OR 4---C(1,1)=SWV1,C(2,1)=PWV1,C(3,1)=PWV2,C(4,1)=SWV2
C AIP=INCIDENT, ANGLE OF P WAVE FOR JJJ=1 OR 3 OF S WAVE FOR JJJ=2 OR 4
C B(I,J)--J=1--AMPLITUDE,J=2---PHASE,J=3---ENERGY,J=4--ANGLE
C B(I,J)--I--COORDINATE AS FOR 1 COORDINATE OF C ARRAY
C RH1 AND RH2 ARE THE DENSITIES OF THE MEDIA
DIMENSION A(5,12),B(5,10),C(5,5)
COMPLEX A,ENCRS,CZERO,SINCF,Z
DATA RTD,PI2/57.29577951308,6.283185307/
COSRF(X)=SQRT(1.-X)*(C(1,1),0.)
COSIF(X)=SQRT(X-1.)
SIN2F(X,Y)=2.*X*Y
SINCF(X,Z)=X*Z IS AND CONSTANT FOR THE A MATRIX
COS2F(X)=1.-2.*X
ABC=2. J=1,10
C ALL J=1-10
C COMPUTES SINE COSINES VELOCITY AND DENSITY RATIOS
C(1,1)=C11
C(3,1)=C31,211
AIP=AI-AL1,11
IF(AIP.GT.PI2/4.0)AIP=PI2/2.0-AIP
C(2,1)=C(1,1)/SQRT(3.)
C(4,1)=C(3,1)/SQRT(3.)
CZERO=CMPLX(0.,0.)
SAI=SIN(AIP),1
CAI=COS(AIP),1
S2AI=SAI**2,11
DRAT=RH2/RH1,1
IF(JJJ.EQ.2.OR.JJJ.EQ.4) GO TO 76
PWV1=C(1,1)
SWV1=C(2,1)

```

```

GO TO 177 SWV1/SWV1*(1/2)*F(1,1,2,3)
76 APWV1=C(2;1)SRAT=(CAI1/C(1,1))*ABC*SIN2F(C(3,2),A(3,1))
SWV1=C(1;1) GO TO 33
77 SRAT=(C(4,1)/SWV1)**2/1/C(4,1)*COS2F(C(4,2))
RAT=SAI/C(1,1)
S1P1=C(2,1)/C(1,1)
34 P2P1=C(3;1)/C(1,1)
S2P1=C(4;1)/C(1,1)
DO 179 I=2;4*P2P1*COS2F(C(4,3))
C(I,2)=RAT*C(I;1)INCF(C(2,2),A(2,1))
C(I,3)=C(I;2)**2S2P1*SINCF(C(4,2),A(4,1))
IF(C(I,3):LE:1.) GO TO 10
A(I,11)=CMPLX(0.,COSIF(C(I,3)))
CCCCC IF(I:GE:3)A(I,11)=-A(I,11)
GO TO 179 14,2)
10 A(I,11)=CMPLX(COSRF(C(I,3)),0.0)
79 CONTINUE 14,11)
C A(3,1)=COS2F(S2A1)
C COMPUTES COEFFICIENTS AND CONSTANT FOR THE A MATRIX
DO 100 I=1,5)*A1C
DO 100 J=1,10(C(4,1)**2)/(SWV1*CAI) (1,1) (1,1) (1,1)
A(I,J)=CZERO/ABC
100 ACONTINUERAT*S2P1*COS2F(C(4,2))
A(1,1)=SAI(2,1)
A(1,2)=A(2;11)A1,CAI)
A(1,5)=-A(1,1)SPF(S2A1)
A(2,1)=-CAI*P2P1*COS2F(C(4,3))
A(2,2)=C(2;2)BC*S2P1*INCF(C(4,2),A(4,1))
A(2,5)=A(2,1)
11 GO TO 177,8,7,8),JJJ
7 A(1;3)=-C(3;2).1.SA.C(3,2).GE:1.0.0.0.14
A(1;4)=A(4,11)
110 A(2,3)=-A(3,11),A,4,1,10.11
A(2;4)=-C(4;2) GO TO 111
A(3;1)=SIN2F(SAI,CAI)

```

```

111 A(3,2)=(PWV1/SWV1)*COS2F(C(2,3))
A(3,3)=DRAT*SRAT*(PWV1/C(3,1))*ABC*SINCF(C(3,2),A(3,1))
IF(JJJ.EQ.3)GO TO 33
A(3,4)=-DRAT*SRAT*(PWV1/C(4,1))*COS2F(C(4,3))
120 GO TO 134
33 A(3,4)=0
34 A(3,5)=A(3,1)
130 A(4,1)=-COS2F(C(2,3))
A(4,3)=DRAT*P2P1*COS2F(C(4,3))
A(4,2)=S1P1*ABC*SINCF(C(2,2),A(2,1))
140 A(4,4)=DRAT*ABC*S2P1*SINCF(C(4,2),A(4,1))
A(4,5)=-A(4,1)
GO TO 110
180 A(1,3)=-A(3,11)
A(1,4)=-C(4,2)
A(2,3)=C(3,2)
190 A(2,4)=-A(4,11)
A(3,1)=COS2F(S2AI)
A(3,2)=(SWV1/PWV1)*SINCF(C(2,2),A(2,1))
A(3,2)=A(3,2)*ABC
A(3,3)=DRAT*((C(4,1)**2)/(SWV1*C(3,1)))*SINCF(C(3,2),A(3,1))
A(3,3)=A(3,3)*ABC
A(3,4)=-DRAT*S2P1*COS2F(C(4,3))
A(3,5)=-A(3,1)
A(4,1)=SIN2F(SAI,CAI)
A(4,2)=S1P1*COS2F(S2AI)
A(4,3)=DRAT*P2P1*COS2F(C(4,3))
A(4,4)=DRAT*ABC*S2P1*SINCF(C(4,2),A(4,1))
200 A(4,5)=A(4,1)
11 ENCONTINUE,5
IF(C(2,2).GE.1.0.OR.C(3,2).GE.1.0.OR.C(4,2).GE.1.0)GO TO 110
260 GO TO 370
110 CALLT MAT(-1,4,5,A,4,1,IDET)
284 IF(IDET.NE.0) GO TO 111
WRITE(6,15)

```

```

      STOP
111  DO 150 II=1,4
      IF(JJJ.EQ.4.AND.II.GE.2) GO TO 141
      IF(AIMAG(A(II,5)))120,130,140
120  B(II,1)=CABS(A(II,5))
      B(II,2)=RTD*(PI2+ATAN2(AIMAG(A(II,5)),REAL(A(II,5))))
      GO TO 150
130  B(II,1)=REAL(A(II,5))
      B(II,2)=0.1X(REAL(A(II,5)),0.1)
      GO TO 150
140  B(II,1)=CABS(A(II,5)) (DET)
      B(II,2)=RTD*ATAN2(AIMAG(A(II,5)),REAL(A(II,5)))
      GO TO 150
141  B(II,1)=0. (MATRIX IS SINGULAR)
      B(II,2)=0.
      B(II,3)=0.1,4
150  CONTINUE (A(II,5))
      ENCRS=A(1,5)**2
      B(1,3)=CABS(ENCRS)
      B(1,4)=AIP
      IF(JJJ.EQ.4) GO TO 284
      DO 281 I=2,4
      IF(C(I,2).LT:1:) GO TO 290 TO 994
      ENCRS=CZERO(C(I,2))
      B(I,4)=999999.**2)*(C(I,1)/C(1,1)-1)*A(I,11)/CAI
      B(I,1)=0. B(I,2)=B(I,3)*DRAT
      B(I,2)=0.
994  GO TO 300
290  B(I,4)=ARSIN(C(I,2))
      ENCRS=(A(I,5)**2)*(C(I,1)/C(1,1))*A(I,11)/CAI
991  IF(I.GE.3) ENCRS=ENCRS*DRAT
300  B(I,3)=CABS(ENCRS)
281  CONTINUE
284  CONTINUE
      AL1=B(3,3)
      SUBROUTINE MAT(IJCB,II,JJ,A,M,N,ICET)
      CD=EX A,B,DET,CZERO,CONST,5
      DIMENSION A(5,12)

```

```

      AL2=B(1,3)
      RETURN KPLX(10.,9.)
C : SOLVES REAL EQUATIONS
370 DO 380 I=1,4
      DO 380 J=1,5
      A(I,J)=CMPLX(REAL(A(I,J)),0.)
380 CONTINUE
      CALL MAT(-1,4,5,A,4,1,IDET)
      IF(IDET.NE.0) GO TO 390
      WRITE(6,15)
15  FORMAT('MATRIX IS SINGULAR')
      STOP
390 DO 371 I=1,4
      B(I,1)=REAL(A(I,5))
      B(I,2)=0.
371 CONTINUE
      B(I,4)=AIP
      B(I,3)=B(I,1)**2
40  DO 991 I=2,4
      IF(JJJ.GE.3.AND.I.GE.3) GO TO 994
      B(I,4)=ARSIN(C(I,2))
      B(I,3)=(B(I,1)**2)*(C(I,1)/C(1,1))*REAL(A(I,11))/CAI
      IF(I.GE.3) B(I,3)=B(I,3)*DRAT
      GO TO 991
994 B(I,4)=0.
      B(I,3)=0.
      B(I,1)=0.
991 CONTINUE=1,4
100 AL1=B(3,3)
      AL2=B(1,3)
110 RETURN
      END
SUBROUTINE MAT(IJOB,II,JJ,A,N,M,IDET)
      COMPLEX A,B,DET,CZERO,CONST,S
      DIMENSION A(5,12)
      DO 120 J=KPL1,H

```

```

EP=1.0E-15  GO TO 170
CZERO=CMPLX(0.,0.)
1  CIDET=1
DET=CMPLX(0.,0.)
DO 180 J=1,3,1
C=CABS(A(J,J))
JP1=J+1
DO 30 I=JP1,N
D=CABS(A(I,J))
IF(C-D)10,30,30
10  DET=-DET
DO 20 K=J,5
B=A(I,K)
A(I,K)=A(J,K)
20  A(J,K)=B
C=D
30  CONTINUE
IF(CABS(A(J,J))-EP)40,70,70
40  IDET=0
IF(IJOB)50,50,60
50  WRITE(6,140)
60  RETURN
70  DO 80 I=JP1,N
CONST=A(I,J)/A(J,J)
DO 80 K=JP1,5
80  A(I,K)=A(I,K)-CONST*A(J,K)
IF(CABS(A(N,N))-EP)40,90,90
90  DO 100 I=1,N
100 DET=DET*A(I,I)
IF(IJOB)110,110,60
110 DO 130 I=1,N
K=N-I+1
KP1=K+1
DO 130 L=5,5
S=0.
DO 120 J=KP1,N

```

```
      IF(KP1.GT.N) GO TO 130  
      S=S+A(K,J)*A(J,L)  
120  CONTINUE  
130  A(K,L)=(A(K,L)-S)/A(K,K)  
      IF(CABS(DET).GT.0.)IDET=1  
140  FORMAT('THE DETERMINANT OF THE SYSTEM EQUALS 0.')
```

RETURN
END

FILE

Seafloor Spreading in the Mozambique Channel

A. G. GREEN

School of Physics, University of Newcastle upon Tyne

Magnetic profiles across the Mozambique Channel limit any interpretation of the movement of Madagascar relative to the African mainland. Recent reconstructions of Gondwanaland are not compatible with this evidence.

RECENT attempts¹⁻³ to reconstruct the southern continents have emphasized the importance of the fit of Madagascar, and in the reconstruction Madagascar has been placed in three positions relative to the African mainland, namely, adjacent to Kenya-Tanzania^{1,2}, adjacent to Mozambique⁴, and in its present position³. Magnetic profiles presented in this article are difficult to reconcile with any of the above positions, but, rather, suggest that Madagascar has moved since the Permian from a position adjacent to southern Africa (Fig. 1).

Profiles and Seafloor Spreading

Profiles were digitized every 3 km and reduced by removing the International Geomagnetic Reference Field (IGRF). The profiles cross various parts of the Mozambique Channel (Fig. 2) from the northern end adjacent to the Somalia basin to the Mozambique Ridge in the south. Two east-west profiles (not shown) north of 8° S and west of 48° E show an extremely flat magnetic character consistent with that found by others⁵⁻⁷. Profiles between 8° S and 14° S are observed to be quite outside the regions defined by the volcanic islands of the Comores and Aldabra groups (Fig. 3). The large anomalies of profile 513 are directly related to the Comores. Most of the magnetic relief outside the islands is below 100 γ with wavelengths between 15 and 60 km. On the records of flight T220, at approximately 47° E, there is a large negative anomaly which indicates a reversely magnetized body for this latitude. The size of the anomaly suggests that the Aldabra islands may be connected by a submarine intrusion or extrusion to the volcanic north-eastern section of Madagascar and/or the Comores. The cross-over section of flights 513 and T225 (a in Fig. 3) produces good correlation between the profiles; the difference in amplitude is due to the different altitudes and flight directions of the two profiles. Magnetic profile 517 and the low altitude flight T225 show very little activity between Madagascar and the mainland, making it improbable that there has been a post-Cretaceous movement of the island across this part of the channel in an east-west direction. There is a marked change of character between lines 517 and 522; the latter, which crosses the Europa group of islands, contains anomalies of 120 γ (peak to trough) with widths \sim 30 km. Most of this magnetic activity can be attributed to the islands, which must be fundamentally volcanic. The change in magnetic relief between profile 522 and the three profiles between 25° S and 32° S is even more noticeable, the latter being typically oceanic in their amplitude and wavelength. Somewhere between the Europa group of islands and flight 540 there must be a drastic change in the age, if not the composition, of the underlying oceanic crust. It is conceivable that this group of islands is a dividing line.

The large amplitude anomalies of the three profiles in the south of the channel extend across the deep sediments (\sim 1.5 km) of the basin east of the Mozambique Ridge onto the Malagasy Ridge where the amplitudes become particularly high. The oceanic nature of this southern region has already been inferred from seismic refraction experiments⁸. Correlations of specific features of the profiles are indicated in Fig. 3, and the correspondence between lines 545 and 523 is particularly good to the west of 43° E. The high activity east of this meridian is directly related to the Malagasy Ridge and fracture zone. Comparison with the simulated anomalies using the time scale of Heirtzler⁹ and Helsley and Stiener¹⁰ modified by Tarling¹¹, using the preliminary results from the deep sea drilling project, yields several possible correlations but no unique match. A more detailed survey in this part of the channel may produce a unique correlation, otherwise it seems that the seafloor may be older than 140 m.y.

As there is no distinct central anomaly, or symmetry of pattern as is usually found on a spreading ridge that is active at present, it is not possible to define the axis of spreading from the magnetics alone. The bathymetry suggests that the most

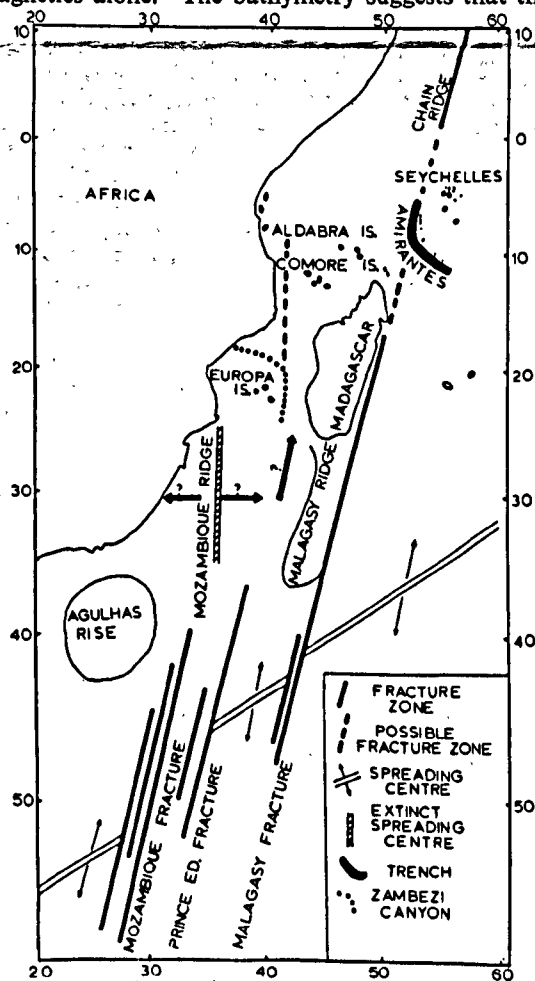


Fig. 1 Sketch of the principal features discussed in the text. The postulated movement of Madagascar is indicated by the wide arrows.

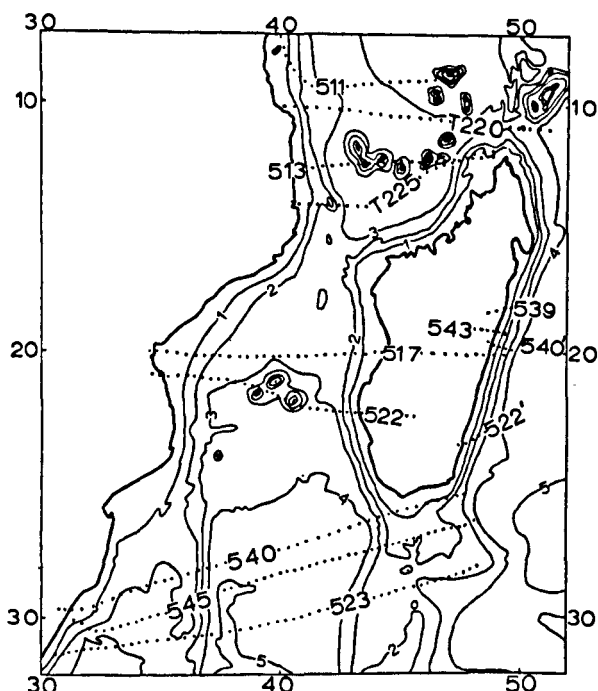


Fig. 2 Map of the Mozambique Channel showing the location of magnetic profiles. The depth contours are in 1,000 m intervals.

probable axis is the Mozambique Ridge (Natal Ridge)¹², which has very high and distinct magnetic anomalies (x in Fig. 3) coincident with its eastern scarp. Additional evidence that the ridge may have been a spreading centre comes from the high free air gravity value^{13,14} observed on one side of the ridge and the seismic activity¹⁵ and magnetic anomalies (A. G. G., in preparation) of its northern extension into the Mozambique-Malawi rift system. Apart from the lack of seismicity on the ridge and of a central positive anomaly, the "normal" heat flow¹⁶ on the ridge and the thick sediments on either side of it¹⁷ are evidence that it is not spreading at present. The sediments⁸ in the west basin are particularly thick, indicating that the ridge has acted as a block to the transportation of sediments from the African mainland. For some time in the past it would also have acted as a sedimentary source. The magnetization, or metamorphic effects on the underlying basalts, of these thick sediments may explain why only long wavelengths are observed to the west of the ridge.

In the section of tracks crossing the east coast of Madagascar (Fig. 4) a very large positive anomaly (500 to 1,000 γ) is coincident with the deeply dipping coastal scarp (Fig. 2) from at

least 18° S to 24° S. This observation would support the idea of a continuous "leaky" fault probably stretching from the South-West Indian Ocean Ridge to as far as the Amirantes ridge-trench system.

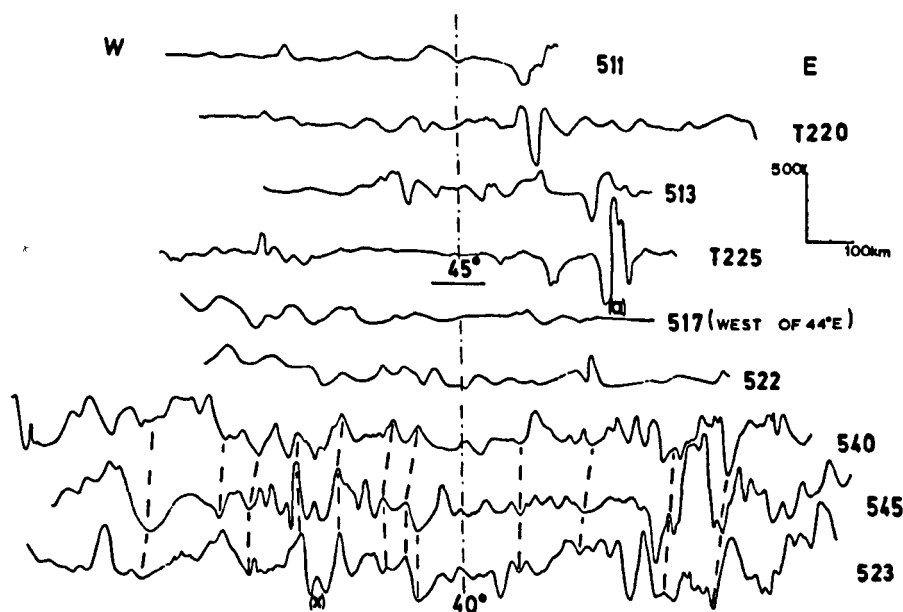
Geological Considerations

The most comprehensive comparisons of the geology of Madagascar and the African continent have been made by Du-Toit¹⁸ and Dixey¹⁹. Much new evidence from geological surveys and radioactive dating on the two land masses, together with the geophysical work in the channel, throws new light on the comparison. There is a significant correlation between the late Precambrian orogeny, which affected three-quarters of the island, and the massive Mozambique orogeny of the mainland. As well as the geological and geophysical similarities^{19,20}, the age determination of the island's orogeny²¹ falls within the 450 to 700 m.y. age for the Mozambique orogeny²². There is a particularly striking correspondence between the rare earths in the pegmatites of the island and those found in the southern parts of the mainland²³; enrichment of scandium is found only in Madagascar and Mozambique, and of lithium and beryllium only in Madagascar, Mozambique and South-West Africa. The pegmatites in the more northern parts of the Mozambique orogeny are particularly deficient in the latter two elements.

More specific correlations for the younger formations indicate a possible fit of the island to the mainland. The lower and middle Karroo of Southern Africa (27° S to 32° S) and South-West Madagascar has been compared by Flores⁴ in a detailed geological analysis. He demonstrates the very close resemblance between the Dwyka (tillites), Eccca (lacustrine and possibly marine deposits), Stormberg (continental deposits) series and the Sakoa, Sakema, Isalo (continental deposits) series of the island. Pallister²⁴ points to the similarities for this period of the "local basins of deposition with intra-formational erosion and unconformities" of Malawi and those indicated by geophysical work in western Madagascar²⁵. For both the island and the mainland to the south of the Limpopo, it is stressed that the Beaufort series, which would lie above the Eccca-Sakema series, is absent⁴. Although Du-Toit¹⁸ favoured a northern fit of Madagascar to the African continent he mentions the similarities for the pre-Stormberg of the island and the southern mainland.

The Upper Karroo is a period of differences rather than similarities between the two continental masses. In Madagascar there is the marine Jurassic, already compared with the coast of Tanzania^{1,18,19}, whereas the southern part of Africa is involved in the spectacular Stormberg volcanics. It is this period in time which is usually recognized as the initiation of

Fig. 3 Magnetic profiles observed across the Mozambique Channel. All profiles shown were obtained at altimeter heights from 8,000 to 11,000 feet except for profiles T225 and 513 which were flown at 4,000 feet and 15,000 feet respectively.



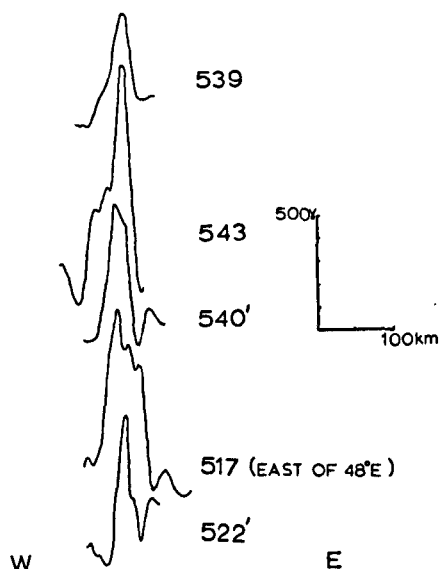


Fig. 4 Magnetic profiles observed across the east Madagascar coastal scarp. All profiles shown were obtained at altimeter heights from 9,000 feet to 11,300 feet.

the principal phase of continental break-up, and it is the most likely time for the drift of Madagascar from the mainland.

Movement of Madagascar

Before examining the possible movements of Madagascar relative to the mainland from the evidence presented, it is worthwhile to emphasize the difficulty that has been found in explaining the tectonics of the South-West Indian Ocean. The dominant feature of this region is the South-West Indian Ocean Ridge with its enormous north to north-east trending fracture zones¹². Although the spreading centre seems to be well defined seismically^{26,27}, the bathymetry and magnetic anomalies have defied reasonable interpretation; a recent survey near 44° S, 38° E shows that the only anomaly that can be correlated, the central anomaly, is unrelated to the prominent bathymetric trend²⁸. It is possible that the confusion associated with this section of the Indian Ocean Ridge system is caused by a change in spreading direction. McKenzie and Sclater²⁹ deduce that this part of the ridge has evolved since the Cretaceous from a large transform fault. Any interpretation of the movement of Madagascar must take this possible change of motion into account.

Geophysical work in the Mozambique Channel, which offers constraints on the movement of Madagascar since at least the Permian, can be summarized as follows. (1) The area north of 9° S (Somalia basin) is overlain by consolidated Jurassic sediments up to 500 km from the African coast, and by Cretaceous sediments almost as far away as the Seychelles⁷. This interpretation of the seismic refraction profiles is supported by an extremely flat magnetic character⁵⁻⁷. (2) Between 9° S and 21° S there is little magnetic relief outside the volcanic Comores and Aldabra islands and possible submarine connexions between them. Profile 517 and the low altitude profile T225 are particularly quiet. (3) There is a marked increase in the magnetic activity between 21° S and 22° S (flights 517 and 522), and most of this increase in activity can be attributed to the Europa group of islands. (4) There is a drastic change of character in the magnetic relief between 22° S and 25° S (between profiles 522 and 540); the region to the south has typical oceanic anomalies. (5) The anomalies correlated all trend in a near north-south direction, parallel to the Mozambique Ridge. (6) Seismic refraction work in the two basins on either side of the Mozambique Ridge indicates an oceanic crust⁸. (7) The Malagasy Ridge, which is intimately related to the Malagasy fracture zone, has very high

magnetic anomalies associated with it. (8) There is a very large linear magnetic anomaly coincident with the scarp of the East Madagascar coast, suggesting the extension of the above fracture zone. (9) Thick sediments, greatly influenced by turbidity currents¹⁷, are found in most parts of the channel. The sediments could be as old as Cretaceous³⁰.

Although these data place strong constraints on the movement of the island with respect to the mainland, it seems futile to attempt a detailed reconstruction of the two land masses until more details about the true pre-drift continental edge are obtained for southern Africa; this edge may be hidden beneath Jurassic-Cretaceous volcanics and younger sediments. Unfortunately, present palaeomagnetic knowledge cannot help because the pole determined from Upper Cretaceous rocks in Madagascar³¹ falls between the Lower Cretaceous and Lower Tertiary poles of the mainland (D. H. Tarling and E. A. Hailwood, personal communication).

From the geological correspondence and the geophysics of the channel, it is only possible to say that the south-west part of the island fitted against South Africa and Mozambique, with the northern tip of the island south of 21° S. I suggest that the Mozambique Ridge, with its landward extension into the Mozambique-Malawi rifts, was the probable spreading centre from late Triassic until late Cretaceous-early Tertiary. The early stage of drifting is inferred, first, from the absence of volcanic materials on Madagascar, which were abundant on the mainland from Jurassic to at least Mid-Cretaceous, and second, from the marine Jurassic sediments on the west coast of the island and the southern tip of the mainland³²; any evidence of this marine incursion on the south-east part of the mainland has been covered by the younger volcanic and sedimentary sequences. The correlation of the Madagascar marine Jurassic fauna with that of the Tanzania coast only implies an intermittent sea connexion between the two areas and not that they were once adjacent.

In the Cretaceous-early Tertiary the whole region was affected by the development of the principal Indian Ocean Ridge system²⁹. In the South-West Indian Ocean, massive faults developed to accommodate the changing stress pattern, and their evolution was possibly controlled to a large extent by the thick crust of the surrounding continental masses. But the differential spreading (faster to the east) due to the changing spreading direction, which may still be a feature of this region, may have pushed the Madagascar and Seychelles sub-continents north relative to the African mainland. East of Madagascar this difference in spreading was taken up by the right lateral Prince Edward and Mozambique fracture zones to the south, and the ridge-like feature discussed by Heirtzler and Burroughs³³ to the north. The present seismicity of the Mozambique channel may indicate a continuous fault¹⁵, of which the Zambezi canyon could be part and the Comores and Aldabra islands compressive features. The differential spreading, which caused the northward movement of the Seychelles relative to Madagascar, would be taken up by the Malagasy fracture zone, and by its extension along the East Madagascar coastal scarp and possibly farther north along the line of topographic features discussed by Fisher *et al.*⁵. The Amirantes may have been a temporary subduction zone during the early phase of the development of the South-West Indian Ocean Ridge and its fracture zones. The present activity of the Mozambique Channel and the fracture zones indicates that the northward movement of Madagascar relative to Africa may still be in progress. Clearly the chief problem remaining is the timing of the various events, particularly the formation of the Amirantes, but the present data are adequate to define the general evolution of the region.

I thank Dr D. H. Tarling for his critical reading of the manuscript and for pointing out several important references, and Drs B. W. Darracott, S. A. Hall and B. Rosen for helpful discussion. I also thank Dr H. Stockard of the US Naval Oceanographic Office for making the magnetic data available

to Dr R. W. Girdler. The work was financed by the Natural Environment Research Council.

Received January 20; revised March 1, 1972.

- ¹ Smith, A. G., and Hallam, A., *Nature*, **225**, 139 (1970).
- ² Dietz, R. S., and Holden, J. L., *J. Geophys. Res.*, **75**, 4939 (1970).
- ³ Tarling, D. H., *Nature*, **229**, 17 (1971).
- ⁴ Flores, G., *Trans. Geol. Soc. South Africa*, **73**, 1 (1970).
- ⁵ Fisher, L. R., Engel, G. G., and Hilde, T. W. C., *Deep Sea Res.*, **15**, 521 (1968).
- ⁶ Bunce, E. T., Langseth, M. G., Chase, R. L., and Ewing, M., *J. Geophys. Res.*, **72**, 2547 (1967).
- ⁷ Francis, T. J. G., Davies, D., and Hill, M. N., *Phil. Trans. Roy. Soc.*, **A**, 259, 240 (1966).
- ⁸ Ludwig, W. J., Nafe, J. E., Simpson, E. S. W., and Sacks, S., *J. Geophys. Res.*, **73**, 3707 (1968).
- ⁹ Heirtzler, J. R., Dickson, G. O., Herron, E. M., Pitman, W. C., and Le Pichon, X., *J. Geophys. Res.*, **73**, 2119 (1968).
- ¹⁰ Helsley, C. E., and Stiener, M. B., *Earth Planet. Sci. Lett.*, **5**, 325 (1969).
- ¹¹ Tarling, D. H., *Principles and Applications of Palaeomagnetism*, 164 (Chapman and Hall, London, 1972).
- ¹² Heezen, B. C., and Tharp, M., *Physiographic Diagram of the Indian Ocean* (Geol. Soc. Amer., New York, 1964).
- ¹³ Venning-Meinesz, F. A., *Publ. Netherlands Geodet. Comm.*, **4**, 233 (1948).
- ¹⁴ Le Pichon, X., and Talwani, M., *Deep Sea Res.*, **16**, 263 (1969).
- ¹⁵ Fairhead, J. D., and Girdler, R. W., *Geophys. J. Roy. Astron. Soc.*, **24**, 271 (1971).
- ¹⁶ Langseth, M. G., and Taylor, P. T., *J. Geophys. Res.*, **72**, 6249 (1967).
- ¹⁷ Ewing, M., Eittreim, S., Truchan, M., and Ewing, J., *Deep Sea Res.*, **16**, 231 (1969).
- ¹⁸ Du-Toit, A. L., *Our Wandering Continents* (Oliver and Boyd, Edinburgh and London, 1937).
- ¹⁹ Dixey, F., *Quart. J. Geol.*, London, **116**, 225 (1960).
- ²⁰ Besairie, J. W., *La Geologie de Madagascar* (Serv. Geol. Tananarive, 1957).
- ²¹ Delbos, L., *CR Acad. Sci. Paris*, **258**, 1853 (1964).
- ²² Cahen, L., and Snelling, N. J., *The Geochronology of Equatorial Africa* (North-Holland, Amsterdam, 1966).
- ²³ Von Knorring, O., in *African Magmatism and Tectonics* (edit. by Clifford, T. N., and Gass, I. G.), 178 (Oliver and Boyd, 1970).
- ²⁴ Pallister, J. W., *Report for UNESCO Tectonic Map of Africa* (E. African section, 1968).
- ²⁵ Cliquet, P. L., *CCTA Reg. Comm. Geol. Second Meeting, CR*, 199 (1957).
- ²⁶ Stover, C. W., *J. Geophys. Res.*, **71**, 2575 (1966).
- ²⁷ Banghar, A. R., and Sykes, L. R., *J. Geophys. Res.*, **75**, 632 (1969).
- ²⁸ Bergh, H. W., *J. Geophys. Res.*, **76**, 6276 (1971).
- ²⁹ McKenzie, D. P., and Sclater, J. G., *Geophys. J. Roy. Astron. Soc.*, **24**, 437 (1971).
- ³⁰ Saito, T., in *The Sea*, **4**, Part 1 (Wiley, New York, 1971).
- ³¹ Andriamirado, R., and Roche, R., *CR Acad. Sci. Paris*, **269**, 16 (1969).
- ³² Dingle, R. V., and Klinger, H. R., *Nature*, **232**, 37 (1971).
- ³³ Heirtzler, J. R., and Burroughs, R. H., *Science*, **174**, 488 (1971).

Magnetic Profile Analysis

A. G. Green

(Received 1972 August 5)*

Summary

The statistical models approach which Spector & Grant applied so successfully to contoured data is described for single profile analysis. The energy spectrum is obtained by simply smoothing the periodogram of the data. Other advantages of the data in the wavenumber domain are described.

1. Introduction

In recent years large regions of the world have been covered by single aeromagnetic profiles (Project Magnet). From these profiles single isolated anomalies may be interpreted by the usual modelling techniques using the geology and the magnetic field vector of the underlying bodies as constraints. This method is practically useless for analysing very large amounts of profile data contaminated with 'noise' which may cross regions for which the geology and magnetic field vector are only poorly known. The approach suggested here is the profile version of the 'Statistical Models Method' which Spector & Grant (Spector 1968; Spector & Grant 1970) applied to contoured data. This is a direct method of finding average depths to ensembles of bodies using the data in the wavenumber domain. Other advantages of using this representation of the data are also described.

2. Profile spectra

(i) *Spectra of a profile crossing a single anomaly*

Much of the versatility of the prism model discussed by Spector & Grant (1970) applies to the 'two-dimensional prism' (Fig. 1) and will, therefore, be used here as the base model for profile analysis. A rectangular co-ordinate system is assumed (Fig. 1), where the x_1 axis is taken to be coincident with the flight line and is at an angle θ with respect to geographic north (θ is positive when measured clockwise from north) and the prism extends to \pm infinity in the x_2 direction. Using mathematics very similar to that described by Bhattacharyya (1966), it can be shown that the energy spectrum of the magnitude of the magnetic field due to the prism shown in Fig. 1 is given by,

$$E(v) = 4\pi^2 \cdot K^2 \cdot R_T \cdot R_K \cdot S \cdot C \cdot P \quad (2.1)$$

* Received in original form 1972 May 31.

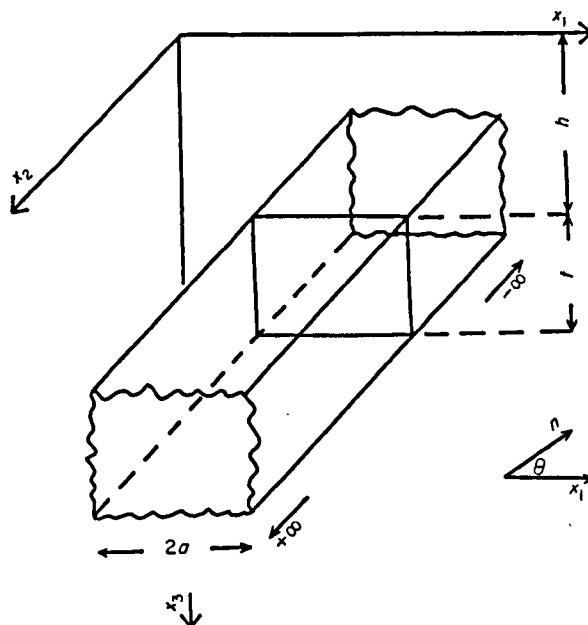


FIG. 1. Diagram of 'two-dimensional' prism used as the base model.

where

$K/2a$ = magnetic moment/unit volume

$$R_T = \sin^2 I_T + \cos^2 (D_T - \theta) \cdot \cos^2 I_T \quad (2.2)$$

I_T is the inclination of the geomagnetic field vector,

D_T is the declination of the geomagnetic field vector,

$$R_K = \sin^2 I_K + \cos^2 (D_K - \theta) \cdot \cos^2 I_K \quad (2.3)$$

I_K is the inclination of the magnetic moment vector,

D_K is the declination of the magnetic moment vector,

$$S = \left(\frac{\sin(va)}{va} \right)^2 \quad (2.4)$$

v is the angular wavenumber equivalent of the space variable x_1 and $2a$ is the width of the prism,

$$C = (1 - \exp(-tv))^2 \quad (2.5)$$

t is the thickness of the body,

$$P = \exp(-2hv) \quad (2.6)$$

h is the depth to the top of the body.

It is clear that the terms S , C , and P contain all the information on the width, thickness and depth respectively.

(ii) Spectrum of a profile crossing a sequence of bodies

The above equations apply only to a single anomaly; to analyse a length of profile which may contain many anomalies, a statistical approach is required. The ensemble approach seems most suitable (Spector 1968; Spector & Grant 1970).

To relate the measurable quantities to those defined by the ensemble theory we use the fundamental postulate that the expectation (most probable value) and the ensemble average of the energy spectrum are equal. We next assume that the profile contains contributions from a single ensemble defined by the parameters $K, D_T, D_K, I_T, I_K, a, t, h$ which are independent of each other and rectangularly distributed in the ranges: $(0 \text{ to } 2\bar{K}), (\bar{D}_T \pm \Delta D_T), (\bar{D}_K \pm \Delta D_K), (\bar{I}_T \pm \Delta I_T), (\bar{I}_K \pm \Delta I_K), (0 \text{ to } 2\bar{a}), (0 \text{ to } 2\bar{t}), (\bar{h} \pm \Delta h)$. The case for the presence of more than one ensemble is discussed later. The ensemble average of the energy spectrum is then given by

$$\langle E(v) \rangle = \langle 4\pi^2 \bar{K}^2 \rangle \langle R_T \rangle \langle R_K \rangle \langle S \rangle \langle C \rangle \langle P \rangle \quad (2.7)$$

where $\langle \rangle$ denotes ensemble average. To make the whole expression additive we simply take the logarithm to give

$$\ln \langle E(v) \rangle = \ln \langle 4\pi^2 \bar{K}^2 \rangle + \ln \langle R_T \rangle + \ln \langle R_K \rangle + \ln \langle S \rangle + \ln \langle C \rangle + \ln \langle P \rangle. \quad (2.8)$$

It is clear that only the last three terms affect the gradient of the power spectrum vs. wavenumber curve. Thus, if an estimate for the average width of the bodies can be obtained, the final gradient (width factor subtracted) will only depend on the average depths and thicknesses of the bodies. A similar argument applies to equation (2.1) for single anomaly analysis. All that follows has a counterpart in the interpretation of single anomalies.

3. Evaluation and discussion of terms related to profile spectra

(i) Geomagnetic field vector term $\langle R_T \rangle$

$$\langle R_T \rangle = \frac{1}{4\Delta I_T \Delta D_T} \int_{I_T - \Delta I_T}^{I_T + \Delta I_T} \int_{D_T - \Delta D_T}^{D_T + \Delta D_T} R_T(I_T, D_T) dD_T dI_T.$$

It follows that

$$\langle R_T \rangle \simeq R_T(\bar{I}_T, \bar{D}_T) \text{ provided } \left. \begin{array}{l} \Delta I_T < 20^\circ \\ \Delta D_T < 20^\circ \end{array} \right\} \quad (3.1)$$

The inclination and declination of the geomagnetic field vector will vary according to the direction and length of profile, but the conditions (3.1) still allow long sections of profile to be analysed by this method.

(ii) Magnetic moment vector term $\langle R_K \rangle$

$$\langle R_K \rangle = \frac{1}{4\Delta I_K \Delta D_K} \int_{I_K - \Delta I_K}^{I_K + \Delta I_K} \int_{D_K - \Delta D_K}^{D_K + \Delta D_K} R_K(I_K, D_K) dD_K dI_K$$

Again it follows

$$\langle R_K \rangle \simeq R_K(\bar{I}_K, \bar{D}_K) \text{ provided } \left. \begin{array}{l} \Delta I_K < 20^\circ \\ \Delta D_K < 20^\circ \end{array} \right\} \quad (3.2)$$

For the induced component of magnetization dominant this term may be set equal to $\langle R_T(I_T, D_T) \rangle$.

If the remanent component is dominant, as is usual, the $R_K(I_K, D_K)$ term may be a highly fluctuating quantity over certain adjacent lengths of profile; the sections of profile for which condition (3.2) may be applicable must then be analysed separately. If (I_K, D_K) are not known for the particular sequence of rocks crossed then either induced magnetization must be assumed or much better an estimate may be obtained

by using the (I_K, D_K) values from nearest neighbour rocks of the same geological age, for which palaeomagnetic results are available. It is emphasized that \bar{R}_K and \bar{R}_T are only needed if an estimate of \bar{K} is required, these factors do not affect the thickness and depth estimates.

(iii) *Width of bodies term* $\langle S \rangle$

$$\langle S \rangle = \frac{1}{2\bar{a}} \int_0^{2\bar{a}} \left(\frac{\sin(va)}{va} \right)^2 da = - \left(\frac{\sin 2v\bar{a}}{2v\bar{a}} \right)^2 + \frac{1}{\bar{a}} \int_0^{2\bar{a}} \frac{\sin 2va}{2va} da \quad (3.3)$$

$$= - \left(\frac{\sin 2v\bar{a}}{2v\bar{a}} \right)^2 + \frac{1}{2v\bar{a}} \int_0^{4v\bar{a}} \frac{\sin Z}{Z} dZ. \quad (3.4)$$

where $Z = 2v\bar{a}$

The second term in (3.4) may be conveniently evaluated numerically using Chebyshev polynomials (Burlirsh 1967). Estimates of the average width $2\bar{a}$ may be obtained by finding the distance between the zeros of the second derivative of the data, which is again conveniently obtained by use of the wavenumber domain. (See Practical Procedure). For induced magnetization only the zeros of the 2nd derivative curve are often found to coincide with the sides of the bodies (see also Vacquier *et al.* 1951; Bhattacharyya 1965) and for remanent magnetization dominant, the distance between the zeros of the second derivative curve was still found to be a fair estimator of the average widths of bodies (see also theoretical models of Bhattacharyya 1965).

(iv) *Thickness of bodies term* $\langle C \rangle$

$$\langle C \rangle = \frac{1}{2i} \int_0^{2i} [1 - \exp(-tv)]^2 dt = 1 - \frac{[3 - \exp(-2iv)][1 - \exp(-2iv)]}{4iv} \quad (3.5)$$

This term is identical to the equivalent derived by Spector & Grant (1970). For sufficient length of profile this term combined with the average depth term (below) has the effect of producing a broad peak in the energy spectrum V wavenumber curve.

(v) *Depth to bodies term* $\langle P \rangle$

$$\langle P \rangle = \frac{1}{2\Delta h} \int_{\bar{h}-\Delta h}^{\bar{h}+\Delta h} \exp(-2hv) dh = \frac{\exp(-2\bar{h}v) \sinh(2v\Delta h)}{4v\Delta h} \quad (3.6)$$

$$\simeq \exp(-2\bar{h}v) \text{ for } \left. \begin{array}{l} \Delta h < \bar{h}/2 \\ v < 1/\bar{h} \end{array} \right\}. \quad (3.7)$$

Again this term is identical to the equivalent expression discussed by Spector & Grant (1970). It is found to be the dominating quantity in the spectrum.

A similar depth dependance for profile spectra was obtained by Treitel, Clement & Kaul (1971) who used line sources for their models. It must be emphasized that these authors erroneously used the gravity potential rather than the magnetic potential in their analysis; for the energy spectrum equation to be generally applicable to magnetic data they would need to have multiplied the complex spectrum by the Fourier transform of the $\partial/\partial s$ operator, where ∂s is an element of length in the direction of the magnetic moment vector. This does not, however, alter the depth dependant term.

4. Practical procedure

There are two ways to the energy spectrum of real data:

- (i) Cosine transform the modified autocorrelation function (Blackman & Tukey 1958).
- (ii) Smooth the modified periodogram (Jones 1965).

With the rediscovery of the Fast Fourier transform algorithm (Cooley & Tukey 1965, see also special issue of I.E.E.E. (A.U.—15) 1967) the latter route is by far the most efficient and offers several additional advantages for magnetic profile analysis. First it allows the data, now in wavenumber form (raw Fourier coefficients) to be conveniently filtered. The application of the conventional filters (continuation, derivatives and cut-off filters) and the design and application of more specialized filters (Spector 1968) are faster and more accurate in the wavenumber domain (Black & Schollar 1969). Secondly the periodogram of separate profiles which cross the same ensemble of bodies may be averaged to obtain a single, more stable estimate of the energy spectrum (Welsh 1967; Tukey 1961). The number of degrees of freedom (Blackman & Tukey 1958) for the spectral estimate will then increase from 2 for a single profile spectrum (unsmoothed) to $2n$ for a spectrum that is the result of averaging over n separate profile spectra (unsmoothed). Lastly, the problem of smoothing (stabilizing) a single profile spectrum or an unstable averaged profile spectrum is more conveniently solved in the wavenumber domain (Black 1970). It is easier to choose a satisfactory smoothing function to be applied to the periodogram than the equivalent problem of choosing the lag window to be applied to the autocorrelation function, (see paper by Treital, Clements & Kaul 1971 who obtained their spectra via the modified autocorrelation function).

For a maximum use of profile data, the following course of action is suggested:

(i) Digitize the data at an interval smaller than the smallest wavelength present; this will depend on the height of the flight above the source and the type of geology crossed. Remove the regional gradient (core effect).

(ii) Fast Fourier transform the digitized data. The shortest wavelength (corresponding to the Nyquist wavenumber) will equal twice the digitizing interval and the longest wavelength will equal the length of data plus the length of one interval. The Fourier coefficients may then be stored, and any of the following operations performed:

(a) Upward or downward continuation—multiply the m th coefficient by

$$\exp\left(-\frac{2\pi mH}{T}\right)$$

where T is the length of profile and H is the change in height (positive H —upwards). (b) n th vertical derivative—multiply the m th coefficient by $(-2\pi m/T)^n$. (c) Low pass filter—simply truncate the Fourier coefficients at the desired wavenumber (e.g. Caner 1969).

Operations (a) and (b) are easily proved by taking the anomaly field vector as independent of the x_2 direction and using equations derived by Bhattacharyya (1965).

The filtered data or second derivative curve may then be rapidly obtained by passing the filtered coefficients through the Fast Fourier transform with the exponent reversed (see special issue I.E.E.E. (AU—15) 1967).

(iii) The raw Fourier coefficients may be convolved with a $(-\frac{1}{4}, \frac{1}{4}, -\frac{1}{4})$ filter to cut down leakage in the resultant energy spectrum (leakage from intermediate spectral estimates—see paper by Bingham, Godfrey & Tukey (1967) in the special issue of I.E.E.E. (AU—15)). This filter has the effect of reducing the energy spectrum by $\frac{3}{8}$ so the final spectrum must be compensated for this (Black 1970). The periodogram

(modified) is then calculated by squaring and adding the real and imaginary modified coefficients. The periodogram can then be smoothed to give a better estimate of the energy spectrum by averaging over different profiles and/or convolving with an appropriate set of filter coefficients. In all the examples studied by the author, a triangular filter set was found adequate to give the required stability (Cooley, Lewis & Welsh 1967). Sharp peaks in the spectrum, which may indicate a periodicity in the underlying structure, must be set equal to the adjacent energy values before smoothing, and replaced subsequently; this process has been termed post-whitening by Black (1970).

(iv) Using the average width of the bodies, which may be obtained by use of the second derivative curve, after any necessary smoothing of the data, the width factor (3.4) may be calculated and subtracted from the energy spectrum. For reliable estimates, the second derivative should be used in conjunction with both the original profile and a series of upward continued versions of the profile; this is especially important when the profile contains contributions from more than one ensemble of bodies.

(v) The energy spectrum curve will now be ready for depth estimates. Appreciable changes in the dominant gradient will indicate the presence of more than a single

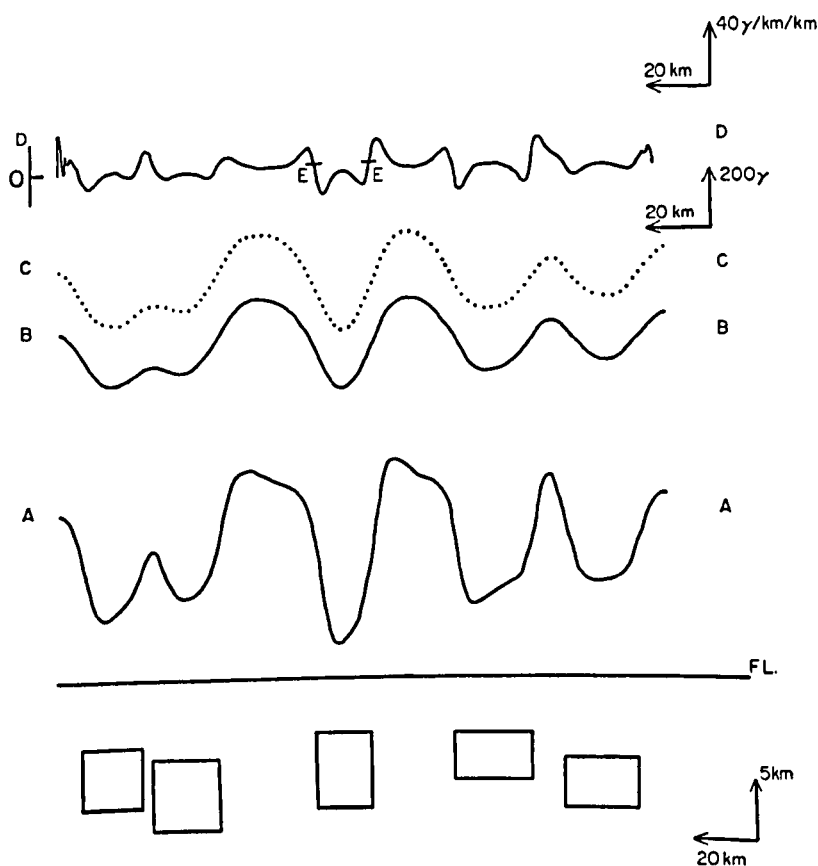


FIG. 2. A set of bodies from a single ensemble shown with (i) computed anomaly curve (A-A), (ii) 5 km upward continued curve using the wavenumber domain calculation (B-B), (iii) Analytically upward continued curve (C-C), (iv) Second derivative curve (D-D). F.L. denotes flight line.

ensemble of bodies and the linear parts of the curve must be analysed separately (Spector & Grant 1970). The average depth is given by

$$\text{gradient} = -2 \times \bar{h} \quad (4.1)$$

The effect of \bar{t} on the gradient of the spectrum after the first few harmonics past the peak is negligible, so that the linear parts of the curve will only depend on \bar{h} .

(vi) The presence of broad peaks may indicate that certain ensembles are depth limited with respect to the length of profile. These particular peaks are defined by

$$\frac{\partial}{\partial v} (\ln \langle C \rangle + \ln \langle P \rangle) = 0$$

or

$$-2\bar{h} - \frac{2}{v} + \frac{4\bar{t}[1 - \exp(-2\bar{t}v)]^2}{4\bar{t}v - [3 - \exp(-2\bar{t}v)][1 - \exp(-2\bar{t}v)]} = 0. \quad (4.2)$$

By substituting into equation (4.2) a value of \bar{h} obtained from the gradient of the curve and the value of v at the peak, it is possible to obtain an estimate of \bar{t} by iteration. Unfortunately, very small errors in \bar{h} will produce a drastically incorrect value of \bar{t} .

There is also the problem of discriminating between peaks due to the above effect and 'non-significant' peaks that are bound to occur when using a limited amount of data. Instead of using equation (4.2) to give thickness estimates it will often be advisable to just say whether or not the bodies are depth limited with respect to the length of data used.

5. Examples

To test some of the ideas discussed, data were simulated using a two dimensional magnetic anomaly computer program (Talwani & Heirtzler 1964). An example of a distribution of bodies, which are members of a single ensemble, is shown in Fig. 2

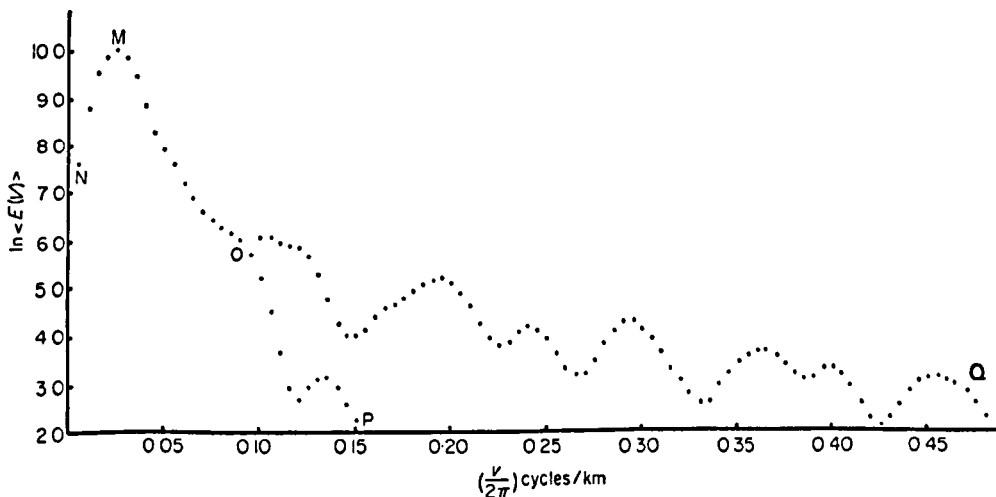


FIG. 3. Logarithm energy spectra smoothed with a triangle filter set $(\frac{1}{16}, \frac{1}{8}, \frac{1}{4}, \frac{1}{2}, \frac{3}{4}, \frac{1}{2}, \frac{1}{4}, \frac{1}{8}, \frac{1}{16})$. The curve NMOP is the significant part of the energy spectrum obtained for the single ensemble of bodies shown in Fig. 2 and the curve NMOQ is the energy spectrum for the two ensembles of bodies shown in Fig. 4. The depth estimate for a particular ensemble was obtained using the slope of the spectrum above the level corresponding to 0.1 per cent of the maximum value of the energy in that ensemble.

with the resultant anomaly curve (line A-A). Also shown are curves continued 5 km upwards by,

- (i) the method described using data in the wavenumber domain (line B-B),
- (ii) recalculation of anomaly field at the new height using the two-dimensional anomaly program (line C-C).

It is clear that the method described here produces a rapid and extremely good representation of the continued field (the two curves are identical on the scale shown, except at the last three points). Also shown in the figure, is the second derivative curve D-D and it is observed that the cross over points with the $y = 0$ axis (example marked E-E) give a fair estimate of the width of the body. These excellent results are to be compared with those which would be obtained by convolving the data with a set of filter coefficients which approximates the above operation (Henderson & Zietz 1949).

The energy spectrum, with the width factor (equation (3.4)) removed is shown in Fig. 3 by the curve NMOP. The peak at M indicates that the ensemble of bodies is

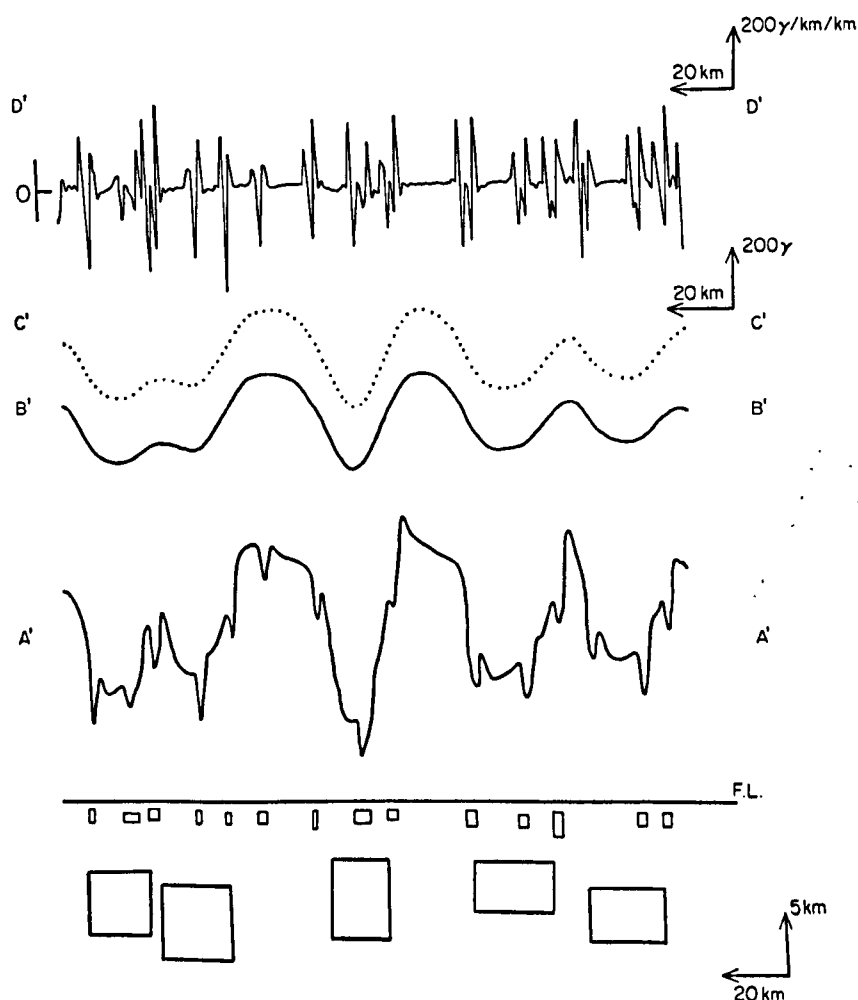


FIG. 4. Two sets of bodies from separate and distinct ensembles. The lower ensemble of bodies corresponds to those shown in Fig. 2. All the curves shown are as described for Fig. 2.

depth limited and the gradient of the curve, which is linear in its decay as predicted, gives a depth by least squares fit of 5.4 km which is to be compared with the true average depth of 5.6 km below the flight line. A wide variety of bodies, which extend to the limits of the conditions set by the ranges of the rectangular distributions of Section 2(ii) were tested with equal success.

In Fig. 4 a second distribution of bodies belonging to a different ensemble is superimposed on the previously defined pattern (compare A'-A' of Fig. 4 with A-A of Fig. 2).

This new curve A'-A' is also continued upward 5 km to give the curve B'-B' in Fig. 4 and this is compared to C'-C', which is the analytically upward continued curve. The two curves B'-B' and C'-C' are identical to the curve C-C of Fig. 2 (except at the end points), demonstrating that only the effect of the broad deep-seated anomalies is observed at the greater height, there seems to be no distortion (on the scale shown at least) for this configuration of bodies from the field of the shallow bodies when using this method of continuation. Again the second derivative curve D'-D' is shown, but now it represents the effect of both sets of bodies. To separate the effect of the deep bodies from the shallow ones, the original anomaly curve was smoothed until only the long wavelength anomalies remained (representing the deeper ensemble of bodies). The second derivative curve calculated for this smoothed anomaly curve, which was found to be very similar to the second derivative curve D-D of Fig. 2, was then used to obtain the average half width for the deeper ensemble of bodies. By comparing the second derivative of this smoothed anomaly curve with the second derivative curve D'-D' it was then possible to distinguish the parts of the curve D'-D' which were attributable to the shallow ensemble of bodies and thus, an estimate of the average half width of the shallow ensemble of bodies was obtained. As the width factor (3.4) is not very sensitive to the value of average half width \bar{a} it was only necessary to obtain the average widths to within 30 or 40 per cent of their true value, and generally this second derivative method produced values well within these limits. If the widths were obtained to the above accuracy then the depth estimates were found to be within 15 per cent of the true value. Without taking the width into account, overestimates in excess of 30 per cent were obtained.

The energy spectrum for this double ensemble case is shown in Fig. 3 by the curve N M O Q. The smaller width of the second ensemble has been used in the width factor (3.4) subtracted from this curve, past the point marked O; this seemed reasonable when considering the domination of the second ensemble past that point. It is clear that the energy spectrum curve marked N M O is not affected at all by the introduction of the second ensemble and, therefore, this section may be used to obtain depth estimates for the first ensemble. The linear section of curve M O yields an average depth of 6.2 km (true average depth 5.6 km) for the first ensemble and the linear trend between O-Q yields an average depth of 0.54 km (true average depth 0.6 km) for the second ensemble of bodies. An indication of the thickness of the second ensemble is obscured by the interaction of the two ensembles where the dominant peak would occur.

Conclusion

With the data in the wavenumber domain, average widths and depths are rapidly estimated for lengths of profile containing a large number of anomalies caused by magnetic bodies belonging to one or more ensembles. If a large number of profiles which cross the same sequence of rocks are available, it may be possible by averaging over profiles to obtain a spectrum which also yields reliable thickness estimates. The wavenumber domain is also an efficient route to most of the filter operations that are commonly applied to magnetic data. A computer program has been written which will obtain the following information: (i) upward or downward continued curve;

(ii) n th vertical derivative curve; (iii) energy spectrum with three different sets of filter coefficients applied; (iv) a least squares fit of a straight line to the linear parts of the curve, all in under 25 s.

The most serious source of error, for real data, is the assumption of two dimensionality, but even the usual modelling techniques use this assumption.

Acknowledgments

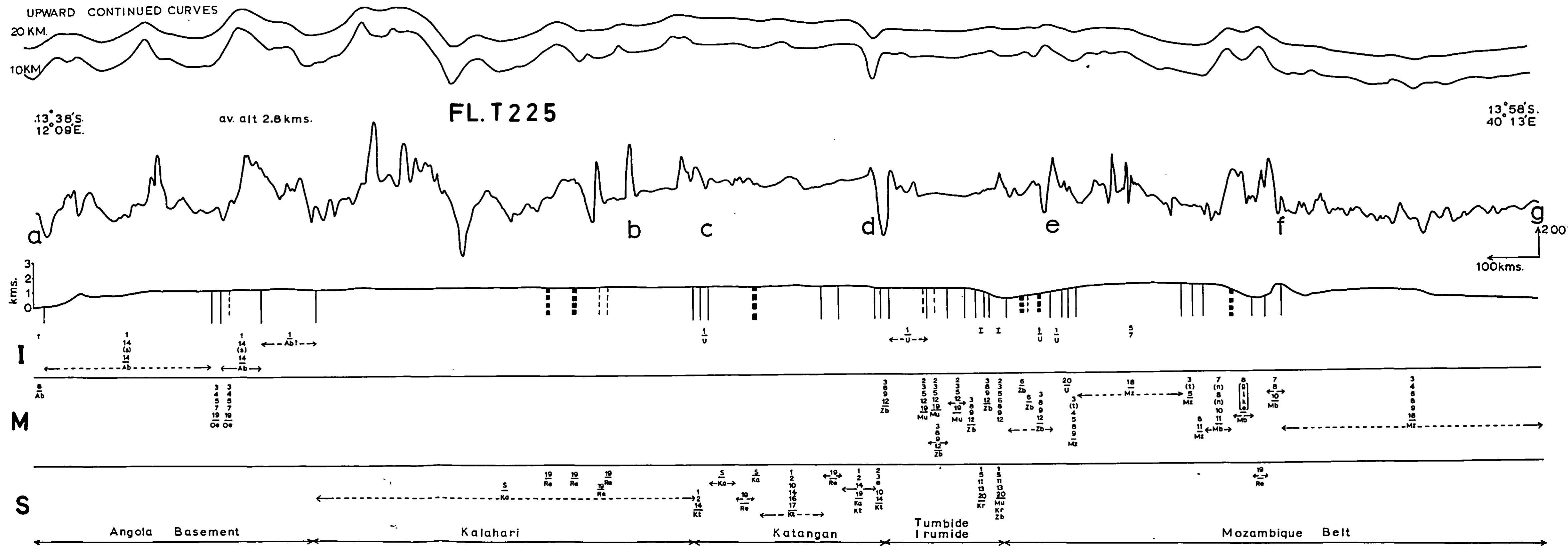
I would like to thank Dr F. Lowes for his critical review of the first draft of this manuscript. This work was supported by the Natural Environment Research Council.

*Department of Geophysics and Planetary Physics,
School of Physics,
The University,
Newcastle-upon-Tyne NE1 YRU.*

References

- Bhattacharyya, B. H., 1965. Two-dimensional harmonic analysis as a tool for magnetic interpretation, *Geophysics*, **30**, 829–857.
- Bhattacharyya, B. H., 1966. Continuous spectrum of the total magnetic field anomaly due to a rectangular prismatic body, *Geophysics*, **31**, 97–121.
- Bingham, C., Godfrey, M. D. & Tukey, J. W., 1967. Modern techniques in power spectrum estimation, *I.E.E.E. Trans. Audio Electroacoust.*, AU-15, 56–66.
- Black, D. I., 1970. Lunar and solar magnetic variations at Abinger: their detection and estimation by spectral analysis via Fourier transforms, *Phil. Trans. R. Soc. Lond. A*, **268**, 233–263.
- Black, D. I. & Schollar, I., 1969. Spatial filtering in the wave vector domain, *Geophysics*, **34**, 916–923.
- Blackman, R. B. & Tukey, J. W., 1958. *The measurement of power spectra*, Dover Publications Inc., N.Y.
- Burlisch, R., 1967. Numerical calculations of sine, cosine and Fresnel integrals, *Num. Math.*, **9**, 380–385.
- Caner, B., 1969. Long aeromagnetic profiles and crustal structure in Western Canada, *Earth Planet. Sci. Lett.*, **7**, 3–11.
- Cooley, J. W. & Tukey, J. W., 1965. An algorithm for the machine calculation of complex Fourier series, *Maths. Comput.*, **19**, 297.
- Cooley, J. W., Lewis, P. A. W. & Welsh, P. D., 1967. The fast Fourier transform and its applications, *I.B.M. Research Report*, RC-1743.
- Henderson, R. G. & Zietz, I., 1949. Computation of second vertical derivatives of geomagnetic fields, *Geophysics*, **14**, 508.
- I.E.E.E. Transactions. Acoust. Electroacoust.*, Au-15, 1967. Special issue on the Fast Fourier transform and its applications.
- Jones, R. H., 1965. A reappraisal of the periodogram in spectral analysis, *Technometrics*, **7**, 531–542.
- Spector, A., 1968. *Spectral analysis of aeromagnetic data*, Ph.D. Thesis. University of Toronto, Toronto, Ontario, Canada.
- Spector, A. & Grant, F. S., 1970. Statistical models for interpreting aeromagnetic data, *Geophysics*, **35**, 293–302.
- Tukey, J. W., 1961. Discussion emphasizing the connection between the analysis of variance and spectrum analysis, *Technometrics*, **3**, 191–219.
- Talwani, M. & Heirtzler, J. R., 1964. Computation of magnetic anomalies caused by two-dimensional structures of any shape in *Computers in the mineral industry*, ed. G. A. Parks, Stanford University.

- Trietel, S., Clement, W. G. & Kaul, R. K., 1971. The spectral determination of depths to buried magnetic basement rocks, *Geophys. J. R. astr. Soc.*, **24**, 415-428.
- Vacquier, V., Steenland, N. C., Henderson, R. G. & Zietz, I., 1951. Interpretation of aeromagnetic maps, *Geol. Soc. Am. Mem.*, **49**, 151.
- Welsh, P. D., 1967. The use of the Fast Fourier transform for estimation of spectra: A method based on time averaging over short modified periodograms, *I.E.E.E., Trans. Audio Electroacoust.*, AU-15, 70-75.



UPWARD CONTINUED CURVES

20KM

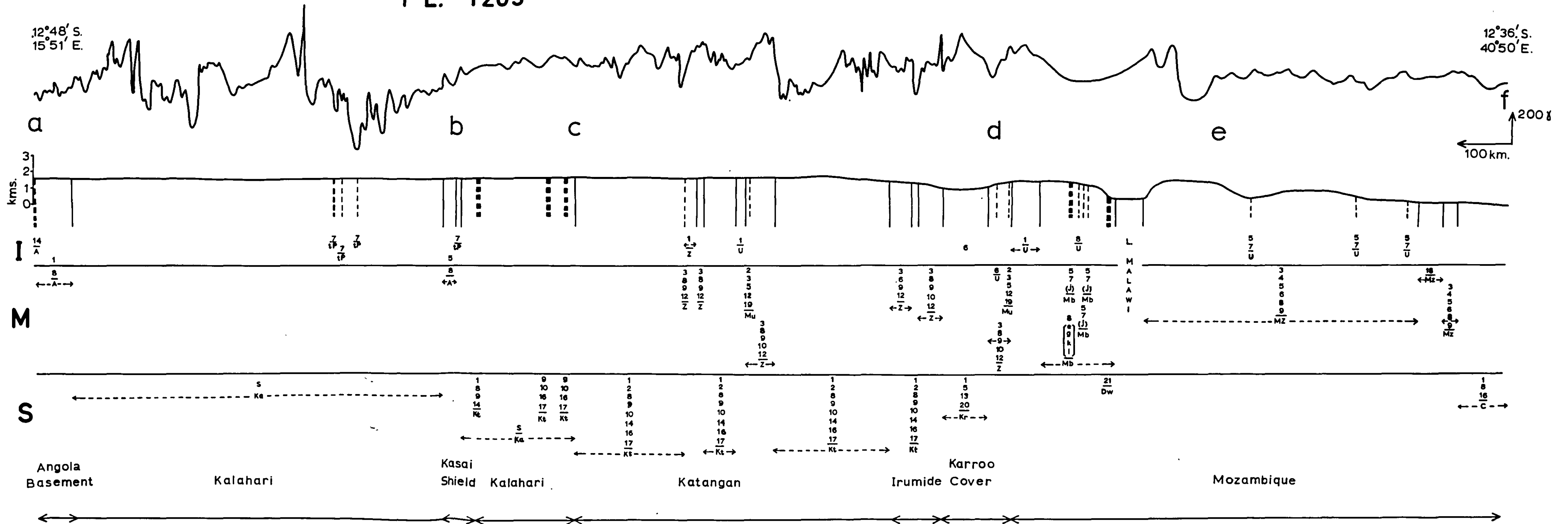
10KM

FL. T203

av. alt. 2.4 km. → 4.6 km. →

12°48' S.
15°51' E.

12°36' S.
40°50' E.



UPWARD CONTINUED CURVES
20KM.
10KM.

04° 49'S
15° 42'E

FL. T 220

av. alt. 1.7 kms. →

av. alt. 3.3 kms. → 2.4 kms. →

10° 06'S.
39° 57'E

a

b

c

d

e

f

200g
100kms

3
2
1
0

I

M

S

Congo Basin

Kasai

Bushimay Kibaran?

Kibaran

Ubendian

Karoo

Mozambique Belt

UPWARD CONTINUED CURVES

20KM.

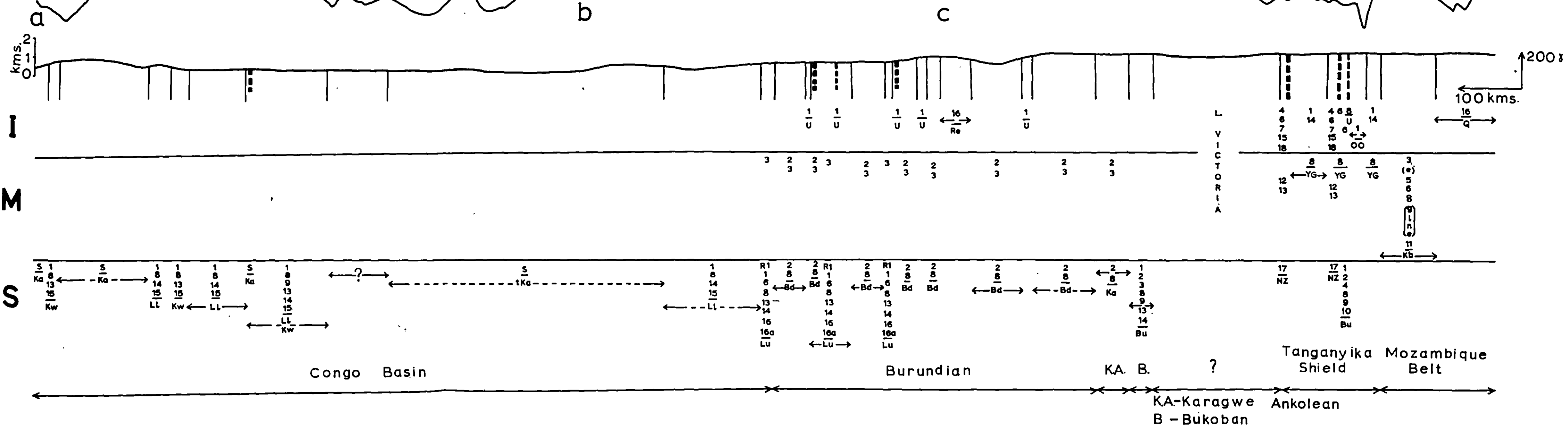
10KM.

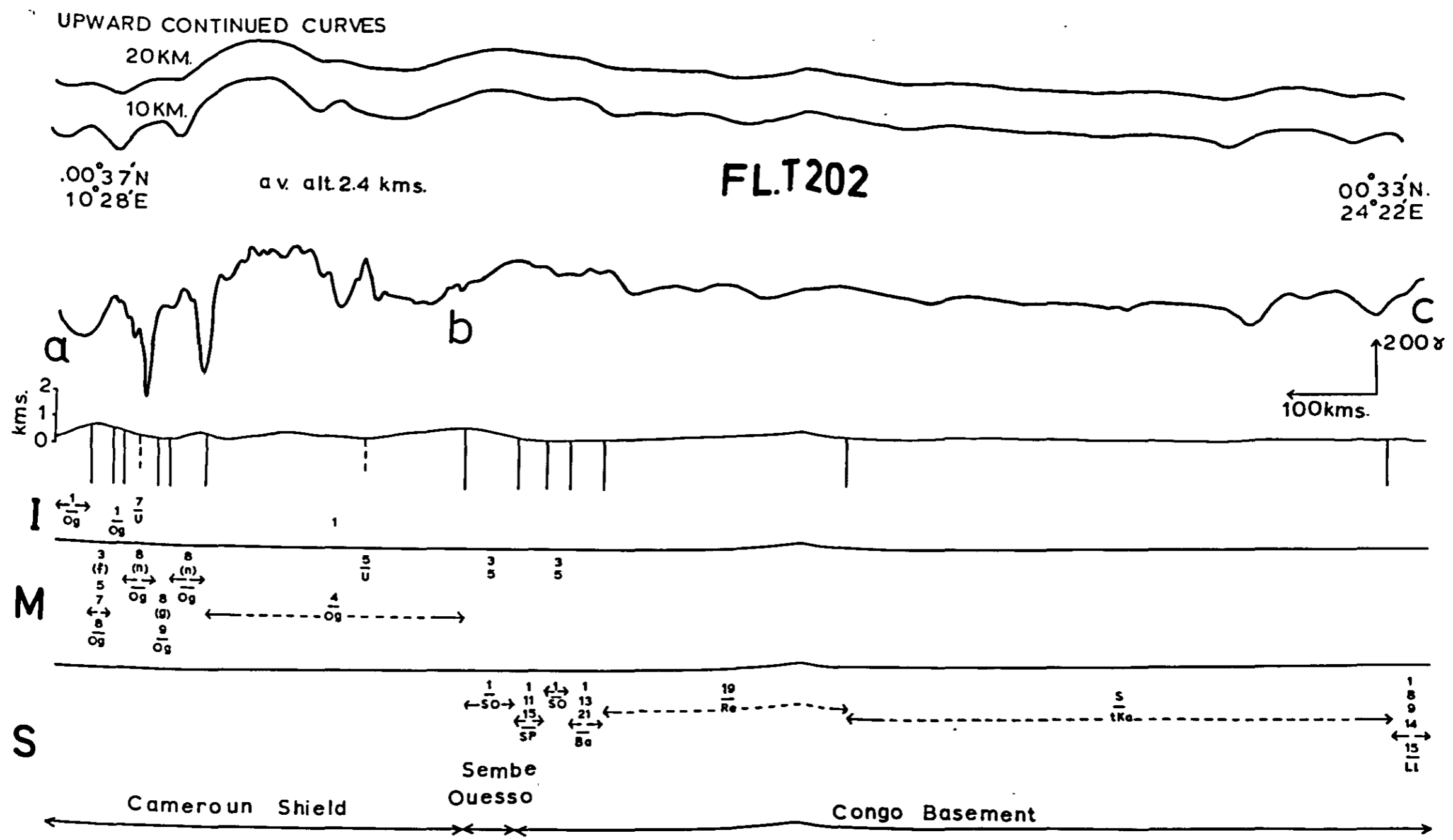
04° 31' S.
15° 23' E.

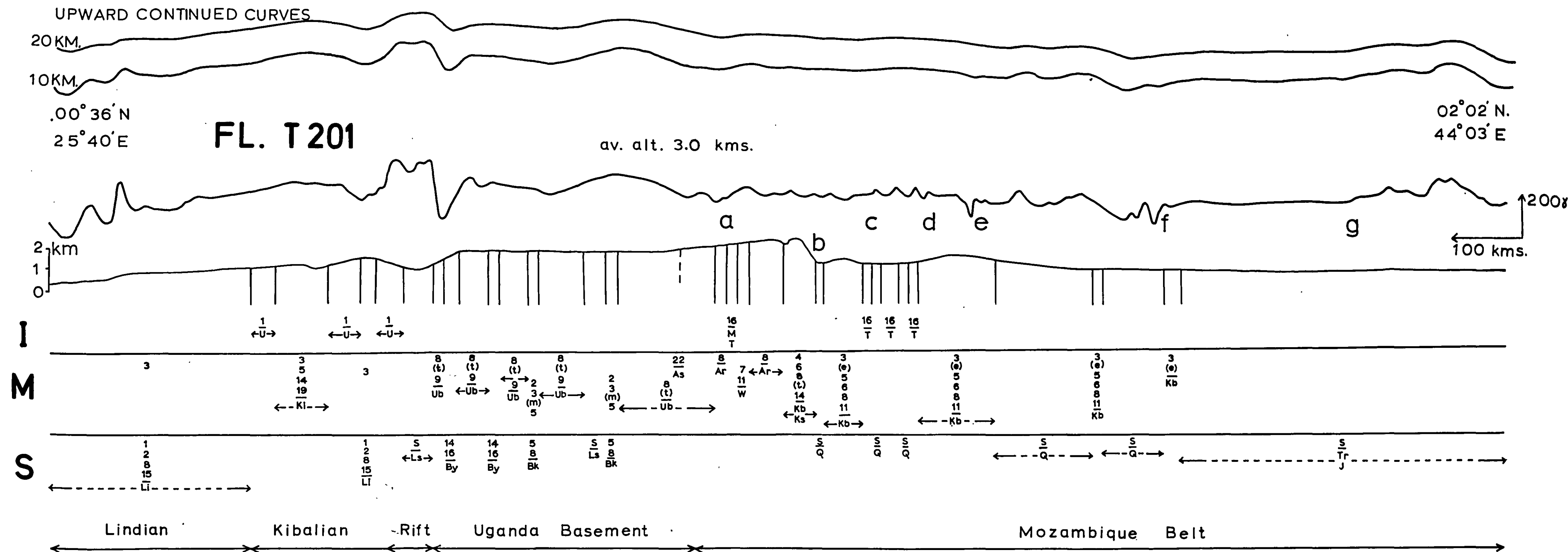
FL. T 219a

av. alt. 3.6 kms.

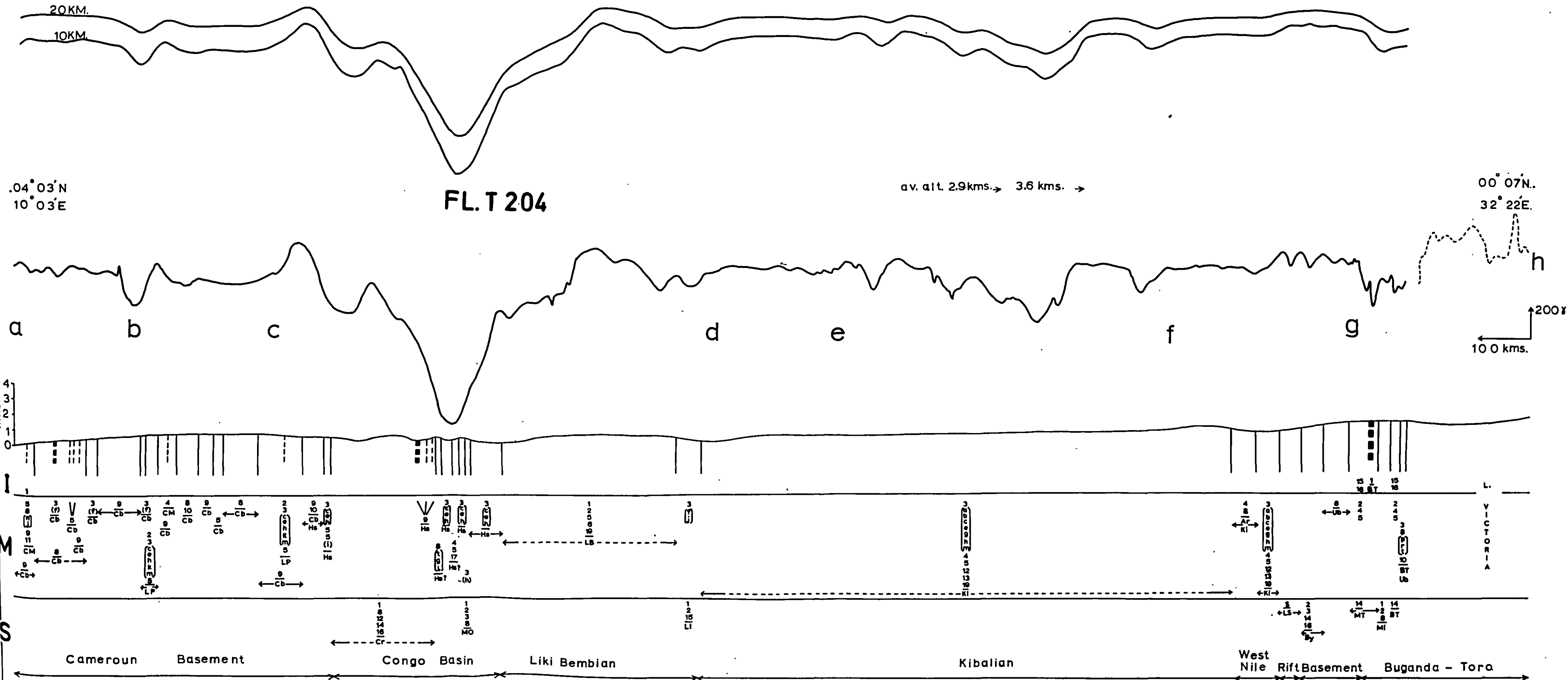
01° 23' S.
36° 41' E.

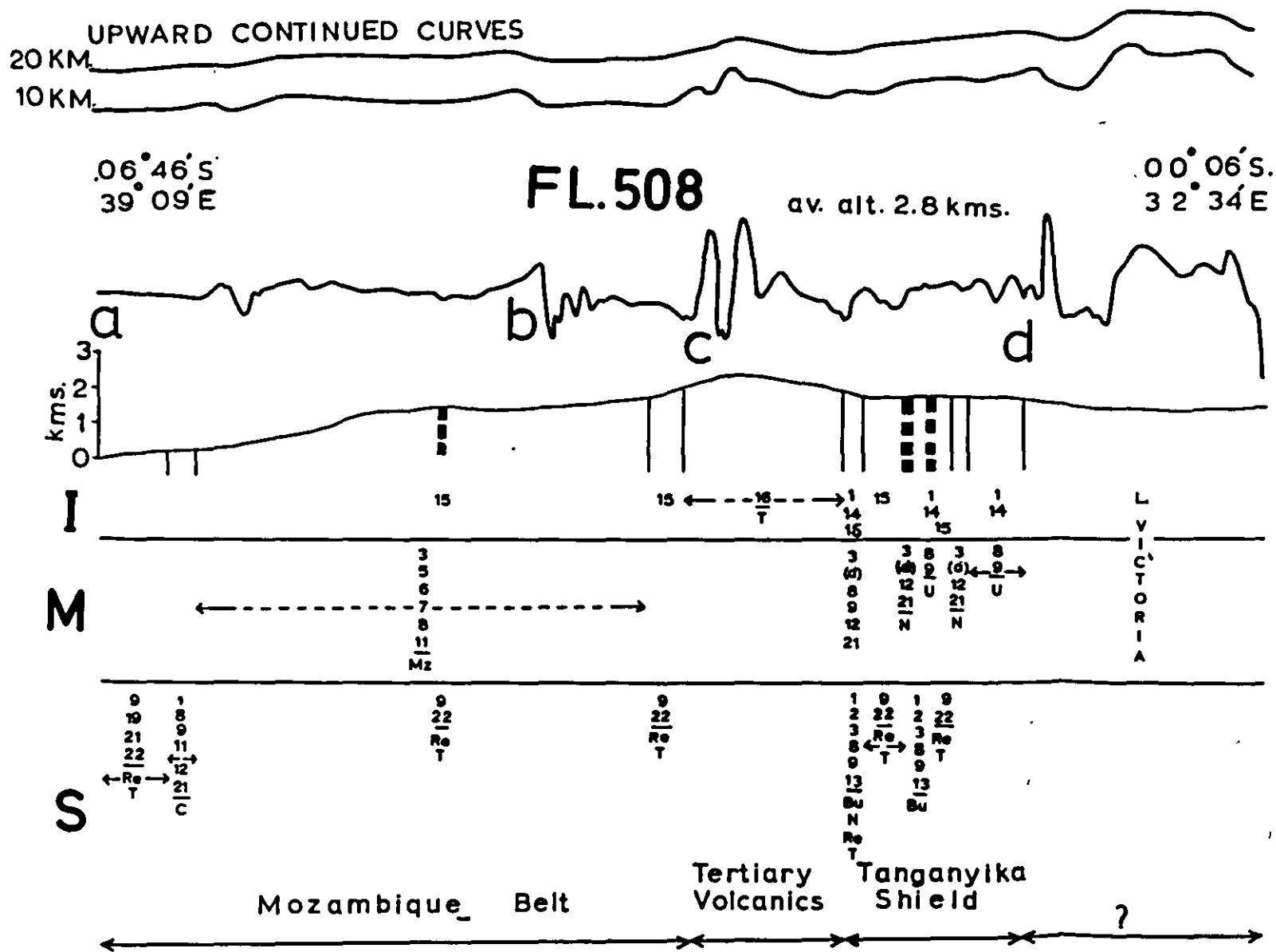






UPWARD CONTINUED CURVES





20 KM

10 KM

.07° 29' S. av. alt. 3.5kms.
40° 04' E.

FL. 511 01.28S.
36 57E

